Natural Computing Series

Koichi Suzumori
Kenjiro Fukuda
Ryuma Niiyama
Kohei Nakajima *Editors*

The Science of Soft Robots

Design, Materials and Information Processing

Springer

Natural Computing Series

Scope

The Natural Computing book series covers theory, experiment, and implementations at the intersection of computation and natural systems. This includes:

- **Computation inspired by Nature**: Paradigms, algorithms, and theories inspired by natural phenomena. Examples include cellular automata, simulated annealing, neural computation, evolutionary computation, swarm intelligence, and membrane computing.
- **Computing using Nature-inspired novel substrates**: Examples include biomolecular (DNA) computing, quantum computing, chemical computing, synthetic biology, soft robotics, and artificial life.
- **Computational analysis of Nature**: Understanding nature through a computational lens. Examples include systems biology, computational neuroscience, quantum information processing.

Koichi Suzumori · Kenjiro Fukuda ·
Ryuma Niiyama · Kohei Nakajima
Editors

The Science of Soft Robots

Design, Materials and Information Processing

Springer

Editors
Koichi Suzumori
School of Engineering
Tokyo Institute of Technology
Tokyo, Japan

Ryuma Niiyama
Graduate School of Science
and Technology
Meiji University
Kanagawa, Japan

Kenjiro Fukuda
RIKEN Thin-Film Device Laboratory
Wako, Saitama, Japan

Kohei Nakajima
Graduate School of Information Science
and Technology
The University of Tokyo
Tokyo, Japan

ISSN 1619-7127 ISSN 2627-6461 (electronic)
Natural Computing Series
ISBN 978-981-19-5173-2 ISBN 978-981-19-5174-9 (eBook)
https://doi.org/10.1007/978-981-19-5174-9

This Springer imprint is published by the registered company Springer Nature Singapore Pte Ltd.
The registered company address is: 152 Beach Road, #21-01/04 Gateway East, Singapore 189721, Singapore

Foreword

When I first started my research in soft robotics, one name recurrently appeared in my literature search on unconventional, continuum robots and flexible actuation technologies: Prof. Koichi Suzumori. Soft robotics is a rapidly growing area, producing new technologies for designing, building, actuating, and controlling soft robots at a fast pace. But Prof. Suzumori started experimenting this original direction at least two decades in advance. Today, together with his colleagues Kenjiro Fukuda, Ryuma Niiyama, and Kohei Nakajima, he is presenting his experience in soft robotics, after leading a large-scale project that gathered the best scientists, all over Japan, to explore the frontiers of soft robots.

These "vague," "imprecise" soft robots, as sometimes called in Japanese with the word "iikagen," have been revolutionizing robotics, breaking the traditional paradigm of rigid bodies operating with high accuracy, speed, and reliability. In soft robotics, "vagueness," "imprecision," or compliance are key to let adaptive behavior emerge, taking advantage of interactions with the environment and with human beings.

Remarkably, the title of the project, and the book, is "the Science of Soft Robots." In one word, "science," it clearly conveys the approach taken and the contents of soft robotics research: not just a direction for technological evolution of robotics, but a deep scientific approach to the study of living beings, to unveiling the secrets of embodied intelligence, to the development of future generation robots. The project aimed at exploring the frontiers of soft robotics, at the merge of disciplines like robotics and engineering, but also biology, physics, and material science. The book consolidates the knowledge produced in the project, and beyond, to the benefit of soft roboticists and those who wish to approach this field.

This book brings the reader along an interdisciplinary journey, outlining how much the new soft robotics approach increases knowledge (and then science) in a variety of fields and provides technologies for many industrial and service sectors. Inspiring illustrations takes the reader to the world of soft robots, of today and of tomorrow. In a timely way, the book re-states the mission and impact of the soft robotics field. It provides the basics for newcomers and systematized knowledge

for the experts. From a unique position, this book opens a window on the current progress of the Science of Soft Robots.

Cecilia Laschi
National University of Singapore
Queenstown, Singapore

Preface

Since the beginning, human beings have sought power, accuracy, and efficiency, leading to the development of Watt's steam engines, Neumann computers, industrial robots, etc. Conventional robots have been designed with rigid bodies, servomotors, and intricate programming to realize these goals, resulting in great success in various industries. However, only a few robots currently work with people in society. This is because their bodies are too hard and stiff to interact gently with their surroundings, and their motions are too accurate to handle the differences between their programming and the actual world. Furthermore, their intelligence is too intricately programmed to adapt to unexpected occurrences in the practical world. Therefore, soft robotics has become one of the most active fields over the last decade to make robots more flexible, gentle, and adaptable.

Simultaneously, new research studies that form the basis of soft robotics have been successively reported in various fields. Examples include flexible electronics in mechatronics, three-dimensional gel printing, biodegradable materials in materials science, and neural networks in computer science. Although these soft technologies have not often been used in conventional robotics aimed at power, accuracy, stability, and certainty, soft robotics has developed rapidly.

Since 2018, a MEXT project titled "Science of Soft Robots (JP18H05465)" has been in progress, wherein many researchers from various fields, such as mechanical engineering, electrical engineering, computer science, materials science, zoology, and biology, have collaborated in soft robotics. Therefore, this book was written by researchers working on the frontiers of soft robotics research.

However, this is not a report of the project results but is intended to be a standard textbook or a technical book on soft robotics. Although soft robotics is still a growing field, an attempt has been made to summarize the standard knowledge and methods found and established in this decade.

After the introduction, the book comprises three parts. Part I, *Design of Soft Robots*; Part II, *Soft Materials*; and Part III, *Autonomous Soft Robots*. Part I comprises soft and biological mechanisms, soft manipulation, and locomotion. In Part II, the basics of polymers, biological materials, flexible and stretchable sensors, and soft actuators are discussed from the viewpoint of material science. Part III contains the

modeling and control of the continuum body, material intelligence, and information processing using soft body dynamics. In addition, some of the latest research results in this project are cutting edge.

I hope this book will be valuable as a textbook or a technical book for students, engineers, and researchers interested in soft robotics.

Tokyo, Japan — Koichi Suzumori
Wako, Japan — Kenjiro Fukuda
Kanagawa, Japan — Ryuma Niiyama
Tokyo, Japan — Kohei Nakajima
July 2022

Contents

1 Introduction 1
Koichi Suzumori and Ryuma Niiyama
1.1 Science of Soft Robots 1
1.1.1 What Are Soft Robots? 1
1.1.2 Configuration of the Soft Robots 2
1.1.3 What Can You Do? 3
1.1.4 Where Do They Fit into the Bio-inspired Robotics Research? 6
1.1.5 Research and Development of Soft Robots 7
1.1.6 E-Kagen Robotics 8
1.2 History of Soft Robots 9
1.2.1 Introduction 9
1.2.2 Seeds of Soft Robotics (1960–) 9
1.2.3 Bioinspiration (1970–) 10
1.2.4 Soft Actuation (1980–) 11
1.2.5 Control of Deformation (1990–) 12
1.2.6 Emergence of Soft Robotics (2000–) 13
1.2.7 Soft Robotics in Growth (2010–) 14
1.2.8 Future of Soft Robots (2020–) 14
References 15

Part I Design of Soft Robots

2 Soft Mechanisms 21
Kenjiro Tadakuma and Hiromi Mochiyama
2.1 Deformable Mechanisms 21
2.1.1 Basic Concepts 21
2.1.2 Basic Function 22
2.1.3 Process of Deformation 22
2.1.4 Soft/Rigid Switching 26
2.1.5 Examples 29

2.2 Typical Soft Mechanisms 31
2.2.1 Continuum, Elastic, and Bistable 31
2.2.2 Examples of Continuum-Elastic Mechanism 33
2.2.3 Example of Continuum-Bistable Mechanisms 34
2.2.4 Exercises 36
References 36

3 Biological Mechanisms 39
Takeshi Yamasaki, Megu Gunji, Yoichi Masuda, and Akira Fukuhara
3.1 Robotics-Inspired Biology 39
3.1.1 Basic Concepts 39
3.1.2 How Do Traditional Biologists Test Their Hypotheses? 41
3.1.3 Experiments with Robots 43
3.1.4 Why Use Robots Rather Than Computer Simulations? 45
3.1.5 Robotics-Inspired Biology: Where to Begin 46
3.1.6 Challenges 46
3.2 Musculoskeletal System 47
3.2.1 Basic Concepts 47
3.2.2 Musculoskeletal Robot 48
3.2.3 Basic Knowledge of Major Musculoskeletal Component 49
3.2.4 Key Anatomical Mechanism 52
3.2.5 How to Start Anatomical Research 54
3.2.6 Challenges 55
References 56

4 Soft Manipulation and Locomotion 59
Shinichi Hirai, Ryuma Niiyama, Taro Nakamura, Takuya Umedachi, Toshiyuki Nakata, and Hiroto Tanaka
4.1 Soft Robot Hands 60
4.1.1 Basic Concept 60
4.1.2 Suction Hands 61
4.1.3 Jamming Hands 62
4.1.4 Bending Fingers Hands 62
4.1.5 Soft Cover Hands 63
4.1.6 Expanding Fingers Hands 64
4.1.7 Hands-on and Challenges 64
4.2 Continuum Arm 65
4.2.1 Introduction 65
4.2.2 Hyper-Redundant Manipulators and Flexible-Link Manipulators 66
4.2.3 Continuum Arms in Living Organisms 67
4.2.4 Typical Structures and Actuation Systems 69

4.2.5 Posture Control ... 69
4.2.6 Features ... 71
4.2.7 Summary ... 71
4.3 Peristaltic Locomotion ... 72
4.3.1 Movement by Peristalsis Motion ... 72
4.3.2 Why Peristaltic Movement?—Principle of Peristaltic Locomotion ... 72
4.3.3 Peristaltic Crawling of Snails and Caterpillars ... 75
4.3.4 Peristaltic Crawling of Earthworm ... 79
4.4 Aerial Flight with Soft Components ... 84
4.4.1 Basic Concepts ... 84
4.4.2 Fluid Mechanics of Flight ... 85
4.4.3 Basic Design of a Soft Aerial Robot ... 87
4.4.4 Flapping Mechanism for Soft Aerial Robots ... 89
4.4.5 Attitude Control of Soft Aerial Robots ... 90
4.4.6 Soft Components for Conventional Drone ... 91
4.4.7 How to Initiate Soft Aerial Robot Research ... 91
4.4.8 Challenges ... 91
4.5 Aquatic Swimming with Soft Fins and Body ... 92
4.5.1 Basic Concepts ... 92
4.5.2 Physical Property of Water ... 92
4.5.3 Conventional Screw Propulsion of Ships ... 93
4.5.4 Propulsion Mechanism in Animals ... 94
4.5.5 How to Start the Soft Fins Research ... 99
4.5.6 Challenges ... 100
References ... 102

5 Nemertea-Inspired Soft Robotic Mechanism ... 107
Kenjiro Tadakuma
References ... 109

6 Life-Machine Fusion Devices ... 111
Yo Tanaka
6.1 Electric Ray Generator ... 113
6.2 Plant-Based Soft Robots ... 114
References ... 116

Part II Soft Materials

7 Basics of Polymer ... 119
Hiroki Uehara, Masaki Kakiage, Tatsuhiro Horii, Toshinori Fujie, Hidemitsu Furukawa, Masaru Kawakami, and Masahito Takakuwa
7.1 Morphology and Physical Property of Polymers ... 119
7.1.1 Macromolecular Characteristics ... 120
7.1.2 Crystalline Structure ... 121
7.1.3 Amorphous Structure ... 124

7.1.4 Molecular Orientation . . . 126
7.1.5 Mechanical Properties . . . 128
7.1.6 How to Start Polymer Property Research . . . 129
7.1.7 Challenges . . . 130
7.2 Structure and Classification of Polymers and Functional Polymers . . . 130
7.2.1 Classifications . . . 130
7.2.2 Chemical Structures . . . 130
7.2.3 Functional Polymers . . . 135
7.2.4 Electro-active Polymers . . . 138
7.2.5 Challenges . . . 143
7.3 Soft Materials (Elastomer, Hydrogels, etc.) . . . 145
7.3.1 Basic Concept of Soft Materials . . . 145
7.3.2 Structure of Polymeric Soft Materials (De Gennes and De Gennes 1979) . . . 145
7.3.3 Functional Gels . . . 152
7.3.4 How to Gain Knowledge on Soft Materials . . . 157
7.3.5 Challenges for Soft Materials . . . 157
7.4 Fabrication of Soft Robot Parts Using Three-Dimensional Printers . . . 157
7.4.1 Designing 3D Models . . . 158
7.4.2 Bonding . . . 162
7.4.3 Conclusion . . . 163
References . . . 166

8 Biological Material . . . 171
Masahiro Shimizu, Yuya Morimoto, and Jun Shintake
8.1 Soft Materials Affected by Biological Processes . . . 171
8.1.1 Introduction . . . 171
8.1.2 Biohybrid Robots Attracting International Attention . . . 172
8.1.3 Mechanical Stimulation as an Interface Between Cells and Control . . . 173
8.1.4 Toward a Growing Biosoft Robot . . . 173
8.1.5 Conclusion . . . 175
8.2 Biological Cells . . . 175
8.2.1 Basic Concepts . . . 175
8.2.2 Actuation of Biological Cells for Soft Robotics . . . 176
8.2.3 Sensing of Biological Cells for Soft Robotics . . . 180
8.2.4 How to Start Using Biological Cells . . . 182
8.2.5 Challenges . . . 183
8.3 Biodegradable Soft Material . . . 183
8.3.1 Approach to Incorporating Biodegradability . . . 184
8.3.2 Materials . . . 186
8.3.3 Biodegradable Soft Robotic Devices . . . 190

8.3.4 Future Outlook ... 192
References ... 193

9 Flexible and Stretchable Electronics and Photonics ... 197
Kenjiro Fukuda and Kuniharu Takei
9.1 Principles and Strategies ... 197
9.1.1 Strain Applied to the Device ... 198
9.1.2 Improvement in Mechanical Robustness ... 199
9.1.3 Flexural Rigidity ... 200
9.1.4 Stretchability ... 200
9.2 Flexible Sensors ... 201
9.2.1 Tactile Pressure Sensor ... 202
9.2.2 Temperature Sensor (Thermistor) ... 208
9.2.3 Summary ... 209
9.3 Flexible and Stretchable Electronics and Photonics ... 210
9.3.1 Stretchable Wires ... 210
9.3.2 Photovoltaics ... 211
9.3.3 Photodiodes ... 214
9.3.4 Thin-Film Transistors and Circuits ... 215
References ... 216

10 Soft Actuators ... 219
Shingo Maeda, Yuhei Yamada, Hiroyuki Nabae, Kenjiro Tadakuma, Koichi Suzumori, Zebing Mao, Jun Shintake, Hideyuki Sawada, Yuya Morimoto, and Masahiro Shimizu
10.1 Overview ... 220
10.1.1 Introduction ... 220
10.1.2 Mathematical Framework ... 220
10.1.3 Energy and Work ... 221
10.1.4 "Softness" of the Actuator ... 222
10.1.5 Types and Classification of Actuators ... 225
10.1.6 Challenges ... 225
10.2 Fluidic Actuators ... 227
10.2.1 Introduction ... 227
10.2.2 Fundamentals, Design, and Modeling ... 229
10.2.3 Fabrication Techniques ... 231
10.2.4 Fluidic Pressure Sources ... 232
10.2.5 Challenges ... 237
10.3 Electroactive Polymer Actuators ... 238
10.3.1 DEAs ... 238
10.3.2 IPMCs ... 244
10.3.3 Future Outlook ... 249
10.4 Thermomechanical Actuators ... 249
10.4.1 Shape-Memory Alloy Actuators ... 249
10.4.2 Physical Properties of SMAs ... 250
10.4.3 Filiform SMAs for Micro-vibration Actuators ... 251

10.4.4 Application to Tactile Displays 253
10.4.5 Application to Fish Robots Having Flexible Bodies 254
10.4.6 Challenges 255
10.5 Bioactuators 256
10.5.1 Biohybrid Frog-Like Robot 256
10.5.2 Biohybrid Robot Actuated by Skeletal Muscle Tissues 258
10.5.3 How to Start 262
10.5.4 Challenges 262
References 263

11 Tissue-Interfaced Electronics 269
Toshinori Fujie and Hajime Fujita
References 271

12 Paper Mechatronics 273
Hiroki Shigemune
References 275

Part III Autonomous Soft Robots

13 Modeling and Control of Continuum Body 279
Shinichi Hirai, Hiromi Mochiyama, Kohei Nakajima, and Nozomi Akashi
13.1 The Physics of Soft Bodies 280
13.1.1 A Basic Concept: The Dimension of Soft Body Models 280
13.1.2 Describing Motion and Deformation 281
13.1.3 Computing Static Deformations 284
13.1.4 Computing Dynamic Deformations 286
13.1.5 Practicalities and Challenges 288
13.2 Rod Theory 289
13.2.1 Kinematics 289
13.2.2 Statics 292
13.2.3 Discretization 293
13.2.4 Rod Integration 297
13.2.5 Computation of Deformation 298
13.3 Nonlinear Dynamics in a Simple Mechanical System 300
13.3.1 Passive Dynamic Walker as Example 300
13.3.2 Attractors and Bifurcations 303
13.3.3 Basin of Attraction and Riddled Basins 306
13.4 Controlling Soft Robots 309
13.4.1 Concept 309
13.4.2 Simultaneous Positioning of Soft Body 309
13.4.3 Orientation Control Through Soft Fingertips 312
13.4.4 Challenges and Perspectives 317
References 317

14 Material Intelligence 319
Yuhei Yamada, Shingo Maeda, Kazuya Furusawa, Masahiro Shimizu, Hiroshi Ito, and Takuma Sugi
14.1 Chemical Information Processing 320
14.1.1 What Is Chemical Information Processing? 320
14.1.2 Active Gels 321
14.1.3 Belousov–Zhabotinsky Reaction 322
14.1.4 Belousov–Zhabotinsky Gels 324
14.1.5 Mathematical Model for Belousov–Zhabotinsky Gels 326
14.1.6 Deformation of Belousov–Zhabotinsky Gels 329
14.1.7 Peristaltic Motion of Belousov–Zhabotinsky Gels 330
14.1.8 Mathematical Model for the Peristaltic Motion of Belousov–Zhabotinsky Gels 331
14.1.9 Challenges 332
14.2 Biological Information Processing 333
14.2.1 Technology for Autonomous Soft Robots that Process Information Using Biomaterials 333
14.2.2 Information Processing Between Biomaterials 333
14.2.3 Living Regulators 334
14.2.4 How to Assemble Robots with Living Regulators 335
14.2.5 Information Transmission Pathways Between Biomaterials 337
14.2.6 Challenges: Programming Robots with Living Regulators 338
14.3 Temporal and Spatial Information Processing 339
14.3.1 Rhythms and Patterns: The Simplest, but Complex Behaviors in Biology 339
14.3.2 Genetic Oscillator 340
14.3.3 Protein Oscillator 343
14.3.4 Synchronization of the Biological Rhythms 345
14.3.5 Biological Pattern Formation by Reaction–Diffusion Systems 347
14.3.6 Biological Pattern Formations by Active Matters 348
14.3.7 Introductory Books and Articles on Biological Rhythms and Patterns 350
14.3.8 Conclusions and Challenges for Artificial Biological Rhythms and Patterns 350
References 352

15 Information Processing Using Soft Body Dynamics 357
Kohei Nakajima, Hideyuki Sawada, and Nozomi Akashi
15.1 Outsourcing Control to a Soft Body: Embodiment Perspectives 357
15.1.1 The Universal Gripper 357

15.1.2 Intelligent Systems as Brain–Body–Environment Systems 359
15.1.3 Evolutionary Robotics: Design Principle of Brain–Body–Environment Systems 362
15.2 Machine Learning for Soft Robots 365
15.2.1 Basic Concepts 365
15.2.2 Self-organizing Map 366
15.2.3 Data Classification Using Soft Tactile Sensors 367
15.2.4 Autonomous Learning the Speaking Skill of a Talking Robot 369
15.2.5 Challenges 370
15.3 Information-Processing Capabilities of Soft Bodies 371
15.3.1 Reservoir Computing: Utilizing Dynamics for Information Processing 371
15.3.2 Reservoir Dynamics and Its Information-Processing Capacity 375
15.3.3 Physical Reservoir Computing in Soft Robots 379
References 387

16 Toward Understanding and Manipulation of Collective Behaviors Using Nematode *Caenorhabditis elegans* 393
Takuma Sugi and Hiroshi Ito
References 396

17 Peristaltic Mixing Pump Based on Intestinal Peristalsis Motion Using Soft Actuators 397
Taro Nakamura
17.1 Basic Concepts 397
17.2 Topic and Principle: Intestinal Anatomy and Peristaltic Motion Patterns 398
17.2.1 Structure of the Intestinal Tract 398
17.2.2 Generation of the Peristaltic Motion 398
17.3 Topic and Principle: Focusing on Mechanisms for Peristaltic Motion 399
17.4 Topic and Principle: Focusing on the Sensor and Control System for Peristaltic Motion 400
References 400

Index 403

Chapter 1
Introduction

Koichi Suzumori and Ryuma Niiyama

1.1 Science of Soft Robots

1.1.1 What Are Soft Robots?

Previously, developments in robotics research focused on two main motivations. The first one is pursuing the value of robots as automated machines to perform tasks efficiently, mainly for industrial applications. The second one is the desire, stemming from intellectual curiosity, to create an artificial being that can move and behave the same as humans or animals. The latter has also led to creating care or welfare robots that support people daily.

Industrial robots have mainly been developed based on the first motivation; hence, their main goals are power, accuracy, reliability, and efficiency. Robots usually have rigid bodies made from hard materials, precise and powerful servomotors, and minutely coded control programs to achieve the abovementioned goals. Thus, these robots have produced significant results in industrial applications.

Meanwhile, considering the second motivation, robotics faces the difficulty that robots still struggle with everyday behaviors that living creatures perform easily. For example, gently cradling a baby is easy for a human but is significantly difficult for existing robots for the following reasons. First, it is difficult for a robot to gently touch a baby's body using its arms and torso and hold it with the appropriate amount of grip force. Second, robots usually have hard and cold skin, which is unpleasant for a baby. Third, babies may move in unexpected ways; if a baby suddenly starts

K. Suzumori (✉)
School of Engineering, Tokyo Institute of Technology, Tokyo, Japan
e-mail: suzumori.k.aa@m.titech.ac.jp

R. Niiyama
Graduate School of Science and Technology, Meiji University, Kanagawa, Japan
e-mail: niiyama@meiji.ac.jp

K. Suzumori et al. (eds.), *The Science of Soft Robots*, Natural Computing Series,
https://doi.org/10.1007/978-981-19-5174-9_1

crying and tries to wriggle out of the robot's arms, the existing robot would be unable to respond appropriately and might forcibly hold the baby to stop it from escaping.

Conventional industrial robots demonstrate excellent performance in environments for which they are designed but are not sufficiently adaptable to work in unknown or changing environments where unexpected situations can arise. In the future, robots will be required to respond flexibly to unpredictable environments and possess characteristics such as precise positioning and high output.

This is where soft robots are introduced. The concept of "soft" includes not only a soft body in a physical sense but also soft movement and the ability to respond flexibly to any situation.

Soft robots can be defined in various ways (RSJ 2023; Laschi 2016; Kim 2013), but researchers have not yet agreed on a clear definition. Moreover, the definition of "robot" itself is still vague, although robotics has been around for over half a century. Considering how the potential of robots has expanded, it is perhaps better to have multiple definitions of soft robots.

To date, most discussions on the definition of soft robots agree on the following points. (1) They have soft bodies composed of soft materials. (2) They have continuous or high degrees of freedom. (3) These physical characteristics are utilized to move and adapt to the environment in ways that are difficult for conventional robots. (4) The science of soft robots or soft robotics is generally considered a new academic field within robotics. It is widely agreed to be an interdisciplinary field that includes materials science and biology.

Therefore, this book defines soft robots as "robots with soft and flexible bodies, which utilize these physical characteristics to adapt to the environment or objects."

The following sections examine soft robots from five perspectives: (1) How does their configuration differ from conventional robots? (2) What tasks can soft robots perform that conventional robots cannot? (3) Where do they fit into research on robots imitating living things? (4) How should they be researched and developed? (5) What is their significance in science and technology?

1.1.2 Configuration of the Soft Robots

Figure 1.1 illustrates the differences between conventional and soft robots based on their configuration.

First, there are differences in the degrees of freedom; conventional robots are systems made of a finite number of joints and rigid links, whereas many soft robots have continuous configurations, where any part can change its shape. In addition, "hyper-redundant" robots, which have a significantly large number of degrees of freedom (Fig. 1.1, middle), are often treated as soft robots.

Using the term "freedom of movement" to refer to the degrees of freedom in the postures that a robot can take and "operational freedom" to refer to the number of operations it can perform, the basic assumption in conventional robotics has been that "freedom of movement = operational freedom." Following this idea, the robot's

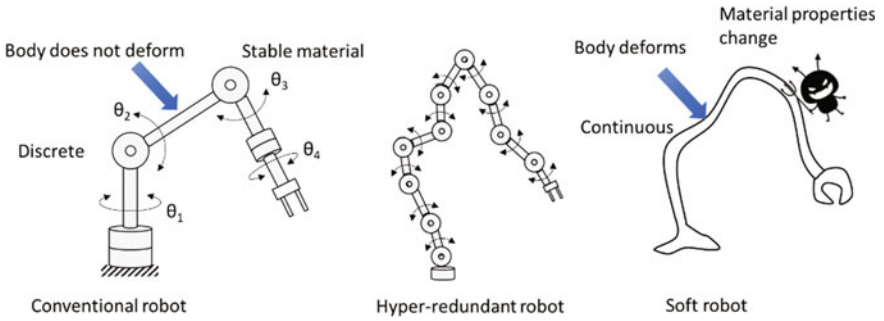

Fig. 1.1 Configuration of conventional/hyper-redundant/soft robots

movements are determined by the computer that controls it; that is, the computer needs to command every movement of every joint, which sometimes results in excessive computer load for robots with high operational freedom or in complex environments.

In contrast, soft robots are generally designed as strongly underactuated drive systems, assuming "operational freedom ≪ freedom of movement." They are typically driven with far fewer operations than degrees of freedom. The movement of a soft robot is passively determined by factors other than the number of operations, such as geometrical or mechanical interference with its surroundings, making it adaptable and flexible.

Second, conventional robots are made of strong and stable materials that do not deform or transform, whereas soft robots are made of deformable materials or materials with alterable properties. For example, suppose a soft robot is made of rubber. In that case, its characteristics will vary depending on the temperature, and its body will deteriorate if exposed to UV rays for a long time.

Conventional robotics has been built on the assumption that the physical characteristics of a robot do not change; however, in soft robotics, the shape, dimensions, and mass distribution of the robot's body change when external forces are applied. In addition, soft robots may be deliberately fabricated using materials with properties that change over time or are affected by temperature. For example, chemically unstable materials such as biodegradable materials and biological tissues have recently been used in soft robotics to enable robots to change their characteristics to suit the environment, return to the natural environment after disposal, or provide self-repair functions.

1.1.3 What Can You Do?

Figure 1.2 shows two illustrations of soft robots from the MEXT Grant-in-Aid for Scientific Research New Academic Area "Soft Robotics" (2018–2022FY) (Suzumori

Fig. 1.2 Future soft robots from the MEXT Grant-in-Aid for Scientific Research on Innovation Area "Science of Soft Robot"

2022): a robot gently cradling a baby and a soft robot car grabbing a child who has run into the road. These examples demonstrate various expectations for soft robots. Therefore, they were divided into three basic functions (shape adaptation, motion control, and information processing), and each is explained in turn (Fig. 1.3).

(a) Shape adaptation

As shown in the two diagrams in Fig. 1.3a, one of the most typical features of a soft robot is that its body can passively adopt an appropriate posture to imitate the shape of the object it handles or the environment around it. This distributes the contact stress between the robot and whatever it is touching, significantly reducing the risk of damage to the robot itself or the other object.

In a gripping task (Fig. 1.3a, left), the body changes shape according to the shape of the gripped object and thus easily achieves a stable hold. This means the robot can grip or handle fragile objects with three-dimensional curved surfaces (such as glass products) or objects of varying shapes, sizes, and softness (such as fruits) without damaging them.

When entering a confined space (Fig. 1.3a, right), the soft robot easily passes through the space by changing its shape passively as it touches its surroundings. In contrast to the control method of a conventional robot (sensing the surroundings, designing a corresponding approach path by computation, and then moving each joint), the soft robot itself works out the path and posture to take.

(b) Motion control

Another typical function of soft robots is to absorb impact energy and achieve dynamic movement. As shown on the left in Fig. 1.3b, a soft robot uses the elasticity of its body to absorb impact energy and thus protects itself and the object. As shown on the right in Fig. 1.3b, the robot can perform a dynamic jumping motion by instantaneously releasing the elastic energy stored in its legs and body.

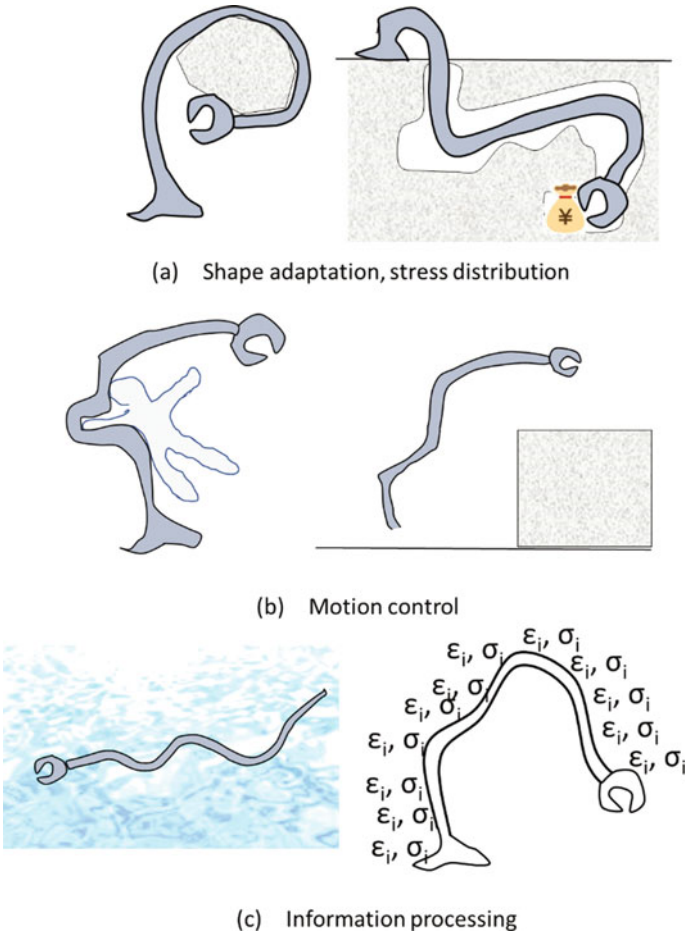

Fig. 1.3 Examples of what soft robots can do (Adapted from RSJ 2023)

When animals run at high speeds, their legs repeatedly hit the ground and perform kicking motions. The elasticity of an animal's body acts as a buffer, temporarily storing mechanical energy to absorb and release energy efficiently. Robots with soft bodies are expected to perform dynamic running motions.

(c) Information processing

The body of a soft robot is expected to process information in two ways.

The first is the ability to generate motion patterns from the interference between the environment and the robot. For example, a soft robot swimming in water (Fig. 1.3c, left) will naturally generate motion patterns suitable for swimming because of mechanical interference with the surrounding water. This is a completely different approach from the control method of conventional robots, in which the body moves

based on the movement patterns devised by the robot's control program designer. A major area of research in soft robotics is identifying the conditions and mechanisms by which appropriate motion patterns are generated.

When multiple robots work together and come into contact, conventional robots with hard bodies often collide, damage each other, and cannot work together. However, soft robots can work closely and come into contact with each other's bodies without complex control. This can also be interpreted as a soft robot's ability to work out how to move its own body to work with other robots using mechanical interference between them.

The second is that the body of a soft robot is a tool for information processing. In conventional robots, variables corresponding to the number of joints (movement and moment of each joint) behave dynamically as the robot moves, but soft robots have a significantly large number of such variables. Nevertheless, by treating the body of a soft robot as an information source comprising many interacting variables (i.e., the strain ε and stress σ of each part of the soft robot's body) and applying physical reservoir computing, it should be possible to achieve excellent information processing ability and construct a highly adaptable robot control system.

(d) Other major possibilities

What soft robots can perform from shape adaptation, motion control, and information processing perspectives have been summarized. There are many other possible explanations for this.

Other essential features of soft robots include that they are lighter than conventional metal robots and can operate in special environments (strong magnetic fields, underwater, etc.). In addition, collision damage is reduced in the event of an abnormal operation, owing to its characteristic light weight.

In the future, soft robots are expected to exhibit self-repair and self-modification functions. This is discussed in Sect. 1.3.

1.1.4 Where Do They Fit into the Bio-inspired Robotics Research?

Soft robots aim for features more common in living creatures than artificial objects, such as supple bodies, movement, intelligence, self-repair, and physical transformation. It can be said that living creatures are the ultimate vision of soft robots.

Figure 1.4 shows how soft robots fit in the study, from conventional to bio-inspired robots.

Suppose a conventional robot is compared to a living creature. In that case, words like "unchanging" and "stable" will characterize the robot, while words like "changing" and "adapting" characterize the living creature. For example, conventional robots have rigid metal bodies, high-power servomotors, and precise programs to

	Conventional robot	Soft robot (soft robot in a narrow sense)	Bio robot (soft robot in a broader sense)	Living creature
	Unchanging/stable	←	→	Changing/adapting
Configuration	Rigid metal structure Servo motor Precise programs	Elastomers, polymers, gels, biodegradable materials Elasstic, continuous body	Living cells, biological tissue	Cells, genes
Features	Force, speed, accuracy, efficiency, reliability	Passive adaptability/ adaptation	Adaptability/adaptation by self-repair and self-modification	Self-repair, self-modification, propagation, mutation, evolution

Fig. 1.4 Soft robots between conventional tobots and living creatures

achieve power, speed, accuracy, efficiency, and reliability. In contrast, living organisms are made of materials that can morph or change in response to their surroundings. They employ this feature to achieve functions such as self-repair, self-modification, propagation, mutation, and evolution. The contrast between "unchanging/stable" and "changing/adapting" also applies to information processing.

For example, the timing of a conventional robot is controlled by a crystal oscillator, which makes it stable and not easily affected by its surroundings. In contrast, a living creature has a biological clock that is unstable and easily affected by its surroundings, but this gives it adaptability to its environment (e.g., when traveling overseas, people recover from jet lag after a few days).

Soft robots and bio-robots fall between conventional robots, which are unstable and stable, and living organisms, which change and adapt.

In a narrow sense, soft robots are made of artificial materials such as rubber and other elastomers, polymers, gels, and biodegradable materials. Furthermore, they demonstrate passive adaptability to their surroundings, as described above. In contrast, bio-robots are made from materials, such as living cells and biological tissues, and they adapt by self-repair and self-modification.

There are various perspectives on whether the concept of soft robots includes bio-robots. Generally, research on soft robots proactively incorporates findings about bio-robots, and bio-robots are sometimes considered soft robots in a broader sense.

1.1.5 Research and Development of Soft Robots

One factor behind the surge in research into soft robots is the string of new research results concerning "softness" in various fields since the beginning of the twenty-first century. Examples include flexible electronics and care/welfare robots in mechatronics, 3D printing of gels and bio-derived materials in materials science, and artificial intelligence and neural computing in information processing.

Biology and zoology have also had major effects on soft robotics research. Living creatures provide treasure troves of valuable ideas and hints for designing soft robots. In addition, extensive research has been conducted on soft robots inspired by the soft configuration and information processing of living things, such as the elephant trunk, octopus, and human intestines. There has also been much research on soft robots made from biological cells or materials derived from living organisms.

An important point in the progress of research and development in soft robotics is that it brings various disciplines together. Previously, robotics developed as an area of engineering, focusing on mechanical engineering, electrical engineering, and information engineering. In addition, soft robotics incorporates new research results and findings in other fields, such as materials science, biology, and zoology.

Soft robots break down the boundaries of physical structure, movement, and intelligence. Conventional robots are made by dividing the work, with mechanical engineering in charge of the robot's body, electrical engineering in charge of movement, and information engineering in charge of intelligence. In contrast, in a soft robot, the boundaries disappear such that the soft skin might make up the body, move by itself, and perform sensing or information processing. This makes interdisciplinary research even more important for soft robotics.

1.1.6 E-Kagen Robotics

Earlier, science and technology have mainly focused on pursuing power, precision, and efficiency to protect ourselves from natural threats, invaders, and hunger and to build a successful society. Conventional robotics developed as part of this pursuit.

However, now that society is prosperous owing to the agricultural, industrial, and information revolutions, the goals of science and technology are shifting from "development/power" to "sustainability/adaptability." Soft robotics is a new academic field in robotics that has emerged in response to this shift.

Conventional robotics was built to solve or eliminate ambiguity and vagueness. By contrast, soft robotics aims at adapting to unpredictable environments by allowing and leveraging the properties of ambiguity and vagueness.

From this perspective, soft robots are sometimes explained using the Japanese word "iikagen or E-kagen," which means "vague," "imprecise," or "irresponsible" (Suzumori 2017). This is one of the keywords indicating the direction of research in the MEXT Grant-in-Aid for Scientific Research New Academic Area "Soft Robotics" (Suzumori 2022). For example, a robot's arm that bends when an external force is applied would be described negatively as "irresponsible" in conventional robotics. In contrast, in soft robotics, it is interpreted as a robot working well by changing its shape in response to its environment or the object it is handling.

However, "iikagen or E-kagen" in soft robotics does not mean vaguely thinking about things. In contrast, it implies incorporating the concepts of ambiguity and vagueness into robotics, handling them logically, and aiming for a new area of robotics suitable for our post-development society.

1.2 History of Soft Robots

1.2.1 Introduction

The word "robot" was first used by Karel Čapek in his 1920 play "R.U.R." to refer to an artificial worker without emotions. Although less conspicuous than this famous word origin, the description of how the original robot was manufactured is fascinating. Rossum's universal robot, as described in the play, is a bio-robot assembled from artificial bones, blood vessels, the nervous system, and internal organs, made from a dough-like artificial protoplasm. Specifically, the concept of a robot originates from synthetic biology, not mechanical or electronic engineering. Hence, softness is inherent to the concept of a robot.

With the development of electronics, computers have enabled the implementation of robots as programmable mechanical devices. Academic robotics research dates back to the servocontrol of a remote-controlled manipulator for handling radioactive materials in the 1950s. Devol developed Unimate, a programmed article transfer device for factory automation, which is the origin of industrial robots. Previously, there had been elaborate mechanical dolls operated by cams and mobile robots, such as "Walter's Tortoise," were operated by analog electric circuits. However, their control units are fixed and less integrated, making it difficult to implement intelligent behaviors in humans and other animals.

The first signs of soft robotics can be observed even during the dawn of robotic research. Let us trace the history of robotics research and discuss the role of softness and flexibility.

1.2.2 Seeds of Soft Robotics (1960–)

Robotics research began worldwide in the 1960s, when researchers in control engineering and computer science recognized robotic manipulators and mobile robots as research subjects. The control of manipulators called artificial arms, and artificial intelligence were established as research fields. This was followed by research into the development of artificial hands and legs. The emerging technologies during this period allowed engineering and replicating of human abilities. In 1960, the terms "cyborg" and "bionics" were introduced. Computer-controlled mechanical hands MH-1 were developed at the Massachusetts Institute of Technology (MIT) (Ernst 1961). The hardware of this age mainly comprised metal machinery with little use of polymer materials. Natural rubber and synthetic fibers were among the few options available for soft materials. The McKibben artificial muscle, a soft actuator, began to be tested as the power source for active prosthetics (Schulte 1961). McKibben-type artificial rubber muscle consists of an elastomeric tube with a braided sheath. Pneumatic artificial muscles (PAMs) with different principles were also developed in Poland and Japan. An artificial arm with seven degrees of freedom (DoF) was

developed using the antagonistic drive of the McKibben artificial muscle (Gavrilović 1969). Notable flexible robotic arms were developed during this period, such as the MA-3, a tentacle arm with 8 DoF from the Minsky's group (Gresser 1968), and the wire-driven tensor arm manipulator (Horn 1968).

Following the development of large computers known as mainframes, small and low-cost minicomputers, such as the programmed data processor (PDP) series by the Digital Equipment Corporation (DEC), appeared in the 1960s and were used to control robots. Computer control enabled "softness" in the sense of feedback control to be implemented by software. It is a primitive force control that modifies the movement of the manipulator in response to the reaction forces from objects or the environment. For example, researchers have shown that a sensor-controlled robot manipulator can adapt to crank-turning and peg-in-hole tasks using information from tactile sensors of the hand and joint torques (Inoue 1971).

1.2.3 Bioinspiration (1970–)

In the 1970s, biomechanics and bioengineering research picked the pace. Biomechanics studies the properties of biological systems and materials from the viewpoint of mechanics, materials, and fluid dynamics. Typical research topics include human blood circulation and bone and joint mechanics, closely related to medical engineering. Although attempts had been made to realize human movement with robots, few studies had linked animal biomechanics with robotics.

Based on a biomechanical study of the undulatory motion of snakes, Umetani and Hirose revealed the principle of snake locomotion using a robot-based synthetic approach (Umetani 1974). This research triggered the development of snake-like robots. Hirose et al. abstracted snake-like mechanisms and named them active code mechanisms (ACMs). The application of ACM is not limited to mobile robots; for example, a multi-joint gripper that can follow curved surfaces has been developed (Hirose 1978).

Meanwhile, due to the influence of the World War, prosthetic and orthotic research was active in Yugoslavia, and research on human motor skills was conducted at the University of Belgrade and the Mihajlo Pupin Institute (MPI). In the International Symposium on External Control of Human Extremities, Ichiro Kato's group, a pioneer in bipedal robotics held discussions with researchers in Yugoslavia. Based on their interest in human muscular control, the early artificial legs developed by Kato et al. were driven by artificial rubber muscles (Lim 2007). However, hydraulic actuators and electric motors have become mainstream with the development of humanoid robots. As it became clear that soft actuators were not essential to the realization of bipedal locomotion, the artificial muscles studied less frequently in the context of humanoid robotics research.

The perspective of biologically inspired robots has encouraged the interdisciplinary engineering interpretation of biological forms and functions, and the scope of robot design had significantly expanded. However, physical softness had not always

been emphasized and the use of soft materials was limited. Learning from animal form and behavior was a new attempt that could be considered an attempt to step away from traditional mechanical engineering. The potential and attractiveness of animal-like machines created in the 1970s played an important role in laying the groundwork for soft robotics.

1.2.4 Soft Actuation (1980–)

In the 1980s, the use of industrial robots began to increase, and the number of robotic actuators gradually improved. Robot arms with large-diameter direct-drive motors without reduction gears have been tested in the lab (Asada 1983). The McKibben artificial muscle used in the 1960s was redesigned and commercialized by Bridgestone, a pneumatic tire and rubber company, under the name "Rubbertuator." Various soft actuators were explored in the 1980–1990s as precursors to soft robotics. The motivation for new actuators was the use of smart materials to simplify mechanisms following the demand for miniaturization. The 1980s were a period of progress in the miniaturization of mechatronics products. In addition, microelectromechanical system (MEMS) research has garnered interest in micromachines. A challenge in miniaturizing machines is the difficulty in manufacturing and assembling components. Research on shape memory alloys and various functional polymers, such as millimeter-scale actuators, had become active.

Robotic applications of actuators utilizing the shape memory effect of Ti-Ni alloys, a type of shape memory alloy, had advanced. An active endoscope was developed using a shape memory alloy (SMA) actuator (Ikuta 1988). The research was initiated using SMA sheets and coil actuators to drive robotic fingers (Kuribayashi 1989; Bergamasco 1989).

Research on polymer actuators had also advanced, and their applications in small machines have been investigated. Polyvinylidene fluoride (PVDF), a piezoelectric material, can be used in bimorph actuators (Davis 1983) and tactile sensors. An artificial muscle with strips of polyvinyl alcohol-polyacrylic acid (PVA-PAA) copolymer that responds to chemical stimulation with water and acetone had been proposed (Caldwell, 1990). A hydrogel with chemo-mechanical properties was applied to inchworm movement in solution (Osada 1992). As an actuator using an electronically conductive polymer, a laminate bipolymer strip using polypyrrole (PPy), which bends in an electrolyte solution, was developed (Pei 1992). A carbon nanotube (CNT) actuator was proposed as a bimorph cantilever actuator, in which two nanotube sheets bend a polymer film (Baughman 1999).

Studies have been conducted on semi-soft robots such as flexible link manipulators and robotic hands with soft fingertips. Flexible link manipulators are robot arms that swing links with rotary joints and handle cases in which the flexure of the link cannot be ignored. The problem of modeling and controlling this particular manipulator had been actively addressed (Hillsley 1993). Most of these manipulators have at most two links and handle in-plane motion; the primary control challenge is vibration control.

Although not directly related to robotics, several studies have been conducted on controlling beam bending using SMA actuation as an example of an active structure (Chaudhry 1991). Dynamics analysis of object grasping by a robotic hand with soft tips on its fingers has also begun (Akella 1989). A review of soft fingertip materials, such as rubber, sponge, and gel, has also been conducted (Shimoga 1996).

1.2.5 Control of Deformation (1990–)

Soft robotics focuses on compliant mechanisms that express functionality through the deformation of soft materials. Classic soft actuators, such as pneumatic muscles and shape memory alloy wires, are only force-generating components and must be integrated with soft materials. Emerging polymer actuators were not immediately suitable for robotic applications owing to their low output and lack of operational stability. Therefore, a flexible microactuator (FMA) (Suzumori 1991), which assumes the form of an integrated actuator and soft material, was an entrance to modern soft robotics. The FMA has a fiber-reinforced elastomeric tube structure with separate chambers and three DoFs in one module. The FMA allows the actuator to serve as a body structure, such as fingers, arms, legs, and trunk. Multi-fingered hands, continuous robotic arms, legged robots, and pipe mobile robots were built using FMA. Meanwhile, a soft finger made of a tube structure with an unbalanced wall thickness was developed (Abo-Ismail 1993).

A novel robot type created during this period was the face robot. In contrast to motor systems such as the hands, arms, and legs, the face is an important organ for social communication. A face can be described as a soft device that conveys information through the continuous deformation of soft materials. A facial robot with 18 FMAs was constructed, and six different facial expressions were realized (Kobayashi 1993).

From 1996 to 2000, the Study on Soft-mechanics and Function Creation in Morpho-functional Machines project was conducted in Japan, with the support of the Japan Society for the Promotion of Science (JSPS). The results of the project, which involved research groups from several institutions, included robotic hands driven by small-diameter McKibben-type artificial muscles (Lee 1999), wearable devices that use granular jamming (Mitsuda 2002), and prototypes of modular and liquid amoeba-like robots (Yokoi 2003). However, these results, which are highly relevant to soft robotics from today's perspective, have rarely been referenced.

The term soft robot did not exist at this time. Suzumori discussed the advantages of elastic materials using the term "compliant robots" and demonstrated that, although many studies have used force control to provide softness to hard robots, only a few have utilized the continuous deformation of soft materials (Suzumori 1996). Robinson and Davies classified the mechanisms of continuum robots into intrinsic, extrinsic, and hybrid forms and provided examples of compliant fingers and continuous manipulators (Robinson 1999).

1.2.6 Emergence of Soft Robotics (2000–)

The field of soft robotics, which currently exists, was first proposed in a study in 2008 (Trivedi 2008). In particular, the features of soft robots were discussed, in contrast to those of hard robots. This discussion was based on a study of continuum robot arms inspired by the hydrostatic skeletons of living organisms found in an octopus's arms and an elephant's trunk (Walker 2005). A field trial was conducted with a system of the OctArm continuum manipulator on a mobile robot to test tasks such as pulling a ball or sticking an object out of a water puddle (McMahan 2006).

More examples of locomotion studies using soft deformations have been published. A caterpillar robot powered by a shape memory alloy actuator was built to study the biomechanics of caterpillars (Trimmer 2006). A deformable robot that rolls and jumps by deformation was also developed (Sugiyama 2006). In addition, a mobile robot with a tensegrity structure has been created (Paul 2006). For underwater locomotion, bending soft actuators have been proposed for manta-like swimming robots (Suzumori 2007). Bio-inspired robots have been established as a research field, and sophisticated collaborations with biology have been demonstrated, such as the StickyBot gecko-inspired robot, which combines functional microstructures with a compliant legged robot (Kim 2008). An early attempt to investigate the connection between softness and perception involved investigating multiple sensors embedded in a soft fingertip (Hosoda 2006).

The word "soft" has a broad meaning, and its implications require clarification. For example, soft robotics realized by force control was proposed based on research on the advanced impedance control of torque-controlled DLR-KUKA robots (Albu-Schäffer 2009). In addition, the term soft sensor refers to a virtual sensor emulated by software from multiple sensor information sources in plant control; it does not refer to a flexible sensor (Kadlec 2009).

The philosophical background of soft robotics is embodied cognitive science. Considerations regarding the embodiment of soft robots later led to the concept of morphological computation (Pfeifer 2006). In the context of embodied intelligence, the OCTOPUS project on octopus-inspired robots, supported by the European Commission (EC), was conducted from 2009 to 2013. Further, the Swiss-Japan Joint Seminar on "Soft Robotics: Morphology, Materials, and Functionalities" was held on embodied intelligence and soft robotics in 2010.

Researchers from Harvard University, Massachusetts Institute of Technology, iRobot, and others have conducted the ChemBots program supported by the Defense Advanced Research Projects Agency (DARPA) from 2008 to 2010. This program attempted to create soft, mobile, and morphing chemical robots and a prototype spherical robot that uses jamming skin to represent this concept (Steltz 2009). Many soft robots have emerged from this program: a rolling caterpillar-inspired robot (Lin 2011), worm-inspired robot Meshworm driven by NiTi coil actuators (Seok 2010), and a soft robotic fish (Marchese et al. 2012). A close research project was the Programmable Matter program supported by DARPA, which resulted in a universal gripper using granular jamming (Brown et al. 2010).

1.2.7 Soft Robotics in Growth (2010–)

The field of soft robotics was established around 2010, with research results from large projects and a mature research community. The 2010s were characterized by several global organizational initiatives. In 2012, IEEE Robotics and Automation Society established the Technical Committee on Soft Robotics. This was followed by the establishment of the RoboSoft Association, with support from the European Commission (EC), in 2013. In South Korea, the Soft Robotics Research Center was established at Seoul National University in 2016 with support from the National Research Foundation of Korea. In Japan, a five-year research project, the Grant-in-Aid for Scientific Research on Innovative Areas "Science of Soft Robots," was launched in 2018. The Soft Robotics, launched in 2014, is an academic journal for global soft robotics projects. The IEEE International Conference on Soft Robotics (RoboSoft) has been conducted annually since 2018.

Continued efforts to pursue basic research on soft robotics will still be necessary, although commercialized soft robotics technology is desired. Soft robots are characterized by safety and redundancy, and their durability is lower than hard robots. The increasing number of collaborative robots (co-robots) shipments could be a positive trend in soft robotics. Soft grippers are an area where commercialization is in progress, and several companies are offering products. Empire Robotics, Inc. closed its business in 2016 after trying to commercialize a jamming gripper in 2012 (Amend et al. 2016). Soft grippers will not replace all robotic hands; however, using soft fingers and compliant mechanisms will occupy a certain share of the market.

Software development is more dominant than hardware development in industrial robot arms, where basic hardware specifications are stable. Because soft robotics is in the exploratory phase and a common mass-produced robot has not yet been developed, the focus is on hardware development. Nevertheless, computation is important, and computational design is a challenge for soft robots (Cheney et al. 2013). Machine learning methods related to deep learning, which have developed rapidly since approximately 2012, have impacted soft robotics (Kim et al. 2021). Machine learning methods are used for robot geometry, actuator placement, and automatic sensor placement (Tapia et al. 2020). The lack of a common platform for soft robots makes it difficult to evaluate and conduct follow-up experiments using the proposed control-and-design method. Similar to the benchmark environments and models available in reinforcement learning, training environments for soft robots have been proposed (Bhatia et al. 2021).

1.2.8 Future of Soft Robots (2020–)

Earlier, soft robotics existed as a counterpart to hard robotics. In the future, the fusion of hardness and softness may be promoted. The body of a living organism, which continues to inspire robots, is a complex system that combines hard and soft materials

in appropriate locations. Hybrid robots or semi-soft robots have already been tested. Furthermore, soft robotics may be elevated from a subcategory of robotics to a higher level of deformable or transformable engineering. Joining such new disciplines would be the fields of flexible electronics, mathematics of soft objects, and morphological computation, which will be introduced in later chapters.

References

Abo-Ismail A (1993) On the development of a new pneumatic versatile gripper. Proc JFPS Int Symp Fluid Power, 1993(2):701–706

Albu-Schäffer A et al (2009) Anthropomorphic soft robotics-from torque control to variable intrinsic compliance. In: International Symposium of Robotics Research (ISRR). pp. 185–207

Amend J, Cheng N, Fakhouri A, Culley B (2016) Soft Robotics commercialization: jamming grippers from research to product. Soft Robot 3(4):213–222

Akella P, Cutkosky M (1989) Manipulating with soft fingers: modeling contacts and dynamics. In: International Conference on Robotics and Automation (ICRA), pp. 764–769

Anderson VC, Horn RC (1968) Tensor arm manipulator, US3497083A, 1968

Asada H, Youcef-Toumi K (1983) Analysis and Design of Semi-Direct-Drive Robot Arms. Am Control Conf 757–766

Baughman RH et al (1999) Carbon nanotube actuators. Sci 284(5418):1340–1344

Bergamasco M, Salsedo F, Dario P (1989) Shape memory alloy micromotors for direct-drive actuation of dexterous artificial hands. Sens Actuators 171:115–119

Bhatia J, Jackson H, Tian Y, Xu J, Matusik W (2021) Evolution gym: a large-scale benchmark for evolving soft robots. In: Advances in Neural Information Processing Systems 34:2201–2214

Brown E et al (2010) Universal robotic gripper based on the jamming of granular material. Proc Natl Acad Sci 107(44):18809–18814

Caldwell DG, Taylor PM (1990) Chemically stimulated pseudo-muscular actuation. Int Eng Sci 28(8):797–808

Chaudhry Z, Rogers CA (1991) Bending and Shape Control of Beams Using SMA Actuators. Intell Mater Syst Struct 2(4):581–602

Cheney N, MacCurdy R, Clune J, Lipson H (2013) Unshackling evolution: evolving soft robots with multiple materials and a powerful generative encoding. In: Annual Conference on Genetic and Evolutionary Computation (GECCO), pp. 167–174

Dario P, Carrozza MC, Lencioni L, Magnani B, D'Attanasio S (1997) A microrobotic system for colonoscopy. In IEEE International Conference on Robotics and Automation (ICRA), pp 1567–1572

Davis AF, Nevill GE (1983) Corrugated PVDF bimorphs as tactile sensors and micro-actuators – A research note. Robotica 1(4):239–240

Ernst HA (1961) MH-1, A computer-operated mechanical hand, Doctoral thesis, massachusetts institute of technology

Gavrilović MM, Marić MR (1969) Positional servo-mechanism activated by artificial muscles. Med Biol Eng 7(1): 77–82

Gresser J-Y (1968) Description and control of manipulation by computer-controlled arm. Artificial Intelligence Memo 165, Massachusetts Institute of Technology

Hosoda K, Tada Y, Asada M (2006) Anthropomorphic robotic soft fingertip with randomly distributed receptors. Rob Auton Syst 54(2):104–109

Hillsley KL, Yurkovich S (1993) Vibration control of a two-link flexible robot arm. Dyn Control 3(3):261–280

Hirose S, Umetani Y (1978) The development of soft gripper for the versatile robot hand. Mech Mach Theory 13(3):351–359

Ikuta K, Tsukamoto M, Hirose S (1988) Shape memory alloy servo actuator system with electric resistance feedback and application for active endoscope. In: IEEE International Conference on Robotics and Automation (ICRA) pp 427–430
Inoue H (1971) Computer controlled bilateral manipulator. Bull JSME 14(69):199–207
Kadlec P, Gabrys B, Strandt S (2009) Data-driven Soft Sensors in the process industry. Comput Chem Eng 33(4):795–814
Kim S, Laschi C, Trimmer B (2013) Soft robotics: a bioinspired evolution in robotics. Trends Biotechnnol. 31:287–294
Kim S, Spenko M, Trujillo S, Heyneman B, Santos D, Cutkosky MR (2008) Smooth vertical surface climbing with directional adhesion. IEEE Trans Robot 24(1):65–74
Kim D et al (2021) Review of machine learning methods in soft robotics. PLoS One 16(2):e0246102
Kobayashi H, F Hara (1993) Study on face robot for active human interface-mechanisms of face robot and expression of 6 basic facial expressions. In: 2nd IEEE International Workshop on Robot and Human Communication, pp. 276–281
Kuribayashi K (1989) Millimeter-sized joint actuator using a shape memory alloy. Sens Actuators 20(1):57–64
Laschi C, Mazzolai B, Cianchetti M (2016) Soft robotics: technologies and systems pushing the boundaries of robot abilities. Sci Robot 1 (1). https://doi.org/10.1126/scirobotics.aah3690
Lee YK, Shimoyama I (1999) A skeletal framework artificial hand actuated by pneumatic artificial muscles. In: IEEE International Conference on Robotics and Automation (ICRA), pp. 926–931
Lim H, Takanishi A (2007) Biped Walking Robots Created at Waseda University: WL and WABIAN Family. Philos Trans Math Phys Eng Sci 365(1850):49–64
Marchese AD, Onal CD, Rus D (2012) Towards a self-contained soft robotic fish: on-board pressure generation and embedded electro-permanent magnet valves. Int Symp Exp Robot 88:1–14
McMahan W et al (2006) Field trials and testing of the OctArm continuum manipulator. In: IEEE Int Conf Robot Autom (ICRA), pp. 2336–2341
Mitsuda T, Kuge S, Wakabayashi M, Kawamura S (2002) Wearable Force Display Using a Particle Mechanical Constraint. Presence Teleoperators Virtual Environ 11(6):569–577
Osada Y, Okuzaki H, Hori H (1992) A polymer gel with electrically driven motility. Nature 355: 242–244
Paul C, Valero-Cuevas FJ, Lipson H (2006) Design and control of tensegrity robots for locomotion," IEEE Trans. Robot 22(5):944–957
Pfeifer R, Iida F, Gómez G (2006) Morphological computation for adaptive behavior and cognition. Int Congr Ser 1291:22–29
Robinson G, Davies JBC (1999) Continuum robots - a state of the art. In: IEEE Int Conf Robo Autom (ICRA) 4:2849–2854
Robotics Society of Japan (2023) Robotics Handbook, 3rd edn. Vol II, Chapter 5, Soft Robots, Corona Publishing: 295-299
Schulte HF (1961) The characteristics of the mckibben artificial muscle. Appl External Power Prosthet Orthot pp. 94–115
Shimoga KB, Goldenberg AA (1996) Soft Robotic Fingertips: Part I: A Comparison of Construction Materials. Int Rob Res 15(4):320–334
Suzumori K, Endo S, Kanda T (2007). A bending pneumatic rubber actuator realizing soft-bodied manta swimming robot. In: IEEE International Conference on Robotics and Automation (ICRA) pp. 10–14
Sugiyama Y, Hirai S (2006) Crawling and jumping by a deformable robot. Springer Tracts Adv Robot 21:281–291
Suzumori K, Iikura S, Tanaka H (1991) Flexible microactuator for miniature robots. In: IEEE Micro Electro Mechanical Systems, pp. 204–209
Suzumori K (1996) Elastic materials producing compliant robots. Rob Auton Syst 18(1):135–140
Suzumori K (2022) Overview of the Kakenhi Grant-in-Aid for scientific research on innovative areas: science of soft robots. J Robot Mechatron 34(2):195–201
Suzumori K (2017) Vague robots. J Jpn Soc Des Eng 52(19):585–589, 2–17

Steltz E, Mozeika A, Rodenberg N, Brown E, Jaeger HM (2009) JSEL: Jamming Skin Enabled Locomotion. In: IEEE/RSJ International Conference on Intelligent Robots and Systems (IROS), pp. 5672–5677

Tapia J, Knoop E, Mutný M, Otaduy MA, Bächer M (2020) Makesense: automated sensor design for proprioceptive soft robots. Soft Robot 7(3):332–345

Trimmer BA, Takesian AE, Sweet BM, Rogers CB, Hake DC, Rogers DJ (2006) Caterpillar locomotion: A new model for soft- bodied climbing and burrowing robots. In: 7th International Symposium on Technology and the Mine Problem, pp. 1–10

Trivedi D, Rahn CD, Kier WM, Walker ID (2008) Soft robotics: Biological inspiration, state of the art, and future research. Appl Bionics Biomech 5(3):99–117

Umetani Y, Hirose S (1974) Biomechanical study of serpentine locomotion. On Theory and Practice of Robots and Manipulators 1:171–184

Walker ID et al. (2005) Continuum robot arms inspired by cephalopods. In: Proc.SPIE

Yokoi H, Nagai T, Ishida T, Fujii M, Iida T (2003) Amoeba-like robots in the perspective of control architecture and morphology/materials. In: Morpho-functional Machines: The New Species, pp. 99–129

Part I
Design of Soft Robots

Chapter 2
Soft Mechanisms

Kenjiro Tadakuma and Hiromi Mochiyama

Abstract Actively exploiting material deformation allows for a variety of new mechanisms, from soft actuators to adjustable stiffness. This chapter will organize and describe deformation induced by fluid forces, compliance of rigid structures, and jamming mechanisms. We then provide the definitions and relationships of three typical classes of soft mechanisms: continuum, elastic, and bistable mechanisms. Continuum mechanisms form an important core in soft mechanisms. Elastic mechanisms are useful and can be applied to understanding animal bodies as well as robotic mechanisms. Bistable mechanisms are effective for generating impulsive forces. A basic understanding of these mechanisms is helpful in designing soft robots.

2.1 Deformable Mechanisms

2.1.1 Basic Concepts

A soft mechanism is literally a "soft" mechanism. Soft mechanisms can be broadly classified into two types: those in which the "motion" is soft, and those in which the "structure" itself is soft. In the former case, rotational and linear joints are often connected by relatively stiff links made of metals or other materials. Generally, compliance control is performed to soften the motion of actuators that move rotary and linear joints using one of two approaches: (i) calibrating the joint based on the value of a joint displacement sensor for an electric motor; or (ii) installing an actuator using a compressible fluid, such as a pneumatic cylinder, artificial muscle, or pouch motor, at a position offset from the rotation axis of the joint. In the second approach, the elasticity of the joint is controlled by changing the internal pressure. In

K. Tadakuma
Graduate School of Information Sciences, Tohoku University, Sendai, Japan
e-mail: tadakuma@rm.is.tohoku.ac.jp

H. Mochiyama (✉)
Graduate School of Systems and Information Engineering, University of Tsukuba, Tsukuba, Japan
e-mail: motiyama@iit.tsukuba.ac.jp

K. Suzumori et al. (eds.), *The Science of Soft Robots*, Natural Computing Series,
https://doi.org/10.1007/978-981-19-5174-9_2

cases where the "structure" itself is soft, robots are often made of materials such as rubber, sponge, or resin, which are softer (lower Young's modulus) than conventional materials of high rigidity such as metals. Recently, plastic materials that can produce elasticity as structures (structural metamaterials) have been developed. Moreover, these metamaterials can be modeled relatively easily with a three-dimensional printer or other similar apparatuses.

Although soft mechanisms with conventional rotational joints are also generally available, in this section, we discuss those in which the structure is made of a flexible material.

2.1.2 Basic Function

Two main types of flexible mechanisms exist active and passive. The former type of mechanism converts input energy into useful work using a combination of actuators and structural materials, and its primary functions are force application and support. The latter is primarily used for shape adaptation to the contacting body and for shock absorption.

Spherical, rod, and surface shapes, as well as combinations of these shapes, are used as fingers, arms, hands, legs, wings, and tails for three main functions: to apply force to the object in contact; to support its own weight, and to propel the mechanism by applying force to the environment. One of the main types of spherical actuators uses a fluid to induce deformation and generate force-applying functions. However, deformation can also be performed using electrostatic actuators and other types of non-fluid actuators. Non-fluid actuators, such as Miura folding used for deployable panels, typically utilize an origami structure.

In addition to support by deformation, functions such as suction and retention are also performed by these mechanisms. An example of these functions is the suction cup.

2.1.3 Process of Deformation

Applying force to an object in contact with a mechanism requires the generation of displacement, which, in turn, requires deformation in the soft mechanism. This section deals primarily with fluid-type mechanisms. Nevertheless, principles analogous to those discussed here can be used to generate curving motion from displacement.

Expansion motion

Flexible mechanisms have a continuous flexible structure, which can deform instead of changing its structural angles, unlike a conventional rigid structure with joints. When internal pressure is applied by a fluid, the thin membrane-like structure tries to expand into a spherical shape. If the film thickness is homogeneous, it expands such that the overall diameter uniformly increases. Uniformity is extremely important in spherical mechanisms.

Stretching motion

As shown in Figs. 2.2 and 2.3, the combination of a flexible membrane and stretching constraint provides displacement anisotropy (Fig. 2.1).

In such cases, a two-step deformation behavior is observed, where the tube is deformed, as illustrated in Fig. 2.3, once it becomes cylindrical, depending on whether it is radially or axially constrained.

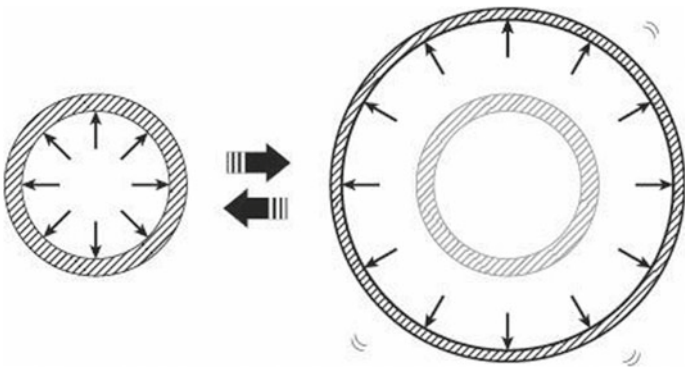

Fig. 2.1 Expansion of flexible membrane due to internal pressure

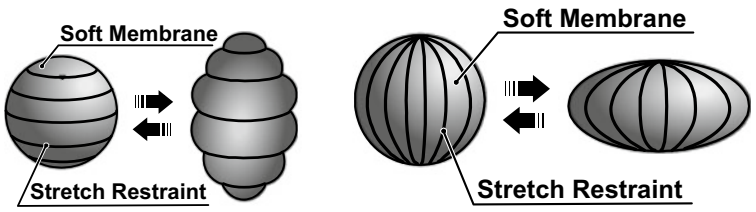

(a) Radial extension constraint (axial expansion) (b) Axial extension constraint (radial expansion).

Fig. 2.2 Addition of displacement anisotropy in combination with extension constraint in mechanisms such as a spherically shaped fiber

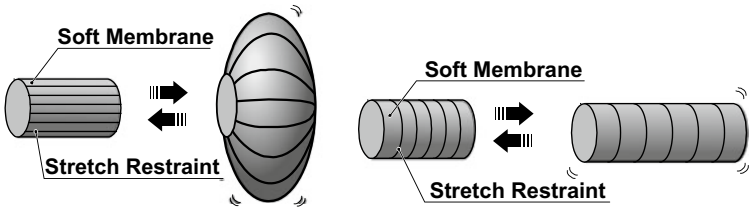

(a) Radial directional extension constraint (axial expansion) and (b) axial directional extension constraint (radial expansion).

Fig. 2.3 Addition of displacement anisotropy in combination with an extension constraint in mechanisms such as a cylindrically shaped fiber

Bending motion

Actuators can be divided into two types: those driven directly by electric motors and rotary joints and those driven by the power transmission of rotary joints. In the latter type, the joints are compact, but the range of motion of the other parts is limited compared to those in the former type.

As is common to all structures, bending and flexion are achieved by inducing relative changes in the physical quantities at geometrically biased positions. Similarly, a change in the physical quantity that induces a large change in the displacement/force only at a geometrically biased position can result in bending or flexion. Conversely, in the natural (neutral) state, the focus is on shaping the object evenly to eliminate bias, or to set the bias of the internal force in the shape and initial state. In addition, fibers or thicker materials are effective in parts of the mechanism that are difficult to deform. The use of these materials facilitates the task of changing the thickness or material in areas that deform easily. Moreover, small actuators that change these high-speed pictures or the physical quantity of the external contact or field can also change the main characteristics of the operation of the mechanism.

The main differences between the various mechanisms are where the actuator is attached and whether it generates an active force in the direction of restoration or passive return.

The most fundamental principle of the flexible mechanism is that the joints are continuously composed of flexible bodies, in contrast to the conventional joints shown in Fig. 2.4. In conventional joints, the extension mechanism is offset from the center of the structure. Moreover, the parts corresponding to A and B in the figure are equivalent in terms of generating bending motion regardless of whether they are exposed or enclosed within the structure. Furthermore, several types of power-transmission methods exist. For instance, Fig. 2.6 illustrates one in which power is transmitted remotely by a wire without an extension mechanism at the position corresponding to A and B. Figure 2.7 illustrates the use of an artificial muscle that fits into A and B. Finally, Figs. 2.8 and 2.9 illustrate a curved structure into which the extension structures are integrated (Fig. 2.5).

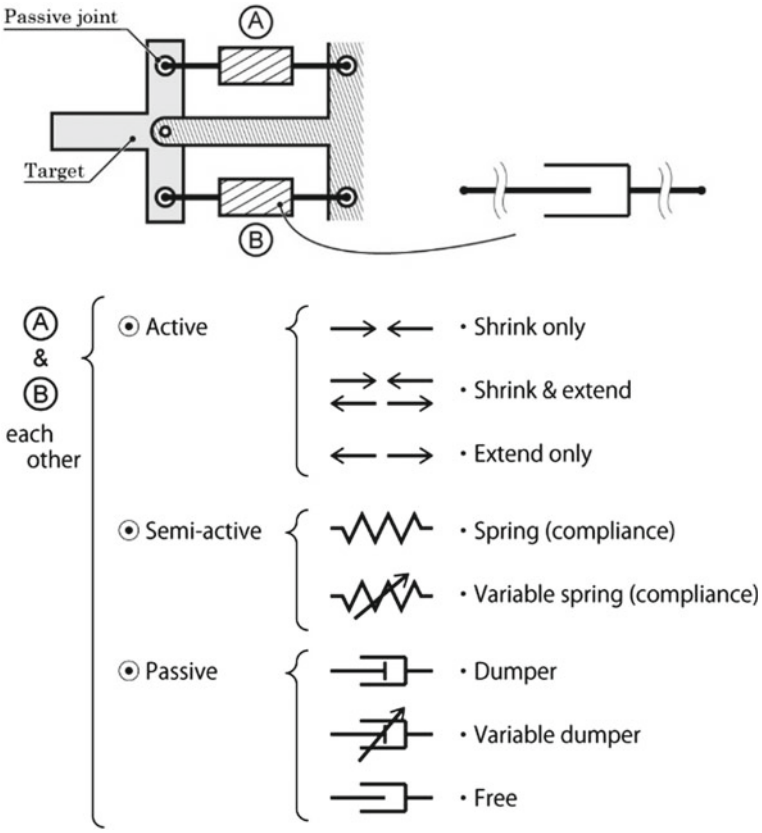

Fig. 2.4 Variable rotational joint system with a conventional rigid structure

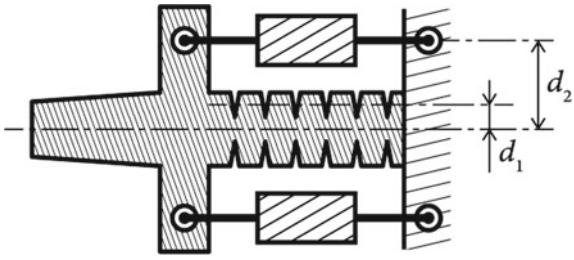

Fig. 2.5 Principle of curved motion achieved using a soft structure

Other structures:

In addition to the abovementioned mechanisms, a torus structure with a propagating tip (Fig. 2.9) and a deformable body with a sponge-like structure inside the membrane (Fig. 2.10) are also available.

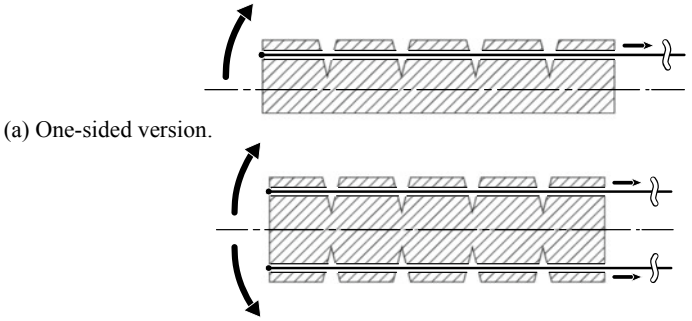

Fig. 2.6 Curvature deformation by extending a point offset from the center

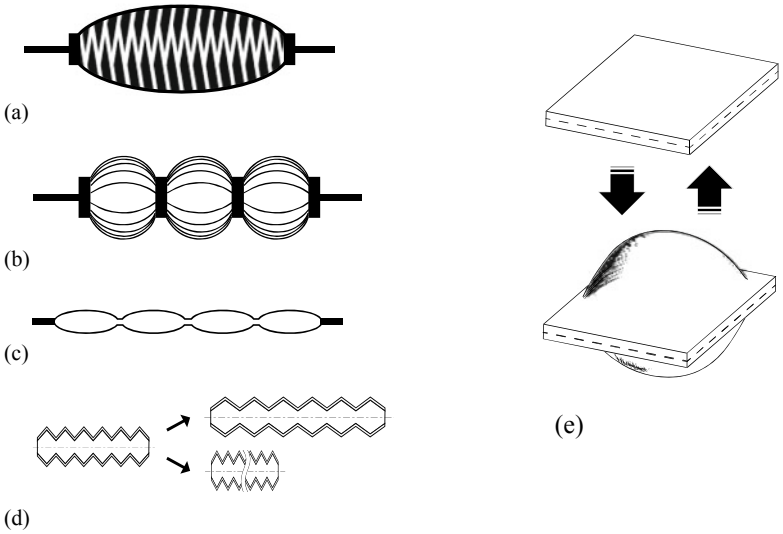

Fig. 2.7 Examples of various artificial muscles. **a** McKibben type (Tondu 2012), **b** Warsaw type (Villegas et al. 2012), **c**Pouch type (connected) (Niiyama et al. 2014), **d**Bellows type (Hashem et al. 2020), **e** Pouch type (single unit) utilizes displacement in the upper direction in the figure

2.1.4 Soft/Rigid Switching

Conventional bag-type flexible/rigid switching mechanisms, as shown in Fig. 2.11, mainly utilize the granular jamming transition phenomenon, in which the powder is sealed inside the closed space of a bag-like membrane. Subsequently, when air, the medium fluid, is removed, the powders jam against each other, resulting in an increase in their rigidity. However, in the case of an elongated bag, buckling tends to occur at its base even in the high-stiffness mode. Furthermore, a structure that generates a stiffness change similar to that induced by the layer jamming transition phenomenon by overlapping multiple plane structures has been proposed. However,

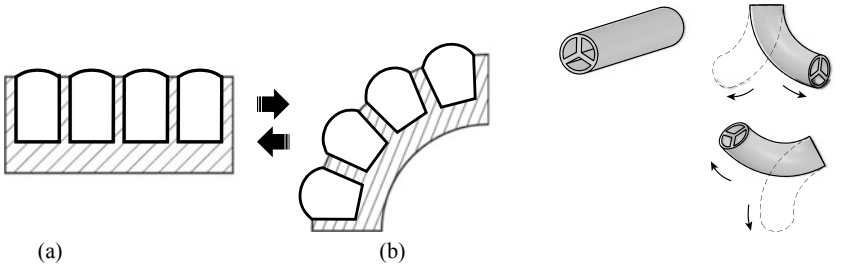

Fig. 2.8 Example of curved displacement generating body. **a** Accordion-type (Mosadegh et al. 2014), **b** 3D curved structure by Suzumori (1989)

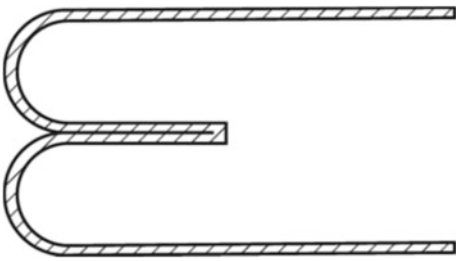

Fig. 2.9 Torus type (Takita et al. 2004)

Fig. 2.10 Combination of membrane and bubble-containing body (Hayakawa et al. 2004)

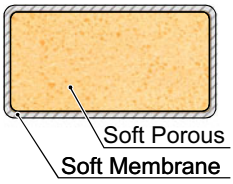

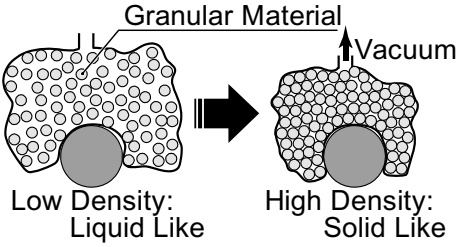

Fig. 2.11 Jamming transition phenomenon

the small bendable radius of curvature in the low-stiffness mode significantly limits the range of motion.

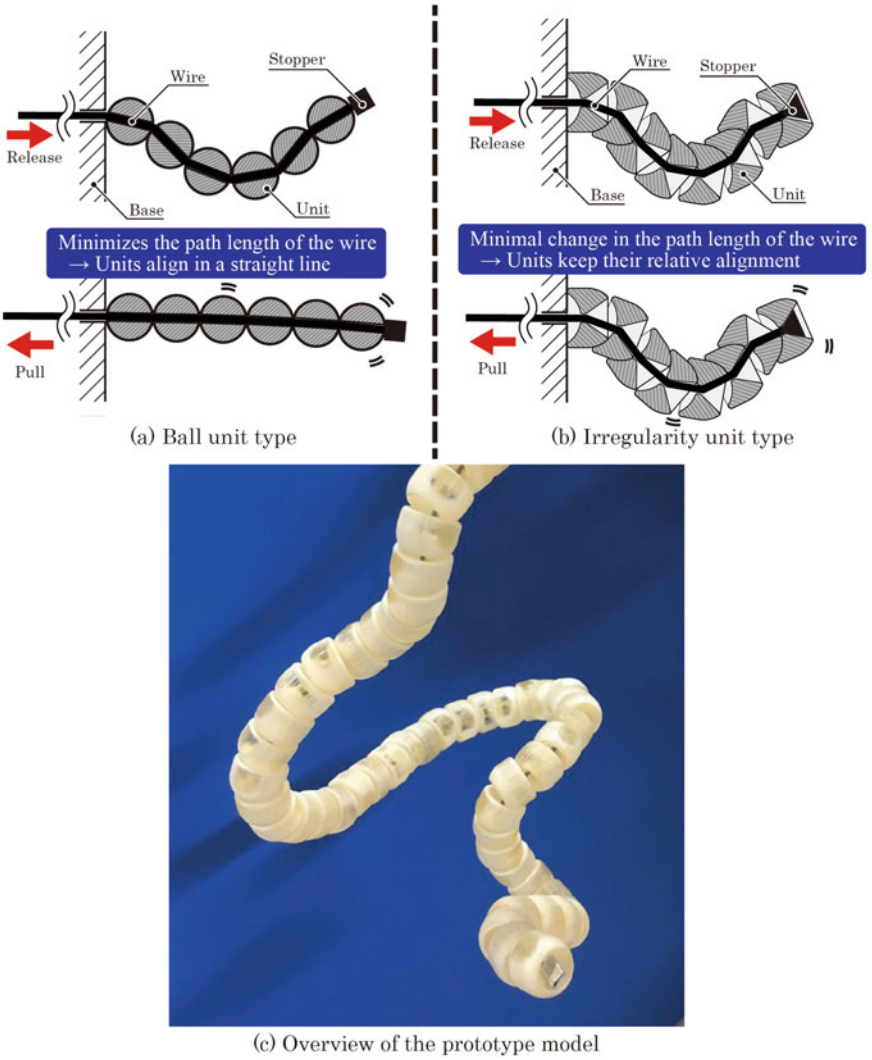

Fig. 2.12 One-dimensional jamming mechanism

Furthermore, a one-dimensional flexible-rigid switching mechanism that uses wires as elements has been realized in actual devices. This mechanism comprises several units with bead-shaped through-holes and a central wire running through these holes. By applying tension to these central wires, the beads touch each other, resulting in high frictional forces and, consequently, improved rigidity. As shown in Fig. 2.12 (left), a simple spherical bead generates a restoring force to minimize the path length, which impairs the posture.

Table 2.1 Classification of mechanisms for switching between soft and stiff

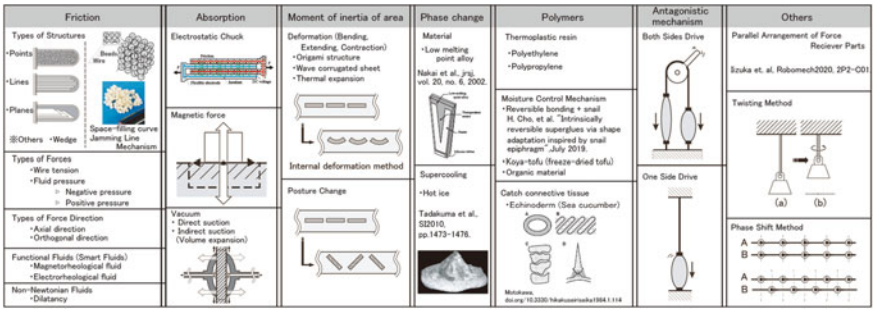

Table 2.1 summarizes the systematization of soft-stiffness switching, including pressurized and wire-traction-type one-dimensional jamming. When configuring the direct-acting jamming mechanism, a two-layer mutual arrangement is more effective than a coaxial arrangement, considering internal wiring. In addition, a configuration that enables flexible and rigid switching in both radial and circumferential directions is possible. This configuration is suitable for multiple joints, which can be driven simultaneously in a simple manner. Another potential method is to change the second cross-sectional moment. This method is an alternative to that of holding by increasing the contact force. However, it requires a design that minimizes the overall dimensional change in flexibility changeover. In terms of practical applications, this method is suitable for paper-gripper mechanisms and soft origami configurations. Another potential method is to place an adsorbent within the device to enclose a negative-pressure-generating organism, magnetic adsorption material, or reversible adhesive material in a fine state.

2.1.5 Examples

In the standard jamming gripper, the granular material was packed into the whole bag and the pressing force for gripping is large. In contrast, a hollow gripper shown in Fig. 2.13 utilizes the variable rigid/flexible switching function to arbitrarily change the rigidity of a structure can grip complex shapes and fragile objects without damaging them. In the industrial field, they are expected to play an active role in the assembly of parts and transportation of goods at high-mix low-volume production sites.

An example of a 1D flexible-rigid switching mechanism is the fire-resistant gripper that can grasp even burning objects, as shown in Fig. 2.14. The gripper is torus-shaped with one-dimensional rigid-flexible switching mechanisms discretely arranged around the circumference in the shape of fingers.

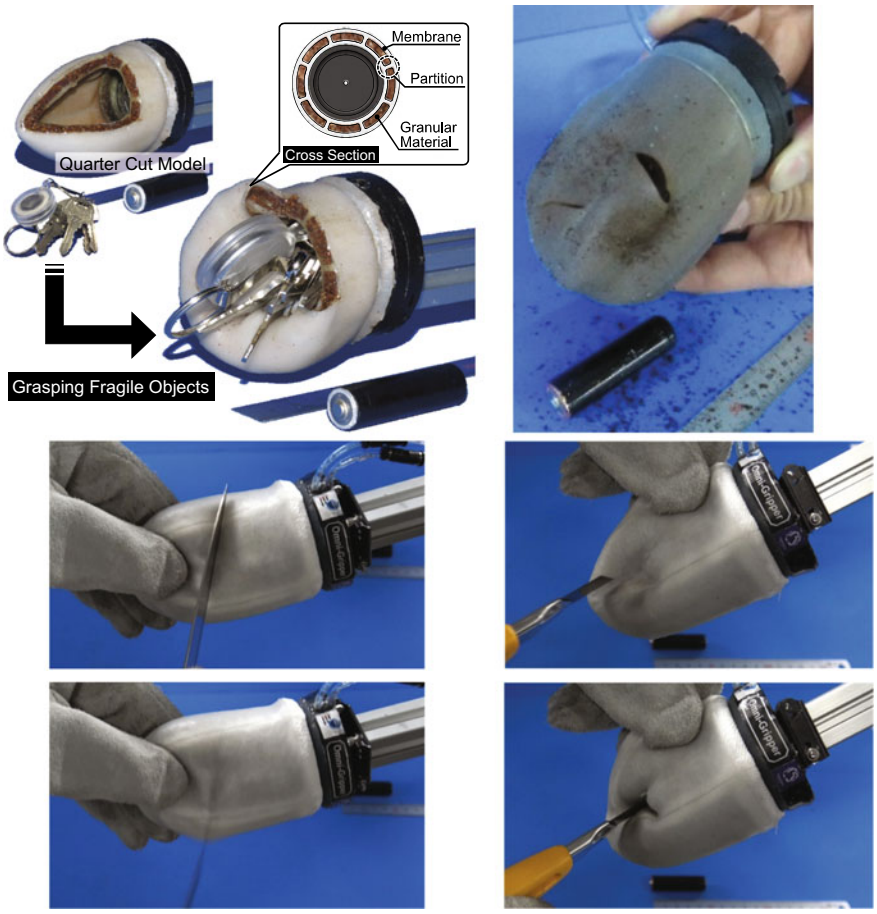

Fig. 2.13 Implementation of flexible-rigid switching membrane gripper mechanism and cut resistance

Flexible mechanisms can be configured to obtain displacement and motion in the desired direction, passively familiarize themselves with the contact object, and effectively apply force by adding a soft-rigid-switching function. In conclusion, these mechanisms have significant potential applications in several fields.

Fig. 2.14 Fire-resistant gripper mechanism equipped with a flexible and rigid switchable linear body (Tadakuma et al. 2008)

2.2 Typical Soft Mechanisms

2.2.1 Continuum, Elastic, and Bistable

In this subsection, the definitions and relationships of typical three classes of soft mechanisms, i.e., continuum, elastic, and bistable mechanisms, are explained.

Continuum Mechanism

Continuum mechanisms consist of continuum bodies that can be characterized by many (approximating infinite) extraordinary kinematic degrees of freedom (DOF). The notion of continuum mechanisms is analogous to that of compliant mechanisms (Howell 2001, 2013) but emphasizes smoothness in shape. For example, the shape of a one-dimensional continuum mechanism is considered as a smooth spatial curve that can be handled by a rigorous geometric model. Although it is possible to consider two-dimensional and three-dimensional continuum mechanisms, most current continuum robots fall into the one-dimensional class. By making full use of their slim bodies, continuum robots are expected to perform useful tasks in narrow spaces that are difficult to access for conventional robots. The term "continuum robots" first appeared in the late 90s (Robinson and Davies 1999), when the term "soft robotics" was not frequently used. Continuum mechanisms form an important "classical" core of soft mechanisms.

Elastic Mechanism

Elasticity is a completely different notion from a continuum. An object is said to be elastic if it deforms when a force is applied but regains its original resting shape once the force is removed. A serial chain of rigid links connected with elastic joints is an elastic mechanism but not a continuum mechanism because its kinematic DOFs

are not necessarily large in number. Elasticity is important for robotic mechanisms because the deformation property of elastic mechanisms allows the achievement of "repeated" transformations of mechanisms by using simple actuation devices. Elasticity is also beneficial from a theoretical perspective because elasticity is related to the concept of potential energy. The behavior of elastic mechanisms can be discussed using the useful concepts of equilibrium and its stability based on potential energy.

Bistable Mechanism

Bistable mechanisms are characterized by two stable equilibrium configurations. Each of the stable equilibria of the mechanism is determined by the elastic potential energy of an elastic mechanism. Therefore, bistable mechanisms consist of elastic mechanisms. However, the bistable mechanism is not entirely elastic. If a certain force is applied to a bistable mechanism and the configuration changes from one equilibrium to another, it does not return to its original shape when the force is removed. Elasticity is necessary for generating bistable properties. However, no bistable mechanism can be elastic. During equilibrium transition, a bistable mechanism is necessary to achieve an unstable configuration. This property may be utilized for a quick motion of the mechanism.

Relationship

The relationships among the three classes of soft mechanisms are shown as a Venn diagram in Fig. 2.15. In this diagram, elasticity in a narrow and wide sense is defined. An object is said to be elastic in a wide sense if it includes an elastic object. The word "elastic in a narrow sense" is used here for mechanisms that are elastic. Bistable mechanisms belong to the region "elastic in a wide sense" and outside "elastic in a narrow sense." Note that important examples of soft mechanisms exist in continuum-elastic or continuum-bistable regions. These examples will be explained in the next section.

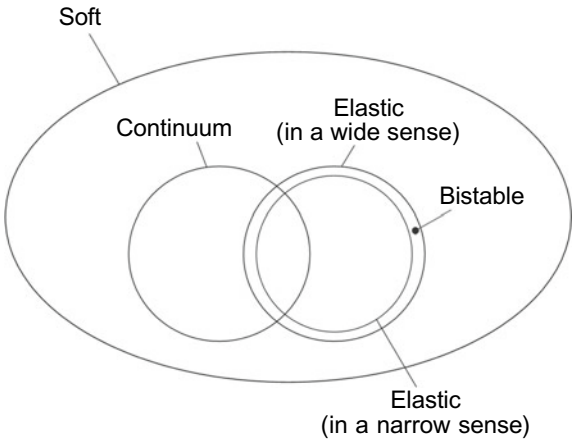

Fig. 2.15 Relationships among the three classes of mechanisms: continuum, elastic, and bistable

2.2.2 *Examples of Continuum-Elastic Mechanism*

In this section, we discuss four typical continuous elastic manipulators. Continuum-elastic locomotors are described in Chap. 4.

An Elastic Rod Pulled by Wires

One of the simplest continuum-elastic mechanisms is an elastic rod pulled by wires. Consider a straight elastic rod with one end fixed to the ground. Let a wire be attached near the other end of the rod with an offset from the center of the cross-section at the end. Let some guides be attached to the rod so that the wire can move along the rod. The elastic rod is bent by pulling the wire. When the wire is loosened, the elastic rod returns to a straight shape. For spatial deformation, multiple wires are attached near the rod tip in different offset directions, as shown in Fig. 2.16a.

Such spatial deformation mechanisms have been observed since the beginning of the 1980s (Hirose et al. 1983). The mechanism is sufficiently simple, and a slender continuum manipulator can thus be embodied. For example, wire-driven mechanisms have been adopted for steerable/active catheters in medical applications (Ganji et al. 2009). For a more complex deformation, we can adopt a multi-section strategy of connecting multiple elastic rods pulled by wires in series. In this case, wire coupling effects should be considered (Camarillo et al. 2008; Carlson et al. 2009).

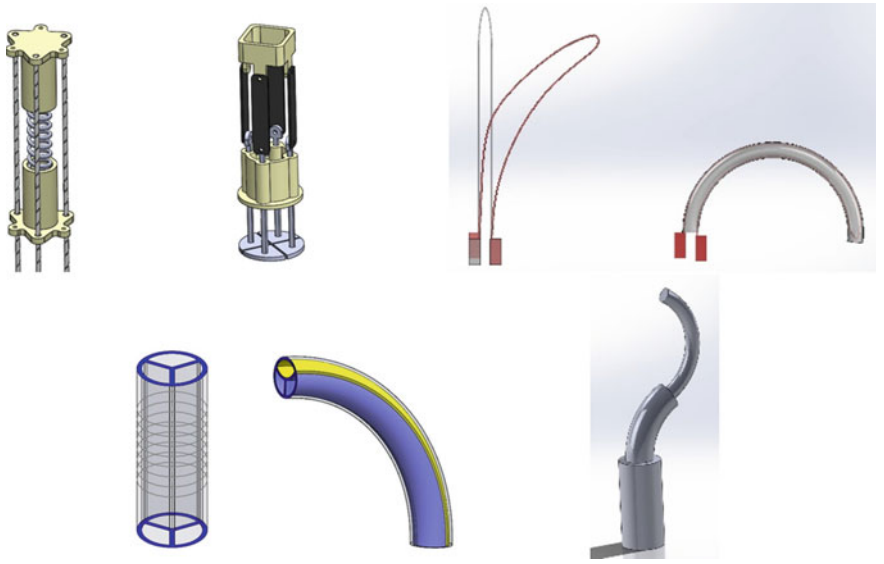

Fig. 2.16 Typical mechanisms of continuum manipulators. **a** Top left: an elastic rod pulled by wires, **b** top center: parallel elastic rods, **c** top right: a sheathed closed elastic rod, **d** bottom left: parallel extensible balloons, **e** bottom right: precurved elastic tubes

An elastic rod can be replaced by a more general viscoelastic object. The recent advancement of wire-driven wearable robot hands is an interesting example (Kang et al. 2016; In et al. 2016).

Parallel Elastic Rods

Two elastic rods are considered. Let one end of each rod be fixed to a linear actuator, and all the other ends be connected to a rigid object with an offset from the center of the cross-section. By pulling/pushing a rod using an actuator, the entire continuum-elastic mechanism ends. When the rod returns to its original position, the shape of the structure also returns to a straight shape. For spatial deformation, multiple elastic rods are fixed in parallel, as shown in Fig. 2.16b. Each end of the rod is fixed to a linear actuator. However, we must be careful about actuation because the inappropriate driving of multiple actuators may generate excessive internal forces. Each pair of opposite rods is driven accordingly. The multi-sections of this mechanism require a nested structure. This makes the entire mechanism large. This mechanism might be useful for adding kinematic DOFs to the tip end of a laparoscopic surgery tool.

The sheathed closed elastic rod has evolved from parallel elastic rods and is shown in Fig. 2.16c. The slender loop of the elastic rod is bent by shifting the end positions of the elastic rods by increasing the loop width. A sheath that covers the loop prevents it from expanding, which significantly contributes to the bending of the entire structure. This advanced continuum mechanism also has medical applications (Yamada et al. 2014).

Parallel Extensible Balloons

We consider three slender balloons, each of which can extend along its length direction by increasing internal pressure. The inside walls of the balloons are sealed with each other. Suppose the shape of the entire mechanism is straight at rest. The mechanism bends by filling air into one balloon, as shown in Fig. 2.16d. The internal pressure control of the three balloons generates spatial deformation. This spatial deformation mechanism was developed in the late 1980s (Suzumori et al. 1992) and is so simple that even a slender manipulator with a submillimeter diameter can be fabricated.

Precurved Elastic Tubes

A complex shape can be formed by inserting a precurved elastic needle into a soft object with rotation. A nested precurved tube can take a more complex shape (Fig. 2.16e). This mechanism was invented for medical use, and the model is described in detail in (Webster et al. 2009, Dupont et al. 2010).

2.2.3 Example of Continuum-Bistable Mechanisms

In this section, snap motors (Mochiyama et al. 2007, Yamada 2007) are described as an illustrative example of continuum-bistable mechanisms.

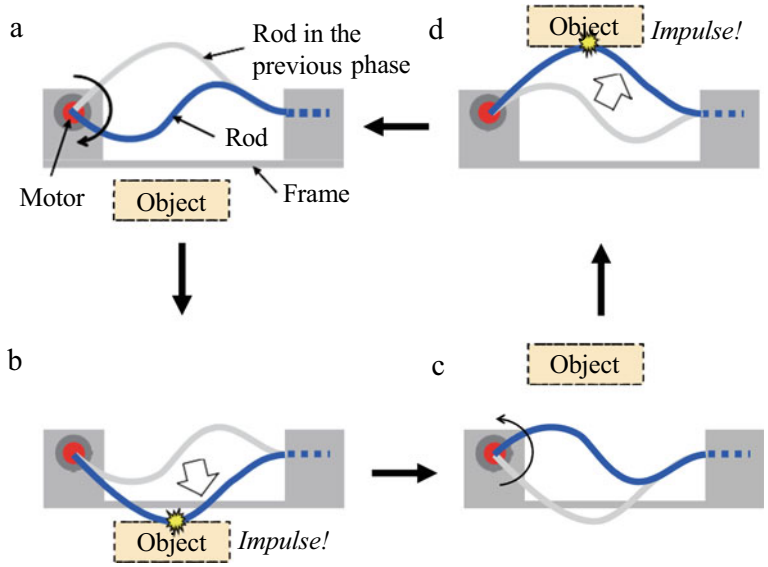

Fig. 2.17 A typical mechanism of snap motors. In this figure, the rod shape in the previous phase is drawn in a light-gray curve

Snap motors are impulse–force generators that utilize a phenomenon called snap-through buckling or snap buckling . A bistable mechanism has two stable equilibrium configurations. Snap-through buckling, unlike simple buckling, is characterized by a sudden change in shape when jumping to the other stable equilibrium configuration through an unstable configuration (Antman 2004). Snap-through buckling can be generated actively by using an actuator. A snap motor is typically represented as a loop mechanism consisting of a large deformable elastic rod, actuator for shape transition, and sufficiently stiff frame, as shown in Fig. 2.17.

In phase A in Fig. 2.17, the snap motor transitions from a stable equilibrium configuration to an unstable configuration by rotating the motor clockwise. In phase B, snap-through buckling occurs; that is, a sudden shape change from an unstable to stable configuration can be observed. In phase C, the snap motor takes a mirrored unstable configuration, as in phase A, by rotating the motor counterclockwise. In phase D, the snap motor undergoes snap-through buckling. Impulsive forces can be generated when the rod contacts an object during a phase shift from A to B or from C to D, where the rod shape changes drastically. This mechanism can effectively generate impulsive forces merely with the repeated motion of one rotational motor. The advantages and disadvantages of the snap motor are as follows:

Advantages

- The mechanism is simple, light, and compact.
- The mechanism does not have any sliding parts. Therefore, it cannot degrade due to wear.

- The mechanism can be repeated to generate impulsive forces with a rather high repeat frequency (about 0.5–2 Hz).

Disadvantages

- The mechanism is difficult to design because its main parts are continuum mechanisms.
- The mechanism is not suitable for generating large impulsive forces because a large elastic rod cannot move quickly due to its large inertia.

2.2.4 Exercises

1. Show some examples of continuum mechanisms and describe the actuators for the mechanisms.
2. Show some examples of elastic mechanisms and describe the actuators for the mechanisms.
3. Show some examples of bistable mechanisms and describe the actuators for the mechanisms.

References

Amend JR, Brown E, Rodenberg N, Jaeger HM, Lipson H (2012) A positive pressure universal gripper based on the jamming of granular material. IEEE Trans Robot 28(2):341–350

Antman S (2004) Nonlinear problems of elasticity, 2nd ed. Springer

Banconand G, Huber B (1982) Depression and grippers with their possible applications. In: 12th ISIR, Paris, pp 321–329

Brancadoro M, Manti M, Grani F, Tognarelli S, Menciassi A, Cianchetti M (2019) Toward a variable stiffness surgical manipulator based on fiber jamming transition. Front Rob AI 6(12):1–12

Camarillo DB, Milne CF, Carlson CR, Zinn MR, Salisbury JK (2008) Mechanics modeling of tendon-driven continuum manipulators. IEEE Trans Rob 24(6):1262–1273

Camarillo DB, Carlson CR, Salisbury JK (2009) Configuration tracking for continuum manipulators with coupled tendon drive. IEEE Trans Robotics 25(4):798–808

Cho H, Wu G, Jolly JC, Fortoul N, He Z, Gao Y, Jagota A, Yang S (2019) Intrinsically reversible superglues via shape adaptation inspired by snail epiphragm. PNAS USA 116(28):13774–13779

Dupont PE, Lock J, Itkowitz B, Butler E (2010) Design and Control of Concentric- Tube Robots. IEEE Trans. Robotics 26(2):209–225

Ganji Y, Janabi-Sharifi F (2009) Catheter kinematics for intracardiac navigation. IEEE Trans Biomed Eng 56(3):621–632

Hashem R, Stommel M, Cheng LK, Xu W (2020) Design and characterization of a bellows-driven soft pneumatic actuator. IEEE/ASME Trans Mechatron 26(5):2327–2338

Hayakawa Y, Morishita K, Aichi M, Thuda R (2004) Development of a pneumatic silicon outer fence mold actuator. Trans Jpn Soc Mech. Eng C 70(690):433–439

Hirose S, Umetani Y (1978) The development of soft gripper for the versatile robot hand. Mech Mach Theory 13(3):351–359

Hirose S (1987) Seibutsu Kikaikogaku (in Japanese). ISBN 978-4-7693-2068-5, Kogyo Chosakai Publishing Co., Ltd.

Hirose S, Kado T, Umetani Y (1983) Tensor-actuated elastic manipulator. Proc. of the Sixth World Congress on Theory of Mechanisms, 978–981.
Howell LL (2001) Comliant mechanisms. Wiley
Howell LL, Magleby SP, Olsen BM (Eds) (2013) Handbook of compliant mechanisms. Wiley
In H, Jeong U, Lee H, Cho K (2016) A novel slack enabling tendon drive that improves efficiency, size and safety in soft wearable robots. IEEE/ASME Trans Mechatron 22(1):59–70
Japan Robot Association (ed) Robot Kogaku Handbook (in Japanese), Corona Publishing Co., Ltd., pp 351–352. ISBN 4-339-04576-4
Kang BB, Lee H, In H, Jeong U, Chung J, Cho K (2016) Development of a polymer-based tendon-driven wearable robotic hand. In: Proceedings of the 2016 IEEE international conference on robotics and automation, pp 3750–3755
Kim Y-J, Cheng S (2013) A novel layer jamming mechanism with tunable stiffness capability for minimally invasive surgery. IEEE Trans Robot 29(4):1031–1042
Masuya K, Ono S, Takagi K, Tahara K (2017) Development of actuator unit consisting of multiple twisted and coiled polymer actuators. In: Proceedings of the 2017 JSME conference on robotics and mechatronics 2A1(A02) Fukushima, Japan, May 2017
Mochiyama H, Watari M, Fujimoto H (2007) Robotic catapult based on a closed elastica and its application to robotic tasks. In: Proceedings of the 2007 IEEE/RSJ international conference on intelligent robots and systems, pp 1508–1513
Morishita S (1996) Applications of electrorheological fluid and its feasibility. Inst Electron Inf Commun Eng 57(318):57–62
Mosadegh B, Polygerinos P, Keplinger C, Wennstedt S, Shepherd RF, Gupta U, Shim J, Bertoldi K, Walsh CJ, Whitesides GM (2014) Pneumatic networks for soft robotics that actuate rapidly. Adv Funct Mater 24(15):2163–2170
Motokawa T (1984) Katasa ga Subayaku Kawaru Ketsugososhiki (in Japanese). Dobutsu Seiri (in Japanese) 1(3):114–120
Nakai Y, Hoshino Y, Inaba M, Inoue H (2002) Softening deformable robot: development of shape adaptive robot using phase change of low-melting-point alloy. J Rob Soc Jpn 20(6):69–74
Niiyama R, Rus D, Kim S (2014) Pouch motors: printable/inflatable soft actuators for robotics. IEEE Int Conf Robot Autom (ICRA2014):6332–6337
Onda I, Ozawa Y, Watanabe M, Takane E, Tadakuma K, Konyo M, Tadokoro S (2020) Jamming transition mechanism that becomes high rigidity by pressure —invention and realization of fluid-driven variable stiffness mechanism. In: Proceedings of 2020 JSME conference on robotics and mechatronics, vol 1P2, no H10
Park Y, Lee J, Jeon S, Ahn H, Koh J, Ryu J, Cho M, Cho K (2016) Dual-stiffness structures with reconfiguring mechanism: design and investigation. J Intell Mater Syst Struct (JIMSS) 27(8):995–1010
Pettersson A, Davis S, Gray JO, Dodd TJ, Ohlsson T (2010) Design of a magnetorheological robot gripper for handling of delicate food products with varying shapes. J Food Engrg 98(3):332–338
Robinson G, Davies JBC (1999) Continuum robots—a state of the art. In: Proceedings of the 1999 IEEE international conference on robotics and automation, pp 2849–2854
Sasaki K, Ishii Y, Iizuka K (2020) Study of availability of slit tread construction for airless variable rigidity wheel. In: Proceedings 2020 JSME conference on robotics and mechatronics 2P2(C01), Kanazawa, Japan, May 2020
Sturges RH Jr, Laowattana S (1993) A flexible, tendon-controlled device for endoscopy. Int J Robot Res 12(2):121–131
Suzuki M, Kamamichi N (2016) Displacement control of antagonistic type Nylon fiber actuator. In: Proceeding 2016 JSME conference robotics and mechatronics 2P2(14b)
Suzumori K (1989) Flexible microactuator (1st report, static characteristics of 3 DOF actuator). Trans Jpn Soc Mech Eng C 55(518):2547–2552
Suzumori K, Iikura S, Tanaka H (1992) Applying a flexible microactuator to robotic mechanisms. IEEE Control Syst Mag 12(1):21–27

Tadakuma K, Tadakuma R, Teshigawara S, Mizoguchi Y, Hasegawa H, Terada K, Takayama T, Omata T, Ming A, Makoto S (2008) The morphing omnidirectional gripper "morphing Omni-gripper" with low melting point alloy. In: The 26th annual conference of the robotics society of Japan 1E1(01)

Tadakuma K, Tanaka H, Fukuda T, Higashimori M, Kaneko M (2010) Hyper flexible agent with variable stiffness and shape. SICE SI2010 2K1(4):1473–1476

Tadakuma K, Fujimoto T, Watanabe M, Shimizu T, Takane E, Konyo M, Tadokoro S (2020) Fire-Resistant deformable soft gripper based on wire jamming mechanism. In: 2020 3rd IEEE international conference on soft robotics (RoboSoft2020), pp 740–747

Takita K, Ochiai A, Aoki T, Hirose S (2004) Development of pneumatic-drive expandable arm to inspect narrow environments—development of the head camera unit. SICE SI2004 1B2(4):54–55

Tondu B (2012) Modelling of the McKibben artificial muscle: a review. J Intell Mater Syst Struct 23(3):225–253

Villegas D, Van Damme M, Vanderborght B, Beyl P, Lefeber D (2012) Third-Generation pleated pneumatic artificial muscles for robotic applications: development and comparison with Mckibben muscle. Adv Robot 26(11):1205–1227

Wang T, Zhang J, Li Y, Hong J, Wang MY (2019) Electrostatic layer jamming variable stiffness for soft robotics. IEEE/ASME Trans Mechatron 24(2):424–433

Webster RJ, Romano JM, Cowan NJ (2009) Mechanics of precurved-tube continuum robots. IEEE Trans Rob 25(1):67–78

Yamada A, Mochiyama H, Fujimoto H (2007) Kinematics and statistics of robotic catapults based on closed elastic. In: Proceedings of the 2007 IEEE/RSJ international conference on intelligent robots and systems, pp 3993–3998

Yamada A, Naka S, Morikawa S, Tani T (2014) MR compatible continuum robot based on closed elastica with bending and twisting. In: Proceedings of the 2014 IEEE/RSJ international conference on intelligent robots and systems, pp 3187–3192

Zhai Z, Wang Y, Jiang H (2018) Origami-inspired, on-demand deployable and collapsible mechanical metamaterials with tunable stiffness. PNAS USA 115(9):2032–2037

Chapter 3
Biological Mechanisms

Takeshi Yamasaki, Megu Gunji, Yoichi Masuda, and Akira Fukuhara

Abstract Collaboration between biology and robotics has been an important trend since before the establishment of modern soft robotics. The chapter began with a discussion of the possibilities of using robots for biological experiments, rather than solely one-way use of biological expertise by robot researchers. We then provide an overview of the musculoskeletal system as the body structure of an organism that combines hardness and softness.

3.1 Robotics-Inspired Biology

3.1.1 Basic Concepts

Swans are fascinating to watch as they fly, walk, swim, and collect food with their flexible necks. Such excellent motion abilities are fundamental for animals and useful for robots as well. Biorobotics is the field of developing robots that perform similarly to living organisms in terms of motion, senses, and other abilities (Ijspeert 2014). Biorobotics is closely related to soft robotics because living organisms are usually made of soft materials and frequently use the softness of their bodies to improve their performance [e.g., see (Tanaka et al. 2022)].

Understanding the motion and senses of living organisms may appear straightforward, but it is not. This problem is high-dimensional because it involves the

T. Yamasaki
Yamashina Institute for Ornithology, Abiko, Chiba, Japan
e-mail: yamasaki@yamashina.or.jp

M. Gunji (✉)
Department of Life Sciences, Faculty of Life Sciences, Toyo University, Ora-gun, Gunma, Japan
e-mail: gunji@toyo.jp

Y. Masuda
Department of Mechanical Engineering, Osaka University, Suita, Osaka, Japan

A. Fukuhara
Research Institute of Electrical Communication, Tohoku University, Sendai, Miyagi, Japan

K. Suzumori et al. (eds.), *The Science of Soft Robots*, Natural Computing Series,
https://doi.org/10.1007/978-981-19-5174-9_3

complex interaction of many elements, such as multiple neurons, muscle fibers, bones, tissues, and all environmental elements (Long 2012; Ijspeert 2014). Many of these elements are soft and transformable (Gravish and Lauder 2018). Moreover, this problem is highly nonlinear, as illustrated by the fact that doubling the amount of a single muscle contraction does not double the speed of motion (Ijspeert 2014). This problem is interdisciplinary because it requires an understanding of robotics and biology (Long 2012; Ijspeert 2014).

Because biorobotics is a collaborative effort between roboticists and biologists, research goals gravitate between robotics and biology (Ijspeert 2014; Iida et al. 2016; Gravish and Lauder 2018). In the former case, biorobotics can be considered a branch of robotics aimed at creating high-performance robots. From the latter standpoint, biorobotics is a branch of biology that aims to improve our understanding of living organisms. Here, biorobotics, as a branch of robotics, is defined as bio-inspired robotics, whereas biorobotics, as a branch of biology, is defined as robotics-inspired biology (Fig. 3.1). As almost all robots are inspired by living organisms in the broadest sense (Iida et al. 2016), bio-inspired robotics has as long a history as robotics itself. Robotics-inspired biology has a long history (Iida et al. 2016), but it has become particularly active since the end of the last century (Gravish and Lauder 2018).

The criteria for deeming a project successful are noticeably different because bio-inspired robotics and robotics-inspired biology have different goals. In bio-inspired robotics, organisms are the only starting point for design ideas. In this field, a project is considered successful if it eventually produces a method that is either better or easier to implement than alternatives in terms of attributes such as locomotor speed and energy efficiency (Ijspeert 2014). Thus, some projects in this field have failed to invest the effort required to fully comprehend biological principles. The term "biomimetic robotics" is occasionally used to distinguish from such research. This term emphasizes that robots are developed based on inspiration from living organisms and attempts to fully comprehend biological principles. However, some researchers avoid this term because it conveys the impression that imitating living things is the

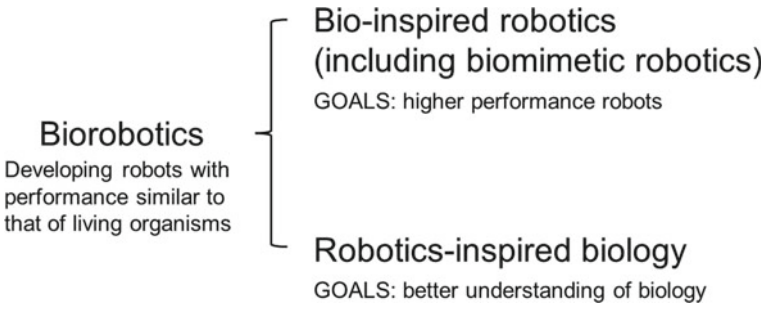

Fig. 3.1 Relationship between biorobotics, bio-inspired robotics, and robotics-inspired biology. These terminologies are used throughout this chapter although the terminologies used to refer to these disciplines are confusing and have no consensus (e.g., see (Webb 2002; Long 2012; Iida et al. 2016; Tamborini 2021))

goal per se (e.g., Griffiths and Page 2022). Although learning from living organisms is crucial, imitating them is not necessarily the best solution for developing high-performing robots. Although organisms have repeated the process of survival of the fittest over many generations, their design is not always optimal; biological designs are usually used for multiple purposes and thus represent a compromise. For example, the barn swallow *Hirundo rustica* uses its tail not only for flight but also to attract females (Møller 1988; Hasegawa 2018). Moreover, the design of organisms is strongly constrained by their evolutionary histories.

Conversely, robots have been developed as biological tools and are used to derive or test biological hypotheses in robotics-inspired biology. In this field, it does not matter whether a robot is elegant; a project is considered successful if it uses robots to produce biological knowledge (Ijspeert 2014). Robots have several properties that make them useful surrogates for experiments involving living organisms. Robots can replicate the same behavior many times, perform actions that are unnatural or dangerous in living organisms, provide access to variables that are difficult to measure in living organisms, and can systematically change their morphology (Ijspeert 2014).

This chapter details robotics-inspired biology, a hot topic in biorobotics in recent years. Although robotics-inspired biology has been successfully applied to various areas of biology, such as biomechanics, neuroscience, and swarm behavior (Webb 2002; Ijspeert 2014; Iida et al. 2016; Gravish and Lauder 2018), examples from evolutionary biology will be the focus of this section. Because hypotheses in evolutionary biology are particularly difficult to test, expectations are high for robotics-inspired biology vis-à-vis hypothesis testing.

3.1.2 How Do Traditional Biologists Test Their Hypotheses?

To understand why biologists now require robotics-inspired biology, let us examine the orthodox methods that biologists use to test their hypotheses. The evolution of the backbone in vertebrates is used as an example (Long 2012).

Vertebrates (i.e., mammals, birds, reptiles, amphibians, and fish) are known to be closely related to ascidians and lancelets (Fig. 3.2), based on evidence such as DNA and anatomical features (Satoh et al. 2014). These animals are collectively known as chordates. Chordates other than vertebrates have a collagen-like rod called the notochord, which serves as their "backbone," and they swim by bending it from side to side. (Ascidians swim only as larvae and live sedentary lives on the ocean floor as adults.) Conversely, vertebrates evolved the vertebral column, which is a collection of bones and/or cartilage that serve as their "backbone" (Kent and Carr 2001; Ota et al. 2011). There are approximately 70,000 living vertebrate species, which is considerably greater than the approximately 3000 living ascidian species and approximately 35 living lancelet species. Vertebrates, such as elephants, whales, humans, bats, eagles, turtles, snakes, frogs, and rays, also have more morphological diversity than the other two groups. Biologists have long wondered what caused this remarkable flourishing of vertebrates, technically called adaptive radiation (Schluter

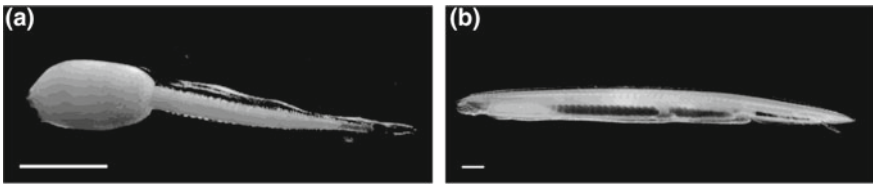

Fig. 3.2 Animals closely related to vertebrates. **a** Tadpole larva of *Syncarpa composita*, an ascidian species. **b** California lancelets, *Branchiostoma californiense*. Scale bars represent 1 mm. Reproduced under a CC BY 4.0 license from Hasegawa and Kajihara (2019) and Campos-Dávila et al. (2019), respectively

2000; Givnish 2015). A favorite hypothesis of biologists is that the evolution of vertebral bones is one of the key innovations that trigger adaptive radiation. A hard axial skeleton could have stored more elastic energy, allowing ancient fish to increase swimming speed and gain a competitive advantage (Long 2012).

This is a hypothesis regarding adaptation. According to biologists, adaptation is the process by which natural selection gradually changes the characteristics of a population of organisms over many generations. It occurs when (1) a trait, such as the backbone, varies among individuals, (2) the trait is partially encoded by genes, and (3) the trait affects the number of offspring produced. Darwin (1859) proposed this theory of evolution by natural selection, and ecological studies on living species, such as fieldwork measuring the beaks of Darwin's finches on a small islet in the Galapagos Islands over several decades, have now confirmed it (Grant and Grant 2008). However, testing hypotheses on adaptations that occurred a considerable time ago, such as the change from notochords to vertebral columns, is difficult. As we do not have time machines, we cannot use direct observations and must rely on circumstantial evidence. In other words, scenarios of such adaptive evolution can never be proven; biologists only consider hypotheses that pass numerous tests as highly plausible.

The statistical approach is an indirect test commonly used by biologists in adaptation studies. For example, biologists will study many living species to statistically determine whether it is possible to conclude that the harder the axial skeleton, the faster is the swimming speed. The discovery of a significant trend can greatly increase the plausibility of this hypothesis. However, this approach has several limitations, as detailed below.

First, collecting data on the variables of interest for many species is challenging, forcing biologists to compromise and use proxies for the variables. For example, it is impractical to collect exhaustive data on spine stiffness and maximum swimming speed. Long et al. measured spine stiffness in marlins and sturgeons, but this took several years for each species (for a review, see Long 2012). Thus, they used the number of vertebral bones as a proxy for this variable in species with spines based on the assumption that fewer vertebrae resulted in a stiffer backbone. They also used the propulsive wavelength, or the degree of body bending during swimming, as a proxy for the maximum swimming speed (Long and Nipper 1996; Long 2012).

They believed that vertebrates with longer propulsive wavelengths, such as tuna, often swim faster than those with shorter propulsive wavelengths, such as eels. However, because the variables of interest for most species have not been measured, we cannot rule out the possibility that the correlations between the variables and proxies are not as strong as we assumed. In this case, the conclusion that a stiffer backbone leads to a faster swimming speed cannot be drawn from the proxy data.

Second, the statistical approach for testing evolutionary scenarios has the additional problem of being unable to meet the assumption of data independence, which is the theoretical foundation of ordinary statistical procedures, because organisms have phylogenetic relationships. To overcome this problem, biologists have developed special statistical methods to test the significance of correlations among traits by considering the tendency of closely related species to resemble each other because of their shared history. These methods are called phylogenetic comparative methods (PCM) (for a review, see Garamszegi 2014). PCMs have been widely used because recent advances in DNA sequencing technology have made it possible to deduce phylogenetic trees with high accuracy.

Third, even if significant correlations among proxies are fortunately detected using PCM, there is still the well-known problem that correlations do not imply causation. Thus, correlation-based research methods that use proxies cannot sufficiently reduce the range of possible interpretations.

3.1.3 Experiments with Robots

As previously demonstrated, the statistical approach has limitations in testing hypotheses concerning adaptations that occurred a long time ago. Conducting experiments on living organisms could be another approach for further testing these hypotheses. For example, artificially hardening the notochords of lancelets and ascidian larvae by surgery could increase swimming speed. However, such surgeries are unlikely to succeed because they have various unforeseen side effects. Changing only the parameter of interest while keeping the other parameters constant is extremely difficult in experiments involving living organisms. What if we could build a robot of lancelets or ascidian larvae with the greatest precision? The stiffness of the robot's backbone can be altered without causing any unforeseen side effects. Biologists would be able to test this hypothesis further using such robots. This is the research style of robotics-inspired biology.

Various types of robots have been designed for robotics-inspired biology. First, depending on the testing method, two types of robots are typically employed to address evolutionary hypotheses. The first type consists of robots that are used as substitutes for the abovementioned surgical experiments on living organisms. These robots are built to estimate adaptive landscapes, which biologists commonly use to discuss adaptive evolution. The adaptive landscape is a plot of an individual's performance (ideally, the average number of offspring it produces, i.e., fitness) against a multidimensional space with the organism's traits as the axes (Schluter 2000). When

two traits of interest exist, the surface becomes rugged and is thus called a "landscape." Biologists can estimate possible adaptive evolutionary pathways using adaptive landscapes. Natural selection is expected to evolve the mean values of traits in a population of organisms in the direction of the upward slope of the adaptive landscape over generations. When the population reaches its peak, no further evolution is expected to occur. Robots created as models of the studied organisms are used to estimate adaptive landscapes. These robots are designed to allow for systematic variation of the traits of interest without any "side effects." A good estimate of the adaptive landscape can be obtained by measuring performance (e.g., speed and power consumption) for different trait values. Notably, this type of robot has the advantage of providing performance values for traits or a combination of traits to which no living organism has ever evolved. Long named this type of robot "Evolutionary Trekker" (ET) (Long 2012) based on its ability to travel through unexplored territories and the title of a well-known science fiction movie.

Long named the second type of robot "Evolvabot" (Long 2012). Thus, these robots can evolve. The concept of evolving robots was inspired by evolutionary robotics, which uses evolutionary principles in the robot production process (Long 2012; Nolfi et al. 2016). Because Evolvabots are designed for robotics-inspired biology, the goal is to test or derive biological hypotheses rather than improve performance. Evolvabots accomplish this by replicating the adaptive evolutionary process. For example, Long (2012) and his collaborators developed a robot called PreyRo (Long 2012), which mimics a Paleozoic fish and evolved a population comprising six individuals over ten generations in an experimental pool (Fig. 3.3a). The robots were designed to be attracted to light, which represents food. Moreover, a non-evolving robot called Tadiator was also placed in the experimental pool to mimic a predator of PreyRos, and PreyRo was designed to escape when it detected the predator with infrared proximity detectors. PreyRos exhibited variations in traits such as the number of vertebrae. The amount of light they gathered and their escape behavior from the predator were used to evaluate their performance in each generation. The traits of high-performing PreyRos were manually copied to produce the next generation of PreyRos. The number of vertebrae exhibited an evolutionary change in this experiment, which mimicked evolution by natural selection. However, after the seventh generation, the number of vertebrae remained almost unchanged, suggesting the presence of an optimal value. Long et al. concluded that the vertebral column has optimal stiffness because a soft axial skeleton improves maneuverability, whereas a hard skeleton improves speed.

Robots designed for robotics-inspired biology can also be classified based on how closely they mimic their target organisms. Robots that closely mimic their targets are called anchor models, whereas those that are highly abstract and simplified are called template models (Full and Koditschek 1999). One might believe that anchor models are always preferable when using robots to derive and/or test hypotheses about organisms. However, building such a robot is typically considerably expensive and requires additional skills and expertise. Furthermore, other than the specific features being studied, organisms have features related to various factors, such as foraging, metabolism, excretion, growth, and reproduction, but an elaborate replica

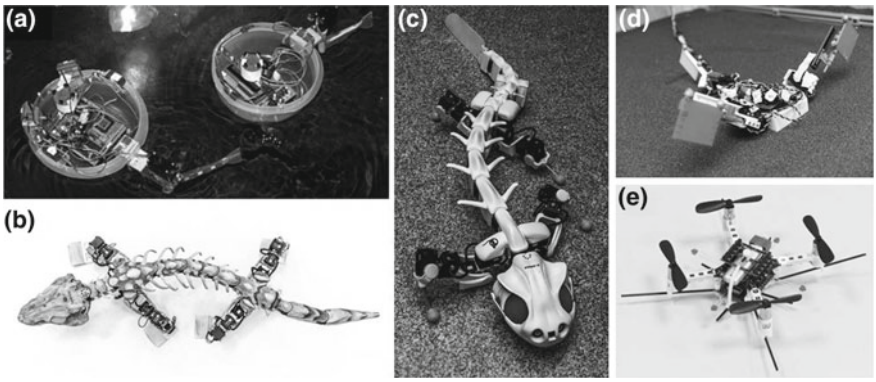

Fig. 3.3 Robots for robotics-inspired biology. **a** PreyRo (left) and Tadiator (right). Reproduced under a CC BY license from Roberts et al. (2014). **b** OroBot. Credit: Kamilo Melo, Tomislav Horvart, and Auke Ijspeert (EPFL Lausanne) and John Nyakatura (HU Berlin). **c** Pleurobot. Credit: Konstantinos Karakasiliotis and Robin Thandiackal (EPFL Lausanne). **d** MuddyBot. Credit: Rob Felt and Daniel I Goldman (Georgia Institute of Technology). **e** Quadcopter for studying a mosquito's flight. Republished with permission of American Association for the Advancement of Science from Nakata et al. (2020); permission conveyed through Copyright Clearance Center, Inc.

of all these would not help solve specific problems. These are the reasons why template models are created. Template models are simpler, save time, and allow for easier interpretation of experimental results. Anchor and template models are two extremes on a continuum of abstraction, rather than discrete categories. In robotics-inspired biology, selecting an appropriate level of abstraction for each problem along this continuum is essential. OroBot, a robot designed to reconstruct walking in early extinct terrestrial vertebrates (Nyakatura et al. 2019), and Pleurobot, a robot designed to study the neural control of walking and swimming in salamanders (Karakasiliotis et al. 2016), are examples of robots on the anchor model side of the continuum (Fig. 3.3b, c). The mudskipper-like robot MuddyBot, which suggests that tail movement may have been important when vertebrates first invaded the land (McInroe et al. 2016), and the quadcopter, which was used to develop the hypothesis that mosquitoes can fly in the dark without colliding with obstacles by sensing flow-field changes, are examples of robots on the template model side of the continuum (Nakata et al. 2020; Fig. 3.3d, e).

3.1.4 Why Use Robots Rather Than Computer Simulations?

As mentioned in the previous section, robots are used to perform simulation studies in robotics-inspired biology. A reader may ask, "Why do we bother building robots? Are computer simulations insufficient?" This is an important question to ask whenever

one is researching robotics-inspired biology because building robots is usually more expensive than creating computer simulations.

It is crucial to understand that computer simulations and building robots are complementary in robotics-inspired biology. Computer simulations offer the advantage of being able to explore a large parameter space in a relatively short time because, unlike robots, minimal effort is required to change their configurations. However, computer simulations involve many simplifications and approximations. Living organisms often have soft bodies that deform and move across rough ground, crumbling sand or mud, fluids, and other environments. The simplification and approximation of these factors can result in the accumulation of errors, thereby reducing the predictive power of computer simulations. When a sufficiently realistic physics engine cannot be prepared, building robots is better than computer simulations, as is typically the case. This is because robots can operate in the real world. When conducting research, one must consider whether computer simulations, robotic experiments, or both, are important.

3.1.5 Robotics-Inspired Biology: Where to Begin

Because robotics-inspired biology aims to derive and test biological hypotheses, it is not necessary to build well-performing and elegant robots. The identification of biologically interesting research topics is the most important factor. For this purpose, it would be beneficial to observe plants and animals from an engineer's perspective and read textbooks on topics such as evolutionary history (e.g., Colbert et al. 2001) and comparative anatomy (e.g., Kent and Carr 2001). It is also an excellent idea to contact researchers specializing in taxonomy, functional morphology, and animal behavior. When considering a research topic, it should be noted that, as previously mentioned, robots are most useful when a realistic physics engine is unavailable.

3.1.6 Challenges

The current surge in robotics-inspired biology has been largely due to the low cost and accessibility of electronic components (e.g., Arduino microprocessors), actuators (e.g., hobby servo motors), sensors (e.g., accelerometers and inertial measurement units (IMUs)), and fabrication equipment (e.g., three-dimensional printers and laser cutters) (Gravish and Lauder 2018). Traditionally, it has been difficult and time-consuming to design and modify robots, particularly from a biologist's perspective. Therefore, the use of robots to derive and/or test biological hypotheses has been impractical. The barriers to the use of robots for biological research have been lowered by the introduction of low-cost, easy-to-use tools, allowing engineering researchers and biologists to design their own mechanical systems and use robots in their research.

This trend is expected to continue. Robotics-inspired biology will become more prevalent in the future.

The field of robotics-inspired biology has flourished in recent years. However, many frontiers remain to be explored. Only a few of the many scenarios for important events in the history of biological evolution, such as the acquisition of spines and invasion into terrestrial environments in vertebrates, have been validated using robotics-inspired biology. Furthermore, many animal behaviors have unknown mechanisms, which opens many opportunities for significant discoveries from an engineer's perspective. For example, Nakata et al. (2020) proposed a hypothesis regarding the mechanism of mosquito flight in the dark. The interactions between the soft bodies of organisms and their environments are complex and difficult to study using computer simulations alone. Thus, it is a major unexplored field where the actual usefulness of robotics-inspired biological methods can be demonstrated.

3.2 Musculoskeletal System

3.2.1 Basic Concepts

To date, many researchers have developed bio-mimetic/bio-inspired robots with functionality based on the body structure of animals. In the field of soft robotics, several studies have focused on the research and development of bio-mimicking systems inspired by the movement and structure of animals and body parts that are completely soft, such as jellyfish, caterpillars, octopus' arms, and elephant trunks, as mentioned in other chapters of this textbook.

However, many characteristics of animals' bodies, other than softness, are of interest to robotics engineers. Arthropods (including crustaceans and insects), shellfish, and echinoderms, such as starfish and sea urchins, have hard exoskeletons made of chitinous material. Moreover, most vertebrates have hard skeletons that are composed mainly of calcium phosphate. These hard tissues function as an "armor" to protect vital tissues inside the body (e.g., the heart and lungs) and provide "leverage" to convert muscle contraction to rapid movement. In addition, especially in animals living on land, the skeleton plays a vital role in protecting the body against gravity.

Recently, by focusing on these characteristics, several soft robots that mimic the musculoskeletal systems of humans and animals have been developed using artificial muscles, whereas robotics engineers have extremely limited access to information about musculoskeletal systems. In this chapter, we briefly introduce the musculoskeletal system, which combines hardness and softness properties essential for the control of movement. We expect that understanding the musculoskeletal structures of various animals can provide hints for the development of soft robots that can achieve versatile behavior on land.

3.2.2 Musculoskeletal Robot

Several robots that mimic the musculoskeletal systems of animals have been developed. In particular, human body structure has been instrumental in the development of bipedal robots and robotic hands. In the field of soft robotics, several musculoskeletal robots that exhibit both rigidity and flexibility have been developed by attaching soft artificial muscles to a hard frame.

A variety of artificial muscles are available today, but pneumatic artificial muscles are convenient actuators for building animal-mimicking robots with sizes ranging from several tens of centimeters to a few meters. Compressed air acts as a spring, easily mimicking the elastic nature of animals. In fact, one study reported that the force–length characteristics of McKibben-type artificial muscles are similar to those of human and animal muscles. In addition, pneumatic actuators are safer than actuators that use heat, high voltage, chemical reactions, or liquids, such as water or oil. Moreover, there is no risk of chemical or liquid leakage. Although pneumatic actuators have excellent characteristics, certain difficulties arise in the development of robots. For example, the application of pneumatic actuators is limited owing to the requirement of an energy source when used in autonomous robots. Current pneumatic musculoskeletal robots quickly stop working without the use of a large pneumatic tank or a loud compressor.

Although some types of artificial muscles can be purchased, most of the latest artificial muscles are not commercially available. Nonetheless, researchers can test the performance of the state-of-the-art artificial muscles. Thus, most artificial muscles are handmade by researchers. Many recipes for designing artificial muscles using typical laboratory equipment have been provided by some researchers based on their studies. We encourage the readers to attempt some recipes and read the corresponding studies. For example, the famous McKibben-type pneumatic artificial muscles can be made for approximately $10–20 per unit. Detailed recipes are available for free at the Soft Robotics Toolkit, Open Soft Machines, and various other websites. We also recommend using a fishing coil actuator, which is inexpensive and easy to prepare.

In addition, recently, realistic skeletal models and CT data of various animals have become available as open sources (e.g., DigiMorph or museum accounts on Sketchfab). It is possible to develop a musculoskeletal robot by printing skeletal models using a 3D printer and attaching artificial muscles to them. For example, if artificial muscles are attached to a Tyrannosaurus skull model, opening and closing of the model's mouth can be achieved. Through this approach, even beginners can have fun and learn about artificial muscles and skeletal models.

Although certain limitations still hinder their large-scale development and application, various artificial muscles have been developed for use in the field of robotics, and musculoskeletal robots are gradually gaining attention.

3.2.3 Basic Knowledge of Major Musculoskeletal Component

The knowledge of basic animal body structures is critical to the development of musculoskeletal robots. In this section, we explain the structure and function of a musculoskeletal robot by focusing on the three most fundamental elements: bones, muscles, and ligaments.

1. Bones

Bones have a wide variety of functions in animals, including serving as a lever for muscle contraction, protecting vital organs from trauma, storing calcium and fat, and generating blood. Bones have different morphologies in different parts of the body; some bones are large and elongated, whereas others are small and round. Even the skeletal components considered as having a homological relationship can vary greatly in shape from one animal species to another. The skull and jaw bones show an adaptive shape related to feeding habits, and limb skeletons exhibit a shape strongly influenced by the locomotion type. The joint structure also differs from position to position in the body. Generally, in robots, joints are designed as simple hinge joints to generate bending motion and produce the same functionality for every part. However, in animals, the shape of joints varies from body part to body part. For instance, the hip is a ball-and-socket joint, and the elbow is a hinge joint. Moreover, some joints move only marginally in animals. An approximate classification of the joint types is shown in Fig. 3.4.

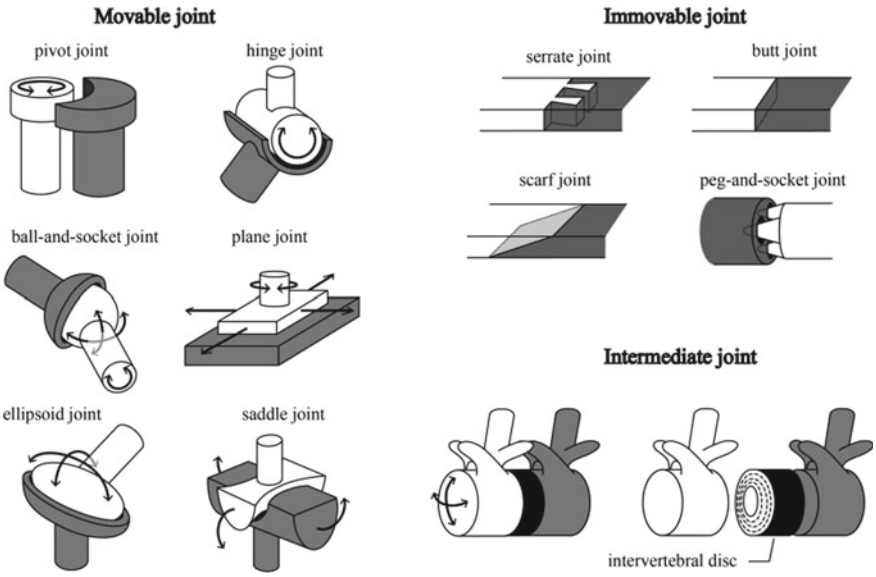

Fig. 3.4 Rough classification and examples of each joint type in vertebrate animals

As most readers know, bone is a hard component. The general Young's modulus of bone is approximately 10 GPa. Interestingly, however, the mechanical properties of bones are not uniform in animals, and this value generally varies from 4 to 33 GPa, depending on the morphology, internal structure, mineral content, and other factors (Turner 2006). For example, a whale's auditory bulla (a hollow bony structure surrounding the middle ear bones) is known to be a bone with high mineral content and high Young's modulus, which is considered an adaptation for whales to gain acoustic impedance in water. In contrast, deer antlers are bones with a relatively low Young's modulus, which makes them less prone to fracture. An extreme example of "soft" bone is the bone in the wingtip of the Mexican free-tailed bat (*Tadarida brasiliensis*). It has no detectable mineral content, and its elastic modulus is approximately 1.5 GPa. These "soft" bone features are important in the development of biomimetic and bio-inspired flying robots.

Soft cartilage also exists around the hard skeleton. Cartilage has a porous structure composed mainly of proteoglycans and collagen and contains a large amount of synovial fluid. When pressure is applied, synovial fluid is pushed outward from inside the cartilage, dispersing the impact load and protecting the bone surface from excessive stress while simultaneously achieving low friction. Plate-like cartilages exist between bones at joints subjected to large forces, such as the jaw and knee joints, which play a role in dispersing impact loads and reducing friction, and then contribute to improving joint stability. In many musculoskeletal robots, bones are often implemented as rigid frames made of a single material. However, as described above, actual bones do not exhibit only a single property.

2. Muscles and tendons

Muscles are the primary actuators in animals. There are three types of muscles in the animal body: cardiac, smooth, and skeletal. The first is the muscle that moves the heart; the second moves the internal organs, and the third is found around the skeleton and causes body movement. Skeletal muscles are further divided into two types according to the type of muscle fiber: fast and slow. The former is composed of fibers that contract quickly but fatigue easily and is suitable for instantaneous motion. The latter is composed of fibers that contract slowly but do not fatigue easily and is a muscle that exhibits high endurance. The bodies of animals are composed of a combination of these muscles and the balance between fast and slow muscles varies among species. Moreover, the muscles function as sensors. There is a sensory organ called a muscle spindle in skeletal muscles that detects and provides feedback on the state of contraction and extension of the muscles. Some robotic researchers have focused on this sensory organ, and several musculoskeletal robots have been developed with these control systems (e.g., Yamada et al. 2011).

At each end of the muscle, there is a hard connective tissue called a tendon that mediates muscle to bone. Its function is to transmit the mechanical force of muscle contraction to the bones. Most tendons are relatively stiff tissues composed of collagen. However, some tendons are highly elastic and can store elastic energy during movement. For instance, the tendon of the gastrocnemius muscle located in the lower hindlimbs, called the Achilles tendon, is responsible for transmitting muscle

force and storing elastic energy during running or hopping. There is also a sensory organ in the tendon called the Golgi tendon organ, which senses the tension applied to the tendon. This prevents tendons from being damaged by excessive tension.

Like bones, muscles have a variety of shapes. Some are simple spindle-shaped muscles that connect two points, whereas other muscles are flat with a wide attachment surface to the bone. Note that if a plate-shaped muscle is implemented with a linear actuator connecting two points, it may not fulfill its original function. Although the external appearance of muscles is similar, the direction of muscle fibers is sometimes different. Some run parallel to the long axis of the muscle, whereas others run at an angle to the long axis. The length of each muscle fiber and total number of muscle fibers are different between these two muscles, even if the muscles have the same volume and length. In other words, even if the external form is the same, the force exerted can be different. Technically, it is virtually impossible to accurately measure all muscle forces using active animals, but the physiological cross-sectional area (PCSA) is commonly used to estimate muscle force (θ: fiber angle to the direction of action of the muscle, ρ: muscle density; see the equation given below) (Sacks 1982). As the balance of muscle antagonism is very important in the musculoskeletal system, it is vital to examine the characteristics of each muscle using indices such as PCSA, as well as simple external shape and weight. Note that errors may occur even when they are used as approximations.

$$\text{PCSA} = \frac{\text{Muscle mass}(g) \times \cos\theta}{\rho \times \text{fiber length}}$$

Additionally, muscles play a role in defining the maximum range of motion of a joint and immobilizing the area around the joint. Examples of the beneficial use of motion limitations owing to muscles and tendons are discussed in detail in Sect. 3.2.4.

3. Ligaments

The ligament is a connective tissue primarily composed of collagen. Tendons and ligaments are very similar in composition. Tendons are tissues that join muscles and bones, whereas ligaments are tissues that join bones. Ligaments vary in shape and size. Some look like strings, thin bands, and broad bands, whereas others are arch-like. The main functions of ligaments are to stabilize joints passively, assist in guiding those joints through their normal range of motion when a tensile load is applied, and sometimes limit the range of motion. Tunnel-shaped ligaments function to hold tendons from floating. In addition, banded ligaments stabilize muscles and tendons (Fig. 3.5). Such structures are particularly important in multi-articular muscles that are attached to several joints. The Young's modulus of the ligaments varies widely among animal species, body regions, and age.

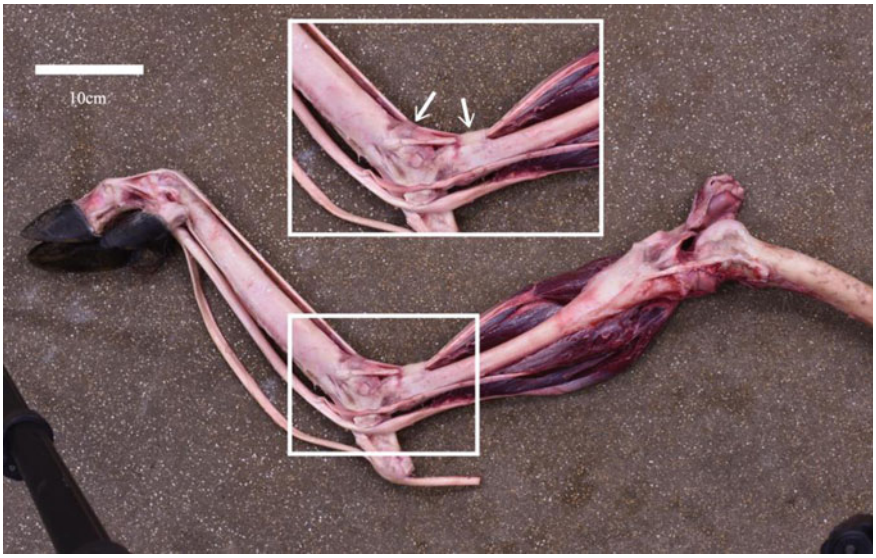

Fig. 3.5 Musculoskeletal structure of the hindlimb in reindeer (*Rangifer tarandus*). The tendon of the long digital extensor muscle that connects from distal part of femur to digit is held by two banded ligaments (arrows in enlarged view) at hock joint. This image is of a specimen donated to the National Museum of Nature and Science, Tokyo (Japan) after it died of natural causes at a zoo

3.2.4 Key Anatomical Mechanism

Until now, we have described the elements that constitute the animal body. In this section, we will introduce the mechanisms that emerge from the integration of these elements from the following two perspectives: the shock-absorbing mechanism and gravity compensation mechanism. The musculoskeletal system of animals has various features and mechanisms that are not present in next-generation musculoskeletal robots. We hope that you will enjoy learning about the great mechanisms of animal body structure.

1. Shock absorbing mechanism

Several shock-absorbing mechanisms exist in the skeletal systems of animals. An example is the immobile joint (Fig. 3.4). This joint type is tightly connected by cartilage or connective tissue, such as a tendon or ligament, and is rarely involved in body movements. Such joints can be flexible enough to provide slight shock absorption, although they are "immovable." This makes them very effective structures that allow hard bones to withstand strong compressive and shear forces without breaking. For example, the teeth are connected to the jawbones by peg-and-socket joints, with cartilage present in the gap. The cartilage absorbs the impact of biting hard objects and prevents damage to the roots of the teeth and jawbone. It also provides a strong bond between the teeth and jawbone.

Furthermore, the intermediate joint acts as a shock absorber. This joint is firmly fixed by strong ligaments and exhibits higher mobility than immobile joints but less mobile than mobile joints. A typical example of this type is the joint between the vertebrae in mammals. In mammals, soft tissue known as the intervertebral disk exists between the vertebrae, and a ring-shaped ligament, known as the annulus fibrosus, joins the two bones (Fig. 3.4).

Furthermore, some animals absorb shock through "loose" joints that do not involve the skeletal system. For instance, in quadrupeds specialized for running (e.g., horses), the scapula is fixed to the trunk only by multiple muscles, without skeletal joints. This loose coupling allows rotational and translational movement of the forelimb basement in the sagittal plane. This structure assists in the absorption of the load applied to the forelimbs during walking and running. It also contributes to positioning the scapula over a wider area of the body and increases the "reach" of the forelimbs.

2. Gravity compensation mechanism

Gravity compensation mechanisms are extremely interesting and important for robots and terrestrial animals. Because energy is finite for animals, some animals undergo gravity compensation mechanisms that enable them to minimize energy consumption as much as possible during rest. This mechanism has been acquired by these animals through evolution.

One example is a joint-stabilizing mechanism that activates during standing using muscle and tendon structures known as the stay apparatus. This is commonly observed in hoofed animals such as horses and giraffes. The major components of the stay apparatus are the deep and superficial digital flexor muscles, which are the typical flexor muscles of the forelimbs. These muscles connect the humerus to the phalanges, possess less compliant and stronger tendons at their distal ends, and interlock the motion of the elbow, carpal, and fetlock joints (Fig. 3.6a). The weight load during standing applies a force in the direction of flexion of each joint and passively lengthens the digital flexor muscles and their tendons. When the tendons achieve equilibrium length, the elbow and fetlock joints are no longer flexed and fixed. Using a similar mechanism, the biceps brachii muscle fixes the shoulder joint while standing (Fig. 3.6a).

Another example is the nuchal ligament that supports the neck and head against gravity. This ligament connects the thorax to the head and neck and has a significantly low Young's modulus with abundant elastin. It generally develops in the cervical region of quadrupeds and passively supports the weight of the neck and head (Fig. 3.6b). The unique "death pose" posture observed in fossil species is due to the contraction of the nuchal ligament when they lie down after death. Furthermore, previous studies have suggested that the nuchal ligament allows the neck to move at the right time during gait, contributing to efficient center-of-gravity transfer during locomotion.

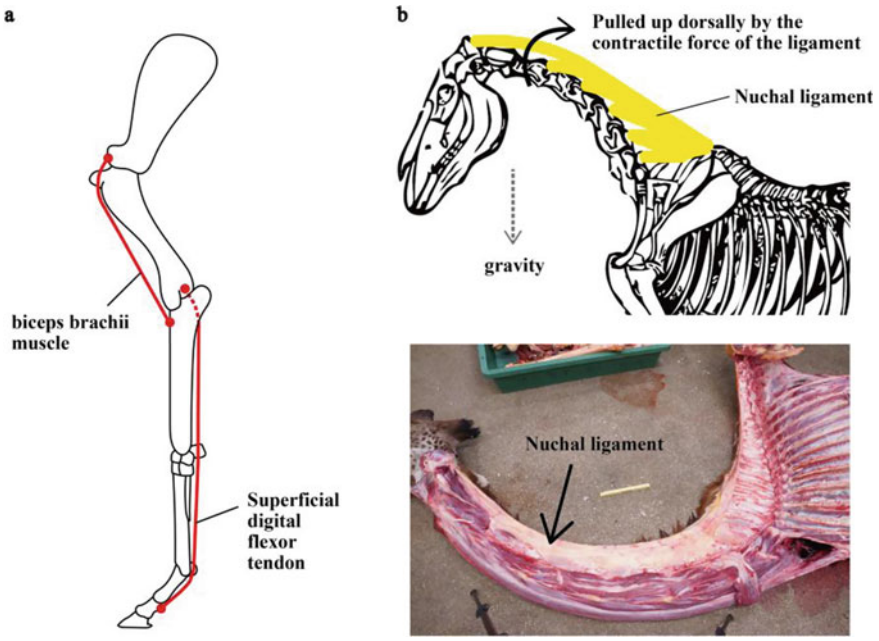

Fig. 3.6 Example of gravity compensation mechanism found in animal body. **a** The musculoskeletal structure called stay apparatus. The biceps brachii muscle prevents the flexion of the shoulder joint and the superficial digital flexor muscle prevents the flexion of elbow joint. **b** The structure of nuchal ligament. Upper image shows a rough explanation of this system, and lower shows a nuchal ligament in giraffe. Note that this is specimen was donated to the National Museum of Nature and Science, Tokyo (Japan) after it died of natural causes at a zoo

3.2.5 How to Start Anatomical Research

As mentioned above, the musculoskeletal structure of animals is an excellent soft system and is expected to provide novel perspectives for the development of soft robots. How can robotics researchers gain anatomical knowledge?

The simplest method is to read a textbook on human or veterinary anatomy. These textbooks contain detailed descriptions of the musculoskeletal structures of animals, such as humans, dogs, and cows, as well as the primary functions of each muscle (e.g., flexion of the elbow). However, as these textbooks are written in a descriptive manner with many technical terms, it may be difficult for beginner students to read them thoroughly. In addition, they are generally written for the purpose of the diagnosis and treatment of diseases, and only a few refer to the function of the structures. If you want to know more about the mechanisms of body structures, as mentioned in 3.2.3, we recommend reading a textbook on functional morphology or comparative anatomy that deals with animal evolution (e.g., Hildebrand and Goslow 2001; Liem et al. 2001). These mechanisms are not often presented in medical and veterinary textbooks, but they are the basic content in classic textbooks on functional anatomy

and comparative morphology. These textbooks are often structured to introduce the adaptive mechanisms of body structures corresponding to topics, such as swimming, fast running, and flight. Therefore, readers can easily select topics that match their interests. These textbooks also feature specialist species adapted to specific environments (e.g., animals living in the deep sea or underground). We hope that these resources will aid in the development of unique robots that perform well in specific environments.

The best way to truly understand the body structure of an animal is to dissect it and observe it in person. Even if you are not an expert in anatomy, it is not difficult to begin animal dissections. Some readers may have purchased whole fish or meat, "dissected" it with a knife in their own kitchen and eaten it for dinner. An interesting exercise could be the following. Suppose you buy a whole chicken. Try to remove the chicken breast and chicken tenderloin. These muscles connect the wings to the breasts. Separate them from the breastbone, leaving the part attached to the wing side. You can observe how the wings flap by pulling on the muscles that have been separated. If you pull on the breast meat, the wing swings down; if you pull on the chicken tenderloin, the wing swings up. Observing the structure of the tendons and skeletal mechanisms will be a great dissection. In addition to chickens, a variety of other animals are sold as meat, including pigs, rabbits, ostriches, and crocodiles. Thus, it is possible to compare the musculoskeletal structures between these species. In addition, using meat animals as specimens for dissections solves the problem of ethical issues in research.

The tissue may get damaged in the first trial. However, as you gain knowledge and experience, you will be able to separate tissue sections successfully. The key point is to carefully separate the tissue in a cold room with an appropriately sharp knife and tweezers. We recommend that you decide on the target part or tissue and take the time to dissect it while observing and sketching it carefully.

3.2.6 Challenges

Musculoskeletal robots usually have complex structures consisting of many elements and are often characterized by robustness and versatility. These characteristics are very important for the development of practical robots, whereas quantitatively evaluating these features and comparing them with those of conventional robots is surprisingly difficult. This problem is particularly pronounced when developing robots that can comprehensively mimic an animal's body. Simplifying the robot structure has the advantages of creating specific functions that are emphasized in research projects and facilitating the evaluation of robot performance, such as energy efficiency. However, with simplification, creating systems that are inherently as versatile as the animals is more difficult.

Additionally, in the anatomical field, while we have abundant knowledge about static functions, our understanding of dynamic functions is poor. This is because anatomy is often learned by studying cadavers. Some studies have investigated the

state of the muscles and skeleton during exercise using electromyography or X-ray movies and have discussed dynamic function by musculoskeletal simulation, but gaps in knowledge remain. In other words, it is quite possible that structures overlooked in traditional anatomy exhibit great performance in dynamic movements. Surprisingly, the detailed functions of some tissues and structures are still not known, even in the human body. For example, fascia (the tissue that surrounds muscles) is distributed throughout the body, yet its specific role is still largely unknown. These tissues and structures are often described in simplified form in anatomy textbooks, sometimes even entirely omitted. The next generation of musculoskeletal robots that combine artificial muscles with real skeletal models may contribute to solving problems and challenges in the field of anatomy.

Finally, many structures in animal bodies have not yet been investigated in the field of robotics. This chapter focuses on the body skeleton. The integrated system of soft and hard tissues is also important, even in very soft internal organs. For example, the cardiac skeleton, commonly formed in the heart of large ruminants, serves as an attachment site for cardiac muscles. It also provides rigidity to prevent the dilation of the valves and outflow tracts. Furthermore, the baculum that forms inside the penis is frequently found in rodents and carnivores. It prevents deformation of the urethra during copulation. This contributes to the maintenance of a channel for sperm flow. We hope that further research focusing on such structures will lead to the development of robots that go far beyond conventional musculoskeletal robots.

Exercises

1. (3.1) Describe the difference between bio-inspired robotics and robotics-inspired biology.
2. (3.1) Explain the advantages and disadvantages of computer simulations and robot construction in robotics-inspired biology.
3. (3.1) Explain anchor and template models.
4. (3.2) Find and read articles about musculoskeletal structure and its function in the fields of functional morphology and comparative anatomy.
5. (3.2) Buy whole chickens or fish from the supermarket, dissect them with a cutter and scissors, and observe their musculoskeletal system.
6. (3.2) Print a skeletal model of an animal available on the Internet using a 3D printer, attach strings or artificial muscles to it, and make it move.

References

Campos-Dávila L, Pérez-Estrada CJ, Rodríguez-Estrella R, Morales-Bojórquez E, Brun-Murillo FG, Balart EF (2019) Seagrass *Halodule wrightii* as a new habitat for the amphioxus *Branchiostoma californiense* (Cephalochordata, Branchiostomidae) in the southern Gulf of California, Mexico. ZooKeys 873:113–131

Colbert EH, Morales M, Minkoff EC (2001) Colbert's evolution of the vertebrates: a history of the backboned animals through time. Wiley-Liss, New York

Darwin C (1859) On the origin of species by means of natural selection, or the preservation of favoured races in the struggle for life. John Murray, London
Full RJ, Koditschek DE (1999) Templates and anchors: neuromechanical hypotheses of legged locomotion on land. J Exp Biol 202(23):332532
Garamszegi LZ (ed) (2014) Modern phylogenetic comparative methods and their application in evolutionary biology: concepts and practice. Springer, Berlin Heidelberg
Givnish TJ (2015) Adaptive radiation versus 'radiation' and 'explosive diversification': why conceptual distinctions are fundamental to understanding evolution. New Phytol 207(2):297–303
Grant PR, Grant BR (2008) How and why species multiply: the radiation of Darwin's finches. Princeton University Press, Princeton
Gravish N, Lauder GV (2018) Robotics-inspired biology. J Exp Biol 221(7)
Griffiths Z, Page J (2022) Biomimicry or bio-inspired design? https://www.animal-dynamics.com/ad-blog/2019/4/10/biomimicry-versus-bio-inspired-design. Accessed 18 Jan 2022
Hasegawa M (2018) Sexual selection mechanisms for male plumage ornaments in Japanese Barn Swallows. Ornithol Sci 17(2):125–134
Hasegawa N, Kajihara H (2019) A redescription of *Syncarpa composita* (Ascidiacea, Stolidobranchia) with an inference of its phylogenetic position within Styelidae. ZooKeys 857:1–15
Hildebrand M, Goslow GE (2001) Analysis of vertebrate structure. Wiley, New York
Iida F, Ijspeert AJ (2016) Biologically inspired robotics. In: Siciliano B, Khatib O (eds) Springer Handbook of Robotics. Springer International Publishing, Cham
Ijspeert AJ (2014) Biorobotics: using robots to emulate and investigate agile locomotion. Science 346(6206):196–203
Karakasiliotis K, Thandiackal R, Melo K, Horvat T, Mahabadi NK, Tsitkov S, Cabelguen JM, Ijspeert AJ (2016) From cineradiography to biorobots: an approach for designing robots to emulate and study animal locomotion. J R Soc Interface 13(119):20151089
Kent GC, Carr RK (2001) Comparative anatomy of the vertebrates. McGraw Hill, New York
Liem KF, Benis WE, Walker WF, Grande L (2001) Functional anatomy of the vertebrates: an evolutionary perspective. Harcourt College Publishers, Fort Worth
Long JH Jr (2012) Darwin's devices: what evolving robots can teach us about the history of life and the future of technology. Basic Books, New York
Long JH Jr, Nipper KS (1996) The importance of body stiffness in undulatory propulsion. Am Zool 36(6):678–694
McInroe B, Astley HC, Gong C, Kawano SM, Schiebel PE, Rieser JM et al (2016) Tail use improves performance on soft substrates in models of early vertebrate land locomotors. Science 353(6295):154–158
Møller AP (1988) Female choice selects for male sexual tail ornaments in the monogamous swallow. Nature 332(6165):640–642
Nakata T, Phillips N, Simões P, Russell IJ, Cheney JA, Walker SM, Bomphrey RJ (2020) Aerodynamic imaging by mosquitoes inspires a surface detector for autonomous flying vehicles. Science 368(6491):634–637
Nolfi S, Bongard J, Husbands P, Floreano D (2016) Evolutionary robotics. In: Siciliano B, Khatib O (eds) Springer Handbook of Robotics. Springer International Publishing, Cham
Nyakatura JA, Melo K, Horvat T, Karakasiliotis K, Allen VR, Andikfar A, Andrada E, Arnold P, Lauströer J, Hutchinson JR, Fischer MS, Ijspeert AJ (2019) Reverse-engineering the locomotion of a stem amniote. Nature 565(7739):351–355
Ota KG, Fujimoto S, Oisi Y, Kuratani S (2011) Identification of vertebra-like elements and their possible differentiation from sclerotomes in the hagfish. Nat Commun 2(1):373
Roberts SF, Hirokawa J, Rosenblum HG, Sakhtah H, Gutierrez AA, Porter ME, Long JH (2014) Testing biological hypotheses with embodied robots: adaptations, accidents, and by-products in the evolution of vertebrates. Front Rob AI 1
Sacks RD, Roy RR (1982) Architecture of the hind limb muscles of cats: functional significance. J Morphol 173:185–195

Satoh N, Rokhsar D, Nishikawa T (2014) Chordate evolution and the three-phylum system. Proc Roy Soc b: Biol Sci 281(1794):20141729

Schluter D (2000) The ecology of adaptive radiation. Oxford University Press, Oxford

Tamborini M (2021) The material turn in the study of form: from bio-inspired robots to robotics-inspired morphology. Perspect Sci 29(5):643–665

Tanaka H, Nakata T, Yamasaki T (2022) Biomimetic soft wings for soft robot science. J Robot Mechatron 34(2):223–226

Turner CH (2006) Bone strength: current concepts. Ann N Y Acad Sci 1068:429–446

Webb B (2002) Robots in invertebrate neuroscience. Nature 417(6886):359–363

Yamada Y, Nishikawa S, Shida K et al (2011) Neural body coupling for emergent locomotion: a musculoskeletal quadruped robot with spinobulbar model. In: IEEE/RSJ international conference on intelligent robots and systems, pp 1499–1506

Chapter 4
Soft Manipulation and Locomotion

Shinichi Hirai, Ryuma Niiyama, Taro Nakamura, Takuya Umedachi, Toshiyuki Nakata, and Hiroto Tanaka

Abstract Soft mechanisms bring a new twist to traditional robotics challenges of object grasping, manipulation, and locomotion. Soft robotic hands are a topic of growing industrial application. A major example of a soft manipulator is a continuum robot arm, which has different features from our human arms. For locomotion, we introduce approaches unique to soft mechanisms, such as peristaltic motion using a deformable body and propulsive motion through interaction with fluid using fins and wings.

S. Hirai
Ritsumeikan University, Shiga, Japan
e-mail: hirai@se.ritsumei.ac.jp

R. Niiyama (✉)
Graduate School of Science and Technology, Meiji University, Kanagawa, Japan
e-mail: niiyama@meiji.ac.jp

T. Nakamura
Chuo University, Hachioji, Japan
e-mail: nakamura@mech.chuo-u.ac.jp

T. Umedachi
Shinshu University, Nagano, Japan
e-mail: umedachi@shinshu-u.ac.jp

T. Nakata
Graduate School of Engineering, Chiba University, Chiba, Japan
e-mail: tnakata@chiba-u.jp

H. Tanaka
School of Engineering, Tokyo Institute of Technology, Tokyo, Japan
e-mail: tanaka.h.cb@m.titech.ac.jp

K. Suzumori et al. (eds.), *The Science of Soft Robots*, Natural Computing Series,
https://doi.org/10.1007/978-981-19-5174-9_4

4.1 Soft Robot Hands

4.1.1 Basic Concept

End-effectors are devices attached to the end points of robot manipulators to manipulate target objects or interact with the environment. For example, when humans peel oranges or apples using their hands or knives, the hands or knives function as end-effectors *grasping* and *manipulation* are important end-effector actions. End-effectors for grasping and manipulation are often called *robotic hands* or *grippers*.

Let us consider the task of picking up a target object from a table (Fig. 4.1a). As the gravitational force acts on the object, lifting forces are applied to the target object against the gravitational force. The lifting forces can be generated directly (Fig. 4.1b) or indirectly as frictional forces (Fig. 4.1c). In direct generation, a robotic hand applies lifting forces to a target object. Surface forces, such as adhesive and electrostatic forces, as well as fluidic forces, such as suction and Bernoulli forces, are direct lifting forces. Depending on the shape of the target object, contact forces can act as lifting forces. When surface forces or fluidic forces are applied, the robot's hands do not have to contact the target objects but should be close to the objects to generate sufficient lifting forces. In indirect generation, a robot hand employs contact forces on a target object, yielding frictional forces that act as lifting forces. Such indirect generation of lifting forces requires contact between the robot's hands and target objects. For example, human fingers contact target objects in our daily lives; therefore, the frictional forces between the fingers and objects act as lifting forces.

Target objects suffer from the risk of being damaged due to contact with robot hands composed of hard materials. Thus, robotic hands composed of soft materials were proposed to reduce the risk (Brown 2010; Ilievski 2011; Fantoni 2014; Shintake 2018; Hao 2021; Wang 2022). Soft robotic hands are categorized as follows:

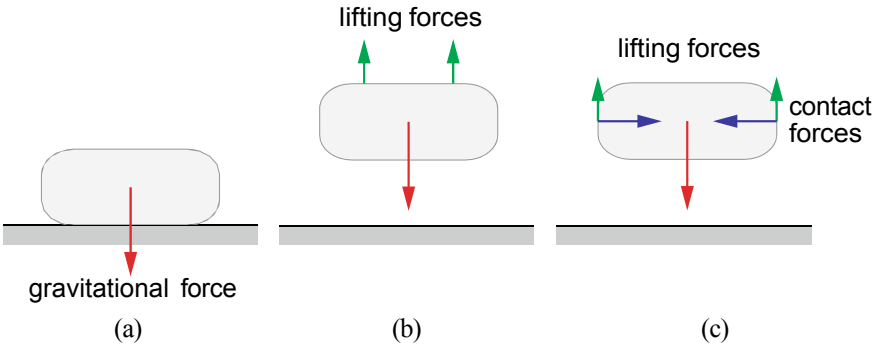

Fig. 4.1 Picking up a target object from a table

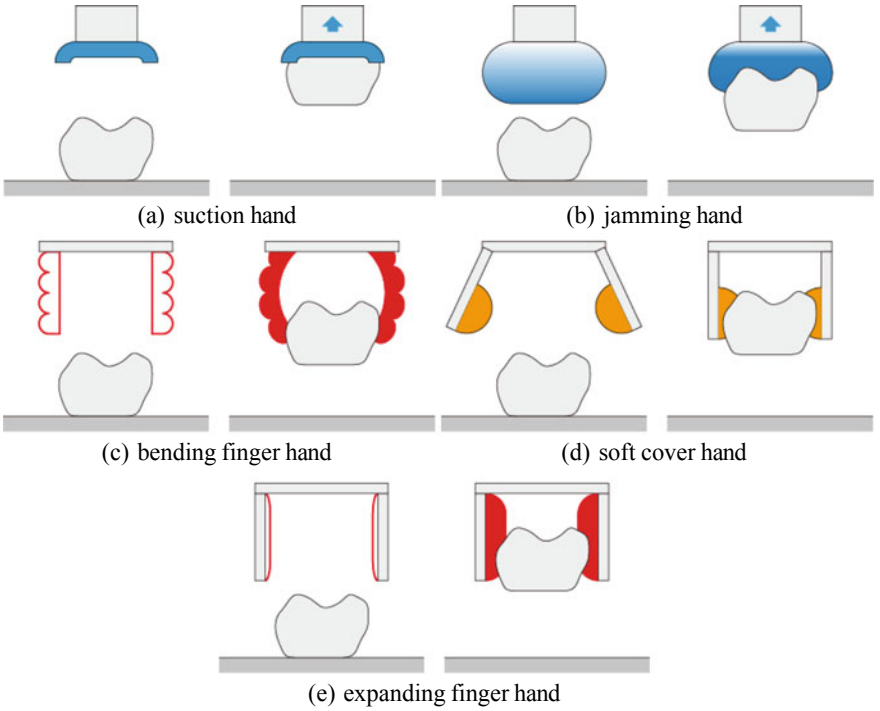

Fig. 4.2 Soft hand categories

- suction hands (Fig. 4.2a)
- jamming hands (Fig. 4.2b)
- bending fingers hands (Fig. 4.2c)
- soft cover hands (Fig. 4.2d)
- expanding fingers hands (Fig. 4.2e)

Suction hands generate lifting forces directly, whereas jamming, bending fingers, soft cover, and expanding fingers hands generate lifting forces indirectly. This section introduces soft robot hands.

4.1.2 Suction Hands

Suction hands (Fig. 4.2a) generate lifting forces by reducing the pressure inside suction cups. Suction cups are made of soft materials to absorb the impact when they contact the target objects and maintain negative pressure inside the cups. Various suction hands are commercially available because of their simple structure and low cost. When the contact surface of a target object is smooth and flat, the suction hand can generate a large lifting force. However, suction hands are not effective when the

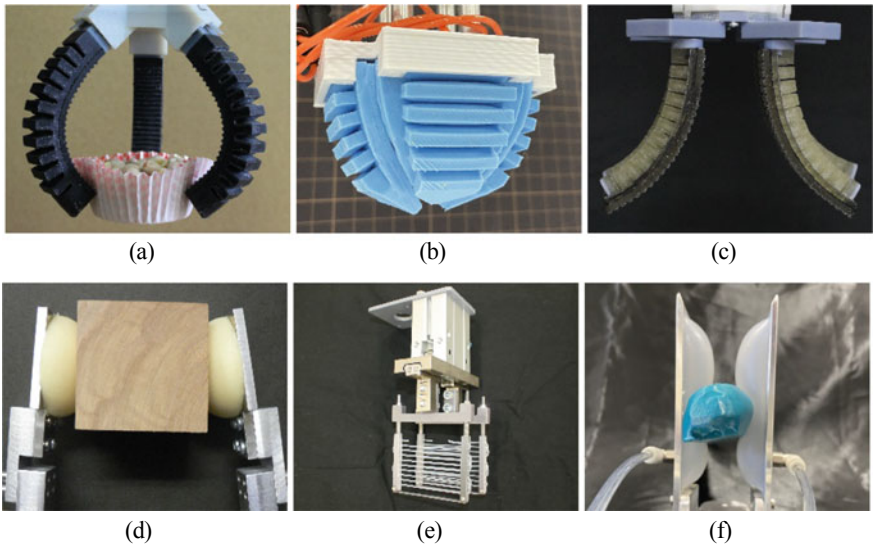

Fig. 4.3 Examples of soft hands

surface is uneven, which may cause a gap between the cups and the surface, resulting in insufficient lifting force. If the surface collapses, the suction hand absorbs the impact on the collapsed surface and reduces suction pressure (Fig. 4.3).

4.1.3 Jamming Hands

Jamming hands consist of elastomer bags and powders (Fig. 4.4a). The bags are filled with the powders. In the natural state, friction between the powders is small, resulting in an external force that easily deforms the bag. When a jamming hand is pushed into a target object in its natural state, the bag deforms according to the object's surface (Fig. 4.4b). When a negative pressure is applied inside the bag, the powders are pushed against one another, increasing the contact forces between the powders. As a result, the frictional forces between the powders increase, making the bag stiff. The bag remains deformed along the object's surface, enabling the target object to be lifted (Fig. 4.4c).

4.1.4 Bending Fingers Hands

Bendable finger hands (Fig. 4.3a) comprise multiple bendable soft fingers (Ilievski 2011). The application of pneumatic or fluidic pressure to bendable fingers causes

(a) (b) (c)

Fig. 4.4 Jamming hand grasping a cup

flexural deformation. For example, let the target object be placed near the bendable fingers.

The deformed fingers contact the object, enabling a set of bendable fingers to grasp the object.

PneuNet actuators are often applied to bendable fingers. These actuators are elastomer tubes with multiple chambers. The chambers are placed on a surface along the tube of the actuator. Applying pneumatic or fluidic pressure to the chambers causes their expansion and adjacent chambers push against each other, resulting in flexural deformation of the actuator. Because the shapes and chamber configurations of bendable fingers affect their flexural deformation, various designs are available. A bendable fingers hand (Fig. 4.3b) with small gaps between adjacent fingers, for example, and another bendable fingers hand (Fig. 4.3c) with fingers bent outward at their natural shapes have both been proposed and fabricated.

4.1.5 Soft Cover Hands

Soft cover hands (Fig. 4.3d) consist of fingers composed of hard material bones covered with a soft material skin. Fingers contact target objects through soft material skins to prevent excessive reaction forces during contact. Moreover, the surfaces of soft material skins have large friction, enabling stable grasping, and manipulation of the target objects. Fabricated surfaces with grooves or irregularities increase friction. Soft cover hands grasp target objects through contact forces originating from torques that drive their hard bones. The driving torques are converted into contact forces with a slight loss, resulting in relatively large contact forces being applied to the target objects.

Soft covers can prevent excess reaction forces and enable stable object grasping. For example, when a soft hemispherical cover is in contact with the flat surface of a target object, the strain potential energy of the cover is formulated as follows:

$$U = \frac{\pi E d_n^3}{3\cos^2\theta} + \pi E(d_n^3 d_t \tan\theta + d_n d_t^2), \tag{4.1}$$

where E denotes Young's modulus of the fingertip material, d_n and d_t are the maximum normal and tangential displacements, respectively, and θ is the relative angle between the fingertip and flat surface. The strain potential energy has its

local minimum under geometric constraints imposed on the fingertip, resulting in the target object being guided to a stable location specified by the local minimum (Inoue 2009).

Instead of soft materials covering hard material bones, flexible threads or deformable films attached between rigid rods have been applied to robotic hands. A scooping-binding hand (Fig. 4.4e) has a pair of fingers, each of which consists of several elastic threads attached between two parallel rods. During grasping, elastic threads contact a target object, adapt to the irregularity of contacting surfaces, and prevent excess contact forces. This scooping-binding hand can grasp slippery objects such as octopuses and raw oysters (Wang 2021).

4.1.6 Expanding Fingers Hands

Expanding fingers hands (Fig. 4.4f) consist of hard material fingers equipped with soft inflatable bags. The bags are inflated by applying pneumatic or fluidic pressure. For example, let a target object be between the bags attached to a pair of fingers opposing each other. Inflating the bags causes contact between the bags and object, enabling the pair of fingers to grasp the object. Note that grasping is performed using inflated bags, implying that the fingers do not have to move during grasping. Moreover, the hard material fingers and soft inflatable bags can be thin. Therefore, the expanding fingers can be thin.

Expanding fingers hands grasp target objects through contact forces from the pressure applied by inflatable bags on the target object. The magnitude of the contact force depends on the pressure and contact area. Thus, increasing the pressure and contact area increases the contact forces.

4.1.7 Hands-on and Challenges

The fabrication method of PneuNet actuators is open source https://softroboticstoolkit.com/parametric-tool-3d-printed-molds, which enables the application of PneuNet actuators to bendable fingers. These are first designed on a computer (Fig. 4.5, left), their deformation is analyzed (Fig. 4.5, center), and then the designed fingers are fabricated through molding or 3D printing (Fig. 4.5, right). Such design-analysis-fabrication steps can be applied to other types of soft hands, enabling the realization of various soft hands according to the requirements.

Soft sensors and actuators are currently available for soft hands, but integrating them into soft hands remains a challenge. Soft sensors and actuators often interfere with one another. Fabrication is often time-consuming, and the fabricated soft hands

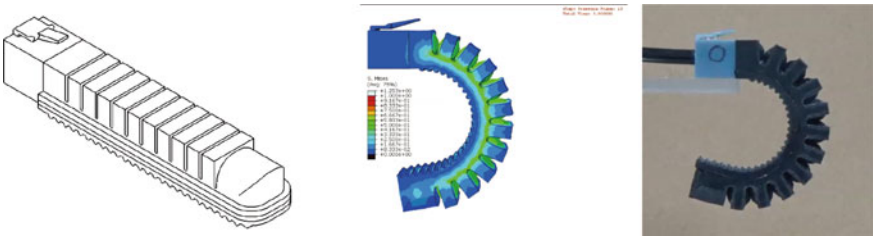

Fig. 4.5 Design, analysis, and fabrication of bendable fingers

suffer from individual variability. The fabrication of soft hands should be investigated further to reduce fabrication costs and variability. Moreover, the actual applications require safety and durability. Therefore, materials that satisfy these requirements should be developed.

4.2 Continuum Arm

4.2.1 Introduction

A continuum robot arm is a type of robot arm made of continuum bodies, such as elastic or fluid, and operates by deformation. The continuum robot arm is characterized by a spatially distributed curvature without local bending points, such as in rigid link robot manipulators. Several continuum robot arms are capable of stretching and twisting movements in addition to bending. Unlike ordinary industrial robot arms, continuum robot arms can penetrate curved tunnels and narrow spaces with obstacles without being trapped. They can also grasp objects by wrapping around them. While the form of a continuum robot arm could have been discovered purely through engineering exploration, it has been developed with inspiration from living organisms, such as the elephant's trunk and octopus's arm. The structural advantages of the continuum robot arm include its ability to achieve complex deformations with a simple structure and a smooth outline with no gaps. Because soft materials are used as support structures, they are easily deformed by external forces, ensuring intrinsic contact safety. However, it is difficult to generate large contact forces in the distal region. The effect of gravity cannot be ignored as an external force, and the arms are often used underwater or in a hanging posture like an elephant's trunk.

The earliest continuum robot arm, Elastor (ACM-7), consisted of a chain of basic units that deformed a spring between two flanges with three wires (Hirose 1983). Walker et al. developed OctArm, a continuum robot arm with a structure of bundled McKibben artificial muscles of an extensible type and mounted it on a mobile robot (Walker et al. 2006).Continuum robot arms range in size from active catheters as small as 1.5 mm in diameter (Ikuta 2006) to inspection balloon arms, 300 mm in

diameter, and 20 m in length (Takeichi 2017).Continuum robot arms are not yet mass-produced; however, Festo, a pneumatic equipment manufacturer, continually releases several types of soft arms (Mahl 2014).

We usually assume that the base of the robotic arm is fixed to the platform and that the platform never moves. If the continuum robot arm could be detached from its platform and still work, it would be a mobile robot similar to an earthworm or snake. In such cases, mechanical constraints and design requirements would change considerably. The similarities and differences between a continuum robot arm and a snake-like mobile robot are interesting topics, although we limit our discussion to the robot arm.

4.2.2 Hyper-Redundant Manipulators and Flexible-Link Manipulators

A typical robot arm consists of a few rigid links connected by rotational joints, similar to a human arm. The minimum number of axes of rotation required to define the three-dimensional position and orientation of the end of a robotic arm is six. Articulated robotic arms made by connecting many short rigid links are called hyper-redundant manipulators (Chirikjian 1994). The kinematic redundancy of these arms allows them to avoid interference with obstacles and to follow the surface of cylindrical objects in the same manner as a continuum robot arm.

A hyper-redundant robot arm consisting of rigid bodies is different from a soft, continuous robot arm. However, similar to an approximation of a smooth curve by a polygonal line, the hyper-redundant robot arm becomes closer to the continuum robot arm as the number of joints increases. These two systems share many characteristics and are herein collectively discussed. In simulators, a continuum robot arm is often modeled as a rigid link system with elasticity. No object is truly a continuum, as is evidenced by the fact that an elastomer is macroscopically smooth, but microscopically it is a collection of molecular chains. In theory, continuum mechanics considers an ideal continuum body, assuming a continuous mass distribution based on the macroscopic behavior of elastic materials and fluids.

Hyper-redundant manipulators are being developed for inspection inside machines and as minimally invasive surgical instruments. The advantages of hyper-redundant manipulators are their high mechanical rigidity, fabrication by assembly, and the ability to bend with little force owing to their well-defined joints. A structure that is easy to bend but strong in compression and torsion can be realized using a 2-DoF joint, such as a universal joint.

The links of an industrial robot arm are sufficiently rigid such that the kinematics and dynamics of an ideal rigid link system can be applied. There is a type of robot arm between the rigid and continuum robot arms called a flexible link manipulator, in which the flexure at the links is not negligible. A particular example of such a robot arm is the long and lightweight space robot. Unlike a continuum robot arm,

the control challenge for flexible link manipulators is primarily vibration control because the deformation of the flexible link cannot be actively controlled. The term "manipulator" refers broadly to mechanical devices for object manipulation and includes devices that do not resemble human arms at all. In many cases, there is no confusion in referring to a robot manipulator as a robot arm; therefore, they are treated here as synonymous.

The term "soft" robot arm may refer to a robot arm in which the links remain rigid, and softness is introduced only at the joints. Joint softness can be achieved by incorporating mechanical elasticity into the joints and drive system as well as by software-based compliance through force control. The addition of feedback-controlled softness to manipulators has been a traditional subject since the beginning of robotics. A compliance-controlled robot arm resembles a continuum robot arm in that it easily changes posture in response to external forces, but it lacks kinematic redundancy. The approach of controlling a hard robot in a soft manner differs from that of exploiting a soft robot in a soft manner in terms of the starting point and philosophy.

Figure 4.6 illustrates a comprehensive classification of robotic arms, including continuum robot arms, hyper-redundant manipulators, flexible link manipulators, and rigid link manipulators. Note here that there are also hybrid manipulators with rigid, discrete mechanisms, and continuous elements in parallel. The materials and structure of the robotic arm are tightly coupled. Hybrid structures may include a mix of discrete and continuous mechanisms in series or in parallel. Redundancy is defined by the system's degree of freedom with respect to the dimensions of the workspace. Continuous robot arms consisting of a limited number of segments of constant curvature in series are not redundant. Conventionally, the workspace of a robotic arm is considered based on the position and orientation of the end effector. On the other hand, in a continuum robot arm, the entire region from the root to the end is often considered the effector. In many cases, the methods of deforming the soft support structure can be selected between wire-driven (extrinsic) and artificial muscle-driven (intrinsic). Therefore, actuation is classified here separately from the structure. Continuum robot arms have infinite passive degrees of freedom unless constrained by constant curvature, resulting in an underactuated system with fewer actuators than the number of DoF in the mechanism.

4.2.3 Continuum Arms in Living Organisms

Hydrostatic skeletons, or hydrostats, are support structures for organisms that do not use hard bones or shells. This structure is a muscular membrane encasing soft tissue with high water content, as seen in the bodies of earthworms and caterpillars. The arms of an octopus, the trunk of an elephant, and the tongue, among others, are entirely composed of muscles and are specifically called muscular hydrostats. Soft robotics was first proposed in the context of research on continuous robotic arms aimed at engineering hydrostatic skeletons (Trivedi 2008).

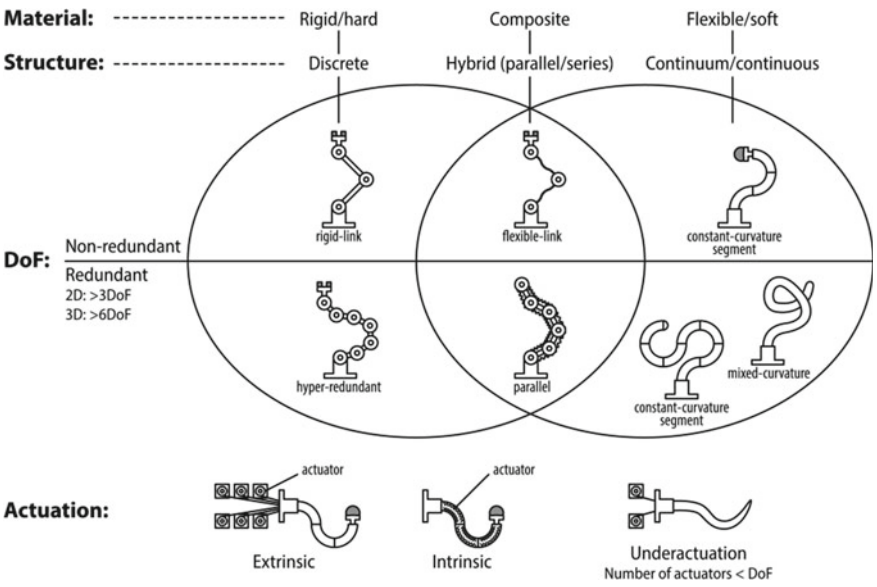

Fig. 4.6 Classification of robot arms/manipulators

Following the functions of a traditional robot arm, the tasks frequently assigned to a continuum robot arm include reaching the end of the desired position and grasping or moving objects. However, in recent years, new tasks have been tested, such as penetrating confined environments, which require not only bending but also the ability of the robot to extend and propel itself while in contact with the environment. Such robots go beyond the concept of an "arm" and are inspired by the roots and vines of plants. For example, a robot based on plant roots uses a 3D printer mechanism to mimic the extension of the root tips through cell division (Sadeghi 2017). In a robot system that mimics vines, a tubular film is inflated with air and unrolled from the inside, allowing meter-scale elongation (Hawkes 2017).

The vertebrate spinal column is a flexible, compression-resistant mechanism that consists of a series of vertebrae. Flexibility and multi-articular muscles of the spinal column are features not found in locomotor organs, such as the arms and legs. The long necks and tails of animals are particularly interesting as bio-inspired mechanisms, although they have received less attention than limbs. The long necks of ducks, herons, ostriches, and emus work as substitutes for arms when feeding or other activities, allowing them to perform skillful movements. Some species of monkeys use their long tails to hang from trees and grasp objects. The spinal column, which includes the neck, backbone, and tail, is a complex structure comprising flexible muscles, connective tissue, and stiff vertebrae. This is a hybrid mechanism that combines the features of a hyper-redundant manipulator and a continuum robot arm, which is open to exploration.

4.2.4 Typical Structures and Actuation Systems

Typical structures of continuum robot arms can be broadly classified into two types: soft actuators embedded in flexible structures, and flexible structures deformed by wires or by other methods. Robinson and Davies referred to the former as intrinsic actuation, and the latter as extrinsic actuation. Examples of hybrids of both types have also been presented. Rubber cylinders, tubes, braided sleeves, bellows, piano wires, and coil springs are used as the supporting continuum. For intrinsic actuation, the actuator itself must be flexible, and fiber-reinforced pneumatic artificial muscles, bellows actuators, and shape memory alloy actuators are used. For extrinsic actuation, the actuator does not need to be flexible and electric motors can be employed. Externally, the force must be transmitted by a soft transmission element, such as a wire. The wire drive requires multiple wires to be led from the root to the target location, where friction in the path and interference with other wires can cause problems.

As a type of intrinsic actuation, bundled soft actuators can serve as flexible structures. The advantage of this structure is that the actuator and structure are integrated and the volume of the actuator can be maximized. This is similar to the muscular hydrostat, which is a bundle of muscles. A snake robot, which cannot be externally driven, usually consists of a series of joint modules with built-in motors.

Extrinsic actuation in the animal kingdom corresponds to structures that are driven solely by tendons with no muscles, although such anatomical structures are difficult to find. In the long necks and legs of birds, intrinsic drive is present in the arrangement of muscles around each joint, whereas long tendons extending from large muscles on the body drive the ends, which can be considered a hybrid of intrinsic and extrinsic actuation.

In hyper-redundant manipulators, extrinsic actuation is commonly used to avoid the increase in weight caused by many actuators and to obtain a sufficient driving force. Actuators are installed on the base, and the angle of each joint is controlled using wires. Because numerous drive wires are arranged in parallel, the section on the root side is complicated by wire concentration. In addition, maintenance and wire replacement are time-consuming.

4.2.5 Posture Control

An ideal continuum robot arm can smoothly control three-dimensional deformations at all regions. However, achieving such deformation requires an infinite number of actuators, which is impractical. Therefore, a common strategy is to limit the mode of deformation and to use only partial deformation patterns. The actual continuum robot arm is an underactuated system with fewer active degrees of freedom (number of actuators) than passive degrees of freedom. Even in the biological control of an elephant's trunk or an octopus's arm, the motor neurons are finite, and it is unlikely that all deformation patterns are utilized.

The most standard continuum robot arm configuration consists of segments of varying curvatures connected in series. The curvature is assumed to be constant within each segment. The length of the neutral axis of the arm is assumed to be constant, with no elongation or contraction. A continuum robot arm that specifies the curvature in each segment can be interpreted as replacing the rotational joints of a serial-link robot arm with flexural joints. The kinematics of such a continuum robot arm can be considered analogously to that of a serial-link robot arm. When using artificial muscles or wires that only generate tension, a minimum of three actuators is required to obtain 2-DoF bending. Therefore, the three actuators are arranged in parallel to form a 2-DoF segment. The minimum configuration for achieving six degrees of freedom for the position and orientation of the end of the continuum robot arm is three 2-DoF segments connected in series, resulting in a total of nine actuators. In this case, there is no redundancy, and more actuators are required if the user wants to specify the path of the middle part of the arm in addition to the position and posture of the end. When the middle part of the robot arm is in contact with the environment, it should be detected by tactile or force sensors, which is a research topic.

If three linear (push–pull) soft actuators are used in parallel to form a segment of a continuum robot arm, the segment has two degrees of freedom for flexion and one degree of freedom for extension and contraction, for a total of three degrees of freedom. Displacement of the segment in the extension and contraction directions is often smaller than that in the flexion direction. A typical example is a robot arm fabricated by connecting multiple flexible microactuators (Suzumori 1991).

Modeling and simulation of the continuum robot arms have been performed for posture control. Modeling a continuum robot arm with constant curvature within a single segment is relatively simple. With respect to kinematics, if the length, curvature, and bending direction of each segment along the neutral axis of the arm are defined as parameters, the overall shape and end position can be expressed by its connection (Jones 2006). For dynamics, it is also possible to consider the mass distribution along the curve through the center of the arm, calculate the homogeneous transformation matrix between segments, and construct the equations of motion by finding the inertia matrix, Coriolis force, centrifugal force matrix, and conserved force vector (Godage 2016). Each term in the equation of motion must be efficiently obtained through recursive computation.

If the continuum robot arm can be simplified as a hyper-redundant manipulator composed of smoothly bent joints, the difference between the two is insignificant. To utilize continuum robot arms, we need to explore their unique functions and applications. Three-dimensional deformations such as elongation, contraction, and diameter changes are difficult to achieve with a rigid hyper-redundant manipulator but are relatively easy with a continuum robot arm. For example, a continuum robot arm with a peristaltic self-propelling function would be useful as a medical device (Burgner-Kahrs 2015). A challenge could be to migrate from a serial mechanism that changes the curvature at each segment to a configuration in which one actuator contributes to the complex deformation of the entire segment.

4.2.6 Features

Let us categorize the typical functions and tasks of a continuum robot arm. The first is to take advantage of the redundant degrees of freedom of the cord-like form. The other is the case in which physical softness is utilized.

Obstacle avoidance

There are infinitely many paths from the root to the end, except for the singular posture. In other words, although the position and posture of the tip may be specified, the path in the middle is arbitrary. For example, an arm can work at the end while avoiding contact with obstacles. Continuum robot arm can also enter and exit tight spaces through the gaps.

Contact in the middle part

In industrial robot arms, contact with any part other than the end effector is avoided because it can either break the opponent or cause damage to the robot itself. The redundancy and flexibility of the continuum robot arm allow it not only to avoid obstacles but also to actively use the middle part of the arm to contact objects and the environment. Wrapping and grasping large objects that cannot be held by an end effector is a unique feature of the continuum robot arm. In addition, if the middle section contacts a stable scaffold, it provides an anchor point to support its own weight and avoids the need to support all loads at the root section.

Passivity

One function that uses deformation in response to external forces is adaptation to complex shapes. For example, if a continuum robot arm is placed on undulating ground in a relaxed state, the shape of the ground can be estimated from the deformation of the arm. In addition, if the arm moves like a pendulum in the hanging position, a large swing can be obtained with a small amount of force. Furthermore, it can move quickly using inertia, such as a lasso or whip.

Use of 3D deformation

Wormlike peristaltic motion, which combines changes in diameter and telescoping, provides propulsion even in narrow spaces that are difficult to penetrate because of friction. Self-propelling continuum robot arms have potential applications in colonoscopes and other diagnostic devices.

4.2.7 Summary

The continuum robot arm has superior features, with potential applications in medical endoscopes, minimally invasive surgical instruments, and inspection equipment in industrial plants. However, they require many actuators and cannot generate large

forces. In addition, there are challenges in tasks involving contact and dynamic control. A commercial and accessible standard platform for continuum robot arms is required for conducting a variety of experiments.

4.3 Peristaltic Locomotion

4.3.1 Movement by Peristalsis Motion

Legged locomotion and Peristaltic locomotion

Arthropods (Arthropoda) and vertebrates (Chordata) possess rigid skeletons that support their bodies. Many of them can move quickly over uneven terrain by supporting their trunk with their exopods (or legs), to keep their trunk off the ground. Alexander (1992); Full (1997); Alexander (2002).

On the other hand, annelids, such as worms and terrestrial mollusks (Mollusca), slugs, and polypod larvae (Lepidoptera), do not have skeletons, and their bodies are mainly formed by muscles with varying arrangements and shapes. These animals are not restricted by their skeletons and can move with great flexibility and freedom (Full 1997; Alexander 2002).

Therefore, they move by flexibly changing their body shape while adapting to the complex surrounding environment. The aforementioned animals, which are particularly good at moving by peristalsis, move by grounding most of their trunk and generating waves in the trunk. This type of movement by the propagation of waves in the trunk is called "peristalsis motion."

Advantages and disadvantages of peristaltic motion: Applicability to soft robots

Movement via peristaltic motion is less efficient than that via wheels or legs. However, movement by peristalsis can support the center of gravity of the trunk over a large area and can flexibly adjust to uneven terrain, thus enabling stable movement without a complicated control system. Soft robotics is most suitable to realize the peristaltic motion seen in such animals because this motion can be realized only by stretching and contracting muscles without skeletons.

4.3.2 Why Peristaltic Movement?—Principle of Peristaltic Locomotion

Robot movement and kinematic pair of elements

The means of motion and movement of a robot depend on the motion of the actuator and kinematic pair of elements. A general robot often uses a revolute pair with a motor, and the wheeled movement method is often adopted. In contrast, animal

muscles are actuated by a rectilinear pair with limited range of motion. Therefore, they require a reciprocating motion for movement.

Peristalsis and Elliptical Motion

The peristaltic movement of animals is also driven by the linear motion of the muscles; therefore, these animals move by reciprocating motion. In this case, a peristaltic animal is flexible, and it can move by propagating waves while flexibly and continuously expanding and contracting its trunk (Quillin 1998). Simultaneously, the trunk generates an elliptical motion with respect to the contact area. This elliptical motion can periodically change the back-and-forth movement in the direction of travel and frictional force with the contact area at a point on the surface. This periodic motion generates movement of the trunk in the direction of travel and its reaction force support (anchor). This motion is continuously propagated against the ground surface by the stretching and contraction of numerous muscles. The propagation of this elliptical motion results in the movement of the trunk by peristalsis.

Direction of wave propagation and direction of trunk movement

Movement by peristalsis can be classified into movement using transverse waves, such as traveling waves, and movement by elastic waves, such as longitudinal waves. The direction of movement of the trunk and direction of propagation of the waves caused by the stretching and contraction of muscles depend on the degrees of freedom and the size, muscle structure, and shape of contraction of the trunk of each animal (Alexander 1992).

For example, one snail species moves by generating traveling waves. In this movement, when a certain point on the surface of the trunk leaves the contact area, and the frictional force, which acts as an anchor, becomes small, the point moves in the direction of muscle contraction. In this case, the direction of wave propagation due to muscle contraction and expansion coincides with the direction of movement of the trunk (direct wave).

However, an earthworm moves by propagating a longitudinal wave. In this movement, the muscles contract in the direction of travel when friction in the contact area increases owing to the radial expansion of the trunk. The direction of wave propagation and trunk movement is reversed in this case (retrograde wave). (Full1997; Alexander 2002).

Types of anchor functions

Animals that move via peristalsis use various methods to realize the anchoring function to counterbalance the propulsive movement of the trunk. For example, there are methods of gripping, including a suction cup, hooking the ground with setae, and using non-Newtonian liquids, such as the Bingham flow. These methods are closely related to the environment in which each animal lives (Alexander 2002; Tanaka 2011a).

When applying peristalsis as a method to enable movement in soft robots, methods to generate “elliptical motion” and “supporting reaction force (anchor)” must be considered.

Animals that produce peristaltic locomotion and their classification

Gastropods are excellent model organisms for discussing direct and retrograde waves, that is, the relationship between the locomotion direction and the propagation direction of the deformation wave of ground-contact body parts, called the foot. This is because both direct and retrograde waves observed in gastropods depend on the species, size, and dynamic mechanical properties of the mucus secreted by them. More fundamentally, according to a theory, direct and retrograde waves are switched depending on the extension/contraction timing and anchoring of ground-contact body parts. For example, slugs and snails locomote in direct waves, whereas limpets locomote in retrograde waves.

First, we explain a direct wave based on Fig. 4.7a. In general, organisms that generate locomotion using direct waves start with the entire abdominal leg/foot "extended" and grounded, then contract the rear foot/leg(s) forward, un-anchoring the contracted foot/leg(s) and sending the contraction wave forward to the front. For example, when a slug or snail is placed on a transparent glass plate and its foot (part sticking to the plate) is observed from the backside, a blackish wave (foot wave) can be observed moving from the rear to the front (direct wave). The wave travels at more than twice the locomotion speed. Direct wave is also employed by caterpillars, which is discussed in detail below.

In contrast, the organisms that generate locomotion using retrograde waves start with the entire abdominal leg "contracted" and grounded, then release and extend the front part/leg(s) forward to grip the ground, followed by sending the extended wave back to the rear (see Fig. 4.7b). The limpet is an excellent example of an organism that generates locomotion using retrograde waves. Mark Denny studied the dynamic viscoelastic properties of mucus in detail (Denny 1980). He found that mussels secrete a particular type of mucus that behaves as an elastic body when the strain is small and as a viscous fluid when the strain is significant. The strain of the mucus in the contracted part/foot is minor, and the mucus becomes anchored, whereas the strain of the mucus in the elongated part is prominent and the mucus behaves as a viscous fluid, thus releasing the anchoring. Earthworms also generate locomotion using retrograde waves. Earthworms, on the other hand, do not use such

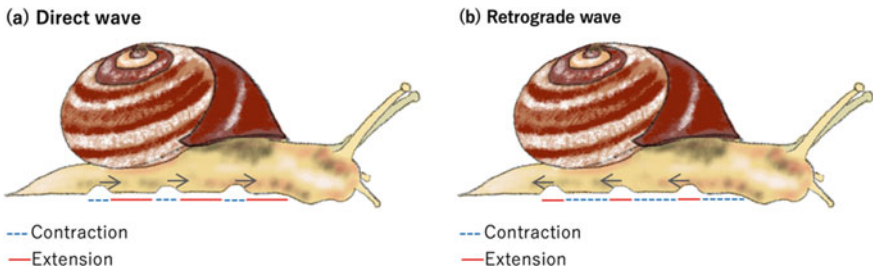

Fig. 4.7 Relation between the locomotion direction and propagation direction of deformation wave of foot: **a** direct wave; and **b** retrograde wave

functional fluids; instead, they use bristles that protrude out from the body segment when it is shortened and anchored to the scaffold.

In summary, a direct wave can be distinguished when a contraction wave is used, as in the case of caterpillars, slugs, and snails, and a retrograde wave can be distinguished when a stretching wave is used, as in the case of limpets and earthworms (Jones 1970). For reference, we roughly classify animals based on direct wave or retrograde wave locomotion below.

- Direct wave: caterpillars, slugs, snails, abalone, lacewings, gobies, and sea cucumbers
- Retrograde wave: serpentine concertina movement, limpets, earthworms, sea hares, chitons.

4.3.3 Peristaltic Crawling of Snails and Caterpillars

Anatomical muscle structure of a slug and caterpillar

Certain species with spires (a part of the coiled shell of mollusks), such as slugs, snails, turban shells, and abalone, are classified as gastropods. Many species of gastropods crawl and move by contracting their feet using muscles that stretch in almost all directions across the part of the body attached to the ground (called the foot). These muscles can be broadly classified as anterior oblique muscles that extend diagonally from the ventral side to the front and posterior oblique muscles that extend diagonally from the ventral side to the back. This anatomical knowledge, along with beautiful illustrations, is available for download at https://www.routledgehandbooks.com/doi/10.1201/9781351115667-3.

A caterpillar's body has a deformable cylindrical shape with a series of body segments and repetitive structures in the axial direction. Three pairs of rigid thoracic legs remain after the caterpillar becomes an adult. The abdomen has two to five pairs of soft leg-like projections called ventral legs, which disappear when the caterpillar becomes an adult. Depending on the presence or absence of these median gastropods, the caterpillar may perform crawling (Fig. 4.8a) or inching locomotion (Fig. 4.8b). A traveling wave flows from the back to the front. Caterpillars contain approximately 4000 muscles. Beautiful anatomical drawings can be found at http://www.printsandprinciples.com/2016/10/anatomy-of-caterpillars-muscles.html.

Peristaltic Locomotion of Snails and Caterpillars

Snails and caterpillars produce peristaltic locomotion in which the direction of propagation of the deformation wave is the same. This is called a direct wave or anterior-grade wave. For example, when a caterpillar starts to produce locomotion, its rear pair releases the branches/ground and bends and contracts its rear body segments. The release of the legs and bending and contraction of the body segments are transmitted to the front. This is how locomotion is performed.

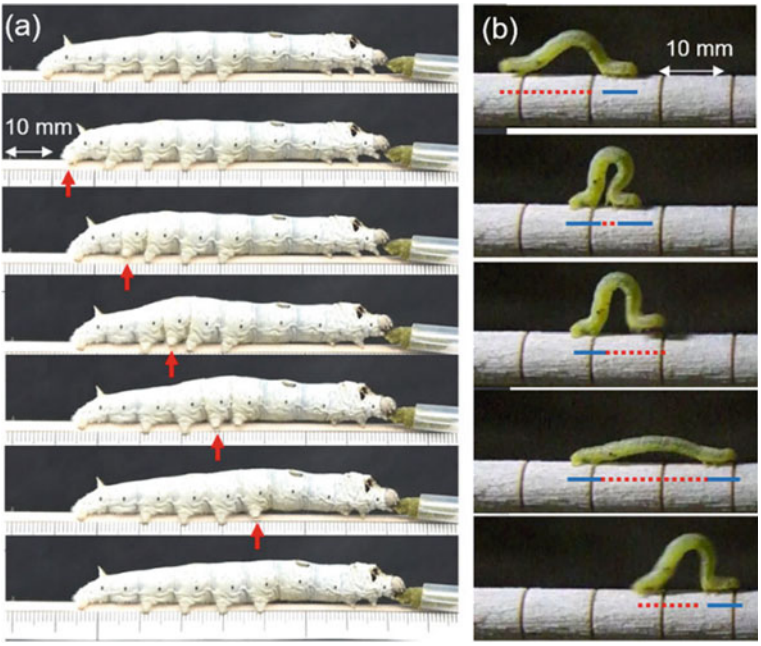

Fig. 4.8 **a** Crawling locomotion and **b** inching locomotion

The point is that both body segment shortening and grip release on the branch/ground almost coincide. This differs significantly from the locomotion of earthworms, described below. Depending on body size, habitat, and other factors, differences in locomotion patterns, such as crawling and inching, have been observed (Griethuijsen 2014).

Crawling is performed by caterpillars that are larvae of relatively large families, such as *Sphingidae, Papilioninae*, and *Bombycidae*. Such caterpillars have many abdominal legs (five pairs), which are used to grasp the substrate and support their large bodies. In the crawling locomotion performed by caterpillars, the abdominal legs are released and grasped in turns from behind. In addition to bending, the body stretches and contracts in the axial direction. Not only bending, but also stretching, and contracting along the body axis, contribute to the propulsion of the caterpillar (Umedachi 2019).

In contrast, inching locomotion is produced by relatively small caterpillars, in which the ventral leg in the middle of the body has been degenerated and lost. The rear prolegs are extended forward to grasp the ground (branch, etc.) just behind the thoracic legs. Because the length of this step is almost equal to the length of the body, the speed of locomotion per body length is greater in species that perform inching locomotion. The middle part of the body remains bent, giving it a characteristic omega (Ω) shape.

Evolutionary developmental studies suggest that a caterpillar with many ventral legs appeared first. The body was then downsized in response to environmental changes, resulting, later, in the appearance of a type with degenerated ventral prolegs in the middle of the body. In some species, this crawling and inching locomotion may use both or a combination of these basic modes (Lin 2011).

Features of Caterpillar-Type Peristaltic Mobile Robot

Peristaltic motion using direct waves is relatively easy to realize robotically. This can be achieved by attaching contraction-type actuators to a wall of flexible skin and contracting the actuators in turn. The contraction-type actuator can be a shape memory array (SMA) coil or a wire tendon wound by a motor. In extreme cases, it can be reproduced with only two actuators, as for example, in the author's earlier work, shown in Fig. 4.9 (Umedachi 2013). This robot is made of a 3D-printed beam of rubber material with only two actuators attached to the front and back of the robot, which are SMAs that contract when electricity is applied. By contracting the SMA in the back and then contracting the SMA in the front after a slight time lag or delay, the robot can generate peristaltic motion. The motion can change from inching to crawling by increasing the time delay.

The recipe for a simplified version of this robot is also available at the following URL; the reader is encouraged to watch and recreate it: http://opensoftmachines.com/2018/02/caterpillar-robot-with-sma/.

Application examples

The following is a typical example of the peristaltic soft robot described above. As explained above, caterpillar-type locomotion robots are relatively easy to make, and newer peristaltic soft robots are being produced elsewhere. Therefore, we will introduce only the typical ones here.

First, let us start with a soft robot with a caterpillar-type movement system. Whitesides' group at Harvard University developed a four-legged soft robot whose technology was originally made of microfluidic channels with silicone rubber. The Soft robotics toolkit (https://softroboticstoolkit.com/) was made by this group.

The Go-Q Bot, developed by Trimmer's group at Tufts University, is also a pioneering caterpillar robot (Lin et al. 2011). The primary function of the Go-Q Bot is to roll, and one of the authors redesigned the caterpillar robot with a ground friction switching mechanism and a few actuators to produce crawling and inching locomotion (Umedachi 2013). The research team originally studied the dynamics and neurophysiology of the tobacco hornworm, *Manduca sexta.* Engineering researchers and students collaborated to build the robot to better understand caterpillars' behavior and locomotion.

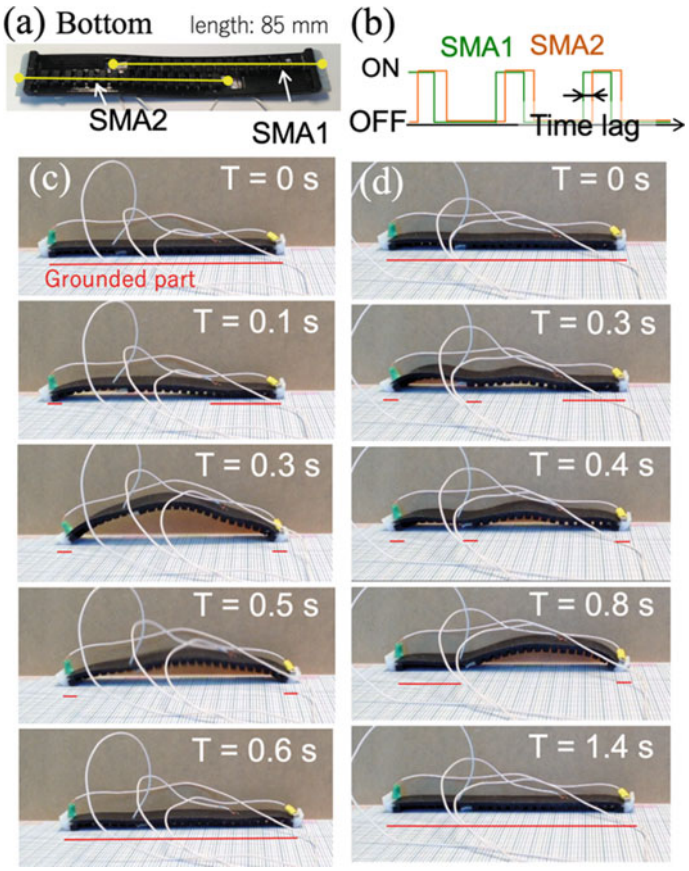

Fig. 4.9 **a** SMA-driven caterpillar-like robot, **b** on–off timing input to the SMA coils, **c** inching locomotion (time lag is set as 0.1 s), and **d** crawling locomotion (time lag is set as 0.4 s). The movie is available at https://youtu.be/0pHOaBnj1po

The peristaltic motion of snails and caterpillars is expected to have various applications because of its unique and useful features, especially the ability to move on a branch, grid wire, vertical wall, or ceiling in the upside-down position. Examples of such applications are as follows:

Environmental and facility monitoring: *The peristaltic locomotion of caterpillars is suitable for moving on branches and electrical grid wires. Therefore, it is expected to be applied to environmental and facility monitoring* (*Carrico* 2019*; Rozen-Levy* 2019*; Morishima et al.* 2020).

Wall Climbing: Snail and caterpillar-like robots are good at climbing upside-down and on vertical walls (*Ewoldt* 2007*; Tang* 2018*; Lam et al.* 2011). *Therefore, they are expected to be used for wall and window cleaning and monitoring of bridges and dams.*

4.3.4 Peristaltic Crawling of Earthworm

Anatomical muscle structure of earthworms

A cross-sectional view of the earthworm is presented in Fig. 4.10 (Sugi 1977). An earthworm consists of numerous segments divided by septa and a coelom containing an alimentary canal and nerve circuits. The inner wall of the body is composed of two main muscle layers. The outer layer, which is arranged radially, is called the circular muscle, and the inner layer, which is arranged axially, is called the longitudinal muscle.

When the longitudinal muscle contracts in the axial direction, the segment becomes increasingly thicker and shorter. At this time, the earthworm grips the soil with the aid of small hair-like projections called setae to increase friction (Fig. 4.11). When the circular muscle is actuated in the radial direction, the segment becomes thinner and longer and extends in the axial direction (Quillin 1999; Tanaka 2011a).

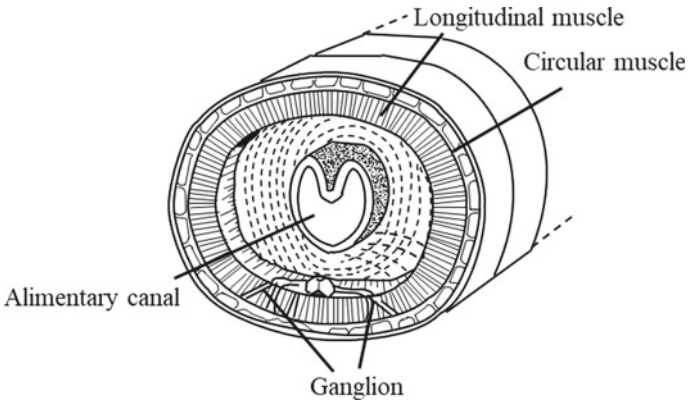

Fig. 4.10 Inner structure of an actual earthworm body (Sugi 1977)

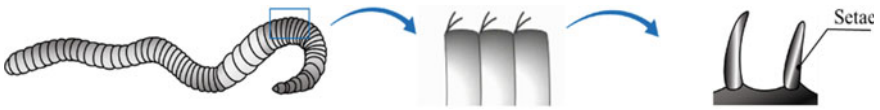

Fig. 4.11 Earthworm's setae as an anchor

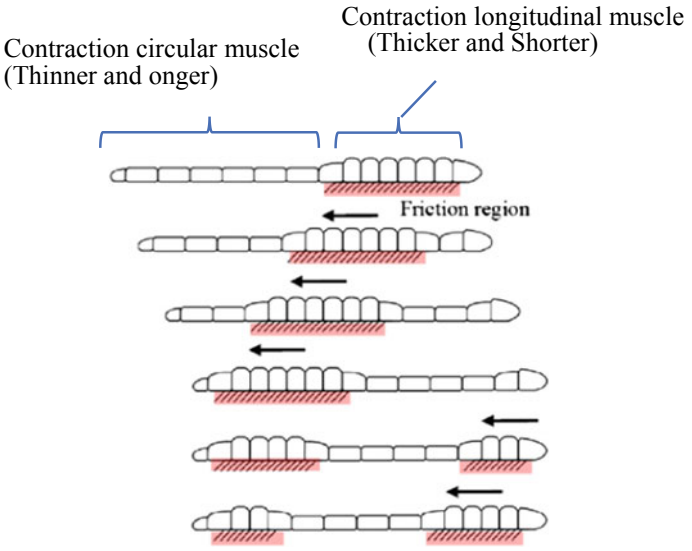

Fig. 4.12 Locomotion pattern of an earthworm with peristaltic crawling

Peristaltic Crawling of Earthworm

Figure 4.12 shows the locomotion pattern of an earthworm during peristaltic crawling.

The earthworm contracts and expands as follows:

- The earthworm contracts an anterior segment using the longitudinal muscles.
- This contraction is transmitted to the rear segments, while the anterior segments are simultaneously elongated by the circular muscles.
- The contraction segments generate a frictional force between the segments and surface. Because of this frictional force, a reaction force is generated to elongate the contraction segments.

Thus, the earthworm can move because of the repetition of thicker and thinner motions (Quillin 1998).

Figure 4.13 shows an analysis of the peristaltic crawling of an actual earthworm. The motion of the earthworm was analyzed using movement-analysis software. Marks were placed on the earthworm's body and captured on video. The figure shows that the contraction waves propagate along the body from the head to the tail (Quillin 1999).

Features of Earthworm-Type Peristaltic Mobile Robot

As observed in earthworms, movement by peristalsis is a slow and inefficient means of locomotion. However, it has an original and practical feature that is not observed in any other movement mechanism. We discuss the space requirements for peristaltic

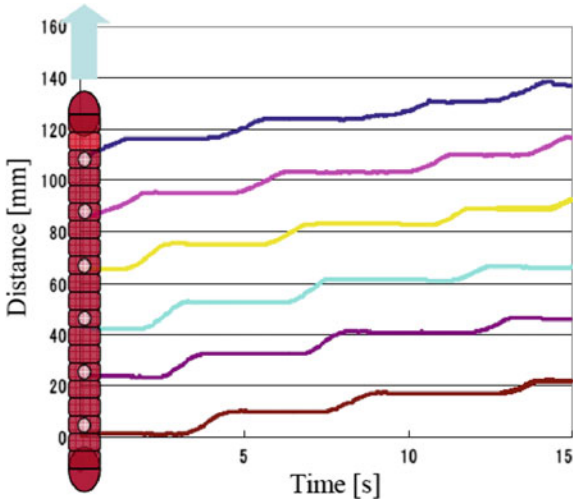

Fig. 4.13 Analysis of an actual earthworm's movement

locomotion compared to other means of transportation. Four features of peristaltic movement are presented.

Figure 4.14 shows a comparison of the moving area with other typical movement methods. The peristaltic movement is based on longitudinal waves, and the movement is caused by the propagation of expansion and contraction in the axial direction. As shown in Fig. 4.14, the worm moves via wave propagation through longitudinal waves and anchoring by setae. Therefore, the earthworm can move provided there is sufficient space for the radial expansion of the body segments. In principle, among all the methods of movement, this method allows an organism to move within the smallest area (Saga 2002a).

- Large contact area for anchor (gripping force)

Wheeled mobility is prone to slipping in localized low-friction areas in the surrounding environment because the contact area where frictional forces, required

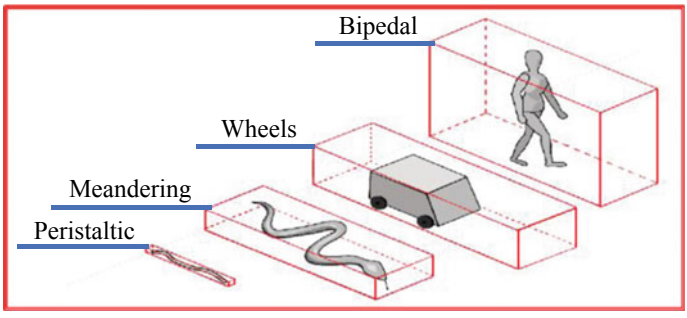

Fig. 4.14 Area required for locomotion by various methods of movements (Saga 2002a)

for gripping, occur is small. Therefore, this mobile method is highly sensitive to changes in the coefficient of friction.

However, the peristaltic motion of earthworms is suitable for movement in narrow tubes. Earthworms can contact and press against the inner wall surface of a tube over a large area by expanding their body segments in the radial direction. By contacting a large area, the pressure for anchoring (gripping) is distributed, which can also smoothen the local changes in the coefficient of friction of the surrounding environment. In addition, the frictional force can be increased by expanding some body segments such that stable running, large traction, and anchoring can be obtained independently of gravity (Tanaka 2011a).

- The inside of the body is hollow.

As shown in Fig. 4.10, the central part of the earthworm is the digestive organ, and the muscles located outside the digestive organ generate surface waves for movement. The presence of this digestive organ indicates that the organism using peristalsis as a method of motion can have space inside its body.

Therefore, the inside of the earthworm robot can also be easily hollowed out. Tools, such as a camera or drill, are easy to mount or replace in this cavity, as is incorporating the tubing and wiring necessary for the actuators.

- Repetition of the same structure

The body of an earthworm is divided into many segments, and the muscle arrangement and motor innervation of most body segments are repetitions of the same structures (Mangan et al. 2002).

Therefore, they are functionally redundant, and the structure of earthworms is highly robust. This ensures that even if a part of the body segment is damaged, overall function will not be significantly affected.

Moreover, when considered from the perspective of robot design, the structure consists of multiple units with the same function connected in series. Therefore, a simpler and less expensive mechanical structure is required.

Realization of Earthworm-Type Peristaltic Mobile Robot

To reproduce the peristaltic motion of earthworms in a robot, it is important to realize soft actuators that can deform to "thicker and shorter" and "thinner and longer," which is the behavior of the body segments of earthworms. The peristaltic motion of an earthworm can be easily realized by connecting several actuator units in series. Some of these methods are presented below.

- Using an external magnetic field

In this method, a flexible rubber tube filled with magnetic fluid is expanded and contracted by an external magnetic field to reproduce the peristaltic motion of an earthworm (Saga et al. 2002). The rubber tube is divided into several segments, and a magnetic field is applied to each segment. The rubber tube is hydrostatic, and the external magnetic field causes the segments to deform. This robot can be miniaturized

owing to its simple structure and is expected to be applied to catheters and similar devices.

- Using braided sleeve

The braided sleeve can continuously reproduce the wormlike peristaltic motion by controlling the braiding angle. Mangan et al. (2002) realized peristaltic motion with a McKibben-type actuator using this sleeve and suggested its application to endoscopes. Boxerbaum et al. (2010) and Seok et al. (2010) realized a continuous longitudinal wave by partially changing the braiding angle by controlling the axial length using a shape memory alloy (SMA) and motor. As most robots are made of flexible materials, they do not break when crushed.

- Using pneumatic artificial muscles

Taking advantage of the similarity between the behavior of a straight fiber-type pneumatic artificial muscle and that of the body segments of an earthworm, Saga et al. (2004) realized an earthworm-type robot with this artificial muscle actuator as one segment. This robot has large traction and grasping forces owing to its artificial muscles. Various practical robot applications have been reported.

- Using an elastic structure (belts, tube, origami)

The robot consists of units with several elastic belts arranged along the circumference of a pair of flanges. By changing the distance between the flanges using an actuator, such as a motor or SMA, the unit changes the radial expansion of the elastic belt or tube, and the movement of the earthworm's body segments can be reproduced (Menciassi et al. 2004; Nakamura 2005). Furthermore, Fang et al. (2017) reproduced peristaltic motion using an origami structure.

Application examples

The peristaltic motion of earthworms is expected to have various applications owing to their unique and useful features, especially when moving in narrow spaces. Examples of such applications are as follows:

Pipe inspection: The peristaltic motion of earthworms is effective for movement in small and flexible pipes, owing to the high gripping and pulling forces inside pipes. Therefore, it is expected to be applied to pipe inspection (Ikeuchi 2012; Yamashita 2011) or cleaning robots (Ito 2019) in factories and infrastructure.

Propulsion equipment for underground excavation: Earthworms are good at moving underground; therefore, earthworm-like robots are expected to be used as propulsion devices for underground excavation, burial of infrastructure pipes, and underground exploration of the moon (Omori 2012) and ocean floor (Isaka 2019).

Medical application: The peristaltic movement of earthworms can occur through thin and soft pipes. Therefore, it is expected to be applied to mobile robots in blood vessels and the digestive tract. (Menciassi et al. 2004; Zou 2005; Hidaka 2009).

4.4 Aerial Flight with Soft Components

4.4.1 Basic Concepts

Drones are composed of inflexible elements. Stable flight of a drone is achieved by controlling the rotation speed of the propeller in response to perturbations. Although drone applications have significantly expanded in recent years, many issues remain to be addressed in terms of safety, flight time, and cruising range. Animals such as birds and insects have outperformed drones in various aspects. Research on animal flight has primarily focused on aerodynamic aspects (Ellington 1984) and reveals that insects use unsteady aerodynamics to stay aloft (Sane 2003). Recently, our understanding of animal flight has advanced further with the development of photogrammetry using high-speed cameras and numerical simulations. As shown in Fig. 4.15, the flapping wings of animals such as insects are passively deformed owing to their softness. This observation emphasizes the significant effect the softness of wings and musculoskeletal systems has on the flight performance of flying animals. The interaction between soft structures and fluids, called fluid–structure interaction, is a complex phenomenon that is difficult to analyze theoretically, and its application to flying robots is very difficult from a design perspective. Elucidation of the pathways for the realization of softness and its effect on the performance of animal flight can significantly improve the performance of aerial robots. In this chapter, a brief introduction to the fluid mechanics of flight is presented, and soft components for aerial robots are subsequently introduced, along with specific examples of the structures and functions of the wings and musculoskeletal systems of flying animals.

Fig. 4.15 High-speed images of various insects. Their flapping wings are dynamically deformed during flight

4.4.2 Fluid Mechanics of Flight

A flying object achieves its movement through interactions between its body and air. Therefore, to fly efficiently and stably, it is important to control the motion of the surrounding air based on the shape and kinematics of the body. Wings that generate a vertical force against the gravitational force can be classified into three categories: fixed, rotary, and flapping. As displayed in Fig. 4.16a, two-dimensional cross-sections of these wings show that the wings undergo two-dimensional motion in the surrounding fluid. Considering that the airfoil is stationary and the surrounding airflows toward the airfoil, the relative angle between the fluid and the airfoil's cross-section is called the angle of attack. The aerodynamic force in the same direction as the fluid motion is called drag, and the aerodynamic force perpendicular to the direction of the fluid motion is called lift. Because drag acts in the direction of blade motion, it is necessary to generate a propulsive force against the drag force to achieve motion in the air. This propulsive force can be generated by a motor in the case of a rotating wing, or by a motor or muscle at the root in the case of a flapping wing. Using the wing area A, reference speed U, and air density ρ, we define the following coefficients that non-dimensionalize the lift F_L and drag F_D:

$$C_L = \frac{F_L}{0.5\rho U^2 A}$$

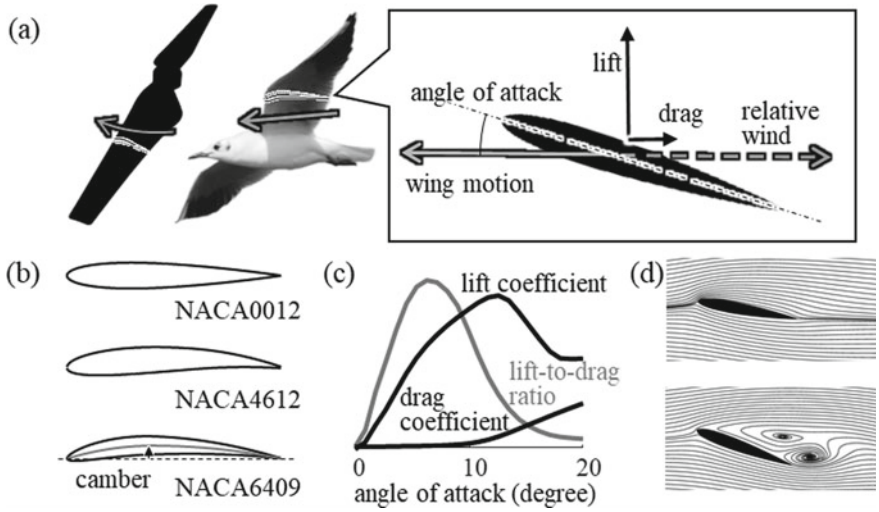

Fig. 4.16 Aerodynamics of a flying object. **a** Motion of a cross-section with lift and drag. **b** Various airfoils. **c** Variations in lift, drag, and lift-to-drag ratio with the angle of attack. **d** Flow field around the wing for a low angle of attack (5°) and high angle of attack (20°) simulated numerically

$$C_D = \frac{F_D}{0.5\rho U^2 A}$$

C_L and C_D are dimensionless coefficients known as lift and drag coefficients, respectively.

It is necessary to generate a high lift with a low drag to expend less energy while moving through air. Therefore, the efficiency of a wing is often expressed in terms of its lift-to-drag ratio.

The shape of the cross-section of a wing is crucial for improving its lift-to-drag ratio. A variety of cross-sectional shapes have been devised and adopted according to the desired performance (Fig. 4.16b). The upward bulge of the wing chord, called camber, is effective in improving the performance of the wing. Another important factor for improving aerodynamic performance is the wing planform. The ratio of wing length to chord length is called the aspect ratio. The larger the aspect ratio, the smaller the effect of the vortices on the lift and the higher the efficiency. Wing loading, which is calculated by dividing the weight of the flying object by the wing area, is also a parameter that determines the turning performance of a flyer.

When the angle of attack of the wing is small, fluid flows smoothly around the wing. As the angle of attack increases, the lift and drag coefficients increase, and the lift-to-drag ratio reaches its maximum at a certain point (Fig. 4.16c, d). As the angle of attack increases further, the fluid detaches, and a phenomenon called a stall occurs (Fig. 4.16d). When the wing is stalled, the lift force decreases rapidly, whereas the drag force increases, which can result in a fall. Therefore, it is important for aerial robots to maintain an appropriate angle of attack.

Consistency in the motion of the surrounding fluid depends on the size and speed of the wing. The dimensionless value that governs this relationship is called the Reynolds number, Re, which is the ratio of the inertia to the viscosity of the fluid. Re is expressed using the reference length of the system (e.g., L, the length of the wing chord), reference velocity (e.g., U, the velocity of the wing), and kinematic viscosity of the fluid ν as follows:

$$\mathrm{Re} = \frac{LU}{\nu}$$

The fluid force on the wing is correlated with Re. In air, as Re increases, the drag coefficient tends to decrease because the viscosity of air is relatively small. In the case of aircraft, Re is on the order of 10^6–10^8, whereas in smaller flyers, such as birds and insects; it is typically on the order of 10^2–10^4 (Shyy 2011). Therefore, small flying objects tend to suffer from high viscous forces and are less efficient.

4.4.3 Basic Design of a Soft Aerial Robot

This section explains and discusses the basic functions and control of soft aerial robots, using a flapping-wing robot model as an example. The flapping-wing aerial robot is a simplified flight robot with wings, a tail, and associated mechanisms that are capable of forward flight and turning (Fig. 4.17a).

The soft elements of the flight robot deform because of interactions with obstacles and air. The interaction between the air and soft elements, known as the fluid–structure interaction, is difficult to analyze theoretically, except in very simplified cases, because it is based on the balance of airflow and structural deformation explained by two different disciplines: fluid mechanics and structural mechanics. As it is difficult to design a soft aerial robot via a purely theoretical approach, it is more effective to mimic animals that already use soft elements. Therefore, in the following sections, we will discuss the effective utilization of soft elements during flight, considering the flight of animals as a template.

4.4.3.1 Wings for Soft Aerial Robots

In a flapping-wing robot, the wings move vertically as the aircraft moves horizontally. As shown in Fig. 4.17b, if the forward speed of the aircraft, vertical speed owing to the flapping of the wings, and direction of the wing cross-section (feathering angle)

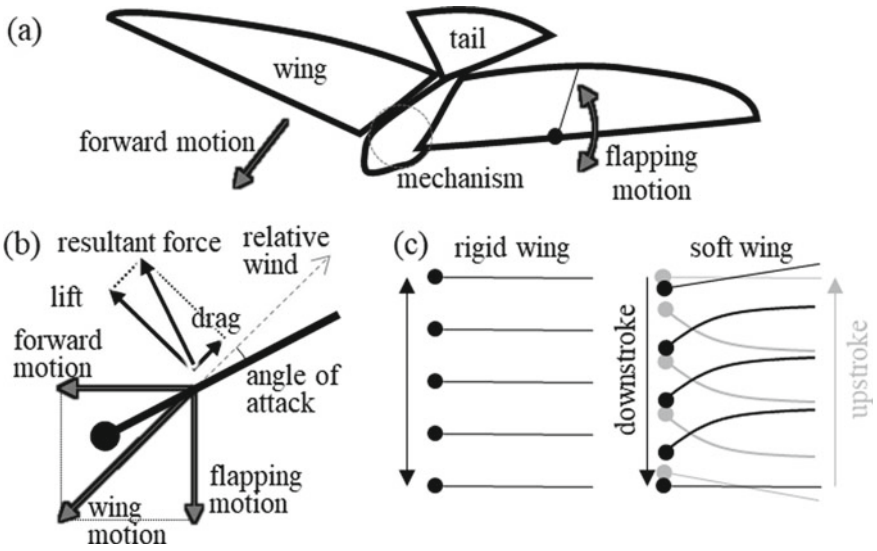

Fig. 4.17 Kinematics and aerodynamics of a flapping-wing robot. **a** Example of a flapping-wing robot. **b** Flapping-wing motion and the direction of lift, drag, and resultant forces. **c** Kinematics of cross-sections of rigid and soft flapping wings

are appropriate, the combined force of lift and drag applied to the wings will be directed upward and forward. Therefore, the wing can simultaneously generate a vertical force against gravity and thrust against drag on the body. If the direction of the wing chord remains the same, the force will be upward during the downstroke and downward during the upstroke, with no thrust generation (Fig. 4.17c). Therefore, the feathering angle must be changed between the downstroke and upstroke to maintain an appropriate angle of attack. Because flapping wings need to be lightweight, soft wing membranes, whose weight can be negligibly small, are often attached to a lightweight skeleton. These skeletons determine the wing shape. If the skeleton and airfoil membrane are appropriately soft, the inertial and aerodynamic forces applied to the airfoil (e.g., upward during downstroke) can change the feathering angle between the downstroke and upstroke (Fig. 4.17c).

The softness of the airfoil surface is crucial for passive deformation. For example, to achieve the above-described feathering angle, the area surrounding the leading edge and root of the wing must be stiffened such that the wing section can rotate around the leading edge. The skeleton of the bird's wing is located near the leading edge, and the rest of the wing consists of relatively soft feathers (Fig. 4.18a). In dragonfly wings, the cross-section near the leading edge is corrugated; therefore, the area near the leading edge is stiffer (Fig. 4.18b). The wings of other insects, such as the hawkmoth, have thicker veins near the anterior margin and thinner veins around the trailing edge (Fig. 4.18c). This might be responsible for the passive control of the wing shape during flapping to maintain the feathering angles, making the flapping wing lighter.

Because the flapping wings rotate around the root, their speed increases from the root to the wing tip. Therefore, the angle of attack near the wing tip significantly affects aerodynamic performance. The wings of hummingbirds and insects produce more force with less power by appropriately twisting and lowering the angle of attack near the wing tip (Maeda 2017). With a structure that is stiff around the leading edge and root while being soft toward the trailing edge (as shown in Fig. 4.18), the wings can be twisted appropriately, and a camber can be introduced to improve the efficiency of the wings (Young 2009). Accordingly, flapping wings that consider the stiffness distribution of insect and bird wings have also been manufactured (Tanaka 2011b).

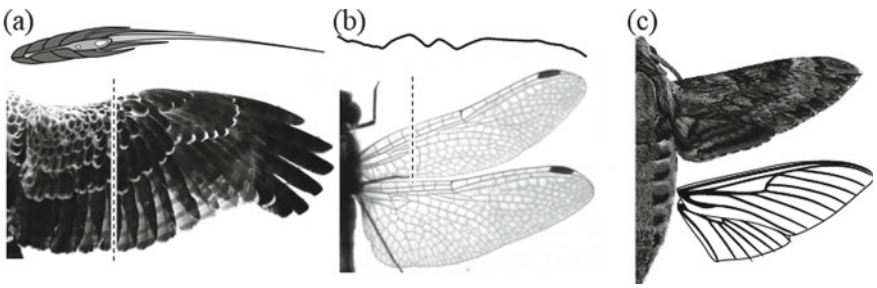

Fig. 4.18 Soft wing structures of flying animals. **a** An example of bird wings and bird wing cross-section. **b** Dragonfly wings and wing cross-section. **c** Venation on a hawkmoth's wing

Like fixed-wing aircraft, the flapping-wing robots described thus far must always move forward and are not capable of hovering, e.g., multicopter drones. To hover like hummingbirds and insects such as hawkmoths, they must stay in the air with a high flapping frequency, large flapping amplitude, and horizontal wing motion. The feathering angles of hovering hummingbirds and hawkmoths vary considerably during their wingbeat to generate leading-edge vortices during both the downstroke and upstroke, which accounts for a large lift that allows them to stay aloft against gravity (Ellington 1996). These leading-edge vortices are ubiquitous in nature and have been observed in the flights of insects such as fruit flies and hawkmoths, birds including hummingbirds and pied-flycatchers, bats, and even around rotating and falling maple seeds (Chin 2016).

In insects, the rotational axis of the wing root is located near the leading edge, and the inertial force during the stroke reversal is applied in the same direction as the torque to change the direction of the wing. Therefore, assuming that the wing root is a simple torsion spring, the feathering angle of an insect wing can be reproduced without precise control of the feathering angle (Kolomenskiy 2019). The same mechanism has been applied to flapping robots (Whitney 2010).

4.4.4 Flapping Mechanism for Soft Aerial Robots

To flap wings, the flapping mechanism must overcome the inertial force to accelerate the wings at the beginning of the stroke and the aerodynamic force in the middle of the stroke. For this purpose, a crank mechanism was used to convert the rotation of the motor into a reciprocating motion (Fig. 4.19a). If the motor is sufficiently light for flight and provides the appropriate power output to overcome inertial and aerodynamic forces, the mechanism can achieve a flapping frequency sufficiently high for flight. Generally, the smaller the wing, the higher the flapping frequency required for flight. If the robot needs to hover, the flapping amplitude of its wings should be higher to support its weight. In contrast, robots in forward flight generally require a lower flapping amplitude because the wings can generate lift with the help of forward motion.

The crank mechanism rigidly controls the motion of the wings. However, no power is required for the motion of the wings during the time the wings decelerate in the later stages of the stroke. In the case of insects, the inertial force for wing deceleration can be stored in the form of musculoskeletal deformation and recycled for wing acceleration in the next stroke (Fig. 4.19b) (Dickinson 1995), which enhances the power economy of the flapping wings. In other words, the flapping mechanism should be soft rather than rigid to facilitate efficient flapping of the wings.

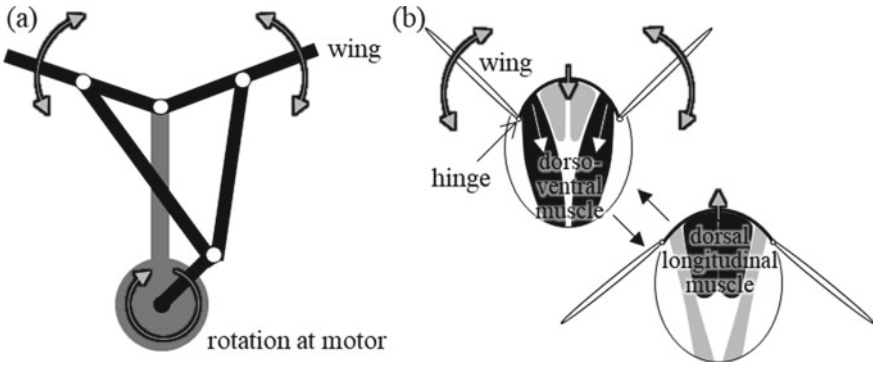

Fig. 4.19 Flapping mechanisms of robots and insects. **a** Crank mechanism commonly used in flapping robots. **b** Cross-section of the soft musculoskeletal system of an insect

4.4.5 Attitude Control of Soft Aerial Robots

To regulate posture and flight direction without falling, aerial robots must control the direction and magnitude of the aerodynamic force applied to their bodies. In the case of a standard flapping-wing robot, the flapping wings oscillate steadily, and the flight direction can be changed by shifting the orientation of the tail. The tail is moved vertically up and down to change the attitude (pitch) of the robot, whereas the tail rotates around the body axis (roll) or in the left–right direction (yaw) to change the flight orientation laterally.

The posture of a multicopter drone is dynamically unstable. It achieves stable stationary flight by adjusting the propeller speed while sensing its own posture. The flight of animals that hover with flapping wings is also considered to be dynamically unstable. Therefore, these animals continuously adjust the speed and feathering angle of their wings by contracting various steering muscles (Dickinson 1997).

In outdoor flight, unpredictable winds may blow, and vortices may be generated around obstacles. Because of these disturbances, aerial robots may collide with obstacles. Therefore, it is necessary to continuously detect obstacles and atmospheric disturbances. However, wind is difficult to predict, and obstacle detection requires the installation of new devices that may increase the weight of the flying object. As a result, it has been proposed that by ensuring appropriate softness of the wings and mechanisms, an aircraft can passively mitigate the effects of wind via deformation at the soft mechanism, reducing the likelihood of losing their posture (Koizumi 2021). In other words, a sufficient level of softness allows for a more robust flight.

4.4.6 Soft Components for Conventional Drone

Thus far, we have analyzed the effect of softness on the performance of flapping-wing robots. However, flapping wings are difficult to manufacture and control. Therefore, using conventional drones with rotary wings is sometimes preferred. An appropriate level of softness is also effective for improving the performance of such conventional drones. Although thin and stiff wings are used in drones to improve performance, they are extremely dangerous owing to their high-speed motion. For example, a lightweight and soft protector with an origami structure is effective in mitigating the impact of collisions (Sareh 2018). A soft propeller has also been reported to reduce the impact of a collision by acting as a cushion (Nguyen 2020). Generally, safety can be improved by replacing conventional elements with softer ones. Under constant application of aerodynamic forces, the wing may deform due to its softness, even under normal conditions. As explained in Sect. 1.1.2, the wing shape has a significant effect on its aerodynamic performance. Therefore, the shape of the wing may become suboptimal because of deformation, which can reduce its aerodynamic performance. Therefore, softer wings must be designed by addressing potential deformation rather than by simply changing materials.

4.4.7 How to Initiate Soft Aerial Robot Research

In this section, we introduce the role of softness in aerial robots. As described, it is difficult to design soft elements by employing a purely theoretical approach owing to the involvement of fluid–structure interactions. Therefore, flying animals that utilize soft wings and musculoskeletal systems can be a good reference (Dudley 2002; Videler 2006). The basic elements of an aerial robot can be fabricated by combining a small motor, crank mechanism, and wings made of carbon rods or films. The stiffness of the carbon rods and films significantly affects the flight performance of the robot. Typically, various combinations of materials must be tested to achieve optimal flight performance. The aerodynamic effects of wing softness can be investigated by measuring thrust using an electronic balance.

4.4.8 Challenges

When a soft structure interacts with air, the balance between structural dynamics and aerodynamics determines the shape of the soft structure and airflow. It is difficult to analyze the fluid–structure interaction theoretically, except for the simplest cases. Therefore, the design of soft elements for aerial robots is difficult. In the case of flight, each component must be sufficiently lightweight and robust to satisfy the weight limitation. It may be possible to improve certain aspects of performance by introducing

softness into existing elements, such as propellers, but these elements may experience deformation owing to fluid–structure interactions, which can adversely affect flight performance. Solving these problems may improve the flight performance of drones and considerably expand their applicability to diverse fields, including logistics and surveillance.

The relationship between flight and softness is also important in animals. The softness of insect wings and bird feathers is maintained by hierarchical structures, which may be the result of weight reduction due to adaptation to flight. Although it is known that softness has certain effects on efficiency and disturbance response, its diverse functions, and effects on flight control, as well as its impact during fluctuating winds, are yet to be investigated. To improve our understanding of these issues, robot-based research, in addition to continued observation of flying organisms, can play a critical role.

4.5 Aquatic Swimming with Soft Fins and Body

4.5.1 Basic Concepts

Soft swimming robots are often modeled on swimming animals, such as fish, dolphins, jellyfish, rays, squid, cuttlefish, sea lions, sea turtles, lobsters, penguins, and snakes (Fish 2020). These swimming organisms propel themselves by moving their fins, arms, legs, or entire bodies. These complex dynamic mechanisms can be qualitatively understood by formulating a simplified model. This model can subsequently be used to estimate propulsion force and efficiency. In this section, a fluid dynamics model of the propulsion mechanism of swimming organisms is introduced to guide the production of soft swimming robots.

4.5.2 Physical Property of Water

Both underwater swimming and aerial flight involve motion in a fluid medium (water or air) that is not in contact with the ground. Therefore, the fluid dynamics model for flight presented in Sect. 4.4 also holds true underwater. However, swimming and flight differ because of the differences between the physical properties of water and air, as presented in Table 4.1.

Water and air have considerably different densities; the density of water is approximately 800 times that of air. Therefore, the buoyancy of a body, which is the fluid density multiplied by the body volume, can be used to support body weight during underwater swimming. Hence, locomotive apparatus such as fins, legs, or undulating bodies can focus on thrust generation with less effort to maintain the body at the same depth level, leading to diverse styles of propulsion methods. In contrast, during aerial

Table 4.1 Physical properties of water and air (at atmospheric pressure (Elger 2016), with source data from the handbook (Bolz 1973)

	Density ρ (kg/m^3)	Viscosity μ (Ns/m^2)	Kinematic viscosity $\nu = \mu/\rho$ (m^2/s)
Water (20 °C)	998	1.00×10^{-3}	1.00×10^{-6}
Water (0 °C)	1000	1.79×10^{-3}	1.79×10^{-6}
Dry air (20 °C)	1.20	1.81×10^{-5}	1.51×10^{-5}
Dry air (0 °C)	1.29	1.72×10^{-5}	1.33×10^{-5}

flight, buoyancy is much smaller than body weight. Thus, the flight apparatus must form a wing shape and support the body weight by aerodynamic force.

A high fluid density causes large drag and lift forces to act on objects in fluid. The following transformations for the formulas for the drag coefficient C_D and lift coefficient C_L presented in Sect. 4.4 show that the drag F_D and lift F_L are proportional to the fluid density ρ.

$$F_D = 0.5\rho U^2 A C_D$$
$$F_L = 0.5\rho U^2 A C_L$$

The viscosity of water is an order of magnitude higher than that of air. However, the kinematic viscosity of water, which is the viscosity per density, is one order of magnitude lower than that of air owing to the high density of water. The Reynolds number, *Re*, is inversely proportional to the kinematic viscosity (see Sect. 4.4). Therefore, the Reynolds number tends to be high during underwater swimming, even at low speeds. Changes in the Reynolds number affect the similarity of the flow field around objects, resulting in changes in C_D and C_L. It is also necessary to consider the temperature dependence of the viscosity and kinematic viscosity of water when calculating the Reynolds number.

4.5.3 Conventional Screw Propulsion of Ships

The general propulsion mechanism of ships and underwater drones relies on rotational wings (screws, propellers, and rotors). The rotational axial component of the wing lift serves as a forward thrust (Fig. 4.20). The radial component of the lift is canceled for each wing rotation. Similar to the aerodynamics of a fixed wing, explained in Sect. 4.4, if a small angle of attack is not maintained for the rotary wing, flow separation will occur, leading to a state where a large lift cannot be obtained (i.e., stall). Therefore, high-speed rotation and an increase in the flow velocity while maintaining a small angle of attack are necessary for a sufficiently large thrust. However, as with the lift, the drag of the wing provides resistance to rotation, resulting in an upper limit on rotational speed due to upper limits on torque and power for rotation. In addition, cavitation occurs at high-speed rotation, in which an extremely

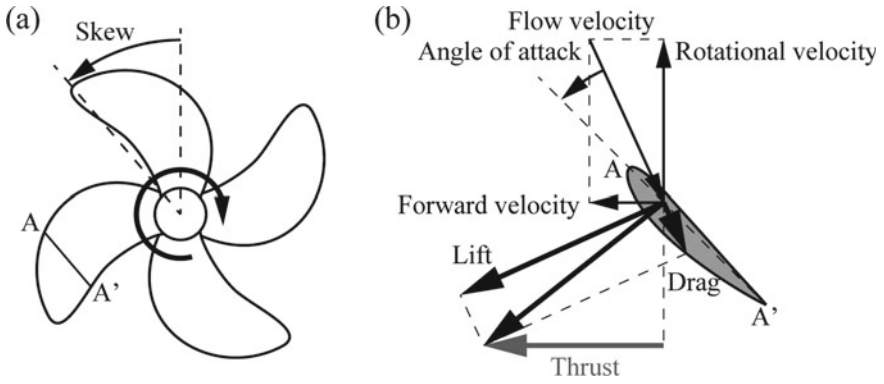

Fig. 4.20 **a** Schematic of the rear view of a skewed propeller rotating in a clockwise direction. **b** Schematic of the cross-section of a wing

low pressure near the wing's surface produces air bubbles. Cavitation may lead to a reduction in thrust, wing vibration, acoustic noise, or wing corrosion. A skewed (sweepback) shape of the wing is adopted to suppress cavitation in ship engineering (Carlton 2012).

4.5.4 Propulsion Mechanism in Animals

This subsection describes the propulsion mechanisms in aquatic animals utilizing soft fins and bodies, such as the jet propulsion of squids, undulating propulsion of sea snakes, paddling propulsion of fish with pectoral fins, and oscillating propulsion of fish with caudal fins. The detailed explanation of theories and calculations for these propulsion models can be found in a reference (Azuma 2006). The swimming mechanism of jellyfish is also discussed. The hydrodynamics of flapping-wing propulsion observed in penguins and mantas are analogous to the aerodynamics of flapping flight, as explained in Sect. 4.4.

1. Jetting

When a squid swims at a high speed, water is drawn into the mantle cavity and expelled through the funnel tube to achieve propulsion. The thrust for the jet propulsion can be described using the bag model shown in Fig. 4.21. The fluid is expelled when the inside of the bag is pressurized and drawn when the pressure decreases. A jet is a pulsating current for which the minimum cross-sectional area S_c is less than the jet expulsion area (opening area of the bag) S. The area ratio S_c/S is 0.62 for a circular orifice (a thin plate with a circular hole).

The thrust T is the integral of the component of the differential pressure acting on the bag ($p_{\text{internal}} - p_0$) in the direction of travel and can also be regarded as the change in the fluid momentum resulting from expulsion and suction. Let V denote

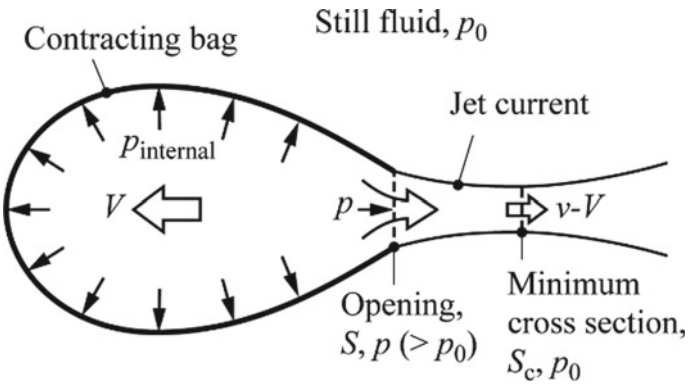

Fig. 4.21 Schematic of the contracting bag model of jetting, based on a reference (Azuma 2006)

the forward velocity of the bag assuming a stationary ambient fluid, and v denote the relative expulsion velocity with respect to the bag where the jet cross-sectional area is a minimum (v is negative for the case of suction). Subsequently, for $v - V > 0$, the jet has a backward velocity with respect to the ambient fluid. In other words, the ambient fluid gains backward momentum, and as a reaction to this action, the bag gains forward momentum. Let $\dot{m}$ denote the mass flow rate per unit time. Then, T is expressed as follows:

$$T = \dot{m}(v - V) = \rho S_c v(v - V)$$

Thus, the maximum efficiency is obtained at $V/v = 0.5$.

For a rocket, the fluid within the bag can be considered a fuel payload on the bag. Expulsion corresponds to a reduction in the total mass of the rocket, including the fuel payload, and T equals $\dot{m}v$.

2. Undulation of a slender body

Sea snakes have slender bodies along which backward-propagating waves can be produced to generate thrust. For a columnar object with a sufficiently small diameter-to-length ratio, the fluid force acting on a part of the object is determined only by the cross-sectional profile of the part and transverse velocity. This model is known as the "slender-body theory." The forces acting on a part of the object consist of the inertial force due to the mass of the part; inertial force due to the mass of the fluid in the vicinity of the part (called the added mass), and drag exerted on the part. The inertial force is proportional to the acceleration of the part. The inertial force due to the mass of the part over one wave cycle averages to zero and, therefore, does not affect the thrust.

The added mass of the ambient fluid per unit length of the body varies with the orientation of the object and its cross-sectional profile. For a circular cross-sectional shape of area S, the added mass with respect to the vertical direction of the object is ρS. The added mass force (the inertial force due to the added mass) acts perpendicular

to the part and can be calculated as $-\rho S a_n$, where a_n is the perpendicular component of the transverse acceleration of the part a_t (Fig. 4.22a, b).

In the case of a uniform cross-sectional profile, the wave amplitude must increase toward the rear of the body for the added mass force to generate thrust (Fig. 4.22a). That is, when the body shape is expressed as $y = ae^{bx} \sin x$, as shown in Fig. 4.22a, b is greater than zero. For a constant wave amplitude, the forward and backward components of the inertial force for both the body part and added mass completely cancel each other such that no thrust is produced (Fig. 4.22b). If the cross-section is as large as that of the rear of the body, the forward component of the inertial force prevails across the entire body to generate thrust even for a constant wave amplitude.

This slender-body theory can be applied to an octopus's arms, which are much longer than their diameters. However, when an octopus closes its arms, the distance

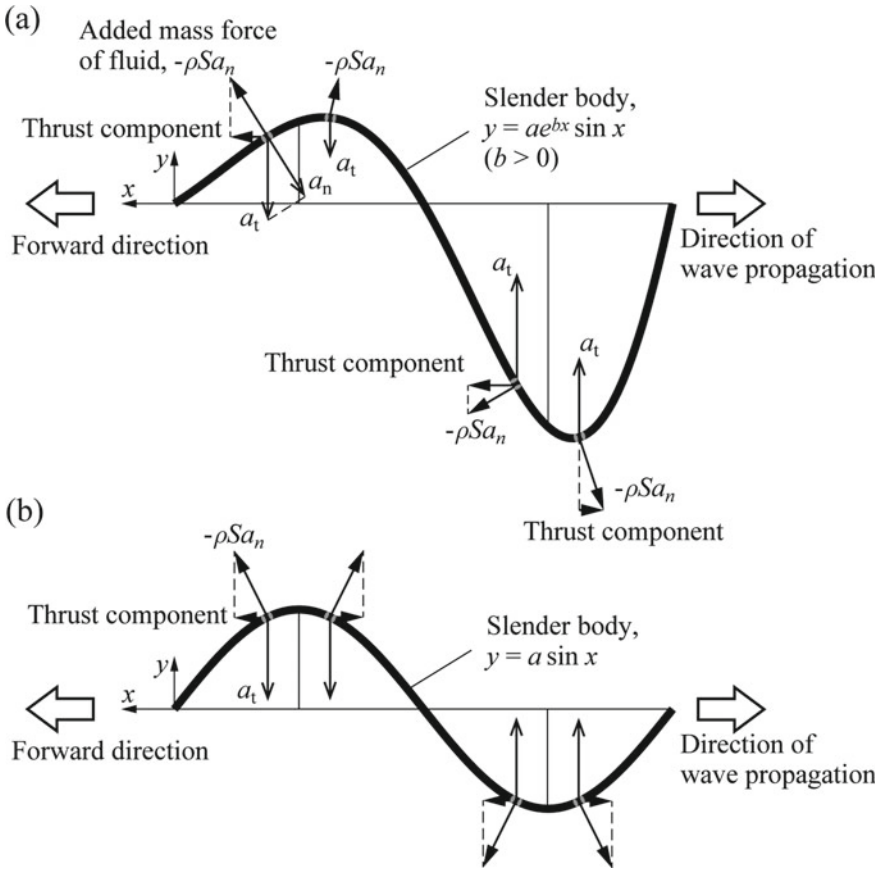

Fig. 4.22 Added mass force in undulating slender bodies, illustrated based on a reference (Azuma 2006). **a** Backward increase in the wave amplitude ($b > 0$) leads to total thrust by the added mass force. **b** Added mass force does not generate thrust with a constant amplitude of the wave. Values for a are different between the schematics of (**a**) and (**b**)

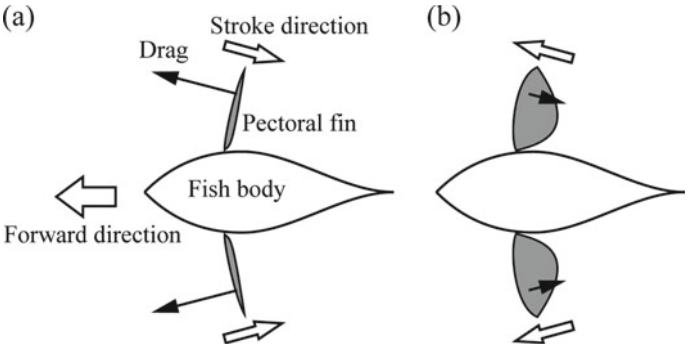

Fig. 4.23 Paddling with pectoral fins in fish. **a** Power stroke. **b** Recovery stroke

between the arms becomes small, and the flow fields around each arm interfere with each other, such that the slender-body theory may not be applicable.

3. Paddling

In paddling propulsion, the drag of plate-like fins or legs is used as thrust. Thus, this is a drag-based propulsion mechanism. Fish that use pectoral fins for paddling move them with a large angle of attack during the power stroke, such that the drag has a large forward component (Fig. 4.23a). The fish reduce the angle of attack during the recovery stroke and return the fins to their original position to prevent the generation of a backward drag component (Fig. 4.23b). Paddling propulsion is suitable for low-speed swimming.

4. Heaving and pitching of caudal fin

Dolphins, whales, and most fish generate thrust by oscillating their caudal fins, in which the forward component of the lift of the caudal fin is utilized. Thus, this is a lift-based propulsion mechanism. When a fish moves forward by oscillating its caudal fins, vortices shed alternately in the rear, as shown in Fig. 4.24, and induce backward flow. The swing styles of the caudal fin can be categorized into one-hinge swing (Fig. 4.25a) and two-hinge swing (Fig. 4.25b). The one-hinge swing is observed in boxfish with a thick caudal peduncle, whereas many other fish adopt the two-hinge swing. In the two-hinge swing of fish with caudal fins, the heaving phase (translational motion in which the fins move away from the central surface) can be offset from the pitching phase (rotational motion of the fins relative to the central surface), and the angle of attack of the caudal fins (the angle between the direction of the relative flow velocity and fin surface) can vary with the phase difference between heaving and pitching.

Cyclic heaving h and pitching θ can be expressed as functions of time t as follows:

$$h = h_c \cos(2\pi f t)$$
$$\theta = \theta_c \cos(2\pi f t + \phi)$$

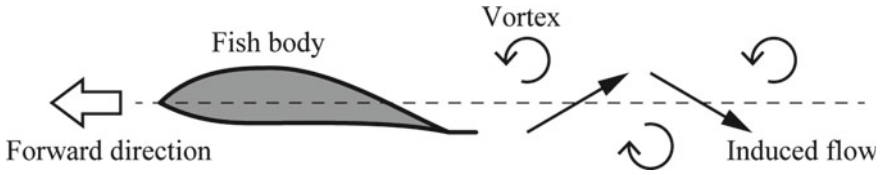

Fig. 4.24 Vortices and flow induced by an oscillating caudal fin

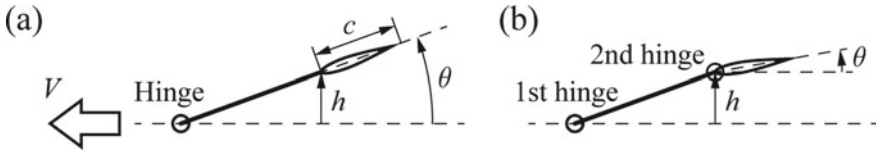

Fig. 4.25 One-hinge model (a) and two-hinge model of an oscillating caudal fin

where h_c and θ_c are the heaving and feathering amplitudes, respectively; f is the frequency; and ϕ is the phase difference between heaving and feathering. In a one-hinge swing, ϕ is zero.

Here, the non-dimensional oscillation frequency k, known as "reduced frequency," is an important parameter related to the performance of caudal fin propulsion. k is expressed as $k = 2\pi f c / V$, where c is a representative length, such as the chord length of the fin. According to the fluid dynamic analysis, to maximize the propulsive force, ϕ should be $\pi/2$ for small k and approach zero for large k. To maximize propulsion efficiency, ϕ should be $-\pi/2$ for sufficiently small k; that is, $k < 0.5$, and a ϕ in the range of $-\pi/2$ to $-3\pi/4$ is suitable for sufficiently large k, that is, $k > 2$. In contrast, propulsion efficiency is poor for $0 < \phi < \pi/2$.

Strouhal number St is also a representative non-dimensional number for caudal fin propulsion and flapping wing propulsion. St is expressed as fh_c/V for caudal fin propulsion. Hydrodynamic experiments of transversal heaving with rotational pitching of wings show that the highest propulsive efficiency usually peaks at an St of approximately 0.3, where the thrust coefficient is also sufficiently large (Anderson et al. 1998). In nature, it is known that the St of cruising fish, sharks, and dolphins ranges from 0.2 to 0.4 (Taylor et al. 2003), implying that these swimmers are optimized for efficient swimming. Note that St of flying birds, bats, and insects also tend to be within a range of $0.2 < \mathrm{St} < 0.4$ (Taylor 2003).

5. Propulsion mechanism of jellyfish

A jellyfish swims via pulsation of its bag-shaped body, which is usually described as jet propulsion. However, careful observation shows that the propulsion mechanism is not simple. Motion measurement of a common jellyfish, *Aurelia aurita*, indicates that the jellyfish accelerates only at the beginning of the ejection phase (the period when the bell volume decreases). In contrast, the moving speed is maintained and does not decelerate, even in the suction phase (the period when the bell volume decreases) (Ichikawa 2008).

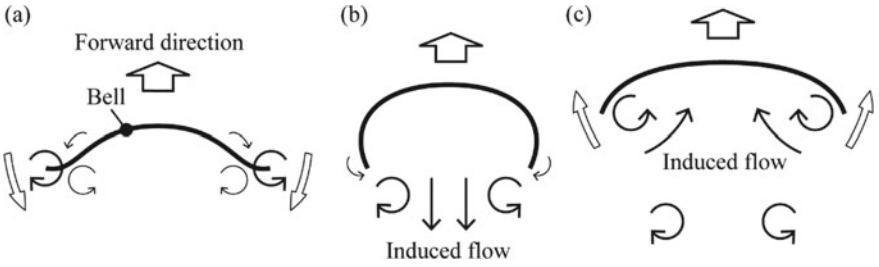

Fig. 4.26 Cross-sectional schematics of jellyfish propulsion based on a reference (Costello et al. 2021)

The bell margin of the jellyfish flaps inward during the ejection phase. Flow visualization reveals that this flapping produces a vortex structure around the jellyfish and contributes to thrust (Fig. 4.26) (Costello et al. 2021). The inward flap of the bell margin (Fig. 4.26a) creates a vortex ring expelling the flow out of the bell cavity (Fig. 4.26b). Another vortex ring is also induced, which draws flow into the bag, thereby providing forward momentum in the suction phase (Fig. 4.26c).

4.5.5 How to Start the Soft Fins Research

Caudal fin propulsion is a suitable subject for evaluating the effectiveness of soft structures. Pitching with a certain phase difference from heaving can be realized by replacing the second hinge with a torsional or plate spring in the two-hinge swing mechanism. The replacement of the rigid fin with an elastic fin in the one-hinge swing mechanism also realizes pitching by the elastic flexion of the fin. Spring or elastic fins have been used in recent fish robots (Clapham 2014; Thandiackal 2021).

The hydrodynamic force and resultant thrust of the fin can be estimated by a quasi-steady calculation based on the following parameters: forward moving speed of the body; heaving speed of the fin; angle of attack, and wing characteristics (relationship between lift and drag coefficients and angle of attack). An empirical survey of the appropriate elasticity is necessary because fluid–structure interactions are complex and difficult to calculate with high accuracy in advance.

The basal swing motion is easily realized by the direct use of a servo motor. For high-frequency swings, it may be suitable to convert the rotary motion of a high-speed motor into reciprocating motion. Typical conversion mechanisms include lever-crank mechanisms (four-bar linkage mechanism), slider-crank mechanisms, and Scotch-yoke mechanisms (slotted link mechanism). For example, scotch-yoke mechanisms have been used in dolphin robots (Peng et al. 2011; Yu 2009). Another mechanism without links can be found in a recent fish robot that uses a rotational bent shaft and a slotted flapper (Thandiackal 2021).

Various types of fish-inspired robots, including caudal fin propulsion, paddling, and undulation, can be found in a review paper (Aditi 2016). A detailed classification of fish swimming modes can be found in the literature (Lindsey 1978; Sfakiotakis 1999).

4.5.6 Challenges

The simplified models of propulsion mechanisms explained in Sect. 4.4.4 are useful in the quantitative understanding and initial design of swimming robots with soft fins and bodies. However, actual performance is difficult to predict before fabrication and experimentation because of the complexity of unsteady fluid dynamics. Moreover, performance can be improved by increasing the degrees of freedom of motion or by continuous deformation of the body. For example, in a one-hinge caudal fin mechanism, the addition of two rotational joints in the link and a flexural spring at the base of the fin has been reported to improve both swimming speed and efficiency (White et al. 2021).

In addition to the aforementioned external motion and deformation, the performance of the internal driving mechanism can also be improved by elastic elements. For example, the implementation of a spring in the transmission of the Scotch yoke mechanism has been reported to enhance efficiency by elastic energy storage and release of the spring (Kwon 2018).

For marine engineering applications, tolerance to water pressure is necessary. Recently, the actuation of a soft flapping-wing robot in deep water has been reported (Li 2021). The body is made of a silicone elastomer, and the dielectric elastomer actuators drive the wing. At a depth of 10,900 m in the Mariana Trench, the robot was tethered to the arm of an underwater vehicle and actuated under a water pressure of 110 MPa. The robot also freely swam at a depth of 3224 m in the lake.

Biomimetic and bio-inspired propulsion mechanisms can realize more agile, robust, and efficient swimming robots in complex and severe underwater environments than conventional screw-type propulsion mechanisms. A broad consideration of real situations, such as water pressure, temperature, current, geography, transparency, and ecosystem, is important in the design of underwater field robots.

Exercises

1. An elastic spherical fingertip is in contact with a flat, rigid surface. Let r be the radius of the fingertip and $r - \delta$ be the distance between the fingertip center and the surface. Let E and ν be Young's modulus and Poisson's ratio of the fingertip material. Then, derive a contact force based on the Hertzian contact model.
2. Design soft hands to grasp the following: (a) a laptop computer, (b) cucumbers, (c) mushrooms, and (d) beans. Investigate the physical properties of each item and consider them to develop the appropriate design for that item
3. Compare an industrial robot arm with a continuum robot arm and list three major differences. (4.2)

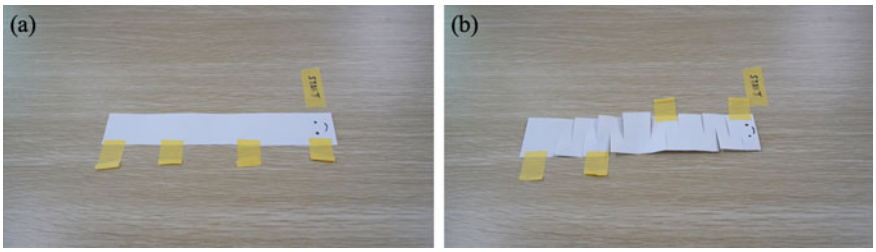

Fig. 4.27 **a** Caterpillar model and **b** Earthworm model

4. Search for species with tentacles that resemble a continuum robot arm. (4.2)
5. Find a paper that applies reinforcement learning to a continuum robot arm. (4.2)
6. Realize a caterpillar model and an earthworm model using paper and tape, as shown in Fig. 4.27. First, procure a rectangular piece of paper (approximately 210 mm × 40 mm), adhesive paper tape that can be pasted and peeled off repeatedly, and scissors. Next, construct the caterpillar and worm models using paper and paper adhesive tape. For the earthworm model, cut a vertically extended slit in the paper, as shown in Fig. 4.27b. **(4.3)**
7. **Realize the caterpillar crawl (4.3)**

   In a caterpillar's crawl, when a body part shrinks, it cannot be anchored because it lifts. Therefore, according to this rule, peel off the tape from the front or back and try to generate caterpillar locomotion by bending motion in the body.
8. **Realize the earthworm crawl (4.3)**

   While crawling, the worm can be anchored when its body contracts (it cannot be anchored when it extends). Following to this rule, try to achieve earthworm locomotion by extending the body part(s) and removing the tape from the front or back.

   Answer Each type of locomotion can be realized as shown in Fig. 4.28.
9. To make efficient flapping-wing robots, what kind of materials can be used for the flapping wings? (4.4)
10. Consider wings attached to the flapping mechanism. If the wings do not generate thrust even when the mechanism consumes a considerable amount of power, how should the wing structure be changed? (4.4)
11. An aerial robot was built using a crank mechanism to flap its wings, which were made of thin uniform plates. However, when flown, the robot fails rapidly and falls. What could be the problems, and how can the robot's flight performance be improved? (4.4)
12. In the jetting propulsion, calculate the relative expulsion velocity v and the thrust T under the following conditions: $S = 0.0004$ m^2; $\dot{m} = 0.4$ kg/s; $\rho = 1000$ kg/m^3; $S_c/S = 0.62$; $V = 1$ m/s. (4.5)

Fig. 4.28 .

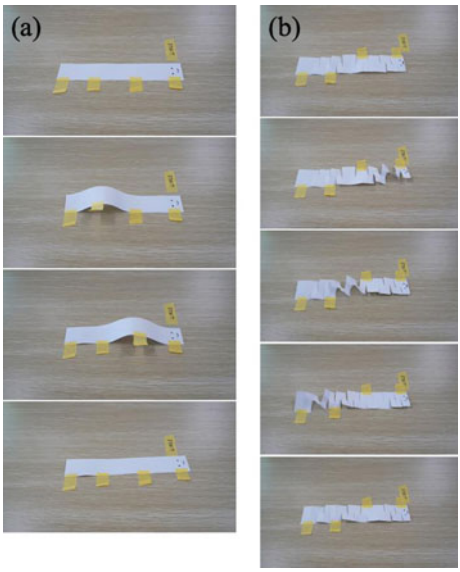

13. In the one-hinge swing propulsion, calculate the frequency f to achieve the reduced frequency $k = 2$ under the following conditions: $c = 0.03$ m; $V = 0.5$ m/s. (4.5)
14. Observe a swimming fish in the sea, at an aquarium, or in a movie and estimate its reduced frequency and Strouhal number. (4.5)

Solution:

1. $$v = \frac{\dot{m}}{\rho Sc} = \frac{4 \times 10^{-1}}{10^3 \times 0.62S} = \frac{4 \times 10^{-1}}{10^3 \times 0.62 \times 4 \times 10^{-4}} = \frac{1}{0.62} \approx 1.61 \text{ m/s}$$
$$T = \dot{m}(v - V) = 4 \times 10^{-1}(1.61 - 1) = 2.44 \times 10^{-1} \text{ N}$$

2. $$k = \frac{2\pi f c}{V}$$
$$\Rightarrow 2 = \frac{2\pi f 0.03}{0.5}$$
$$\Rightarrow f = \frac{0.5}{0.03\pi} \approx 5.3$$

References

Aditi R, Atul T (2016) Fish-inspired robots: design, sensing, actuation, and autonomy—a review of research. Bioinspir Biomim 11(3):031001
Alexander RM (1992) Exploring biomechanics, animals in motion. W.H. Freeman and Company
Alexander RM (2002) Principles of animal locomotion. Princeton Univ. Press, Princeton

Anderson JM, Streitlien K, Barrett DS, Triantafyllou MS (1998) Oscillating foils of high propulsive efficiency. J Fluid Mech 360:41–72
Azuma A (2006) The biokinetics of flying and swimming, 2nd edn. AIAA, Virginia, USA
Bolz RE, Tuve GL (1973) Handbook of tables for applied engineering science. CRC Press Inc., Cleveland, USA
Brown E, Rodenberg N, Amend J, Mozeika A, Steltz E, Zakin MR, Lipson H, Jaeger HM (2010) Universal robotic gripper based on the jamming of granular material. Proc Natl Acad Sci 107(44):18809–18814. https://doi.org/10.1073/pnas.1003250107,Nov
Boxerbaum AS et al. (2010) A new theory and methods for creating peristaltic motion in a robotic platform. In: Proceeding of the international conference on robotics and automation (ICRA2010), pp 1221–1227
Burgner-Kahrs J, Rucker DC, Choset H (2015) Continuum robots for medical applications: a survey. IEEE Trans Rob 31(6):1261–1280. https://doi.org/10.1109/TRO.2015.2489500
Carlton J S, (2012) Propeller design. In: Marine propellers and propulsion, 3rd edn. Butterworth-Heinemann, Oxford, UK, pp 431–458
Carrico JD et al (2019) 3D-Printing and machine learning control of soft ionic polymer-metal composite actuators. Sci Rep 9. Article number: 17482
Chin DD, Lentink D (2016) Flapping wing aerodynamics: from insects to vertebrates. J Exp Biol 219:920–932
Chirikjian GS, Burdick JW (1994) A hyper-redundant manipulator. IEEE Robot Autom Mag 1(4):22–29. https://doi.org/10.1109/100.388263
Clapham RJ, Hu H (2014) iSplash-II: realizing fast carangiform swimming to outperform a real fish. In: Proceedings of IEEE/RSJ international conference on intelligent robots and systems (IROS), pp 1080–1086
Costello JH, Colin SP, Dabiri JO, Gemmell BJ, Lucas KN, Sutherland KR (2021) The hydrodynamics of jellyfish swimming. Ann Rev Mar Sci 13:376–396
Denny M (1980) The role of gastropod pedal mucus in locomotion. Nature 285:160–161
Dickinson MH, Lighton JRB (1995) Muscle efficiency and elastic storage in the flight motor of Drosophila. Science 268:87–90
Dickinson MH, Tu MS (1997) The function of dipteran flight muscle. Comp Biochem Physiol A Physiol 116:223–238
Dudley R (2002) The biomechanics of insect flight: From, function, evolution. Princeton University Press, New Jersey.
Elger DF, Lebret BA, Crowe CT, Robertson JA (2016) Engineering fluid mechanics 11th edition international student version. Wiley, New York, USA
Ellington CP (1984) The aerodynamics of hovering insect flight. I. The quasi-steady analyses. Philos Trans R Soc B 305:1–15
Ellington CP, van den Berg C, Willmott AP, Thomas ALR (1996) Leading-edge vortices in insect flight. Nature 384:626–630
Ewoldt R et al (2007) Rheological fingerprinting of gastropod pedal mucus and synthetic complex fluids for biomimicking adhesive locomotion. Soft Matter 24;3(5):634–643. https://doi.org/10.1039/b615546d
Fantoni G, Santochi M, Dini G, Tracht K, Scholz–Reiter B, Fleischer J, Lien TK, Seliger G, Reinhart G, Franke J, Hansen HN, Verl A (2014) Grasping devices and methods in au- tomated production processes. CIRP Ann Manufact Technol 63(2):679–701
Fang H et al (2017) Origami-based earthworm-like locomotion robots. Bioinspiration Biomimetics 12(6)
Full RJ (1997) Invertebrate locomotor systems. Oxford University Press, New York
Godage IS, Medrano-Cerda GA, Branson DT, Guglielmino E, Caldwell DG (2016) Dynamics for variable length multisection continuum arms. Int J Rob Res 35(6):695–722. https://doi.org/10.1177/0278364915596450
Hao Y, Visell Y (2021) Beyond soft hands: efficient grasping with non-anthropomorphic soft grippers. Front Robot AI. https://doi.org/10.3389/frobt.2021.632006

Hawkes EW, Blumenschein LH, Greer JD, Okamura AM (2017) A soft robot that navigates its environment through growth. Sci Robot 2(8). https://doi.org/10.1126/scirobotics.aan3028
Hidaka Y et al (2009) Peristaltic crawling robot with artificial rubber muscles for large intestine endoscopy. In: Proceedings of 12th International conference on climbing and walking robot (CLAWAR2009), pp 225–232
Hirose S, Kado T, Umetani T (1983) Tensor actuated elastic manipulator. In: 6th World congress on theory of machines and mechanisms, pp 978–981
Ichikawa S, Mochizuki O (2008) The flow induced by a jellyfish. J Visualization 11(3):257–264
Ilievski F, Mazzeo AD, Shepherd RF, Chen X, Whitesides GM (2011) Soft robotics for chemists. Angew Chem Int Ed. https://doi.org/10.1002/anie.201006464
Ikeuchi M et al (2012) Development of an in-pipe inspection robot for narrow pipes and elbows using pneumatic artificial muscles. In: IEEE/RSJ international conference on intelligent robots and systems (IROS2012), pp 926–931
Ikuta K, Ichikawa H, Suzuki K, Yamamoto T (2003) Safety active catheter with multi-segments driven by innovative hydro-pressure micro actuators. In: The 16th IEEE international conference on micro electro-mechanical systems (MEMS), pp 130–135. https://doi.org/10.1109/MEMSYS.2003.1189704
Inoue T, Hirai S (2009) Mechanics and control of soft-fingered manipulation. Springer. ISBN 978-1-84800-980-6. https://doi.org/10.1007/978-1-84800-981-3
Isaka K et al (2019) Development of underwater drilling robot based on earthworm locomotion. IEEE Access
Ito F et al (2019) Proposal of a peristaltic motion type duct cleaning robot for traveling in a flexible pipe. In: IEEE/RSJ international conference intelligent robot and systems (IROS2019), pp 6614–6621
Jones HD et al (1970) Locomotion of the Limpet, Patella Vulgata L. J Exp Biol 52:201–216
Jones BA, Walker ID (2006) Kinematics for multisection continuum robots. IEEE Trans Robot 22(1):43–55. https://doi.org/10.1109/TRO.2005.861458
Koizumi S, Nakata T, Liu H (2021) Flexibility effects of a flapping mechanism inspired by insect musculoskeletal system on flight performance. Front Bioeng Biotechnol 9:612183
Kolomenskiy D, Ravi S, Xu R, Ueyama K, Jakobi T, Engels T, Nakata T, Sesterhenn J, Schneider K, Onishi R, Liu H (2019) The dynamics of passive feathering rotation in hovering flight of bumblebees. J Fluids Struct 91:102628
Kwon SR, Lee DY, Jeong U, Park YJ, Cho KJ (2018) Development of efficiency enhanced scotch yoke mechanism for robotic fish. Int J Precision Eng Manuf 19(10):1507–1513
Lam TL et al (2011) A flexible tree climbing robot: treebot—design and implementation. In: 2011 IEEE international conference on robotics and automation. https://doi.org/10.1109/ICRA.2011.5979833
Li G, Chen X, Zhou F, Liang Y, Xiao Y, Cao X, Zhang Z, Zhang M, Wu B, Yin S, Xu Y, Fan H, Chen Z, Song W, Yang W, Pan B, Hou J, Zou W, He S, Yang X, Mao G, Jia Z, Zhou H, Li T, QUu S, Xu Z, Huang Z, Luo Y, Xie T, Gu J, Zhu S andYang W (2021) Self-powered soft robot in the Mariana Trench. Nature 591(7848):66–71
Lin H et al (2011) GoQBot: a caterpillar-inspired soft-bodied rolling robot. Bioinspir Biomim 6(2):026007. https://doi.org/10.1088/1748-3182/6/2/026007
Lin HT (2011) Biomechanical strategies for locomotion in soft-bodied animals. PhD Thesis, Tufts University. https://dl.tufts.edu/concern/pdfs/p8419067q
Lindsey CC (1978) Form, function, and locomotory habits in fish. In: Fish physiology. Academic Press, Massachusetts, USA, pp 1–100
Maeda M, Nakata T, Kitamura I, Tanaka H, Liu H (2017) Quantifying the dynamic wing morphing of hovering hummingbird. Roy Soc Open Sci 4:170307.
Mahl T, Hildebrandt A, Sawodny O (2014) A variable curvature continuum kinematics for kinematic control of the bionic handling assistant. IEEE Trans Robot 30(4):935–949. https://doi.org/10.1109/TRO.2014.2314777

Mangan EV et al (2002) Development of a peristaltic endoscope. In: Proceedings of IEEE international conference on robotics and automation, pp 347–352
Menciassi et al (2004) A SMA actuated artificial earthworm. In: Proceedings of IEEE international conference on robotics and automation, pp 347–352
Morishima M, Umedachi T, Kawahara Y (2020) Caterpillar-inspired soft robot that locomotes upside-down by utilizing environmental skeleton. Eng Res Expr 2:035022
Nakamura T et al (2005) Development of a peristaltic crawling robot based on earthworm locomotion. J Rob Mechatron 18(3):299–304
Omori H et al (2012) Development of a novel bio-inspired planetary subsurface explorer: Initial experimental study by prototype excavator with propulsion and excavation units. IEEE/ASME Trans Mechatron 18(2):459–470
Peng L, Kai H, Xiefeng O, Ruxu D (2011) Mechanical design, kinematic modeling and simulation of a robotic dolphin. In: Proceedings of IEEE international conference on information and automation, pp 738–743
Quillin KJ (1999) Kinematic scaling of locomotion by hydrostatic animals: ontogeny of peristaltic crawling by the earthworm lumbricus terrestris. J Exp Biol 202(6):661–674
Quillin KJ (1998) Ontogenetic scaling of hydrostatic skeletons: geometric, static stress and dynamic stress scaling of the earthworm lumbricus terrestris. J Exp Biol 21;201(12):1871–83
Rozen-Levy S et al (2019) The design and development of Branch Bot: a branch-crawling, caterpillar-inspired, soft robot. Int J Res Rev. https://doi.org/10.1177/0278364919846358
Sadeghi A, Mondini A, Mazzolai B (2017) Toward self-growing soft robots inspired by plant roots and based on additive manufacturing technologies. Soft Robot 4(3):211–223. https://doi.org/10.1089/soro.2016.0080
Saga N et al (2004) A prototype of peristaltic robot using pneumatic artificial muscle. Intell Auton Syst 8(1):85–95
Saga N et al (2002a) Development of peristaltic crawling robot using magnetic fluid on the basis of locomotion mechanism of earthworm. In: Proceedings of SPIE, smart structures, devices, and systems, pp 369–377
Saga N et al (2002b) Elucidation of Propulsive force of micro-robot using magnetic fluid. J Appl Phys 91(10–2,3):7003–7005
Saga N et al (2003) Study on peristaltic crawling robot using artificial muscle actuator. In: IEEE/ASME international conference on advanced intelligent mechatronics (AIM2003), pp 679–684
Sane SP (2003) The aerodynamics of insect flight. J Exp Biol 206:4191–4208
Seok S et al (2010) Peristaltic locomotion with antagonistic actuators in soft robotics. In: Proceedings of IEEE international conference robotics and automation (ICRA2010), pp 1228–1233
Sfakiotakis M, Lane DM, Davies JBC (1999) Review of fish swimming modes for aquatic locomotion. J Oceanic Eng 24(2):237–252
Shintake J, Cacucciolo V, Floreano D, Shea H (2018) Soft robotic grippers. Adv Mater 30(29)
Shyy W, Lian Y, Tang J, Viiery D, Liu H (2011) Aerodynamics of low reynolds number flyers. Cambridge University Press, UK
Sugi H (1977) Evolution of muscle motion. The University of Tokyo Press, Tokyo
Suzumori K, Iikura S, Tanaka H (1991) Flexible microactuator for miniature robots. IEEE Micro Electro Mech Syst 1991:204–209. https://doi.org/10.1109/MEMSYS.1991.114797
Takeichi M, Suzumori K, Endo G, Nabae H (2017) Development of a 20-m-long Giacometti arm with balloon body based on kinematic model with air resistance. In: IEEE international conference on intelligent robots and systems (IROS), pp 2710–2716. https://doi.org/10.1109/IROS.2017.8206097
Tanaka Y et al (2011a) Mechanics of peristaltic locomotion and role of anchoring. J Roy Soc Interface 9(67):222–233
Tanaka H, Whitney JP, Wood RJ (2011b) Effect of flexural and torsional wing flexibility on lift generation in hoverfly flight. Integr Comp Biol 51:142–150

Tang Y et al. (2018) Switchable Adhesion Actuator for Amphibious Climbing Soft Robot. Soft Robotics 5(5)
Taylor GK, Nudds RL, Thomas ALR (2003) Flying and swimming animals cruise at a Strouhal number tuned for high power efficiency. Nature 425(6959):707–711
Thandiackal R, White CH, Bart-Smith H, Lauder GV (2021) Tuna robotics: hydrodynamics of rapid linear accelerations. Proc Roy Soc B: Biol Sci 288(1945):20202726
Trivedi D, Rahn CD, Kier WM, Walker ID (2008) Soft robotics: biological inspiration, state of the art, and future research. Appl Bionics Biomech 5(3):99–117
Umedachi T et al (2019) Caterpillar-inspired crawling robot using both compression and bending deformations. IEEE Rob Autom Lett. https://doi.org/10.1109/LRA.2019.2893438
Umedachi T et al (2013) Highly deformable 3-D printed soft robot generating inching and crawling locomotions with variable friction legs. In: IEEE/RSJ international conference on intelligent robots and systems (IROS 2013), WeAT11.5
van Griethuijsen LI et al (2014) Locomotion in caterpillars. Biol Rev 89(656–670):656. https://doi.org/10.1111/brv.12073
Wang Z, Furuta H, Hirai S, Kawamura S (2021) A scooping-binding robotic gripper for handling various food products. Front Robot AI. https://doi.org/10.3389/frobt.2021.640805
Wang Z, Hirai S, Kawamura S (2022) Challenges and opportunities in robotic food handling: a review. Front Robot AI Algorithms Technol Towards Robot Food Manipulation. https://doi.org/10.3389/frobt.2021.789107
White CH, Lauder GV, Bart-Smith H (2021) Tunabot Flex: a tuna-inspired robot with body flexibility improves high-performance swimming. Bioinspiration Biomimetics 16(2):026019
Whitney J, Wood RJ (2010) Aeromechanics of passive rotation in flapping flight. J Fluid Mech 660:197–220
Yamashita A et al (2011) Self-localization and 3-D model construction of pipe by earthworm robot equipped with omni-directional rangefinder. In: Proceedings of IEEE international conference on robotics and biomimetics, pp 1017–1023
Young J, Walker SM, Bomphrey RJ, Taylor GK, Thomas ALR (2009) Details of insect wing design and deformation enhance aerodynamic function and flight efficiency. Science 325:1549–1552
Yu J, Hu Y, Huo J, Wang L (2009) Dolphin-like propulsive mechanism based on an adjustable Scotch yoke. Mech Mach Theory 44(3):603–614
Zou J et al (2005) A micro creeping robot for colonoscopy based on the earthworm. J Medical Eng Tech 29(1):1–7

Chapter 5
Nemertea-Inspired Soft Robotic Mechanism

Kenjiro Tadakuma

A torus structure can enter a narrow area without sliding because it can extend from its tip. It is a characteristic structure of several living organisms. For instance, they are found in the growing tips of plant roots and branches. Hirose et al. developed an extension hose (Mishima et al. 2003). Allison et al. recently developed a growing robot with tube structure (Blumenschein et al. 2018).

To better understand the deployable mechanism of the nemertean proboscis, we analyzed the structure of the nemertean nose in detail (Fig. 5.1). It has a torus structure that rapidly extends and branches. The nemertean proboscis is typically housed in a void in its own body called the nasal cavity, which is independent of the digestive tract. Moreover, it can be extended from the body by increasing the internal pressure of the nasal cavity to capture prey. Several nemertean proboscises are straight, and seven types of nemertean proboscises have been identified. However, the mechanism used by nemertea to extend the branched structure remains unclear from both the biological and engineering perspectives. If the nemertean rostral structure could be reproduced, a mechanism capable of comprehensive exploration of multiple paths in challenging environments, such as debris, could be realized. Furthermore, it can be expected to grasp objects of various irregular shapes and branch stent grafts in the blood vessels, in addition to performing a wide range of tasks, such as in-pipe inspection.

In this study, we developed a prototype mechanical model of a robotic nemertean proboscis (Tadakuma et al. 2022, Takahashi et al. 2021). A deployable mechanical prototype with branches is shown in Fig. 5.2. Internal pressure was used to develop the prototype using polyurethane sheets; it has branches that extend from its roots. Its limitation is that the branches do not retract into the tip but shrink in the radial direction while maintaining their length in the longitudinal direction.

K. Tadakuma (✉)
Tohoku University, Sendai, Japan
e-mail: tadakuma@rm.is.tohoku.ac.jp

K. Suzumori et al. (eds.), *The Science of Soft Robots*, Natural Computing Series,
https://doi.org/10.1007/978-981-19-5174-9_5

Fig. 5.1 Example of nemertean proboscis: Nemertea has a tip-extending mechanism in the proboscis that can branch, extend, and bend. The proboscis can also be retracted by pulling it from the tip (this picture was taken by Prof. Kajihara at the laboratory at Hokkaido University)

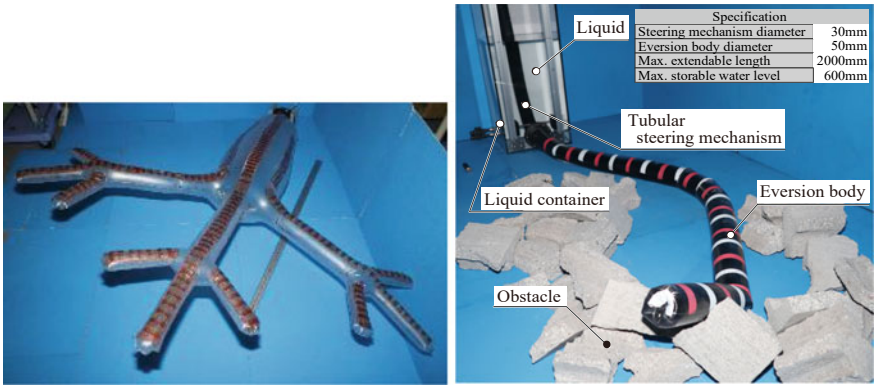

Fig. 5.2 Left: the branched torus mechanism based on nemertean proboscis. Right: retractable and steerable prototype mechanism

To realize the retraction function, we inserted the internal mechanism and extended the eversion robot simultaneously by opening the upper surface of the eversion robot using a liquid as the working fluid. An overview of the prototype model is shown in Fig. 5.2. We experimentally confirmed that obstacle avoidance and step-overcoming tasks could be realized by steering the long prototype in a 2D plane.

The results show that the model can steer in any direction, overcome steps, and retract if operated manually. Furthermore, even though the entire structure is a simple curved line without a branching configuration, the retracting motion from the tip was realized through experiments. In future studies, a retractable mechanism with a stiffness-changing function should be developed for pneumatic driving.

References

Blumenschein LH, Gan LT, Fan JA, Okamura AM, Hawkes EW (2018) A tip-extending soft robot enables reconfigurable and deployable antennas. IEEE Robot Autom Lett 3(2):949–956

Mishima D, Aoki T, Hirose S (2003) Development of pneumatically controlled expandable arm for search in the environment with tight access. In: Proceedings of international conference on field and service robotics (FSR2003), pp 315–320

Tadakuma K, Kawakami M, Furukawa H (2022) From a deployable soft mechanism inspired by a Nemertea Proboscis to a robotic blood vessel mechanism. J Robot Mechatron 34(2)

Takahashi T, Tadakuma K, Watanabe M, Takane E, Hookabe N, Kajihara H, Yamasaki T, Konyo M, Tadokoro S (2021) Eversion robotic mechanism with hydraulic skeleton to realize steering function. IEEE Robot Autom Lett 6(3):5413–5420

Chapter 6
Life-Machine Fusion Devices

Yo Tanaka

The fusion of microdevices and biological cells has become a noteworthy trend in the field of microfluidics, or lab-on-a-chip, because it exploits the capability of their scale to accommodate various cell sizes. Many recent researchers have utilized the sizes and functional properties of micro-or nanodevices and cellular mechanical components to construct biomicroactuators based on microelectromechanical system (MEMS) technology. These biomicroactuators have distinctive features. This is because cells are naturally integrated and biocompatible driving parts actuated by the biochemical energy from adenosine triphosphate (ATP). One prominent approach to the development of cell-based biomicroactuators is the use of microorganisms, including bacteria. Although these devices are useful for application in a small area, muscle cells or tissues are more accommodating for dynamic actuation owing to their large force. Some groups have reported cardiomyocyte robots. These devices are interesting because relatively large structures can be actuated compared with microorganism-based actuators.

However, because fluids are not easily actuated, an efficient structure to communicate force to the fluids as well as check valves to regulate flow are necessary. We focused on this point and developed cell-based fluidic devices, which are introduced below.

Y. Tanaka (✉)
Laboratory for Integrated Biodevice, Center for Biosystems Dynamics Research (BDR), Riken, Tokyo, Japan
e-mail: yotanaka1980@gmail.com

K. Suzumori et al. (eds.), *The Science of Soft Robots*, Natural Computing Series,
https://doi.org/10.1007/978-981-19-5174-9_6

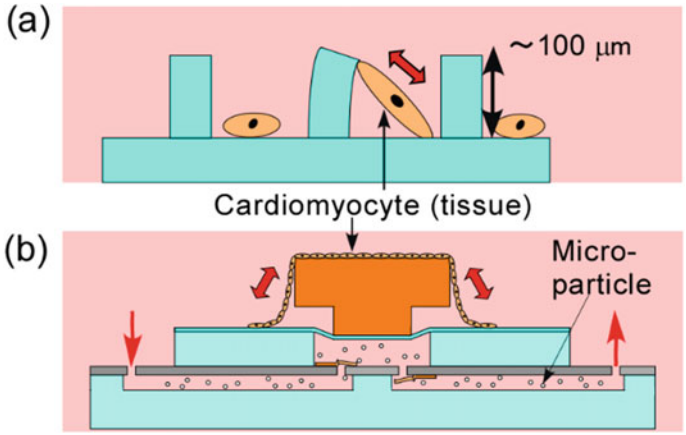

Fig. 6.1 Cultured cardiomyocyte devices. **a** Measurement of the contractile force of cardiomyocytes using micropillars (Tanaka et al. 2006a). **b** A bio-micropump using a cardiomyocyte sheet (Tanaka et al. 2006b)

To understand the fundamental properties of cultured cardiomyocytes, we prepared a micropillar array and cultured muscle cells on it (Tanaka et al. 2006a). Polydimethylsiloxane (PDMS) micropillars were fabricated by casting from a silicon mold. The pillars were then driven by the attached pulsating cardiomyocytes (Fig. 6.1a). The contractile forces of the cultured cardiomyocytes were estimated by the displacement of the driving pillars. It was greater than 3.5 μN.

This force is large for single cells but not sufficient for the actuating fluid. Therefore, we used a cardiomyocyte sheet to create a micropump (Tanaka et al. 2006b). As shown in Fig. 6.1b, spontaneous oscillating fluid motion in the microchannel was observed through microparticle tracking from repeated, regular pulsatile stroke movements of the cell sheet, which were attached to the push bar and observed at 37 °C. Directional fluid pumping within the microchannels was confirmed (2 nL/min) using the microcheck valves.

The cardiomyocyte actuators were further developed and their applications have been demonstrated recently. For instance, not only cardiomyocytes but also smooth muscle cells have been demonstrated for use in this actuator (Tanaka et al. 2008). In addition, iPS cell-derived cardiomyocytes can be used with thin PDMS membranes as substitutes for cell sheets. Moreover, by exploiting the 3D self-assembling property of cardiomyocytes, an ultrasmall cardiomyocyte pump (under 200 μm) was demonstrated (Tanaka et al. 2019a). However, these techniques limit the fabrication of cardiomyocyte pumps. For applications, performance tests of cell sheets and drug testing have demonstrated the high sensitivity of this device (Abulaiti et al. 2020).

From the viewpoint of energy conversion, these cardiomyocyte pumps utilize glucose (chemical energy) input and produce fluid driving energy (dynamic energy) output. This is the most unique feature compared to conventional machines.

6.1 Electric Ray Generator

The contractile force of cultured muscle cells is lower than that of natural muscle tissue because mimicking natural tissue by the cultured system is currently very difficult. The use of natural muscle tissue is the most effective way to generate large forces.

An example of a natural-tissue-based device is an earthworm pump (Tanaka et al. 2017). Using the strong force (mN) of the earthworm muscle, a flow rate 2500 times higher than that of a cardiomyocyte pump was achieved. An earthworm valve was also installed (Tanaka et al. 2019b).

Another example is an electric power generator using the electric organs of electric rays (Tanaka et al. 2016), which generate large electric pulses using the ATP molecules produced from glucose as energy sources to capture prey. As shown in Fig. 6.2, electric power generation was controlled using simple pressure-driven fluidic control as an alternative nervous system, and 1.5 V of voltage and 0.64 mA of current were achieved.

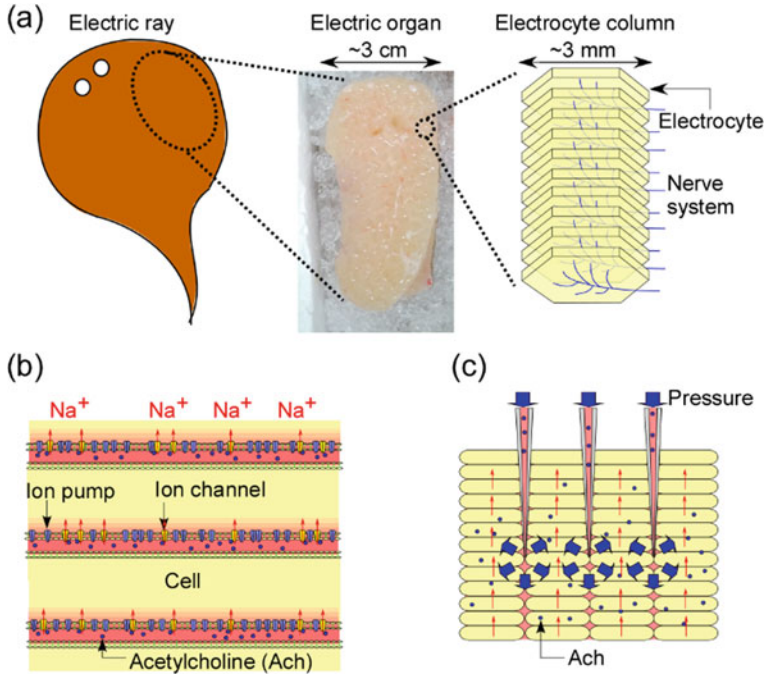

Fig. 6.2 Structure and electric power generation principle of electric organs (Tanaka et al. 2016). **a** Structure of the electric organ and electrocyte columns in it. **b** Principle of electric power generation by Ach chemical stimulation from a nerve terminal. **c** Power generation by an alternative nervous system (needles) using fluid pressure

From the viewpoint of energy conversion, this generator also utilizes glucose (chemical energy) input and cardiomyocyte pumps to produce electric energy output. This is also a unique feature of this generator compared to conventional power generators.

6.2 Plant-Based Soft Robots

Microfluidic actuators, including valves and pumps, are being increasingly adopted in on-chip applications at both the micro- and nanoscale. Such devices are commonly used in various fields, especially in the biomedical field and integrated bioanalysis systems. However, most conventional devices require an electrical power source for their operation. This increases the complexity of the device and limits its integration with lab-on-a-chip devices.

Instead, systems actuated by living biological materials have gradually attracted attention to address these conventional shortcomings. In our previous work, for instance, bio-actuated microfluidic valves and pumps were developed, which are driven by cardiomyocytes and vascular muscle cells (Tanaka and Fujita 2015; Tanaka et al. 2008). However, there are many limitations to the practical application of these living actuators. For example, these living actuators include neurons, blood vessels, and intestines and require strict environmental control, delicate handling, and complicated preparation procedures such as vascular system construction and recovery (Yamashita et al. 2011). Furthermore, ethical restrictions remain a critical issue in their applications. Therefore, living actuators that are free of these concerns are highly preferred.

In contrast, there are approximately 320,000 plant species worldwide. Plants constantly produce energy mainly from sunlight via photosynthesis. Plants can remain alive even when they are cut into slices if water, air, and light are provided. In addition, plant-related experiments are completely free of ethical issues. Although most plants are not active, some have the ability to sense environmental stimuli and respond promptly. Mimosa pudica is a typical stimuli-responsive plant whose leaves shrink and branches drop rapidly in response to external stimuli, such as light, temperature, mechanical forces, or attacks by insects and pathogens. When a Mimosa pudica branch is stimulated, the branch on the main stem drops by bending its pulvinus. The pulvinus is a joint-like bulging structure that controls the internal and external ion concentrations of the plant motor tissue. This reversible and repetitive stimuli-responsive feature of Mimosa pudica is useful for the development of living actuator systems driven by reactive stimulation. Additionally, Mimosa pudica is useful for device experiments from the viewpoint of high reproduction, in addition to the general advantages of using plants explained above (Fig. 6.3).

We have developed a plant-actuated microfluidic valve system (Aishan et al. 2022). The actuation of this valve is controlled by the reaction of the Mimosa pudica branch to external stimuli. The motion of the branch was used to control the open and closed states of the valve in a microfluidic chip. In a plant-actuated valve system, a

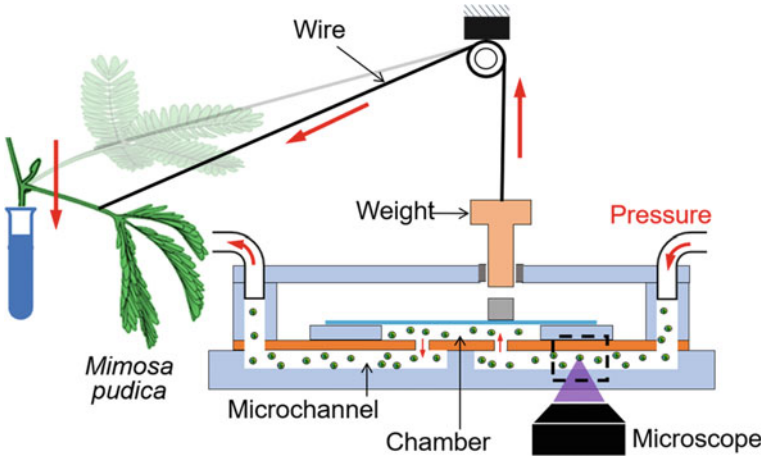

Fig. 6.3 Structure and principle of the microfluidic valve using Mimosa pudica

stable flow is constantly applied to the valve by a pressure regulator. Before stimulation, the Mimosa pudica branch remains in its initial position, and the weight presses down on the push bar. When a deflectable thin PDMS layer blocks one orifice, the microchannel is not connected and the valve system is in the closed state. However, when the branch is stimulated by mechanical contact, the petiole bends downward to pull up the weight via a plastic wire. At this moment, the valve switches to an open state.

Likewise, control of valve opening and closing was realized by the Mimosa pudica branch upon external physical stimulation. One mature, single, uncut Mimosa pudica branch produced an average force of approximately 16 mN. This force was sufficient for actuating and keeping the valve open for approximately 8 min in a stimulation–recovery cycle of 30 min. Additionally, two separately cut Mimosa pudica branches were able to keep the valve open for approximately 2 min in a stimulating-recovery cycle of 45 min. The pressure resistance and response time of the valve were approximately 4 kPa and 0.8 s, respectively.

Compared with other stimuli-responsive plants, Mimosa pudica is well-known for its pharmacogenetic aspects because of its anti-asthmatic, aphrodisiac, analgesic, and antidepressant properties. In addition, Mimosa pudica can adapt well to various environments with high growth rates and produce more drastic stimuli-responsive forces. This demonstration of plant-microfluidics integration encourages the exploitation of more applications of microfluidic platforms that involve plant science and plant energy harvesting.

References

Abulaiti M, Yalikun Y, Murata K, Sato A, Sami MM, Sasaki Y, Fujiwara Y, Minatoya K, Shiba Y, Tanaka Y, Masumoto H (2020) Establishment of a heart-on-a-chip microdevice based on human iPS cells for the evaluation of human heart tissue function. Sci Rep 10:19201

Aishan Y, Funano S, Sato A, Ito Y, Ota N, Yalikun Y, Tanaka Y (2022) Bio-actuated microvalve in microfluidics using sensing and actuating function of Mimosa pudica. Sci Rep 12:7653

Tanaka Y, Fujita H (2015) Fluid driving system for a micropump by differentiating iPS cells into cardiomyocytes on a tent-like structure. Sens Actuators, B Chem 210(1):267–272

Tanaka Y, Morishima K, Shimizu T, Kikuchi A, Yamato M, Okano T, Kitamori T (2006a) Demonstration of a PDMS-based bio-microactuator using cultured cardiomyocytes to drive polymer micropillars. Lab Chip 6(2):230–235

Tanaka Y, Morishima K, Shimizu T, Kikuchi A, Yamato M, Okano T, Kitamori T (2006b) An actuated pump on-chip powered by cultured cardiomyocytes. Lab Chip 6(3):362–368

Tanaka Y, Sato K, Shimizu T, Yamato M, Okano T, Manabe I, Nagai R, Kitamori T (2008) Demonstration of a bio-microactuator powered by vascular smooth muscle cells coupled to polymer micropillars. Lab Chip 8(1):58–61

Tanaka Y, Funano S, Nishizawa Y, Kamamichi N, Nishinaka M, Kitamori T (2016) An electric generator using living Torpedo electric organs controlled by fluid pressure-based alternative nervous systems. Sci Rep 6:25899

Tanaka Y, Noguchi Y, Yalikun Y, Kamamichi N (2017) Earthworm muscle driven bio-micropump. Sens Actuators, B Chem 242:1186–1192

Tanaka N, Yamashita T, Yalikun Y, Amaya S, Sato A, Vogel V, Tanaka Y (2019a) An ultra-small fluid oscillation unit for pumping driven by self-organized three-dimensional bridging of pulsatile cardiomyocytes on elastic micro-piers. Sens Actuators, B Chem 293:256–264

Tanaka Y, Funano S, Noguchi Y, Yalikun Y, Kamamichi N (2019b) A valve powered by earthworm muscle with both electrical and 100% chemical control. Sci Rep 9:8042

Yamashita T, Tanaka Y, Idota N, Sato K, Mawatari K, Kitamori T (2011) Cultivation and recovery of vascular endothelial cells in microchannels of a separable micro-chemical chip. Biomaterials 32:2459–2465

Part II
Soft Materials

Chapter 7
Basics of Polymer

Hiroki Uehara, Masaki Kakiage, Tatsuhiro Horii, Toshinori Fujie, Hidemitsu Furukawa, Masaru Kawakami, and Masahito Takakuwa

Abstract Polymers are essential building blocks for soft robots, and therefore, must maintain their structural integrity under compliant performance. In this regard, it is important to understand the structure, properties, and functions of polymers, including process and engineering of polymeric materials. In this chapter, we will introduce the basics of polymers represented by morphology; physical properties of polymers; structure and classification of polymers and functional polymers; soft materials (elastomers, hydrogels, etc.); and fabrication of soft robot parts using three-dimensional printers.

7.1 Morphology and Physical Property of Polymers

Muscles are composed of various proteins, including actin and myosin, and their structural changes are induced by the energy supplied from adenosine triphosphate (ATP), resulting in the stretching and shrinking of muscles. Although such a drive by biopolymers provides a lower torque than that provided by conventional mechanical engines or electrical motors, the light weight of muscles is advantageous for reducing the carbon dioxide exhaustion during energy conservation. These muscles support the human backbone as they are lightweight and can exert a force ten times stronger

H. Uehara · M. Kakiage
Division of Molecular Science, Faculty of Science and Technology, Gunma University, Tokyo, Japan

T. Horii · T. Fujie
School of Life Science and Technology, Tokyo Institute of Technology, Tokyo, Japan

H. Furukawa (✉) · M. Kawakami
Soft and Wet Matter Engineering Lab (SWEL), Department of Mechanical Systems Engineering, Yamagata University, Tokyo, Japan
e-mail: furukawa@yz.yamagata-u.ac.jp

M. Takakuwa
Waseda University, Tokyo, Japan

K. Suzumori et al. (eds.), *The Science of Soft Robots*, Natural Computing Series,
https://doi.org/10.1007/978-981-19-5174-9_7

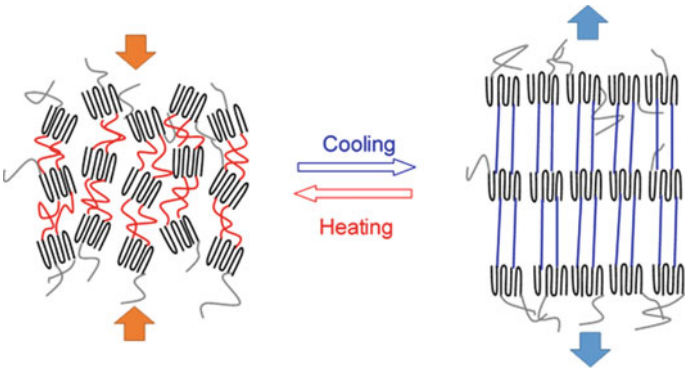

Fig. 7.1 Tie-molecule-driven shrunk state on heating (left) and stretched state on cooling (right) for drawn polyethylene film

than the force of gravity. This is one of the outstanding characteristics of living things compared to man-made machines.

Various soft actuators mimicking the mechanisms by which proteins induce movement have been developed. Typical examples are polymeric gels, which exhibit desirable flexibility, quietness, and light weight. However, their maximum drivable loads are much lower than those of mechanical engines or electrical motors. The movement of these gels is limited under wet conditions. By contrast, synthetic polymer actuators, which are composed of coiled fishing lines, can repeatedly shrink on heating and stretch on cooling even under dry conditions (Haines 2014). These actuators achieve a 20% strain change between heating and cooling even with 10 MPa loading, which is 30 times higher than a muscle output (Hiraoka 2016). These values exceed the required value for power-assisting suits (Madden 2004), whose development has been desired for elderly care.

The driving principle of the abovementioned coiled-fishing-line actuator has been attributed to the entropic shrinkage and elongation of amorphous tie molecules, which transmit the stress between crystalline lamellae (Yoshizawa 2021), as shown in Fig. 7.1. Therefore, the design, manufacturing, and application of such soft actuators require understanding of the morphology and physical properties of crystalline and amorphous phases of polymeric materials.

7.1.1 Macromolecular Characteristics

Polymeric materials exhibit anisotropy of both structural and property characteristics owing to the chain moieties of their macromolecular architectures. Polymeric anisotropy is caused by a pair of strong covalent bonds along molecular chains and a weak interaction between these chains. Polar polymers often show moderate interactions, for example, hydrogen bonding, but these interactions are weaker than

covalent bonding. This molecular anisotropy provides superior mechanical and polarizing properties. A parallel arrangement of molecular chains allows self-assembling crystallization to form crystalline phases.

Another characteristic of polymeric chains is their self-entanglement with other polymeric chains owing to the ease of rotation of C–C covalent bonds. Such entanglement characteristics lead to the formation of amorphous phases that are composed of random coils without a periodic arrangement of molecular chains. The enhanced molecular motion of amorphous phases provides elasticity and transparency to polymeric materials.

Crystalline phases are also present in metals and inorganic materials. However, amorphous phases are limited to polymeric materials. The fractionation and arrangement of these phases dominate the mechanical properties of polymeric materials.

7.1.2 Crystalline Structure

The crystalline phase is effective for improving the physical properties of polymeric materials. In particular, mechanical properties of polymeric materials reflect the molecular conformation within a crystalline lattice, as described in Sects. 7.1.4 and 7.1.5.

1. Morphology

Generally, polymeric materials are composed of extended-chain crystals (ECCs), folded-chain crystals (FCCs), and amorphous random coils (Uehara 2007), as shown in Fig. 7.2. ECCs are thermodynamically stable and formed at high temperatures and pressures. High temperature induces molecular slippage in a parallel chain arrangement, and high pressure causes entropic reduction in oriented crystallization. Molecular ends align along ECC edges, inducing rigid but brittle features.

By contrast, FCC growth is induced by the lateral propagation of chain folding, resulting in a lamellar appearance. FCC surfaces are covered by loose loops, which indicates the lower stability of FCCs than that of ECCs. However, the crystallization

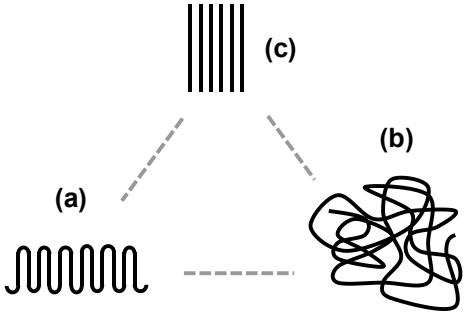

Fig. 7.2 Schematic representation of typical solid structures of crystalline polymers, including extended-chain crystal (**a**), folded-chain crystal (**b**), and amorphous random coil (**c**)

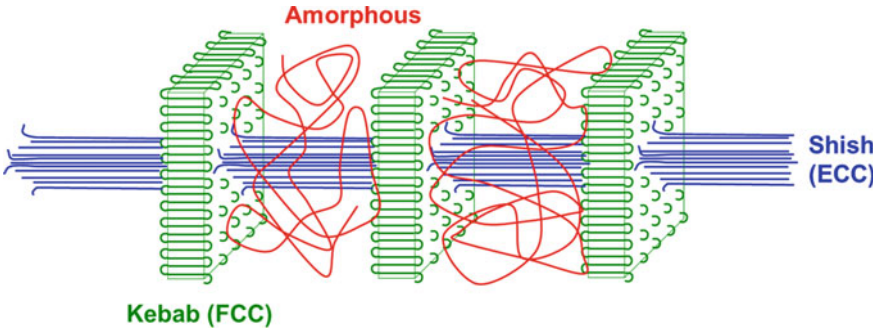

Fig. 7.3 Shish-kebab morphology with combination of extended-chain crystals and folded-chain crystals

rate of FCCs is much higher than that of ECCs. Therefore, under usual atmospheric conditions, conventional crystallization from melt kinetically results in the formation of FCC. Radial growth with lamellar rotation results in a spherulite morphology.

A combination of ECCs and FCCs is called a shish-kebab morphology. As shown in Fig. 7.3, shish (ECC) arrays are linked by kebab (FCC) platelets, which are perpendicular to the shish direction. An ECC is first formed by molecular orientation, and the formation of FCC from the ECC nucleus allows perpendicular growth, linking ECC arrays. Several examples have been reported for polyethylene (PE) fibers or films prepared by the Couette flow (Zwijnenburg 1978) or melt-drawing (Nakae 2000).

2. Molecular conformation

The crystalline segments within crystalline phases reflect the chemical structures of macromolecules. The simplest conformation is the trans (T) zigzag of PE and polytetrafluoroethylene (PTFE) consisting of a straight segment without branching, as shown in Fig. 7.4a.

Polypropylene (PP), which is included in polyolefin, has different stereoregularities of isotactic and syndiotactic moieties. Isotactic PP (i-PP) exhibits alternate propagation of T and gauche (G) conformations, resulting in a 3_1-helix appearance, as shown in Fig. 7.4b. By contrast, syndiotactic PP (s-PP) exhibits T_2G_2 propagation, resulting in an eight-shaped projection, as shown in Fig. 7.4c.

3. Crystalline form

The packing arrangement of these molecular conformations determines the crystalline form. Figure 7.5a depicts the most stable orthorhombic lattice of PE, where T-zigzag conformations are most closely packed. Often, metastable packing results in polymorphism. Sometimes, heating the T-zigzag conformation within the oriented PE produces a small amount of G conformation, leading to a hexagonal arrangement allowing molecular rotation (Uehara et al. 1996), as shown in Fig. 7.5b.

By contrast, the 3_1-helix conformation of i-PP results in right-hand and left-hand helices. The packing of a pair of these symmetric helices forms the most stable

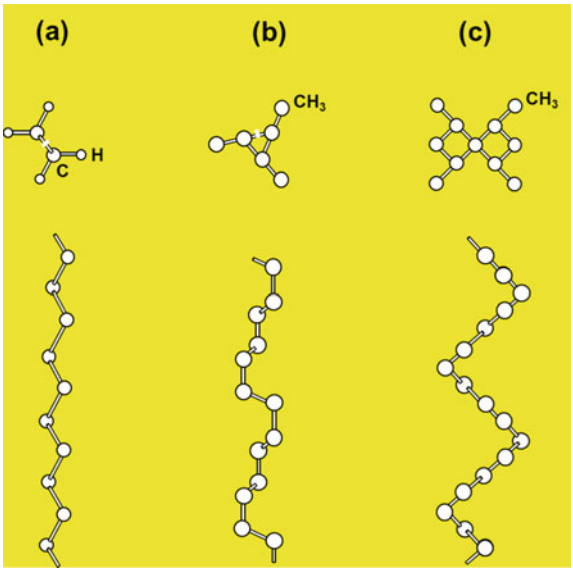

Fig. 7.4 Molecular conformation for trans zigzag (**a**), -$(TG)_2$- (**b**), and -$(T_2G_2)_2$- (**c**) for PE and PP

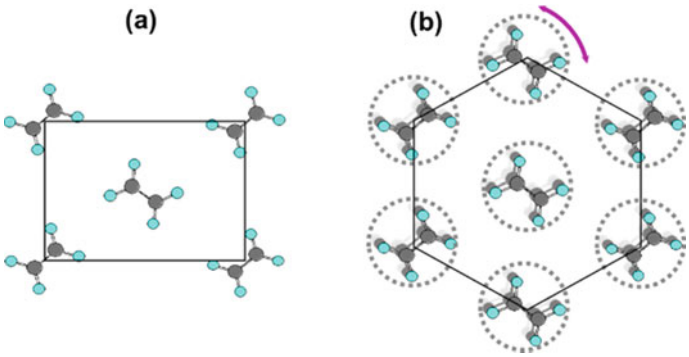

Fig. 7.5 Molecular packing of stable orthorhombic (**a**) and metastable hexagonal crystalline lattices (**b**). The former lattice is composed of an entirely T-zigzag conformation; however, the G contribution traveling along the molecular chain allows the remarkable rotation around the chain axis

monoclinic arrangement (α-form), whereas the asymmetrical arrangement of these helices provides a hexagonal arrangement (β-form) (Yamamoto 2007).

4. Crystallinity

Crystallinity, χ_c is defined as the ratio of the crystalline phase to the total fraction of crystalline and amorphous phases. Crystallinity is evaluated using various methods. The most popular evaluation method uses sample density.

$$\chi_c = \frac{\rho_c(\rho - \rho_a)}{\rho(\rho_c - \rho_a)} \tag{7.1}$$

Here, ρ, ρ_c, and ρ_a are the sample density, crystalline density, and amorphous density, respectively.

Crystallinity can be determined using the melting entropy calculated from the endothermic peak area on differential scanning calorimetry (DSC) profile. The observed entropy (ΔH_f) is divided by the entropy value reported for the perfect crystal (ΔH_f^o).

$$\chi_c = \frac{\Delta H_f}{\Delta H_f^o} \tag{7.2}$$

Another method to determine crystallinity is based on the peak resolution of various spectrum profiles obtained using the X-ray or infrared (IR) analysis. The peak area (A) of crystalline phase corresponds to crystallinity, as represented by the following equation:

$$\chi_c = \frac{A_{crystal}}{A_{crystal} + A_{amorphous}} \tag{7.3}$$

7.1.3 Amorphous Structure

As mentioned above, even semi-crystalline polymers, such as PE, PP, and PTFE, contain amorphous phase because of defects such as chain entanglements and ends. However, there are amorphous polymers that contain only amorphous phase and no crystalline phase. Among the PP families, i-PP and s-PP are crystalline polymers, as described above. However, atactic PP (a-PP) is totally an amorphous polymer that is composed of random propagation of racemic and meso configurations.

1. Chain entanglement

In particular, for polymeric materials with a high molecular weight, chain entanglements are inevitably formed. During crystallization, the entanglements are segregated from the crystalline phase into the amorphous phase. Previously, the average amount of entanglement was determined from rheological melt viscosity. However, the coexistence of different types of entanglements has recently been confirmed by the oriented crystallization during melt-drawing of PE with an ultrahigh molecular weight (Uehara 2006). Several studies on melt-drawing behavior revealed that "deep" entanglements are maintained on drawing and "shallow" engagements disentangle during drawing (Kato 2015), as shown in Fig. 7.6.

Controlling the molecular entanglements results in the formation of a homogeneous FCC with a constant thickness (Uehara et al. 2012), which corresponds

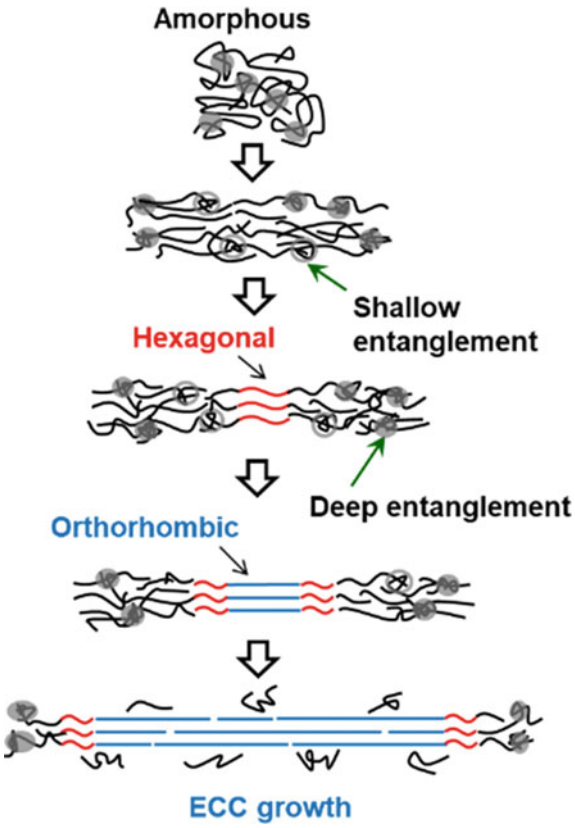

Fig. 7.6 Schematic representation of structural changes during melt-drawing for entangled amorphous state, oriented amorphous, hexagonal crystallization, orthorhombic transformation, and ECC growth. Shallow and deep entanglements are indicated by open circles and filled circles, respectively

to the average distance between entanglements estimated from the melt viscosity (Graessley 1974), as shown in Fig. 7.7. Such structural formation utilizing an entanglement arrangement is characteristic of polymeric materials.

2. Tie-molecule

By contrast, amorphous segments that link crystalline phases are recognized as tie molecules. They contribute to the structure and properties of drawn polymers (Ono et al. 2011). In particular, these tie molecules generate the driving force for polymer actuators, which shrink on heating and stretch on cooling (Yoshizawa 2021) (see

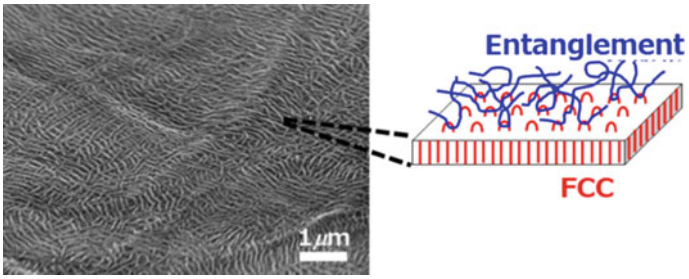

Fig. 7.7 Homogeneous FCC morphology resulting from periodic arrangement of molecular entanglements

Fig. 7.1). Currently, various analytical methods, including nuclear magnetic resonance and Raman and IR spectroscopies, for the evaluation of these tie molecules are being examined in academia and industries.

3. Cross-link

Most cross-linked polymers are amorphous. A typical example is cross-linked rubber containing sulfide—sulfide bonds between poly (butadiene) segments. When cross-linked rubber is tensile drawn, it acquires an oriented-crystalline phase but returns to the non-oriented amorphous phase upon the release of the applied strain. This mechanism of stretching and shrinking of cross-linked rubber provides entropic elasticity and is also observed in thermal actuators, which show similar dimensional changes on heating and cooling.

7.1.4 Molecular Orientation

The molecular orientation of polymeric materials has been achieved by various drawing methods, such as gel drawing (Smith 1980), reactor-powder drawing (Kanamoto et al. 1987), and melt-drawing (Uehara et al. 1999). All of these drawing techniques target the ultimate structure, as described below.

1. Ultimate structure

To derive the maximum anisotropy of polymeric chains, several conditions are required: (1) molecular extension, (2) high orientation, and (3) solidification by crystallization. Various drawing techniques have been developed to orient the polymeric molecules. During such drawing processes, a transition from FCCs to ECCs causes necking deformation spreading over the entire sample length, corresponding to the natural draw ratio (*NDR*). The tensile modulus rapidly increases at this stage.

By contrast, the development of tensile strength further requires (4) randomization of the arrangement of chain ends. This deformation stage surpasses *NDR*, which indicates super-drawing (Kanamoto and Porter 1989). In the case of ECCs crystallized

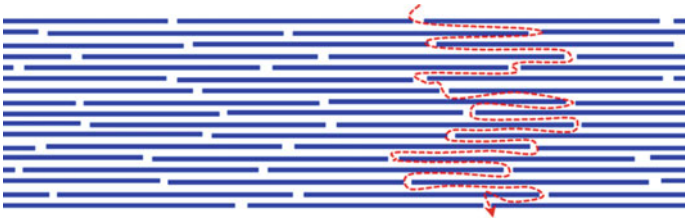

Fig. 7.8 Ultimate structure obtained by super-drawing. A sample break travels through chain ends, as indicated by the red dotted line

at high temperatures and pressures, a straight path of break propagation confers the brittle characteristic, as shown in Fig. 7.2c. Conversely, the maze of paths of chain ends within ECCs obtained through super-drawing improves the tensile strength. Satisfaction of all of these requirements leads to the ultimate structure (Uehara 2007), as shown in Fig. 7.8.

A comparison of the improvements in tensile modulus and strength suggests that the strength is more difficult than the tensile modulus because the strength requires molecular sliding to achieve random arrangement of chain ends.

2. Drawing effect

The structural and property changes induced by tensile drawing are explained for PE. Structural parameters, including crystallinity, crystalline orientation, and melting temperature, increase with increasing *DR*, but saturate at a *DR* greater than 30 (Kanamoto and Porter 1989). The amorphous orientation is less detectable owing to the decrease in the number of amorphous phases with increasing *DR*. However, the tensile properties such as modulus and strength continue to increase even at a *DR* greater than 100. The crystallite size along the oriented molecules, corresponding to ECC length, increases at the later stage of drawing. Such coincidence indicates that the structural continuity dominates the mechanical properties of polymeric materials, which are controlled by the arrangement of defects, as described above.

3. Maximum achievable properties

Molecular sliding is necessary for achieving the ultimate structure, which means that a weaker interaction between molecules is desirable. PE is one of the few polymers whose ultimate structure has been achieved. The experimentally achieved tensile modulus for a superdrawn PE sample was 220 GPa (Kanamoto et al. 1988), which is comparable to the crystalline modulus of 240 GPa (Sakurada et al. 1966). When superdrawn, fluoro-polymers, including PTFE, experimentally achieve the crystalline modulus (Uehara et al. 1997). In superdrawn PE with the ultimate structure, the thermal conductivity, which is another important property of polymeric materials, also approaches the theoretical value of 400 W m^{-1} K^{-1} (Choy et al. 1985). By contrast, the polymers that undergo strong interactions with other molecules, such as polyamides or polyesters, restrict the crystalline modulus achievability to 10% owing to their lower crystallinities than those for polyolefins.

7.1.5 *Mechanical Properties*

Mechanical properties of polymeric chains depend on chain conformation (Tashiro 1993). Crystallinity affects the modulus of crystalline polymers.

1. Tensile modulus

The tensile modulus reflects the molecular architecture of polymeric materials. The chain conformation within a crystalline lattice determines the crystalline modulus, which corresponds to a theoretical value. The f value corresponds to the spring constant of a single segment. This f value is constant for the same conformation even when the chemical structures are different (Tashiro 1993).

Among conventional polymers, PE exhibits the highest crystalline modulus. A crystalline segment of a PE chain forms an entirely T-zigzag conformation, exhibiting the highest f value. As described above, combining T conformation with the smallest molecular cross section results in a high crystalline modulus of 240 GPa. In the case of PP with the second simplest polymeric architecture, the crystalline modulus of i-PP with the 3_1 helix is 35 GPa (Kanamoto et al. 1988), but that of s-PP with the 8_1 helix is 8 GPa (Uehara et al. 1996). This change in crystalline modulus is due to the helix winding.

The actual tensile modulus (E) depends on the arrangement of crystalline and amorphous phases, assuming parallel and series arrangements, as shown in Fig. 7.9 (Takayanagi et al. 1964). That of the parallel arrangement mainly reflects the crystalline modulus, but that of the series arrangement is dominated by the amorphous modulus, which is much lower than the crystalline modulus.

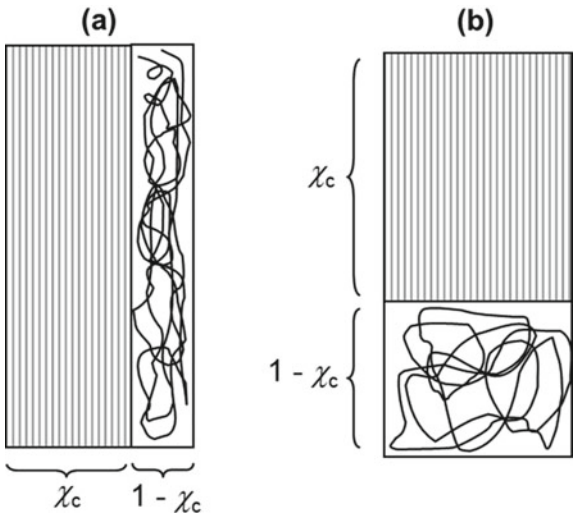

Fig. 7.9 Parallel and series arrangements of crystalline and amorphous phases. The strain is induced along the vertical direction. χ_c indicates crystallinity

$$\text{Parallel arrangement: } E = \chi_c E_c + (1 - \chi_c) E_a$$

$$\text{Series arrangement: } \frac{1}{E} = \frac{\chi_c}{E_c} + \frac{1 - \chi_c}{E_a}$$

Here, E_c and E_a are the crystalline and amorphous moduli, respectively.

Therefore, the parallel arrangement gives a higher modulus than the series arrangement even with the same crystallinity.

2. Tensile strength

By contrast, the theoretical value of tensile strength depends on the calculation assumption. The most widely accepted value for a PE chain is 30 GPa, which is calculated from the extrapolation of ECC length (Pennings et al. 1990). However, the maximum achievable tensile strength is less than 3 GPa (Kanamoto et al. 1988), which corresponds to one-tenth of the abovementioned theoretical value. This means that the chain ends also cause break propagation, similar to the boundaries between crystalline and amorphous phases.

3. Strain at break

Breaking strain is one of the most important properties for polymeric materials. Cross-linked polymers, such as synthetic rubber, exhibit a large strain at break but retain their original length; thus, they have excellent stretchability. Often, 1000% breaking strain is achieved even with low modulus. By contrast, the oriented crystallization for superdrawn polymers provides a higher modulus but lower breaking strain. For example, high-modulus and high-strength fibers of ultrahigh-molecular-weight PE or polyaramide exhibit a breaking strain lower than 3%.

7.1.6 How to Start Polymer Property Research

Tensile tests provide a basic understanding of the relationship between polymer structure and properties. They can provide estimations of mechanical properties and ductility, that is, processability. Both these characteristics reflect on the polymeric morphology, which is composed of crystalline and amorphous phases.

The textbook recommended for beginners is "Macromolecular Physics" (Wunderlich 1973). In this book, the polymer structures and properties ascribed to chain moieties are explained on the basis of theoretical and experimental results. Various crystalline morphologies are shown in many beautiful photographs. It also provides new insights on polymer analysis and processing for beginners.

7.1.7 Challenges

The theoretical value of tensile strength has not been achieved, even for the simplest PE, as described above. This means that there is still room for property development of polymeric materials when the continuity of ECCs is further enhanced. A material with theoretical strength can be prepared. Since the light weight of polymeric materials is beneficial for their practical applications in soft robotics, achieving the ultimate structure is a meaningful challenge in polymer research.

7.2 Structure and Classification of Polymers and Functional Polymers

7.2.1 Classifications

Polymers are gigantic molecules formed by the repetition of monomer molecules via polymerization reaction that are composed of hundreds of monomer units. Physical properties of polymers are determined by the type of binding between constituent atoms of monomer molecules (i.e., chemical structure). Figure 7.10 shows the structural classifications of various polymers. An open and a closed circle symbols represent monomer units. A homopolymer, which consists of single monomers is shown in Fig. 7.10a. Copolymers are obtained from the polymerization of two or more different monomer units (A and B monomers), as shown in Fig. 7.10b–e and are classified depending on the sequence of the comonomer units. Blocks of homopolymers of monomers A and B are bound together to produce (b) a block copolymer combining the characteristics of blocks A and B, whereas (c) an alternating copolymer, (d) a periodic copolymer, and (e) a random copolymer are composed of a sequence in which the monomers A and B are enchained alternatively, periodically, and randomly, respectively. Furthermore, (f) a star polymer, (g) grafted polymer, (h) hyperbranched polymer, and (i) cyclic polymer are produced depending on the binding modes of the backbone chains.

7.2.2 Chemical Structures

Molecular structures within a single polymer chain and aggregated structures (solid-state) of polymer chains tend to affect the physical properties of polymers. We would like to introduce the primary structure determining the bonding mode of monomer units, the stereoregularity and the molecular weight distribution, and the secondary structure equivalent to the spatial arrangements of polymer chains induced by intra- and inter-molecular interactions.

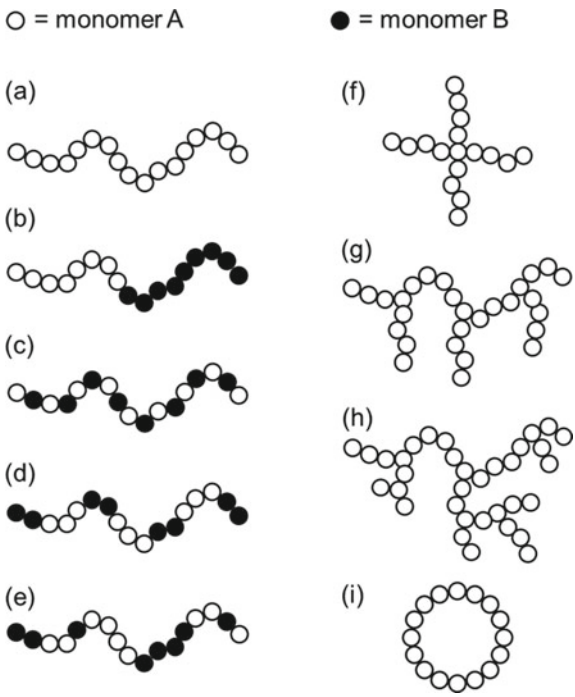

Fig. 7.10 Schemes of various polymer chains

Primary structure

Considering the polymerization of vinyl monomer (e.g., $CH_2 = CH(A)$), three types of bonding modes of monomer units are produced, as shown in Fig. 7.11b, c. Each monomer unit is enchained in one of the three directions, resulting in head-to-tail (Fig. 7.11b), head-to-head, and tail-to-tail bonding structures (Fig. 7.11cm α, β)). In general, the reactive species have an advantage in binding with the tail side of the monomer owing to the steric hindrance. The reactive species generated by head-to-tail bonding tend to be more stable than those generated by head-to-head bonding. The chemical structural formula of the polymer produced by polymerization of the vinyl monomer is described, as shown in Fig. 7.11a. Furthermore, the polymerization of conjugated diene monomers, such as 2-methyl butadiene, produces polymer chains with various chemical structures, as shown in Fig. 7.12. In addition, polymerization of diene monomers, 1,2- and 3,4-enchainment of the monomers, produces 1,2- and 3,4-addition structure, respectively. 1,4-enchainment of the monomers produces *trans*-1,4 and *cis*-1,4 geometric isomers whose double bond in the polymer chain inhibits a rotational interconversion of these isomers. Natural rubber consists of almost 100% *cis*-1,4-polyisoprene. Ziegler–Natta catalyst enables the production of 100% *cis*-1,4-polyisoprene, whereas *trans*-1,4-polyisoprene named as gutta-percha does not exhibit any rubber properties.

Considering that all monomers (shown in Fig. 7.11a) bonded in the head-to-tail direction, carbons substituted in the polymer main-chain have the possibility for

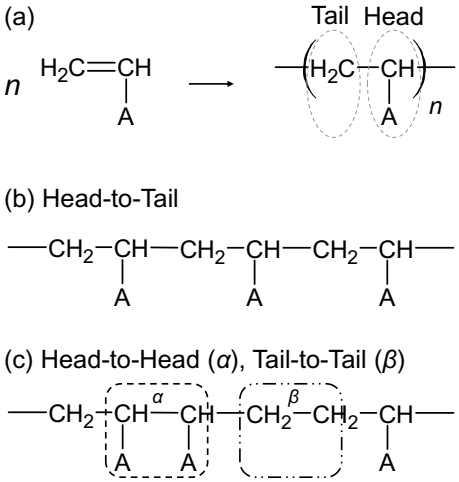

Fig. 7.11 **a** Reaction formula for the polymerization of vinyl monomers. **b**, **c** Different bonding structures of polymerized monomer units

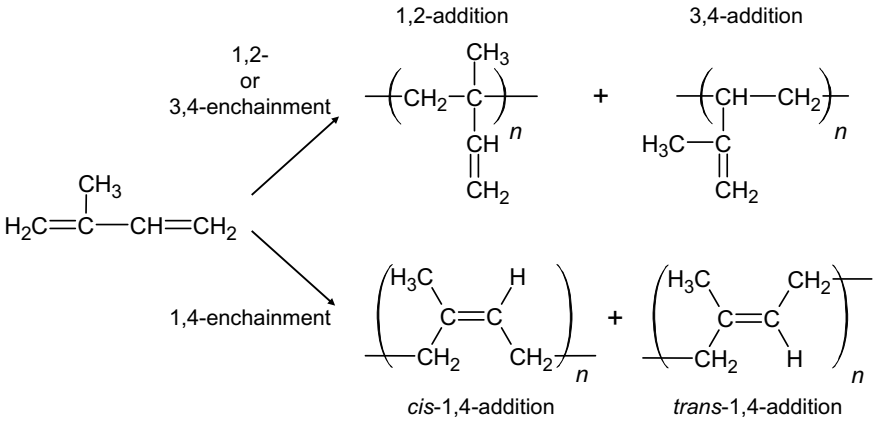

Fig. 7.12 Reaction formula for the polymerization of vinyl monomers. **b**, **c** Different bonding structures of polymerized monomer units

relative handedness. Hence, the carbons are termed pseudo asymmetric carbons. The configuration of the pseudo asymmetric carbons leads to three types of possible stereochemical arrangements that are illustrated in Fig. 7.13. Bold lines and broken lines represent the bonding directions of the front and opposite sides, respectively. Either of the substituents A and hydrogen H of the stereoregular structures are on the same side of the main-chain backbone plane (*isotactic*) or bonded with the pseudo asymmetric carbons alternatively from side to side (*syndiotactic*), as shown in Fig. 7.11b,

c. The random arrangement of the substituent group on either side of the backbone plane is termed *atactic*.

The above structures, which are configurated during polymerization of monomers, are termed configuration.

Secondary structure

Although the monomer sequences determine the configuration of the polymer chains, the rotation around the C–C bonding axis allows the polymers to form various chain shapes, which is the secondary structure of a polymer. Then, the spatial arrangement between the atoms and the atomic groups is termed conformation, and it can affect the properties of polymer materials. Figure 7.14 shows a part of the chemical structure of *n*-butane, conformations of a four-carbon fragment, and dependence of potential energy of rotation around the bond axis between adjacent carbons. Bold lines and broken lines represent the bonding directions of the front and opposite sides, respectively. The Newman projection is helpful to understand the rotation around the bond axis between adjacent carbons, as shown in Fig. 7.14b. The rotation angle of the *trans* (T) conformation is 0°, and the potential energy is minimum. *Gauche*$^+$ (G^+) and *gauche*$^-$ (G^-) represent angles of + 120° and – 120°, respectively, at which the potential energy has a local minimum value. At an angle of 180°, where the maximum potential energy results in the formation of an unstable structure, the conformation is

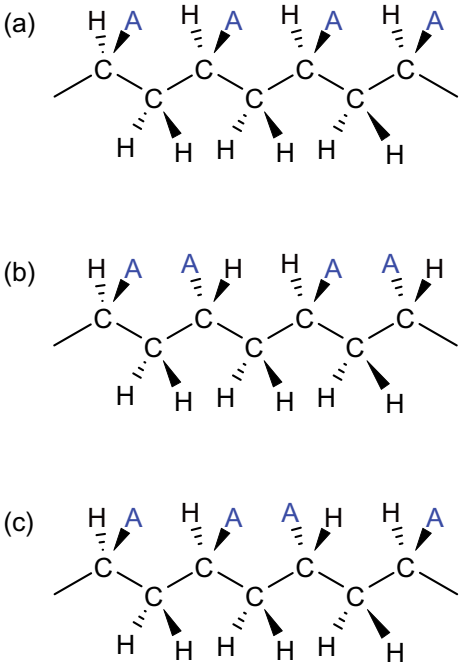

Fig. 7.13 Schemes of various stereoregularities of a linear chain polymer; **a** *isotactic*, **b** *syndiotactic*, and **c** *atactic*

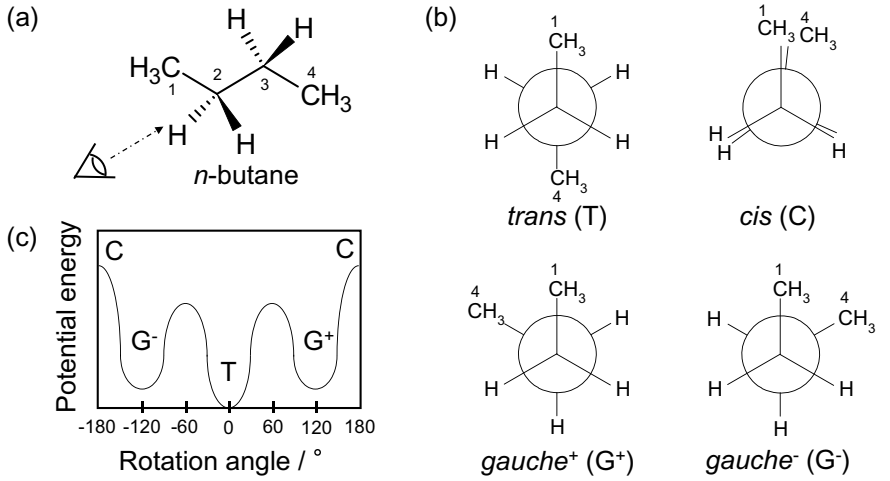

Fig. 7.14 Schemes of **a** chemical formula of *n*-butane and **b** four types of rotational isomer (Newman projection). **c** Dependence of the rotational potential energy of *n*-butane on rotation angle around C2–C3 bonding axis

called *cis* (C) or eclipsed. The potential energy barriers (600–800 cal/M) between T and $G^{\pm}$ are comparable to the thermal energy in the molecules at room temperature.

Numerous C–C bonds at intra-polymer molecular sites form various conformations of polymer chains, rotating around the bonds. The chain structure of *isotactic*-polypropylene has a regular spiral structure that has one period for three methyl groups (side-chains) in a crystalline state. Large substituent groups of side-chains can extend the spiral interval of a polymer.

Solid-state structures of polymers

In the previous sections, we described the formations of a polymer chain, such as the sequences of monomers and conformations. We often use polymer materials as a solid-state. The solid-state polymers are formed by evaporating solvents from the polymer solutions and cooling molten polymers to a melting temperature (T_m). The crystals in the solid-state polymer materials are formed by polymer chains parallelly close to each other and atom sequences ordered in three-dimension. The ordered sequences give rise to reduced entropy, whereas crystallization results in negative enthalpy exceeding the reduction of the entropy, which results in negative Gibbs free energy in the solid-state. The polymers that can undergo crystallization are termed crystalline polymers, in which not all polymer chains form crystallites. The crystalline polymers show not only T_m but also a glass transition temperature (T_g), as shown in Fig. 7.15d. Conversely, amorphous polymers (non-crystalline polymers) show no crystalline state but only show T_g. In crystalline polymers, the stereoregularity may or may not affect the crystallization of the polymers. The regularly arranged polymers show crystalline states, such as *isotactic*-polypropylene, *syndiotactic*-polypropylene, *isotactic*-polystyrene, and *syndiotactic*-polystyrene.

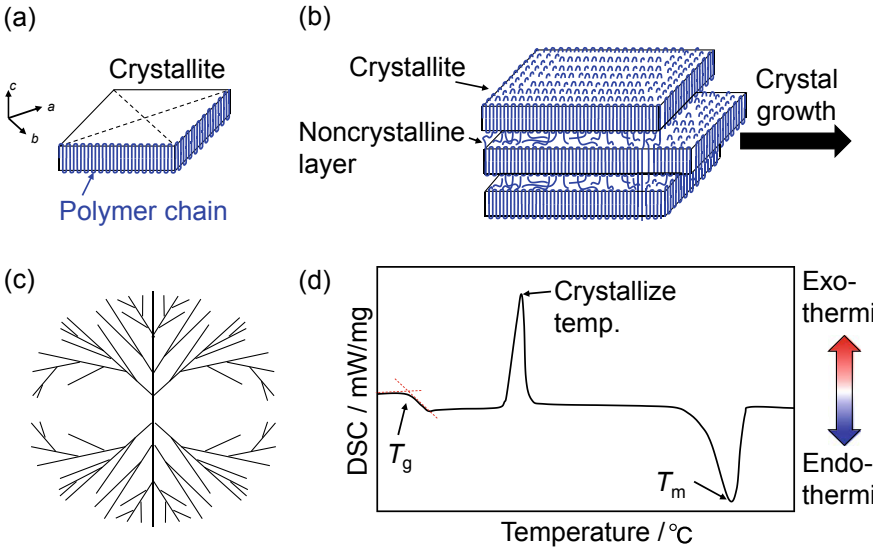

Fig. 7.15 Schemes of **a** a single crystal, **b** stacked lamella crystallites, and **c** a spherulite composed of grown stacked lamella crystallites. The lines show the direction of the crystal growth. **d** Scheme of typical differential scanning calorimetry (DSC; exo- and endo-thermic values) curve of the crystalline polymer (e.g., polyethylene terephthalate)

The crystalline structure depends on the fabrication conditions and processes. In 1957, A. Keller et al. prepared a ca. 10 nm thick and several micrometers wide single crystal (lamella crystal) of polyethylene by cooling a dilute xylene solution of polyethylene, and they discussed that the folded polyethylene chains constructed a crystallite, considering the difference between the crystallite thickness of ca. 10 nm and the chain length of hundreds of nanometers (Fig. 7.15a). On the other hand, we can easily obtain the crystalline state on a larger scale than that of a single crystal by gently cooling down a melted bulk polymer under the melting point (Fig. 7.15b). The crystals consist of lamella crystals stacked on top of each other along the thickness direction via non-crystalline layers, where the polymer chains do not form any ordered structures. Furthermore, the crystal growth of the stacked lamella crystal in the direction of the arrow in Fig. 7.15b, resulting in fibrils, leads to the formation of a spherulite, as shown in Fig. 7.15c.

7.2.3 Functional Polymers

Functional polymers change their dimensions (shapes) and characteristics in response to external stimulations, such as light irradiation, electric field, magnetic field, temperature, pH changes, and enzymes.

Liquid crystal polymers have been widely used as a driving source in soft robotics and microfluidics by introducing photo-reactive groups in the polymer backbone networks, such as azobenzene (Fig. 7.16) (Lv et al. 2016; Gelebart et al. 2017; Wang et al. 2019). By introducing azobenzene groups to poly(pentafluorophenyl acrylate), freestanding fibers are fabricated, which show bending and recovering motion under UV and visible light irradiation, respectively (Fig. 7.17) (Chen et al. 2021). The azobenzene is isomerized from the *trans* to the *cis* form by UV irradiation, resulting in an actuation behavior in the above studies (Ikegami et al. 2016)].

pH-responsive polymers are useful materials for releasing drugs, pesticides, and fertilizers (Stuart et al. 2010; Ma et al. 2013b; Qin et al. 2017; Dararatana et al. 2020). For the drug release, Dararatana et al. designed the polymer nanoparticles that enable the release of various corrosion inhibitors under an acidic state. The inhibitors conjugated to functional groups of the copolymers are incorporated into the nanoparticles under a neutral state and then released under an acidic state (pH 3.5). The releasing rate increases as the pH value decreases (Fig. 7.18).

Poly-(N-isopropylacrylamide) (PNIPAm) is one of the thermoresponsive polymers that dissolves in aqueous media at a temperature lower than the lower critical solution temperature (LCST) and becomes insoluble and milky white in color at higher temperatures. Meanwhile, in certain hydrophobic ionic liquids, PNIPAm exhibits an upper critical solution temperature (UCST), in which the phase separation occurs at a temperature lower than UCST and dissolution occurs at a higher temperature (Ueki et al. 2015). L. Ionov's group fabricated a star-shaped self-folding capsule using a bilayer structure comprising a biodegradable hydrophobic polycaprolactone (PCL) layer and a PNIPAm layer for reversible encapsulation of yeast cells (Fig. 7.19). The PCL layer restrains the deformation of the PNIPAm layer, which swells and shrinks depending on temperature changes, resulting in the bending motion of the star-shaped capsules (Stoychev et al. 2011).

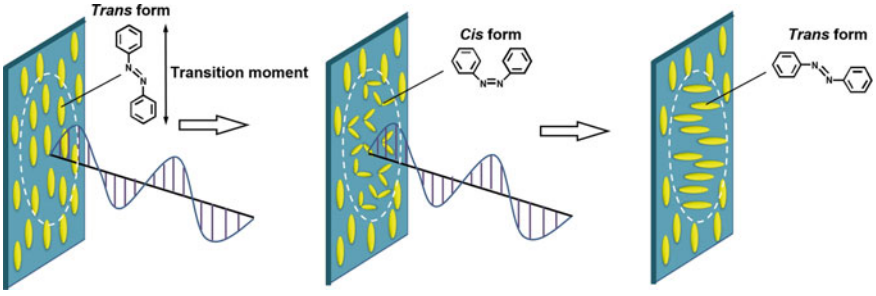

Fig. 7.16 Schematics demonstrating the mechanism of photoalignment of azobenzene mesogens under linear polarized blue light (Lv et al. 2016)

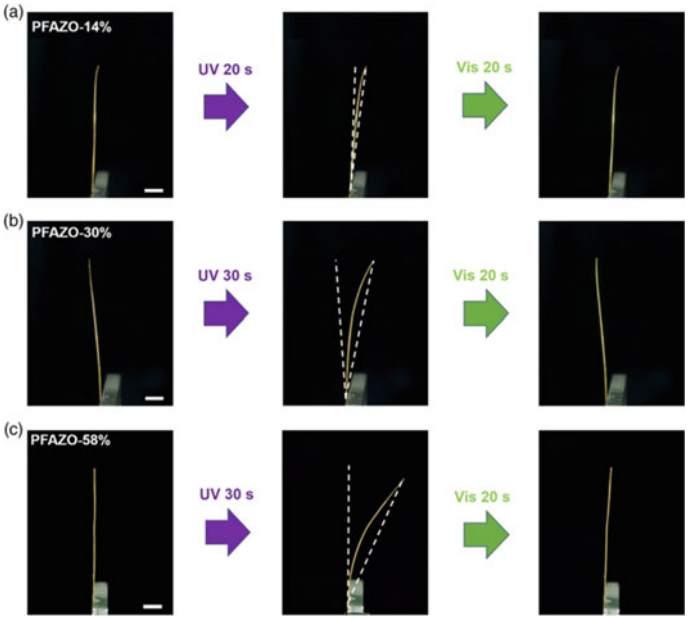

Fig. 7.17 Photo deformation behaviors of **a** PFAZO-14%, **b** PFAZO-30%, and **c** PFAZO-58% cross-linked fibers. The bending and recovery are induced by 365 nm UV light (10 mW cm^{-2}) and 530 nm green light (10 mW cm^{-2}) (Chen et al. 2021)

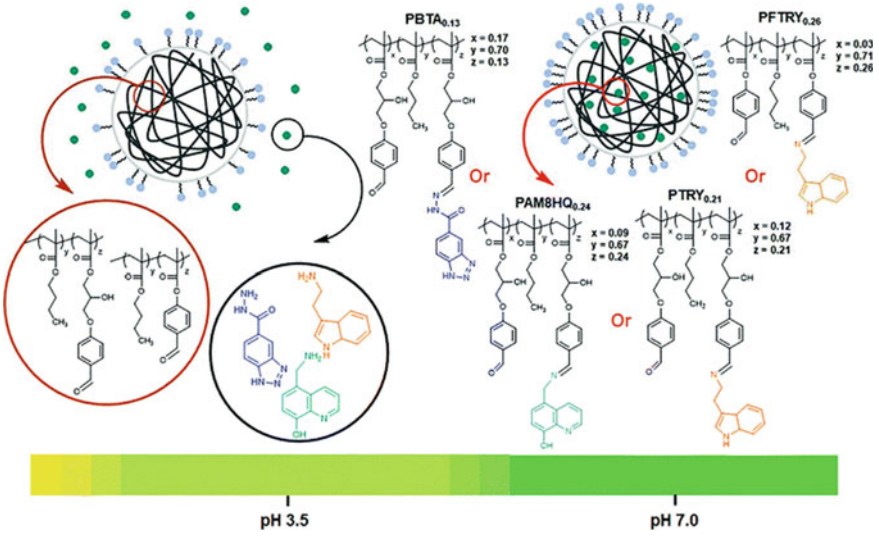

Fig. 7.18 Schematic showing the chemical structure of polymer conjugates containing the corrosion inhibitors BTA hydrazide (PBTA0.13), AM8HQ (PAM8HQ0.24), and tryptamine (PTRY0.21 and PFTRY0.26) releasing corrosion inhibitors upon lowering the pH value. Reproduced with permission from the Royal Society of Chemistry

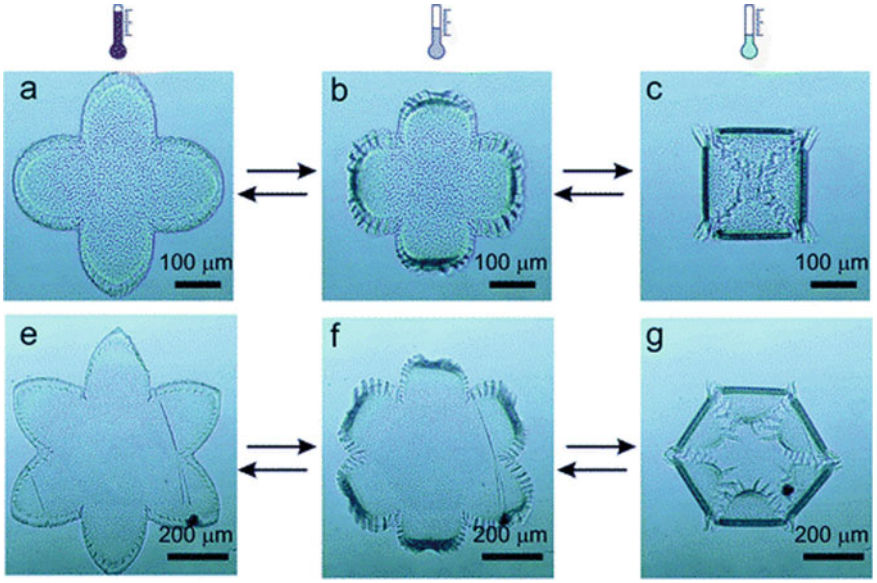

Fig. 7.19 Bright field optical microscopy images of self-folding of the star-like patterned polymer bilayer. The polymer bilayer is undeformed at elevated temperatures when the poly-(NIPAM–ABP) layer is shrunk. Cooling results in swelling of the poly-(NIPAM–ABP) layer and folding of the bilayer. Reproduced with permission from the Royal Society of Chemistry

7.2.4 Electro-active Polymers

Referring to previous studies, this section introduces electro-active polymers (EAPs) in detail. EAPs are deformable when electric stimulation is applied, displaying the potential to be used as polymer actuators. In addition, some EAPs exhibit electric signals (i.e., voltage and electric current) while applying external forces and displacements, ensuring the fabrication of mechanical sensors. Considering the driving mechanisms, EAPs are roughly divided into three categories: ionic-, non-ionic-, and electronic-EAPs (Table 7.1).

7.2.4.1 Ionic-EAPs

Electric conductive polymers

In general, π-conjugated polymers, such as polypyrrole (PPy), polyaniline, and poly(3,4-ethylenedioxythiophene) (Fig. 7.20a), exhibit electron conductivity in the polaron and/or bipolaron state when they are electrochemically doped with counter anions (oxidized state). The solid films of these polymers change their volume in electrolyte solutions depending on the degree of oxidation and reduction (doping and dedoping), as shown in Fig. 7.20b. Several reports demonstrate the evaluation of

Table 7.1 Comparison of actuating performance among natural skeletal muscles and various soft actuators

Type	Deformation type	Driving voltage (V)	Strain (%)	Stress (MPa)	Response speed (s)	Cycle	Environment
Muscles (Mirfakhrai 2007)	Contracting	-	20	0.1–0.4	0.1	10^9	Solvent
Light (Wang 2019; Qin 2020)	Bending/Contracting	-	20–80	ca. 0.07	> 10	-	Air
pH (Yu 2015)	Expanding	-	43	-	-	-	Solvent
Temperature (Stoychev 2011)	Expanding/Contracting/Bending	-	-	-	5–10	-	Solvent
Ionic-EAP (Hara 2003; Asaka 1995; Kamamichi 2021)	Expanding/Bending	3	3–35	3.5	ca. 0.1–2	1×10^5	Solvent/Air
Non-ionic-EAP (Horii 2016; Ma 2013)	Contracting	14	7.8	27	> 3	-	Air
Electronic-EAP (Pelrine et al. 2000; Li et al. 2015)	Expanding	600–6000	10–68 in thickness direction	0.8–2.4	< 0.1	$> 5 \times 10^6$	Air

the electric conductive polymers as electrochemical actuators that convert electrical energy to mechanical energy (Baughman et al. 1990; Pei and Inganas 1992; Otero et al. 1992; Kaneto et al. 1995). K. Kaneto et al. developed a linear PPy actuator comprising tubular PPy films and PPy-Au coil composites for tactile displays and micro-valves. The linear PPy actuators displayed an electrochemical strain and stress of ca. 35% and 2.6–3.5 MPa, respectively (skeletal muscles: 20–40%, ca. 0.3 MPa) (Hara et al. 2003). The diffusion of dopant ions in the polymers limits the rate of reactions, and the response speed of the actuator was 13.8%/s, which is less than that of a skeletal muscle (300%/s).

Ionic conductive polymers

Ionic conductive polymers are generally divided into two structural classifications: polymers with side-chains of ionic functional groups and composites of anions and cations supported in polymer matrixes (Fig. 7.21). K. Oguro conducted a study related to ionic polymer–metal composite (IPMC) actuators composed of an ionic conducting polymer sandwiched between two film electrodes (Oguro 1992); he also applied for a patent for the same. K. Asaka et al. demonstrated the bending motion of a Nafion membrane plated with gold or platinum toward the anode on applying a voltage in water solution. The cation flux, the electro-osmotic drag of water from the anode to the cathode, changes in the interfacial tension, and concentration in the electric double layer between the electrode and the Nafion membrane induced the bending motion toward the anode (Asaka and Mizuhata 1995). The changes in the concentration of electrolyte solution and the evaporation of solvent from the swollen membrane

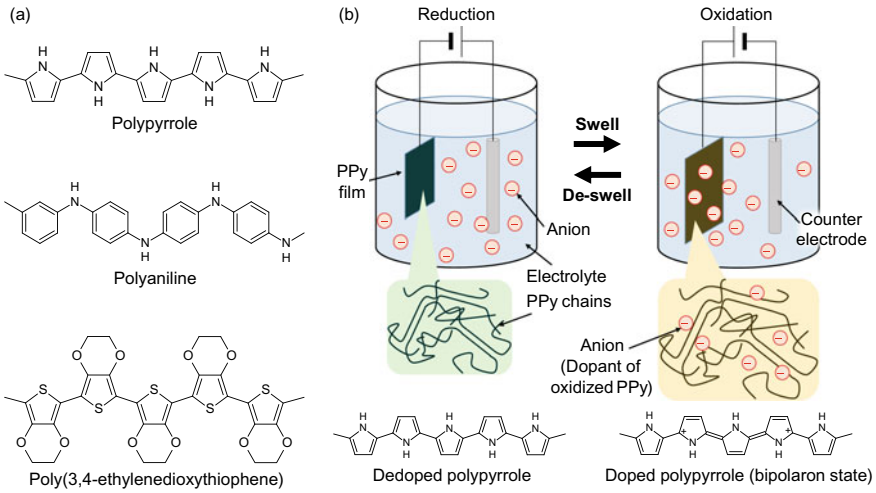

Fig. 7.20 Schemes of **a** chemical structures of representative conductive polymers and **b** de-swelling and swelling behavior via reduction–oxidation reaction of polypyrrole in an electrolyte solution on applying a voltage

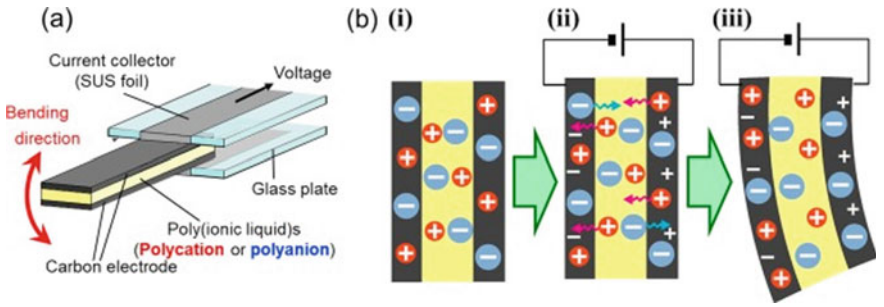

Fig. 7.21 Schematic of **a** structure of polymer actuator in this study and **b** driving mechanism of the polymer actuator using ionic liquids or ionic salts as electrolytes in the case of ($t+ > t-$); (i) before applying voltage, (ii) after applying voltage, ion migration to both EDL associated with charging, and (iii) deformation toward positive electrode owing to the increase in the volume of negative electrode. Reproduced with permission from Elsevier

in air affect the mechanical performance. IPMCs controllable in atmospheric conditions were developed using polymer/ionic liquid (Fukushima et al. 2005; Imaizumi et al. 2013; Shioiri et al. 2019) and elastomer/ionic liquid (ILs) (Okuzaki et al. 2014) composites. S. Imaizumi et al. derived an equation for the displacement considering the difference of transference number between a cation and an anion and theoretically and experimentally discussed the association of displacement with bending direction (Imaizumi et al. 2012).

Polymerized ionic liquids (PILs), a type of ionic conductive polymers, can be used for harvesting electric energy. S. Ono et al. developed a soft electret comprising ionic liquids (ILs) anchored to a polymer network. UV light was exposed to a mixed solution of ILs, polymer, polymerization initiator to polymerize the ILs with functional groups including unsaturated bond and the polymer with the same functional groups as the ILs. On polymerization, by applying 2–3 V DC (within the electrochemical windows of ILs) to the solution, the soft electret displayed current densities as high as 9–200 $\mu A/cm^2$ (Mitsuya et al. 2015; Ono et al. 2017).

7.2.4.2 Non-ionic-EAPs

Humidity is one of the core factors responsible for EAP deformation in the electric field. The electric conductive polymers are sensitive to the existence of water vapor. Accordingly, applying an electric field to the PPy film in air induces Joule heating and generates desorbed water vapor from the film, resulting in a 1% contraction in the strain, which is smaller than that in other EAP actuators (Fig. 7.22) (Okuzaki and Funasaka 2000). Horii et al. evaluated the solid films of chemically synthesized poly(3,4-ethylenedioxythiophene) doped with poly(4-styrene sulfonate acid) (PEDOT:PSS) with different PSS composition ratios as humido-sensitive actuators. The contractile strain of PEDOT:PSS film increased with the increase in the PSS composition ratio, reaching up to 7.8%, corresponding to an electric power density

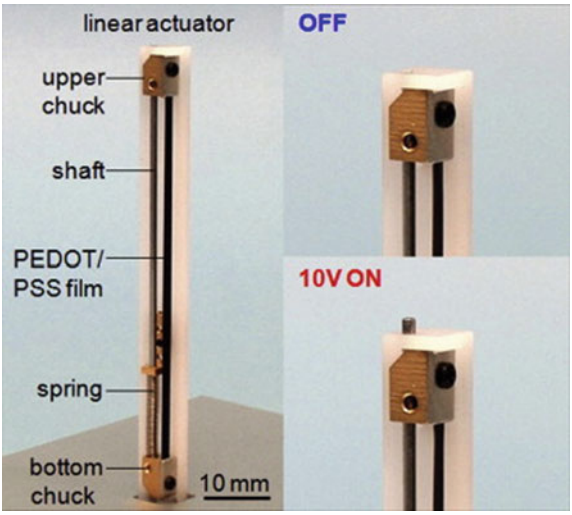

Fig. 7.22 Photographs of a linear actuator using a PEDOT/PSS film. Reproduced with permission from Elsevier

of ca. 0.4 kW/cm^3 (Horii et al. 2016). Ma et al. developed an actuator comprising polyol-borate as a dynamic network and polypyrrole as a rigid matrix for rapid and continuous responses (Ma et al. 2013a).

7.2.4.3 Electronic-EAPs

Polymers generating electric signals and displacements via applications of forces and voltages, respectively, are termed piezoelectric polymers. Polyvinylidene fluoride (PVDF) shows significant piezoelectric effect ($g_{31} = 150–70 \times 10^{-3}$ V/g) on applying high voltage (300 kV/cm) to the highly elongated PVDF film (Kawai 1969). In general, the piezoelectric polymers are stable in air, vacuum, and water, whereas the electric strain of poly(vinylidene fluoride-trifluoroethylene) is approximately 4% in an electric field of 150 V/μm (Zhang et al. 1998).

A dielectric elastomer actuator (DEA), comprising a dielectric elastomer (DE) sheet sandwiched between two compliant electrodes, contracts along the thickness direction and expands along the in-plane direction owing to the attractive electrostatic force (Maxwell stress) generated by applying a kV-scale potential difference across the electrodes (Fig. 7.23) (Pelrine et al. 2000). DEAs have attracted great attention as potential actuation systems in wearable devices, such as artificial muscles of motion assisting suits and haptic devices (Duduta et al. 2019; Qiu 2019). Recently, some research groups developed thin-type DEA, which requires less applied voltage (several 100 V) and is suitable for haptics and speaker applications (Hosoya et al. 2019; Ji et al. 2021; Wiranata et al. 2021).

Dielectric gels, such as polyvinyl alcohol (PVA) gel with dimethyl sulfoxide and polyvinyl chloride (PVC) gel, show amoeba-like creep deformation along the anode surface in the presence of an electric field (Fig. 7.24). K. Asaka and M. Hashimoto

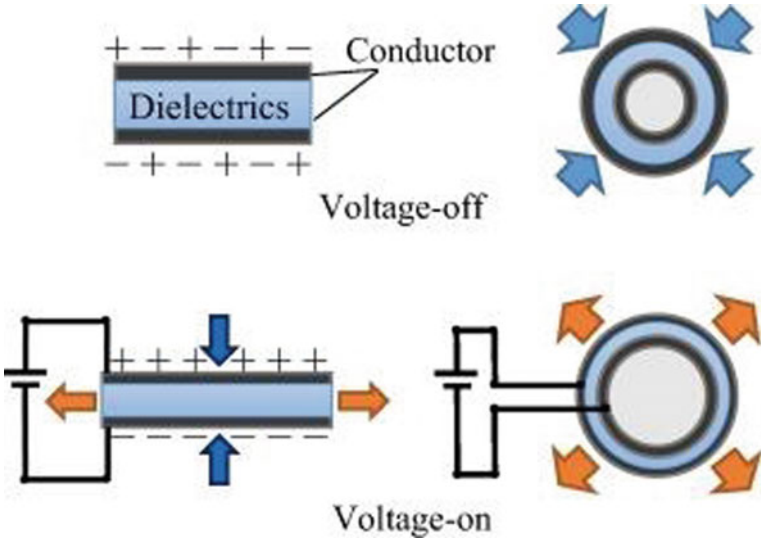

Fig. 7.23 Operational principle of the balloon dielectric elastomer actuator. Reproduced with permission from Elsevier

concluded that the creep deformation of the gel near the anode surface is due to the Maxwell stress. When a voltage was applied to the electrodes located on both sides of a PVC gel sheet, negative charges were accumulated in the PVC gel near the surface of the anode, which was demonstrated by space-charge measurement (Xia et al. 2010), resulting in the separation of the PVC gel into two layers with different resistances and capacitances. The voltage is applied to the thin and solvent-rich layer with high resistance formed near the anode surface (Asaka and Hashimoto 2018). M. Hashimoto et al. developed stacked-layer PVC gel actuators by alternatively laminating PVC gel sheets and metal mesh electrodes and thus, developed various planer PVC gel actuator types for walking and body motion assistive suits (Fig. 7.25) (Li et al. 2015, 2019).

7.2.5 Challenges

The advancement of an aging society with decreasing childbirth rate is a serious problem both in Japan and in rapidly developing countries (Cabinet Office 2020). Aging causes illness and injury, which reduces muscle strength and body movement capability. In addition, loss of body parts and biological tissues as a result of injury and inhibition of body movement owing to brain and nervous system diseases, such as dystonia, can occur in people of any generation. Therefore, the development of motion support wearables and therapeutic devices to assist human physical and motor functions has attracted great attention. These devices consist of functional

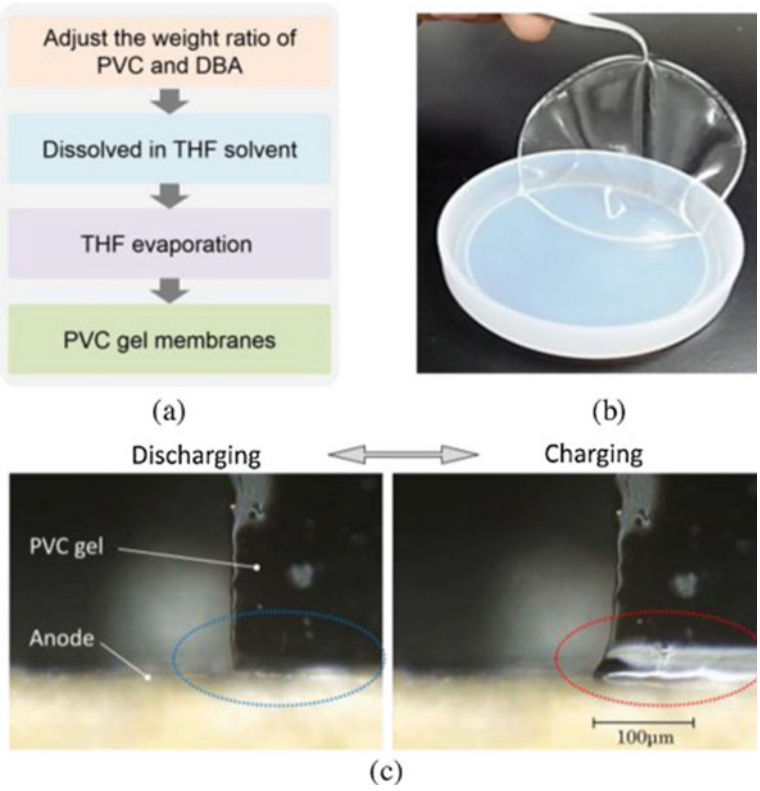

Fig. 7.24 **a** Process of preparation of PVC gel membranes. **b** Photograph of a fabricated PVC gel membrane. **c** Deformation of a PVC gel membrane under a DC field in front view. Reproduced with permission from Elsevier

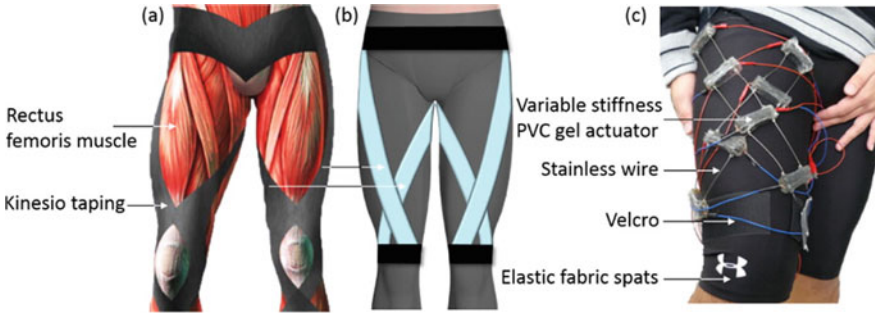

Fig. 7.25 Design and prototype of variable stiffness gel spats; **a** upper leg muscle anatomy with taping; **b** design concept; and **c** actual prototype. Copyright 2015 International Journal of Advanced Robotic Systems

polymers that offer high degree of followability to motion, affinity to the tissues, and safety. They are extremely important to create soft robots. Furthermore, there is an urgent need to practically apply these devices to society. As described in this section, characteristics of functional polymers and devices, such as actuators, have been studied in detail, and numerous original ideas have been published. Meanwhile, further investigations are required to implement these devices in real-time industrial and medical products. An enhancement in the durability of EAP actuators, their mass fabrication process, and automation are essential. Reducing the driving voltage of the actuators will improve their applicability to in-vivo applications and direct contact with biological tissues, such as haptic devices integrated with operating circuits and power sources. In addition, improving the response speed and durability of pH- and light-stimuli-responsive polymers will generate synergistic effects with other functional polymers.

7.3 Soft Materials (Elastomer, Hydrogels, etc.)

7.3.1 Basic Concept of Soft Materials

In this section, we will discuss the soft materials, such as rubbers and gels, including the fundamental concepts of polymer chains, elastic modus, and estimates of crosslink densities in accordance with de Gennes' scaling theory (De Gennes and De Gennes 1979). An overview of entropy elasticity, Brownian motion, and examples of actuator measurements will be discussed.

7.3.2 Structure of Polymeric Soft Materials (De Gennes and De Gennes 1979)

1. *Scaling rule for the spread of an isolated polymer*

Polymeric soft materials are usually composed of polymers. Polymers are made up of monomers linked like chains, as shown in Fig. 7.26.

Considering the conformation of the polymer from the origin O, the connection of each monomer can be evaluated using the end-to-end vector $\boldsymbol{R}$, which is the sum of $\boldsymbol{r}$ vectors.

$$\boldsymbol{R} = \sum_{i=1}^{N} \boldsymbol{r}_i \tag{7.4}$$

Assuming that the polymer randomly changes conformation at room temperature, the average size of the conformation is calculated. The square of the end-to-end vector is calculated as follows:

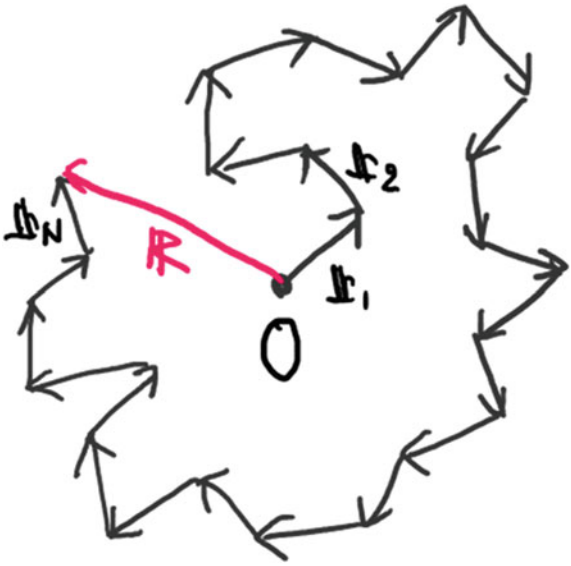

Fig. 7.26 Conformation of an isolated polymer chain

$$|\mathbf{R}|^2 = (\mathbf{r}_1 + \mathbf{r}_2 + \cdots + \mathbf{r}_N)^2 = \mathbf{r}_1^2 + \mathbf{r}_2^2 + \cdots + \mathbf{r}_N^2 + 2\mathbf{r}_1 \cdot \mathbf{r}_2 + \cdots \tag{7.5}$$

The inner product of the cross terms is zero if the monomer segments are randomly oriented moment-to-moment with each other.

$$\langle \mathbf{r}_i \cdot \mathbf{r}_j \rangle = 0, \text{ when } i \neq j \tag{7.6}$$

Therefore, if we take the average of the squares of the inter-terminal vectors,

$$\langle |\mathbf{R}|^2 \rangle = \langle \mathbf{r}_1^2 \rangle + \langle \mathbf{r}_2^2 \rangle + \cdots + \langle \mathbf{r}_N'^2 \rangle = a^2 N \tag{7.7}$$

where a is the size of monomer segment. This gives the average radius of a randomly conforming chain (ideal chain) as follows:

$$R_0 \cong a N^{\frac{1}{2}} \tag{7.8}$$

The above calculations assumed that all segments move randomly. In actual polymers (real chains), the segments repel each other, as shown in Fig. 7.27.

Considering this self-avoiding interaction, the radius R_F (Flory radius) of the real chain is obtained by raising N to the power of 3/5.

$$R_\mathrm{F} = a N^{\frac{3}{5}} \tag{7.9}$$

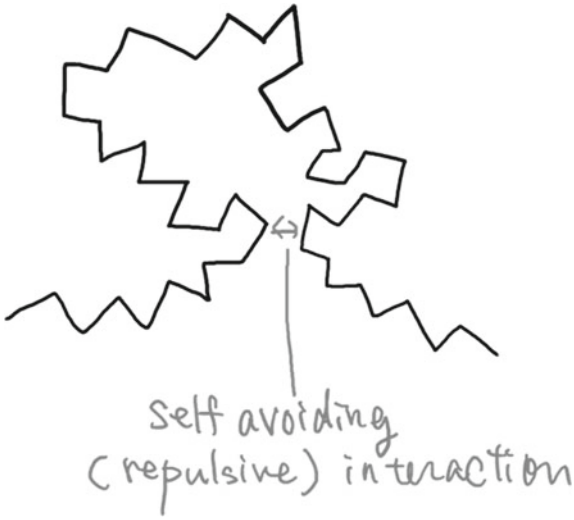

Fig. 7.27 Self-avoiding volume effect working between monomers of a real chain

The 3/5 rule was first obtained by Flory's approximation, which was later confirmed to be the power of 0.6 by rigorous discussion based on the renormalization group. In a good solvent, the polymer chain is spread out. However, when the quality of the solvent is poor, there is a state in which it behaves as an ideal chain. Such a state is called the theta state, and such a solvent is called a theta solvent. When the solubility is further lowered, the isolated chains condense into a collapse state. This corresponds to the globule state in the case of proteins. The most compact size of the collapsed chain is proportional to the number of monomers ($R \propto N$), and the radius of the collapsed chain is expressed as follows:

$$R_{\text{collapse}} \propto N^{\frac{1}{3}} \tag{7.10}$$

In addition, polyelectrolytes and other polymers can spread further than real chain formula due to the electrostatic repulsion acting between charged monomers.

$$R_{\text{Ex}} \propto N^{\nu_{\text{Ex}}}, \text{ when } \frac{3}{5} \leq \nu_{\text{Ex}} \leq 1 \tag{7.11}$$

This behavior is called the scaling law. As described above, the conformation of chains in various states is expressed as an exponent of the degree of polymerization. The spreading exponent ν changes between 1/3 and 1 as the spreading changes.

Summarizing the above, the following can be concluded using the exponent ν of the spread of the isolated chain.

$$R \propto N^{\nu} \begin{cases} \nu = \frac{3}{5} & \text{for real chain in good solvent} \\ \nu = \frac{1}{2} & \text{for ideal chain in theta solvent} \\ \nu = \frac{1}{3} & \text{for collapsed chain in poor solvent} \\ \frac{3}{5} \leqq \nu \leqq 1 & \text{for extended chain} \end{cases} \tag{7.12}$$

2. *Internal structure of polymer solutions and gels*

So far, we have considered the behavior of isolated chains that exist alone in solutions. Actual polymers overlap with each other as their concentration increases in a solution, as shown in Fig. 7.28.

Chemically cross-linked gels are produced by inserting crosslinking points into a polymer solution at a concentration higher than that of a pure dilute solution. If a crosslinking reaction is applied to a polymer solution with a concentration lower than Φ*, the chains do not spread across the vessel and therefore do not gel.

At the overlap concentration, the concentration at which the concentration in the chain and the concentration outside the chain coincide can be determined as follows:

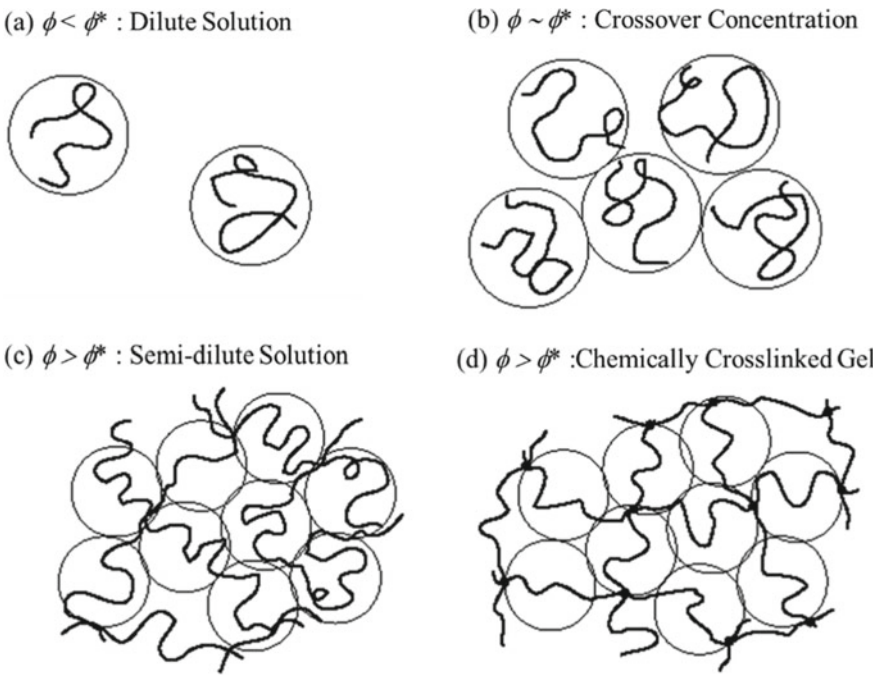

Fig. 7.28 Concentration dependence of polymer solutions. The thick lines represent polymer chains. The circles drawn with thin lines represent concentration blobs. The dots at the thick line crosses in Figure (**d**) indicate the crosslinking points

$$\phi^* \cong \frac{a^3 N}{R^3} \cong \frac{a^3 N}{(aN^\nu)^3} \cong N^{1-3\nu} \tag{7.13}$$

where R is the radius of the subchain, N is the degree of polymerization, and a is the segment length (monomer size). As mentioned above, the spread exponent ν is expressed as $\nu = \frac{1}{2}$ for ideal chains and $\nu = \frac{3}{5}$ for real chains.

If the degree of polymerization of subchains in the semi-dilute concentration blob is g,

$$\phi \cong g^{1-3\nu} \tag{7.14}$$

If the size of the concentration blob, which corresponds to the mesh size of the network structure due to entanglement, is ξ,

$$\xi \cong a g^\nu \tag{7.15}$$

Thus, using these two equations, we obtain

$$\xi \cong a\phi^{\frac{\nu}{1-3\nu}} \tag{7.16}$$

For the case of an ideal chain, $\nu = \frac{1}{2}$,

$$\xi \cong a\phi^{-1} \tag{7.17}$$

For the case of a real chain, $\nu = \frac{3}{5}$,

$$\xi \cong a\phi^{-\frac{3}{4}} \tag{7.18}$$

These equations suggest that the higher the concentration, the smaller the mesh size. The characteristic size of the interior of an entangled polymer solution or chemically cross-linked gel is in one-to-one correspondence with the concentration.

3. *Rubber elasticity*

When a rubber band is placed between the nose and mouth, we feel the temperature of the rubber band. When the rubber band is pulled, it feels warm, and when it is squeezed and relaxed, it feels cold (Fig. 7.29).

The change in rubber's temperature is due to the thermal motion of the rubber chain molecules. For example, few children are connected by a rope, as illustrated in Fig. 7.30. When an adult tries to pull from one end, they move forward while remaining connected. When the opposite end of the rope is tied to a pole, the adult can straighten the rope when the children are calm, but if the children move actively, the adult will be pulled and hence will be unable to keep the rope straight.

The intensive physical activity of the child corresponds to heat. If the rubber band is stretched, the child cannot move, so the heat gets dissipated. A diagram of this principle applied to a molecular model of rubber is shown in Fig. 7.31.

Fig. 7.29 Rubber band experiment

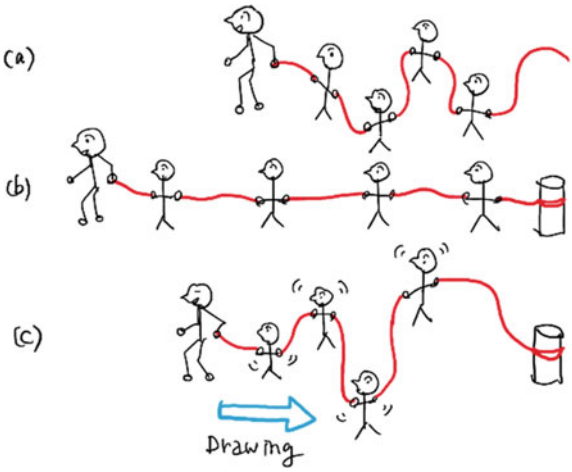

Fig. 7.30 Illustration of molecular motion and polymer tension in rubber

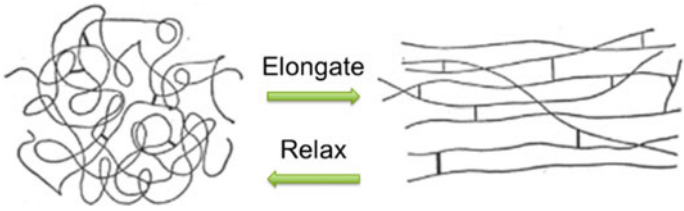

Fig. 7.31 Molecular model of rubber

When a rubber mesh is stretched, the chains are oriented such that the entropy is reduced and heat is released. By contrast, when the rubber shrinks, the chains become disorganized and the entropy increases. This leads to the absorption of heat, making the rubber cooler.

We can calculate the elastic modulus of rubber bands E by dividing the stress σ by the strain ε, which yields a value of approximately 0.1 MPa, as shown below.

$$\sigma = E\varepsilon \tag{7.19}$$

The distribution function of a single Gaussian chain (ideal chain) of extension rate λ can be written as follows:

$$P\left(\lambda_x, \lambda_y, \lambda_z\right) = \left(\frac{3}{2\pi R_0^2}\right)^{\frac{3}{2}} \exp\left[-\frac{3}{2}\left(\lambda_x + \lambda_y + \lambda_z\right)^2\right] \tag{7.20}$$

The free energy of a single Gaussian chain is then obtained from the fact that the distribution function of the chain is the origin of entropy.

$$F\left(\lambda_x, \lambda_y, \lambda_z\right) = -TS\left(\lambda_x, \lambda_y, \lambda_z\right) = k_{\mathrm{B}}T \ln P\left(\lambda_x, \lambda_y, \lambda_z\right) \tag{7.21}$$

where S is the entropy, k_{B} is the Boltzmann constant, and T is the absolute temperature.

The stress due to the free energy in the x direction is calculated as follows:

$$\sigma_x = \frac{1}{\lambda_y \lambda_z} \frac{\partial}{\partial \lambda_x} F\left(\lambda_x, \lambda_y, \lambda_z\right) = k_{\mathrm{B}}T\left(\lambda^2 - \frac{1}{\lambda}\right) \tag{7.22}$$

where

$$\lambda_x = \lambda, \quad \lambda_y = \lambda_z = \frac{1}{\lambda} \tag{7.23}$$

Finally, we obtain

$$\sigma_x = k_{\mathrm{B}}T\left[(1+\varepsilon)^2 - \frac{1}{1+\varepsilon}\right] \cong 3k_{\mathrm{B}}T \cdot \varepsilon \tag{7.24}$$

Thus, the Young's modulus of a single Gaussian chain is obtained by combining Eqs. (7.19) and (7.24).

$$E_{\mathrm{chain}} \cong 3k_{\mathrm{B}}T \tag{7.25}$$

Finally, the Young's modulus of ideal rubber is obtained as

$$E_{\mathrm{bulk}} = 3\nu_{\mathrm{e}}k_{\mathrm{B}}T \tag{7.26}$$

where ν_{e} is the number of chains per unit volume, and it contributes to the entropic elasticity. Rubber elasticity is proportional to the absolute temperature. So the higher

the temperature, the harder the rubber. It should be noted that the initial elasticity, i.e., the Young's modulus is independent of the molecular weight.

7.3.3 *Functional Gels*

When two types of monomers are connected to form rigid oligomers that are then cross-linked at the ends of the oligomers, a lattice-like polymer network can be created, as shown in Fig. 7.32 (Furukawa et al. 2012). By adding azobenzene, which bends with light, to the main-chain, functional gels that bend with light can be created.

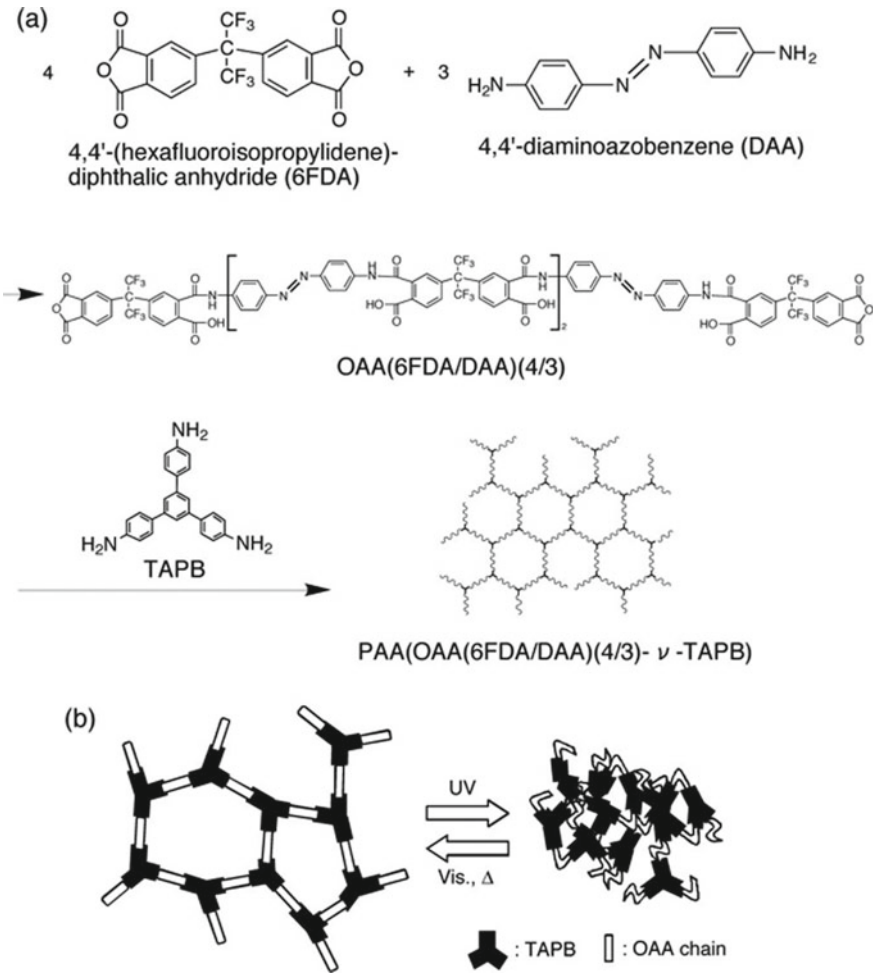

Fig. 7.32 Photoresponsive end-cross-linked gels (Furukawa et al. 2012)

As shown in Fig. 7.33, when UV light is applied, the gel bends in the area where the chain bends and the volume of the lattice-like polymer network shrinks. By contrast, when visible light is applied, the reverse reaction occurs, and the gel returns to its original straight state.

As shown in Fig. 7.34, the Brownian motion of the gel mesh can be observed through dynamic light scattering while it bends with light.

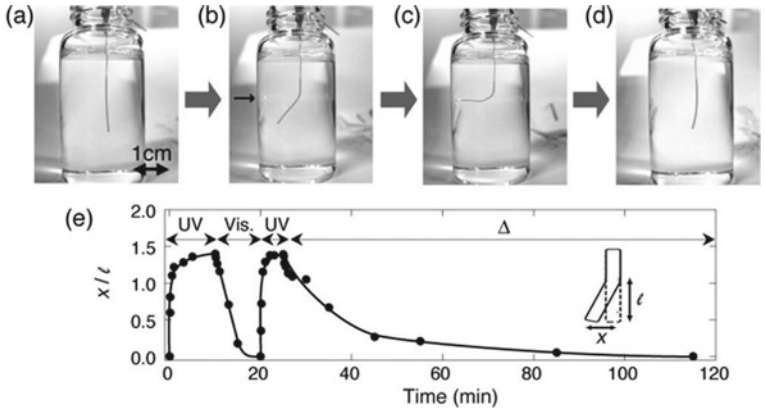

Fig. 7.33 Gel that bends with light (Furukawa et al. 2012)

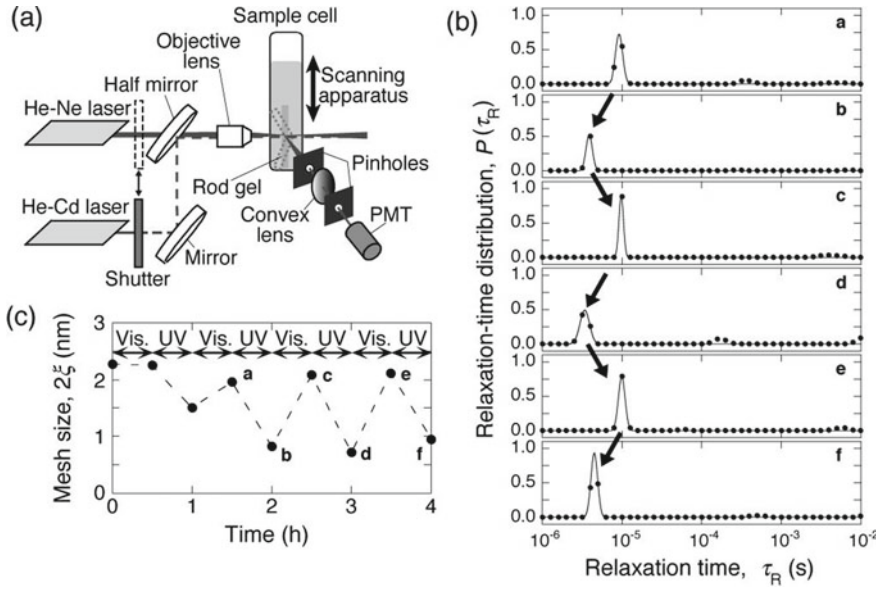

Fig. 7.34 In-situ non-destructive evaluation of mesh size measurement of gels that bend with light (Furukawa et al. 2012)

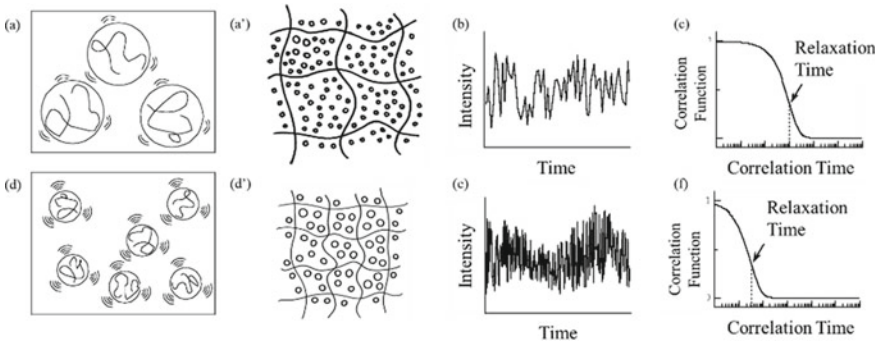

Fig. 7.35 Relationship between the Brownian motion of isolated polymer chains (**a** and **d**) and polymer gel meshes (**a′** and **d′**), fluctuation of scattered intensity (**b** and **e**), and measurement of correlation functions by dynamic light scattering (**c** and **f**)

The scattered light is scanned microscopically (Furukawa et al. 2003) based on dynamic light scattering to measure the Brownian motion of the mesh network.

$$D = \frac{k_B T}{6\pi\eta R} \tag{7.27}$$

where D is the diffusion coefficient, η is the viscosity of the solvent, and R is the size of the unit of motion that undergoes Brownian motion.

The radius of spread of the polymer can be determined through R if the diffusion coefficient of Brownian motion D can be measured by light scattering. As shown in Fig. 7.35, the larger blobs move more slowly and the smaller blobs move quickly, allowing us to observe the sizes of the concentration blobs.

In the case of gels, the unit of motion is the mesh, as shown in Fig. 7.35a′ and d′.

$$R \cong 2\xi \tag{7.28}$$

As shown in Fig. 7.36, the crosslinking density of the gels can be determined in three ways (Furukawa et al. 2013).

First, as observed in the above discussion, the crosslinking density ν_s determined from scattering can be determined using the following equation:

$$\nu_s = \frac{1}{d^3} \cong \frac{1}{\xi^3} \tag{7.29}$$

where d is the size of a piece of the cubic lattice model.

Second, the crosslinking density obtained from the water content (solvent content) ν_w can be determined from the concentration of the synthesized gels and the swelling state of the gels when synthesized.

$$\nu_w = \frac{\left(\frac{f}{2}\right) n_{cross}}{V} \cong \frac{N_A \rho_w f}{2M_{cross}} \psi_{cross}(1 - \phi_w) \tag{7.30}$$

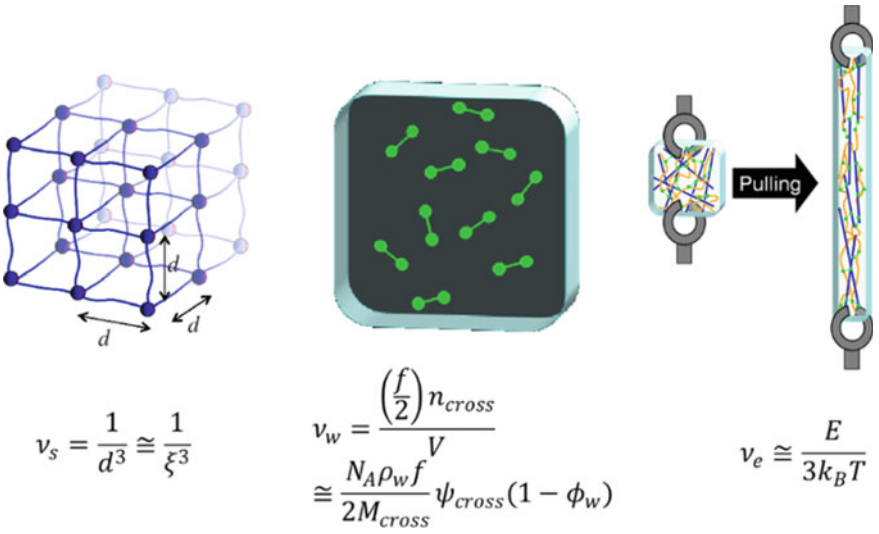

Fig. 7.36 Three ways to determine the crosslinking density of gels (Furukawa et al. 2013)

where f is the functionality of the crosslinking point, n_{cross} is the number of crosslinkers in the gel, V is the volume of the gel in the swollen state, M_{cross} is the molecular weight of the crosslinker, N_{A} is the Avogadro's number, ρ_{G} and ρ_{W} are the specific densities of the gel's solute, and ψ_{C} is the crosslinker density in preparation. $\psi_{\text{C}} \equiv w_{\text{C}}/w_{\text{G}}$, where w_{C} and w_{G} are the weights of the crosslinker content and the entire gel solute content including the polymers and the crosslinker, respectively.

Third, the crosslinking density can be determined from the Young's modulus of the gel ν_{e}, as determined using Eq. (7.26).

$$\nu_{\text{e}} \cong \frac{E}{3k_{\text{B}}T} \tag{7.31}$$

Usually, the three different methods to determine the three types of crosslinker concentrations do not match. Their comparison is shown in Fig. 7.37 (Watanabe et al. 2013).

When the mesh size of the swelling ratio and Young's modulus is smaller than the mesh size determined by dynamic light scattering, as shown in inset (a) of Fig. 7.37, it is expected that the chains are entangled with each other, resulting in a smaller mesh than the determined one and the actual gels may be harder than those determined from the mesh size. By contrast, as shown inset (c) of Fig. 7.37, there may be more defects and the actual gels may be softer than those determined from the mesh size.

The gels in the middle, as shown inset (b) of Fig. 7.37, are probably considered to be the gels with the most uniform mesh. It has also been confirmed with acrylamide (Furukawa et al. 2003) and polyimide gels (Furukawa et al. 2012) that gels made under intermediate concentration conditions tend to be uniform.

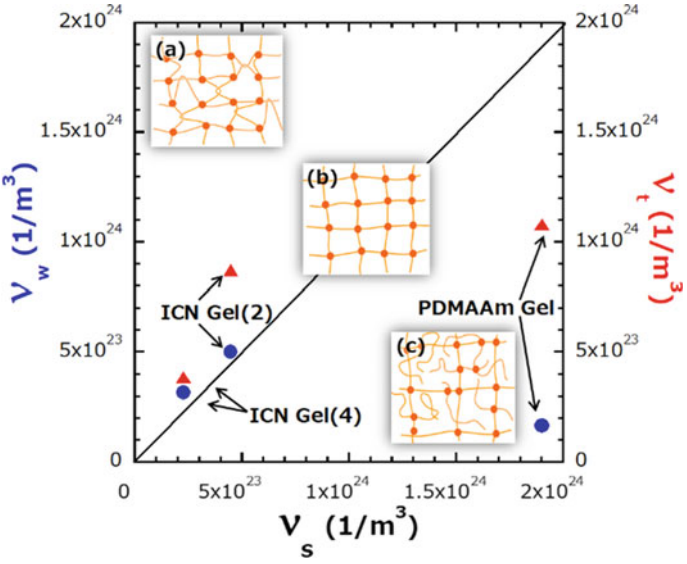

Fig. 7.37 Comparison of the three crosslink densities (Watanabe et al. 2013)

Additionally, the above-described equations can also be used to qualitatively calculate the elastic modulus of rubber and the molecular weight between crosslinking points. In the case of ideal rubber, it has been investigated that the rubber takes an ideal chain-like conformation in the molten state, with a spreading index ν of ½ predicted historically by Flory (De Gennes and De Gennes 1979).

Let us estimate the length of the chain (in the case of rubber) that can be stretched and spreads as an ideal chain. Theoretically, the elongation of the chain is calculated, based on Eq. (7.8) as follows:

$$\frac{R_{\mathrm{Ex}}}{R_0} \simeq g^{1-\frac{1}{2}} = g^{\frac{1}{2}} \tag{7.32}$$

Thus,

$$\frac{\xi}{a} \cong g^{\frac{1}{2}} \tag{7.33}$$

When $\xi \cong 3$ nm and $\alpha \cong 0.1$ nm, the magnification factor that becomes fully extended is 30 times. Theoretically, if $N = 100$ and N corresponds to θ, it will elongate 10 times, and if $N = 10{,}000$, it will elongate 100 times.

(The elastic modulus gives the spatial crosslink density, and the effective mesh size gives the molecular weight between entanglement points, which in turn gives the approximate length of elongation.)

In the case of a gel, because it is a real chain, the exponent of elongation is $1 - 3/5 = 2/5$, i.e., the power of 0.4.

7.3.4 How to Gain Knowledge on Soft Materials

De Gennes' textbook is a good source of information on the scaling theory of polymer physics explained here. Although not mentioned here, PNIPA gels have the property of shrinking in a volumetric phase transition with respect to temperature, and their application to actuators has long been studied.

Also, the high-strength mechanism of high-strength gels has been widely studied, and guidelines for sturdy gels are useful. Other studies, such as the theory of phase separation and gelation, are also useful for actuator design, manufacturing, and control.

7.3.5 Challenges for Soft Materials

With the development of 3D printing and printed electronics, it will become possible to create rubber and gel of targeted hardness and softness at targeted locations in the near future. Thus, the origin and basic concepts of entanglement density and elasticity discussed here are useful. In the future, soft robotics researchers will be able to create new soft materials with the softness of their choice, and the development of new soft materials will bring new value to soft robots. Even then, a new generation of soft robots designed from materials can be created by understanding the response mechanism of gels to external fields and their molecular theory and by linking molecular models and macroscopic physical quantities.

7.4 Fabrication of Soft Robot Parts Using Three-Dimensional Printers

Three-dimensional (3D) printers have been used for the fabrication of robotic parts in laboratories and technical colleges for almost a decade. Very soft robot parts, such as the hands of pneumatic balloon robots, can be fabricated either by casting soft materials into molds modeled using 3D printers or through conventional machining processes such as computer numerical control or injection molding. However, 3D printers have many advantages, such as the ability to print complex shapes, low cost, short turnaround time, low material wastage, and high customizability. The direct modeling of robot parts using 3D printers is preferred for manufacturing soft parts that are soft enough not to break and injure people even if they encounter an accident.

7.4.1 Designing 3D Models

Because the robot parts are "directly" printed by a 3D printer, the 3D data can be used as-is for designing the robot's shape. By contrast, in the casting method, the 3D data needs to be converted to a cast (mold) data first. Free software for designing 3D models is sufficient for academic institutions and small-scale companies. Typically, 3D model created using 3D computer-aided design (CAD) is saved in the stereolithography (STL) format, and the slicing software automatically calculates the operation of the 3D printer using this model (Fig. 7.38). In particular, when using soft materials, the nozzle movement speed, material extrusion speed, and distance between layers should be accurately set because the success rate of the print and quality of the finished product vary considerably depending on these settings.

Different 3D printers are used for different materials depending on the deposition method. However, the fabrication of soft materials using 3D printers is challenging. In the following section, the characteristics of each method, status of manufacturing methods using soft materials, and technical challenges owing to differences in printing methods are discussed.

Inkjet Method

In this method, a monomer solution of photocurable resin is sprayed vertically downward on a table using an inkjet head to draw a cross-sectional image. Immediately after spraying, the drawn layer is cured by exposing it to a powerful ultraviolet (UV) lamp, and subsequently, another layer is sprayed on top of it. Thus, a 3D layer of the cured material can be obtained by repeating this process (Fig. 7.39).

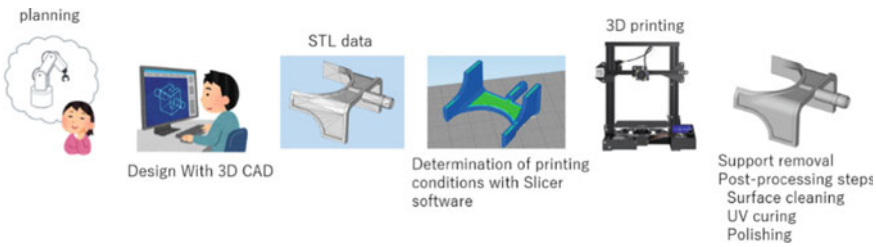

Fig. 7.38 Steps involved in robot part fabrication using a 3D printer

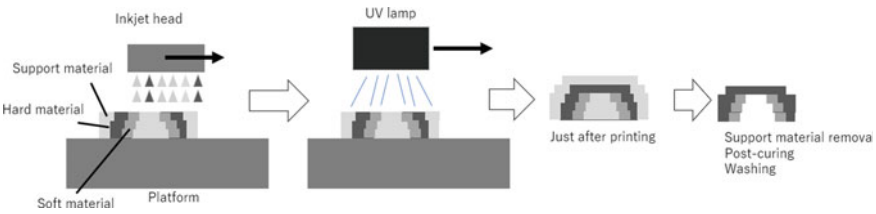

Fig. 7.39 Schematic of inkjet 3D printing

Unlike other 3D printing methods, the main and supporting materials are packed together to form the desired object in this method, and the supporting materials are removed by dissolving them in a solvent or through heating. For modeling with soft materials, depending on the printer model, "rubber-like materials" (flexible and bendable; suitable for prototyping rubber products) can be used. This material is soft, with a Shore A hardness of 90–30. Urethane resin should be used carefully because the softer the material is, the stickier it becomes on the surface of the object, which often becomes an obstacle when using the object as a robot component.

An example of a soft robot fabrication using soft materials is a pneumatically operated soft robot hand. Depending on the printer model, multiple materials can be used for modeling. For example, rubber-like materials of different hardness or a combination of hard and rubber-like materials can be used.

The main limitations of using soft materials for 3D printing are that their physical properties differ from those of normal rubber materials, and their viscosity is high. Specifically, the speed at which rubber-like materials deform and recover in response to air pressure and mechanical expansion and contraction is considerably slower than that of normal rubber. Furthermore, soft-material resin deteriorates quickly because of UV rays (or sunlight) and hydrolysis.

This method is typically not used for robot fabrication because of the high cost of equipment and materials. However, robot hands of complex shapes and composite material elements of hard and soft materials can be fabricated using this method (Wang et al. 2017a, b).

Thermal Melt Lamination Method (Fused Deposition Molding (FDM)/Fused Filament Fabrication (FFF))

In this method, the molten material is drawn like whipped cream on the XY plane by matching the timing of nozzle movement and extrusion. This process is repeated one layer at a time to create the desired shape (Fig. 7.40).

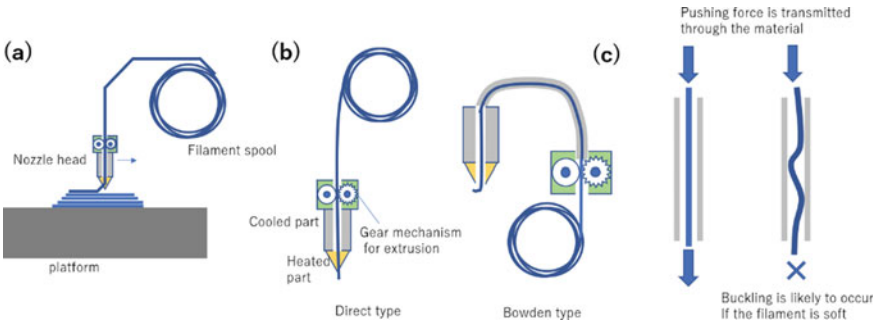

Fig. 7.40 **a** Printing principle of the thermal melting method (FDM/FFF). **b** Explanation of the Bowden/direct method. **c** Filament bucking

The fused deposition method (FDM) is used extensively, and polylactic acid (PLA) is widely used because it is inexpensive, exhibits low toxicity, and is less prone to warping that cause failure during molding.

The choice of printer is critical for printing soft materials using this method. FDM printers feed the material by pushing the filament. The filament is held between a pulley and gear, and the gear rotates to push the filament out. Two types of FDM printers currently exist; the Borden type, in which the extrusion mechanism is located far from the nozzle, and the direct type, where the extrusion mechanism is located just before the nozzle. The Borden method exhibits a faster nozzle movement than that in the direct type because the nozzle head does not have an extrusion mechanism, which requires a heavy motor. Therefore, as the nozzle is light, it undergoes less vibration during printing. In the FDM method, a thermoplastic polymer based on polyurethane is typically used as the flexible material. In the Bowden method, the long flexible material between the push-in and nozzle parts often bends (buckles) under the pressure of the push-in, and the push-in force is not transmitted properly. The direct method with a shorter distance is suitable for flexible materials; however, buckling typically occurs when the material is too soft. Moreover, buckling is probable if the material feed rate or printing speed is not set considerably lower than when using hard materials. In general, a printing speed four to five times lower than that of hard materials is appropriate. Ordinary direct-type FDM printers can only print materials with a Shore A hardness of approximately 85. Even when a special equipment (nozzles for flexible filament extrusion) or filament (such as urethane foam) is used, the lower limit for A hardness is approximately 60.

When using flexible materials, in addition to the lower limit of hardness, this method is not suitable for producing complex shapes and cannot be used for pneumatically driven parts because gaps between layers reduce the strength of fabricated parts and cause air leaks. The low cost of this method is advantageous over other methods. This type of printer can be purchased for less than 100,000 yen ($1000), and the filament used can be purchased for a few thousand yen per kilogram ($10/kg). This method is suitable for creating robot bodies that do not require very soft properties.

Stereo Lithography (SLA)/Digital Light Processing (DLP)

These methods have distinct names depending on whether the light source is a laser, projector, or light-emitting diode (LED). After each layer has been cured, the platform is lifted to detach the object from the bottom film, and the object is brought back to the film at the stacking pitch distance. This process is repeated until the final object is obtained (Fig. 7.41). To model overhangs or beam structures, it is necessary to place support structures that must be removed after modeling. Therefore, cavity-shaped parts with narrow entrances are not ideal for this method because removing the support inside the cavity after molding is difficult.

High-performance DLP method printers as well as FDM method printers are commercially available at low cost. DLP can be used to produce objects with high precision. However, modeling should be performed accurately in a confined space, such as a tube, because the resin may harden in areas that were not originally irradiated, leaving behind uncured resin.

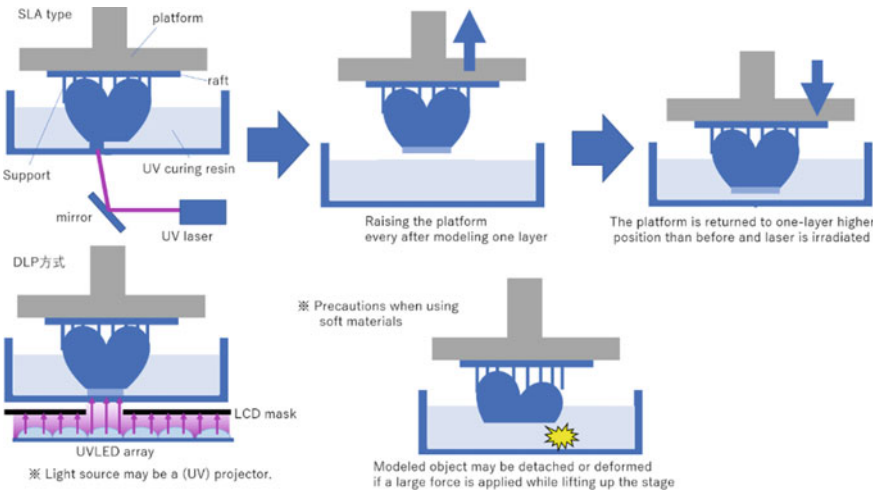

Fig. 7.41 SLA (upper left)/DLP (lower left) method printing principle

Furthermore, because an object is "lifted" in this method, the weight of the object may cause distortion when large parts are modeled. Moreover, because the process of "peeling off the object from the film" is repeated, this method is not suitable for modeling shapes with large cross-sectional areas because if large force is applied during the peeling process, it may cause deformation or the object may peel off from the platform.

Acrylic resin is the most commonly used material, but flexible resin is also available from various companies under names such as "flexible," "elastic," or "rubber-like."

SLA/SLS/Binder Jet Method

In the SLA method, a resin tank is filled with photocurable resin, and a UV laser beam is irradiated and scanned over the liquid surface to form a single layer. Next, the formed part is submerged in the liquid, and the stage is raised again to a position that is one molding pitch lower than that in the previous molding. Furthermore, the liquid surface is irradiated once again to draw the next cross-sectional image. This process is repeated until the final product is obtained, which is submerged in the resin tank (Fig. 7.42 left).

The SLS method is similar to the SLA method, but instead of liquid resin, fine powder is used as the material, and the irradiated area is sintered through laser irradiation to create a cross-sectional image. This process is repeated until the final object is obtained buried in the unused powder material.

In the binder jet method, a binder (adhesive) is sprayed from the inkjet head onto the surface of the powder sample to solidify the cross-sectional image at each layer (Fig. 7.42 right).

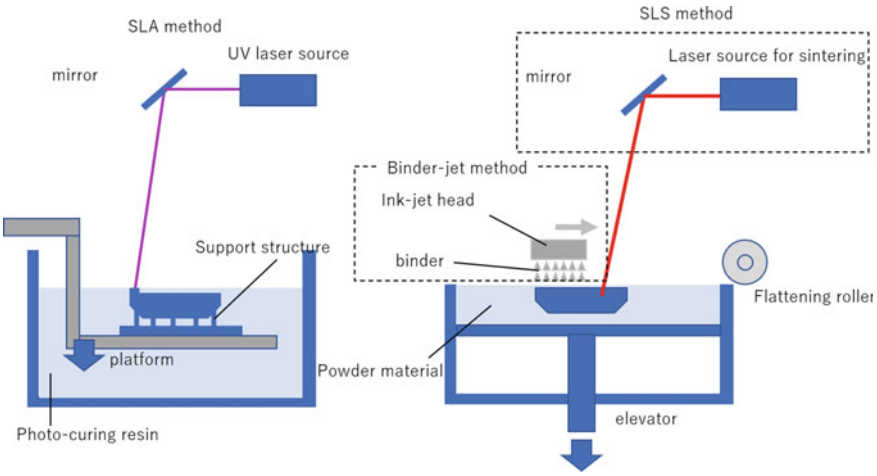

Fig. 7.42 Illustration of the printing principle of the SLA/SLS/binder jet method

Both SLA and SLS can use flexible materials. In SLA, photocurable resin is used as the material; thus, the material characteristics are identical to those described for the inkjet and DLP methods. In SLS, flexible materials such as urethane rubber (Shore A 60) and rubber-like resin (Shore A 45–75) can be used as printable resins.

7.4.2 Bonding

Mount electronics or integrated multiple flexible electronics and the joining/bonding technology that appropriately integrates various parts of soft robots are essential. This section focuses on the joining/bonding techniques for integrating the required components while preserving the advantages of flexibility and elasticity of materials in soft robots.

Chemical adhesives have been widely used to bond polymer resin materials thicker than a few hundred micrometers. They can be used in the ambient air atmosphere and can easily be used in multiple materials. However, many resin materials cannot be used because of the pollution problem caused by solvents. Therefore, a liquid-phase bonding method was used. A part of the resin material is heated above the melting point, and the materials are welded to each other without using an adhesive layer. The heating process can be roughly classified into three types. First, metals or gases, heated from the outside, are brought into contact with each other using the heat conduction or convection effect. Second, the mechanical or ultrasonic vibration is applied to the materials to be joined. Third, an electromagnetic energy, such as infrared rays or lasers, is applied locally to the joint part (Grewell et al. 2003).

Solid-phase bonding is more appropriate for bonding polymer thin films with thicknesses of several hundred micrometers or less. Solid-phase bonding is a method

for directly bonding polymers to each other by heating, pressurizing, or increasing the activation energy within the range of the solid-phase state, in which the material to be bonded is not melted. Therefore, it is possible to suppress thin film damage during the bonding process. In particular, surface-activated room-temperature bonding is useful as a flexible resin bonding technology (Howlader et al. 2007). In general, oxides and organic substances are adsorbed on the surface of a solid film. Bonding is achieved by contacting the bonding surfaces in vacuum and removing this impurity layer from the surface through ion irradiation under high vacuum conditions with a neutron atom beam. Because surface-activated room-temperature bonding does not require heat or mechanical stress for bonding, it is possible to bond even a low-melting-point polymer thin film that is more sensitive to thermal processes.

Direct bonding between the cyclo-olefin polymer and glass is achieved in an ambient atmosphere by activating the bonding surface using plasma steam gas (Terai et al. 2018). In the conventional surface activation bonding methods, which use reaction gases such as oxygen, pure surface activation is hindered owing to reattachment of reaction gas atoms and a chemical reaction. By using water vapor derived from water as a gas source, functional groups such as carboxylic groups (–COOH) and hydroxyl groups (–OH), derived from water, are attached to the bonding surface. Hydrogen bonding occurs by contacting the bonding surface, where the maximum bonding strength reaches up to 20 kPa. In this method, the resin material can be directly bonded in the ambient atmosphere using chemical bonds without heating or pressure, considering the reaction gas.

Furthermore, a solid-phase bonding method is developed to directly bond metal electrodes in the atmosphere. This method helps in the electrical bonding of flexible electronics built on a polymer thin film. Water–vapor plasma-assisted bonding (WVPAB) enables direct bonding of gold electrodes deposited on ultra-thin polymer films (Takakuwa et al. 2021). The surfaces of two Au electrodes deposited on ultra-thin polymer films are treated with water vapor plasma before being placed in contact with each other in the ambient air. Gold–gold direct bonding can be achieved by leaving it for approximately 12 h or longer without additional heating and pressure.

Applying such surface-activated bonding technology guarantees that thin-film polymer substrates and electronics formed on such substrates can be flexibly bonded and integrated.

7.4.3 Conclusion

In this chapter, the various types of 3D printers and soft materials used in different scenarios are described. The following figure depicts the hardness distribution of the materials that can be used in the methods described thus far (Fig. 7.43).

The use of 3D printers for the fabrication of robots ensures that prototypes can be produced many times in a short period of time at low cost. Therefore, institutions involved in soft robotics research and manufacturing should have an inexpensive FDM or DLP printer to fabricate soft robots. If a special model is required for

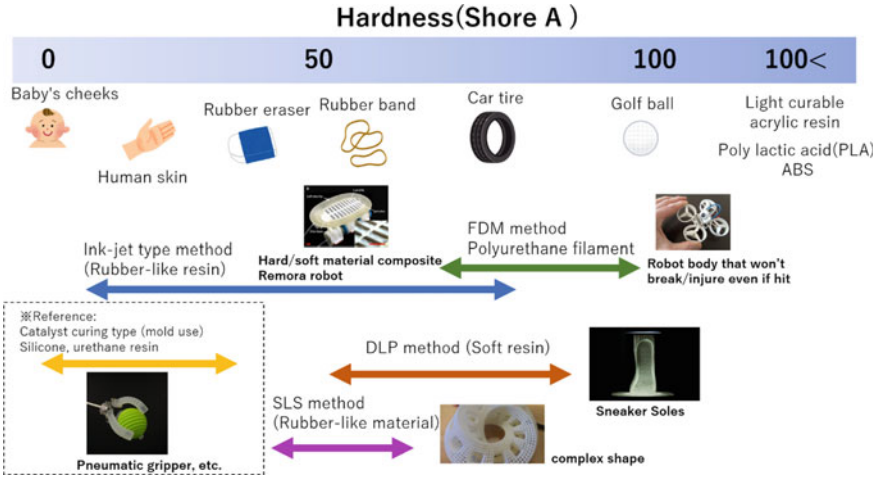

Fig. 7.43 Distribution of hardness of materials achieved using each printing method and examples of modeling

printing very soft or a combination of soft and hard materials, the most reasonable choice is to use a modeling service that uses inkjet or SLS/SLA. Furthermore, to design robot parts to the desired shape, proficiency in 3D CAD software is critical.

With the advent and widespread use of 3D printers, designing customizable robots, production of prototypes in a short time, and fabricating functional soft robots at low costs have become possible. Soft robotics research will continue to develop in this environment.

Exercises

- (5.1) Explain the morphologies characteristic of polymeric crystals with corresponding illustrations.
- (5.1) Explain the molecular conformation and packing in the crystalline lattice of polyethylene with corresponding illustrations.
- (5.1) Explain the ultimate structure achievable by super-drawing.
- (5.2) Explain the difference in mechanical properties between *cis*-1,4-polyisoprene and *trans*-1,4-polyisoprene.
- (5.2) For crystalline polymers, name the steric regularities that exhibit crystallinity.
- (5.2) Because a single polymer chain contains many C–C bonds, the degree of freedom of intramolecular rotation increases, and the polymer chain can adopt various conformations. As a result, the polymer chains exhibit helical structures and take on several helical intervals depending on the size of the substituents and physical interactions such as hydrogen bonding intra- and inter-molecularly in the polymer chains. Let's find out the helical structure of the polymers in detail, such as those of polypropylene and polypeptides (one of the biopolymers).

- (5.2) Let's study the properties and applications of the functional polymers, except for actuators, discussed in this section and their mechanisms using journal articles and books.
- (5.2) When devices such as actuators and sensors using functional polymers are applied to living bodies or plants, the connection of the devices to the power supply and operating circuits is challenging. Using journal articles and books, let's consider how to solve this problem.
- (5.3) Estimate the Young's modulus E (Pa) of a rubber band in the following situation using Eq. (7.19). F: force, 100 gf $\approx$ 1 N. A: area, 1 mm^2 = 1 $\times$ 10^{-6} m^2. (1 Pa = 1 N/m^2) Strain: $\varepsilon = 5$.
- (5.3) Estimate the chain density per unit volume ν in the rubber hand of 1 at 300 K, where the rubber band behaves as an ideal rubber, using Eq. (7.26). Additionally, estimate the volume of a chain in the rubber band by using Eq. (7.29).
- (5.3) Estimate the molecular weight M_w of the chain in the rubber band of 1 when the density ρ of the rubber is 0.7 g/cm^3 using the formula $M_W \nu = \rho$.
- (5.3) Estimate the polymerization degree N of the rubber band of 1 made from isoprene, where the molecular weight M_{mono} of isoprene (C_5H_8) $\approx$ 70 g/mol, using the formula $M_W / M_{mono} = N$.
- (5.3) Estimate the radius of the subchain R_0 in the rubber band of 1 swollen in toluene based on the ideal chain (Gauss chain) model, where the segment size a = 0.3 nm, using Eq. (7.8).
- (5.3) Estimate the Flory radius of the subchain R_F in the rubber band of 1 swollen in toluene (as assumed good solvent for isoprene) based on the real chain model, where the segment size a = 0.3 nm, using Eq. (7.9).
- (5.4) Choose which type of 3D printer/casting method is suitable for fabricating a robot part with the following characteristics:

1. Robotic components with pneumatic mechanisms
2. Soft robot parts with small and fine shapes
3. Robot parts made of a complex combination of hard and soft materials
4. Soft outer shell frame for a drone

a. FDM method
b. Inkjet method
c. DLP method
d. Mold casting with elastic resin

Answer: d, c, b, a.

References

Asaka K, Hashimoto M (2018) Electrical properties and electromechanical modeling of plasticized PVC gel actuators. Sens Actuators B Chem 273:1246–1256

Asaka K, Mizuhata M (1995) Bending of polyelectrolyte membrane-platinum composites by electric stimuli I. Response characteristics to various waveforms modeling polymer fiber artificial muscle. View project Modeling ionic polymer sensors and actuators View project. Polym J

Baughman RH, Shacklette LW, Elsenbaumer RL, Plichta E, Becht C (1990) Conducting polymer electromechanical actuators. Conjug Polym Mater Oppor Electron Optoelectron Mol Electron 559–582

Chen Y, Liu Q, Theato P, Wei J, Yu Y (2021) A Convenient route to prepare reactive azobenzene-containing liquid crystal polymers and photodeformable fibers. Adv Intell Syst 3:2000254

Choy CL, Wong SP, Young K (1985) Model calculation of the thermal conductivity of polymer crystals. J Polym Sci Polym Phys Ed 23(8):1495–1504

Dararatana N, Seidi F, Hamel J, Crespy D (2020) Controlling release kinetics of pH-responsive polymer nanoparticles. Polym Chem 11:1752–1762

De Gennes PG, Gennes PG (1979) Scaling concepts in polymer physics. Cornell University Press

Duduta M, Hajiesmaili E, Zhao H, Wood RJ, Clarke DR (2019) Realizing the potential of dielectric elastomer artificial muscles. Proc Natl Acad Sci USA 116:2476–2481

Fukushima T, Asaka K, Kosaka A, Aida T (2005) Fully plastic actuator through layer-by-layer casting with ionic-liquid-based Bucky gel. Angew Chem Int Ed 44:2410–2413

Furukawa H, Horie K, Nozaki R, Okada M (2003) Swelling-induced modulation of static and dynamic fluctuations in polyacrylamide gels observed by scanning microscopic light scattering. Phys Rev E 68(3):031406

Furukawa H, Yoshikawa M, Yamada K, Watanabe T, Hidema R, Horie K (2012) Photo-responsible gel actuator developed with scanning microscopic light scattering. In: Active and passive smart structures and integrated systems 2012 (International Society for Optics and Photonics), vol 8341, p 83411T

Furukawa H, Hidema R, Takada G, Amano Y, Kabir MH, Gong J (2013) Smart hydrogels developed with inter-crosslinking network (ICN) structure. J Solid Mech Mater Eng 7(2):245–250

Gelebart AH, Jan Mulder D, Varga M, Konya A, Vantomme G, Meijer EW, Selinger RLB, Broer DJ (2017) Making waves in a photoactive polymer film. Nature 546:632–636

Graessley WW (1974) The entanglement concept in polymer rheology. Adv Polym Sci 16:1–179

Grewell D, Benatar A, Park J (2003) Plastics and composites welding handbook. Hanser Publishing, p 271

Haines CS, Lima MD, Li N, Spinks GM, Foroughi J, Madden JDW, Kim SH, Fang SL, de Andrade MJ, Goktepe F, Goktepe O, Mirvakili SM, Naficy S, Lepro X, Oh JY, Kozlov ME, Kim SJ, Xu XR, Swedlove BJ, Wallace GG, Baughman RH (2014) Artificial muscles from fishing line and sewing thread. Science 343(6173):868–872

Hara S, Zama T, Sewa S, Takashima W, Kaneto K (2003) Highly stretchable and powerful polypyrrole linear actuators. Chem Lett 32:576–577. https://doi.org/10.1246/cl.2003.576

Hiraoka M, Nakamura K, Arase H, Asai K, Kaneko Y, John SW, Tagashira K, Omote A (2016) Power-efficient low-temperature woven coiled fibre actuator for wearable applications. Sci Rep 2016:6

Horii T, Endo S, Okuzaki H (2016) High-strain electro-active PEDOT/PSS solid actuators. Trans Mater Res Soc Jpn 41:21–24

Hosoya N, Masuda H, Maeda S (2019) Balloon dielectric elastomer actuator speaker. Appl Acoust 148:238–245

Howlader MMR, Suga T, Kim MJ (2007) A novel bonding method for ionic wafers. IEEE Trans Adv Packag 30:598–604

Ikegami T, Kageyama Y, Obara K, Takeda S (2016) Dissipative and autonomous square-wave self-oscillation of a macroscopic hybrid self-assembly under continuous light irradiation. Angew Chem 128:8379–8383

Imaizumi S, Kato Y, Kokubo H, Watanabe M (2012) Driving mechanisms of ionic polymer actuators having electric double layer capacitor structures. J Phys Chem B 116:5080–5089
Imaizumi S, Ohtsuki Y, Yasuda T, Kokubo H, Watanabe M (2013) Printable polymer actuators from ionic liquid, soluble polyimide, and ubiquitous carbon materials. ACS Appl Mater Interfaces 5:6307–6315
Ji X, Liu X, Cacucciolo V, Civet Y, El Haitami A, Cantin S, Perriard Y, Shea H (2021) Untethered feel-through haptics using 18-μm thick dielectric elastomer actuators. Adv Funct Mater 31:2006639
Kamamichi N (2021) Research and development trends of polymer actuators. J Japan Soc Precis Eng 87:39–42. https://doi.org/10.2493/JJSPE.87.39
Kanamoto T, Ohama T, Tanaka K, Takeda M, Porter RS (1987) Two-stage drawing of ultra-high molecular weight polyethylene reactor powder. Polymer 28:1517–1520
Kanamoto T, Porter RS (1989) Maximum properties achieved by uniaxial drawing of high molecular weight polyolefins. In: Lemstra PJ, Kleintjens (eds) Integration of fundamental polymer science and technology, vol 3. Springer, Dordrecht, pp 168–177
Kanamoto T, Tsuruta A, Tanaka K, Takeda M, Porter RS (1988) Super-drawing of ultrahigh molecular weight polyethylene. 1. Effect of techniques on drawing of single crystal mats. Macromolecules 21(2):470–477
Kaneto K, Kaneko M, Min Y, MacDiarmid AG (1995) Artificial muscle: electromechanical actuators using polyaniline films. Synth Met 71:2211–2212
Kato S, Tanaka H, Yamanobe T, Uehara H (2015) In situ analysis of melt-drawing behavior of ultra-high molecular weight polyethylene films with different molecular weights: Roles of entanglements on oriented crystallization. J Phys Chem B 119(15):5062–5070
Kawai H (1969) The piezoelectricity of poly (vinylidene fluoride). Jpn J Appl Phys 8:975
Li Y, Li Y, Hashimoto M (2019) Low-voltage planar PVC gel actuator with high performances. Sens Actuators B Chem 482–489
Li Y, Maeda Y, Hashimoto M (2015) Lightweight, soft variable stiffness gel spats for walking assistance. Int J Adv Robot Syst 1
Lv JA, Liu Y, Wei J, Chen E, Qin L, Yu Y (2016) Photocontrol of fluid slugs in liquid crystal polymer microactuators. Nature 537:179–184
Ma M, Guo L, Anderson DG, Langer R (2013a) Bio-inspired polymer composite actuator and generator driven by water gradients. Science 339:186–189
Ma ZY, Jia X, Zhang GX, Hu JM, Zhang XL, Liu ZY, Wang HY, Zhou F (2013b) pH-responsive controlled-release fertilizer with water retention via atom transfer radical polymerization of acrylic acid on mussel-inspired initiator. J Agric Food Chem 61:5474–5482
Madden JDW, Vandesteeg NA, Anquetil PA, Madden PGA, Takshi A, Pytel RZ, Lafontain SR, Wieringa PA, Hunter IW (2004) Artificial muscle technology: Physical principles and naval prospects. IEEE J Oceanic Eng 29:706–728
Mirfakhrai T, Madden JDW, Baughman RH (2007) Polymer artificial muscles. Mater Today 10:30–38. https://doi.org/10.1016/S1369-7021(07)70048-2
Mitsuya H, Ono S, Miwa K, Ataka M, Toshiyoshi H, Fujita H (2015) Soft electret gel for low frequency vibrational energy harvesters. J Phys Conf Ser 660:012004
Nakae M, Uehara H, Kanamoto H, Zachariades AE, Porter RS (2000) Structure development upon melt drawing of ultra-high molecular weight polyethylene: Effect of prior thermal history. Macromolecules 33:2632–2641
Oguro K (1992) Bending of an ion-conducting polymer film-electrode composite by an electric stimulus at low voltage. J Micromach Soc 5:27–30
Okuzaki H, Funasaka K (2000) Electromechanical properties of a humido-sensitive conducting polymer film. Macromolecules 33:8307–8311
Okuzaki H, Takagi S, Hishiki F, Tanigawa R (2014) Ionic liquid/polyurethane/PEDOT:PSS composites for electro-active polymer actuators. Sens Actuators B Chem 194:59–63

Ono Y, Kakiage M, Yamanobe T, Yukawa Y, Higuchi Y, Arai K, Kamiya H, Uehara H (2011) Structural and property changes during uniaxial drawing of ethylene-tetrafluoroethylene copolymer films as analyzed by in-situ X-ray measurements. Polymer 52(4):1172–1179

Ono S, Miwa K, Iori J, Sano C, Toshiyoshi H, Fujita H, Mitsuya H, Ishibashi K (2017) New type of energy harvester with electric double layer electrets. In: 2017 symposium on design, test, integration and packaging of MEMS/MOEMS (DTIP)

Otero TF, Angulo E, Rodríguez J, Santamaría C (1992) Electrochemomechanical properties from a bilayer: polypyrrole / non-conducting and flexible material—artificial muscle. J Electroanal Chem 341:369–375

Pei Q, Inganas O (1992) Electrochemical applications of the bending beam method. 1. Mass transport and volume changes in polypyrrole during redox. J Phys Chem 96:10507–10514

Pelrine R, Kornbluh R, Pei Q, Joseph J (2000) High-speed electrically actuated elastomers with strain greater than 100%. Science (80-) 287:836–839

Penning PJ, van der Werff H, Roukema M, Pennings AJ (1990) On the theoretical strength of gelspun/hotdrawn ultra-high molecular weight polyethylene fibres. Polym Bull 23:347–352

Qin P, Xu X, Cai Y, Bai B, Wang H, Suo Y (2017) Fabrication of phytic acid-modified wheat straw platform and its pH-responsive release performance for the pesticide imidacloprid. RSC Adv 7:32777–32785

Sakurada I, Ito I, Nakamae K (1966) Elastic moduli of the crystal lattices of polymers. J Polym Sci Part C 15:75–91

Shioiri R, Kokubo H, Horii T, Kobayashi Y, Hashimoto K, Ueno K, Watanabe M (2019) Polymer electrolytes based on a homogeneous poly(ethylene glycol) network and their application to polymer actuators. Electrochim Acta 298:866–873

Smith P, Lemstra PJ (1980) Ultra-high-strength polyethylene filaments by solution spinning/drawing. J Mater Sci 15:505–514

Stoychev G, Puretskiy N, Ionov L (2011) Self-folding all-polymer thermoresponsive microcapsules. Soft Matter 7:3277–3279

Stuart MAC, Huck WTS, Genzer J, Müller M, Ober C, Stamm M, Sukhorukov GB, Szleifer I, Tsukruk VV, Urban M, Winnik F, Zauscher S, Luzinov I, Minko S (2010) Emerging applications of stimuli-responsive polymer materials. Nat Mater 92(9):101–113

Takakuwa M, Fukuda K, Yokota T, Inoue D, Hashidume D, Umezu S, Someya T (2021) Direct gold bonding for flexible integrated electronics. Sci Adv 7:eable6228

Takayanagi M, Uemura S, Minami S (1964) Application of equivalent model method to dynamic rheo-optical properties of crystalline polymer. J Polym Sci Part C: Polym Symp 5(1):113–122

Tashiro K (1993) Molecular theory of mechanical properties of crystalline polymers. Prog Polym Sci 18(3):377–435

Terai H, Funahashi R, Hashimoto T, Kakuta M (2018) Heterogeneous bonding between cyclo-olefin polymer (COP) and glass-like substrate by newly developed water vapor-assisted plasma, Aqua Plasma Cleaner. Electr Eng Jpn 205:48–56

Uehara H, Yamazaki Y, Kanamoto T (1996) Tensile properties of highly syndiotactic polypropylene. Polymer 37:57–64

Uehara H, Jounai K, Endo R, Okuyama H, Kanamoto T, Porter RS (1997) High modulus films of PTFE prepared by two-stage drawing of reactor powder. Polym J 29:198–200

Uehara H, Nakae M, Kanamoto T, Zachariades AE, Porter RS (1999) Melt drawability of ultra-high molecular weight polyethylene. Macromolecules 32:2761–2769

Uehara H (2007) Structure and property development for conventional polymers utilizing molecular anisotropy and entanglement characteristics. Kobunshi Ronbunshu 64:525–538

Uehara H, Kakiage M, Yamanobe T, Komoto T, Murakami S (2006) Phase development mechanism during drawing from highly entangled polyethylene melts. Macromol Rapid Commun 27(12):966–970

Uehara H, Tamura T, Kakiage M, Yamanobe T (2012) Nanowrinkled and nanorporous polyethylene membrane via entanglement arrangement control. Adv Funct Mater 22(10):2048–2057

Ueki T, Nakamura Y, Usui R, Kitazawa Y, So O, Lodge TP, Watanabe M (2015) Photoreversible gelation of a triblock copolymer in an ionic liquid. Angew Chem Int Ed 54:3018–3022

Wang Y, Yang X, Chen Y, Wainwright DK, Kenaley CP, Gong Z, Liu Z, Liu H, Guan J, Wang T, Weaver JC, Wood RJ, Wen L (2017a) A biorobotic adhesive disc for underwater hitchhiking inspired by the remora suckerfish. Sci Robot 2(10):eaan8072. https://doi.org/10.1126/scirobotics.aan8072. Epub 2017 Sept 20. PMID: 33157888

Wang Z, Torigoe Y, Hirai S (2017b) A Prestressed soft gripper: design, modeling, fabrication, and tests for food handling. IEEE Robot Autom Lett 2(4):1909–1916. https://doi.org/10.1109/LRA.2017.2714141

Wang Z, Li K, He Q, Cai S, Wang Z, Li K, He Q, Cai S (2019) A light-powered ultralight tensegrity robot with high deformability and load capacity. Adv Mater 31:1806849

Watanabe Y, Maekawa K, Hidema R, Kabir MH, Gong J, Furukawa H (2013) Structural analysis and mechanical properties of dry-synthesis gels. J Solid Mech Mater Eng 7(2):224–227

Wiranata A, Kanno M, Chiya N, Okabe H, Horii T, Fujie T, Hosoya N, Maeda S (2021) High-frequency, low-voltage oscillations of dielectric elastomer actuators. Appl Phys Express 15:011002

Wunderlich B (1973) Macromolecular physics, vol 1: crystal structure, morphology, defects. Academic, New York

Xia H, Takasaki M, Hirai T (2010) Actuation mechanism of plasticized PVC by electric field. Sens Actuators A Phys 157:307–312

Yamamoto Y, Inoue Y, Onai T, Doshu C, Takahashi H, Uehara H (2007) Deconvolution analyses of differential scanning calorimetry profiles of β-crystallized polypropylenes with synchronized X-ray measurements, Macromolecules 40(8):2745–2750

Yoshizawa H, Takazawa A, Kakiage M, Yamanobe T, Hayashi N, Hiraoka M, Masunaga H, Aoyama K, Uehara H (2021) Actuation mechanism of drawn polyethylene evaluated by structural change during cyclic stretching/shrinking, Sens. Actuators A Phys 323:112634

Yu C, Yuan P, Erickson EM, Daly CM, Rogers JA, Nuzzo RG (2015) Oxygen reduction reaction induced pH-responsive chemo-mechanical hydrogel actuators. Soft Matter 11:7953–7959. https://doi.org/10.1039/C5SM01892G

Zhang QM, Bharti V, Zhao X (1998) Giant electrostriction and relaxor ferroelectric behavior in electron-irradiated poly(vinylidene fluoride-trifluoroethylene) copolymer. Science (80-) 280:2101–2104

Zwijnenburg A, van Hutten PF, Pennings AJ, Chanzy HD (1978) Longitudinal growth of polymer crystals from flowing solutions V.: Structure and morphology of fibrillar polyethylene crystals, Colloid Polym Sci 256:729–740

Chapter 8
Biological Material

Masahiro Shimizu, Yuya Morimoto, and Jun Shintake

Abstract Biological materials are characterized as active soft materials. These materials can behave as actuators or processors based on biological mechanisms. In addition, biodegradable materials are required in the future as they are less invasive to the environment. Based on the above discussion, this chapter introduces soft materials affected by biological processes, biological cells, and biodegradable soft materials.

8.1 Soft Materials Affected by Biological Processes

8.1.1 Introduction

The purpose of studying soft materials affected by biological processes is to realize a growing biosoft robot by constructing a robot with living cell parts. The main feature of the machine is its physical plasticity, which allows it to modify itself. The morphology and function of an organism are simultaneously improved by improving the physiological and physical responses of its cells to the mechanical stimuli generated by its own movement. Therefore, this type of materials aims to realize an intelligent robot that grows both its mechanical and control systems by directly incorporating cells as soft and intelligent components of the robot and implementing them as an autonomous distributed system. Therefore, this study plays a role in clarifying

M. Shimizu (✉)
Department of Systems Innovation, Graduate School of Engineering Science, Osaka University, Toyonaka, Japan
e-mail: m_shimizu@nagahama-i-bio.ac.jp

Y. Morimoto
Department of Mechano-Informatics, Graduate School of Information Science and Technology, The University of Tokyo, Tokyo, Japan

J. Shintake
Department of Mechanical and Intelligent Systems Engineering, The University of Electro-Communications, Tokyo, Japan

K. Suzumori et al. (eds.), *The Science of Soft Robots*, Natural Computing Series,
https://doi.org/10.1007/978-981-19-5174-9_8

the requirements necessary for "direct implementation of biological information to create a growing robot."

To achieve biosoft robots, it is essential to create technologies that integrate and control the functions of cell groups. Specifically, by targeting muscle cells, we will elucidate the mechanism of function emergence in a system, in which cells themselves act as sensors, CPUs, and actuators. The fact that it is possible to design a system that integrates sensing, judgment, and motion is important for soft robotics; this is possible only by using biological materials and is a point of focus unique to the authors. Biosoft robots provide not only mechanical flexibility but also "flexible self-modification of the entire system" based on the inherent capabilities of living organisms. In many cases, the fusion of biology and engineering that has been promoted in the past has been limited to biology to develop robots or robotics to understand living organisms. In response to the current situation, we are developing an autonomous decentralized control system that links organisms and machines, including the growth and self-healing of biological materials, to promote the world's first interface between organisms and robots.

8.1.2 Biohybrid Robots Attracting International Attention

In Japan, Morishima et al. presented a biomechanical fusion system using insect cells (Akiyama et al. 2012). They showed that insect cells are robust against temperature and pH changes and are promising for application as biomechanical components. Kanzaki et al. developed a system combining a silkworm moth and wheeled robot (Minegishi et al. 2012). The cranial nervous system of the silkworm moth is extracted, and the direction of travel of the wheeled robot is controlled by the cranial nervous system of the living organism according to the direction of detection of pheromones. Here, by intervening the relationship between commands from the silkworm moth's cranial nervous system and the wheel drive, we have achieved a biomechanical fusion system that can manipulate the silkworm moth's "body-environment interaction." Outside Japan, Park et al. (2016) developed a ray-type robot driven by muscle cells. Warwick et al. (2010) developed a feedback system between the cells and the environment by culturing neurons and applied sensor information to a wheeled robot as electrical stimuli. A feedback system between the cells and the environment was developed. It was shown that a wheeled robot moving on a flat surface surrounded by walls can run without colliding with the walls through the feedback between the cells and the environment.

As described above, various cross-disciplinary efforts are being promoted in Japan and overseas. There have been many studies in recent years that cannot be introduced here owing to space constraints, and this research area is gaining attention only recently. As mentioned in the beginning of this section, it is expected that machines will grow by using living cells as parts. However, many studies have not yet achieved the design theory of "growing" by applying self-assembly of cells in response to mechanical stimuli. It is expected that the results of many domestic and international

efforts, including those of the authors, will be published in the coming years and will serve as a milestone to design theory.

8.1.3 Mechanical Stimulation as an Interface Between Cells and Control

What is the technology that can integrate and control individual functions to achieve a growing biosoft robot? In recent years, it has become clear in biology that mechanical stimulation of cells has a significant impact on morphological and functional differentiations. In Japan, Sogabe et al. demonstrated that mechanical stimulation can change the orientation of muscle cells in a short period of time (Hayakawa et al. 2011). Engler et al. revealed that mesenchymal stem cells can recognize the mechanical strength of the adhesive site, change their gene expression according to the firmness of the scaffold, and differentiate them into bone, muscle, and nerve cells (Engler et al. 2006). These findings are currently attracting a great deal of interest in the medical field, including the use in regenerative medicine, transplantation, and cancer treatment. Interestingly, from the viewpoint of robotics, bone = mechanism, muscle = actuator, and nerve = control circuit; this suggests the feasibility of a robot to be made entirely from biomaterials.

Mechanical stimulation is a phenomenon, in which cells show physiological and physical changes in response to external physical input. When one thinks about it, "physical input" is a technology that engineers use on a daily basis. This point of view implies that engineers may be able to control the physiological response of the cell by using their expertise. The importance of engineering techniques is not limited to external observation of cells, as in the case with many other past techniques. The authors expect that engineering technology will bring breakthroughs as an interface to control the cells themselves by using mechanical stimuli.

8.1.4 Toward a Growing Biosoft Robot

The authors specifically target muscle cells among many cell types. Muscle cells are very interesting because they themselves produce mechanical actions as actuators and also play the role of "biological sensors" that receive mechanical stimuli. This point of view implies that myocytes can be used not only as a device but also as a control system in itself.

Based on the above ideas, the authors are (1) constructing a direct coupling interface between machine and cell by developing a frog cyborg driven by biological muscle and clarifying the efficient use of elastic energy and the long-term cultivation method of muscle tissue; (2) fabricating a growing cellular tactile sensor by developing a sensor for tactile sensation using growing cells; (3) developing a growing

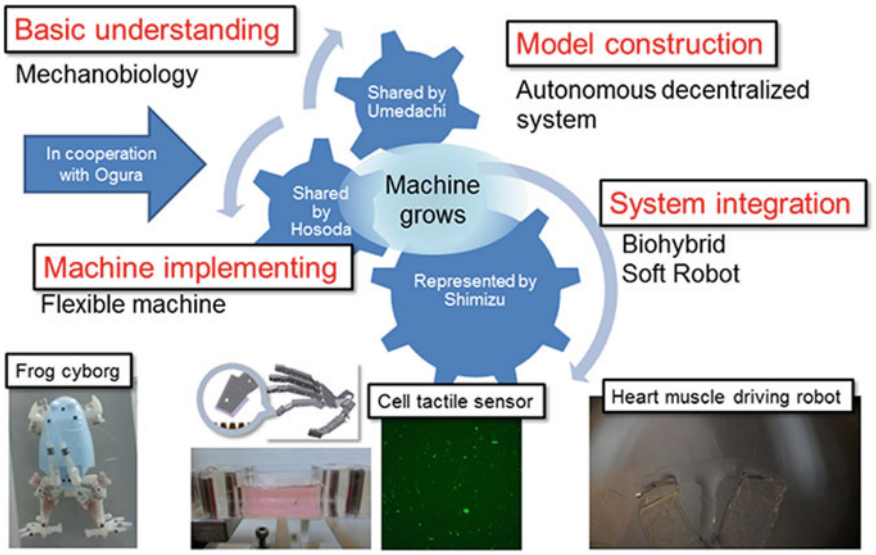

Fig. 8.1 Biosoft robotics based on soft materials affected by biological processes

cell tactile sensor by creating a cell tactile sensor device that can acquire the ability to detect specific tactile stimuli based on past experience and identify the intensity of tactile stimuli; (4) constructing autonomous distributed control for biosoft robots by developing a micro robot driven by a group of cardiac muscle cells and a distributed control system on the micro robot (see Fig. 8.1).

The pulsation of cardiomyocytes organized through gap junctions is modeled as a nonlinear oscillator network. Furthermore, starting from the caterpillar and worm-like string structures that we have been working on, we will formulate a theory on how beating rhythms are spontaneously generated from the distribution of myocardial cells that change depending on the body structure when the myocardium is arranged in three dimensions. The beating rhythm of the myocardium is critical for a cardiomyocyte robot that drives it as an actuator and uses it as an active mechanical stimulus to itself. We believe that it is also essential for cellular control that applies the mechanical stimulus response of cells.

In addition, we are working on developing a technique for prototyping the biosoft robot rapidly by 3D printing a cell-embedding gel to design and construct a body for the growing machine. We expect that the robot will not be finished after molding, but will serve as a platform for a growing machine, in which muscle cells function as a part of a flexible body.

8.1.5 Conclusion

We have outlined a methodology to realize growing machines using cells. The elasticity and microstructure that constitute the "flexible body," which form the basis of this research, are properties and technologies shared by the same group in the new academic field, and the organic coupling of biological information and mechanical electronics will accelerate the project. Furthermore, the research on materials (inorganic nanomaterials and polymeric soft materials) conducted by other groups is also essential for this research, and the results of this study are expected to play a role in connecting the entire field of study.

Cells exhibit an intrinsic self-repair function. Therefore, they are expected to create the world's most advanced robotics technology, in which biorobots themselves can autonomously repair malfunctioned parts. The biorobot in this study is powered by the culture medium, which is a substantial source of energy. Therefore, the biorobot is expected to be more energy-efficient than conventional electrically powered robots. In the future, biorobots are expected to make a significant contribution to solving Japan's energy problems. The market for medical products related to regenerative medicine is currently estimated to be over 10 trillion yen worldwide and 1 trillion yen in Japan, and the ripple effects of this research are extremely large. The technology for manufacturing biosoft robots using muscle cells created in this research is also expected to be applied to regenerative medicine for joint and muscle tissue. Thus, the approach of actively using living cells is not only novel but also has the potential to solve future scientific problems.

8.2 Biological Cells

8.2.1 Basic Concepts

Cells are the fundamental elements that form living organisms. Cells are generally between 10 and 20 μm in size, allowing us to easily manipulate and observe them with the latest advanced micro-nanoengineering techniques. Cells have organelles inside the cell membrane made of a lipid bilayer. The main organelles are the nucleus, endoplasmic reticulum, and mitochondria. The nucleus stores deoxyribonucleic acid (DNA), which constitutes the genetic information and is capable of expressing specific functions depending on the cell type. The endoplasmic reticulum is responsible for the production of proteins that perform a variety of functions, ranging from sensing to actuation. Mitochondria can produce energy by converting glucose into energy. One of the advantages of using cells as a material for soft robots is that they can run on glucose, avoiding the use of electricity that is required to drive general soft robots.

Another advantage of using cells in soft robotics is easy preparation in the required quantities, as they can generally be proliferated. Cells also have the ability to differentiate, i.e., change into different cell types, by external stimuli so that the experimenters can control the functions of cells by inducing the differentiation. Depending on their ability to proliferate and differentiate, cells are mainly classified into three types: primary cells, cell lines, and stem cells. Primary cells are isolated from living tissue by enzymatic, mechanical, or other processes (Fig. 8.2a). As their multiplication occurs only a finite number of times, they cannot proliferate any more after a certain number of multiplies for each cell type. Some primary cells, such as primary cardiomyocytes (heart muscle cells), do not have the ability to proliferate. Primary cells are more functional than cell lines and stem cells because they have a high potential to express the functions of original living tissue. Cell lines become immortalized by some factors and have acquired the ability to proliferate semi-permanently with certain functions (Fig. 8.2b). The experimenters can obtain various cell lines from cell banks and culture them. Although cell lines are clearly superior to primary cells in terms of proliferative properties, primary cells are more homogeneous to living cells in terms of biological functions. Pluripotent stem cells are specialized cells that have the ability to proliferate and differentiate into various types of cells (pluripotency). Induced pluripotent stem cells (iPSCs) have been widely used as experimental stem cells (Fig. 8.2c). Because the target cells can be obtained by differentiating stem cells after their proliferation, stem cells have been widely used for various applications, such as in the preparation of cardiomyocytes which do not proliferate (Fig. 8.2d). In addition, stem cells ease the ethical problem caused by primary cells requiring animal experiments. However, the cell preparation by differentiation of stem cells requires a complicated procedure for experimenters who are inexperienced in cell culture and brings cost-related issues. Through appropriate selection and use of these cells, experimenters can effectively utilize them as materials in soft robotics. Actuation and sensing are attractive functions of biological cells in the view of soft robotics. The following sections describe the characteristics of cellular actuation and sensing.

8.2.2 Actuation of Biological Cells for Soft Robotics

In living organisms, muscles are used as actuators to control postures, generate body movements, and pump blood throughout the body. Muscles usable in soft robotics are mainly cardiac (heart muscle) and skeletal muscles. Cardiac muscles achieve spontaneous pulsed contractions, twitches. Cardiac muscle is composed of cardiomyocytes. As cardiomyocytes can also achieve twitches, they are easy-to-use actuators for soft robots because they can contract spontaneously without external stimulations (Tanaka et al. 2007). On the other hand, skeletal muscles are capable of strong and long-time contractions by superimposing twitches, called tetanus. Skeletal muscles consist of skeletal myofibers formed by the fusion of myoblasts (skeletal muscle cells). Although it takes time and effort to prepare contractile myofibers or skeletal muscle tissue in cell culture because cell fusion is required (Fig. 8.3), they

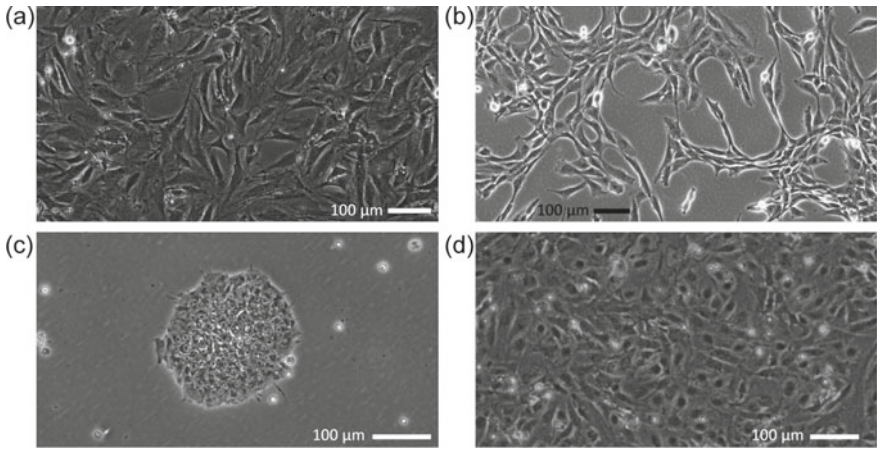

Fig. 8.2 Images of cells usable in soft robotics. **a** Primary tenocytes collected from bovine tendon. **b** Skeletal muscle cell line (C2C12 cells). **c** Human iPSCs. **d** Human iPSC-derived cardiomyocytes

have high contraction controllability, making them easier actuators to use than cardiac muscles. Primary cardiomyocytes, iPSC-derived cardiomyocytes, primary skeletal myoblasts, and myoblast cell lines (C2C12 cells) have been mainly used in soft robotics. Although the contractility of cell lines and iPSC-derived cells are generally lower than that of primary cells, we believe that cell lines and iPSC-derived cells will mainly be used in soft robotics in the future because they offer good usability and less ethical issues.

The advantages of using muscles in soft robotics are good driving energy efficiency and wide controllability (Hunter and Lafontaine 1992). Muscle contractions have high energy efficiency, ranging from 10 to 40% in single cyclic motion, so their power-to-weight ratio is superior to mechanical robotic actuators equipped with a heavy energy source (Ricotti and Menciassi 2012; Ricotti et al. 2017). For example, the power-to-weight ratio of skeletal muscle contractions is ~ 1 kW/kg. Furthermore, muscle contractions can be triggered in various ways including neuronal transmission (Witzemann 2006), electrical stimulation (Fujita et al. 2007), and optical stimulation (in the case of recombinant light-sensitive muscle) (Asano et al. 2012). Note that these stimuli are not used as an energy source and are just triggers for contractions. Muscles use sugar as energy source.

Muscle contraction is mediated by the intracellular sliding motion between motor proteins, myosin, and actin (Huxley 1974). In skeletal muscles, there are two basic relationships: the force–length relationship, in which the contractile force depends on the change in skeletal muscle length (Ramsey and Street 1940), and the force–velocity relationship, in which the contractile force depends on the contraction velocity (Hill 1938) (Fig. 8.4). In this case, the contractile force F increases with increasing muscle activity level α $(0 \leq \alpha \leq 1)$, where α represents the degree of activation of the skeletal muscle. Based on the skeletal muscle length L, the contractile force F is

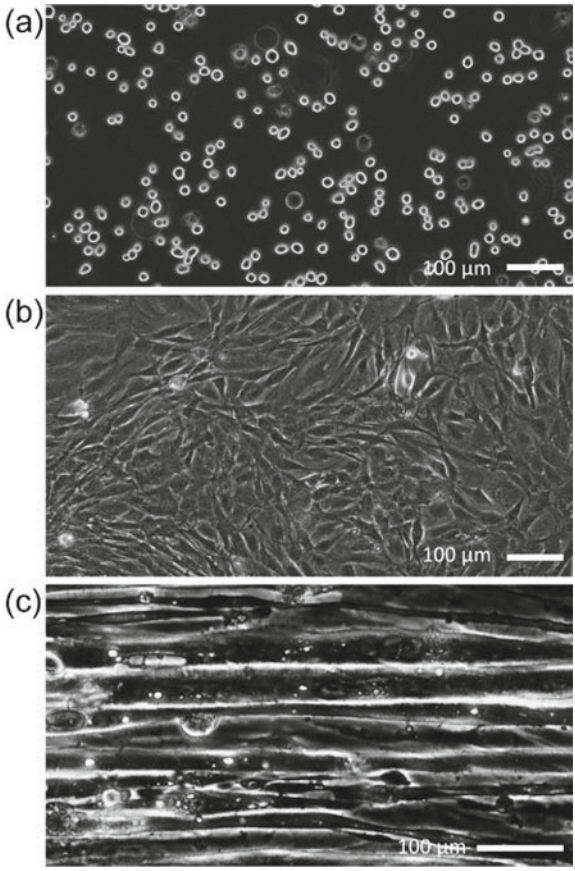

Fig. 8.3 Images of differentiation of C2C12 cells into myofibers (myotubes). **a** C2C12 cells before adhering on a culture dish. **b** C2C12 cells after confluent growth on the culture dish using the growth medium. **c** Myotubes after differentiation of C2C12 cells using the differentiation medium

assumed to be the product of the muscle activity level α and a nonlinear function $g\left(L, \dot{L}\right)$, which represents the contractile force when the activity level α is 1. Here, approximating $g\left(L, \dot{L}\right)$ in the vicinity of an arbitrary muscle length L_0 and zero contraction velocity, the contractile force can be expressed as follows (Ito and Tsuji 1985):

$$F \approx \alpha(F_0 + kx + c\dot{x}),$$

where F_0 is the contraction force when activity level α is 1 at skeletal muscle length L_0, k is the virtual elastic constant of skeletal muscle, c is the virtual viscous constant of skeletal muscle, and x is the change in skeletal muscle length expressed as $L - L_0$.

By contrast, the muscle contractile force can be regarded as the sum of active tension (tension generated by external stimulation) and passive tension (tension of

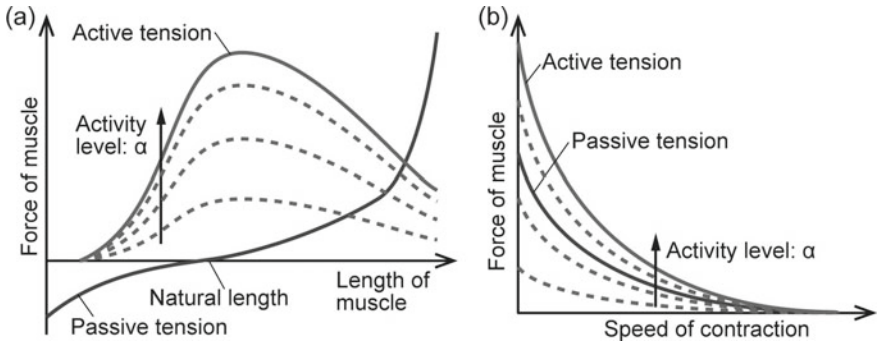

Fig. 8.4 Conceptual diagram of the relationship between contractile force and activity level of muscle. **a** Force–length relationship. **b** Force–velocity relationship

skeletal muscle acting as a spring) (Delp and Loan 2000). Therefore, the muscle activity level α is not equal to the activation level of the muscle, meaning that the passive tension cannot be represented in the above equation. In the application of muscle to soft robotics, it is essential to consider the passive tension. In order to represent the passive tension, we divide the muscle contractile force F into active tension F_a and passive tension F_p and assume that the active tension changes depending on the activity level α ($0 \leq \alpha \leq 1$), while the passive tension is independent of the activity level. Then, the contraction force can be modeled in the vicinity of skeletal muscle length L_0 as follows:

$$F \approx \alpha(F_{a0} + k_a x + c_a \dot{x}) + \left(F_{p0} + k_p x + c_p \dot{x}\right), \tag{8.1}$$

where k_a and c_a are the elastic constant and viscous constant under active tension, respectively; k_p and c_p are the elastic constant and viscous constant under passive tension, respectively; F_{a0} is the maximum active tension at muscle length L_0 and zero contraction speed; and F_{p0} is the passive tension at muscle length L_0 and zero contraction speed. By designing a soft robot with this relationship, muscle and muscle cells will be used efficiently as actuators.

By aggregating muscle cells into a muscle tissue, the contractile force is increased compared to when the cells are alone. It is well known that the contractile force is dependent on the cross-sectional area of tissue. However, this property is conditional on the cardiomyocytes or myofibers being aligned in the same direction. Since each of these cells is an independent linear actuator, if they are randomly arranged, they will contract in all directions with a weak force and will not be able to contract strongly in one direction like living muscle. Defining the expected contractile direction of muscle tissue as 90°, its F_{a0} is considered to change based on the direction of each cell as follows:

$$F_{a0} \approx \frac{F_f}{n_L} \rho A \int_0^{\pi} \delta\left(\theta_f\right) \sin\theta_f d\theta_f, \tag{8.2}$$

where F_f is the contractile force of single cell, n_L is the number of cells required per unit length to form myofiber (1 for cardiomyocytes), ρ is the cell density of myoblasts in the muscle tissue, A is the cross-sectional area of the tissue, θ_f is the angle between the expected contractile direction of the tissue and the long axis direction of cells, and $\delta\left(\theta_f\right)$ is the distribution of existence probability of cells at an angle θ_f. Here, ρ and A are controlled in the construction of muscle tissue. However, F_f, n_L related to the tissue maturation and $\delta\left(\theta_f\right)$ related to the tissue shape would depend on the culture condition. Therefore, it is necessary to establish appropriate culture conditions to adjust these values, resulting in the increase of the contractile force of the muscle tissue.

Extracellular matrices (ECMs) such as collagen, Matrigel, and fibrin gel have been used in the tissue construction to control the culture conditions of the muscle tissue. By gelling cardiomyocyte-laden ECMs in molds, cardiac muscle tissues are formed in various shapes such as rods (Morimoto et al. 2016) (Fig. 8.5a) and rings (Zimmermann et al. 2002) (Fig. 8.5b). The orientation of cardiomyocytes in the cardiac muscle tissue is determined by shaping the cardiomyocyte-laden ECMs into striped structures with narrow width (Morimoto et al. 2016). In the case of skeletal muscle tissue, culturing myoblasts in the ECM while fixing their ends to prevent shrinkage is an attractive method for tissue construction (Smith et al. 2012a; Shima et al. 2018) (Fig. 8.5c). Myofibers in the skeletal muscle tissue are generally aligned between fixed ends by the unidirectional traction force of the muscle fibers. Furthermore, the alignment of skeletal muscle fibers becomes higher when culturing narrow striped myoblast-laden ECMs shaped with molds (Morimoto et al. 2013). Therefore, using these methods, the maturation and alignment of muscle tissue are controllable to express strong contractile force.

8.2.3 Sensing of Biological Cells for Soft Robotics

When a mammal inhales an odor, the odorant is sucked into the nasal cavity along with the air and dissolves into the mucous membrane. Then, olfactory neurons fire when the odorant binds to them. Since each of the neurons expresses only one type of odorant receptor, it responds only to specific odorants. This highly sensitive and selective mechanism of odor detection in living organisms is being mimicked for application to robotics.

To use cells as sensor elements, many researchers have proposed methods to separate cells from tissues (Corcelli et al. 2010) and produce odor-responsive cells by transgenesis (Oda et al. 2021). Mammalian cells (Sato and Takeuchi 2014) and insect cells (Mitsuno et al. 2015) have been mainly used for this. In both cell types, olfactory receptors located on the cell membrane are responsible for responding to

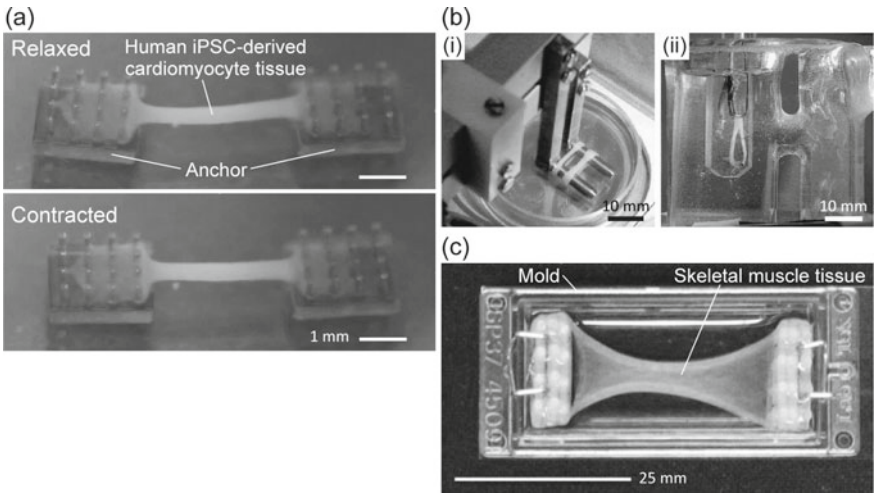

Fig. 8.5 Muscle tissues formed by culturing cell-laden ECMs. **a** Rod-shaped cardiac tissue made of cardiomyocytes derived from human iPSC-derived. **b** Ring-shaped cardiac tissues mounted on mechanical arms. **c** Rod-shaped skeletal muscle tissue fabricated by the culture of myoblasts in a mold—images are reprinted with **a** permission from Morimoto et al. (2016), 2016 licensed under Creative Commons Attribution-NonCommercial 3.0 Unported License, **b** permission from Zimmermann et al. (2002), ©2001 Wolters Kluwer Health, Inc., and **c** permission from Smith et al. (2012a), ©2012 John Wiley and Sons

odorants. When an odorant is detected, olfactory receptors first transmit a signal into the cell, which amplifies the signal from a single odor molecule to multiple molecules, resulting in a high signal-to-noise ratio.

Using electrodes and fluorescence, there are two ways to detect the response of cells to odorants. By seeding olfactory neurons or olfactory receptor-expressing cells on the microelectrode array (MEA) (Fig. 8.6a, b) (Liu et al. 2011), the response of the olfactory cells on the MEA to the odorants can be obtained as electrical signals. Although this method provides easy and quantitative detection of odor responses, the high price of MEA limits general application. In the method using fluorescence, by incorporating calcium fluorescence indicators into olfactory neurons or olfactory receptor-expressing cells, the response to the odorants is measurable by fluorescence intensity through observation of the cells using a fluorescence microscope (Fig. 8.6c, d) (Smith et al. 2012b). Because fluorescence microscopy is commonly used in biological research, it seems to be the preferred method for using the cells as sensor elements. Using these methods, experimenters will use olfactory cells as odor sensor elements in soft robots.

Moreover, the sensing responses of olfactory cells to odorants are easily detectable by tissue construction with the cells. For example, by shaping an olfactory cell-laden hydrogel into a cylindrical shape, the cells are stacked in the hydrogel (Fig. 8.7) (Hirata et al. 2019). This method allows for enhancing the fluorescence intensity by superimposing the fluorescence emitted from each olfactory cell, including calcium

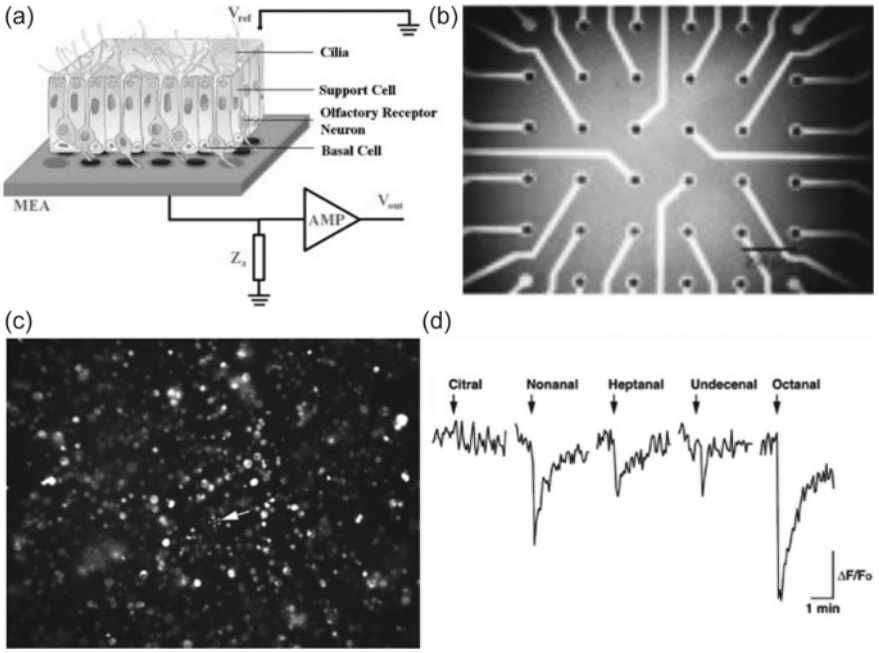

Fig. 8.6 Method for detecting the response of cells to odorants. **a** Olfactory epithelium on MEA for detecting the responses to odorants. **b** Electrode pattern of MEA. **c** Fluorescent image of olfactory cells with calcium indicators. **d** Change in the fluorescence intensity in response to different odorants—images are reprinted with (**a**, **b**) permission from Liu et al. (2011), ©2011 Elsevier, and (**c**, **d**) permission from Smith et al. (2012b)

fluorescence indicators, inducing the fluorescence detection using a small and inexpensive image sensor. As a result, the system can be used as a portable odorant sensor. In addition, by placing the hydrogel cylinders on a hydrogel substrate, the cells are protected from drying damage even when they are exposed to the gas phase by replenishing the culture medium from the substrate. Therefore, by carrying out tissue construction with olfactory cells, it is possible to measure the response to odorants with low-sensitivity image sensors and prevent cells from drying out, which were difficult to use in single cell. The tissue improves the applicability of cells as odor sensor elements.

8.2.4 How to Start Using Biological Cells

To use cells in your experiments, it is necessary to prepare equipment, such as clean benches that can work in isolation from bacteria and mold and incubators that allow culturing cells at a constant temperature and carbon dioxide concentration. It is preferable to culture cells at universities or research institutes where such equipment

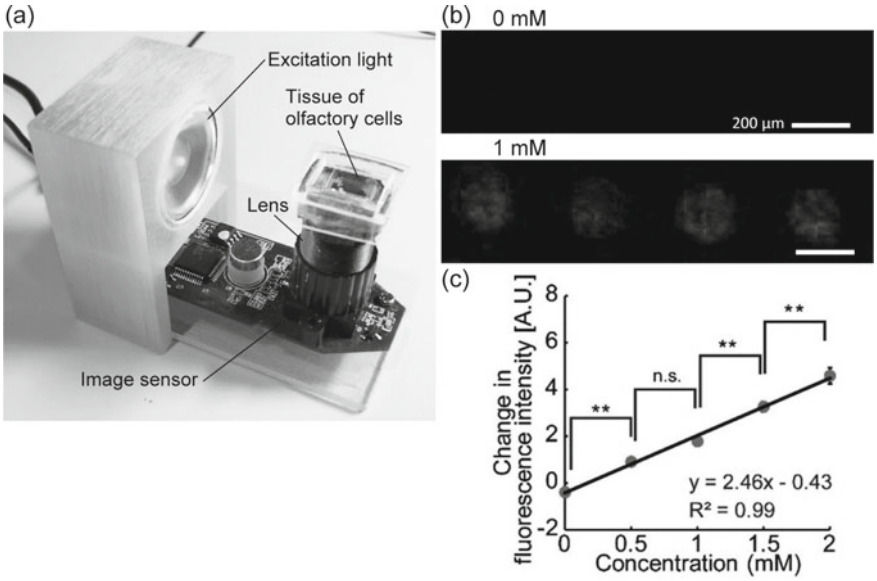

Fig. 8.7 Odorant sensing using tissue of olfactory cells. **a** Portable odorant sensor with the tissue and image sensor. **b** Fluorescence image of the tissue according to the concentration of target odorants. **c** Change in fluorescence intensity after the addition of target odorants at different concentrations—images are reprinted with permission from Hirata et al. (2019), ©2019 Royal Society of Chemistry

is available. The procedures for cell culture have been described in various books, and it is advisable to acquire cell culture techniques by referring to such books.

8.2.5 Challenges

To improve the contractile properties of the muscle tissue, construction of large-sized muscle tissue is required because animals have muscles up to a meter long, whereas current cultured muscle tissue is a maximum of a centimeter in size. For engineering large muscles in the future, it is necessary to clarify the methods for integrating blood vessels or flow paths into the muscle, allowing delivery of nutrients and oxygen.

8.3 Biodegradable Soft Material

When plants and trees wither, they return to the soil. Likewise, a robot that naturally decomposes at the end of its activity is the ultimate form of a machine that is in harmony with the environment. One possible way to realize such a system is to create

a robot using biodegradable materials, which have the property of being blended into the earth. Ultimately, biodegradable materials are decomposed into carbon dioxide and water by microbial activity and are then returned to nature. Thus, biodegradable materials are closely related to biological activities, and in this sense, they can be interpreted as a type of biological material. In fact, some biodegradable materials can be synthesized by the fermentation of biological organisms.

Elastomeric materials, such as silicone rubbers, are commonly used in soft robotics. Elastomers are easy to handle and highly versatile. They are chemically stable, which is preferable for most soft robotic systems. However, this feature renders the materials difficult to recycle, causing them to have a high environmental impact. This also contributes to environmental destruction when soft robots performing tasks in natural fields are discarded due to malfunctions and accidents. From this point of view, the incorporation of biodegradability into robots is of great significance.

Numerous biodegradable materials are of natural origin, and building a robot with these materials is equivalent to incorporating sustainability. Given that the Sustainable Development Goals (SDGs) have been advocated and international efforts are underway, the development of biodegradable robotic materials, elements, and systems is an important research direction that is expected to bring forth sustainable and environmental-friendly soft robots and subsidiary novel technologies that expand the use of robots and contribute to future society.

This section discusses the approach, type of materials, and implementation of soft robotic biodegradable materials, which pave the way for the realization of sustainable and environmental-friendly soft robots.

8.3.1 Approach to Incorporating Biodegradability

Many different types of biodegradable materials exist. However, they are not intended for use in robotics. Therefore, some sort of criteria is required to select, synthesize, and apply the materials to soft robotics.

One solid approach is to match the mechanical and electrical properties of the materials to those of soft robots. In soft robotics, most of the devices are made of elastomers, such as silicone rubbers (Rus and Tolley 2015). These materials display an elongation at break of over 100% and an elastic modulus (Young's modulus) in the order of 0.1–1 MPa. The specific values of these mechanical properties can be used as metrics to incorporate biodegradability into soft robotics. To better capture the compliance of the materials used in soft robotics, the Young's modulus of some representative materials is shown in Fig. 8.8.

Soft actuators and sensors are often electrically driven. When incorporating biodegradability into these elements, it is necessary to ensure electrical properties in addition to mechanical properties, more specifically, insulation and conductivity. Among the materials considered as insulators, deionized water (pure water) with a low resistivity in the order of $1 \times 10^5\,\Omega\,\mathrm{m}$ is considered. Among the materials that are considered as conductors, silicon (Si) has a high resistivity in the order of

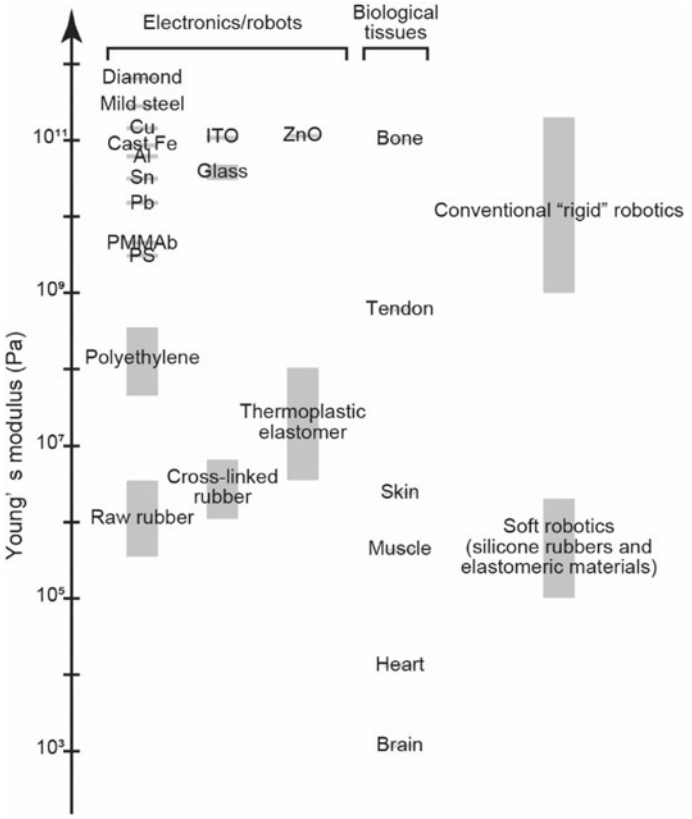

Fig. 8.8 Young's moduli of biological tissues and typical materials used in electronics, soft robotics, and conventional "rigid" robotics (Yamagishi 2019)

$1 \times 10^3\ \Omega\,\mathrm{m}$. These values can be an indicator to apply or develop biodegradable materials to build electrically driven soft robotic elements. For instance, insulating properties should maintain a resistivity above $1 \times 10^5\ \Omega\,\mathrm{m}$ and conductive properties below $1 \times 10^3\ \Omega\,\mathrm{m}$.

In addition to the mechanical and electrical properties discussed above, there are several other aspects that should be considered. Viscoelasticity is often found in soft materials, and high viscosity slows down physical movements, creates hysteresis characteristics, and reduces efficiency due to energy dissipation. Mechanical and electrical durability against repeated deformation and loading is also important. Even if the robot is biodegradable, it will be difficult for it to function as a robotic system if it breaks down quickly.

Biodegradable materials are preferable if they are compatible with existing manufacturing methods in soft robotics. Soft actuators and sensors are mainly fabricated by molding and 3D printing, and most of these methods handle the material in the liquid state and allow it to cure (Schmitt et al. 2018; Gul et al. 2018; Stano and Percoco

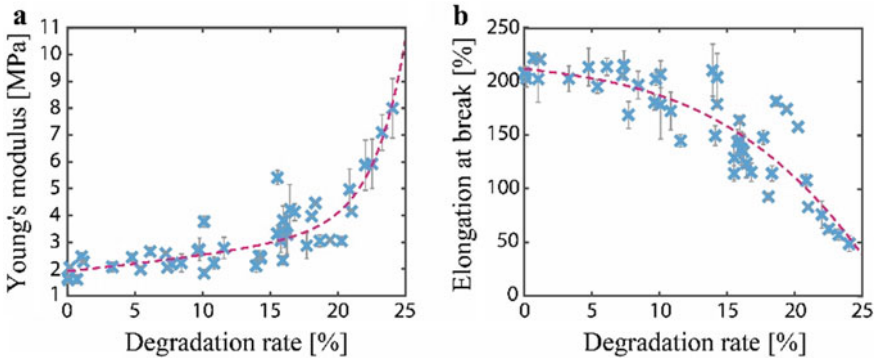

Fig. 8.9 **a** Young's modulus and **b** elongation at break of a gelatin-based soft robotic biodegradable material as functions of the degradation rate. Adopted from Nagai et al. (2021)

2021). If biodegradable materials can be handled in the same manner, fabrication will be much easier and the design will be more flexible. Indeed, several studies have already demonstrated soft robotic devices fabricated through molding and 3D printing of biodegradable materials (Shintake et al. 2017; Zolfagharian et al. 2018; Digumarti et al. 2021).

What is unique about biodegradable materials is that their properties change during the degradation process. For example, in the case of gelatin, which is a typical biodegradable soft material, the elongation at break decreases and Young's modulus increases as the degradation progresses, as shown in Fig. 8.9. This implies that even if the input is the same, the motion of the actuator will not be identical. The same applies to the output of sensors. Hence, the relationship between the denaturation rate and the properties of the materials should be analyzed prior to use in devices. Based on this, the robot can be properly designed for a given mission period and controlled effectively. The mission period could also be adjusted by setting up a mechanism that triggers the decomposition of the robot.

8.3.2 Materials

Research on sustainable and environmental-friendly "green" soft robots is just in its early stages, and there are numerous materials waiting to be applied, including muscle cells discussed in Sects. 8.1 and 8.2. Among the many candidates, one of the most promising classes of materials is biodegradable polymers (Middleton and Tipton 2000; Nair and Laurencin 2007; Vroman and Tighzert 2009). This is because, depending on the type, their mechanical properties, such as modulus and elongation at break, are comparable to those of silicone rubbers. Moreover, many of the biodegradable polymers are liquid in the prepolymer state, making them compatible with existing soft robotics manufacturing methods, such as molding and 3D printing.

Microorganisms, chemical synthesis, and natural products are all sources of biodegradable polymers. These polymers are referred to as bio-based polymers or green plastics. Microbially derived polymers are made by bacterial fermentation, and a typical example is polyhydroxybutyrate (PHB), also known as bio-polyester. Biodegradable polymers made by chemical synthesis include polylactic acid (PLA), which is made by the fermentation of starch. Polymers in this class include polycaprolactam (PCL) and poly(butylene succinate) (PBS), which are synthesized from petroleum-based raw materials. Polymers derived from natural products are basically raw materials extracted from plants and animals. Gelatin, starch, cellulose, chitin, chitosan, and natural rubbers fall into this category.

Polymers derived from natural products, simply referred to as natural polymers in this section, are relatively easy to prepare in that the raw materials can be used directly to prepare them. Therefore, they are suitable for application to soft robotics in the sense that they are readily handled. In fact, many soft actuators and robots have been developed based on this type of biodegradable polymer. Natural polymers can be divided into two main categories depending on the substance: proteins and polysaccharides (carbohydrates). Protein-based polymers include casein, gelatin, gluten, silk, and zein. They also include those extracted from fish, soy, and milk (whey). Silk is mainly composed of natural protein fiber (fibroin) produced by silkworms. Polysaccharide-based natural polymers consist of cellulose, chitosan, and starch. It is worth mentioning that the compliance and elasticity of natural polymers can be adjusted by the amount of plasticizers, such as glycerol and polyethylene glycol (PEG).

Figure 8.10 maps the tensile strength and elongation at break of natural polymers reported in the literature along with those of commercially available silicone rubbers. Natural polymers have long been developed for use in edible packaging films, as well as in drug delivery. As such, there is a rich source of experimental data. The figure includes a data point for an acrylic elastomer, which is frequently used in soft matter devices. For natural polymers, the difference in properties of the same base material is owing to composition, such as plasticizers, additives, and their ratios. The figure shows that with those ingredients, the mechanical properties can be comparable to those of silicone rubbers. To further specify, Tables 8.1 and 8.2 summarize the values of typical examples of natural polymers and commercially available silicone rubbers plotted in Fig. 8.10. While the elongation at break of silicone rubbers is approximately 1000% for the larger ones, it is approximately 600% for the natural polymers. However, this is not a major concern as the deformation that occurs in the majority of soft robotic devices is below these values. It should also be noted that for soft matter devices, an elongation at break of 100% or more is generally considered to be an indicator of high stretchability.

Thus far, the discussion has focused on the mechanical properties of biodegradable materials, in particular, polymers. Next, the focus will be on biodegradable materials with electrical conductivity. Needless to say, conductive materials are essential for the electrodes of soft robotic elements such as actuators and sensors, which ensure the proper operation of the robots. Among the conventional conductive materials used, gold, silver, platinum, and carbon are chemically stable and have no direct impact on

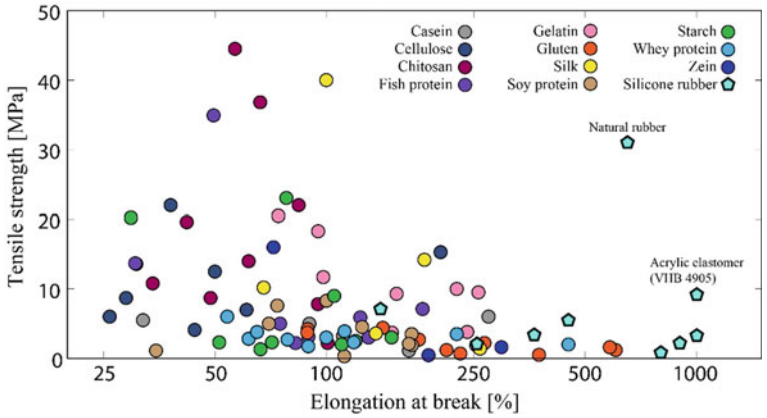

Fig. 8.10 Tensile strength and elongation at break of selected biodegradable natural polymers and commercially available polymers

Table 8.1 Mechanical properties and composition of selected natural polymers

Base material	Remark on composition	Tensile strength (MPa)	Elongation at break (%)	References
Casein	Beta-casein	6	274	(Mauer et al. 2000)
Cellulose	Hydroxypropyl cellulose	15.3	203.5	(Park et al. 1993)
Chitosan	Lactoferrin	2.2	100.8	(Bourbon et al. 2011)
Fish protein	Essential oil	7.1	181.9	(Pires et al. 2013)
Gelatin	Glycerol	1.9	254	(Baumgartner et al. 2020)
Gluten	Wheat gluten, glycerol	1.2	604	(Micard et al. 2000)
Silk	Fibroin	1.4	260	(Lu et al. 2010)
Soy protein	Glycerol	2.1	167	(Ou et al. 2005)
Starch	Potato starch, glycerol	3	150	(Ehivet et al. 2011)
Whey protein	Zein hydrolysate, transglutaminase	2	450	(Oh et al. 2004)
Zein	p-hydroxybenzoic acid	0.5	188.6	(Arcan et al. 2011)
Natural rubber		31	650	(Piersol and Harris 2010)

Table 8.2 Mechanical properties of commercially available silicone rubbers

Product name	Manufacturer	Tensile strength (MPa)	Elongation at break (%)	References
Ecoflex 00-10	Smooth-On	0.8	800	(Smooth-On 2015)
Ecoflex 00-30	Smooth-On	1.4	900	
Dragon Skin 10	Smooth-On	3.3	1000	
Dragon Skin 30	Smooth-On	3.4	364	
Sylgard 184	Dow Corning	7.1	140	(Dow Chemical Company)
Sylgard 186	Dow corning	2.1	255	(Dow Chemical Company)
VHB 4905	3M	9.2	1000	(Shintake et al. 2022)
Elastosil Film 2030	Wacker Chemie	6.0	450	(Wacker Chemie AG 2021)

the environment. Magnesium, zinc, and iron are minerals found in the environment. Sodium chloride, used in water-soluble and gel electrodes, is also composed of minerals. However, these inorganic materials are not biodegradable and accumulate in nature. For this reason, these conductors may not be suitable for soft robots, in which all the elements are desired to be completely biodegradable. In any case, the ratio of electrodes to the volume of a robot, actuator, sensor, or other device is usually small. Therefore, they could be used in systems where most but not all of them are biodegradable. In such a case, it would be possible to apply a conductive material in the form of particles or film or mix it with a biodegradable polymer to form electrodes. In this sense, the above-mentioned inorganic conductive materials are still good candidates for biodegradable soft robots. As for organic materials, the approach of blending conductive polymers, such as polypyrrole, polyacetylene, polyaniline, polythiophene, and poly(3,4-ethylenedioxythiophene) (PEDOT), with biodegradable elastomeric materials has been widely studied (Feig et al. 2018; Kenry 2018; Liu et al. 2020). Here, the main challenge for soft robotics is to achieve both high conductivity and stretchability while attaining fully biodegradable functionality, as the conductive polymers themselves are inherently not biodegradable.

As mentioned earlier, when applying biodegradable materials to soft robotics, it is important to identify the change in material properties, such as viscoelasticity, hysteresis, and repeatability, in addition to elastic modulus and elasticity, during the degradation process. Since degradation also affects the electrical conductivity, its characterization is vital. The dominant factors that determine the biodegradation rate of a material are the level of microbial activity and the elapsed time. However, there are other environmental factors that can affect the characteristics of these materials. For instance, temperature and humidity change the moisture content of a material, which in turn varies its mechanical and electrical properties. A material could dissolve when in contact with water. Additionally, the ultraviolet rays in sunlight can degrade many types of materials. The development of biodegradable materials and following

characterizations should take into account these factors. This also implies that the improvement in antimicrobial and environmental resistance of materials by coatings and additives is a meaningful approach in development.

This research may have a strong aspect of accumulating experimental data. It will create a database, in which properties of materials are expressed in terms of various factors. Such a library may enable the efficient design and control of devices, such as soft actuators, sensors, and robots. There, analytical models and numerical simulations, as well as traditional control theories, would be useful. Owing to the vast amount of data, machine learning, represented by deep learning and neural networks, may be an effective approach for control. As an example of a design approach, a recent study has presented a framework, in which finite element analysis of soft biodegradable actuators is conducted with the implementation of parameters acquired experimentally (Nagai et al. 2021). The study shows that the performance of actuators under biodegradation can be predicted. Furthermore, it will be possible to effectively operate biodegradable soft robots by prior assessment of the climate and environmental conditions of the target area, together with the duration of the task to be performed.

8.3.3 Biodegradable Soft Robotic Devices

Gelatin has been frequently employed in the study of biodegradable soft robotic devices. It is a common material that can be bought in supermarkets, is inexpensive, can be adjusted to realize different mechanical properties with a plasticizer such as glycerol, has a low melting point, and is liquid in the prepolymer state, making it easy to handle and suitable for a variety of fabrication methods. Figure 8.11 shows an example of a fluid elastomer soft actuator using gelatin (Nagai et al. 2021). As shown in Fig. 8.11a, the actuator can bend and deform when pressurized air is applied. Additionally, as shown in Fig. 8.11b, the actuator is able to return to the soil after a certain time elapses. In addition to the fluidic actuation, gelatin also exhibits deformations under electrical stimuli (Chambers et al. 2014).

Gelatin-based materials have also been demonstrated for use in other robotic devices. Figure 8.12a shows a soft gripper that can hold a variety of objects (Shintake et al. 2017). Because many biodegradable materials are also biocompatible, it may be possible to expand the types of objects and situations, in which they can be manipulated. Figure 8.12b shows a mobile robot that has multiple actuation parts (Hughes and Rus 2020). The surface of the cylindrical structure can be selectively inflated, enabling a rolling motion on the ground. Further research on such mobile robots can lead to the realization of biodegradable soft robots that can perform tasks in natural environments. The conductivity of gelatin can be adjusted depending on the amount of water, plasticizer, and additives. Its conductivity also changes in response to deformation, which can be exploited to detect deformations. Figure 8.12c shows an example of a gelatin sensor (Wang et al. 2020), where the response of the sensor placed on a finger changes according to the amount of deformation.

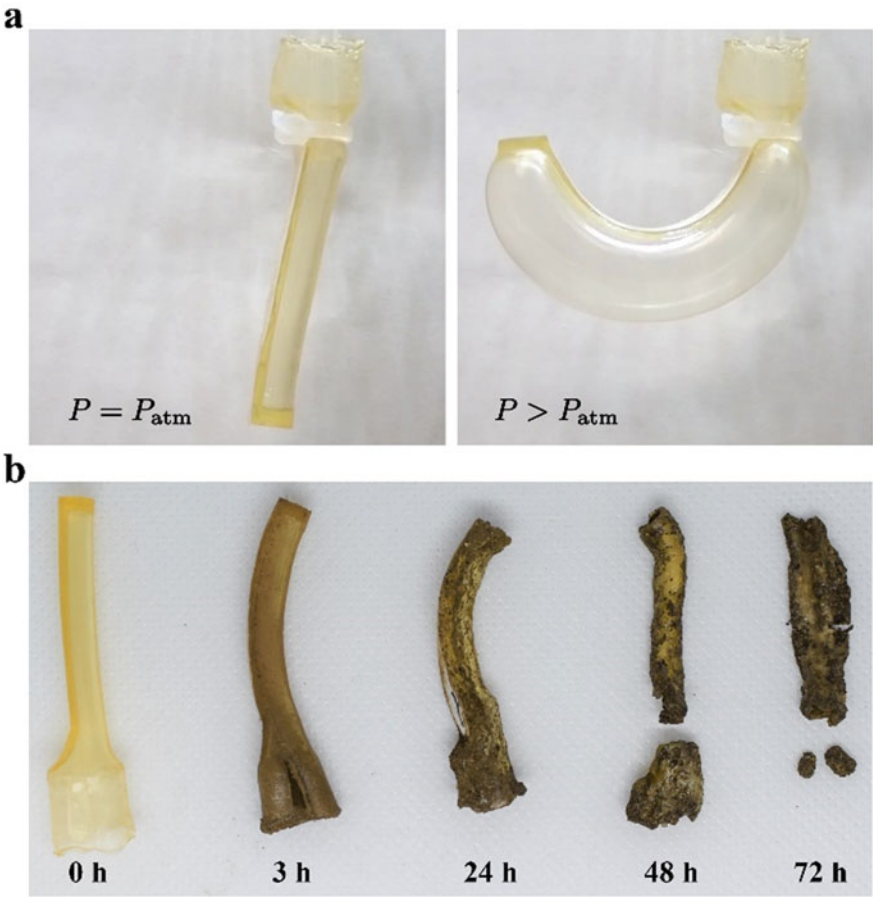

Fig. 8.11 **a** Fluidic elastomer actuator using a gelatin-based material. Pressurizing the actuator realizes a bending motion. **b** Biodegradation process of the actuator (adopted from Nagai et al. 2021). After 72 h, the device is almost merging into the soil

Here, only a specific material and limited number of devices are introduced. Many types of robots and actuation and sensing principles are available in the field of soft robotics (Laschi et al. 2016; Amjadi et al. 2016; Hines et al. 2017; Rich et al. 2018; El-Atab et al. 2020). It is easy to imagine that the fusion of this knowledge and technologies with biodegradable materials will bring forth unprecedented robotic devices for various applications.

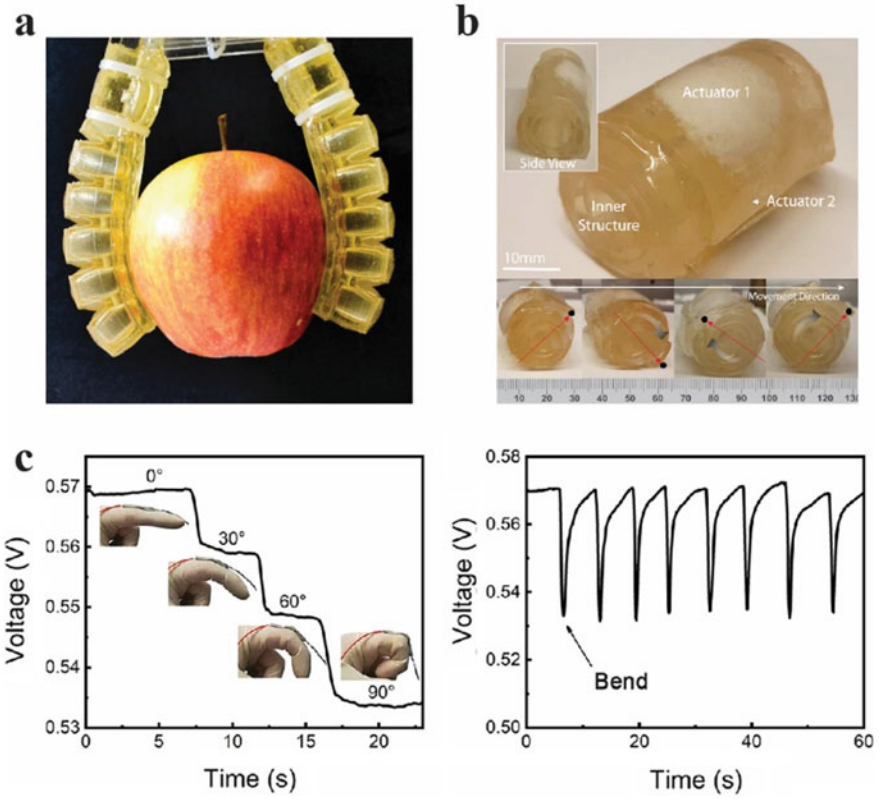

Fig. 8.12 Soft robotic devices based on gelatin materials. **a** Soft gripper holding an apple (Shintake et al. 2017). **b** Rolling robot (Hughes and Rus 2020). **c** Soft sensor to detect motion of a human finger (Wang et al. 2020)

8.3.4 Future Outlook

Research on sustainable, environmental-friendly soft robots is a new trend, for which a rich source of potentially applicable materials and principles is available. Given their diversity and high potential, remarkable research efforts in various aspects are expected. Specifically, developments may take place in three directions: (1) biodegradable materials that are not only highly elastic but also insulating and conductive; (2) actuators, sensors, and other functional elements that are driven by different stimuli such as fluids and electricity; and (3) soft robotic systems. In these initiatives, integration with green electronics (Irimia-Vladu 2014; Li et al. 2020) will be essential, particularly in terms of creating robotic elements and systems. In the end, these research efforts can form a scientific field beyond soft robotics, namely green robotics.

Exercises

- (6.1) Let's consider what kind of soft robotic application is good for growth owing to mechanical stimulation.
- (6.2) What types of cells are mainly classified according to proliferation and differentiation?
- (6.2) When evaluating muscle contraction force, it is common to measure the isometric contraction force. Discuss the reasons.
- (6.2) What are the two common methods to use cells as sensors for odorant detection?
- (6.3) What are the expected advantages of being biodegradable in soft robotics?
- (6.3) What are the representative properties to consider when incorporating biodegradable materials into soft robots?
- (6.3) List the applications of biodegradable soft robots.

Acknowledgements This work is supported by the JSPS KAKENHI Grant-in-Aid for Scientific Research on Innovative Areas "Science of Soft Robot" project (grant number 21H00324).

References

Akiyama Y, Odaira K, Sakiyama K, Hoshino T, Iwabuchi K, Morishima K (2012) Rapidly-moving insect muscle-powered microrobot and its chemical acceleration. Biomed Microdevice 14(6):979–986

Amjadi M, Kyung K-UU, Park I, Sitti M (2016) Stretchable, skin-mountable, and wearable strain sensors and their potential applications: a review. Adv Funct Mater 26:1678–1698. https://doi.org/10.1002/adfm.201504755

Arcan I, Yemenicioğlu A (2011) Incorporating phenolic compounds opens a new perspective to use zein films as flexible bioactive packaging materials. Food Res Int 44:550–556. https://doi.org/10.1016/j.foodres.2010.11.034

Asano T, Ishizua T, Yawo H (2012) Optically controlled contraction of photosensitive skeletal muscle cells. Biotechnol Bioeng 109(1):199–204

Baumgartner M, Hartmann F, Drack M et al (2020) Resilient yet entirely degradable gelatin-based biogels for soft robots and electronics. Nat Mater 19:1102–1109. https://doi.org/10.1038/s41563-020-0699-3

Bourbon AI, Pinheiro AC, Cerqueira MA et al (2011) Physico-chemical characterization of chitosan-based edible films incorporating bioactive compounds of different molecular weight. J Food Eng 106:111–118. https://doi.org/10.1016/j.jfoodeng.2011.03.024

Chambers LD, Winfield J, Ieropoulos I, Rossiter J (2014) Biodegradable and edible gelatine actuators for use as artificial muscles. In: Bar-Cohen Y (ed) Electroactive polymer actuators and devices (EAPAD) 2014. International Society for Optics and Photonics, p 90560B

Corcelli A, Lobasso S, Lopalco P, Dibattista M, Araneda R, Peterlin Z, Firestein S (2010) Detection of explosives by olfactory sensory neurons. J Hazard Mater 175(1–3):1096–1100

Delp SL, Loan JP (2000) A computational framework for simulating and analyzing human and animal movement. Comput Sci Engi 2(5):46–55

Digumarti KM, Gosden D, Le NH, Rossiter J (2021) Toward stimuli-responsive soft robots with 3D printed self-healing konjac glucomannan gels. 3D Print Addit Manuf. https://doi.org/10.1089/3dp.2020.0289

Dow Chemical Company T (2017a) SYLGARDTM 184 Silicone Elastomer FEATURES & BENEFITS
Dow Chemical Company T (2017b) SYLGARDTM 186 Silicone Elastomer
Ehivet FE, Min B, Park M-K, Oh J-H (2011) Characterization and antimicrobial activity of sweetpotato starch-based edible film containing Origanum (*Thymus capitatus*) oil. J Food Sci 76:C178–C184. https://doi.org/10.1111/j.1750-3841.2010.01961.x
El-Atab N, Mishra RB, Al-Modaf F et al (2020) Soft actuators for soft robotic applications: a review. Adv Intell Syst 2:2000128. https://doi.org/10.1002/aisy.202000128
Engler JA, Sen S, Sweeney LH, Discher ED (2006) Matrix elasticity directs stem cell lineage specification. Cell 126(4):677–689
Feig VR, Tran H, Bao Z (2018) Biodegradable polymeric materials in degradable electronic devices. ACS Cent Sci 4:337–348. https://doi.org/10.1021/acscentsci.7b00595
Fujita H, Nedachi T, Kanzaki M (2007) Accelerated de novo sarcomere assembly by electric pulse stimulation in C2C12 myotubes. Exp Cell Res 313(9):1853–1865
Gul JZ, Sajid M, Rehman MM et al (2018) 3D printing for soft robotics—a review. Sci Technol Adv Mater 19:243–262. https://doi.org/10.1080/14686996.2018.1431862
Hayakawa K, Tatsumi H, Sokabe M (2011) Actin filaments function as a tension sensor by tension-dependent binding of cofilin to the filament. J Cell Biol 195(5):721–727
Hill AV (1938) The heat of shortening and the dynamic constants of muscle. Proc Roy Soc Ser b: Biol Sci 126(843):136–195
Hirata Y, Morimoto Y, Nam E, Takeuchi S (2019) Portable biohybrid odorant sensors using cell-laden collagen micropillars. Lab Chip 19:1971–1976
Hines L, Petersen K, Lum GZ, Sitti M (2017) Soft actuators for small-scale robotics. Adv Mater 29:1603483. https://doi.org/10.1002/adma.201603483
Hughes J, Rus D (2020) Mechanically programmable, degradable ingestible soft actuators. In: 2020 3rd IEEE international conference on soft robotics, RoboSoft 2020. Institute of Electrical and Electronics Engineers Inc., pp 836–843
Hunter IW, Lafontaine S (1992) A comparison of muscle with artificial actuators. In: IEEE solid-state sensor and actuator workshop, pp 178–185
Huxley AF (1974) Muscular-contraction—review lecture. J Physiol Lond 243:1–43
Irimia-Vladu M (2014) "Green" electronics: biodegradable and biocompatible materials and devices for sustainable future. Chem Soc Rev 43:588–610. https://doi.org/10.1039/C3CS60235D
Ito K, Tsuji T (1985) The bilinear characteristics of muscle-skeletomotor system and the application to prosthesis control. IEEJ Trans Inst Electr Eng Jpn C (jpn) 105(10):201–208
Kenry LB (2018) Recent advances in biodegradable conducting polymers and their biomedical applications. Biomacromol 19:1783–1803. https://doi.org/10.1021/acs.biomac.8b00275
Laschi C, Mazzolai B, Cianchetti M (2016) Soft robotics: technologies and systems pushing the boundaries of robot abilities. Sci Robot 1:1–12. https://doi.org/10.1126/scirobotics.aah3690
Li W, Liu Q, Zhang Y et al (2020) Biodegradable materials and green processing for green electronics. Adv Mater 32:2001591. https://doi.org/10.1002/adma.202001591
Liu Q, Hu N, Ye W, Cai H, Zhang F, Wang P (2011) Extracellular recording of spatiotemporal patterning in response to odors in the olfactory epithelium by microelectrode arrays. Biosens Bioelectron 27(1):12–17
Liu K, Tran H, Feig VR, Bao Z (2020) Biodegradable and stretchable polymeric materials for transient electronic devices. MRS Bull 45:96–102. https://doi.org/10.1557/mrs.2020.24
Lu Q, Hu X, Wang X et al (2010) Water-insoluble silk films with silk I structure. Acta Biomater 6:1380–1387. https://doi.org/10.1016/j.actbio.2009.10.041
Mauer L, Smith D, Labuza T (2000) Water vapor permeability, mechanical, and structural properties of edible β-casein films. Int Dairy J 10:353–358. https://doi.org/10.1016/S0958-6946(00)00061-3
Micard V, Belamri R, Morel M-H, Guilbert S (2000) Properties of chemically and physically treated wheat gluten films. J Agric Food Chem 48:2948–2953. https://doi.org/10.1021/jf0001785
Middleton JC, Tipton AJ (2000) Synthetic biodegradable polymers as orthopedic devices. Biomaterials 21:2335–2346. https://doi.org/10.1016/S0142-9612(00)00101-0

Minegishi R, Takashima A, Kurabayashi D, Kanzaki R (2012) Construction of a brain-machine hybrid system to evaluate adaptability of an insect. Robot Auton Syst 5(60):692–699
Mitsuno H, Sakurai T, Namiki S, Mitsuhashi H, Kanzaki R (2015) Novel cell-based odorant sensor elements based on insect odorant receptors. Biosens Bioelectron 65:287–294
Morimoto Y, Kato-Negishi M, Onoe H, Takeuchi S (2013) Three-dimensional neuron-muscle constructs with neuromuscular junctions. Biomaterials 34(37):9413–9419
Morimoto Y, Mori S, Sakai F, Takeuchi S (2016) Human induced pluripotent stem cell-derived fiber-shaped cardiac tissue on a chip. Lab Chip 16(12):2295–2301
Nagai T, Kurita A, Shintake J (2021) Characterization of sustainable robotic materials and finite element analysis of soft actuators under biodegradation. Front Robot AI 8:383. https://doi.org/10.3389/FROBT.2021.760485/BIBTEX
Nair LS, Laurencin CT (2007) Biodegradable polymers as biomaterials. Prog Polym Sci 32:762–798. https://doi.org/10.1016/j.progpolymsci.2007.05.017
Oda H, Kihara K, Morimoto Y, Takeuchi S (2021) Cell-based biohybrid sensor device for chemical source direction estimation. Cyborg Bionic Syst 1(1):8907148
Oh J-H, Wang B, Field PD, Aglan HA (2004) Characteristics of edible films made from dairy proteins and zein hydrolysate cross-linked with transglutaminase. Int J Food Sci Technol 39:287–294. https://doi.org/10.1111/j.1365-2621.2004.00783.x
Ou S, Wang Y, Tang S et al (2005) Role of ferulic acid in preparing edible films from soy protein isolate. J Food Eng 70:205–210. https://doi.org/10.1016/j.jfoodeng.2004.09.025
Park HJ, Weller CL, Vergano PJ, Testin RF (1993) Permeability and mechanical properties of cellulose-based edible films. J Food Sci 58:1361–1364. https://doi.org/10.1111/j.1365-2621.1993.tb06183.x
Park S, Gazzola M, Park KS, Park S, Santo VD, Blevins EL, Lind JU, Campbell PH, Dauth S, Capulli AK, Pasqualini FS, Ahn S, Cho A, Yuan H, Maoz BM, Vijaykumar R, Choi J, Deisseroth K, Lauder GV, Mahadevan L, Parker KK (2016) Phototactic guidance of a tissue-engineered soft-robotic ray. Science 6295(353):158–162
Piersol A, Harris C (2010) Harris' shock and vibration handbook
Pires C, Ramos C, Teixeira B et al (2013) Hake proteins edible films incorporated with essential oils: physical, mechanical, antioxidant and antibacterial properties. Food Hydrocoll 30:224–231. https://doi.org/10.1016/j.foodhyd.2012.05.019
Ramsey RW, Street SF (1940) The isometric length-tension diagram of isolated skeletal muscle fibers of the frog. J Cell Comp Physiol 15:11–34
Rich SI, Wood RJ, Majidi C (2018) Untethered soft robotics. Nat Electron 1:102–112. https://doi.org/10.1038/s41928-018-0024-1
Ricotti L, Menciassi A (2012) Bio-hybrid muscle cell-based actuators. Biomed Microdevice 14(6):987–998
Ricotti L, Trimmer B, Feinberg AW, Raman R, Parker KK, Bashir R, Sitti M, Martel S, Dario P, Menciassi A (2017) Biohybrid actuators for robotics: a review of devices actuated by living cells. Sci Robot 2(12):eaaq0495
Rus D, Tolley MT (2015) Design, fabrication and control of soft robots. Nature 521:467–475. https://doi.org/10.1038/nature14543
Sato K, Takeuchi S (2014) Chemical vapor detection using a reconstituted insect olfactory receptor complex. Angew Chem Int Ed 53(44):11798–11802
Schmitt F, Piccin O, Barbé L, Bayle B (2018) Soft robots manufacturing: a review. Front Robot AI 5. https://doi.org/10.3389/frobt.2018.00084
Shima A, Morimoto Y, Sweeney HL, Takeuchi S (2018) Three-dimensional contractile muscle tissue consisting of human skeletal myocyte cell line. Exp Cell Res 370(1):168–173
Shintake J, Sonar H, Piskarev E et al (2017) Soft pneumatic gelatin actuator for edible robotics. In: IEEE international conference on intelligent robots and system, pp 6221–6226. https://doi.org/10.1109/IROS.2017.8206525

Shintake J, Matsuno K, Kumegawa S et al (2022) Characterization of slide ring materials for dielectric elastomer actuators. Smart Mater Struct 31:025028. https://doi.org/10.1088/1361-665X/ac42e9

Smith RS, Peterlin Z, Araneda RC (2012a) Pharmacology of mammalian olfactory receptors In: Crasto C (ed) Olfactory receptors. Methods in molecular biology (methods and protocols), vol 1003. Humana Press, Totowa, NJ

Smith AST, Passey S, Greensmith L, Mudera V, Lewis MP (2012b) Characterization and optimization of a simple, repeatable system for the long term in vitro culture of aligned myotubes in 3D. J Cell Biochem 113(3):1044–1053

Smooth-On (2015) EcoflexTM Series—Smooth-On. https://www.smooth-on.com/tb/files/ECOFLEX_SERIES_TB.pdf

Stano G, Percoco G (2021) Additive manufacturing aimed to soft robots fabrication: a review. Extreme Mech Lett 42:101079. https://doi.org/10.1016/j.eml.2020.101079

Tanaka Y, Sato K, Shimizu T, Yamato M, Okano T, Kitamori T (2007) Biological cells on microchips: new technologies and applications. Biosens Bioelectron 23(4):449–458

Vroman I, Tighzert L (2009) Biodegradable polymers. Materials 2:307–344. https://doi.org/10.3390/MA2020307

Wacker Chemie AG (2021) ELASTOSIL® Film 2030

Wang J, Tang F, Wang Y et al (2020) Self-Healing and highly stretchable gelatin hydrogel for self-powered strain sensor. ACS Appl Mater Interfaces 12:1558–1566. https://doi.org/10.1021/acsami.9b18646

Warwick K (2010) Implications and consequences of robots with biological brains. Ethics Inf Technol 12(3):223–234

Witzemann V (2006) Development of the neuromuscular junction. Cell Tissue Res 326(2):263–271

Zimmermann WH, Schneiderbanger K, Schubert P, Didie M, Munzel F, Heubach JF, Kostin S, Neuhuber WL, Eschenhagen T (2002) Tissue engineering of a differentiated cardiac muscle construct. Circ Res 90(2):223–230

Zolfagharian A, Kaynak A, Khoo SY, Kouzani AZ (2018) Polyelectrolyte soft actuators: 3D printed chitosan and cast gelatin. 3D Print Addit Manuf 5:138–150. https://doi.org/10.1089/3dp.2017.0054

Chapter 9
Flexible and Stretchable Electronics and Photonics

Kenjiro Fukuda and Kuniharu Takei

Abstract In soft robots, it is not only important to make the actuator soft and flexible, but it is also important to fabricate the electronic devices, including logic circuits and sensors, using soft materials. In this chapter, we will discuss the principles and strategies for realizing flexible electronics and photonics. Subsequently, we will introduce the principles of tactile pressure and temperature sensors, wiring, photovoltaics, photodiodes, and transistors as specific devices.

9.1 Principles and Strategies

Both flexible and stretchable electronics should be clearly defined to avoid confusion, as many different definitions have been presented in different texts. In this text, the term "flexible electronics" refers to electronic circuits and other components that are fabricated on flexible substrates, making them bendable. The term "stretchable electronics" refers to electronic circuits and other components that possess the capability of stretching strains.

Moreover, mechanical flexibility and stretchability are completely different parameters. Flexible electronics assume bending capability. However, elasticity is not considered in most cases. This concept can be recognized by considering an extremely thin polymer film, such as a food wrap. Such thin polymer films can be easily bent. However, they easily become torn by adding a small percentage of tensile strain. In addition, many stretchable electronics possess some degree of bending capability. Therefore, it is reasonable to consider stretchable electronics as a narrow classification for flexible electronics.

Young's modulus (E) and thickness are important parameters in exploring flexibility or mechanical robustness. Indeed, both parameters are used to determine the

K. Fukuda (✉)
RIKEN, Saitama, Japan
e-mail: kenjiro.fukuda@riken.jp

K. Takei
Osaka Metropolitan University, Osaka, Japan
e-mail: takei@omu.ac.jp

K. Suzumori et al. (eds.), *The Science of Soft Robots*, Natural Computing Series,
https://doi.org/10.1007/978-981-19-5174-9_9

applied strain and flexural rigidity. As shown in Fig. 8.1 in Sect. 8.3, a polymer possesses a Young's modulus of several tens of MPa to several GPa and therefore has a smaller bending rigidity than that of the existing silicon-based rigid electronics and photonics, in which Young's modulus varies in the range of several tens to hundreds of GPa (Fig. 8.8).

9.1.1 Strain Applied to the Device

The cyclic durability of a fixed bending radius or angle is often discussed while evaluating the mechanical stability of flexible electronics. Although this approach is significantly important in industrial applications, the bending radii and angles of devices prohibit proper physical analyzes to determine the amount of applied strain in the electronics. Instead, evaluating the strain applied to the device is better when considering the mechanical robustness of different materials and structures.

Strain calculation by approximation using a two-layer model has long been used to estimate thin-film electronics fabricated on a flexible film substrate (Gleskova et al. 1999). A device on a relatively thick substrate can be simplified into a two-layer model of "substrate" and "device" when the substrate is sufficiently thicker than the device. In this model, the strain ε applied to the top surface of the device is expressed as

$$\varepsilon = \left(\frac{s+d}{2R}\right)\frac{\left(1+2\eta+\chi\eta^2\right)}{(1+\eta)(1+\chi\eta)}, \tag{9.1}$$

where R is the bending radius applied to the substrate, d is the thickness of the device, s is the thickness of the substrate $\eta = d/s$, and $\chi = \frac{\text{Young's modulus of device } (E_d)}{\text{Young's modulus of substrate } (E_s)}$.

If $d \ll s$ then Eq. (9.1) can be approximated to

$$\varepsilon \approx \frac{s}{2R}. \tag{9.2}$$

This approximation is effective when the thin film electronics are relatively thick with respect to the substrate film, which can be considered as a single plate.

However, in recent years, as the thickness of substrates has been extremely reduced, the approximation of the two-layer model can be hardly applied. In addition, thin-film electronics are usually composed of a multi-layered structure of conductors, semiconductors, and insulators, which are composed of a plurality of materials with different resistances to strain. Therefore, the strain applied to critical layers of electronics should be estimated.

An estimation of strains that considers Young's modulus and thickness of all layers in multi-stack structures is more favorable for comparison of the mechanical robustness. The bending strain at an arbitrary position r from the bottom surface of the multilayer stack when the first layer is at the bottom and the nth layer is at the

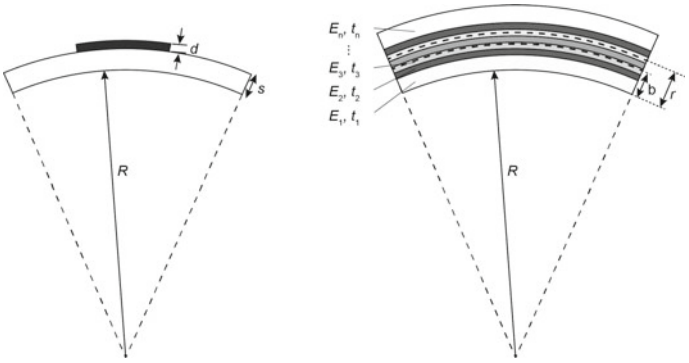

Fig. 9.1 Strategies to realize stretchable electronics. Left: two-layer model with a thick substrate and device. Right: multi-stack model, where n layers with different materials are stacked to form an electronic/photonic device

top is expressed as (Fukuda et al. 2016)

$$\varepsilon = \frac{r-b}{R+b}, \tag{9.3}$$

where R and b are the bending radius and neutral mechanical plane (zero-strain position), respectively (Fig. 9.1). Position b is expressed as (Kim et al. 2008a, b)

$$b = \frac{\sum_{i=1}^{n} E_i t_i \left[\sum_{j=1}^{i} t_j - \frac{t_i}{2}\right]}{\sum_{i=1}^{n} E_i t_i}, \tag{9.4}$$

where E_i and t_i are Young's moduli and thicknesses of the individual layers, respectively.

9.1.2 Improvement in Mechanical Robustness

Minimization of the bending strain applied to the weakest layer is an essential strategy to improve mechanical robustness. Equation (9.3) indicates that the performance degradation of the device can be minimized using bending strain by arranging a layer or an interface that yields the weakest strain response at a neutral mechanical plane. This neutral strain-position strategy with a thin substrate and encapsulation yields excellent bending robustness for flexible electronics/photonics even if brittle materials, such as oxide materials, are used (Park 2018).

Another effective strategy is to replace brittle materials with more robust materials. In general, inorganic materials are the most brittle ones, whereas metals are more robust than inorganic materials owing to their ductility and malleability. As

for organic materials, polymers are more robust than small molecules. Additionally, higher crystallinity tends to degrade the mechanical robustness, and delamination should also be considered for multi-stack structures.

Moreover, indium tin oxide (ITO) is a specific example that is typically used as a transparent electrode in photonic devices, such as photovoltaics and light-emitting diodes (LEDs). Indeed, ITO is one of the most brittle layers used in photonic devices. An existing study proved that a strain of 2% could crack ITO films (Cairns et al. 2001). Therefore, the applied strain to the ITO layer during bending should be maintained at less than 2% using the neutral strain-position strategy. The replacement of transparent electrodes with highly flexibility materials effectively enhances the mechanical robustness. Some effective substitutes for transparent electrodes include graphene (Woo 2018), PEDOT:PSS, silver nanowires, and silver nanonetworks (Seo et al. 2019).

9.1.3 Flexural Rigidity

Flexural rigidity D is a crucial parameter for achieving mechanically conformable electronic devices, which is defined as follows (Yamagishi et al. 2019):

$$D = \frac{Et^3}{12\left(1 - v^2\right)}, \tag{9.5}$$

where t, E, and v denote the thickness, Young's modulus, and Poisson's ratio of the film, respectively. Equation (9.3) describes a strategy to produce conformable electronics. The most effective approach for decreasing flexural rigidity is reducing the thickness because it is proportional to the third power of the thickness. An existing study clearly presented improved conformability using materials with the same substrate at a reduced thickness (Kim et al. 2010).

9.1.4 Stretchability

For some electrical applications, such as wearable electronics used in sportswear, stretchability is considerably more important than flexibility and conformability (Matsuhisa et al. 2019). In addition, stretchability is required when film-type electronics are adhered onto nondevelopable surfaces, such as spheres (Rich 2022).

Five strategies have been introduced to apply stretchability to electronic devices (Fig. 9.2) (Lee 2021). The first strategy involves the fabrication of devices with intrinsically stretchable materials. The second strategy uses stretchable substrates and conductors with "rigid islands." Nonstretchable device components are placed

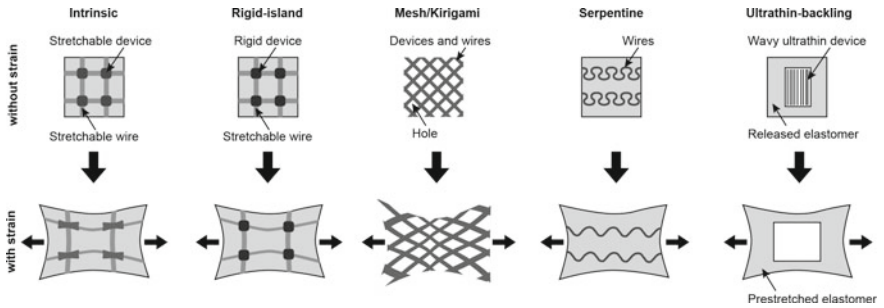

Fig. 9.2 Strategies to realize stretchable electronics

within rigid islands and wired to the surrounding stretchable substrate using stretchable interconnects. In the third strategy, meshes or kirigami structures are constructed, in which the strain can be drastically reduced in devices to withstand stretching. The fourth strategy is to create serpentine patterns of nonstretchable wires and devices. When the strain is applied, the shape is deformed, and wires and devices receive lower stress concentrations owing to the serpentine design. The fifth strategy combines ultrathin devices with prestretched elastomers. In this approach, ultrathin devices are attached to the prestretched elastomers. When the elastomer is relaxed, random wrinkles are formed on devices. The performance is not degraded under severe deformation conditions owing to the excellent bending stability of ultrathin devices.

The first approach, in which intrinsically stretchable materials are used in electronics, is the most straightforward strategy, and thus an ideal approach. The current bottleneck is the decreased performance of the device owing to the limited performance of stretchable materials. The fifth strategy requires both ultrathin electronics and prestretched elastomers. This strategy requires the integration of ultrathin devices on stretched surfaces, which may cause complicated process conditions when industrialization is considered. Applying ultrathin organic solar cells with the rigid island strategy, mesh/Kirigami strategy, or serpentine design is considered a moderate method that does not compromise the required performance. Adequately high performance can be achieved by flexible electronics on thin polymer films that have small or no stretchability, and stretchability can be achieved with stretchable interconnects. This strategy can minimize the active area changes following stretching, which can lead to stable outputs. In addition, this approach yields a reasonable conformability for the entire system.

9.2 Flexible Sensors

As discussed in the previous section, materials are easily strained under bending and stretching conditions, based on mechanical phenomena. Utilizing this strain, strain

and tactile pressure sensors can be fabricated on flexible and stretchable films, which can be integrated into soft robots. In particular, artificial electronic skin (e-skin) is one of the most interesting sensor systems which imitates functionalities of human skin, such as detection of tactile pressure and temperature. In this section, fundamental mechanisms of tactile pressure and temperature sensors are explained.

9.2.1 Tactile Pressure Sensor

Three types of tactile pressure sensors are often used, employing resistive, capacitive, and piezoelectric mechanisms. All three types have advantages and disadvantages when incorporated into soft robot e-skin, and the sensor type should be selected depending on system integration and sensing requirements. For resistive sensors, also called piezoresistive sensors, the measurement system can be simplified, while a flexible and/or stretchable conductive layer must be developed. For capacitive sensors, a parallel-plate structure using dielectric elastomers can be used. Such a system is simpler and easier to realize in most cases than using resistive sensors. However, cases requiring capacitive measurement systems are somewhat complicated compared to resistive sensors. Lastly, for piezoelectric sensors, since a piezoelectric material, such as polyvinylidene difluoride, generates power when tactile pressure is applied, it can be used for low-power operations. However, output power is generated only by dynamic change of the structure, with the result that data analysis is required to read the tactile pressure when pressure is applied to the sensor. Furthermore, the output power cannot support operation of signal processing circuits, because too little power is generated. In this section, resistive and capacitive pressure sensors are discussed because they are easy to fabricate and reproduce for soft robotics application.

Resistive tactile pressure sensors

To understand sensing mechanisms, strain effects on flexible/stretchable conductive materials must first be understood. Conductive flexible materials are often formed by using conductive polymers or by adding conductive particles to the elastomer (Fig. 9.3). Because piezoresistive sensors often read tunnel currents between conductive particles through the elastomer, the distance between particles l is important. Since these particles are less flexible than the elastomer, only the distance between particles changes under strain. That is, no change in particle size d occurs (Fig. 9.3). When tensile strain ΔL is applied, the distance between particles changes by Δl, which causes a lower probability path of tunnel current than that without strain, resulting in increased resistance.

To consider the theoretical calculation of the resistance change caused by the particle distance change, a three-dimensional model is shown in Fig. 9.4. The resistance is defined by Eq. (9.6),

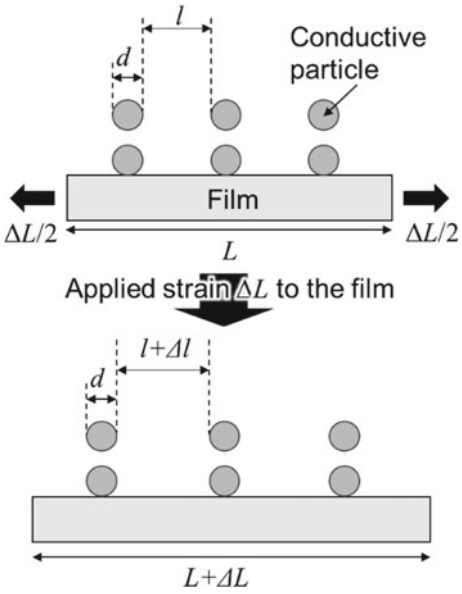

Fig. 9.3 Explanation of the particle distance change in the film under applied strain

$$R = \frac{N}{MK} R_{\mathrm{T}} \tag{9.6}$$

where N, M, and K are the number of particles (Fig. 9.4). R_{T} is the tunnel resistance between conductive particles, and is described by

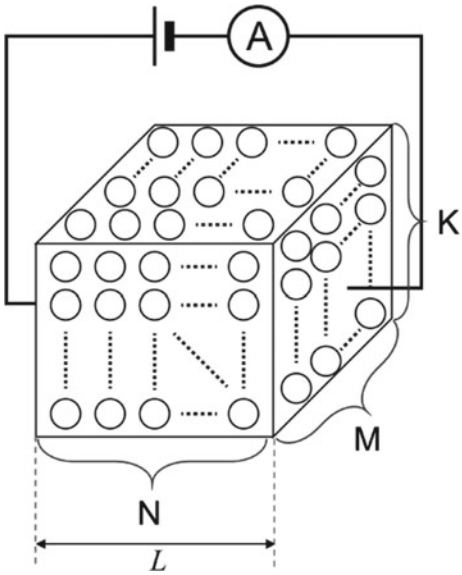

Fig 9.4 Strain sensor using conductive particles embedded in an elastomer

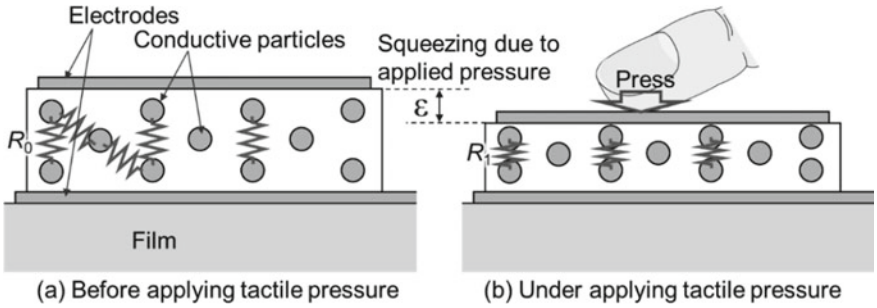

Fig 9.5 Sensing mechanism of a resistive tactile pressure sensor. **a** Before applying tactile pressure and **b** during the application of tactile pressure to the sensor

$$R_{\mathrm{T}}(l) \propto \mathrm{e}^{\beta l} \tag{9.7}$$

where β is the coefficient of the conductive particle material. The length L shown in Fig. 9.4 can be appropriately expressed as

$$L \cong N(d + l) \tag{9.8}$$

Since conductive particles generally do not stretch under strain because of their hardness, the length change ΔL can be expressed as

$$\Delta L \cong N \Delta l \tag{9.9}$$

Based on Eqs. (9.8) and (9.9), Δl is extracted as

$$\Delta l = \frac{\Delta L}{L}(d + l) = (d + l)\varepsilon \tag{9.10}$$

where ε is the strain applied to the material, expressed as

$$\varepsilon = \frac{\Delta L}{L} \tag{9.11}$$

Finally, using Eqs. (9.6), (9.7), and (9.8), the resistance change is expressed as

$$\begin{aligned} \frac{\Delta R}{R} &= \frac{\mathrm{e}^{\beta(l+\Delta l)} - \mathrm{e}^{\beta l}}{\mathrm{e}^{\beta l}} = \mathrm{e}^{\beta \Delta l} - 1 \\ &= \mathrm{e}^{\beta(d+l)\varepsilon} - 1 \end{aligned} \tag{9.12}$$

Because $\beta(d + l)$ for the tunnel current mechanism is usually small, the resistance change ratio can be simplified to

$$\frac{\Delta R}{R} \cong \beta(d+l)\varepsilon = g\varepsilon \tag{9.13}$$

where $g = \beta(d + l)$, and g is called a gage factor. The gage factor is often used to evaluate the sensitivity of the strain sensor. It should be noted that the gage factor is often calculated using $\Delta R/R = g\varepsilon$, without considering the tunnel current. This is because flexible and stretchable strain sensors are widely studied without using the tunnel current mechanism. However, this factor is very useful to understand the sensitivity of the sensor to compare with other strain sensors and also for calibration of sensor outputs.

Now, we understand the sensing mechanism using tunnel current change caused by deformation of the flexible materials. Using this mechanism, resistive tactile pressure sensors can be developed in addition to the strain detectors discussed above. Tactile pressure sensors can also be fabricated from conductive elastomers containing nanoparticles (Fig. 9.5). A pair of electrodes is vertically located on the upper and lower surfaces of the conductive elastomer, or the electrodes are placed on either surface of the elastomer (not shown). Depending on the application, electrode location and design should be tuned. In general, the design of vertically placed electrodes shows lower initial resistance and higher sensitivity, whereas laterally integrated electrodes have good scalability and are easier to integrate as planar structures. As the sensing mechanism is almost the same between vertical and lateral integration, this section explains the vertical structure.

Figure 9.5 illustrates a sensor before and during the application of tactile pressure. Before applying pressure, owing to conductive particles embedded in elastomer, the resistance R_0 between the top and bottom electrodes is high. Once pressure is applied, the distance between conductive particles is reduced because the elastomer is squeezed. This shorter distance ε is the same parameter as the strain, discussed before. This results in a higher probability of tunnel current, and the sensor resistance R_1 is lower than that in the initial state without pressure (i.e. $R_0 > R_1$). The applied pressure can be calculated by measuring the resistance change. It should be noted that depending on the density of conductive particles in an elastomer, initial resistance and sensitivity are different. Particularly, lower initial resistance due to a higher density of conductive particles often implies lower sensitivity. For lateral integration, the electrical current path is between the electrodes instead of a vertical path, as discussed above.

For pressure sensor development, in addition to sensitivity, hysteresis of the resistance change is another important parameter to detect the applied pressure precisely. It often takes time for elastomeric materials to return to their initial shape after deformation caused by applied pressure. In the worst case, the resistance never returns to its initial value. The reason for this is most likely permanent structure change of the elastomer or damage, including position changes of conductive particles embedded in the elastomer. To characterize the hysteresis, the time dependence of resistance changes owing to applying and releasing pressure is studied. From this time-dependence study, the operational speed of the tactile pressure sensor is determined from the

time it stabilizes under pressure until it returns to the initial value. For the resistance-change dependence as a function of pressure, permanent change is also monitored. Furthermore, for practical use, cycle testing and applying and releasing the pressure multiple times must be performed.

Unlike conventional inflexible pressure sensors, bending or stretching of sensor outputs must be considered because mechanical deformation causes structural change. As discussed in the previous section, when the substrate is bent, upper and lower surfaces experience tensile or compressive strain, and the thickness of the elastomer is slightly diminished. Because this generates a resistance change, selectivity or specific application is important for targeted pressure monitoring. In other words, this sensor can also be used as a strain sensor.

Capacitive tactile pressure sensors

Next, using the same structural concept, capacitive tactile pressure sensors are briefly discussed. For capacitive measurements, conductivity paths between two electrodes should be removed. For this purpose, conductive particles are not required in the elastomer. If the capacitance value needs to be high, then small amounts of conductive particles that do not form conductive tunnel current paths, even under applied pressure, are dispersed in the elastomer. As with resistive sensors, depending on the applied tactile pressure, the elastomer is deformed (Fig. 9.6). Because there is no conductive material in the elastomer, the capacitance is changed by varying the applied pressure. For example, a parallel plate capacitor model is applied to the structure shown in Fig. 9.6. The capacitance is calculated using

$$C_0 = \varepsilon\varepsilon_0 \frac{S}{d} \tag{9.14}$$

where ε is the dielectric constant of the elastomer, ε_0 is the permittivity of space, S is the electrode area, and d is the distance between the electrodes (the thickness of the elastomer). By applying pressure, owing to deformation of the elastomer (Fig. 9.6), the distance decreases from d to $d - \Delta d$ $(= \varepsilon)$, resulting in increased capacitance.

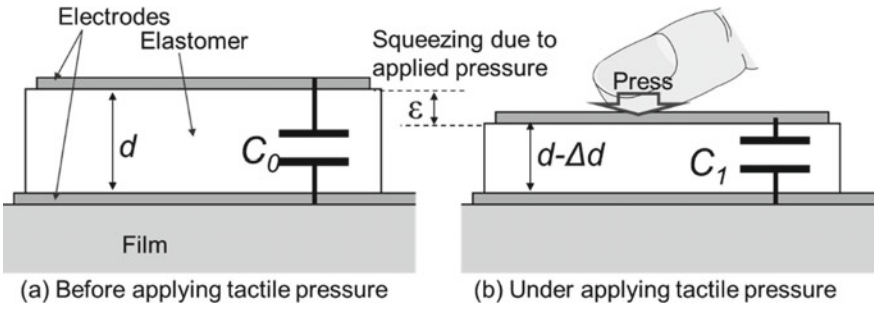

Fig 9.6 Sensing mechanism of a capacitive tactile pressure sensor. **a** Before applying tactile pressure and **b** on applied tactile pressure

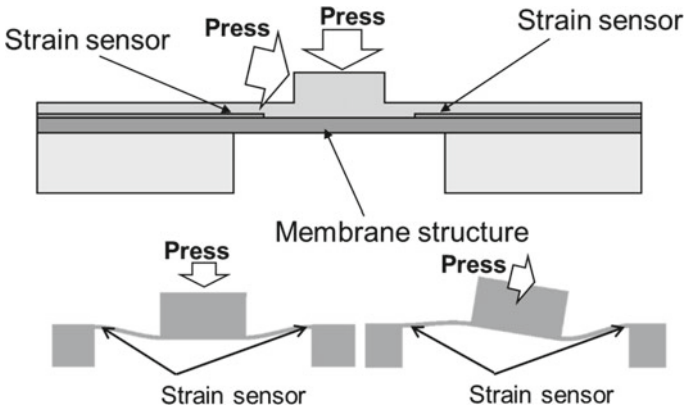

Fig. 9.7 Structure of a multi-directional tactile pressure sensor and its membrane structure change extracted using the finite element method. Reproduced with permission (Harada et al. 2014), Copyright 2014 American Chemical Society

From the capacitance change, the applied pressure is calculated. Characterization parameters to evaluate the sensor are almost the same as those for resistive sensors. Compared to the resistive type, it is not necessary to have conductive materials in the elastomer. Thus, these are easier structures to fabricate. However, sometimes owing to environmentally induced changes in the dielectric constant, the capacitance changes without applied tactile pressure. To prevent this effect, the electrical ground should be carefully designed, depending on the application. Furthermore, the readout circuit is somewhat complicated compared to that of the resistive type because of the capacitance measurement.

Multi-directional tactile pressure sensor

To imitate the functions of human skin or for different applications, multi-directional tactile pressure monitoring is sometimes required. For example, fingers usually detect tactile pressure and slipping forces to hold objects without dropping them. In this section, multi-directional tactile pressure/force sensors are briefly discussed. To monitor tactile pressure and slipping force, an out-of-plane structure like a fingerprint is prepared (Fig. 9.7). The structure is located on a membrane, and depending on the pressure direction, deformation of the membrane occurs. By monitoring this deformation change, the tactile pressure amount and direction can be measured by integrating a strain sensor surrounding the out-of-plane structure. This concept is also used for joysticks. Furthermore, in fact, if a mass is attached to the center of the membrane instead of the out-of-plane structure and the structure is optimized, this can be also used as an acceleration sensor (Yamamoto et al. 2016, 2017). Although this section has only explained one type of structure, there are probably other possibilities to monitor different forces and directions using strain/pressure sensors.

9.2.2 Temperature Sensor (Thermistor)

For soft robotic applications, important functions may be similar to those of human skin. As we have already discussed tactile pressure sensors in the previous section, this section explains temperature detection on a flexible film. Resistive temperature sensor (thermistor) mechanisms include three main types: negative temperature coefficient (NTC), positive temperature coefficient (PTC), and critical temperature resistor (CTR). The resistance of NTC decreases as the temperature increases, whereas the resistance of PTC increases with increasing temperature. For CTR, in a certain temperature range, resistance suddenly changes. These mechanisms depend strongly on material composition and structure. In this section, NTC-based temperature sensors are explained further. For flexible temperature sensors, mixtures of different materials are often used to realize solution-based fabrication on a flexible film. By mixing two materials, some junctions are formed between them (Fig. 9.8a). Owing to material differences, a barrier forms at these junctions, and this barrier suppresses current flow. However, as the temperature increases, electrons have more energy, resulting in more electrons passing through the barrier. As electrons behave as though they are jumping over the barrier, this mechanism is known as "electron hopping." The hopping probability changes depending on the barrier height and electron energy. By measuring the current flow, i.e., the resistance, as a function of temperature, activation energy, which is strongly related to the barrier height, is calculated using

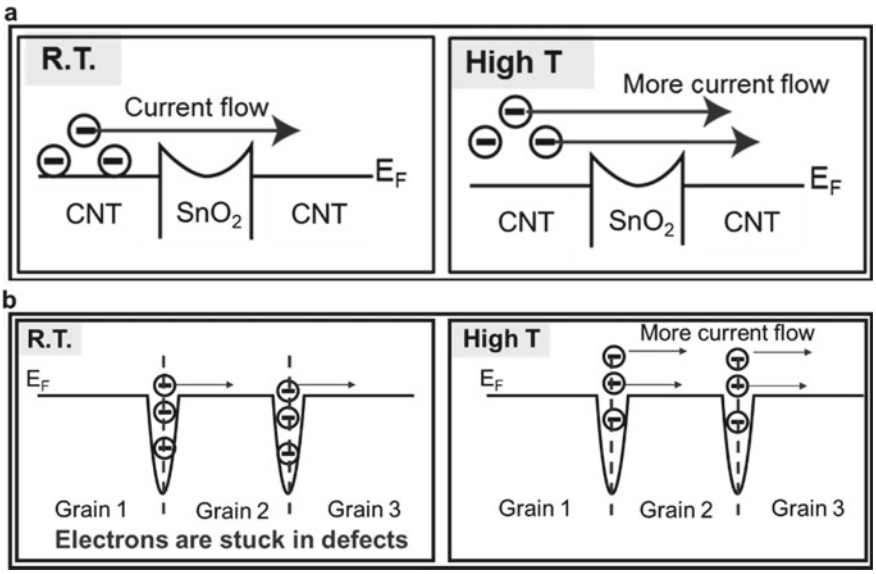

Fig 9.8 Sensing mechanisms of temperature sensors using **a** heterojunctions and **b** homojunctions with grains or defects

$$R = R_0 \exp\left(\frac{E_a}{2kT}\right) \tag{9.15}$$

where E_a is the activation energy, k is the Boltzmann constant, T is temperature, and R_0 is the resistance at the defined temperature. It should be noted, based on the equation, that the resistance does not change linearly as a function of temperature.

In addition to the heterojunction structure, sometimes multiple grained or defective single-material films are used as temperature sensors. This sensing mechanism is almost the same as the heterojunction sensor explained above. The only difference is that this single-material film sensor traps electrons in wells created by grain boundaries or defects (Fig. 9.8b), whereas heterojunction sensors use the barrier height to control the current flow. Briefly, at low temperature, most electrons are trapped in the well, such that electrons hardly exit the well, i.e., the resistance is high. However, at higher temperatures, electrons acquire sufficient thermal energy and exit the well more easily as free electrons, i.e., the resistance is low. As the mechanism of electron movement is the same as that in heterojunction sensors, the same equation can be used to calculate the resistance in both cases.

For temperature sensors, stability is one of the most important parameters. In particular, because it is used in soft robotic applications, the sensor itself has high probability of bending during use. To achieve stability and mechanical flexibility, strain distribution should be carefully considered. As discussed in the previous section, strain should be minimized under bending conditions by designing the sensor in the neutral region for strain. For this purpose, passivation/protection layers are required to cover the sensor, and it is better to fabricate thin sensor films to prevent the strain effect. By combining these two points, in general, the effect of strain can be eliminated. Furthermore, long-term stability should also be tested at different temperatures. Because temperature sensors require absolute values of temperature, long-term stability without sensor output drift is very important. Stability is often a problem when using solution-based temperature sensors.

9.2.3 Summary

In this section, fundamental mechanisms of tactile pressure and temperature sensors were explained for applications in soft robotics such as e-skin, which imitates functionalities of human skin. Various mechanisms have been reported previously. In this section, examples of common mechanisms were introduced, and depending on the application, different sensing mechanisms may be suitable. When a soft robot is designed, strain distribution, temperature effects, and detection of other stimuli should be considered for each application. For more specific details about sensor applications, the engineering literature should be consulted as this section offers only a few examples. Furthermore, if other sensing functionalities are required, it

is also possible to design and develop sensors, such as chemical sensors and other physical sensors. However, when they are integrated into the soft robot, bending and temperature effects should be characterized to monitor each stimulus separately and precisely because specific applications often change with strain and temperature.

9.3 Flexible and Stretchable Electronics and Photonics

When electronics or photonics are directly fabricated on a substrate on a film, the desired function can be achieved by constructing a multi-stacked structure of conductive, semiconductor, and insulating materials. The simplest device is wiring, which is achieved by simply forming a conductive material on the substrate. Transistors are typical elements of electronic circuits. Metal-oxide-semiconductor field-effect transistors (MOSFETs) are used in silicon technology, and thin-film transistors (TFTs), such as amorphous Si, and oxide semiconductors, such as indium gallium zinc oxide, are used in the field of flexible electronics. TFTs have a multistacked structure consisting of three electrodes (gate, source, and drain), an insulating layer that divides the gate and source/drain electrodes, and a semiconductor layer that controls the current modulation between the source and drain. Typical photonics include LEDs and photovoltaics. This method uses a semiconductor material that exhibits a photoelectric conversion effect. LEDs convert electricity to light and photovoltaics convert the light energy to an electrical output. In either case, the transparent electrode collects electrons or holes, and the counter electrode (not necessarily transparent) collects the other carrier. It has a structure in which photoactive semiconductor materials are laminated to be sandwiched between both electrodes, as shown in Fig. 9.9. Furthermore, each transport material is typically formed at the interface between the electrodes and semiconductors to improve the collection efficiency of holes and electrons.

9.3.1 Stretchable Wires

Normal metals and conductive polymers help achieve flexibility by forming on flexible substrates. The layer can withstand the force as long as it does not receive strains larger than its critical strain threshold caused by a harsh bending that includes an extremely small bending radius. Therefore, stretchability is an important research topic with regard to wires and conductors.

As discussed in Sect. 9.1.4, both structure- and material-based approaches can be considered. The structure-based approach can be applied to conventional nonstretchable conductive materials for use as stretchable wires. The strategies for achieving stretchable conductive materials can be classified into five categories (Matsuhisa et al. 2019). The first strategy uses liquid metals, such as eutectic gallium indium

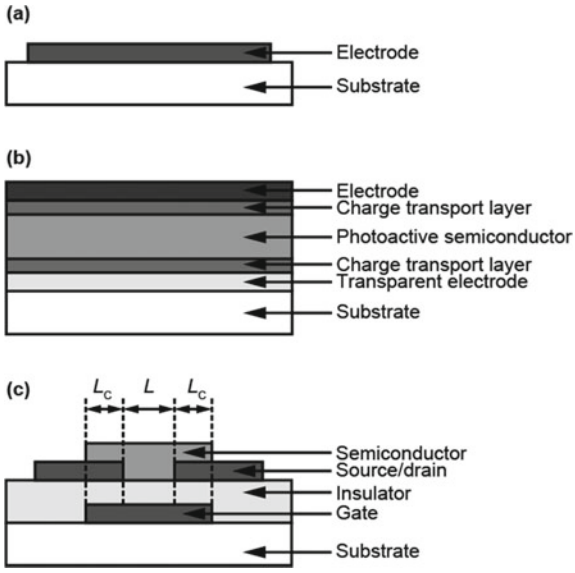

Fig. 9.9 Typical device structures for electronics and photonics: **a** wire, **b** photovoltaics, photodiode, or LED, and **c** thin-film transistor

(EGaIn). Theoretically, they have an infinite stretchability and a reasonable conductivity (> 10^4 S cm^{-1}). The second strategy uses ionic conductors. Hydrogels with ions or ionic liquids exhibit a high stretchability (> 600%), and their deformation has a negligible effect on ion conduction. They normally do not possess sufficient conductivity for wiring. However, a low sheet resistance can be obtained with an increased thickness. The third strategy uses conductive polymers because polymers have superior intrinsic stretchability compared to that of other materials. One of the most promising candidates for conductive polymers is poly(2,3-dihydrothieno-1,4-dioxin)–poly(styrenesulfonate) (PEDOT:PS). The fourth strategy uses metal nanowires with a high aspect ratio of length/diameter. Although each metal nanowire has limited stretchability, appropriately aligned nanowires with contact points exhibit mesh-like structures when stretched, which retains conductivity. In the fifth strategy, a composite of conductive and stretchable materials is fabricated. Stretchable materials, which are insulating for most cases, can support conductive networks of conductive nonstretchable materials during the application of stretching strains. The optimization relies on the type of materials used and the mixing method.

9.3.2 Photovoltaics

Energy harvesting is a principal technology in fabricating untethered soft robots. With such technologies, a battery can be recharged repeatedly in a discrete application. The required electric power should be carefully supplied. However, most

energy harvesting technologies cannot supply the required operating power for actuators. Therefore, energy harvesting technologies supply power to electronic components, such as sensors and circuits, in soft robots. In particular, the power output is normally proportional to the device area. Therefore, a large-area harvesting device with sufficient thinness and softness is an acceptable shape for soft robots.

Table 9.1 summarizes typical expected power output of various energy harvesting technologies. Energy harvesting from light, or a photovoltaic cell (a solar cell) can yield the highest power output when used under light conditions, particularly in the outdoors.

Figure 9.10a shows an equivalent circuit diagram of a solar cell. Actual solar cells have parasitic series resistance (R_s) and shunt resistance (R_{sh}), which are related to leakage current path. An ideal solar cell exhibits a zero R_s and an infinite R_{sh}. However, actual solar cells are not ideal and provide a lower efficiency than that of an ideal solar cell.

The performance of solar cells can be evaluated by recording their current density–voltage (J–V) characteristics, where J is the current per effective area of the solar cell. Figure 9.10b shows typical J–V characteristics of a solar cell. Principal parameters, such as the short-circuit current density (J_{SC}), open-circuit voltage (V_{OC}), fill factor (FF), and power conversion efficiency (PCE), can be obtained from the J–V characteristics. From the J–V curve, we can also draw the power per area P–V curve using the following equation:

$$P = JV \tag{9.16}$$

The maximum output power (P_{Max}) of the solar cell and the corresponding values of J and V (J_{Max} and V_{Max}) can be obtained using the P–V curve as follows:

$$P_{Max} = J_{Max} V_{Max} \tag{9.17}$$

The PCE η can be obtained as

$$\eta = \frac{P_{Max}}{P_{Light}} \tag{9.18}$$

Table 9.1 Summary of various energy harvesting technologies

Energy sources	Specific source	Power output (W cm^{-2})
Light	Outdoor (sun light)	$10^{-3} \sim 10^{-2}$
Light	Indoor light	$10^{-5} \sim 10^{-4}$
Vibration	Walking, machine	$10^{-7} \sim 10^{-4}$
Thermal/chemical	Body temperature, chemical reaction	$10^{-5} \sim 10^{-3}$
Radio wave	Broadcast wave, wireless LAN	10^{-6}

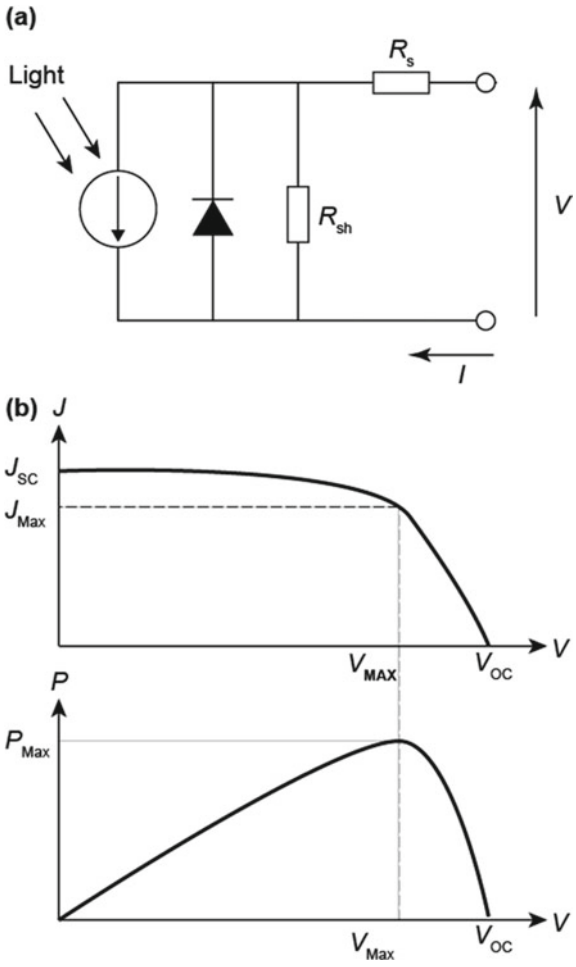

Fig. 9.10 **a** Equivalent circuit diagram of a solar cell. **b** Typical *J*–*V* and *P*–*V* curves of a solar cell

where P_{Light} is incident light intensity. Thus, PCE can be expressed as

$$\eta = \frac{J_{\text{SC}} V_{\text{OC}} \text{FF}}{P_{\text{Light}}} \tag{9.19}$$

where FF can be expressed as follows:

$$\text{FF} = \frac{J_{\text{Max}} V_{\text{Max}}}{J_{\text{SC}} V_{\text{OC}}} \tag{9.20}$$

In an ideal solar cell FF = 1; however, actual solar cells display FF values in the range of 0–1 because of R_{s} and R_{sh}.

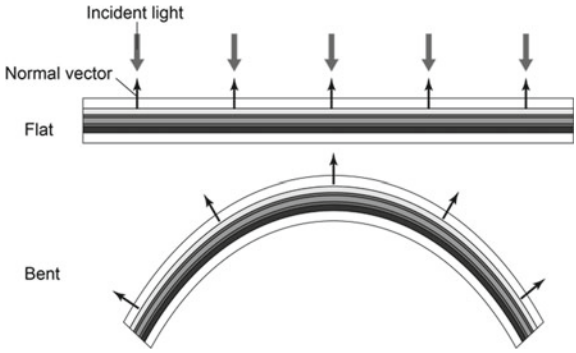

Fig. 9.11 Schematic illustration of two strain conditions (flat and bent) and normal vectors at some specific points on the effective area. In the flat condition, the angle difference between each normal vector and incident light is 0, whereas the angle at the specific point varies greatly for bent condition

When a solar cell is connected to a load, resistance matching is needed to achieve the largest power output. If the solar cell performance is independent of the effective area, the area can be modified to match the power output of the cell and resistance of the load.

The J–V characteristics of solar cells without (plane)/with (bending) strains should be considered to determine performance changes, particularly owing to changes in current. Moreover, the geometrical changes in the effective area should be considered to evaluate the performance under strains. Because the solar cell current value depends on the angle of the incident light, angles between the normal vectors and incident light at certain points in the effective area can determine the performance, as shown in Fig. 9.11.

9.3.3 Photodiodes

Photodiodes are the most commonly used flexible optical sensors (Yokota 2021). Their device structure and operation principle are the same as those of photovoltaics. A photodiode has a two-terminal structure, in which a transparent electrode, such as ITO, is an active layer for photoelectric conversion, and another electrode whose transparency is not required is vertically stacked. It can be easily integrated with switching elements, such as transistors. Therefore, they are often used in flexible image sensors. Normally, the operation bias of photodiodes is negative, whereas that of photovoltaics is positive. Photodetectors convert the light intensity to current. Therefore, the on–off current ratio between the light and dark conditions is a crucial parameter for photodetectors (Fig. 9.12). Other important parameters include sensitivity, responsivity, response speed, and linearity.

Moreover, wavelength response is an important parameter. Different wavelengths have different potential applications. Visible wavelengths can be used in normal imaging devices. The near-infrared region with a wavelength of 700 nm or longer has a high tissue permeability owing to the smaller absorption/scattering caused by water than those of ultraviolet and visible lights. Such light is typically used

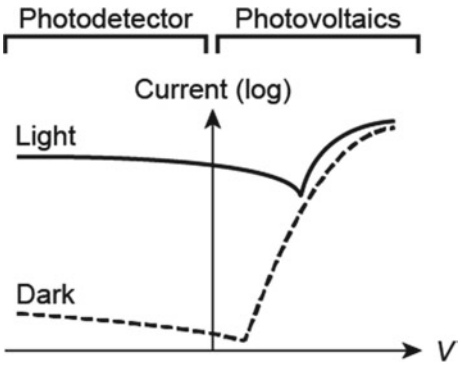

Fig. 9.12 Typical current–voltage curve of photodetectors

for in-vivo observations. Responsive wavelength can be modified by modifying the photoactive layer.

9.3.4 Thin-Film Transistors and Circuits

Transistors are most the commonly used switching elements in multipoint sensors and constitute an essential element in integrated circuits. In the field of flexible electronics, thin-film transistors can be used to achieve flexible integrated circuits. Amorphous silicon, polysilicon, metal oxides, carbon nanotubes, and organic semiconductors are potential semiconducting materials.

The cutoff frequency f_T is a key parameter that expresses a boundary in a system's frequency response at which energy flowing through the system begins to reduce (attenuated or reflected) rather than passing through. Thus, the cutoff frequency determines the operating speed of the transistor. In addition, the cutoff frequency of a field-effect transistor is often calculated as follows (Ante 2012):

$$f_T = \frac{\mu_{eff}(V_{GS} - V_{th})}{2\pi L(L + 2L_C)} \tag{9.21}$$

where μ_{eff} is the effective charge-carrier mobility, V_{GS} is the gate–source voltage, V_{th} is the threshold voltage, L is the channel length, and L_C is the contact length. The threshold voltage is the minimum gate-to-source voltage required to create a conducting path between the source and drain terminals. The contact length is the distance at which the gate electrode overlaps the source and drain contacts. This equation shows that higher effective mobility and decreased length are crucial to achieve a high operation speed; the effective mobility depends on the semiconducting material, and the length depends on the process.

Hybrid systems have been recently used to produce flexible integrated circuits. Silicon-based, extremely small, and rigid integrated circuits are used in hybrid

systems to secure a high frequency. The integrated circuits are mounted on a flexible film with other flexible device components.

Exercises

- (7.1) A device having thickness of 100 nm is fabricated onto flexible substrate having a thickness of 100 μm. Calculate the strain value of the device when the bending radius R of 5 mm is applied to the film. You can consider that device thickness is much smaller than substrate thickness.
- (7.1) Consider a three layer stacked structure, whose Young's modulus (E) and thickness (t) are given as follows: E_1: 2 GPa, t_1: 2000 nm, E_2: 4 GPa, t_2: 400 nm, E_3: 8 GPa, t_3: 200 nm. Calculate the neutral strain position (b) from the bottom surface and the strain value at top surface when the multistack film is bent at bending radius of 1 mm.
- (7.2) Initial resistance of a strain sensor based on tunnel current mechanism is 1 kΩ, and it increases to 1.5 kΩ under 10% tensile strain. What is the gauge factor of this strain sensor?
- (7.3) Calculate the fill factor (FF) and conversion efficiency of a solar cell whose other parameters are as follows: short current density (J_{SC}): 25.0 mA cm^{-2}, open-circuit voltage (V_{OC}): 0.820 V, current density at maximum power point (J_{Max}): 21.2 mA cm^{-2}, voltage at maximum power point (V_{Max}): 0.650 V.
- (7.3) Calculate the cut-off frequency of a transistor under the given parameters. Gate-source voltage (V_{GS}): 10 V, threshold voltage (V_{TH}): 0 V, effective mobility (μ_{eff}): 10 cm^2 V^{-1} s^{-1}, channel length (L): 1 μm, contact length (L_C): 1 μm.

References

Ante F, Kälblein D, Zaki T, Zschieschang U, Takimiya K, Ikeda M, Sekitani T, Someya T, Burghartz JN, Kern K, Klauk H (2012) Contact resistance and megahertz operation of aggressively scaled organic transistors. Small 8:73–79. https://doi.org/10.1002/smll.201101677

Cairns DR, Paine DC, Crawford GP (2001) The mechanical reliability of sputter-coated indium tin oxide polyester substrates for flexible display and touchscreen applications. In: Proceedings, annual technical conference—society of vacuum coaters, vol 666, pp 160–165. https://doi.org/10.1557/proc-666-f3.24

Fukuda K, Sekine T, Shiwaku R et al (2016) Free-standing organic transistors and circuits with sub-micron thicknesses. Sci Rep 6:27450. https://doi.org/10.1038/srep27450

Gleskova H, Wagner S, Suo Z (1999) Failure resistance of amorphous silicon transistors under extreme in-plane strain. Appl Phys Lett 75:3011–3013. https://doi.org/10.1063/1.125174

Harada S et al (2014) Fully printed flexible fingerprint-like three-axis tactile and slip force and temperature sensors for artificial skin. ACS Nano 8:12851–12857

Kim DH, Ahn JH, Won MC et al (2008a) Stretchable and foldable silicon integrated circuits. Science 320:507–511. https://doi.org/10.1126/science.1154367

Kim DH, Song J, Won MC et al (2008b) Materials and noncoplanar mesh designs for integrated circuits with linear elastic responses to extreme mechanical deformations. Proc Natl Acad Sci USA 105:18675–18680. https://doi.org/10.1073/pnas.0807476105

Kim D-H, Viventi J, Amsden JJ et al (2010) Dissolvable films of silk fibroin for ultrathin conformal bio-integrated electronics. Nat Mater 9:511–517. https://doi.org/10.1038/nmat2745

Lee H, Jiang Z, Yokota T, Fukuda K, Park S, Someya T (2021) Stretchable organic optoelectronic devices: design of materials, structures, and applications. Mater Sci Eng: R: Reports 146:100631. https://doi.org/10.1016/j.mser.2021.100631

Matsuhisa N, Chen X, Bao Z, Someya T (2019) Materials and structural designs of stretchable conductors. Chem Soc Rev 48:2946–2966. https://doi.org/10.1039/c8cs00814k

Park S, Fukuda K, Wang M, Lee C, Yokota T, Jin H, Jinno H, Kimura H, Zalar P, Matsuhisa N, Umezu S, Bazan GC, Someya T (2018) Ultraflexible near-infrared organic photodetectors for conformal photoplethysmogram sensors. Adv Mater 30:1802359. https://doi.org/10.1002/adma.201802359

Rich SI, Lee S, Fukuda K, Someya T (2022) Developing the nondevelopable: creating curved-surface electronics from nonstretchable devices. Adv Mater 34:2106683. https://doi.org/10.1002/adma.202106683

Seo K, Lee J, Jo J et al (2019) Highly efficient (>10%) flexible organic solar cells on PEDOT-free and ITO-free transparent electrodes. Adv Mater 31:1902447. https://doi.org/10.1002/adma.201902447

Woo YS (2018) Transparent conductive electrodes based on graphene-related materials. Micromachines 10:24–28. https://doi.org/10.3390/mi10010013

Yamagishi K, Takeoka S, Fujie T (2019) Printed nanofilms mechanically conforming to living bodies. Biomater Sci 7:520–531. https://doi.org/10.1039/c8bm01290c

Yamamoto Y et al (2016) Printed multifunctional flexible device with an integrated motion sensor for health care monitoring. Sci Adv 2:e1601473

Yamamoto D et al (2017) A planar, multisensing wearable health monitoring device integrated with acceleration, temperature, and electrocardiogram sensors. Adv Mater Technol 2:1700057

Yokota T, Fukuda K, Someya T (2021) Recent progress of flexible image sensors for biomedical applications. Adv Mater 33:2004416. https://doi.org/10.1002/adma.202004416

Chapter 10
Soft Actuators

Shingo Maeda, Yuhei Yamada, Hiroyuki Nabae, Kenjiro Tadakuma, Koichi Suzumori, Zebing Mao, Jun Shintake, Hideyuki Sawada, Yuya Morimoto, and Masahiro Shimizu

Abstract We will discuss typical soft actuators in this chapter. In the overview, we showed that actuators are generally divided into equilibrium and non-equilibrium types in terms of energy dissipation and efficiency. We introduce the following categories of soft actuators: fluidic actuators, electroactive polymer actuators, thermomechanical actuators, and bioactuators. Furthermore, the types of actuators are summarized. Finally, we discuss the mechanical properties and performance of the various actuators.

S. Maeda (✉) · H. Nabae · K. Suzumori · Z. Mao
Department of Mechanical Engineering, Tokyo Institute of Technology, Tokyo, Japan
e-mail: maeda.s.ao@m.titech.ac.jp

H. Nabae
e-mail: nabae.h.aa@m.titech.ac.jp

K. Suzumori
e-mail: suzumori.k.aa@m.titech.ac.jp

Z. Mao
e-mail: mao.z.aa@m.titech.ac.jp

S. Maeda · Y. Yamada · K. Suzumori
Living Systems Materialogy (LiSM) Research Group, International Research Frontiers Initiative (IRFI), Tokyo Institute of Technology, Yokohama, Japan
e-mail: yamada.y.bw@m.titech.ac.jp

K. Tadakuma
Tohoku University, Sendai, Japan
e-mail: tadakuma@rm.is.tohoku.ac.jp

J. Shintake
Department of Mechanical and Intelligent Systems Engineering, The University of Electro-Communications, Chōfu, Japan
e-mail: shintake@uec.ac.jp

H. Sawada
Department of Applied Physics, Faculty of Science and Engineering, Waseda University, Tokyo, Japan
e-mail: sawada@waseda.jp

K. Suzumori et al. (eds.), *The Science of Soft Robots*, Natural Computing Series,
https://doi.org/10.1007/978-981-19-5174-9_10

10.1 Overview

10.1.1 Introduction

An actuator is a device that controls the mechanical movement of a machine system. The word "actuator" is often used ambiguously. In this chapter, we define an actuator as any device that converts energy into mechanical energy. Unlike conventional actuators that are usually hard in the sense of the material and control mechanism, actuators with a soft body or fuzzy controllability are called soft actuators. Herein, we introduce a mathematical framework for actuators and discuss the meaning and role of "softness."

10.1.2 Mathematical Framework

We consider an actuator as "a system whose state at a given time is uniquely determined by a set of variables and that exerts a force on the outside through deformation." For simplicity, let us denote the variable that characterizes the shape of the actuator as x (which corresponds to the length if it is a piston-type actuator) and the variable that characterizes the force that balances the external load as f. We then consider a one-dimensional motion in which the direction of deformation and that of the force are parallel. Note that generalization of the discussion to a multidimensional case or transformation of variables to corresponding ones is straightforward.

When the state of the actuator is fully specified by x, f, and n variables $\boldsymbol{\theta} = (\theta_1, \theta_2, \ldots, \theta_n)$ that characterize the internal state, the variables are related by a function Φ as

$$f = \Phi(x, \boldsymbol{\theta}) \tag{10.1}$$

We refer to Eq. (10.1) as the equation of state of the actuator, and we denote the state of the actuator at time t as $(f, x, \boldsymbol{\theta}; t)$ (Fig. 10.1).[1]

Y. Morimoto
Department of Mechano-Informatics, Graduate School of Information Science and Technology, The University of Tokyo, Tokyo, Japan
e-mail: y-morimo@hybrid.t.u-tokyo.ac.jp

M. Shimizu
Department of Systems Innovation, Graduate School of Engineering Science, Osaka University, Toyonaka, Japan
e-mail: m_shimizu@nagahama-i-bio.ac.jp

[1] When we replace f with pressure P, x with volume V, and θ with temperature T, Eq. (10.1) corresponds to the thermodynamic equation of state. However, the variables here do not necessarily have to be thermodynamic variables; we can say that Eq. (10.1) is a generalized equation of the thermodynamic equation of state. Although this formulation apparently ignores the effect of hysteresis,

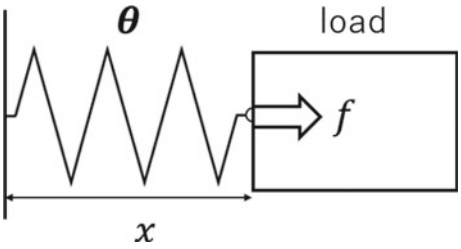

Fig. 10.1 Schematic of an actuator

10.1.3 Energy and Work

Actuators are often designed to work repetitively through cyclic operations. In this case, it is convenient to define efficiency as the ratio of the energy required to change the state of an actuator to the work output for a cycle. Suppose that, during time Δt, the state of the actuator changes by Δf, Δx, and $\Delta \boldsymbol{\theta}$. We denote the energy required to cause the change as

$$\mathrm{d}E[(f, x, \theta; t) \to (f + \Delta f, x + \Delta x, \boldsymbol{\theta} + \Delta \boldsymbol{\theta}; t + \Delta t)] \tag{10.2}$$

By repeating the change, we can define a sequential process that returns to its original state. We refer to the sequential process as a cycle and denote it by C. The energy required to realize the cycle can be expressed as

$$E = \oint_C \mathrm{d}E \tag{10.3}$$

We can calculate f and $\mathrm{d}x$, the displacement of x, for each small change in the state. Integrating the product of f and $\mathrm{d}x$ over a cycle, we obtain the work output W as

$$W = \oint_C f \mathrm{d}x \tag{10.4}$$

The efficiency of the actuator for a cycle C is then defined as

$$\eta_C = \frac{W}{E} \tag{10.5}$$

Depending on the nature of $\mathrm{d}E$, we can divide actuators into two types. Consider the process of time Δt maintaining its state. When the energy required for the process is zero, i.e.,

---

the effect can be discussed within the same framework if we can add variables that characterize the effect as $\boldsymbol{\theta}$.

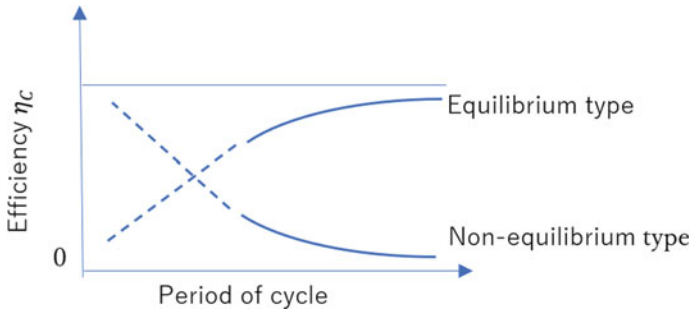

Fig. 10.2 Schematic of the relationship between efficiency and time for equilibrium- and non-equilibrium-type actuators

$$\mathrm{d}E[(f, x, \boldsymbol{\theta}; t) \rightarrow (f, x, \boldsymbol{\theta}; t + \Delta t)] = 0 \tag{10.6}$$

the actuator is classified as an "equilibrium-type." Examples include heat engines, shape-memory alloys (SMAs), piezo actuators, and dielectric elastomer actuators (DEAs). However, when the energy required for the process is not zero, i.e.,

$$\mathrm{d}E[(f, x, \boldsymbol{\theta}; t) \rightarrow (f, x, \boldsymbol{\theta}; t + \Delta t)] \neq 0 \tag{10.7}$$

the actuator is classified as a "non-equilibrium type." Examples include actuators that use electromagnetic motors and fluid pumps. The relationship between operation time and efficiency of actuators exhibits contrasting behaviors depending on the type. Because the dissipation of an equilibrium-type actuator becomes smaller with increasing Δt, E becomes the minimum at the limit of $\Delta t \rightarrow \infty$, which corresponds to the quasi-static process of thermodynamics. Subsequently, the η_C becomes maximum when the cycle is composed of the quasi-static process. However, in a non-equilibrium-type actuator, both the dissipation and E increase with increasing Δt because energy dissipation occurs constantly. Then, E becomes infinitely large and η_C becomes zero when the cycle is composed of the quasi-static process. In practical use, we can utilize some mechanisms such as valves for a non-equilibrium-type actuator to avoid energy consumption and maintain its state. We can then prevent the decrease in efficiency by increasing the time of a cycle (Fig. 10.2).

10.1.4 "Softness" of the Actuator

One of the characteristics of soft actuators is that they are composed of soft materials. Softness physically means that a large deformation is induced by a small force. When a tensile or compressive force is applied to an object, the stress–strain relationship between the "hard" and "soft" objects is typically represented as shown in Fig. 10.3. What effect does this softness have on the performance of actuators? As a typical

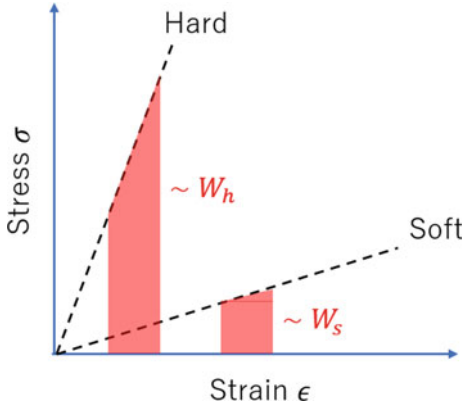

Fig. 10.3 Stress–strain relationship for hard and soft actuators

example, consider a one-stroke process of a piston-type actuator in which the control variable $\boldsymbol{\theta}$ is functionally switched stepwise from $\boldsymbol{\theta}_0$ to $\boldsymbol{\theta}_1$ at $t = 0$ and in which work is produced by quasi-static changes in x and f. Suppose that x increases monotonically during this process and $f \geq 0$. Additionally, suppose that x varies from x_0 to x_1 and that f varies from f_0 to f_1. The relationship between x and f during this process is expressed using the equation-of-state Eq. (10.1) as $\boldsymbol{\theta} = \boldsymbol{\theta}_1$:

$$f = \Phi(x, \boldsymbol{\theta}_1) \tag{10.8}$$

We now define the strain as

$$\epsilon = \frac{x_1 - x}{x_1} \tag{10.9}$$

and the stress σ is defined as the amount of f divided by the cross-sectional area A on which the force acts. The relationship between ϵ and σ then corresponds to the stress–strain relationship obtained from mechanical measurements when $\boldsymbol{\theta} = \boldsymbol{\theta}_1$. The work output of the process is equal to the integral of the stress–strain curve with the change in strain multiplied by $A \times x_1$. As shown in Fig. 10.3, compared with hard actuators, soft actuators usually encounter greater difficulty generating large forces, and the work produced by a soft actuator W_s tends to be smaller than that produced by a hard actuator W_h. However, when adaptability to the environment is considered, soft actuators are often more capable than hard actuators. Because soft actuators are deformable, they offer the advantage of allowing a certain degree of freedom in selecting the load. By defining the input energy as E_in, work output as W', and energy required for deformation as E_d, we can express the relationship as

$$E_\mathrm{in} = W' + E_\mathrm{d} \tag{10.10}$$

Here, we ignore the dissipated energy. Because hard actuators are difficult to deform, E_d becomes smaller than W' and the opposite takes place for soft actuators.

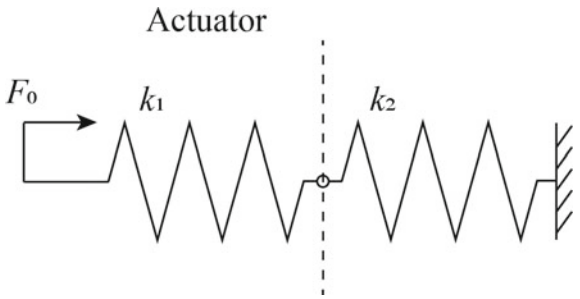

Fig. 10.4 Simple model of a soft actuator (and work object) using linear spring elements

Let us consider the energy distribution through a simple model in which the actuator and load are modeled using linear springs (Fig. 10.4). Parameters k_1 and k_2 are the spring constants of the actuator and load, respectively, and F_0 denotes the input force to the actuator. For example, in the case of a pneumatic actuator, this input corresponds to the force (or pressure) exerted by a pump and the elasticity represents the mechanical property of a composite composed of air and the actuator's body. Consider the energy E_d used to deform the actuator and the work W' performed on the load. The displacement of the actuator is F_0/k_1 and that of the load is F_0/k_2. Then, E_d and W' become

$$E_\mathrm{d} = \frac{F_0^2}{2k_1} \tag{10.11}$$

$$W' = \frac{F_0^2}{2k_2} \tag{10.12}$$

In the case of soft actuators, $k_1 < k_2$ and then $E_\mathrm{d} > W'$, as previously discussed. The present example is an extremely idealized model used to discuss the interaction between the actuator and load. In practical cases, we need to consider nonlinearities of elasticity to evaluate the energies, especially those for soft actuators, because they often exhibit large deformations in their operation. Moreover, other characteristics of the actuator, load, and interacting environment also affect the energy distribution. Such individual cases should be treated separately.

Finally, the discussion here is just a brief comparison of the softness of actuators.[2] Hard and soft actuators should not be treated as superior or inferior; they are complementary concepts. Both types of actuators are needed depending on the situation.

[2] We are discussing a typical case here; however, methods such as "soft-rigid switching," in which the stiffness is temporarily changed to increase the work output W', have also been proposed for soft actuators.

10.1.5 Types and Classification of Actuators

In this section, we focus on (1) the physical process of extracting work and (2) the state of the working material and describe the characteristics of each of these. Although there are various viewpoints for classifying actuators, we classify actuators for extracting motion into five major types: thermodynamic type, light type, mechanical type, electromagnetic type, and bio-type. We classified each type by the index of the control parameter and driving principle and organized the entire classification. The thermodynamic, light, mechanical, electromagnetic, and bio types correspond to the physical phenomena that govern each type.

Thermal actuators, SMAs/shape-memory polymers (SMPs) (Higuchi et al. 2009), and thermoresponsive gel actuators (Yeghiazarian et al. 2005) are typical examples of thermodynamic-type actuators. The fishing-line artificial muscle (Haines et al. 2014) is a thermal-type actuator. By fabricating the fiber structure in the form of a coil, researchers have achieved large expansion and contraction.

Piezoelectric actuators (Higuchi et al. 2009), DEAs (Ji et al. 2019), IPMC actuators (Kodaira et al. 2019), polyvinyl chloride (PVC) gel actuators (Li and Hashimoto 2016), and EHD actuators (Cacucciolo et al. 2019) are examples of electromagnetic-type actuators. There are several actuators whose control parameter is electric field (Table 10.1).

Importantly, the driving principles of actuators driven by electrostatic force, such as DEAs and HASELs, and those driven by ion conduction, such as IPMC actuators, differ fundamentally. In the field of artificial muscle research, electroactive polymers have been attracting attention as polymers that can be electrically driven (Cohen 2004).

Figure 10.5 shows the relationship among various actuators. Numerous graphs have been reported by many researchers. However, because the experimental conditions differ, the graphs are inconsistent. We therefore note that we created Fig. 10.5 intuitively. Herein, we used Huber et al. (1997) wherein the authors considered the process of one stroke, in which an actuator does work against a load. They defined actuation stress σ_a as the force divided by the cross-sectional area A on which the force acts and actuation strain ϵ_a as the displacement produced by the actuator divided by the original length L of the actuator.

10.1.6 Challenges

Throughout this section, we have discussed the characteristics of soft actuators. Although we have attempted to keep the discussion as general as possible, there are still some important issues that could not be addressed here. For example, the following issues were not discussed:

- How can we describe the efficiency in a non-steady state when considering the efficiency of equilibrium- and non-equilibrium-type actuators shown in Fig. 10.2?

Table 10.1 Classes of actuators

Type	Control parameter	Driving principle	Actuator
Thermodynamic type	Temperature	Entropic force	Thermal actuator
		Phase transition (solid)	SMA/SMP
		Phase transition (liquid–vapor)	Phase-change actuator/pouch motor
		Osmotic pressure	Gel actuator
	Concentration	Osmotic pressure	Gel actuator
		Equilibrium hydrogen pressure	Hydrogen storage alloy
Light type	Light	Photomechanical effect	Photomechanical actuator
		Photostrictive	Photostrictive actuator
Mechanical type	Pressure	Hydraulic pressure	Hydraulic actuator
		Air pressure	Pneumatic actuator
Electromagnetic type	Electric field	Piezoelectric effect	Piezoelectric actuator
		Electrostatic force	DEA
			HASEL
			ERF actuator
		Ion conduction	IPMC actuator
			Gel actuator
			Conducting polymer actuator
			PVC gel actuator
			EHD actuator
	Magnetic field	Magnetic force	Electromagnetic actuator
			MR fluid actuator
Bio type	Concentration	Molecular machine[3]	Bioactuator

- How can we calculate the work that the actuator can do on the object under a load? How can we calculate the efficiency in such a situation?
- What happens if the system shown in Fig. 10.4 is a nonlinear one? How can we generalize the actuator and the load?
- How can we understand the cycle of the actuator in finite time and dissipation in the actuator?

Here, we provide additional explanations of these issues. First, although we omitted the discussion of finite-time operation of actuators, it is a critical issue in

[3] Biological system is quite complex, and there are still many concepts about various mechanisms in living beings that are yet to be understood. Therefore, at present, it is quite difficult for us to state the driving principle of the bio-type actuators.

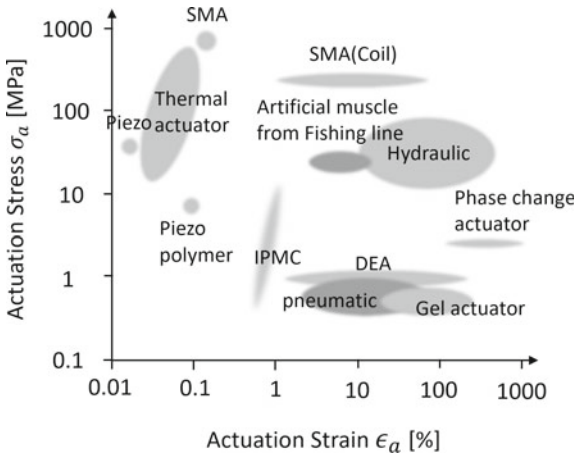

Fig. 10.5 Actuation stress–strain for actuators

actual applications. In most cases, soft materials take longer to respond to mechanical forces than hard materials. For example, when considering the work production by a periodic signal input, soft actuators will have an upper operational frequency limit because of the limited deformation speed. To calculate the operational frequency limit, we must consider the material's viscosity. Another critical issue is the interaction of soft actuators with loads. As discussed in Sect. 10.1.3, the work output depends greatly on the nature of the load. Although the same issue arises in hard actuators, it is more serious in soft actuators because a greater amount of energy is used to deform soft materials. In practical applications, the choice of load (or the design and selection of the actuator) that maximizes the work output is an important issue for improving energy efficiency. We need to develop systematic theories for methods of matching loads and actuators depending on the nature of the materials. Moreover, it is important to consider energy dissipation in soft actuators. In soft materials, heat dissipation is often associated with deformation. Because large and fast deformations of the material induce greater dissipation, understanding and controlling dissipation is important for soft actuators.

10.2 Fluidic Actuators

10.2.1 Introduction

Conventional fluidic actuators or cylinders consist of a hollow cylinder with a piston inserted into them (Fig. 10.6a). Fluidic actuators acquire power from a pressurized working fluid such as fluidic oil. Structurally, fluidic actuators consist of a cylindrical barrel in which a piston rod can move back and forth. To seal the fluidic actuators, the piston usually comprises sliding seals and rings. A biased pressure provided by a

mechanical pump is applied to the piston, which can move an external load. In the case of a single action, the piston can move unidirectionally when fluid pressure is applied to one side of the piston. A spring is then used to provide the piston a return stroke for a single-acting cylinder. As a force difference exists between the two sides of the piston, the piston can move from one side to the other. The fluidic actuators can precisely control the linear displacement of the piston when incompressible fluid is used as the working fluid. Conventional fluidic actuators are extensively used in numerous applications (e.g., excavators, vehicles, drilling rigs, and conveyors). Compared with their rigid counterparts, fluidic elastomer actuators (FEAs) are a new type of highly extensible, adaptable, low-power soft actuators that are flexible, resilient to perturbations, and safe for human–robot interactions (Fig. 10.6b). The fluidic actuation can be used to inflate the elastomer chamber and induce the desired deformation. Therefore, fluidic actuators are typically fabricated from advanced organic elastomers and are operated by the deformation of the chamber or embedded channels by pressurized fluids. These organic elastomers, which are readily available from commercial vendors (e.g., Dow-Corning and Shin-Etsu), have low hysteresis and high flexibility with low elastic moduli. Stress–strain curves of these elastomers are used to evaluate their suitability. The slope of the curves reveals some of the elastomers' properties, including their elastic modulus (E) and toughness (G). Therefore, the soft fluidic actuators rely on pressurization due to the used properties of the intrinsic materials (Polygerinos et al. 2017). FEAs operate pneumatically or hydraulically because fluids are advantageous for generating large forces at the expense of increased weight and viscosity.

Various FEAs have emerged since the earliest research in 1989 by Suzumori et al. (1992). They can be roughly classified into four types on the basis of their locomotion: expanding, contracting, twisting, and bending (Fig. 10.7). Fluidic actuators can

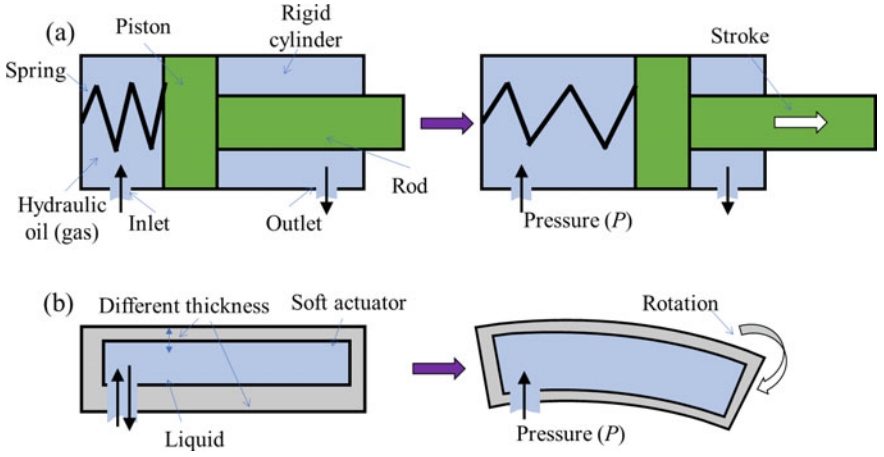

Fig. 10.6 **a** Conventional and **b** soft fluidic actuators

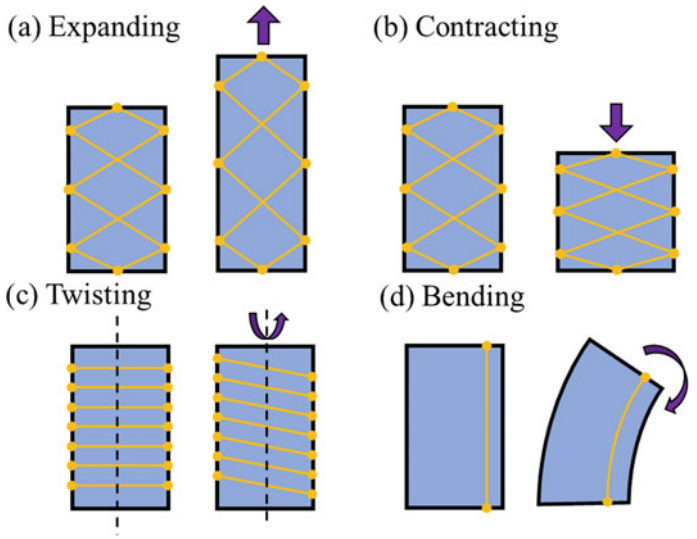

Fig. 10.7 Categories of fluidic actuators according to their deformation: **a** expanding, **b** contracting, **c** twisting, and **d** bending

be inflated by a pressurized fluid because of their carefully designed flexible structures. The structures of expanding and contracting actuators typically have symmetrical cross-sections; linear motion is induced as the fluid pressure is transmitted to the inner chamber. The famous contracting motion of McKibben actuators can be achieved using strain-limiting fibers (Hiramitsu et al. 2019). In twisting actuators, asymmetric structures composed of spiraling fibers can generate twisting motions. In the case of bending actuators, the design of the fluidic actuators is often asymmetrical, which enables deflection when a liquid is pressurized. When sophisticated fluidic actuators are studied, their motion path can be divided into one or more of the four aforementioned elements. Interesting or targeted motions such as gripping, rolling, quadrupedal locomotion, grasping, jumping, and snake-like undulation can be achieved via a combination of the four elements (Gorissen et al. 2017).

10.2.2 Fundamentals, Design, and Modeling

1. **Fundamentals**

Pressure (p or P) and flow rate (q or Q) are often used to evaluate the power driving a fluidic actuator. Pressure is defined as the force applied perpendicular to the surface of an object per unit area, which obeys Pascal's law (Elger et al. 2020). According to this law, when an external pressure is applied to an incompressible liquid, it is transmitted equally throughout the liquid (Fig. 10.8a). The SI unit of pressure is

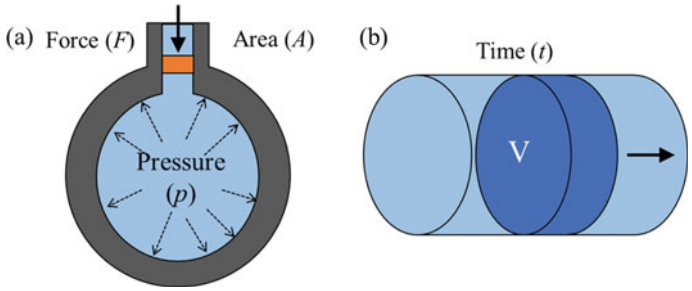

Fig. 10.8 Schematics demonstrating **a** Pascal's law and **b** the volumetric flow rate

pascal (Pa), which is defined as one newton per square meter (N/m^2). Pressure is calculated using

$$p = \frac{F}{A} \tag{10.13}$$

where p, F, and A are the pressure, the magnitude of the force, and the area of the contact surface, respectively. Fluid pressure, which often refers to the compressive stress at some point in a fluid, can be divided into two categories: open-channel flow (e.g., the ocean/atmosphere) or closed-conduit flow (e.g., a closed chamber). Soft fluidic actuators belong to the closed-conduit type. In the closed body of the soft liquid actuators, the fluid is either "static" or "dynamic." When the fluid is not moving, the pressure at any given point is referred to as the hydrostatic pressure. The following Bernoulli equation is used to determine the pressure at any point in a fluid. The underlying assumption is that the ideal and incompressible fluid is inviscid (i.e., lacks viscosity). Note that ρ, g, v, and z are density, acceleration of gravity, velocity of the fluid, and elevation, respectively.

$$\frac{p}{\rho g} + \frac{v^2}{2g} + z = \text{const.} \tag{10.14}$$

The flow rate is known as the volumetric flow rate, which is defined as the volume of fluid per unit time (Fig. 10.8b). The SI unit of volumetric flow rate is cubic meters per second (m^3/s). The change in volume is the amount of liquid that flows through the boundary within a given period. Therefore, the volumetric flow rate is defined as

$$Q = \frac{dV}{dt} \tag{10.15}$$

where V, Q, and t are the liquid volume, flow rate, and time, respectively. This volumetric flow rate is a scalar quantity because it is the time derivative of the volume and not the difference between the final and initial volumes at the boundary. To calculate the pressure and flow rate of fluid under complex conditions, we can

use the Navier–Stokes equations, which describe the motion of viscous fluids. The Navier–Stokes equations mathematically express the conservation of momentum and conservation of mass for Newtonian fluids (Constantin and Foias 1988). Although this equation is useful because it can describe many phenomena in fluidic engineering, it has not yet been proven to have smooth solutions. The equation can be written as

$$\frac{D\mu}{Dt} = \frac{1}{\rho}\nabla \cdot \sigma + f \tag{10.16}$$

where μ, t, ρ, σ, and f are the flow velocity, time, density, stress tensor, and body forces, respectively; $D\mu/Dt$ and $\nabla \cdot \sigma$ are the material derivative of μ and the divergence of the stress tensor, respectively.

2. **Design and Modeling**

Soft fluidic actuators have been designed using conventional three-dimensional (3D) computer-aided design (CAD) software. Because fluidic actuators relate to two or more fluid-related fields, including mechanics (large deformation), electronics, and chemistry, the design and modeling methods can be categorized into three types: empirical methods, mathematical methods, and finite element methods (FEMs). As fast design methods, empirical methods are primarily based on experimental results. Mathematical methods are beneficial for designing simple fluidic actuators with eccentric or three chambers, which can be easily explained on the basis of the Euler–Bernoulli beam theory. Even fluidic actuators subjected to external loads have been modeled in terms of edge and tip loading via a mathematical method. However, in some cases of delicate structures, explaining the relationship between the deformation and applied pressure through mathematic models is difficult. To address these limitations, more precise FEM models have been developed to optimize actuator geometry and couple it with large deformations of soft fluidic actuators.

10.2.3 Fabrication Techniques

Soft fluidic actuators can be fabricated using molding replication, 3D printing technology, or digital additive manufacturing. Among these, the most popular process is molding the elastomeric material to a structure with a fluid pathway and then adhering it to other fabricated molds (Shepherd et al. 2011). Fibers can be added to further modify the stiffness of soft actuators. The process mainly includes three steps: (a) preparing molds using machining or 3D printing technology; (b) casting the elastomer liquid into the molds; and (c) curing the elastomer using a thermal polymerization or photopolymerization process and subsequently removing the mold (Fig. 10.9a). Fluidic actuators can be fabricated at the microscale using stereolithography techniques. These miniature soft fluidic actuators can potentially be used in medicine (e.g., microsurgery). In addition, 3D printing technology (e.g., digital mask projection stereolithography) (Peele et al. 2015) and direct ink writing (Robinson et al.

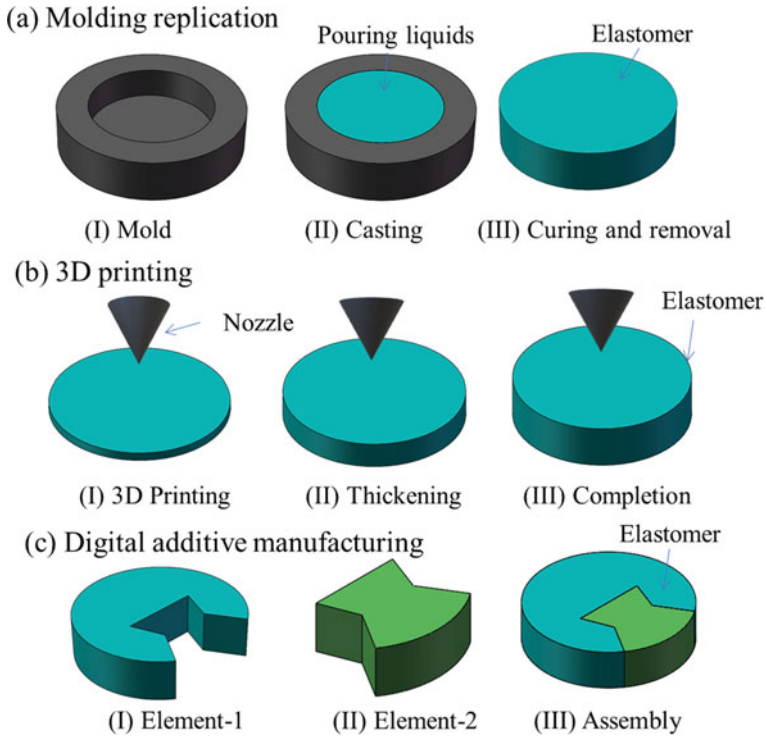

Fig. 10.9 Fabrication techniques: **a** molding replication, **b** 3D printing technology, and **c** digital additive manufacturing

2015) have been explored as alternative methods of producing soft fluidic actuators directly (Fig. 10.9b). Moreover, the digital additive manufacturing method is now emerging as a method for manufacturing soft actuators (Fig. 10.9c). The digital manufacturing method takes advantage of simple assemblers to complete traditional and complicated manufacturing tasks, similar to the use of tiles and bricks (Morin et al. 2014). The motions of soft fluidic actuators can be programmed by changing the stiffness of each block in the body. In addition, multifunctional devices can be realized by modifying internal structures.

10.2.4 Fluidic Pressure Sources

Fluid soft actuators are stretchable. However, their power source is often bulky and not entirely soft. Although numerous methods of driving fluidic actuators have been developed, we here focus on the actuators that operate on the basis of internal pressurization induced by fluids. The choice of fluid depends largely on the application. Fluids help produce large forces at the expense of increased viscosity and

weight. Here, we do not consider micropumps because it is difficult to power soft robots through them. The pressure sources of soft actuators can be mainly categorized into two types: offboard and onboard pumps. An offboard pump can be (a) an air compressor/microcompressor (Onal et al. 2017) (Fig. 10.10a), (b) mechanical hydraulic pump (Fig. 10.10b) (Katzschmann et al. 2018; Aubin et al. 2019; Xu et al. 2017), (c) thermomechanical pump (Garrad et al. 2019; Tse et al. 2020) (Fig. 10.10c), or (d) an electrostatic pump (Fig. 10.10d) (Acome et al. 2018; Diteesawat et al. 2021). An onboard pump can be (e) a chemical reaction pump (Fig. 10.10e) (Tolley et al. 2014; Wehner et al. 2016; Suzumori et al. 2013) or (f) a direct electricity–fluid conversion pump (Fig. 10.10f) (Cacucciolo et al. 2019; Mao et al. 2021).

1. **Air Compressor/Microcompressor (McKibben Artificial Muscle)**

Air pressure in soft robots is extensively used in many surgical robots, therapeutic applications, and wearable devices. Air, compressed by mechanical pumps, can be stored and released via various methods. Energy is transferred to the actuators as the pressurized air expands. Many soft actuators have been powered by an offboard air compressor or microscale air compressor to achieve simple or sophisticated motions. As one of the most efficient and commonly used fluidic artificial muscles, the McKibben artificial muscle is a prominent invention because of its simple design and the similarity of its behavior to that of human muscles (Kurumaya et al. 2016). The McKibben artificial muscle has an inner elastic tube, which is surrounded by

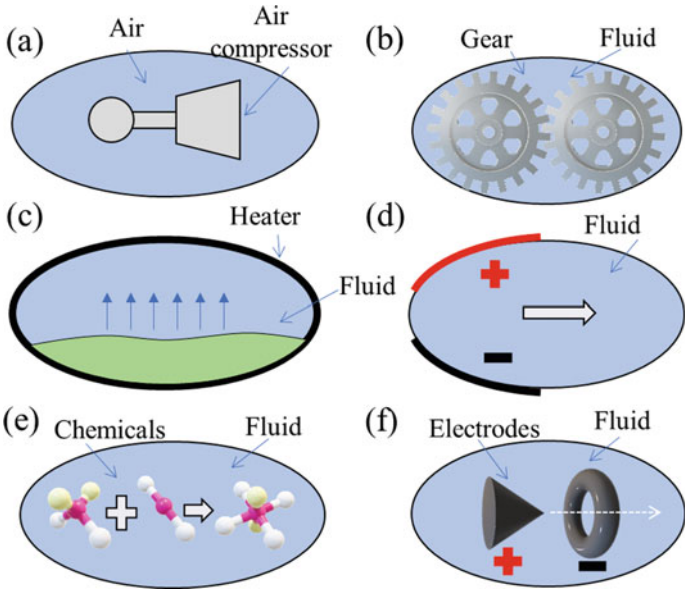

Fig. 10.10 Fluidic pressure sources: **a** air compressor/microcompressor, **b** mechanical hydraulic pump, **c** thermomechanical pump, **d** electrostatic pump, **e** chemical reaction pump, and **f** direct electricity–fluid conversion pump

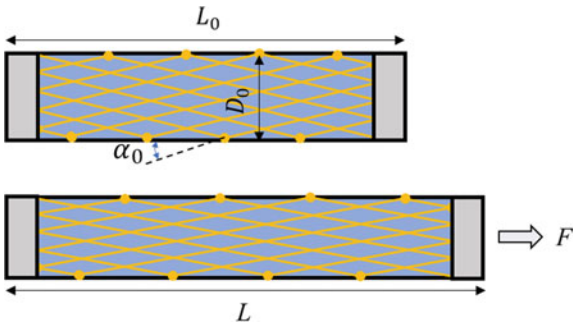

Fig. 10.11 Simplified geometrical model of a McKibben artificial muscle, where L is the initial length, L_0 is the length after stretching, α_0 is the initial braid angle, F is the actuating force, and D_0 is the initial muscle diameter

a double-helix-braided sheath (Fig. 10.11). The artificial muscle contracts when an internal pressure exists and returns to its original shape as the pressure is released. Therefore, if the McKibben artificial muscle is assumed to be completely cylindrical and distortion effects from the two ends and the frictional force between the flexible tube and mesh are neglected, the internal pressure (P) is given by

$$P = \frac{4F \sin^2 \alpha_0}{\pi D_0^2 \{3(1-\varepsilon)^2 \cos^2 \alpha_0 - 1\}} \tag{10.17}$$

where F, α_0, ε, and D_0 are the actuating force, initial braid angle, contraction rate, and the initial muscle diameter, respectively. The contraction rate can be defined as

$$\varepsilon = \frac{L - L_0}{L_0} \tag{10.18}$$

where L and L_0 are the initial nominal length and the length after stretching, respectively.

2. **Mechanical Hydraulic Pump (Gear Pump)**

Pneumatic energy sources are extensively used for actuating soft robots on the ground. By comparison, fluidic actuating systems can be used in underwater environments. Offboard fluidic pumps, which include gear pumps and impeller pumps, are often rigid mechanical moving parts integrated with several rigid components such as rotating valves. Such offboard pumps are also used in several systems such as sophisticated soft robotic fish (Katzschmann et al. 2018), electrolytic vascular systems (Aubin et al. 2019), and traditional fluidic systems (Xu et al. 2017). Because gear pumps have been reported to drive soft fluidic actuators, we here focus on gear pumps in terms of their working principle (Katzschmann et al. 2018).

The operating principle of gear pumps is to use the meshing of gears to pump fluids via displacement. As the gears rotate in the pumps, the void between two gears is occupied by the fluid. The gears then carry the fluid from the inlet to the outlet of the pump. Because of tight mechanical tolerances, leakage of liquid to the inlet can be effectively prevented. This meticulous design enables the pumping of

high-viscosity fluids. Structurally, gear pumps are divided into two main groups: internal and external gear pumps. The external gear pumps have two external spur gears, whereas the internal ones have an internal and external spur gear. A gear pump can produce a fixed-volume displacement; thus, the volumetric displacement can be described using

$$V = \frac{\pi}{4}\left(D_{\mathrm{o}}^2 - D_{\mathrm{i}}^2\right)L \tag{10.19}$$

where D_{o}, D_{i}, and L are the outer diameter, inner diameter, and width of the gear teeth, respectively.

3. **Thermomechanical Pump (Ball Actuators)**

A thermomechanical pump relies on the use of low-boiling point fluids (LBPFs), which can be transformed from the liquid state to the gaseous state by controlling the temperature (Garrad et al. 2019). In principle, exterior heat causes LBPFs to boil in the closed chamber, thus causing a shape change. This pump is highly compatible with FEAs because the fluids used in FEAs can be selected on the basis of their ability to undergo the liquid–gas phase change. When a compliant heating element is used, the phase-change process can function as a power source to actuate the gas. Also, other pumps based on the thermomechanical mechanism have been developed using super-coiled polymer (SCP) artificial muscles (Tse et al. 2020). The pump's structure is composed of a flexible bellow and SCP artificial muscles. Models of these two thermomechanical pumps are still under development.

4. **Electrostatic Pumps (Hydraulically Amplified Self-healing Electrostatic [HASEL] Actuators)**

Electrostatic actuators are attractive because they operate silently and exhibit high energy efficiency and self-sensing properties. By exploiting the electrical and hydraulic properties of dielectric fluids, researchers have developed some interesting actuators, including hydraulically amplified self-healing electrostatic (HASEL) (Acome et al. 2018) and electro-ribbon actuators. Structurally, two electrodes are zipped to pump the liquid via electrostatic forces. To complete the zipping process, a small amount of dielectric liquid is required to ensure that the two electrodes are placed at the closest possible position. When dielectrophoretic liquid zipping (DLZ) is used, this pump can pump either a gas or a liquid. The output energy ($E_{\mathrm{output}}(t)$) can be described using (Diteesawat et al. 2021)

$$E_{\mathrm{output}}(t) = (P_{\mathrm{atm}})(V_{\mathrm{in}} + V_{\mathrm{connector}}) \cdot \log\left(\frac{P_{\mathrm{i}} + P_{\mathrm{atm}}}{P_{\mathrm{a}}(t) + P_{\mathrm{atm}}}\right) \tag{10.20}$$

where P_{atm}, V_{in}, $V_{\mathrm{connector}}$, P_{i}, and $P_{\mathrm{a}}(t)$ are the atmospheric pressure, injected air volume, volume of the connecting tube, input power, initial pressure at no actuation, and the actuated pressure at time t, respectively.

5. **Chemical Reaction Pump (Combustion Actuators)**

Chemical reactors, such as those that operate by combustion (methane (butane) + oxygen) or peroxide decomposition, have been developed to realize directional jumping maneuvers and soft, autonomous robots (Tolley et al. 2014; Wehner et al. 2016). This type of pressure source can be operated portably and can generate pressurized gas or new chemicals using combustible fuels. To maximize the energy density of the fuel, pure oxygen is used instead of air. In this pump, an enriched oxygen environment is provided by the catalytic decomposition of H_2O_2. In the presence of a Pt catalyst, the following reaction occurs:

$$2H_2O_2(l) \rightarrow 2H_2O(l) + O_2(g) \tag{10.21}$$

Methane and butane are used as fuel because they are easily controlled to ignite the reaction, are commercially available, release sufficient energy, and work over a wide temperature range (Tolley et al. 2014; Wehner et al. 2016).

For methane, the reaction follows:

$$CH_4(g) + 2O_2(g) \rightarrow CO_2(g) + 2H_2O(l) \tag{10.22}$$

For butane, the reaction follows:

$$2C_4H_{10}(g) + 13O_2(g) \rightarrow 8CO_2(g) + 10H_2O(l) \tag{10.23}$$

If the temperature at the moment of ignition and the temperature after the combustion reaction are represented as T_1 and T_2, respectively, the generated pressure of the pump can be calculated as

$$P_2 = P_1 \frac{T_2}{T_1} \tag{10.24}$$

where P_1 and P_2 are the pressure at the moment of ignition and after the combustion reaction, respectively.

To achieve not only gas generation but also gas absorption, the following reversible chemical reaction can be used for driving fluidic actuators:

$$2H_2O(l) \rightarrow 2H_2(g) + O_2(g) \tag{10.25}$$

$$2H_2(g) + O_2(g) \rightarrow 2H_2O(l) \tag{10.26}$$

6. **Direct Electricity–Fluid Conversion Pump (Electrohydrodynamic Pump)**

Fluidic pressure can be achieved using functional/dielectric liquids under applied high voltages. The viscous forces generated by the liquid are used to drive the actuator. This pump, known as an electrohydrodynamic (EHD) pump, has been widely researched in recent years (Cacucciolo et al. 2019; Mao et al. 2021). The EHD jet can

be observed when the electrodes are connected to a power source. The EHD effect is governed by the electric force ($\vec{F}$), which can be expressed as (Stratton 2007)

$$\vec{F} = q\vec{E} - \frac{\varepsilon_0}{2}E^2\nabla\varepsilon_r + \frac{\varepsilon_0}{2}\nabla\left(E^2\frac{\partial\varepsilon_r}{\partial\rho}\rho\right) \tag{10.27}$$

where q, ρ, $\vec{E}$, ε_0, and ε_r are the charge density, density of the dielectric liquid, electric field, permittivity of vacuum, and the relative permittivity of the dielectric liquid, respectively. The electric forces include three types of forces—Coulomb force, dielectric force, and electrostriction force—that contribute to the pressure and flow rate of EHD pumps. In addition, the EHD flow can be described using the Navier–Stokes equation as follows:

$$\frac{\partial\vec{\mu}}{\partial t} = -(\vec{\mu}\cdot\nabla)\vec{\mu} - \frac{1}{\rho}\nabla p + \frac{\eta}{\rho}\nabla^2\vec{\mu} + \frac{1}{\rho}q\vec{E} \tag{10.28}$$

where $\vec{\mu}$, p, and η are the velocity, pressure, and viscosity, respectively. EHD jets and pumps have been used to drive various interesting actuators (e.g., finger, hand, and soft fish actuators).

10.2.5 Challenges

1. *Soft powerful and continuous pressure sources onboard*

Currently, most robotic systems in laboratories are strongly dependent on rigid, heavy, offboard power sources (e.g., air compressors or hydraulic pumps). These offboard pumps cannot easily be softened. Onboard pumps, such as chemical pumps that use combustible fuels, can generate instantaneous pressure. The reliability of the interfaces between the integrated electrical, chemical, pneumatic, and hyperplastic systems is still under investigation because the explosive forces can easily disable the system. Also, refilling fuel for chemical pumps is cumbersome and requires disassembling the robot, which eventually leads to difficulty in generating continuous pressure. In addition, direct electricity–fluid conversion pumps usually generate limited pressure, which makes actuating soft systems with loads difficult. Therefore, the development of soft, powerful, and continuous onboard pressure sources is urgently needed for fluidic actuators.

2. *Modeling of fluidic actuators driven by pressure sources*

Fluidic actuators powered by offboard pumps have been extensively studied because hydraulic and pneumatic systems have been well developed. In addition, two models for the relationship between hyperplastic deformation and fluidic systems have been developed. However, fluidic actuators driven by onboard pumps are difficult to model because their technology spans several fields, including the fluid, hyperplastics,

chemical, and electrical fields. This complexity complicates the modeling process for fluidic actuators, making dynamic models, in particular, difficult to develop.

3. *Untethered soft fluidic systems on the ground*

An autonomous, mobile system is necessary as an imperative part of the field of human–robot interactions, such as in search and rescue operations. However, most robotic systems in laboratories are strongly dependent on rigid and heavy power sources (air compressors or hydraulic pumps) connected via electrical tethers. Carrying heavy power sources and overcoming gravity can disable the locomotion of soft robots. Although untethered mobile systems that operate underwater have been developed, an untethered system (Kitamori et al. 2016) on the ground remains a formidable challenge in this field because the robots' ability to lift against gravity and the supply of power must be considered.

10.3 Electroactive Polymer Actuators

Electroactive polymers (or electromechanically active polymers, EAPs), refer to polymers that deform in response to external electric stimuli (Bar-Cohen 2004; Carpi 2016). EAPs are often referred to as artificial muscles because of the ability of the material to deform in response to stimuli (Mirvakili and Hunter 2018). In addition, these polymers are smart materials as they can be used to perform sensing and actuation (Shahinpoor 2020).

Two types of EAPs are widely used in soft robotics: dielectric elastomer actuators (DEAs) and ionic polymer–metal composites (IPMCs) (Carpi 2016; Shahinpoor 2020). Both materials deform in response to electrical stimuli. The difference is that in the case of the former material, the attraction of opposing electric charges directly moves the structure, whereas in the case of the latter material, the actuation is performed by the physical movement of mobile cations, that is, positively charged ions.

In the recent decade, DEAs and IMPCs have contributed to advancements in the field of soft robotics. This section describes the underlying principles, characteristics, materials, manufacturing methods, and applications of the two types of EAP actuators.

10.3.1 DEAs

Positive and negative charges attract each other. This attractive force, that is, the Coulomb force or electrostatic force, is the driving force for DEAs. Although the electrical deformation of solid materials was observed in the late eighteenth century, the operating principles of DEA were established in the late 1990s (Pelrine et al. 1998).

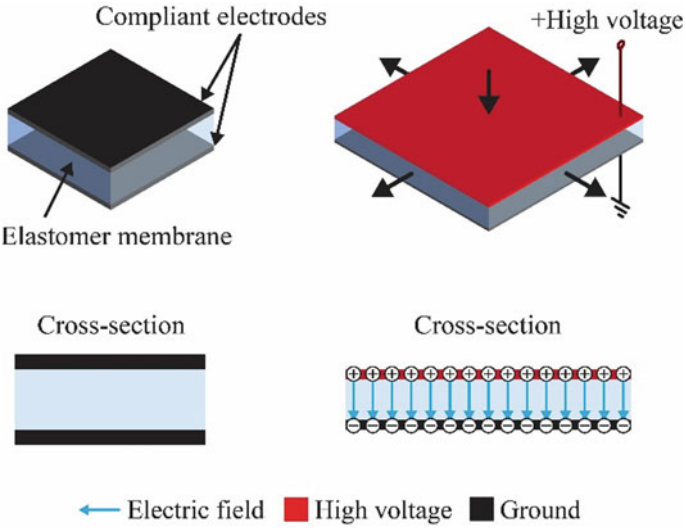

Fig. 10.12 Working principle of dielectric elastomer actuators (DEAs)

A typical DEA consists of a thin elastomer membrane sandwiched between compliant electrodes, as shown in Fig. 10.12. Elastomer is a general term for polymers with viscoelasticity. The Young's modulus of elastomers used in DEAs ranges from 0.1 to 1 MPa. When a high potential difference of several kV is applied between the electrodes, the elastomer membrane compresses in the thickness direction and expands in the planar direction as the opposing charges on the electrodes experience attraction. This deformation can be exploited as actuation motion. In addition, the current flowing through DEAs during actuation is approximately 100 μA because of the electrostatic nature.

DEAs can generate large deformations of over 100% strain with a fast response time of a few milliseconds and a high energy density of more than 3 MJ/m^3. Moreover, because of their simple structure, the electromechanical efficiency of DEAs, which is the rate of conversation of electrical input into mechanical output, is theoretically more than 90%.

The fundamental characteristic of DEAs, which enables the interconversion of electrical and mechanical inputs and outputs, is quasi-reversibility. Owing to this property, DEAs are often termed dielectric elastomer transducers. This property allows DEAs to be used as sensors or energy harvesting elements. DEAs, which have a simple structure consisting of an elastomeric membrane and a couple of electrode layers, can be used in a diverse range of actuator configurations. Moreover, these actuators can be adopted in robots of various forms in a wide range of scales, from millimeters to meters. In addition, DEAs, as mechatronic elements, have been applied in various scientific fields. Details regarding these applications can be found in the literature (Brochu and Pei 2010; Anderson et al. 2012; Rosse and Shea 2016; Gu et al. 2017; Guo et al. 2021).

Working Principle

In the actuation of DEAs, the electrostatic force that compresses the elastomer membrane in the thickness direction is known as the Maxwell stress and can be expressed as

$$\sigma_{\mathrm{M}} = \varepsilon_0 \varepsilon_{\mathrm{r}} E^2 = \varepsilon_0 \varepsilon_{\mathrm{r}} \left(\frac{V}{d} \right)^2 \tag{10.29}$$

where ε_0 and ε_{r} denote the permittivity of free space and relative permittivity (or dielectric constant) of the elastomer, respectively. E is the electric field between the electrodes, which is a product of the voltage potential difference V and membrane thickness d. Using Eq. (10.29), the strain in the thickness direction can be defined as

$$S_z = -\frac{\sigma_{\mathrm{M}}}{Y} = -\frac{\varepsilon_0 \varepsilon_{\mathrm{r}} E^2}{Y} \tag{10.30}$$

where Y is the Young's modulus of the elastomer. The sign of the strain is negative because the deformation is induced in the direction of decreasing membrane thickness. Assuming that the elastomer membrane is incompressible, that is, its volume is constant under deformation and the Poisson's ratio approaches 0.5 (as in the case of most elastomeric materials), the strains in the planar directions can be defined as

$$\begin{aligned} &(S_x + 1)\big(S_y + 1\big)(S_z + 1) = 1 \\ &\therefore S_x = S_y = (S_z + 1)^{-\frac{1}{2}} - 1 \end{aligned} \tag{10.31}$$

Equations (10.29) and (10.30) indicate that the actuation of DEAs is proportional to the relative permittivity, square of the electric field, and inverse of the Young's modulus. These equations can guide the selection and study of materials for DEAs. In general, soft elastomers that exhibit a high relative permittivity and dielectric strength are promising candidate materials. To enhance the relative permittivity and dielectric strength, fillers can be added to the elastomer materials, or the elastomeric membrane can be prestretched. The degree of prestretching determines the behavior of actuation. It has been experimentally demonstrated that prestretching an elastomer enhances its dielectric strength (Huang et al. 2012). Moreover, Eq. (10.29) indicates that a target actuation output can be achieved at low voltages with small membrane thicknesses. Therefore, previously, we focused on developing thin DEAs driven at certain voltages (for instance, to realize actuation below 500 V (Ji et al. 2018)).

Equations (10.29)–(10.31) represent the simplest and most basic expressions for modeling the actuation behavior of DEAs. However, the results often lack accuracy, particularly in the case of large deformations. In such cases, a hyperelastic material model that can consider the high stretchability and nonlinearity of elastomers can be used in analytical analyses, or a finite element analysis software can be used to model the actuator. ABAQUS (Dassault Systemes Co. Ltd.) and ANSYS (Ansys Software Pvt. Ltd.) are typical finite element analysis software used for such modeling. When

modeling DEAs, the presence of electrodes must be considered to obtain accurate predictions. In particular, electrodes are passive elements, and their stiffness and dimensions can affect the amount of resulting actuation.

Materials and Fabrication Methods

Acrylic and silicone materials are mainly used to prepare elastomeric membranes in DEAs. Acrylic elastomers usually correspond to a high output but low response speed, and silicone elastomers correspond to a low output but high response speed. Several types of these materials are commercially available as cured and formed tapes or sheets, for instance, as VHB 4905/4910 (3M Co. Ltd.) and ELASTOSIL Film 2030 (Wacker Chemie AG), which represent acrylic and silicone elastomers, respectively.

Despite the easy availability of such materials, commercial elastomers are often provided in an uncured, liquid state. Consequently, membrane fabrication must be performed, such as forming the material into a thin layer and curing it, and the related equipment must be procured. Thin elastomeric membranes can be prepared through centrifugal spin coating, spray coating, inkjet printing, 3D printing, pad printing, or blade casting. The formed membranes are then cured by heat or light, depending on the material characteristics.

Electrodes in DEAs can be prepared using a wide variety of materials, such as carbon grease, carbon black, carbon nanotubes, graphene, metal particles, silver nanowires, liquid metals, and conductive gels. These materials can be mixed with elastomers to endow conductivity. These electrode materials can be applied to the elastomer manually using a brush or in a manner similar to the thin-film forming process described previously.

Actuator Configurations

The actuator configuration is of significance to decrease the thickness and increase the area of the elastomeric film for usable movement.

Figure 10.13a summarizes the representative configurations of DEA prepared in the early stages of development (late 1990s to early 2000s), specifically, diamond-shaped, rolled, tubular, planer, folded, and bended configurations. In the diamond-shaped form, the expansion of DEA is converted into vertical extension using a structure equipped with flexible hinges. When a DEA is rolled, it exhibits elongation in the longitudinal direction. The tubular form operates with a similar principle, but its internal structure is hollow. In the planar form, the expansion of the DEA area is exploited as deformation in the plane. The movement direction depends on the shape of the DEA. For example, in the rectangular form, the lengthwise elongation is dominant. The elongation is transformed to bending actuation when a DEA is laminated onto a hinged structure or a flexible substrate, as in the folded and bended forms. The use of a hinged structure or flexible frame enables folding of the entire structure owing to the mechanical compliance. Notably, these configurations rely on the area expansion of the DEA. If thickness reduction is employed as the main actuation principle, the actuator exhibits a linear contraction such as that in a muscle.

This type of configuration is prepared by stacking multiple DEAs or folding a long DEA, as shown in Fig. 10.13b.

Soft Robotic Applications

The intrinsic compliance and diverse actuator configurations of DEA have enabled the development of various soft robots. Figure 10.14 shows several representative soft robotic applications based on DEAs. A soft gripper, shown in Fig. 10.14a, is suitable for grasping several types of objects. The device compliance allows the gripper to conform to the target in contact (Shintake et al. 2016, 2018a). This structural conformation at the interface is a type of automated behavior that simplifies control, and in certain cases, enables the accomplishment of tasks with only an on/off input.

As mentioned, DEAs operate through the application of a high potential difference of several kV. This aspect appears to imply that a high-voltage power supply or converter must be used to drive the actuators. However, miniaturized DC/DC converters, weighing only a few grams, can be used. Using such devices, untethered

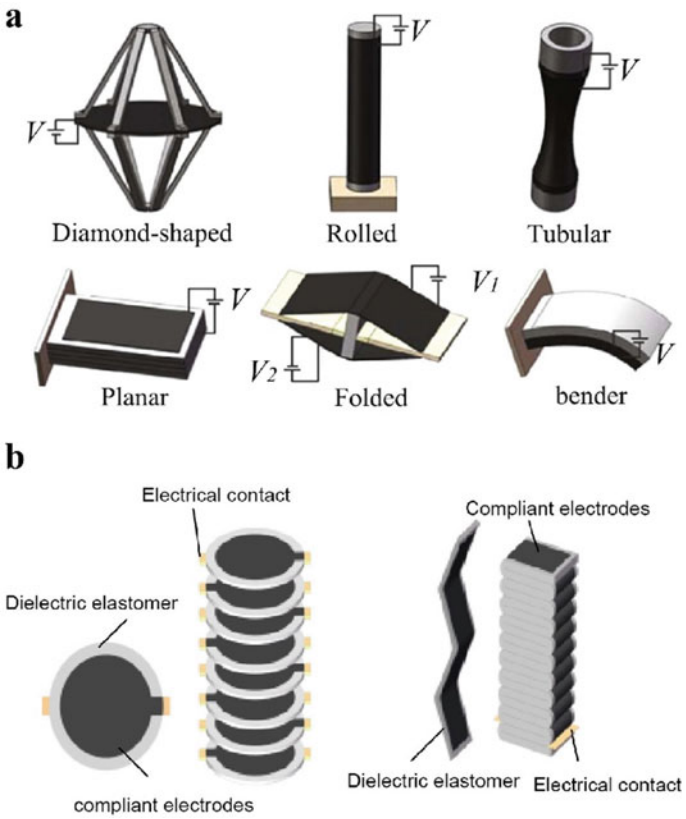

Fig. 10.13 **a** Typical configurations of DEAs, adopted from Gu et al. (2017). **b** Stacked and folded configurations, adopted from Wang et al. (2018)

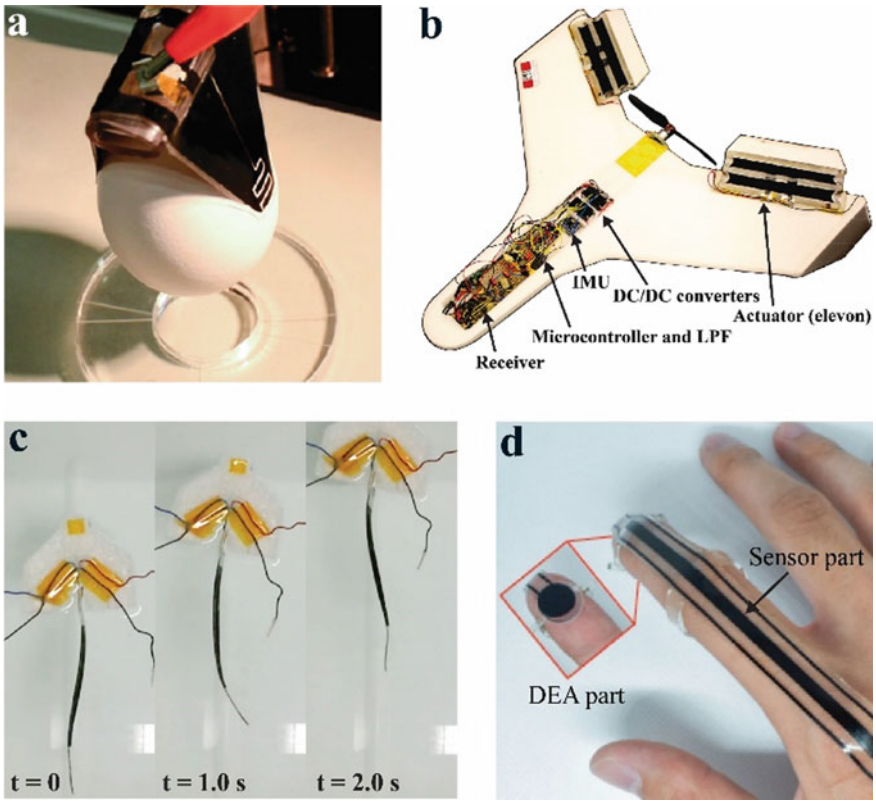

Fig. 10.14 Representative soft robotic applications based on DEAs. **a** Soft gripper. **b** Flying drone. **c** Underwater robot. **d** Multifunctional wearable device

DEA robots containing all the components, such as a driving circuit, controller, and battery, can be prepared. A representative device is shown in Fig. 10.14b, that is, a small flying drone with control surfaces made of DEAs (Shintake et al. 2015).

With sufficient insulation, DEAs can operate underwater. This property can enable the development of biomimetic underwater robots, as shown in Fig. 10.14c (Shintake et al. 2018b). In such robots, the short-circuiting of electrodes on the high-voltage side is prevented, although the electrodes on the outside are often not insulated. This configuration is established because the water surrounding the robot is used as the electrode on the ground side.

Because DEAs are soft and thin, they can conform to the surface of the human body and thus promote the realization of wearable systems. An example is haptic devices that can apply vibration and force. As shown in Fig. 10.14d, a circular DEA attached to the thumb can provide a vibrating haptic sensation, and through its multifunctional nature, it can detect bending deformation of the finger (Kanno et al. 2021).

This discussion demonstrates the high applicability of DEA to soft robotics. More types of robots, including practical systems, can be expected to be realized in the future.

10.3.2 IPMCs

IPMCs consist of a cation exchange resin membrane (thickness: 100–300 μm) with flexible electrodes attached on both sides (Asaka et al. 1995). To prepare the membrane, a sulfonated tetrafluoroethylene-based fluoropolymer-copolymer, also known as Nafion (DuPont Inc.), is commonly used because of its high water content ratio and cation exchange capacity. Gold and platinum are commonly used to prepare electrodes, although carbon materials, particularly carbon nanotubes, have attracted attention recently. Moreover, IPMCs can function as sensors or as polymer electrolyte fuel cell membranes for pumping fluid-driven soft actuators (Nabae et al. 2019).

A typical structure of IPMCs is illustrated in Fig. 10.15a. When a potential difference of a few volts (1–3 V) is applied to the electrodes, the cations in the membrane migrate to the negative side. This movement causes the negative side of the membrane to swell and the entire structure to bend toward the positive side, leading to a bending motion defined as actuation. The deformation of IPMCs is large, and more than 180° of bending actuation can usually be achieved. Because the actuation principle relies on the physical movement of ions, the speed of actuation is relatively low. An energy density of 5.5 kJ/m^3 has been reported (Park et al. 2008).

When an IPMC is bent by an external force, it generates a voltage of 0.1–1 mV corresponding to the amount of deformation, which allows it to act as a sensor, as represented in Fig. 10.15b. When water is filled around an IPMC and voltage is applied to the electrodes, hydrogen and oxygen gases are generated by electrolysis, as displayed in Fig. 10.15c. When the voltage application is terminated, water is synthesized by the gases. In this manner, the IPMC functions as a chemical pump for fluid-driven soft actuators.

As mentioned, gold is usually used to prepare the electrodes in IPMC actuators, although several researchers have employed platinum as well. Notably, platinum is extremely hard to bend and is often damaged by actuator movements. Gold is relatively soft and does not incur damage during actuation. To attach gold electrodes to a cation exchange resin membrane, non-electrolytic plating must be performed to ensure the mobility of ions between the membrane and electrodes, which is essential for actuation.

For IPMC sensors, non-electrolytic plating does not need to be performed. Instead, metal sheets can be simply placed on the surfaces of the cation exchanger resin membrane. However, the caustic action of the membrane must be addressed. For example, Nafion includes a sulfonate group, which acts as an acid and base in the presence of H^+ and Na^+, respectively. Therefore, aluminum and copper cannot be used as the electrodes because they will melt. In such scenarios, corrosion-resistant metals such as stainless and gold can be applied.

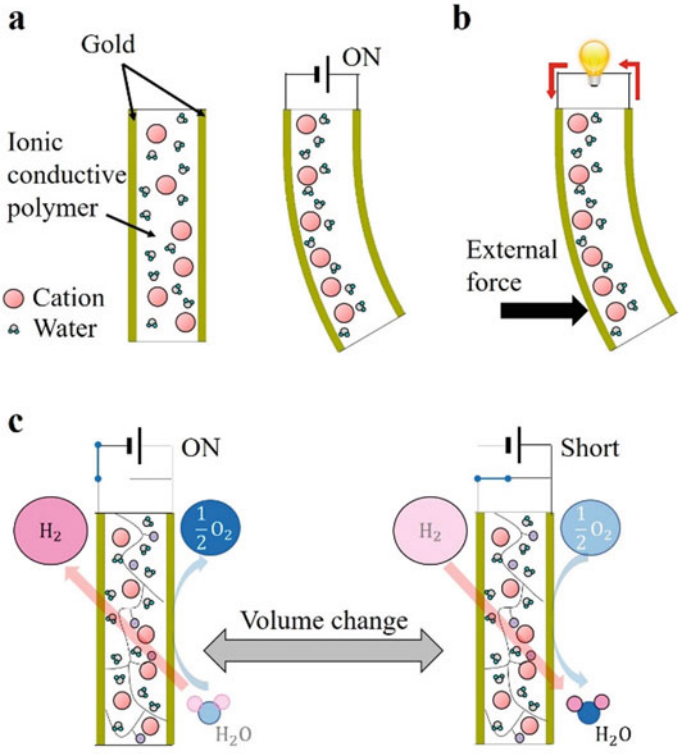

Fig. 10.15 Working principles of IPMCs. **a** Actuation. **b** Sensing. **c** Chemical pumping

Working Principle of IPMC Actuators

The performance of IPMC actuators is highly influenced by the length and thickness of the cation exchange resin membrane. Consequently, the geometric design of the actuator is of significance.

In a bending state, as shown in Fig. 10.16, the deformation of the actuator can be considered as strain in an infinitesimal interval of its length $\Delta l/l$, where l is the length of the device. The strain is influenced by the size and number of cations and magnitude of the applied voltage. In the case of thick IPMC actuators, the surface area and thickness of the electrodes are also important. In particular, to generate a large actuation, a material with large cations (for example, tetramethylammonium) must be used. Furthermore, increasing the membrane roughness by sandblasting prior to attaching the electrodes also increases the strain.

The strain of the actuator $\Delta l/l$ can be calculated considering the radius of curvature R. As shown in Fig. 10.16, Δx and L_{dis} are defined as the tip displacement and length between the actuator base and measurement point, respectively. Using the Pythagorean theorem, we obtain

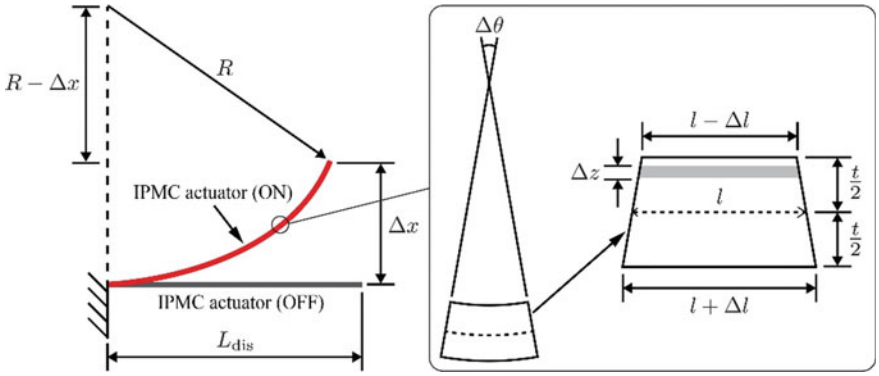

Fig. 10.16 Schematic of an IPMC actuator in a bending state

$$R^2 = (R - \Delta x)^2 + L_{\text{dis}}^2 \tag{10.32}$$

Transforming this equation yields the expression of R.

$$R = \frac{\Delta x^2 + L_{\text{dis}}^2}{2\Delta x} \tag{10.33}$$

The following relationship holds for R and the bending angle of infinitesimal interval, $\Delta\theta$.

$$\begin{cases} R\Delta\theta = l \\ \left(R + \frac{t}{2}\right)\Delta\theta = l + \Delta l \end{cases} \tag{10.34}$$

Transforming Eq. (10.34) yields

$$\Delta l = \frac{tl}{2R} \tag{10.35}$$

where t is the membrane thickness. The strain is defined as

$$\frac{\Delta l}{l} = \frac{t}{2R} \tag{10.36}$$

Substituting Eq. (10.33) into Eq. (10.36) yields

$$\frac{\Delta l}{l} = \frac{t\Delta x}{\Delta x^2 + L_{\text{dis}}^2} \tag{10.37}$$

According to Eq. (10.37), if $\Delta l/l$ is constant, t and Δx are nearly inversely proportional to each other. $\Delta l/l$ can be increased by increasing t because an actuator

with a large thickness has a large number of cations in the membrane. However, in this case, it is necessary to increase the surface area and thickness of electrodes.

The blocking force is another metric that represents the performance of IPMC actuators. The force can be calculated based on the power and moment generated by the expansion and contraction in an infinitesimal interval of an actuator. The moment M represents an integral ranging from $-t/2$ to $t/2$ of the moment of the volume illustrated in Fig. 10.16. M is calculated by multiplying the power by the distance from the neutral line in the actuator structure. The power is computed by multiplying the expansion by the spring rate, which is calculated using the Young's modulus of the cation exchange resin membrane E and actuator size.

$$\begin{cases} M = \int_{-t/2}^{t/2} \text{Power} \cdot z \mathrm{d}z \\ \text{Power} = \text{Expansion} \cdot \text{Spring rate} \\ \text{Spring rate} = E\frac{w\mathrm{d}z}{l} \\ \text{Expansion} = \Delta l \frac{z}{t/2} \end{cases} \tag{10.38}$$

where w is the width of the actuator. Transforming Eq. (10.38) yields an expression of M as

$$M = 2\int_{0}^{t/2} \Delta l \frac{z}{t/2} E \frac{w}{l} \mathrm{d}z = Ewt\frac{\Delta l}{l} \tag{10.39}$$

The blocking force F is defined as

$$F = \frac{M}{L_{\text{force}}} \tag{10.40}$$

Equation (10.40) can be rewritten as

$$F = \frac{Ewt}{L_{\text{force}}}\frac{\Delta l}{l} \tag{10.41}$$

Equation (10.41) indicates that when the length of the actuator (L_{force}) is large, the blocking force decreases because of the principle of leverage. Moreover, increasing the width and thickness of the actuator increases the blocking force. As described previously, the strain $\Delta l/l$ can be increased by increasing the thickness. Therefore, increasing the thickness is the optimal approach to increase the power and thus the force.

Soft Robotic Applications

Owing to their low-voltage application and simple structure, IPMCs are widely applied in soft robotics. Figure 10.17 shows several representative soft robotic applications based on IPMCs. The early developments were focused on using IPMC actuators in a tethered condition, and promising applications such as soft grippers (Fig. 10.17a) and underwater robots (Fig. 10.17b) were demonstrated (Bar-Cohen et al. 1998; Takagi et al. 2006). Recently, untethered robots were developed, as shown in Fig. 10.17c, in which electrical components such as a controller and battery were included. Because IPMCs can be driven at low voltages, a single cell lithium polymer battery can adequately power all the electric components. The bending motion of the actuator can be transformed to inchworm-like locomotion that drives the robot forward.

In addition to soft robots, the low-voltage application of IPMCs renders them suitable for medical devices. A representative example is shown in Fig. 10.17d, indicating the use of IPMC actuators in intraocular lenses (Horiuchi et al. 2017).

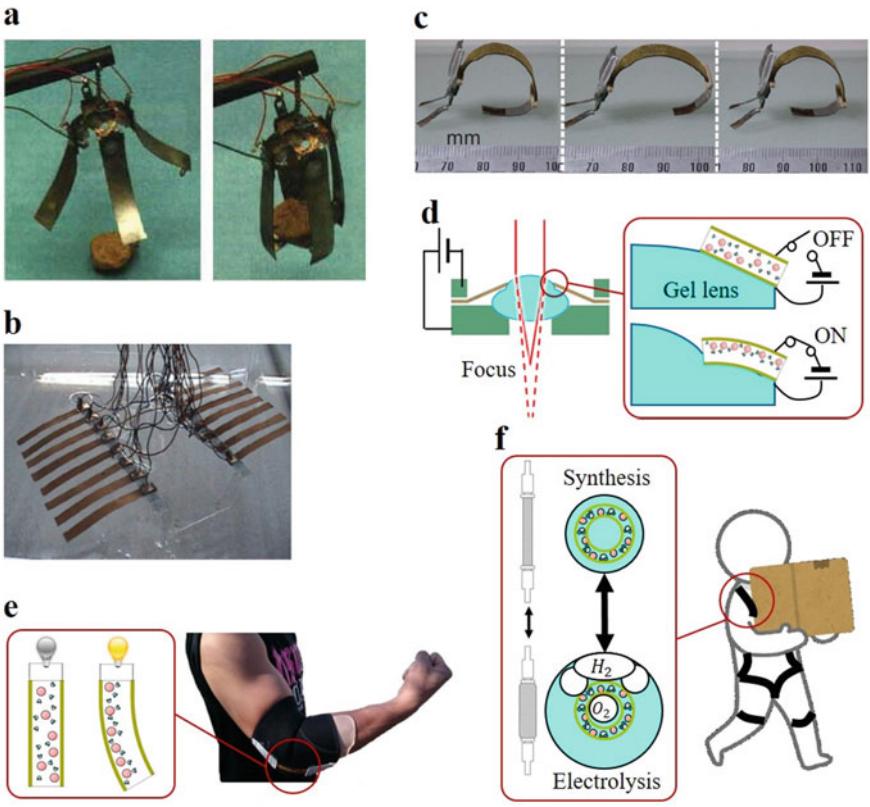

Fig. 10.17 Representative soft robotic applications based on IPMCs

Intraocular lenses are promising medical devices for cataract surgery. The extremely thin actuators can be used inside of the eye. When voltage is applied, the bending motion of the actuators deforms the gel lens part, leading to voltage-controlled focus change.

Another application of IPMCs is wearable devices to detect, for instance, the motion of a human joint, as shown in Fig. 10.17e. IPMC sensors are adequately soft to safely follow the deformations of the human body. When used as a chemical pump, IPMCs can drive power suits (Nabae et al. 2019), as illustrated in Fig. 10.17f. Conventional pneumatic power suits require the connection of tubes to supply air from an external source, which can limit the movement of workers wearing the device. IPMC pumps eliminate the need for introducing air tubes, and thus, the suits can be used in an untethered manner.

10.3.3 Future Outlook

Owing to their unique properties, such as intrinsic softness, simplicity, high performance, and multifunctionality, EAPs can serve as ideal actuators in soft robotics. To this end, further research and development must be performed in the areas of materials, structure, manufacturing, and implementation. These research efforts involve many scientific fields, such as materials, mechanics, electronics, and control. The advancement of EAP technology is expected to facilitate the development of soft robotics and related fields and to enrich future society.

10.4 Thermomechanical Actuators

10.4.1 Shape-Memory Alloy Actuators

A shape-memory alloy (SMA) is an alloy that remembers its original shape. It is deformable by the application of external force in the martensite phase at lower temperatures and returns to its pre-deformed shape when heated to transit into the austenite phase (Melton and Mercier 1981; Piao et al. 1992). Shape-memory alloys have been widely applied to various engineering and medical fields to introduce thermomechanical actuators such as shape-memory springs, thermo-reactive valves and catheters, and efficient energy transducers (Reynaerts et al. 1999; Singh et al. 2003; Kennedy et al. 2004; Fukui et al. 2004; Kim et al. 2006; Mizukami and Sawada 2006; Pan and Cho 2007; Juan et al. 2008; Bellini et al. 2009; Sun et al. 2011). Owing to their lightweight, compact size, and the generatable force, the SMA actuators are expected to act as alternatives to conventional electronic actuators, electric motors, and pneumatic and hydraulic actuators. Their transformation speed is, however, comparatively slow, since the phase transformation between the martensite and austenite phases is

led by the temperature, which is conducted by supplying heat to the material body or radiating heat to the surrounding environment.

A filiform SMA wire with the diameter of 50–100 μm presents unique characteristics, swiftly responding to temperature related to the martensite and austenite phases. By applying weak current to an SMA wire, heat is generated owing to internal resistance, and the wire shrinks by up to 5% lengthwise. When the current stops flowing and the temperature drops, then it returns to the original length. The SMA wire is thin and flexible enough to be cooled down right after the current stops flowing, and it returns to the pre-deformed length according to the temperature shifts from the austenite to martensite states. This means that the contraction and returning of the SMA wire can be precisely controlled by the properly prepared pulse current.

The authors have also discovered that the deformation caused by a given stress to a SMA wire generates a change in the electric resistance. With this characteristic, the SMA wire works as a force sensor with high sensitivity, while generating microvibration. The SMA wires have been applied to tactile displays and sensors that react to the force applied to the display by a user as a feedback (Hafiz and Sawada 2011; Zhao et al. 2012; Takeda and Sawada 2013; Jiang et al. 2014; Danjo et al. 2016, 2017; Geier et al. 2020; Chen et al. 2020). The detailed properties of an SMA wire are introduced herein, together with possible robotic applications.

10.4.2 Physical Properties of SMAs

SMAs display two representative effects as physical properties related with the body temperature and the applied force; they are the shape memory effect and pseudoelasticity, as shown in Fig. 10.18.

The shape memory effect, shown in blue in Fig. 10.18, is observed as a result of heat exchange in the body. An SMA in the martensite state is deformable under the application of a load, and the shape returns to the original one by receiving heat to transit to the austenite state. The transition between the martensite and austenite states is reversible under the application of heat to the body or the radiation of heat from the body.

The pseudoelasticity, on the other hand, is the phenomenon observed in the austenite phase, shown in orange in Fig. 10.18. A loaded SMA in the austenite state shows the deformation to transit to the martensite state, which is called stress-induced martensite phase, and the strain is released by removing the load. This transformation exhibits the change of electric resistance, and in particular, the transformation between the austenite state and R-phase shows a quick response in time.

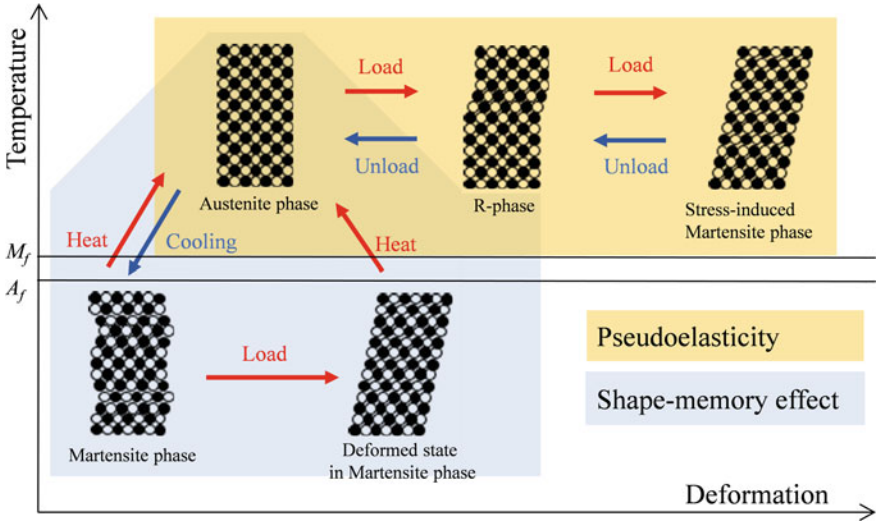

Fig. 10.18 Physical properties of the deformation of a SMA

10.4.3 Filiform SMAs for Micro-vibration Actuators

The authors have developed a micro-vibration actuator electrically driven by pulsed current. Figure 10.19 shows a vibration actuator composed of a 5-mm-long SMA wire with a diameter of 0.05 mm. On applying weak current to the alloy, the temperature rises to T_2 owing to the heat generated inside the wire body, and the length of the alloy shrinks by up to 5% of the original length. When the current stops flowing and the temperature drops to T_1 owing to heat radiation, the alloy returns to its original length. Figure 10.20 shows the temperature characteristics of the SMA wire employed in this study having the specific temperatures $T_1 = 68°$ and $T_2 = 72°$ (Mizukami and Sawada 2006).

The SMA wire is so thin that it rapidly cools down after the current stops flowing and returns to its original length when the temperature shifts from T_2 to T_1. This

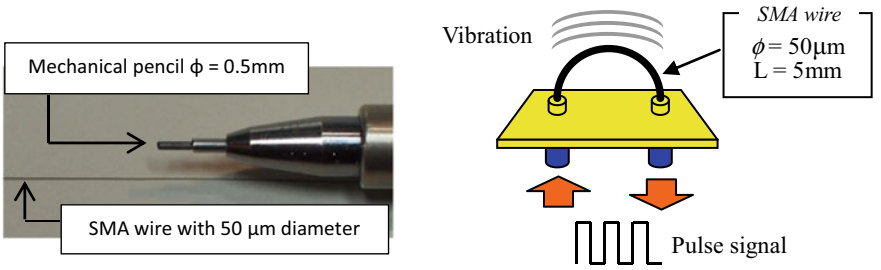

Fig. 10.19 SMA wire and vibration actuator

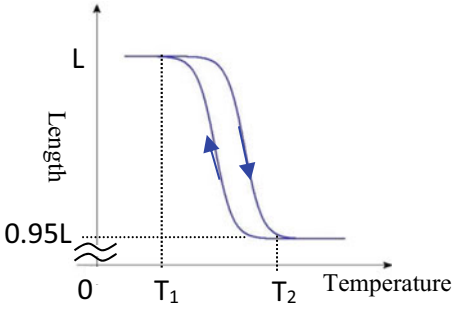

Fig. 10.20 Temperature characteristics of an SMA wire

means that the shrinkage and the return to initial length of the SMA wire can be controlled by controlling the pulse current. By driving the SMA wire with pulse current as shown in Fig. 10.21, micro-vibration with an amplitude of several micrometers is generated, which is perceived by the human body as tactile sensation although the vibration is invisible. We employed pulse-width modulated (PWM) current to control the vibration mode of the SMA wire generated from a specially designed amplifier. The control pulse signal has the amplitude of H (V) and a width of W (ms). The duty ratio W/L determines the heating and cooling time of the SMA. $W \times H$, which is equivalent to the calories exchanged during the lengthwise deformation, determines the amplitude of a vibration, and the vibration frequency is completely controlled by regulating L. While generating micro-vibrations of 50 and 100 Hz, a high-speed camera verified that the SMA wire perfectly synchronized with the ON/OFF pulse current and shrunk in the contraction state to approximately 2 μm lengthwise. We confirmed that the vibration frequency was properly controlled up to 400 Hz by the pulse current using our control circuit.

The actuator has an advantage of a compact structure, together with the low energy consumption of approximately 10 mW that enable it to quickly respond to generating vibration. We have also developed a simple structure to amplify the vibration displacement (Zhao et al. 2012). One of the amplification methods is to employ a pin, as shown in Fig. 10.22, which illustrates the structure of the pin-type

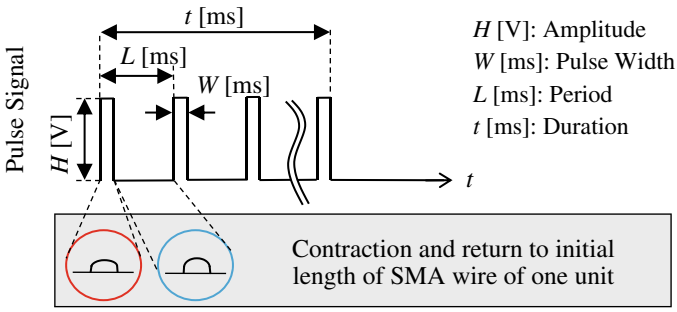

Fig. 10.21 Pulse current for driving SMA actuators

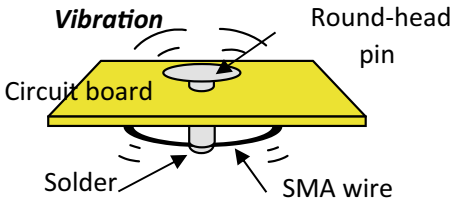

Fig. 10.22 Pin-type actuator

actuator consisting of a 50 μm (diameter) × 3 mm (length) SMA wire and a 1.5 mm (diameter) × 3 mm (length) round head pin. The tip of the pin is soldered at the middle of the SMA wire so that the micro-vibration is efficiently conducted to the pin to be mechanically amplified at the round head.

10.4.4 Application to Tactile Displays

Frequency-controlled vibration generated by the SMA actuators is efficiently applied to present various tactile sensations to human skin. A tactile display is constructed by arranging multiple vibration actuators. Figure 10.23 shows five examples of tactile displays developed in our laboratory, namely (a) tactile mouse, (b) tactile pen, (c) tactile pad, (d) tactile glove, and (e) Braille display. The tactile mouse is equipped with 16 actuators arranged in a 4 × 4 matrix. The 16 actuators are independently driven by the current-control amplifier to present various tactile sensation synchronizing with pictures and movies in a visual display.

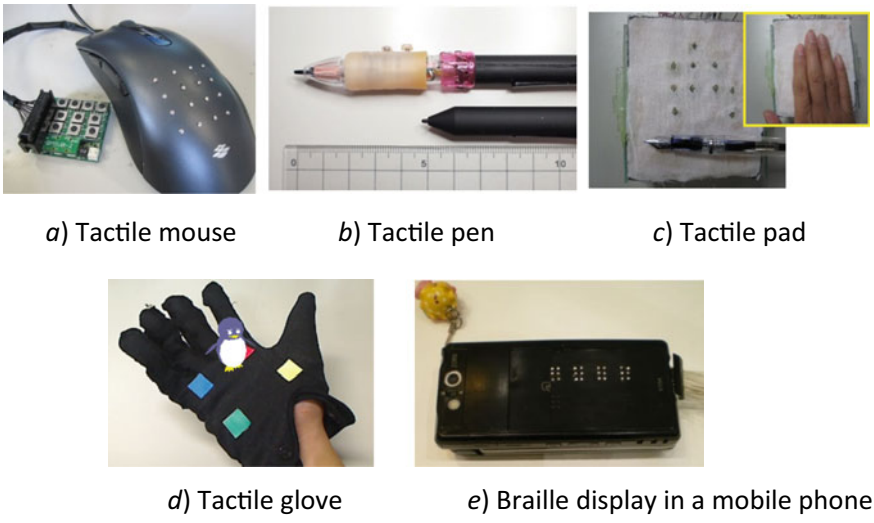

Fig. 10.23 Tactile displays using SMA actuators

Humans feel the texture sensations of an object by touching it with the hand and are also able to imagine the surface textures and tracing sensations from visual information. We tried to extract visual features from a picture by using an image processing technique, and then converted them into pulse signals by selectively determining the frequency, amplitude, and duty ratio (Takeda and Sawada 2013; Jiang et al. 2014). We paid attention to the cyclic patterns included in a picture and tried to relate them with the features of tactile sensations. Cyclic patterns were extracted using Fourier Transform, and parametric values were obtained as the spatial frequency and spectrum amplitude. By relating the spatial frequency with the pulse frequency and the spectral intensity with the duty ratio of a pulse signal, the driving pulse signals for tactile actuators can be automatically generated. In addition, the tactile sensation perceived while stroking an object surface should be changed according to the speed of the hand motion.

In this study, we assumed the following relations among the spectral features of a texture image and the presented tactile sensations:

$$f_{\mathrm{p}} = \alpha\left(v_{\mathrm{p}}\right) \cdot g(f_{\mathrm{s}}) \tag{10.42}$$

$$p_{\mathrm{w}} = h(i_{\mathrm{s}}) \tag{10.43}$$

where f_{p} represents the driving pulse frequency, p_{w} shows the pulse width, f_{s} presents the spatial frequency extracted from an input image, i_{s} represents the spectral intensity of the second peak in a FT image, and v_{p} presents the speed of a stroking motion on an object. The function α modifies the driving frequency of the actuators according to the speed of the hand motion so that the user perceives the different responses of a tactile sensation reacting to the actions. The functions α, g, and h give the conversion from the image features and user's stroking actions into the driving parameters for the tactile actuators, which are determined by experiments conducted by users.

10.4.5 Application to Fish Robots Having Flexible Bodies

The flexibility of SMA wires are applicable to the bending motion of soft robots (Chen et al. 2020). The authors developed a bionic robotic fish having a soft tail. Two sets of SMA wires were stitched to the two sides of the silicone-fabricated soft tail, allowing the tail to bend on either side, as shown in Fig. 10.24.

The robotic fish body is divided into two parts, a hard body shell in which control systems are installed and the soft silicone tail. The control system includes a control circuit, an infrared transmitter/receiver, and a compact rechargeable lithium battery, and all of them are installed inside the body shell, as shown in Fig. 10.25, to realize an untethered swimming control.

By alternately supplying pulse current to the SMA wires settled in the two sides of the fin, the fin undergoes a flipping motion to propel in water. The swinging motion

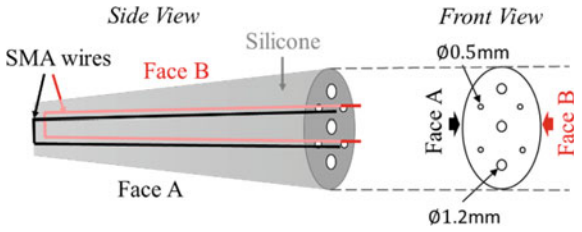

Fig. 10.24 Bionic robotic fish tail using SMA actuators

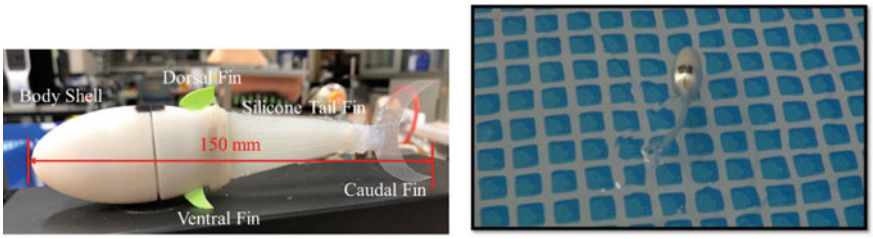

Fig. 10.25 Untethered bionic fish robot using SMA actuators and its swimming behavior

of the fin is controlled by the frequency of pulse current. For example, a 0.5 Hz fin motion implies slow swimming, while a 3 Hz motion implies swift swimming found in the escaping behavior.

10.4.6 Challenges

In this chapter, novel micro-vibration actuators using shape-memory alloy wires were introduced. As applications, first, the tactile displays consisting of filiform SMA wires with a 50 μm diameter were presented. The display generated micro-vibrations with various frequencies to display various tactile sensation synchronizing with visual and auditory information for VR/AR applications. The actuator features compactness and low energy consumption and is applied to mobile tactile displays and tactile interaction systems by attaching or stitching SMA wires to any surface of a conventional interface device. Second, the application of bionic soft robotic fish was presented. Two SMA wires were installed in the silicone-made fin, and the behavior of bionic fish was successfully realized.

10.5 Bioactuators

10.5.1 Biohybrid Frog-Like Robot

One method for studying the motion of living organisms is to use a biohybrid robot in which a part of the living organism is replaced by a machine. This system is also interesting as an engineering system that directly implements the adaptability of an organism into a machine. In this section, we introduce a bio-muscle-driven frog robot developed by us that implements the muscles of the African clawed frog, which performs excellent swimming locomotion using its legs. Experimental results showed that the frog robot equipped with bioactuators can be driven outside the culture medium.

Movement of living organisms is caused by the interaction between the nervous system, musculoskeletal system, and environment. One method to intervene between these interactions and study their dynamics is to use a biohybrid robot. This method replaces a part of a living body with a machine and investigates changes in its behavior. In this study, we focused on the African clawed frog, Xenopus, which has excellent swimming locomotion, and we created a bio-muscle-driven frog-like robot that realizes the locomotion function of frogs. Frogs have been used in many biohybrid robots that used biological muscles in the past because of their ease of handling, such as the removal of muscles. When biomuscle is driven outside of the culture medium, it has the disadvantage of shorter drive time owing to desiccation and internal ion leakage. Therefore, in previous studies, water tanks were filled with culture medium and the robots were driven inside the tanks. However, this method does not allow the robot to be driven outside of the culture medium, which is a problem that needs to be solved. The authors have developed a bioactuator that packages biomuscle and culture fluid, prevents contact between the biomuscle and the driving environment, and transmits the output of the muscle to the robot.

Various studies have been conducted on the biohybrid robot using frog muscles. Herr et al. extracted semitendinosus muscle from a leopard frog to drive the tail fin structure of a fish-like robot and demonstrated that the muscle could be used as an actuator for the robot by performing swimming motions, such as straight and turning motions (Herr and Dennis 2004). Richards et al. developed robots that can rotate the tibialis posterior muscle of African clawed frogs and swim using servomotors based on the measured output, and they measured the reaction force of water using the sensors on the foot fins (Richards 2011). Using the developed robot, the researchers showed that the thrust force generated by the tibialis posterior muscle varies with the size of the fin, moment arm of the tibialis posterior muscle, and length of the muscle.

Muscle cell actuators are composed of tissue units. Therefore, muscle tissue must be isolated from an individual. The output is large because mature muscle tissue is utilized. However, it is important to conduct the experiment in an ethical manner. The goal is to create an actuator by combining the acquired muscle tissue with the connecting parts of an external mechanical structure. A centimeter-scale myocyte actuator can be obtained, which pulls between two points, and its function is to

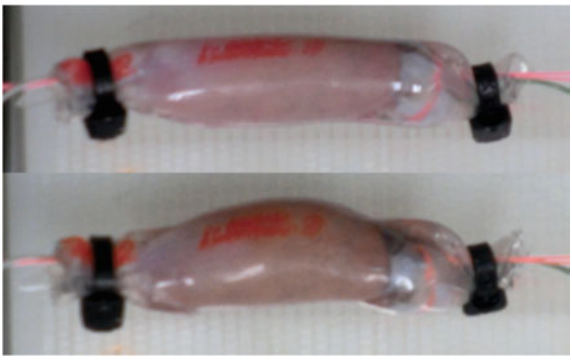

Fig. 10.26 Skeletal muscle tissue actuator surrounded by a silicone membrane. The upper figure indicates natural length. The lower figure shows contraction of the actuator

perform a contracting action upon electrical stimulation. Here, leg muscle tissue (tibialis posterior muscle) isolated from an African clawed frog was employed. The completed actuator is shown in Fig. 10.26. Here, the muscle tissue is surrounded by a silicone membrane and closed at both ends. The silicone membrane is filled with saline solution (Ringer's solution) prepared for frogs. Polyethylene threads were sewn onto the tendon portions at both ends of the muscle tissue to connect it to the external mechanical structure. The polyethylene threads have low elongation owing to external force and can efficiently extract displacement. Simultaneously, electrodes were inserted at both ends of the muscle tissue and extracted externally. The build procedure is described as follows:

Step 1: Isolate the tibialis posterior muscle from the leg of the African clawed frog in compliance with ethical standards.

Step 2: Package the muscle tissue. Polyethylene thread is sewn onto the tendon portions at both ends of the muscle tissue. Simultaneously, an electrode (Junflon wire, conductor length: 0.32 mm) is inserted into the muscle. Wrap the electrode in a silicone membrane (Dragonskin 30) and fill the inside with Ringer's solution. Both ends of the membrane are closed.

Step 3: Electrical stimulation is applied to the electrodes (a stimulus group of 7 inputs of square waves of 3.3 V amplitude and 1 ms width at 20 ms intervals, applied at 1000 ms intervals) to drive the robot.

A biohybrid frog-like robot modeled based on an African clawed frog is shown in Fig. 10.27. The body contains an electrical circuit for electrical stimulation of muscles and communication with a PC for remote control. The hind legs reproduce the musculoskeletal system of a frog and are driven by skeletal muscle tissue actuators attached to the legs and thighs. The forelegs are omitted because they do not contribute to the frog's locomotion, such as swimming.

The robot requires a foot structure that mimics the musculoskeletal system of the African clawed frog. The anatomical knowledge and dissected African clawed frogs were used as references for the foot structure. Many of the robot's components

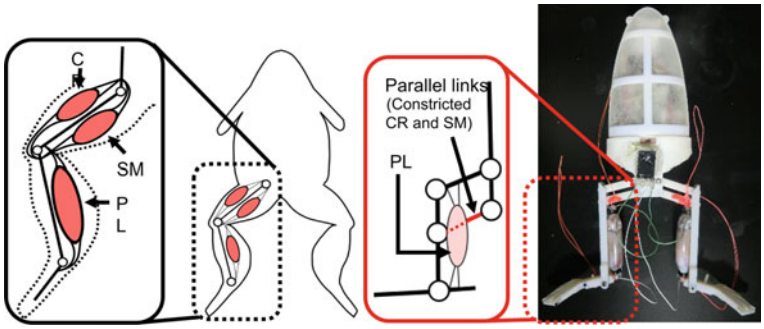

Fig. 10.27 Biohybrid frog-like robot driven by skeletal muscle tissue actuators

are made of Vero White Plus resin printed by a 3D printer (Connex 260TM 3D printing system, Stratasys, Ltd.). Ball bearings are incorporated to reduce friction at each joint. In addition, torsion springs are incorporated in the hip and ankle joints to compensate for the drive of the actuators other than the myocyte actuators. When swimming, the frog extends its legs and scrapes the water with its flippers, thereby increasing the area of its flippers. We reproduced this mechanism. The robot can be divided into three parts: the robot legs driven by biomuscles, the system part consisting of electronic components such as microcontroller, and the exoskeleton part that reproduces the exoskeleton of the frog body. In particular, electronic components including microcontroller and Li–Po batteries are mounted inside the robot.

In the future, we intend to improve the musculoskeletal design of the frog robot, add other muscles to the developed robot, and incorporate sensors and feedback from the environment into the robot, so that the developed frog robot can acquire the motor functions of a frog.

10.5.2 Biohybrid Robot Actuated by Skeletal Muscle Tissues

Skeletal muscle tissue is an attractive bioactuator owing to its strong contractile force, ON/OFF controllability, and dimensional designability. The culture of myoblasts on a device for constructing the tissue allows for the integration of the device and skeletal muscle tissue, enabling the skeletal muscle tissue to be used as an actuator to drive the device. However, simply placing skeletal muscle tissue on a device does not work efficiently. Because the intrinsic traction force, the passive tension, causes a spontaneous shrinkage of the skeletal muscle tissue, leading to malfunction of its contraction, a load of a counter force to the traction force is necessary to prevent shrinkage and maintain the morphology and contractility. There are two main ways to apply a counter force to the skeletal muscle tissue: placement of an antagonistic skeletal muscle tissue and the use of a bendable substrate. The design theory for the device differs depending on the method used.

In biological systems, antagonistic pairs of skeletal muscles are used to overcome shrinkage; the balance of the tension between antagonistic muscles prevents spontaneous shrinkage. By mounting an antagonistic pair of skeletal muscle tissues on a robotic skeleton with a joint similar to that in a biological system, a biohybrid robot can balance the tension between the two tissues. In one study, when selectively applying electrical stimulation to the tissue, joint rotation was achieved, according to the contractions of each tissue. In the robot motion, a large contraction with a strain of the skeletal muscle tissues of 0.2 and joint rotation of 90° was achieved, similar to the motions of the living skeletal muscle and human finger joints (Morimoto et al. 2018) (Fig. 10.28a). Furthermore, the biohybrid robot succeeded in hooking, carrying, and placing a ring by the selective contraction of each skeletal muscle tissue (Fig. 10.28b). Therefore, these results show that the antagonistic pair of skeletal muscle tissues not only prevents shrinkage of the tissue, but can also replicate various finger- and arm-like movements. For the smooth motions, it is important to consider that the configuration of the skeleton influences the robot motion. The motions of the biohybrid robot are determined by the balance between the friction force at the joint and the tensions of skeletal muscle tissues; when this balance does not hold, the joint rotates. It is assumed that the balance can be expressed as follows (Morimoto et al. 2018):

$$F_{\mathrm{f}} - F_{\mathrm{e}} \leq \mu(F_{\mathrm{f}} + F_{\mathrm{e}} - (2W_{\mathrm{a}} + W_{\mathrm{b}})) \tag{10.44}$$

Here, F_{f} is the tension of the flexor muscle tissue (contracted muscle tissue), F_{e} is the tension of the extensor muscle (extended muscle tissue), W_{a} is the weight of the anchor connected to the end of each tissue, W_{b} is the weight of the bar attached to the joint, and μ is the friction constant at the joint. Because the tension of the skeletal muscle tissue is much larger than the weights of the anchor and bar, they are negligible in the above equation. Therefore, the friction constant is an important factor in determining the magnitude of the joint rotation. In this research, the friction constant at the joint was large (0.46 ± 0.04 (mean $\pm$ s.d., $n = 7$)); thus, the frictional force imparted resistance to the tension of the tissue, causing a limitation to the joint rotation. Thus, when using skeletal muscle tissue as an actuator, it is important not only to improve its contractility but also to adjust the device characteristics, as smoother joint rotations are possible when the friction constant of the joint is reduced, even if the muscle contractility remains the same. In the case of a bending biohybrid device composed of a flexible sheet and an antagonistic pair of skeletal muscle tissues, the deformation of the sheet can be predicted using a finite element method (FEM) simulation (Morimoto et al. 2019). These results suggest that by understanding the contractility of skeletal muscle tissue and the driving characteristics of the corresponding device, it is possible to design biohybrid robots driven by the tension balance of the antagonistic pair of muscle tissues while predicting the driving style, as in conventional robotics.

Using a bendable substrate, the elastic force of the bent substrate is used as the source of the counter force to the passive tension of the skeletal muscle tissue. The advantage of this method is that it can be driven by a single skeletal muscle tissue. In

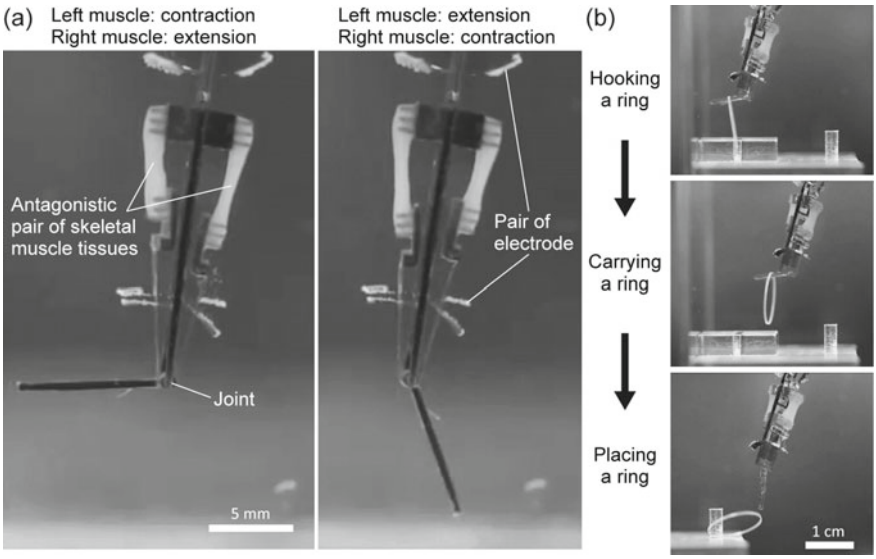

Fig. 10.28 Movements of a biohybrid robot with a joint powered by an antagonistic pair of skeletal muscle tissues. **a** Rotation of the joint according to selective contractions of each skeletal muscle tissue. **b** Manipulation of a ring with the joint rotation—images are reprinted with permission from Morimoto et al. (2018), ©2018, The American Association for the Advancement of Science

addition, by using FEM simulations, it is possible to design a device with appropriate stiffness, i.e., one that does not deform under only the passive tension of the skeletal muscle tissue, but also deforms when its active tension is generated. Although the design of the device must be carefully adjusted to generate a counter force to escape spontaneous muscle shrinkage and malfunctions of the contractility, this method allows for easy tissue construction and electrical stimulation for beginners, as it requires only a single skeletal muscle tissue. In biohybrid robots with a bendable substrate, walking is a typical motion. In the study, when a flexible substrate with two hard pillars was used and the skeletal muscle tissue was bridged between the pillars, its muscle contractions were controlled by the electrical stimulation-induced deformation of the flexible substrate. As a result of the deformation, the locomotion of a biohybrid robot was achieved by kicking the bottom of a culture dish at the tips of the pillars (Cvetkovic et al. 2018; Pagan-Diaz et al. 2018) (Fig. 10.29). Furthermore, by using a method with optogenetically modified skeletal muscle tissues, the robot could walk according to the deformation of its flexible substrate based on light exposure (Raman et al. 2016). As skeletal muscle tissue is made of cells and is vulnerable to desiccation, all of the above biohybrid robots can only work in a culture medium. To overcome this issue, a biohybrid robot with a collagen layer has been proposed. The collagen layer keeps the culture medium inside to prevent the tissue from drying out, even when the robot is in the air. In addition, because flexible electrodes are placed in the collagen layer, the electrical stimuli are transmitted to the skeletal muscle tissue covered with the layer. In one biohybrid robot, deformation of the bendable

substrate and collagen layer was caused by muscle contraction in air (Morimoto et al. 2020) (Fig. 10.30). As a result, the biohybrid robot achieved bending motions in air and successfully accomplished tasks that could not be performed in liquid, such as pushing a bead. The use of skeletal muscle tissue as a driving source is still in its infancy, and further practical applications are expected to emerge in the future.

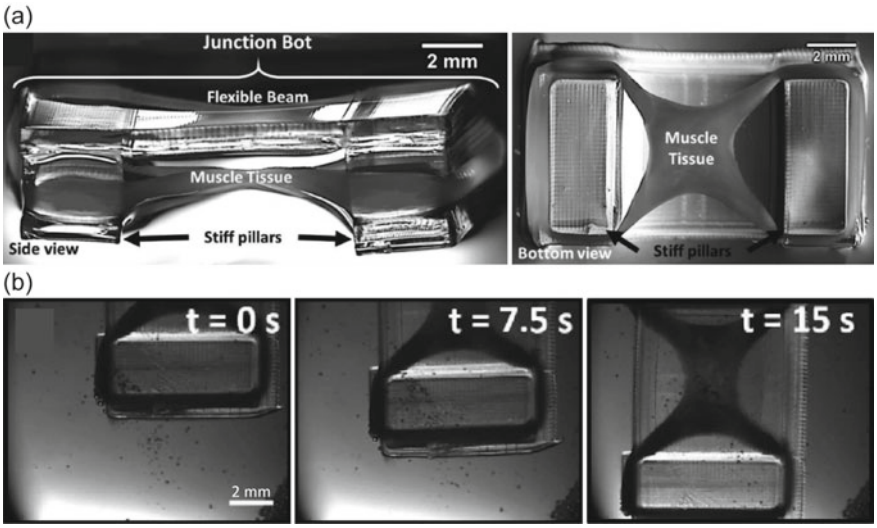

Fig. 10.29 Locomotion of the biohybrid robot on culture dish. **a** Side and bottom view and **b** sequential bottom view of the locomotion—images are reprinted with permission from Pagan-Diaz et al. (2018), ©2018 John Wiley and Sons

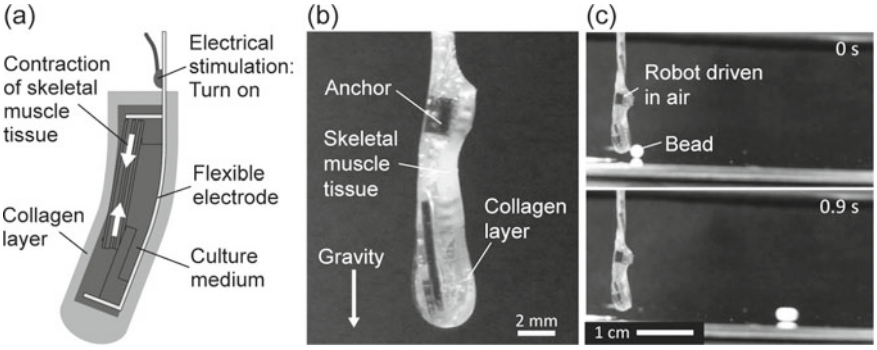

Fig. 10.30 Biohybrid robot driven in air. **a** Conceptual illustration and **b** image of the biohybrid robot covered with a collagen layer. **c** Pushing a bead with the robot—images are reprinted from Morimoto et al. (2020), ©2020 Authors, licensed under a Creative Commons Attribution (CC BY) license

10.5.3 How to Start

To use skeletal muscle tissue as an actuator, it is necessary to prepare equipment for cell culturing and master tissue construction skills. There are many published books and papers on tissue construction, so it is good to refer to them. However, I think the best way is to learn from professors and researchers who specialize in this field, as it requires technical expertise. Meanwhile, as long as the robotic devices are biocompatible and made from materials that do not damage cells, there are no restrictions on how they are fabricated. In addition, at the beginning of research on biohybrid robots with skeletal muscle tissue, I think that it is better to use muscles exploited from living organisms instead of cultured skeletal muscle tissues, so as to check if the robotic device will work with the muscles as desired before starting the work.

10.5.4 Challenges

One of the limitations of using skeletal muscle tissue as an actuator is that the optimal environment is strict, such as a temperature of 37 °C and a pH of approximately 7. Although conventional biohybrid robots have solved this issue by regulating the surrounding environment, it is desirable to be able to adjust these factors internally, such as in living organisms. Therefore, biohybrid robots with such systems will be required in the future.

Exercises

- (8.1) Calculate the ratio of work output and deformation energy W'/E_{d} in the case where the spring constant of actuator $k_1 = ax_1$ and external load a, $k_2 = \text{const.}$ in Fig. 10.4.
- (8.1) Consider the generalized case where the force–displacement relation of the actuator and external load in Fig. 10.4 are $f_1(x)$ and $f_2(x)$, respectively. How does the discussion change?
- (8.2) State the basic motions of fluidic actuators and analyze the possible compositions of basic motions for an octopus' leg.
- (8.2) List the commonly used fabrication techniques for soft fluidic actuators.
- (8.2) Specify the types of fluidic pressure sources and compare the pros and cons of each pressure source.
- (8.3) What are the parameters to derive the Maxwell stress?
- (8.3) What is the role of cations in IPMCs?
- (8.3) Discuss the best application for DEAs and IPMCs.
- (8.4) Considering the physical properties of shape-memory alloy actuators, propose possible applications for the actuation of robots.
- (8.4) By applying the pseudoelasticity of shape-memory alloys, propose a new force-sensing method or a device applicable to robots.

- (8.5) What methods are mainly used to load the counter force to the passive tension of the skeletal muscle tissue?

Acknowledgements This work is supported by the JSPS KAKENHI Grant-in-Aid for Scientific Research on Innovative Areas "Science of Soft Robot" project (grant number 21H00324).

References

Acome E, Mitchell SK, Morrissey TG, Emmett MB, Benjamin C, King M, Radakovitz M, Keplinger C (2018) Hydraulically amplified self-healing electrostatic actuators with muscle-like performance. Science 359:61–65

Anderson IA, Gisby TA, McKay TG et al (2012) Multi-functional dielectric elastomer artificial muscles for soft and smart machines. J Appl Phys 112:041101. https://doi.org/10.1063/1.4740023

Asaka K, Oguro K, Nishimura Y et al (1995) Bending of polyelectrolyte membrane–platinum composites by electric stimuli I. Response characteristics to various waveforms. Polym J 27:436–440. https://doi.org/10.1295/polymj.27.436

Aubin CA, Choudhury S, Jerch R, Archer LA, Pikul JH, Shepherd RF (2019) Electrolytic vascular systems for energy-dense robots. Nature 571(7763):51–57

Bar-Cohen Y (2004) Electroactive polymer (EAP) actuators as artificial muscles: reality, potential, and challenges, 2nd edn. SPIE, Bellingham, WA

Bar-Cohen Y, Xue T, Shahinpoor M et al (1998) Flexible, low-mass robotic arm actuated by electroactive polymers and operated equivalently to human arm and hand. In: Robotics 98. American Society of Civil Engineers, Reston, VA, pp 15–21

Bellini A, Colli M, Dragoni E (2009) Mechatronic design of a shape memory alloy actuator for automotive tumble flaps: a case study. IEEE Trans Ind Electron 56(7):2644–2656

Brochu P, Pei Q (2010) Advances in dielectric elastomers for actuators and artificial muscles. Macromol Rapid Commun 31:10–36. https://doi.org/10.1002/marc.200900425

Cacucciolo V, Shintake J, Kuwajima Y, Maeda S, Floreano D, Shea H (2019) Stretchable pumps for soft machines. Nature 572(7770):516–519

Carpi F (2016) Electromechanically active polymers. Springer International Publishing, Cham

Chen X, Shigemune H, Sawada H (2020) An untethered bionic robotic fish using SMA actuators. In: Proceedings of IEEE international conference on mechatronics and automation (IEEE ICMA2020), pp 1768–1773

Cohen YB (2004) Electroactive polymer (EAP) actuators as artificial muscles: reality, potential, and challenges. SPIE Press

Constantin P, Foias C (1988) Navier-stokes equations. University of Chicago Press

Cvetkovic C, Raman R, Chan V, Williams BJ, Tolish M, Bajaj P, Sakar MS, Asada HH, Saif MTA, Bashir R (2018) Three-dimensionally printed biological machines powered by skeletal muscle. Proc Natl Acad Sci USA 111(28):10125–10130

Danjo J, Danjo S, Nakamura Y, Uchida K, Sawada H (2016) Micro-vibration patterns generated from shape memory alloy actuators and the detection of an asymptomatic tactile sensation decrease in diabetic patients. IEICE Trans Inf Syst E99-D(11):2759–2766

Danjo J, Sawada H, Uchida K, Danjo S, Nakamura Y (2017) Efficacy of a new microvibration sensation measurement device at detecting diabetic peripheral neuropathy using a newly devised finger method. J Gen Fam Med 18(4):155–161

Diteesawat RS, Helps T, Taghavi M, Rossiter J (2021) Electro-pneumatic pumps for soft robotics. Sci Robot 6(51)

Elger DF, LeBret BA, Crowe CT, Roberson JA (2020) Engineering fluid mechanics. Wiley
Fukui Y, Inamura T, Hosoda H, Wakashima K, Miyazaki S (2004) Mechanical properties of a Ti–Nb–Al shape memory alloy. Mater Trans 45(4):1077–1082
Garrad M, Soter G, Conn AT, Hauser H, Rossiter J (2019) Driving soft robots with low-boiling point fluids. In: IEEE international conference on soft robotics, pp 74–79
Geier A, Tucker RCY, Somlor S, Sawada H, Sugano S (2020) End-to-end tactile feedback loop: from soft sensor skin over deep GRU-autoencoders to tactile stimulation. IEEE Robot Autom Lett 5(4):6467–6474. https://doi.org/10.1109/LRA.2020.3012951
Gorissen B, Reynaerts D, Konishi S, Yoshida K, Kim JW, De Volder M (2017) Elastic inflatable actuators for soft robotic applications. Adv Mater 29(43):1604977
Gu G-Y, Zhu J, Zhu L-M, Zhu X (2017) A survey on dielectric elastomer actuators for soft robots. Bioinspir Biomim 12:011003. https://doi.org/10.1088/1748-3190/12/1/011003
Guo Y, Liu L, Liu Y, Leng J (2021) Review of dielectric elastomer actuators and their applications in soft robots. Adv Intell Syst 3:2000282. https://doi.org/10.1002/aisy.202000282
Hafiz M, Sawada H (2011) Presentation of button repulsive sensations on touch screen using SMA wires. In: IEEE international conference on mechatronics and automation, pp 1–6
Haines CS, Márcio DL, Li N, Spinks GM, Foroughi J, Madden JDW, Kim SH, Fang S, Andrade MJD, Göktepe F, Göktepe Ö, Mirvakili SM, Naficy S, Lepró X, Oh J, Kozlov ME, Kim SJ, Xu X, Swedlove BJ, Wallace GG, Baughman RH (2014) Artificial muscles from fishing line and sewing thread. Science 343:868–872
Herr H, Dennis RG (2004) A swimming robot actuated by living muscle tissue. J Neuroeng Rehabil 1(1):6
Higuchi T, Suzumori K, Tadokoro S (eds) (2009) Next-generation actuators leading breakthroughs. Springer
Hiramitsu T, Suzumori K, Nabae H, Endo G (2019) Experimental evaluation of textile mechanisms made of artificial muscles. In: IEEE international conference on soft robotics (RoboSoft). IEEE, pp 1–6
Horiuchi T, Mihashi T, Fujikado T et al (2017) Voltage-controlled IPMC actuators for accommodating intra-ocular lens systems. Smart Mater Struct 26:045021. https://doi.org/10.1088/1361-665X/aa61e8
Huang J, Shian S, Diebold RM et al (2012) The thickness and stretch dependence of the electrical breakdown strength of an acrylic dielectric elastomer. Appl Phys Lett 101:122905. https://doi.org/10.1063/1.4754549
Huber JE, Fleck NA, Ashby MF (1997) The selection of mechanical actuators based on performance indices. Proc R Soc Lond A 453:2185–2205
Ji X, El Haitami A, Sorba F et al (2018) Stretchable composite monolayer electrodes for low voltage dielectric elastomer actuators. Sens Actuators B Chem 261:135–143. https://doi.org/10.1016/j.snb.2018.01.145
Ji X, Liu X, Cacucciolo V, Imboden M, Civet Y, Haitam AE, Cantin S, Perriard Y, Shea H (2019) An autonomous untethered fast soft robotic insect driven by low-voltage dielectric elastomer actuators. Sci Robot 4:eaaz6451
Jiang C, Uchida K, Sawada H (2014) Research and development of vison based tactile display system using shape memory alloys. Int J Innov Comput Inf Control 10(3):837–850
Juan JS, No ML, Schuh CA (2008) Superelasticity and shape memory in micro- and nanometer-scale pillars. Adv Mater 20(2):272–278
Kanno R, Nagai T, Shintake J (2021) Rapid fabrication method for soft devices using off-the-shelf conductive and dielectric acrylic elastomers. Adv Intell Syst 3:2000173. https://doi.org/10.1002/aisy.202000173
Katzschmann RK, DelPreto J, MacCurdy R, Rus D (2018) Exploration of underwater life with an acoustically controlled soft robotic fish. Sci Robot 3(16)
Kennedy DK, Straub FK, Schetky LMD, Chaudhry Z, Roznoy R (2004) Development of an SMA actuator for in-flight rotor blade tracking. J Intell Mater Syst Struct 15(4):235–248

Kim B, Lee MG, Lee YP, Kim Y, Lee G (2006) An earthworm-like micro robot using shape memory alloy actuator. Sens Actuators A Phys 125(2):429–437
Kitamori T, Wada A, Nabae H, Suzumori K (2016) Untethered three-arm pneumatic robot using hose-free pneumatic actuator. In: 2016 IEEE/RSJ international conference on intelligent robots and systems (IROS). IEEE, pp 543–548
Kodaira A, Asaka K, Horiuchi T, Endo G, Nabae H, Suzumori K (2019) IPMC monolithic thin film robots fabricated through a multi-layer casting process. IEEE Robot Autom Lett 4:1335–1342
Kurumaya S, Suzumori K, Nabae H, Wakimoto S (2016) Musculoskeletal lower-limb robot driven by multifilament muscles. Robomech J 3(1):1–15
Li Y, Hashimoto M (2016) Design and prototyping of a novel lightweight walking assist wear using PVC gel soft actuators. Sens Actuators A Phys 239:26–44
Mao Z, Iizuka T, Maeda S (2021) Bidirectional electrohydrodynamic pump with high symmetrical performance and its application to a tube actuator. Sens Actuators A Phys 332:113168
Melton KN, Mercier O (1981) The mechanical properties of NiTi-based shape memory alloys. Acta Metall 29(2):393–398
Mirvakili SM, Hunter IW (2018) Artificial muscles: mechanisms, applications, and challenges. Adv Mater 30:1704407. https://doi.org/10.1002/adma.201704407
Mizukami Y, Sawada H (2006) Tactile information transmission by apparent movement phenomenon using shape-memory alloy device. Int J Disabil Hum Dev 5(3):277–284
Morimoto Y, Onoe H, Takeuchi S (2018) Biohybrid robot powered by an antagonistic pair of skeletal muscle tissues. Sci Robot 3(18):eaat4440
Morimoto Y, Onoe H, Takeuchi S (2019) Biohybrid device with antagonistic skeletal muscle tissues for measurement of contractile force. Adv Robot 33(5):208–218
Morimoto Y, Onoe H, Takeuchi S (2020) Biohybrid robot with skeletal muscle tissue covered with a collagen structure for moving in air. APL Bioeng 4(2):026101
Morin SA, Kwok SW, Lessing J, Ting J, Shepherd RF, Stokes AA, Whitesides GM (2014) Elastomeric tiles for the fabrication of inflatable structures. Adv Funct Mater 24(35):5541–5549
Nabae H, Kodaira A, Horiuchi T et al (2019) Soft polymer-electrolyte-fuel-cell tube realizing air-hose-free thin McKibben muscles. In: 2019 IEEE/RSJ international conference on intelligent robots and systems (IROS). IEEE, pp 8287–8293
Onal CD, Chen X, Whitesides GM, Rus D (2017) Soft mobile robots with on-board chemical pressure generation. In: Robotics research. Springer, Cham, pp 525–540
Pagan-Diaz GJ, Zhang XT, Grant L, Kim Y, Aydin O, Cvetkovic C, Ko E, Solomon E, Hollis J, Kong H, Saif T, Gazzola M, Bashir R (2018) Simulation and fabrication of stronger, larger, and faster walking biohybrid machines. Adv Funct Mater 28(23):1801145
Pan Q, Cho C (2007) The investigation of a shape memory alloy micro-damper for MEMS applications. Sensors 7(9):1887–1900
Park I-S, Jung K, Kim D et al (2008) Physical principles of ionic polymer–metal composites as electroactive actuators and sensors. MRS Bull 33:190–195. https://doi.org/10.1557/mrs2008.44
Peele BN, Wallin TJ, Zhao H, Shepherd RF (2015) 3D printing antagonistic systems of artificial muscle using projection stereolithography. Bioinspir Biomim 10(5):055003
Pelrine RE, Kornbluh RD, Joseph JP (1998) Electrostriction of polymer dielectrics with compliant electrodes as a means of actuation. Sens Actuators A Phys 64:77–85. https://doi.org/10.1016/S0924-4247(97)01657-9
Piao M, Miyazaki S, Otsuka K (1992) Characteristics of deformation and transformation in $Ti_{44}Ni_{47}Nb_9$ shape memory alloy. Mater Trans JIM 33(4):346–353
Polygerinos P, Correll N, Morin SA, Mosadegh B, Onal CD, Petersen K, Cianchetti MT, Michael T, Shepherd RF (2017) Soft robotics: review of fluid-driven intrinsically soft devices; manufacturing, sensing, control, and applications in human-robot interaction. Adv Eng Mater 19(12):1700016
Raman R, Cvetkovic C, Uzel SGM, Platt RJ, Sengupta P, Kamm RD, Bashir R (2016) Optogenetic skeletal muscle-powered adaptive biological machines. Proc Natl Acad Sci USA 113(13):3497–3502

Reynaerts D, Peirs J, Brussel HV (1999) Shape memory micro-actuation for a gastro-intestinal intervention system. Sens Actuators A Phys 77(2):157–166
Richards CT (2011) Building a robotic link between muscle dynamics and hydro-dynamics. J Exp Biol 214(14):2381–2389
Robinson SS, O'Brien KW, Zhao H, Peele BN, Larson CM, Mac Murray BC, Shepherd RF (2015) Integrated soft sensors and elastomeric actuators for tactile machines with kinesthetic sense. Extreme Mech Lett 5:47–53
Rosset S, Shea HR (2016) Small, fast, and tough: shrinking down integrated elastomer transducers. Appl Phys Rev 3:031105. https://doi.org/10.1063/1.4963164
Shahinpoor M (2020) Fundamentals of smart materials. Royal Society of Chemistry
Shepherd RF, Ilievski F, Choi W, Morin SA, Stokes AA, Mazzeo AD, Whitesides GM (2011) Multigait soft robot. Proc Natl Acad Sci 108(51):20400–20403
Shintake J, Rosset S, Schubert BE et al (2015) A foldable antagonistic actuator. IEEE/ASME Trans Mechatron 20:1997–2008. https://doi.org/10.1109/TMECH.2014.2359337
Shintake J, Rosset S, Schubert B et al (2016) Versatile soft grippers with intrinsic electroadhesion based on multifunctional polymer actuators. Adv Mater 28:231–238. https://doi.org/10.1002/adma.201504264
Shintake J, Cacucciolo V, Floreano D, Shea H (2018a) Soft robotic grippers. Adv Mater 30. https://doi.org/10.1002/adma.201707035
Shintake J, Cacucciolo V, Shea H, Floreano D (2018b) Soft biomimetic fish robot made of dielectric elastomer actuators. Soft Robot 5:466–474. https://doi.org/10.1089/soro.2017.0062
Singh K, Sirohi J, Chopra I (2003) An improved shape memory alloy actuator for rotor blade tracking. J Intell Mater Syst Struct 14(12):767–786
Stratton JA (2007) Electromagnetic theory. Wiley
Sun F, Hao YL, Nowak S, Gloriant T, Laheurte P, Prima F (2011) A thermo-mechanical treatment to improve the superelastic performances of biomedical Ti–26Nb and Ti–20Nb–6Zr (at.%) alloys. J Mech Behav Biomed Mater 4(8):1864–1872
Suzumori K, Iikura S, Tanaka H (1992) Applying a flexible microactuator to robotic mechanisms. IEEE Control Syst Mag 12(1):21–27
Suzumori K, Wada A, Wakimoto S (2013) New mobile pressure control system for pneumatic actuators, using reversible chemical reactions of water. Sens Actuators A Phys 201:148–153
Takagi K, Yamamura M, Luo Z et al (2006) Development of a rajiform swimming robot using ionic polymer artificial muscles. In: 2006 IEEE/RSJ international conference on intelligent robots and systems. IEEE, pp 1861–1866
Takeda Y, Sawada H (2013) Tactile actuators using SMA micro-wires and the generation of texture sensation from images. In: IEEE/RSJ international conference on intelligent robots and systems (IROS2013), pp 2017–2022
Tolley MT, Shepherd RF, Karpelson M, Bartlett NW, Galloway KC, Wehner M, Wood RJ (2014) An untethered jumping soft robot. In: IEEE/RSJ international conference on intelligent robots and systems, pp 561–566
Tse YA, Wong KW, Yang Y, Wang MY (2020) Novel design of a soft pump driven by super-coiled polymer artificial muscles. In: IEEE/RSJ international conference on intelligent robots and systems (IROS), pp 8789–8794
Wang N, Cui C, Guo H et al (2018) Advances in dielectric elastomer actuation technology. Sci China Technol Sci 61:1512–1527. https://doi.org/10.1007/s11431-017-9140-0
Wehner M, Truby RL, Fitzgerald DJ, Mosadegh B, Whitesides GM, Lewis JA, Wood RJ (2016) An integrated design and fabrication strategy for entirely soft, autonomous robots. Nature 536(7617):451–455
Xu B, Hu M, Zhang JH, Mao ZB (2017) Distribution characteristics and impact on pump's efficiency of hydro-mechanical losses of axial piston pump over wide operating ranges. J Cent South Univ 24(3):609–624

Yeghiazarian L, Mahajan S, Montemagno C, Cohen C, Wiesner U (2005) Directed motion and cargo transport through propagation of polymer-gel volume phase transitions. Adv Mater 17:1869–1873
Zhao F, Jiang C, Sawada H (2012) A novel Braille display using the vibration of SMA wires and the evaluation of Braille presentations. J Biomech Sci Eng 7(4):416–432

Chapter 11
Tissue-Interfaced Electronics

Toshinori Fujie and Hajime Fujita

One of the major goals of tissue-interfaced electronics is efficient sensing or treatment by taking advantage of the proximity to tissue, while reducing the burden on the user as much as possible. To achieve this goal, a wide range of innovative medical devices have been developed in recent years. In this column, we will outline the recent trends, mainly from the viewpoint of technological disciplines, such as material mechanics, biomaterials science, and wireless communication engineering (Fig. 11.1).

A key method to alleviate the mechanical mismatch between the tissue and the electronics is by minimizing the thickness of the device to obtain flexibility that is equivalent to that of the tissue. According to the equation of flexural rigidity (or bending stiffness), the body conformability of sheet materials is greatly affected by the thickness (Park et al. 2008). Taking advantage of this rule, the flexural rigidity of metallic and semiconductive materials is reduced by thinning. Furthermore, polymeric materials used as substrates can be thinned by coating a polymer solution on a substrate and peeling it off. For example, the body conformability of polymeric ultra-thin films (referred to as "nanosheets") was validated using various functional polymers, such as biodegradable polymers (i.e., polylactic acid) (Saito et al. 2021).

Controlling degradability and adhesiveness of materials from the viewpoint of biomaterials science is also important to improve device usability. Flexible electronics with degradability have been called "transient electronics," and biodegradable polymers, such as silk and polylactic acid, have been widely used because their crystalline structures dissolve over time under wet conditions on biological tissues (Altman et al. 2003). Alternatively, gold, which is not easily oxidized, is the most common metal in circuits considering the effect of metal oxides on cells. Recently, the integration of bioadhesives with tissue–electronic interfaces has been spotlighted. Bioadhesives can ensure the fixation of electronics at ideal spots and avoid the drawbacks of conventional suturing methods, such as a high infection rate and extensive

T. Fujie (✉) · H. Fujita
School of Life Science and Technology, Tokyo Institute of Technology, Tokyo, Japan
e-mail: t_fujie@bio.titech.ac.jp

K. Suzumori et al. (eds.), *The Science of Soft Robots*, Natural Computing Series,
https://doi.org/10.1007/978-981-19-5174-9_11

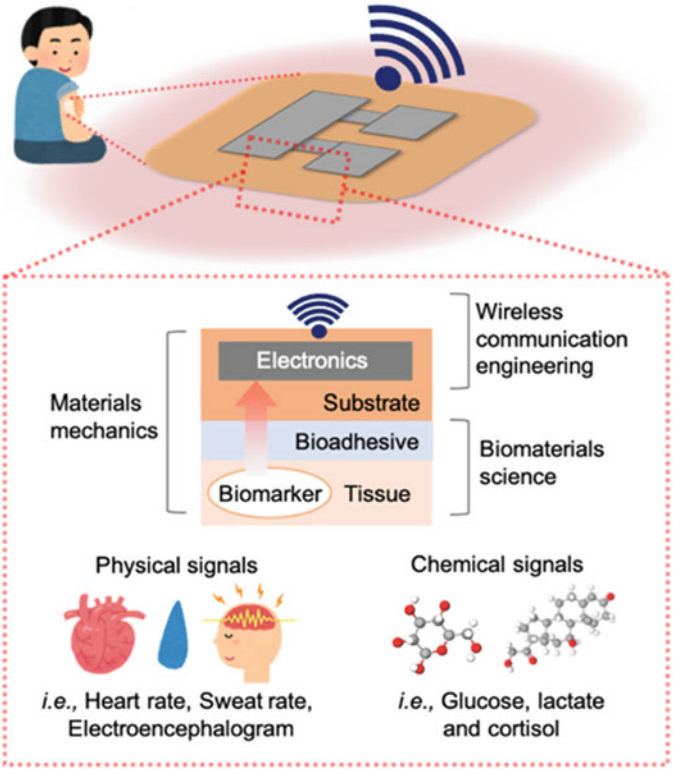

Fig. 11.1 Overview of tissue-interfaced electronics at an intersection of materials mechanics, biomaterials science, and wireless communication engineering

handling (Mehdizadeh and Yang 2013). One study demonstrated the simple fixation of plastic electronics by photo-crosslinking a biodegradable composite material of poly(ethylene glycol) (PEG), chitosan, and alginate at a tissue–electronics interface (Yang et al. 2021). Other potential bioadhesives, such as gelatin, albumin, polysaccharide, and dextran, can be achieved by chemical, photo-chemical, and enzymatic approaches.

Integrating wireless communication with tissue-interfaced electronic materials will help us monitor health conditions and take appropriate measures. One study demonstrated a unique combination of materials and device design using a glucose-responsive phenylboronic acid (PBA) hydrogel integrated with an inkjet-printed interdigitated capacitor (IDC) that had a rapid response (< 5 min) to glucose concentration changes (Fujita et al. 2021). This study inferred that the controlled design and fabrication of tissue-interfaced sensing materials is imperative to ensuring sufficient signal transduction for battery-free biosensing. In addition to wireless biosensors, studies have shown various applications of wireless tissue-interfaced devices for treating diseases. Another study reported the use of light-emitting devices (LEDs)

by combining a polymeric nanosheet with a wirelessly powered LED. These devices were applied to implantable photodynamic cancer therapy in a mouse model, and the tumor was eliminated by the localization of light to the tumors with a photosensitizer (Yamagishi et al. 2019). In addition, a flexible and expandable light-emitting device and a flexible induction heating device were fabricated by inkjet printing of metal coils on a polymer thin film, indicating the potential for biomedical applications, such as localized drug delivery (Tetsu et al. 2020). These previous studies imply that wireless communication is a major factor that should be considered when designing tissue-interfaced electronics.

In conclusion, a comprehensive approach to device design and fabrication from the perspective of material mechanics, biomaterial science, and wireless communication engineering is indispensable for advanced tissue-interfaced electronics.

References

Altman GH, Diaz F, Jakuba C et al (2003) Silk-based biomaterials. Biomaterials 24:401–416

Fujita H, Yamagishi K, Zhou W et al (2021) Design and fabrication of flexible glucose sensing platform toward rapid battery-free detection of hyperglycaemia. J Mater Chem. 9:7336–7344

Mehdizadeh M, Yang J (2013) Design strategies and applications of tissue bioadhesives. Macromol Biosci 13:271–288

Park S-I, Ahn J-H, Feng X et al (2008) Theoretical and experimental studies of bending of inorganic electronic materials on plastic substrates. Adv Funct Mater 18:2673–2684

Saito M, Kanai E, Fujita H et al (2021) Flexible induction heater based on the polymeric thin film for local thermotherapy. Adv Funct Mater 31:2102444

Tetsu Y, Kido Y, Hao M et al (2020) Graphene/Au hybrid antenna coil exfoliated with multi-stacked graphene flakes for ultra-thin biomedical devices. Adv Electron Mater 6:1901143

Yamagishi K, Kirino I, Takahashi I et al (2019) Tissue-adhesive wirelessly powered optoelectronic device for metronomic photodynamic cancer therapy. Nat Biomed Eng 3:27–36

Yang Q, Wei T, Yin RT et al (2021) Photocurable bioresorbable adhesives as functional interfaces between flexible bioelectronic devices and soft biological tissues. Nat Mater. 20:1559–1570

Chapter 12
Paper Mechatronics

Hiroki Shigemune

This paper presents research on paper mechatronics to construct mechatronic devices using inkjet printing (Shigemune et al. 2016). Compact mechatronic devices are characterized by seamlessly integrating mechanics and electronics. Mechatronic devices are developed by incorporating electronics into sheet materials and folding them. While digital fabrication methods can be developed by directly providing circuits to the 3D printed structure, this technology is not reliable. Therefore, paper mechatronics is considered a desirable prototyping technology for mechatronic devices in the subsequent Internet of Things (IoT) era.

One of the major contributions of paper mechatronics to soft robotics is the development of a novel control system for active matter using printers and reactions. Usually, computers are used in mechatronic systems to achieve programmed behavior. In paper mechatronics, the mechanics (structure and movement) and functions of the material are programmed using a printer and an ink. The structure is formed by creating a physicochemical reaction between the ink and sheet material (Shigemune et al. 2016). The self-folding part is controlled by the position of the ink to be printed. Furthermore, the self-folding dynamics can be controlled by varying the reaction speed (Shigemune et al. 2021). Conductive inks are printed on parts that should be intelligent, whereas electrical circuits comprising (LCR) elements are embedded in the mechanics (Shigemune et al. 2017). Therefore, in paper mechatronics, the printing of the structure, motility, and electronics can be accomplished using a single printer (Fig. 12.1).

Additionally, paper mechatronics contributes to the development of origami devices. Origami, a traditional Japanese art form, is a method of creating 3D object structures using sheet materials. In Japanese, “ori” means folding and “gami” means paper; hence, “origami” means the folding of paper. Because of its ability to impart properties, such as development, stretching, cushioning, and strengthening to sheet

H. Shigemune (✉)
Shibaura Institute of Technology, Tokyo, Japan
e-mail: hshige.shalab@gmail.com

K. Suzumori et al. (eds.), *The Science of Soft Robots*, Natural Computing Series,
https://doi.org/10.1007/978-981-19-5174-9_12

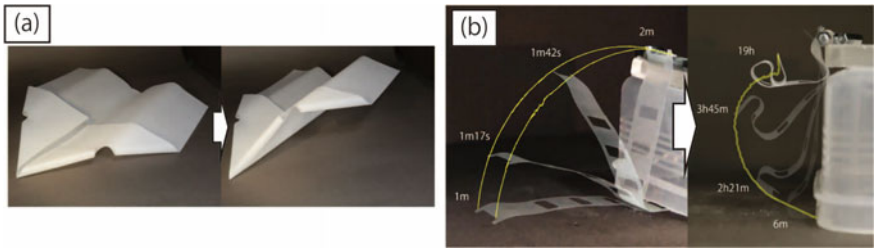

Fig. 12.1 Printed mechanics. **a** structure and **b** motility using self-folding paper. (Programming motility stepwise into a sheet of paper using inkjet printing/H. Shigemune et. al/Advanced Intelligent Systems/Vol. 3/Issue. 1 Copyright ©2021 Wiley)

materials without using additional components, origami has attracted wide attention from both mathematical and engineering researchers. Origami technology is one of the primary methods for forming sheet material structures, while paper mechatronics is created by folding electrical circuits. In other words, the device constructed using paper mechatronics is also considered an origami device, exhibiting unique mechanical properties.

Owing to the usefulness of origami technology, self-folding technology has been actively studied to automatically fabricate origami structures. Researchers have used heat, light, mechanical energy, and chemical energy to actuate the material. We developed a self-folding technique that automatically forms an origami structure by creating a physicochemical reaction between the printed paper and the printing solution. Consequently, the self-folding process continued without any human intervention or external stimuli. Paper is a unique material with high flexibility and has high water absorption. It has a thin film and is low-cost, lightweight, and environmentally friendly. The development of biodegradable green devices has increased owing to the use of paper electronics. Therefore, to meet the SDG's goal of recycling-oriented development, we successfully developed a quick and easy self-folding origami structure using the properties of paper.

Flexible and stretchable origami devices can be created by printing electrodes on self-folding paper. Figure 12.2 shows an origami device prototype fabricated using paper mechatronics. As shown in Fig. 12.2, the circuit and structure are formed on the same sheet of paper, whereas the circuit is formed on a different sheet and attached to another paper that self-folds (Shigemune et al. 2015). To date, we have developed an essential platform for creating origami devices. In the future, we hope to contribute to the further development of soft robotics by developing paper mechatronics for various applications, such as medicine, nursing care, transportation, agriculture, and space.

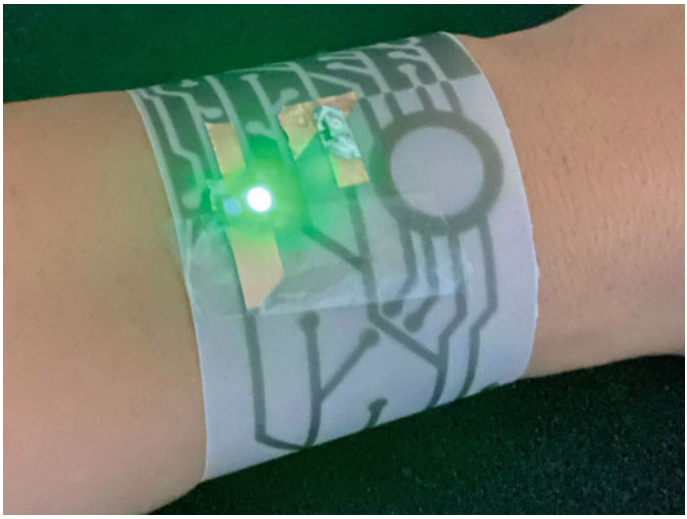

Fig. 12.2 Origami wearable device

References

Shigemune H, Maeda S, Hara Y, Koike U, Hashimoto S (2015) Kirigami robot: Making paper robot using desktop cutting plotter and inkjet printer. In: 2015 IEEE/RSJ international conference on intelligent robots and systems (IROS). IEEE, pp 1091–1096

Shigemune H, Maeda S, Hara Y, Hosoya N, Hashimoto S (2016) Origami robot: a self-folding paper robot with an electrothermal actuator created by printing. IEEE/ASME Trans Mechatron 21(6):2746–2754

Shigemune H, Maeda S, Cacucciolo V, Iwata Y, Iwase E, Hashimoto S, Sugano S (2017) Printed paper robot driven by electrostatic actuator. IEEE Robot Autom Lett 2(2):1001–1007

Shigemune H, Maeda S, Iwase E, Hashimoto S, Sugano S, Sawada H (2021) Programming stepwise motility into a sheet of paper using inkjet printing. Adv Intell Syst 3(1):2000153

Part III
Autonomous Soft Robots

Chapter 13
Modeling and Control of Continuum Body

Shinichi Hirai, Hiromi Mochiyama, Kohei Nakajima, and Nozomi Akashi

Abstract Modeling the motion and deformation of soft bodies is essential for understanding the behavior of soft robots. In this chapter, we formulate the static and dynamic behaviors of the soft robot bodies. Section 13.1 focuses on the statics and dynamics of soft-material robots based on the strain potential and kinetic energy of soft bodies. Section 13.2 explains the kinematics and statics of an elastic rod, which is one of the most common flexible parts used in soft robots, to gain a better understanding of its deformation nature. Section 13.3 introduces the fundamental concepts of nonlinear dynamical systems using examples from a simple mechanical system, known as a passive dynamic walker. Section 13.4 demonstrates how soft materials contribute to soft body control using two basic examples: simultaneous positioning of a soft body and orientation control through soft fingertips. An elastic rod is one of the most common flexible parts of a soft robot. In this chapter, the deformations of an elastic rod are considered based on their efficient computation and physical understanding, which require knowledge from various fields including differential geometry (O'Neill in Elementary differential geometry, Revised 2nd edn. Academic Press, 2006), mechanics (Timoshenko and Goodier in Theory of elasticity, 3rd edn. McGraw-Hill, 1970; Antman in Nonlinear problems of elasticity, 2nd edn. Springer, 2004), computer science (Keller in Numerical methods for two-point boundary value problems. Blaisdell Publishing, 1968), and robotics (Zodiac in Theory of robot control. Springer, 1996; Murray et al. in A mathematical introduction to robotic manipulation. CRC Press, 1994).

S. Hirai (✉)
Department of Robotics, Ritsumeikan University, Shiga, Japan
e-mail: hirai@se.ritsumei.ac.jp

H. Mochiyama
Graduate School of Systems and Information Engineering, University of Tsukuba, Tsukuba, Japan
e-mail: motiyama@iit.tsukuba.ac.jp

K. Nakajima
Graduate School of Information Science and Technology, The University of Tokyo, Tokyo, Japan
e-mail: k-nakajima@isi.imi.i.u-tokyo.ac.jp

N. Akashi
Graduate School of Informatics, Kyoto University, Kyoto, Japan
e-mail: akashi.nozomi.2a@kyoto-u.ac.jp

K. Suzumori et al. (eds.), *The Science of Soft Robots*, Natural Computing Series,
https://doi.org/10.1007/978-981-19-5174-9_13

13.1 The Physics of Soft Bodies

13.1.1 A Basic Concept: The Dimension of Soft Body Models

Soft robots move and deform. Here, we formulate the motion and deformation of soft robots. All actual soft robots have three-dimensional (3D) bodies that act in a 3D space. Therefore, it is natural to build soft 3D robot models. However, when the main motion and deformation of a soft robot are in a one-dimensional (1D) or two-dimensional (2D) space, 1D or 2D models are built to focus on the main motion and deformation of the robot. Consequently, the following models can be built: 1D models (Fig. 13.1a), 2D models (Fig. 13.1b), and 3D models (Fig. 13.1c). 1D models focus on translational motion and extensional deformation in a 1D space. 2D models focus on translational/rotational motion and extensional/shear deformation in a 2D space. 3D models focus on translational/rotational motion and extensional/shear deformation in a 3D space. It should be noted that rotational motion and shear deformation appear in both 2D and 3D models. Soft robots comprising soft materials are referred to as *soft-material robots*. These three models are applicable to soft-material robots.

When one or two dimensions of the body are dominant over the other dimension(s), the body may deform. Soft robots with these bodies are referred to as

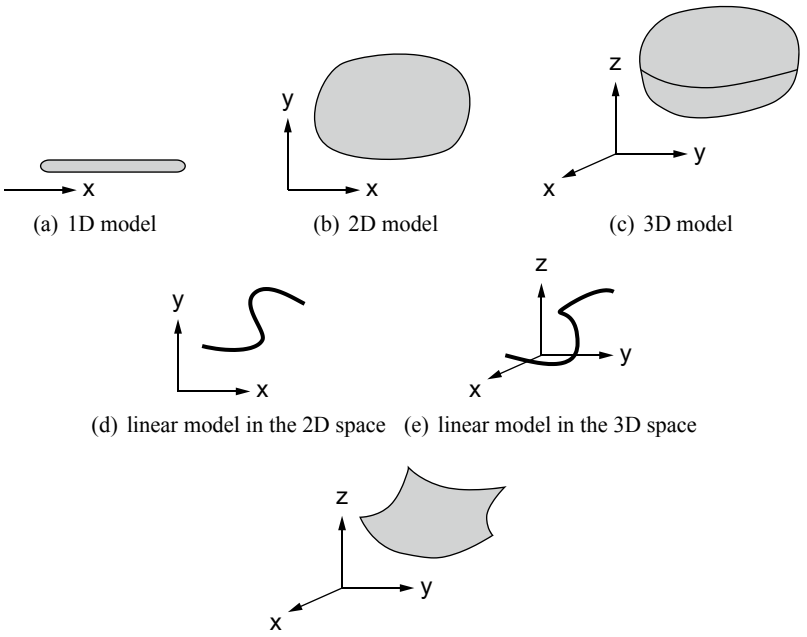

(a) 1D model (b) 2D model (c) 3D model

(d) linear model in the 2D space (e) linear model in the 3D space

(f) planar model in the 3D space

Fig. 13.1 Soft robot models

geometrically deformable robots. The models were built by focusing on the dominant dimension(s). *Deformable linear models* have one dominant dimension; that is, the other two dimensions are negligible. Deformable linear models in 2D space (Fig. 13.1d) focus on bending and extensional deformations. Deformable linear models in 3D space (Fig. 13.1e) focus on bending, twisting, and extensional deformations. *Deformable planar models* (Fig. 13.1f) have two dominant dimensions, that is, the third dimension is negligible. They focus on bending and extensional deformations in 3D space.

13.1.2 Describing Motion and Deformation

Let us formulate the motion and deformation of a 2D soft robot in 2D space. A 2D soft robot comprises a 2D region S in its natural state (Fig. 13.2a). Let $P(x, y)$ be an arbitrary point in the soft robot, where $(x, y) \in S$. We assume that this 2D soft robot moves and deforms (Fig. 13.2b). The displacement of point $P(x, y)$ is then given by a 2D vector as follows:

$$\boldsymbol{u}(x, y) = \begin{bmatrix} u(x, y) \\ v(x, y) \end{bmatrix}. \tag{13.1}$$

The motion and deformation of a 2D soft robot can be described by a vector function $\boldsymbol{u}(x, y)$, that is, by its two components $u(x, y)$ and $v(x, y)$. 2D soft robots perform translational motion, rotational motion, and deformation. Let us describe the deformation of a 2D soft robot using partial derivatives as follows: $u_x = \frac{\partial u}{\partial x}$, $u_y = \frac{\partial u}{\partial y}$, $v_x = \frac{\partial v}{\partial x}$, and $v_y = \frac{\partial v}{\partial y}$. The translational motion of a 2D soft robot does not affect these partial derivatives, because any translational motion yields constant displacement components over the region S. The deformation of a 2D soft robot can be classified into extension along the x-axis, extension along the y-axis, and shear deformation. Additionally, rotational motion affects the partial derivatives. The partial derivatives are related to the extensional/shear deformations and rotational motion as follows:

$$\frac{\partial u}{\partial x} = \text{extension along } x\text{-axis}, \qquad \frac{\partial v}{\partial y} = \text{extension along } y\text{-axis},$$
$$\frac{\partial v}{\partial x} = \text{shear} + \text{rotation}, \qquad \frac{\partial u}{\partial y} = \text{shear} - \text{rotation}.$$

Let ε_{xx} and ε_{yy} be the normal strain components along the x- and y-axes at point P and ε_{xy} be the shear strain at point P. Thus, it is possible to express the following:

$$\varepsilon_{xx} = \frac{\partial u}{\partial x}, \qquad \varepsilon_{yy} = \frac{\partial v}{\partial y}, \qquad 2\varepsilon_{xy} = \frac{\partial u}{\partial y} + \frac{\partial v}{\partial x}, \tag{13.2}$$

which are referred to as *Cauchy strain components*, or simply *strain components*. Let us define

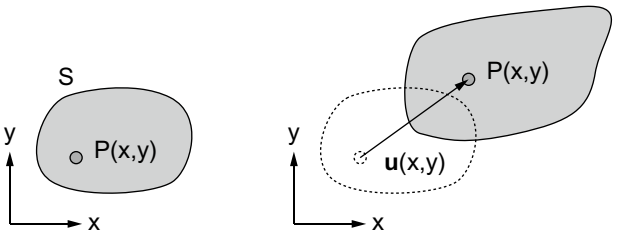

(a) natural state (b) moved and deformed state

Fig. 13.2 Displacement function of a 2D soft robot

$$\boldsymbol{\varepsilon} \triangleq \begin{bmatrix} \varepsilon_{xx} \\ \varepsilon_{yy} \\ 2\varepsilon_{xy} \end{bmatrix} \tag{13.3}$$

which is referred to as a *pseudo-strain vector*, or simply a *strain vector*. This strain vector describes the deformation of a soft robot at arbitrary point P.

The deformation of the soft robot yields strain potential energy. We now formulate the strain potential energy of a 2D soft robot. Assuming that the robot material exhibits *linear isotropic elasticity*, the strain energy density at point $P(x, y)$ is formulated as follows:

$$\frac{1}{2}\boldsymbol{\varepsilon}^{\mathrm{T}}(\lambda I_\lambda + \mu I_\mu)\boldsymbol{\varepsilon} \tag{13.4}$$

where λ and μ are Lamé's constants, and

$$I_\lambda = \begin{bmatrix} 1 & 1 & \\ 1 & 1 & \\ & & \end{bmatrix}, \quad I_\mu = \begin{bmatrix} 2 & & \\ & 2 & \\ & & 1 \end{bmatrix}. \tag{13.5}$$

Lamé's constants λ and μ are specific to the robot material and are related to the Young's modulus E and Poisson's ratio ν as follows:

$$\lambda = \frac{\nu E}{(1+\nu)(1-2\nu)}, \qquad \mu = \frac{E}{2(1+\nu)}.$$

Let h be the thickness of the robot at point $P(x, y)$. The volume element at point $P(x, y)$ is then described as follows: $h\,\mathrm{d}S = h\,\mathrm{d}x\,\mathrm{d}y$. Integrating the product of the energy density and volume element over the 2D region, S yields the strain potential energy. Consequently, the strain potential energy stored in a 2D soft robot can be formulated as follows:

$$U = \int_S \frac{1}{2}\boldsymbol{\varepsilon}^{\mathrm{T}}(\lambda I_\lambda + \mu I_\mu)\boldsymbol{\varepsilon}\, h\,\mathrm{d}S. \tag{13.6}$$

It is noteworthy that λ, μ, and h may depend on (x, y).

The soft robot motion yields kinetic energy. We now formulate the kinetic energy of a 2D soft robot. The velocity vector at the point $P(x, y)$ is given by $\dot{\boldsymbol{u}} = [\dot{u}, \dot{v}]^{\mathrm{T}}$. The kinetic energy density was then formulated as follows:

$$\frac{1}{2}\rho\, \dot{\boldsymbol{u}}^{\mathrm{T}}\dot{\boldsymbol{u}} = \frac{1}{2}\rho\left(\dot{u}^2 + \dot{v}^2\right) \tag{13.7}$$

where ρ denotes the density of robot material. Integrating the product of the energy density and volume element over the 2D region, S yields kinetic energy. Consequently, the kinetic energy of a 2D soft robot can be formulated as follows:

$$T = \int_S \frac{1}{2}\rho\, \dot{\boldsymbol{u}}^{\mathrm{T}}\dot{\boldsymbol{u}}\, h\, \mathrm{d}S. \tag{13.8}$$

It is noteworthy that ρ and h may depend on (x, y).

The strain potential energy U and kinetic energy T of a 2D soft body S are described as integrals over the region S. Finite element approximation (Fish and Belytschko 2007) provides a method for calculating these integrals. We approximated the 2D region S using a set of small triangles. The integral over the 2D region S can then be approximated by the sum of the integrals over the small triangles:

$$\int_S \approx \sum_{\Delta P_i P_j P_k} \int_{\Delta P_i P_j P_k},$$

where $\Delta P_i P_j P_k$ denotes a small triangle identified by three vertices P_i, P_j, and P_k. Let P_i for $i = 1, \ldots n$ be the vertices of all small triangles. These vertices are referred to as the *nodal points*. Let $\boldsymbol{u}_1$ through $\boldsymbol{u}_n$ be the displacement vectors of the nodal points P_1 through P_n, respectively. The motion and deformation of a 2D body can be approximated by the displacements $\boldsymbol{u}_1$ through $\boldsymbol{u}_n$. Let $\boldsymbol{u}_{\mathrm{N}}$ be a collective vector consisting of $\boldsymbol{u}_1$ through $\boldsymbol{u}_n$, the motion and deformation of a 2D body can be described by vector $\boldsymbol{u}_{\mathrm{N}}$, which is referred to as a *nodal displacement vector*.

Assume that Lamé's constants λ and μ as well as the density ρ and width h are uniform over the body, indicating that they are constants. By approximating region S using a finite number of triangles, the strain potential and kinetic energies can be described as follows:

$$U = \frac{1}{2}\boldsymbol{u}_{\mathrm{N}}^{\mathrm{T}}\, K\, \boldsymbol{u}_{\mathrm{N}}, \qquad T = \frac{1}{2}\dot{\boldsymbol{u}}_{\mathrm{N}}^{\mathrm{T}}\, M\, \dot{\boldsymbol{u}}_{\mathrm{N}},$$

where M denotes the inertia matrix, and K represents the stiffness matrix. Consequently, the strain potential energy U is described in quadratic form with respect to $\boldsymbol{u}_{\mathrm{N}}$, and the kinetic energy T is given by another quadratic form with respect to $\dot{\boldsymbol{u}}_{\mathrm{N}}$.

The strain potential energy U and kinetic energy T of a 3D soft body V are described as integrals over the region V. Using the finite element approximation, we observed that the strain potential and kinetic energies are also described by the above equations.

13.1.3 Computing Static Deformations

We calculated the static deformation of the elastic body. We applied the variational principle in statics for the calculation. Let U be the potential energy of a body. External forces applied to the body deform it. Let W be the work done by external forces. The geometric constraints imposed on the body cause its deformation. Let $\boldsymbol{R}$ be a collective vector of geometric constraints. The variational principle in statics states that internal energy $I = U - W$ reaches its minimum under a set of geometric constraints $\boldsymbol{R} = \boldsymbol{0}$ at equilibrium. In other words, the static deformation of the body can be calculated by minimizing the internal energy under geometric constraints as follows:

$$\begin{aligned} &\text{minimize } I = U - W \\ &\text{subject to } \boldsymbol{R} = \boldsymbol{0}. \end{aligned} \tag{13.9}$$

In the finite element approximation, the deformation of an elastic body is described by the nodal displacement vector $\boldsymbol{u}_{\mathrm{N}}$, which implies that the internal energy and geometric constraints are functions of the vector $\boldsymbol{u}_{\mathrm{N}}$. Calculating the vector $\boldsymbol{u}_{\mathrm{N}}$ that minimizes the internal energy $I(\boldsymbol{u}_{\mathrm{N}})$ under the geometric constraints $\boldsymbol{R}(\boldsymbol{u}_{\mathrm{N}}) = \boldsymbol{0}$ yields the static deformation of the body.

Subsequently, we calculate the deformation of an elastic membrane deformed by the air pressure. It was assumed that the elastic membrane was attached to a rigid shell. Pressure p was applied to the chamber, which was surrounded by the membrane and shell. The applied pressure deformed the membrane. The work done by constant pressure p is formulated as follows:

$$W = pV, \tag{13.10}$$

where V denotes the increment in the chamber volume. In 2D deformations, V is given by hS, where S denotes the increment in the chamber area.

We attached to the rigid shell an elastic membrane with width 10 cm, height 1 cm, thickness $h = 1$ cm, Young's modulus $E = 0.1$ MPa, and Poisson's ratio $\nu = 0.48$. The membrane region is divided into $10 \times 1 \times 2$ triangles (Fig. 13.3a). Pressure is applied to the bottom edges P_1P_2 through $P_{10}P_{11}$. The increment in the chamber area is described by polygon $P_{11}P_{10} \cdots P_2P_1$. The signed polygon area $S(\boldsymbol{u}_{\mathrm{N}})$ takes a positive value when the membrane expands, and a negative value when it shrinks. Finally, we obtain the following conditional optimization problem:

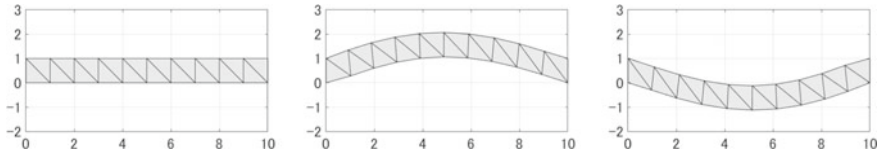

(a) natural (b) positive pressure (c) negative pressure

Fig. 13.3 Deformation of a membrane under pressure

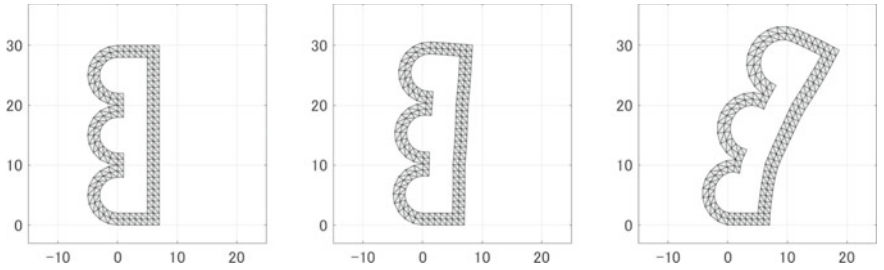

(a) natural (b) 500 kPa (c) 700 kPa

Fig. 13.4 Deformation of a PneuNet actuator

$$\begin{aligned} &\text{minimize } I(\boldsymbol{u}_{\mathrm{N}}) = \frac{1}{2}\boldsymbol{u}_{\mathrm{N}}^{\mathrm{T}} K\, \boldsymbol{u}_{\mathrm{N}} - ph\, S(\boldsymbol{u}_{\mathrm{N}}) \\ &\text{subject to } A^{\mathrm{T}}\boldsymbol{u}_{\mathrm{N}} = \boldsymbol{0}. \end{aligned} \tag{13.11}$$

It is worth noting that $A^{\mathrm{T}}\boldsymbol{u}_{\mathrm{N}} = \boldsymbol{0}$ corresponds to a set of geometric constraints: $\boldsymbol{u}_1 = \boldsymbol{0}, \boldsymbol{u}_{11} = \boldsymbol{0}, \boldsymbol{u}_{12} = \boldsymbol{0}$, and $\boldsymbol{u}_{22} = \boldsymbol{0}$. By applying a conditional optimization algorithm to the above problem, we obtain the nodal displacement vector $\boldsymbol{u}_{\mathrm{N}}$, which describes the deformed shape of the membrane. Figure 13.3b shows the computation result at an applied pressure $p = 2$ kPa. The membrane deforms outward. Because $S(\boldsymbol{u}_{\mathrm{N}})$ denotes the signed area, which can take a negative value, we can calculate the deformation corresponding to a negative pressure. Figure 13.3c shows the computation result at a negative pressure $p = -2$ kPa. The membrane deforms inward, which describes the actual phenomenon.

Subsequently, we calculate the static deformation of a PneuNet actuator (Fig. 13.4a). This actuator is composed of an elastic material with Young's modulus $E = 0.1$ MPa and Poisson's ratio $\nu = 0.48$ and consists of three air chambers along its left side. Air pressure was applied inside the actuator, expanding the air chambers, which yielded the bending deformation of the actuator (Fig. 13.4b, c). The actual PneuNet actuators are 3D actuators; the junctions between neighboring air chambers and the right side of the actuator are connected by front and back elastic covers, resulting in the distance between the junction and the right side remaining almost constant. Therefore, in this calculation, we impose two geometric constraints: (i) the distances between individual junctions and the right side remains constant, and (ii) the nodal

points on the bottom edge are fixed to the floor. We calculate the deformed shape of the actuator at a specified air pressure. Figure 13.4b shows the deformation at an applied pressure of 500 kPa, and Fig. 13.4c shows the deformation at an applied pressure of 700 kPa. It was observed that the application of a 500 kPa caused little deformation, whereas a 700 kPa pressure induced considerable deformation.

13.1.4 Computing Dynamic Deformations

Next, we formulate the dynamic deformation of a 2D elastic body described by S. Assume that Lamé's constants λ and μ as well as the density ρ and width h are uniform over the body. The kinetic and strain potential energies can be described as follows:

$$T = \frac{1}{2}\dot{\boldsymbol{u}}_{\mathrm{N}}^{\mathrm{T}} M\, \dot{\boldsymbol{u}}_{\mathrm{N}}, \qquad U = \frac{1}{2}\boldsymbol{u}_{\mathrm{N}}^{\mathrm{T}} K\, \boldsymbol{u}_{\mathrm{N}},$$

where $\boldsymbol{u}_{\mathrm{N}}$ denotes the nodal displacement vector, M denotes the inertia matrix, and K denotes the stiffness matrix. The work done by external forces can be formulated as follows:

$$W = \boldsymbol{f}^{\mathrm{T}}\boldsymbol{u}_{\mathrm{N}}.$$

A set of geometric constraints imposed on the body can be described as follows:

$$\boldsymbol{R} = A^{\mathrm{T}}\boldsymbol{u}_{\mathrm{N}} - \boldsymbol{b}(t) = \boldsymbol{0},$$

where $\boldsymbol{b}(t)$ denotes a collective vector that describes the position of the constrained points at time t. Consequently, the following Lagrangian is obtained:

$$\begin{aligned}\mathcal{L}(\boldsymbol{u}, \dot{\boldsymbol{u}}) &= T - U + W + \boldsymbol{\lambda}^{\mathrm{T}}\boldsymbol{R} \\ &= \frac{1}{2}\dot{\boldsymbol{u}}_{\mathrm{N}}^{\mathrm{T}} M\, \dot{\boldsymbol{u}}_{\mathrm{N}} - \frac{1}{2}\boldsymbol{u}_{\mathrm{N}}^{\mathrm{T}} K\, \boldsymbol{u}_{\mathrm{N}} + \boldsymbol{f}^{\mathrm{T}}\boldsymbol{u}_{\mathrm{N}} + \boldsymbol{\lambda}^{\mathrm{T}}\left(A^{\mathrm{T}}\boldsymbol{u}_{\mathrm{N}} - \boldsymbol{b}(t)\right),\end{aligned} \tag{13.12}$$

where $\boldsymbol{\lambda}$ denotes a collective vector of Lagrange multipliers corresponding to a set of constraints. Because M and K are constant matrices, we obtain the following:

$$\frac{\partial \mathcal{L}}{\partial u_{\mathrm{N}}} = -K\boldsymbol{u}_{\mathrm{N}} + \boldsymbol{f} + A\boldsymbol{\lambda}, \qquad \frac{\partial \mathcal{L}}{\partial \dot{\boldsymbol{u}}_{\mathrm{N}}} = M\dot{\boldsymbol{u}}_{\mathrm{N}}$$

which directly yields

$$-K\boldsymbol{u}_{\mathrm{N}} + \boldsymbol{f} + A\boldsymbol{\lambda} - M\ddot{\boldsymbol{u}}_{\mathrm{N}} = \boldsymbol{0} \tag{13.13}$$

The equation for stabilizing the constraint $A\boldsymbol{u}_{\mathrm{N}} = \boldsymbol{0}$ is expressed as follows:

$$\left(A^{\mathrm{T}}\ddot{\boldsymbol{u}}_{\mathrm{N}} - \ddot{\boldsymbol{b}}(t)\right) + 2\alpha\left(A^{\mathrm{T}}\dot{\boldsymbol{u}}_{\mathrm{N}} - \dot{\boldsymbol{b}}(t)\right) + \alpha^2\left(A^{\mathrm{T}}\boldsymbol{u}_{\mathrm{N}} - \boldsymbol{b}(t)\right) = \boldsymbol{0}, \tag{13.14}$$

where α is a positive constant. By introducing $\boldsymbol{v}_{\mathrm{N}} = \dot{\boldsymbol{u}}_{\mathrm{N}}$, the above two ordinary differential equations (ODEs) collectively become the following:

$$\begin{bmatrix} M & -A \\ -A^{\mathrm{T}} & \end{bmatrix} \begin{bmatrix} \dot{\boldsymbol{v}}_{\mathrm{N}} \\ \boldsymbol{\lambda} \end{bmatrix} = \begin{bmatrix} -K\boldsymbol{u}_{\mathrm{N}} + \boldsymbol{f} \\ C(\boldsymbol{u}_{\mathrm{N}}, \boldsymbol{v}_{\mathrm{N}}) \end{bmatrix} \tag{13.15}$$

where

$$\boldsymbol{C}(\boldsymbol{u}_{\mathrm{N}}, \boldsymbol{v}_{\mathrm{N}}) = -\ddot{\boldsymbol{b}}(t) + 2\alpha(A^{\mathrm{T}}\boldsymbol{v}_{\mathrm{N}} - \dot{\boldsymbol{b}}(t)) + \alpha^2 \left(A^{\mathrm{T}}\boldsymbol{u}_{\mathrm{N}} - \boldsymbol{b}(t)\right).$$

The above equation provides a canonical form of the ODEs, which can be solved numerically using a standard ODE solver.

Next, we calculate the dynamic behavior of an elastic ring driven by eight spring actuators (Sugiyama and Hirai 2006). We focused on the 2D deformation of the cross-sectional area of the ring (Fig. 13.5a). The outer and inner radii of the ring were 5 and 4 mm, respectively, in its natural shape. The ring material exhibited isotropic linear elasticity, which is described by $E = 0.1$ MPa and $\nu = 0.48$. Green strain is used during the calculation. Let the density and viscous modulus of the ring material be $\rho = 1\,\mathrm{g/cm^3}$ and $c = 0.04$ kPa s. Eight spring actuators labeled A_1 through A_8 counterclockwise were radially distributed inside the ring. Mass m supports the spring actuators; that is, one end of each spring actuator is connected to the mass, and the other end is connected to the inner surface of the ring. In its natural state, actuator A_1 is below the mass. Let the mass be $m = 1$ g and the acceleration of gravity be $g = 9.8\,\mathrm{m/s^2}$. We assume that the natural length of all actuators is $L = 4$ mm; that is, the natural length is equal to the inner radius of the ring. Let the spring constant of all the actuators be $k = 20\,\mathrm{N/m}$.

Next, we simulate the dynamic rolling of a ring on the floor. Rolling on the floor is described by the penalty method with a normal spring constant $K_{\mathrm{p}} = 1000\,\mathrm{N/m}$ and tangential damping constant $B_{\mathrm{t}} = 20\,\mathrm{N/(m/s)}$. Figure 13.5 shows a snapshot of the computation result. The natural shape (Fig. 13.5a) of the elastic ring deformed under gravity. Subsequently, the pair of opposite spring actuators A_2 and A_6 applied a shrinking force of 5 N (Fig. 13.5b–d). After relaxing all spring actuators (Fig. 13.5e), another pair of opposite spring actuators, namely A_3 and A_7, applied a shrinking force of 5 N (Fig. 13.5f–h). After relaxing all spring actuators (Fig. 13.5i), the pair of opposite spring actuators A_4 and A_8 applied a shrinking force of 5 N (Fig. 13.5j–l). This result demonstrates that the elastic ring rolls rightward through its deformation caused by successive activation of the spring actuators: A_2 and A_6, A_3 and A_7, and then A_4 and A_8.

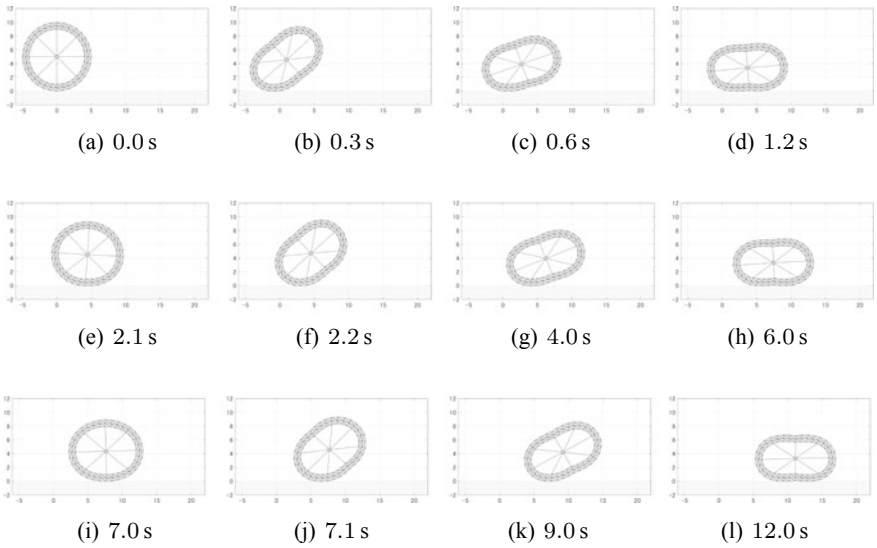

Fig. 13.5 Rolling of an elastic ring driven by spring actuators

13.1.5 Practicalities and Challenges

Commercial software, such as ANSYS and Abaqus, can be used for the finite element calculation of soft body deformations. Additionally, open-source software, such as MFEM (https://mfem.org/) and SOFA (https://hal.inria.fr/SOFA/), is available.

We can compute the static/dynamic deformation of soft bodies. However, the design of soft bodies remains dominated by trial-and-error methods, because systematic approaches are lacking. Investigations into the design of soft hands for grasping given items and soft bodies for faster locomotion and higher jumping have already begun. The design of soft bodies will be a future challenges. The behavior of soft bodies in contact with the environment depends not only on the material properties but also on the surface properties, such as friction and adhesion. Contact modeling that incorporates friction and adhesion remains an issue that must be addressed.

Exercises

1. A soft robot moves inside a smooth rigid tube. The robot's body consists of a cylindrical soft tube (length L, outer radius R, and inner radius r) and thin rigid plates attached to both ends of the tube. Young's modulus of the tube material is given by E. Air pressure P is applied inside the tube through its one end. Assume that the robot extends along its central axis alone and radial deformation

is negligible. Let $L = 100\,\text{mm}$, $R = 10\,\text{mm}$, $r = 6\,\text{mm}$, $E = 1.0\,\text{MPa}$, and $P = 0.10\,\text{MPa}$, estimate the extensional deformation of the robot.

2. Assume that $P(x, y)$ and $Q(x + \delta x, y + \delta y)$ are neighboring points. Let δs be the distance between P and Q in the natural shape and $\delta s'$ be the distance in the deformed shape. Introduce $u_x = \partial u/\partial x$, $u_y = \partial u/\partial y$, $v_x = \partial v/\partial x$, and $v_y = \partial v/\partial y$. Show that

$$(\delta s')^2 - (\delta s)^2 = 2\begin{bmatrix}\delta x & \delta y\end{bmatrix}\begin{bmatrix}E_{xx} & E_{xy}\\ E_{xy} & E_{yy}\end{bmatrix}\begin{bmatrix}\delta x\\ \delta y\end{bmatrix}$$

where

$$\begin{aligned} E_{xx} &= u_x + \frac{1}{2}\left(u_x^2 + v_x^2\right)\\ E_{yy} &= v_y + \frac{1}{2}\left(u_y^2 + v_y^2\right)\\ 2E_{xy} &= u_y + v_x + \left(u_x u_y + v_x v_y\right)\end{aligned}$$

are referred to as *Green strain components*.

13.2 Rod Theory

13.2.1 Kinematics

Consider a slender elastic rod. It is assumed that the rod is inextensible and unshearable. To understand the essence of the analysis here, consider the rod to be a rectangular prism with length L, width w, and thickness t at rest. We can draw a curve by connecting the cross-sectional centers perpendicular to the direction of the length. This curve characterizes the shape of an elastic rod. This curve is known as the backbone curve. The curve is straight when no external force is applied to the rod. However, with some external force, the rod deforms and the backbone curve changes its shape accordingly. Therefore, rod deformations can be expressed by the shapes of the backbone curves. One end of the elastic rod is fixed to the ground, referred to as the base, and the other end is called the tip.

In this section, the kinematics of the backbone curve are discussed. First, let $\sigma \in [0\ L]$ be the arc length parameter of the backbone curve. Let $\boldsymbol{p}(\sigma) \in \Re^3$ denotes the position vector of a point on the curve at σ. From the perspective of differential geometry, the most natural method to study the shape of a curve is to measure the rate of change of the frames attached along the curve. A frame comprises a set of three orthogonal unit vectors. These unit vectors are called the x-, y-, and z-axes of the frame. The x-axis of each frame is aligned with the tangent line of the curve. The z-axis of each frame is aligned with the major bending axis of the rod. In this case, the z-axis is in the width direction. The y-axis of each frame is aligned to

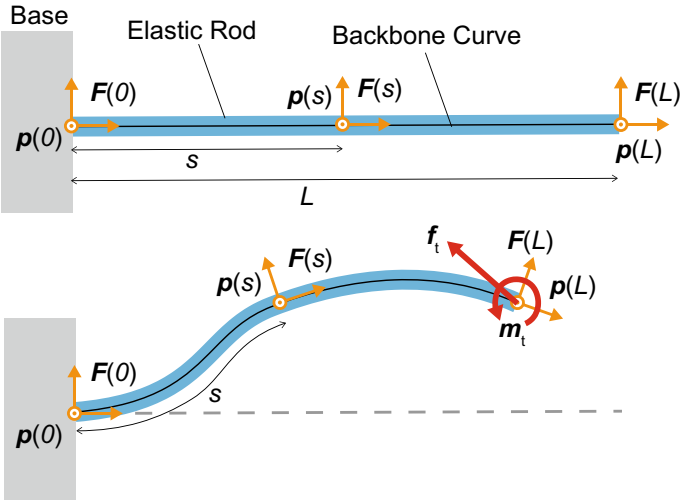

Fig. 13.6 Continuum model of an elastic rod

complete a right-handed frame. Let $\boldsymbol{F}(\sigma) \in \mathrm{SO}(3)$ be the orientation matrix of frame, where $\mathrm{SO}(3) := \left\{ \boldsymbol{F} \in \Re^{3\times 3} \mid \boldsymbol{F}^{\mathrm{T}}\boldsymbol{F} = \boldsymbol{I}_3, \det \boldsymbol{F} = 1 \right\}$ denotes the three-dimensional special orthogonal group, and $\boldsymbol{I}_3$ denotes the three-dimensional identity matrix. The orientation matrix of a frame is one of the most typical methods of expressing the orientation of a rigid body. This matrix is created by arranging the three unit vectors of the x-, y-, and z-axes of a frame in a row. Note that all orientation matrices on the backbone curve are identical if they are straight (Fig. 13.6).

Let $\boldsymbol{p}_{\mathrm{b}} \in \Re^3$ and $\boldsymbol{F}_{\mathrm{b}} \in \mathrm{SO}(3)$ be the position vector and orientation matrix, respectively, for the fixed base end of the rod. The constraints at the base are expressed as follows:

$$\boldsymbol{p}(0) = \boldsymbol{p}_{\mathrm{b}} \tag{13.16}$$

$$\boldsymbol{F}(0) = \boldsymbol{F}_{\mathrm{b}} \tag{13.17}$$

The shape of the backbone curve is characterized by the following differential equations:

$$\frac{\mathrm{d}\boldsymbol{p}}{\mathrm{d}\sigma}(\sigma) = \boldsymbol{F}(\sigma)\boldsymbol{e}_x \tag{13.18}$$

$$\frac{\mathrm{d}\boldsymbol{F}}{\mathrm{d}\sigma}(\sigma) = \boldsymbol{F}(\sigma)\left[\boldsymbol{\theta}(\sigma)\times\right] \tag{13.19}$$

where $\boldsymbol{\theta}(\sigma) := [\theta_{\mathrm{t}}(\sigma)\ \theta_{\mathrm{n}}(\sigma)\ \theta_{\mathrm{b}}(\sigma)]^{\mathrm{T}} \in \Re^3$ is a vector that expresses the bending and twisting of the backbone curve and its elements $\theta_{\mathrm{t}}(\sigma)$, $\theta_{\mathrm{n}}(\sigma)$, and $\theta_{\mathrm{b}}(\sigma) \in \Re$ are infinitesimal rotations around the corresponding axes of a frame at σ. Symbol $[\cdot\times] : \Re^3 \to \mathrm{so}(3)$ represents an operator that expands a three-dimensional vector

into a corresponding three-dimensional skew-symmetric matrix. For example, for $\boldsymbol{x}, \boldsymbol{y} \in \Re^3$, $[\boldsymbol{x}\times]\,\boldsymbol{y} = \boldsymbol{x} \times \boldsymbol{y}$ holds, where '$\times$' on the right-hand side represents the outer product of two vectors and so(3) denotes the set of three-dimensional skew-symmetric matrices. Vector $\boldsymbol{e}_x := [1\ 0\ 0]^{\mathrm{T}}$ is the unit vector in the x-direction and $\boldsymbol{e}_y$ and $\boldsymbol{e}_z$ are defined in a similar manner. Note that $\boldsymbol{\theta}(\sigma)$ is a geometric quantity, that is, it is coordinate-free. If $\theta_{\mathrm{n}}(\sigma) \equiv 0$, $\theta_{\mathrm{t}}(\sigma)$ and $\theta_{\mathrm{b}}(\sigma)$ correspond to curvature and torsion of a spatial curve, respectively, in this case, differential equations reduce to the famous Frenet–Serret functions. Therefore, (13.18) and (13.19) can be supposed to be an extended version of the Frenet–Serret formulas. These equations suggest the following: three parameters are necessary for considering the deformation of the elastic rod, whereas it is sufficient for the geometry of a spatial curve to have two parameters, that is, the curvature and torsion.

In the planar case, the differential equations have the following solutions:

$$\boldsymbol{p}(\sigma) = \left[\int_0^\sigma \cos\phi(\eta)\mathrm{d}\eta \quad \int_0^\sigma \sin\phi(\eta)\mathrm{d}\eta \quad 0\right]^{\mathrm{T}} \tag{13.20}$$

$$\boldsymbol{F}(\sigma) = \begin{bmatrix} \cos\phi(\sigma) & -\sin\phi(\sigma) & 0 \\ \sin\phi(\sigma) & \cos\phi(\sigma) & 0 \\ 0 & 0 & 1 \end{bmatrix} \tag{13.21}$$

where $\phi(\sigma) \in C := (-\pi, \pi]$ is the absolute angle, that is, angle of the tangent line of the curve at σ measured from the x-axis, which can be expressed as follows:

$$\phi(\sigma) = \int_0^\sigma \theta_{\mathrm{b}}(\eta)\,\mathrm{d}\eta + \phi_{\mathrm{b}} \tag{13.22}$$

where $\phi_{\mathrm{b}} \in C$ denotes the absolute angle of the tangent line of the curve at the base, and is used instead of $\boldsymbol{F}_{\mathrm{b}}$.

Deformation of an elastic rod requires external forces and/or moments. We assumed that external forces/moments were applied only at the base and tip of the rod. Therefore, we introduced additional constraints on the position and orientation of the tip. Suppose that the tip of an elastic rod is fixed at position $\boldsymbol{p}^* \in \Re^3$ with orientation $\boldsymbol{F}^* \in \mathrm{SO}(3)$. The boundary conditions can then be expressed as follows:

$$\boldsymbol{p}(L) = \boldsymbol{p}^* \tag{13.23}$$

$$\boldsymbol{F}(L) = \boldsymbol{F}^* \tag{13.24}$$

13.2.2 Statics

It has been assumed that an elastic rod is inextensible and unshearable. In addition, we assume a linear constitutive equation: Moment at each point on the backbone curve $\boldsymbol{\tau}(\sigma) := [\tau_{\mathrm{t}}(\sigma)\ \tau_{\mathrm{n}}(\sigma)\ \tau_{\mathrm{b}}(\sigma)]^{\mathrm{T}} \in \Re^3$ is proportional to the infinitesimal rotation around the frame axes. An elastic rod that satisfies these assumptions is called a Kirchhoff. Let E and ν be the Young's modulus and Poisson's ratio of the material used for the elastic rod, respectively. The linear constitutive equation is given as follows:

$$\boldsymbol{\tau}(\sigma) = \boldsymbol{K}\boldsymbol{\theta}(\sigma) \tag{13.25}$$

where $\boldsymbol{K} = \mathrm{diag}\{k_{\mathrm{t}}, k_{\mathrm{n}}, k_{\mathrm{b}}\}$ is a three-dimensional diagonal matrix, and its three diagonal elements k_{t}, k_{n}, and k_{b} are the parameters of rotational stiffness around the axes of the frame. Let I_{b} and I_{n} be the moments of inertia of the cross section of the rod with respect to the z- and y-axes of the frame, respectively. Let I_{t} be the polar moment of inertia of the cross section. Let $G = E/2(1+\nu)$ be the modulus of rigidity. The stiffness parameters can then be expressed as $k_{\mathrm{t}} = GI_{\mathrm{t}}$, $k_{\mathrm{n}} = EI_{\mathrm{n}}$, and $k_{\mathrm{b}} = EI_{\mathrm{b}}$. Using this rotational stiffness matrix $\boldsymbol{K}$, the strain potential energy stored in an elastic rod $U \in [0\ \infty)$ can be represented as follows:

$$U = \int_0^L \frac{1}{2}\boldsymbol{\theta}^{\mathrm{T}}(\sigma)\boldsymbol{K}\boldsymbol{\theta}(\sigma)\mathrm{d}\sigma \tag{13.26}$$

In planar cases, the constitutive equation can be written as follows:

$$\tau_{\mathrm{b}}(\sigma) = k_{\mathrm{b}}\theta_{\mathrm{b}}(\sigma) \tag{13.27}$$

The planar strain potential energy is expressed as follows:

$$U = \int_0^L \frac{1}{2}k_{\mathrm{b}}\theta_{\mathrm{b}}^2(\sigma)\mathrm{d}\sigma \tag{13.28}$$

We now formulate the problem that we would like to solve. In a statically balancing situation, an elastic rod takes the shape where the strain potential energy is locally minimal.

Shape computation problem For an elastic rod model (13.18) and (13.19), under boundary conditions (13.23) and (13.24), determine the shape (i.e., bending and twisting) $\boldsymbol{\theta}(\sigma)$, $\sigma \in [0\ L]$ which locally minimizes strain potential energy (13.26). ◊

It is important to note that if an elastic rod forms a statically balanced shape, the following Euler equation holds for any $\sigma \in [0\ L]$ value.

$$\boldsymbol{F}(\sigma)\boldsymbol{K}\boldsymbol{\theta}(\sigma) = \{\boldsymbol{p}(L) - \boldsymbol{p}(\sigma)\} \times \boldsymbol{\lambda}_{\mathrm{e}} + \boldsymbol{\tau}_{\mathrm{e}} \tag{13.29}$$

where $\boldsymbol{\lambda}_{\mathrm{e}} \in \Re^3$ and $\boldsymbol{\tau}_{\mathrm{e}} \in \Re$ represent the constraint force and moment at the tip, respectively. This pair of forces and moments was used to fix the tip position and orientation at the designated positions (13.23) and (13.24). The Euler equation represents the moment balance. The moment generated by the tip constraint force and moment must be equal to the reaction moment against the rod deformation. Note that the moment balance equation (13.29) holds at any point on the backbone curve.

In planar cases, the Euler equation is reduced to the following scalar equation:

$$k_{\mathrm{b}}\theta_{\mathrm{b}}(\sigma) = \boldsymbol{e}_z^{\mathrm{T}}\{(\boldsymbol{p}(L) - \boldsymbol{p}(\sigma)) \times \boldsymbol{\lambda}_{\mathrm{e}}\} + \tau_{\mathrm{e}} \tag{13.30}$$

where $\tau_{\mathrm{e}} := \boldsymbol{e}_z^{\mathrm{T}}\boldsymbol{\tau}_{\mathrm{e}}$ has been introduced because the x- and y-elements of $\boldsymbol{\tau}_{\mathrm{e}}$ are always zero. Again, even in planar cases, the Euler equation (13.30) holds for arbitrary $\sigma \in [0\ L]$.

Here, we show a better expression of the Euler equation for a subsequent computational discussion. Let $\boldsymbol{f}_{\mathrm{b}} \in \Re^3$ and $\boldsymbol{m}_{\mathrm{b}} \in \Re^3$ be the force and the moment applied from the rod to the base. Then, the Euler equation can be rewritten as follows:

$$\boldsymbol{F}(\sigma)\boldsymbol{K}\boldsymbol{\theta}(\sigma) = \{\boldsymbol{p}(0) - \boldsymbol{p}(\sigma)\} \times \boldsymbol{f}_{\mathrm{b}} + \boldsymbol{m}_{\mathrm{b}} \tag{13.31}$$

The planar version is expressed as follows:

$$k_{\mathrm{b}}\theta_{\mathrm{b}}(\sigma) = \boldsymbol{e}_z^{\mathrm{T}}\{(\boldsymbol{p}(0) - \boldsymbol{p}(\sigma)) \times \boldsymbol{f}_{\mathrm{b}}\} + m_{\mathrm{b}} \tag{13.32}$$

where $m_{\mathrm{b}} := \boldsymbol{e}_z^{\mathrm{T}}\boldsymbol{m}_{\mathrm{b}}$.

The Euler equation is nonlinear and infinite-dimensional because it includes the arc length parameter σ which can take any value from 0 to L. This implies that the static balancing shape of an elastic rod is nontrivial. Generally, we cannot expect to obtain an analytical solution. An approximated value of the solution must be considered using a numerical method. Hereafter, we consider a discretized rod model to obtain a smart numerical method.

13.2.3 Discretization

Consider a serial chain of rigid bodies connected with rotational elastic joints as a discretized rod model of a continuum rod model for a better understanding of the rod deformation. In this discretized model, the rod does not deform at rigid bodies, but deforms only at rotational elastic joints. In spatial cases, the rotational elastic joints are three dimensional. However, in planar cases, they are one dimensional.

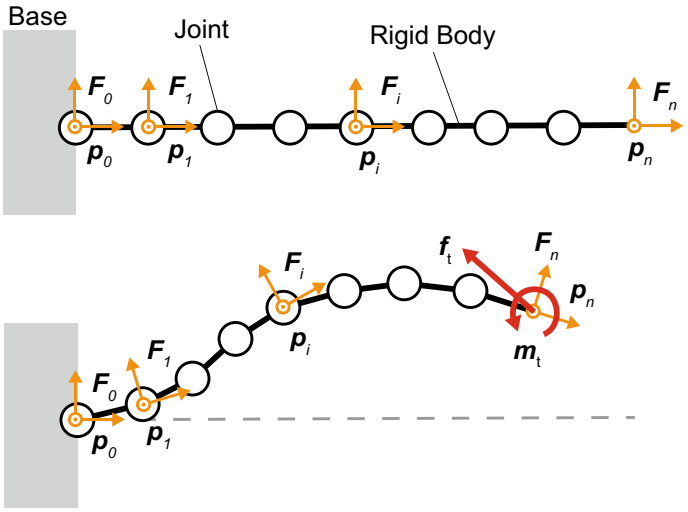

Fig. 13.7 Serial chain of rigid bodies connected with elastic joints

The shape of a continuum rod model is represented by a backbone curve. However, in a discretized model, the shape is expressed by a zigzag line. Let n denote the total number of joints. This constant is called the partition number because we approximate the rod by partitioning it into n segments. The joints and rigid bodies were numbered from base to tip. Without a loss of generality, all the segments (called links) are identical in length. Let $l := L/n$ denote link length (Fig. 13.7).

Here, the kinematics of a zigzag line is discussed. Let $i \in \{0, 1, 2, \ldots n\}$ be the index of the joint and rigid body numbers. Let $\boldsymbol{p}_{i-1} \in \Re^3$ be the position vector of joint i which corresponds to the ith node of a zigzag line. (Note: We number from 0 for joints, which results in a deviation of the index by -1.) To measure the orientation of each rigid body, we assigned a frame to each rigid body in a manner similar to the continuum case. Let $\boldsymbol{F}_i \in \mathrm{SO}(3)$ be the orientation matrix of rigid body i that corresponds to the ith line segment of a zigzag line. All orientation matrices on rigid bodies are identical when the zigzag line is straight at rest. The boundary conditions at the base can be written as follows:

$$\boldsymbol{p}_0 = \boldsymbol{p}_\mathrm{b} \tag{13.33}$$

$$\boldsymbol{F}_0 = \boldsymbol{F}_\mathrm{b} \tag{13.34}$$

Then, the shape of a zigzag line can be represented by the following differential equations with respect to i:

$$\boldsymbol{p}_i = \boldsymbol{p}_{i-1} + l\boldsymbol{F}_i\boldsymbol{e}_x \tag{13.35}$$

$$\boldsymbol{F}_i = \boldsymbol{F}_{i-1}\boldsymbol{R}_\mathrm{J}(\boldsymbol{\theta}_i) \tag{13.36}$$

where the matrix $\boldsymbol{R}_{\mathrm{J}} \in \mathrm{SO}(3)$ represents the rotational action of the three-dimensional elastic joint. Explicitly, this matrix is defined as follows:

$$\boldsymbol{R}_{\mathrm{J}}(\boldsymbol{\theta}_i) = \boldsymbol{R}(\boldsymbol{e}_x, \theta_{\mathrm{t}i})\boldsymbol{R}(\boldsymbol{e}_y, \theta_{\mathrm{n}i})\boldsymbol{R}(\boldsymbol{e}_z, \theta_{\mathrm{b}i}) \tag{13.37}$$

where $\boldsymbol{R}(\boldsymbol{a}, \theta) : U \times C \to \mathrm{SO}(3)$ denotes a rotational action around axis $\boldsymbol{a}$ with a rotational angle θ, and U is a set of unit vectors. Variables $\theta_{\mathrm{t}i}$, $\theta_{\mathrm{n}i}$, and $\theta_{\mathrm{b}i} \in C$ are the relative angles of the ith joint around the x-, y-, and z-axes, respectively. Vector $\boldsymbol{\theta}_i \in C^3$ is constructed by arranging these angles in a column, that is, $\boldsymbol{\theta}_i := [\theta_{\mathrm{t}i}\ \theta_{\mathrm{n}i}\ \theta_{\mathrm{b}i}]^{\mathrm{T}}$. In planar cases,

$$\boldsymbol{p}_i = \begin{bmatrix} \sum_{j=1}^{i} l\cos\phi_j & \sum_{j=1}^{i} l\sin\phi_j & 0 \end{bmatrix}^{\mathrm{T}} \tag{13.38}$$

$$\boldsymbol{F}_i = \begin{bmatrix} \cos\phi_i & -\sin\phi_i & 0 \\ \sin\phi_i & \cos\phi_i & 0 \\ 0 & 0 & 1 \end{bmatrix} \tag{13.39}$$

where $\phi_i \in C$ is the absolute angle of link i measured from the x-axis. The relationship between the absolute and relative angles of the links can be written as follows:

$$\phi_i = \sum_{j=1}^{i} \theta_{\mathrm{b}j} + \phi_{\mathrm{b}} \tag{13.40}$$

where $\phi_{\mathrm{b}} \in C$ denotes the absolute angle of the base, and corresponds to the absolute angle of the tangent line of the backbone curve, at the base in the continuum rod model. The corresponding boundary conditions at the tip are expressed as follows:

$$\boldsymbol{p}_n = \boldsymbol{p}^* \tag{13.41}$$

$$\boldsymbol{F}_n = \boldsymbol{F}^*. \tag{13.42}$$

The discretized version of the constitutive equation represents the rotational stiffness of the elastic joint. The linear constitutive relation assumption implies that reaction moment at each elastic joint $\boldsymbol{\tau}_i := [\tau_{\mathrm{t}i}\ \tau_{\mathrm{n}i}\ \tau_{\mathrm{b}i}]^{\mathrm{T}} \in \Re^3$ is proportional to the joint angle vector $\boldsymbol{\theta}_i$ and can be expressed as follows:

$$\boldsymbol{\tau}_i = \boldsymbol{K}_{\mathrm{d}}\boldsymbol{\theta}_i \tag{13.43}$$

where $\boldsymbol{K}_{\mathrm{d}} = \mathrm{diag}\{k_{\mathrm{dt}}, k_{\mathrm{dn}}, k_{\mathrm{db}}\}$ is a three-dimensional diagonal matrix whose diagonal elements, k_{dt}, k_{dn}, and k_{db} are the rotational spring constants of an elastic joint around the x-, y-, and z-axes of the joint frame, respectively. This matrix is related to the rational stiffness matrix of the continuum rod model with $\boldsymbol{K}_{\mathrm{d}} = \boldsymbol{K}/l$. Strain potential energy $U \in [0\ \infty)$ can be approximated using $\boldsymbol{K}_{\mathrm{d}}$ as follows:

$$U \approx \sum_{i=1}^{n} \frac{1}{2} \boldsymbol{\theta}_i^{\mathrm{T}} \boldsymbol{K}_{\mathrm{d}} \boldsymbol{\theta}_i \tag{13.44}$$

In planar cases,

$$\tau_{\mathrm{b}i} = k_{\mathrm{db}} \theta_{\mathrm{b}i} \tag{13.45}$$

and

$$U \approx \sum_{i=1}^{n} \frac{1}{2} k_{\mathrm{db}} {\theta_{\mathrm{b}i}}^2 \tag{13.46}$$

The discretized version of the Euler equation represents the moment balance at all the elastic joints.

$$\boldsymbol{A}_i \boldsymbol{K}_{\mathrm{d}} \boldsymbol{\theta}_i = \left(\boldsymbol{p}_0 - \boldsymbol{p}_{i-1} \right) \times \boldsymbol{f}_{\mathrm{b}} + \boldsymbol{m}_{\mathrm{b}}, \tag{13.47}$$

where $\boldsymbol{A}_i = [\boldsymbol{a}_{\mathrm{t}i}\ \boldsymbol{a}_{\mathrm{n}i}\ \boldsymbol{a}_{\mathrm{b}i}]$ is a matrix obtained by arranging the three unit vectors of the ith joint axes. The vectors of the joint axes are explicitly represented as follows:

$$\boldsymbol{a}_{\mathrm{t}i} = \boldsymbol{F}_{i-1} \boldsymbol{e}_x \tag{13.48}$$

$$\boldsymbol{a}_{\mathrm{n}i} = \boldsymbol{F}_{i-1} \boldsymbol{R}(\boldsymbol{e}_x, \theta_{\mathrm{t}i}) \boldsymbol{e}_y \tag{13.49}$$

$$\boldsymbol{a}_{\mathrm{b}i} = \boldsymbol{F}_{i-1} \boldsymbol{R}(\boldsymbol{e}_x, \theta_{\mathrm{t}i}) \boldsymbol{R}(\boldsymbol{e}_y, \theta_{\mathrm{n}i}) \boldsymbol{e}_z \tag{13.50}$$

In planar cases, the moment balance at the joints can be written as follows:

$$k_{\mathrm{db}} \theta_{\mathrm{b}i} = {\boldsymbol{e}_z}^{\mathrm{T}} \left\{ (\boldsymbol{p}_0 - \boldsymbol{p}_{i-1}) \times \boldsymbol{f}_{\mathrm{b}} \right\} + m_{\mathrm{b}}. \tag{13.51}$$

As we can expect that the discretized rod model shown above converges to the continuum rod model by considering a large partition number n, the solution of the following problem will provide a good approximation for the original shape computation problem we would like to solve.

Discretized shape computation problem For a discretized elastic rod model (13.35), (13.36) and (13.37), under boundary conditions (13.41) and (13.42), determine the shape (i.e., a set of joint angles) $\boldsymbol{\theta}_i$, $i = 1, 2, \ldots, n$, that satisfies the discretized Euler equation (13.47). ◊

This problem has $(3n + 6)$ equations for $(3n + 6)$ unknown variables. Therefore, it implies solving $(3n + 6)$-dimensional nonlinear equations. This essentially corresponds to a two-point boundary problem involving nonlinear differential equations. One of the typical numerical methods is the shooting method. The shooting method uses a strategy to identify a solution by numerically solving the initial value problem repeatedly for the boundary problem of differential equations. First, we assumed the initial values. Second, we determined the final values by numerically integrating the differential equations. Third, we checked the boundary conditions for the final values

and updated the initial values based on the error at the final values. We repeated these procedures until a sufficiently small error was obtained. We will utilize the property of an elastic model called 'rod integration' for efficient use of the shooting method. To better understand the essence of the concept, hereafter, we treat only the planar cases. To provide an appropriate guide to the extension of special cases, we have provided some references during its explanations.

13.2.4 Rod Integration

Before explaining rod integration, we normalize and nondimensionalize the planar discretized rod model. Without a loss of generality, we assume $\boldsymbol{p}_{\mathrm{b}} = \boldsymbol{0}$ and $\phi_{\mathrm{b}} = 0$.

<Kinematics>

$$\tilde{\boldsymbol{p}}_i = \left[\frac{1}{n} \sum_{j=1}^{i} \cos\phi_j \;\; \frac{1}{n} \sum_{j=1}^{i} \sin\phi_j \;\; 0 \right]^{\mathrm{T}} \tag{13.52}$$

$$\phi_i = \sum_{j=1}^{i} \theta_{\mathrm{b}j} \tag{13.53}$$

Static Balance (Euler Equation)

$$\theta_{\mathrm{b}i} = \boldsymbol{e}_z{}^{\mathrm{T}} \left\{ (\tilde{\boldsymbol{p}}_0 - \tilde{\boldsymbol{p}}_{i-1}) \times \tilde{\boldsymbol{f}}_{\mathrm{b}} \right\} + \tilde{m}_{\mathrm{b}} \tag{13.54}$$

<Boundary Constraints>

$$\tilde{\boldsymbol{p}}_n = \tilde{\boldsymbol{p}}^* \tag{13.55}$$

$$\phi_n = \phi^* \tag{13.56}$$

where the newly introduced non-dimensional variables have the following relationships with the corresponding original variables:

$$\boldsymbol{p}_i = L\tilde{\boldsymbol{p}}_i \tag{13.57}$$

$$\boldsymbol{p}^* = L\tilde{\boldsymbol{p}}^* \tag{13.58}$$

$$\boldsymbol{f}_{\mathrm{b}} = \frac{k_{\mathrm{db}}\tilde{\boldsymbol{f}}_{\mathrm{b}}}{L} \tag{13.59}$$

$$m_{\mathrm{b}} = k_{\mathrm{db}} \tilde{m}_{\mathrm{b}} \tag{13.60}$$

Note that the rod length L and the bending stiffness k_{db} are no longer included in this non-dimensionalized model (13.52)–(13.56), respectively. Therefore, except for scale differences, the static balancing rod shape is independent of these values. For example, when the width and/or thickness of an elastic rod is changed, its stiffness changes, but its shape does not change under the same boundary conditions.

Here, one of the most important properties in computing rod shapes 'rod integration' is explained. The rod integration property is based on the fact that mapping from the base force and moment to a static balancing shape except that the straight shape was bijective.

Here, we explain the computational process of rod integration using a planar model. Suppose that the base force $\tilde{\boldsymbol{f}}_{\mathrm{b}}$ and the base moment $\tilde{m}_{\mathrm{b}}$ are provided. The partition number n is also provided, because this is a design parameter that can be selected. First, by substituting $i = 1$ for the planar Euler equation (13.54), we obtain $\theta_{\mathrm{b}1} = \tilde{m}_{\mathrm{b}}$. Subsequently, from the second kinematic equation (13.53), we obtain $\phi_1 = \theta_{\mathrm{b}1}$. Then, from the first kinematic equation (13.52), we obtain $\tilde{\boldsymbol{p}}_1 = [(\cos\phi_1)/n \ (\sin\phi_1)/n \ 0]^{\mathrm{T}}$. Incrementing i yields

$$\theta_{\mathrm{b}2} = \boldsymbol{e}_z{}^{\mathrm{T}} \left\{ (\tilde{\boldsymbol{p}}_0 - \tilde{\boldsymbol{p}}_1) \times \tilde{\boldsymbol{f}}_{\mathrm{b}} \right\} + \tilde{m}_{\mathrm{b}} \tag{13.61}$$

$$\phi_2 = \sum_{j=1}^{2} \theta_{\mathrm{b}j} \tag{13.62}$$

$$\tilde{\boldsymbol{p}}_2 = \left[\frac{1}{n} \sum_{j=1}^{2} \cos\phi_j \ \frac{1}{n} \sum_{j=1}^{2} \sin\phi_j \ 0 \right]^{\mathrm{T}} \tag{13.63}$$

By repeating these processes recursively with respect to i, we obtain all $\theta_{\mathrm{b}i}$, which implies that the rod shape is determined. We can achieve such rod integration computation even in more general spatial deformation cases by introducing an appropriate approximation. For more details, see Takano et al. (2017) and Nakagawa and Mochiyama (2018) and the references therein.

13.2.5 Computation of Deformation

The rod integration property is as follows: From the base force and moment, the corresponding static balancing shape can be computed. Here, we explain an efficient method to obtain a numerical solution of the discretized shape computation problem using the shooting method with rod integration.

In the discretized shape computation problem, the base force $\tilde{\boldsymbol{f}}_{\mathrm{b}}$ and the base moment $\tilde{m}_{\mathrm{b}}$ are unknown. Then, we tentatively determined these values. Subse-

quently, from the estimated base force and moment, we compute the corresponding statically balanced shape by rod integration, which also provides the tip position $\tilde{\boldsymbol{p}}_n$ and tip orientation ϕ_n as the results of the computation. These values are expected to be equal to the desired tip position $\tilde{\boldsymbol{p}}^*$ and orientation ϕ^* under tip boundary conditions. Therefore, we evaluated the errors using the following indices:

$$\boldsymbol{e} = \begin{bmatrix} \tilde{\boldsymbol{p}}^* - \tilde{\boldsymbol{p}}_n \\ \phi^* - \phi_n \end{bmatrix} \tag{13.64}$$

Note that for these error indices, $\tilde{\boldsymbol{p}}_n$ and $\tilde{\boldsymbol{p}}^*$ are treated as two-dimensional vectors by removing z elements. Thus, the error vector above is three dimensional. If the magnitude of the error was unacceptably large, we updated the estimated values of the base force $\tilde{\boldsymbol{f}}_\mathrm{b}$ and base moment $\tilde{m}_\mathrm{b}$ based on the tip error. These processes were repeated until the tip error became sufficiently small.

For efficient shape computation, an appropriate updated law for the base force $\tilde{\boldsymbol{f}}_\mathrm{b}$ and the base moment $\tilde{m}_\mathrm{b}$ is necessary. The Newton method, one of the most fundamental numerical methods for optimization, suggests that the direction of convergence to the solution is provided by the inverse of the Jacobi matrix of the mapping from the search variables to the variables for the final boundary conditions. In the case of the shape computation for an elastic rod, the search variables are the base force and base moment, and the variables for the final boundary conditions are the tip position and orientation. Both variables are three dimensional, the Jacobi matrix is a three-times-three matrix. Here, we present an updated law based on the Levenberg–Marquardt method which is a modified version of Newton's method:

$$\begin{bmatrix} \tilde{\boldsymbol{f}}_\mathrm{b}(k) \\ \tilde{m}_\mathrm{b}(k) \end{bmatrix} = \begin{bmatrix} \tilde{\boldsymbol{f}}_\mathrm{b}(k-1) \\ \tilde{m}_\mathrm{b}(k-1) \end{bmatrix} + \left\{ \boldsymbol{J}^\mathrm{T}(k)\boldsymbol{J}(k) + \lambda \boldsymbol{I}_3 \right\}^{-1} \boldsymbol{J}^\mathrm{T}(k)\boldsymbol{K}_\mathrm{p}\boldsymbol{e}(k) \tag{13.65}$$

where k denotes the step number in the repeated computations, $x(k)$ denotes the value of variable x in the kth step, $\boldsymbol{K}_\mathrm{p} \in \Re^{3\times 3}$ is a positive-definite matrix as the gain for tuning the search variable per step, and λ is the damping factor in the Levenberg–Marquardt method and must be set to a non-negative real value. It is more reasonable to obtain the Jacobi matrix in each step numerically than its analytical counterpart because of the high dimensionality of the rod model. Rod integration is also useful for obtaining the numerical Jacobi matrix. Specifically, we perturbed the elements of the estimated values of the base force and moment sequentially, obtained the corresponding values of the tip position and orientation by rod integration, and then arranged the computation results in a row.

Exercises

1. Find the explicit matrix expression of $[\boldsymbol{v}\times]$ for vector $\boldsymbol{v} = [v_1\ v_2\ v_3]^\mathrm{T}$ in $\Re^3$.
2. Prove that $[\boldsymbol{v}\times]^\mathrm{T} = -[\boldsymbol{v}\times]$ for any vector $\boldsymbol{v}$ in $\Re^3$.

3. Prove that $[(\boldsymbol{R}\boldsymbol{v})\times] = \boldsymbol{R}[\boldsymbol{v}\times]\boldsymbol{R}^{\mathrm{T}}$ for any $\boldsymbol{v}$ in $\Re^3$ and $\boldsymbol{R}$ in SO(3).
4. Find the explicit matrix expression of the rotation action $\boldsymbol{R}(\boldsymbol{a}, \theta)$ for unit vector $\boldsymbol{a} = [a_1\ a_2\ a_3]^{\mathrm{T}}$ and angle θ.
5. Derive the normalized and non-dimensionalized version of the planar discretized rod model expressed by Eqs. (13.52)–(13.56) from the original Eqs. (13.38)–(13.42) and (13.51).

Answers to Exercises

1. $\begin{bmatrix} 0 & -v_3 & v_2 \\ v_3 & 0 & -v_1 \\ -v_2 & v_1 & 0 \end{bmatrix}$.
2. $[\boldsymbol{v}\times]^{\mathrm{T}} = \begin{bmatrix} 0 & -v_3 & v_2 \\ v_3 & 0 & -v_1 \\ -v_2 & v_1 & 0 \end{bmatrix}^{\mathrm{T}} = \begin{bmatrix} 0 & v_3 & -v_2 \\ -v_3 & 0 & v_1 \\ v_2 & -v_1 & 0 \end{bmatrix} = -[\boldsymbol{v}\times]$.
3. Let $\boldsymbol{R}^{\mathrm{T}} = [\boldsymbol{e}_1\ \boldsymbol{e}_2\ \boldsymbol{e}_3]$ and note that $\boldsymbol{e}_1$, $\boldsymbol{e}_2$ and $\boldsymbol{e}_3$ are mutually orthonormal. Then
$\boldsymbol{R}[\boldsymbol{v}\times]\boldsymbol{R}^{\mathrm{T}} = \begin{bmatrix} \boldsymbol{e}_1{}^{\mathrm{T}}(\boldsymbol{v}\times\boldsymbol{e}_1) & \boldsymbol{e}_1{}^{\mathrm{T}}(\boldsymbol{v}\times\boldsymbol{e}_2) & \boldsymbol{e}_1{}^{\mathrm{T}}(\boldsymbol{v}\times\boldsymbol{e}_3) \\ \boldsymbol{e}_2{}^{\mathrm{T}}(\boldsymbol{v}\times\boldsymbol{e}_1) & \boldsymbol{e}_2{}^{\mathrm{T}}(\boldsymbol{v}\times\boldsymbol{e}_2) & \boldsymbol{e}_2{}^{\mathrm{T}}(\boldsymbol{v}\times\boldsymbol{e}_3) \\ \boldsymbol{e}_3{}^{\mathrm{T}}(\boldsymbol{v}\times\boldsymbol{e}_1) & \boldsymbol{e}_3{}^{\mathrm{T}}(\boldsymbol{v}\times\boldsymbol{e}_2) & \boldsymbol{e}_3{}^{\mathrm{T}}(\boldsymbol{v}\times\boldsymbol{e}_3) \end{bmatrix} = \begin{bmatrix} 0 & -\boldsymbol{v}^{\mathrm{T}}\boldsymbol{e}_3 & \boldsymbol{v}^{\mathrm{T}}\boldsymbol{e}_2 \\ \boldsymbol{v}^{\mathrm{T}}\boldsymbol{e}_3 & 0 & -\boldsymbol{v}^{\mathrm{T}}\boldsymbol{e}_1 \\ -\boldsymbol{v}^{\mathrm{T}}\boldsymbol{e}_2 & \boldsymbol{v}^{\mathrm{T}}\boldsymbol{e}_1 & 0 \end{bmatrix}$
which corresponds to $[(\boldsymbol{R}\boldsymbol{v})\times]$.
4. $\begin{bmatrix} {a_1}^2(1-\cos\theta)+\cos\theta & a_2a_1(1-\cos\theta)-a_3\sin\theta & a_3a_1(1-\cos\theta)+a_2\sin\theta \\ a_1a_2(1-\cos\theta)+a_3\sin\theta & {a_2}^2(1-\cos\theta)+\cos\theta & a_3a_2(1-\cos\theta)-a_1\sin\theta \\ a_1a_3(1-\cos\theta)-a_2\sin\theta & a_2a_3(1-\cos\theta)+a_1\sin\theta & {a_3}^2(1-\cos\theta)+\cos\theta \end{bmatrix}$.
5. Check it by yourself using the relationships (13.57)–(13.60).

13.3 Nonlinear Dynamics in a Simple Mechanical System

13.3.1 Passive Dynamic Walker as Example

A controller-body-environment system can be regarded as a system in which multiple nonlinear elements interact and evolve over time, or in other words, a large nonlinear dynamical system. For example, a salamander robot has been conceived to switch between different types of locomotion (swimming and walking) based on its environmental conditions by coupling multiple nonlinear oscillators and designing central pattern generator models (Ijspeert et al. 2007). The behavior of nonlinear dynamical systems must be elucidated to understand such intelligent systems. Here, the dynamical system approach is introduced, using a passive dynamic walker as an example (McGeer 1990). A passive dynamic walker does not have a brain (controller). Instead, walking behavior is achieved only through interactions between the body and environment. Therefore, one of the simplest models is introduced here. However, a diverse and essential repertoire of dynamics is observed in this example.

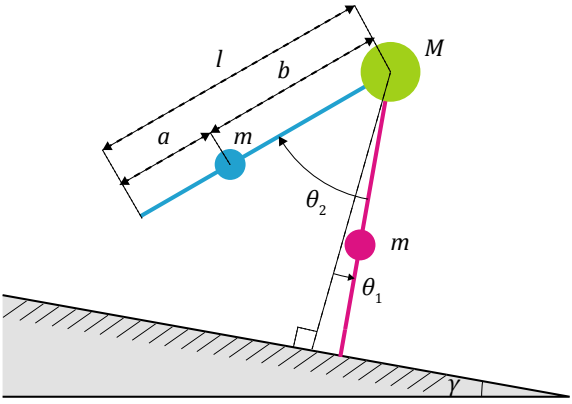

Fig. 13.8 Schematic diagram of compass-gait model. The red line shows the stance leg, and the blue line shows the swing leg

The 'compass-gait' model, which is one of the simplest forms of passive dynamic walkers, is introduced here (Garcia et al. 1998; Goswami et al. 1996; Obayashi et al. 2016). The compass-gait was a kneeless bipedal model, as shown in Fig. 13.8. It achieves a passive gait that draws energy from gravity and does not require control because appropriate axial foot switching is defined. The model parameters are the mass (m) of the leg, mass (M) of the point mass at the rear, length ($l = a + b$) of the leg, distance (b) from the rear to the center of gravity of the leg, and inclination angle (γ). The model has four degrees of freedom, consisting of the angles and angular velocities of the two legs.

The dynamics of compass-gait were explained. Of the two legs, the one that is in contact with the ground is called the stance leg, and one that is not in contact with the ground is called the swing leg. Its dynamics consist of repeated alternating of two phases: the swing phase, where the legs are swinging, and the impact phase, where the stance leg and swing leg switch when the swing leg comes into contact with the ground (the dynamical system that is described by these multiple time evolution rules is called a hybrid dynamical system (or switch dynamical system)). The state of this model is illustrated in Fig. 13.8, where the angle of the stance leg with respect to the vertical direction of the incline is set as θ_1, and the angle from the stance leg to the swing leg is set as θ_2, where $\Theta = (\theta_1 \theta_2)^{\mathrm{T}}$ and its velocity $\dot{\Theta} = (\dot{\theta_1} \dot{\theta_2})^{\mathrm{T}}$, for a total of four variable sets.

First, the dynamics of the swing phase are explained. As can be observed, the swing phase is a double pendulum that immobilizes the contact point of the stance leg and can be described by the ordinary differential equation based on the equation of motion, as follows (Goswami et al. 1996; Obayashi et al. 2016):

$$\begin{pmatrix} 1+2\beta+2r\beta(-1-\cos\theta_2+r) & \beta r(\cos\theta_2-r) \\ r\cos\theta_2-r^2 & r^2 \end{pmatrix}\begin{pmatrix} \ddot{\theta}_1 \\ \ddot{\theta}_2 \end{pmatrix} + \begin{pmatrix} r\beta(2\dot{\theta}_1-\dot{\theta}_2)\dot{\theta}_2\sin\theta_2 \\ -r\dot{\theta}_1{}^2\sin\theta_2 \end{pmatrix} + \frac{g}{l}\begin{pmatrix} -(1+\beta(2-r))\sin(\theta_1-\gamma)-\beta r\sin(\theta_2-\theta_1+\gamma) \\ r\sin(\theta_2-\theta_1+\gamma) \end{pmatrix} = \begin{pmatrix} 0 \\ 0 \end{pmatrix}, \tag{13.66}$$

where g is the gravitational acceleration, $r = \frac{b}{l}$ and $\beta = \frac{m}{M}$.

Subsequently, the dynamics of the impact phase are explained. The impact phase occurred instantaneously when the contact conditions were satisfied. The impact phase involves switching the orientations of the stance and swing legs and the change in velocity that preserves the momentum associated with ground contact. The states before and after contact are expressed as Θ^- and Θ^+, respectively, and the transition rule is defined as follows:

$$\begin{aligned} \Theta^+ &= -\Theta^-, \\ Q^+(\theta_1^-)\dot{\Theta}^+ &= Q^-(\theta_1^-)\dot{\Theta}^-, \end{aligned} \tag{13.67}$$

$$\begin{aligned} Q^+(\theta_1^-) &= \begin{pmatrix} Q_{11}^+(\theta_1^-) & br\cos 2\theta_1^- - \beta r^2 \\ r\cos 2\theta_1^- - r^2 & r^2 \end{pmatrix}, \\ Q_{11}^+(\theta_1^-) &= 1+\beta(1-r)^2+\beta-2\beta\cos 2\theta_1^-+\beta r^2, \\ Q^-(\theta_1^-) &= \begin{pmatrix} Q_{11}^-(\theta_1^-) & br(1-r) \\ r(1-r) & 0 \end{pmatrix}, \\ Q_{11}^-(\theta_1^-) &= (1+2\beta-2\beta r)\cos 2\theta_1^- - 2\beta r(1-r). \end{aligned} \tag{13.68}$$

The contact conditions are defined as follows:

$$\begin{aligned} h_1(\Theta) &= 2\theta_1-\theta_2 = 0, \\ h_2(\Theta) &= \theta_1 < 0, \\ h_3(\dot{\Theta}) &= 2\dot{\theta}_1-\dot{\theta}_2 < 0, \end{aligned} \tag{13.69}$$

where $h_1(\Theta)$ indicates that the swing leg is in contact with the ground, and when combined with $h_2(\Theta)$ and $h_3(\dot{\Theta})$, it indicates the condition in which the swing leg is in front of the stance leg and the swing leg is swung down toward the ground. Note that $h_2(\Theta)$ and $h_3(\dot{\Theta})$ are necessary because the compass-gait model involves a simplification in which the knees are eliminated. Thus, the swing leg will almost certainly penetrate the ground when the two legs cross each other. Therefore, $h_2(\Theta)$ and $h_3(\dot{\Theta})$ are added such that the impact phase occurs when the swing leg swings

downward. Furthermore, in the walking model, it is possible to evaluate whether walking can be achieved by defining a fall state. Here, the rear coming into contact with the ground is deemed a fall, which is defined as a state that satisfies $\theta_1 = \pm\pi/2$.

In the compass-gait model, the limits of $\beta = m/M \to 0$ and $r = b/l \to 1$ were applied, and it was made dimensionless on the timescale $\sqrt{l/g}$ as the simplest walking model (Garcia et al. 1998; Obayashi et al. 2016). The swing phase time evolution in Eq. (13.66) is simplified as follows:

$$\begin{aligned} &\ddot{\theta}_1 - \sin(\theta_1 - \gamma) = 0, \\ &(\cos\theta_2 - 1)\ddot{\theta}_1 + \ddot{\theta}_2 - \dot{\theta}_1^2 \sin\theta_2 + \sin(\theta_2 - \theta_1 + \gamma) = 0. \end{aligned} \tag{13.70}$$

Furthermore, the impact phase update is as follows:

$$\begin{pmatrix} \theta_1^+ \\ \dot{\theta}_1^+ \\ \theta_2^+ \\ \dot{\theta}_2^+ \end{pmatrix} = \begin{pmatrix} -\theta_1^- \\ \dot{\theta}_1^- \cos 2\theta_1^- \\ -2\theta_1^- \\ \dot{\theta}_1^- \cos 2\theta_1^- (1 - \cos 2\theta_1^-) \end{pmatrix}. \tag{13.71}$$

The simplest walking model is used for subsequent analyses.

13.3.2 Attractors and Bifurcations

We conducted various analyses using the simplest walking model introduced in the previous section. Here, we introduce the basic terms of dynamical systems to analyze the dynamics of the simplest walking model. A dynamical system (of continuous time) is described by a set of states X, and a function $F : X \times \mathbb{R} \to X$, which describe its time evolution. This set of states is called the phase space, and if this is the simplest walking model, then $X = \Theta \times \dot{\Theta}$. Function F is called flow, and function $x : \mathbb{R} \to X$ in the phase space that follows the flow $x(t) = F(x(0), t)$ is called the solution trajectory, where $x(0) \in X$ is the initial state of the solution trajectory. Analyzing the type of subspace in which the state remains within the phase space with time evolution is useful for understanding the properties of dynamical systems. Here, an attractor is a subset, $A \subset X$, of the phase space that has the property of attracting trajectories (Broer and Takens 2011; Hirsch et al. 2012) for an exact definition of the terms for dynamical systems such as attractors). Attractors are broadly classified into four types: fixed point, periodic, quasiperiodic, and strange attractors. Here, we consider the example of an attractor used by the model. In the simplest dimensionless walking model, the incline slope γ is the only parameter.

Figure 13.9a, b shows the gaits and time series of $\dot{\theta}_2$, respectively, for time $t \in [650, 750]$ at incline angle $\gamma = 0.01$ and $\gamma = 0.019$. The red and blue lines represent the stance and swing legs of the simplest walking model, respectively. Walking is done without falling from these initial states. It can also be observed that the gait with

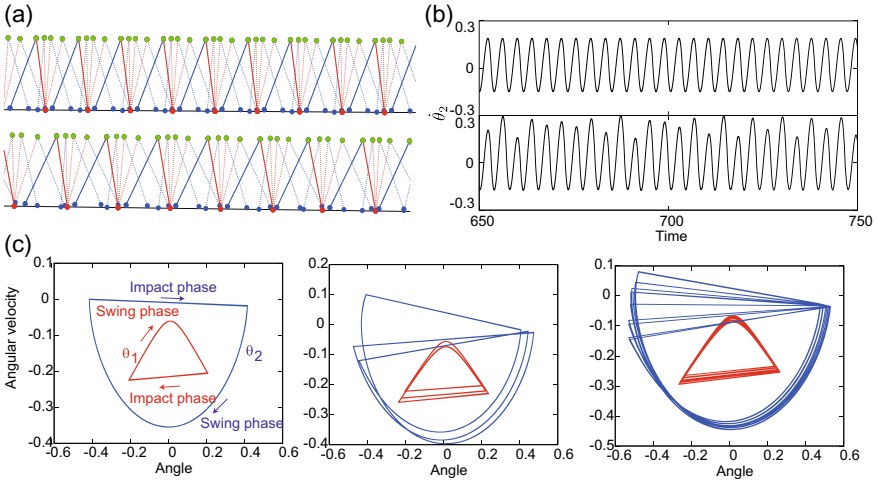

Fig. 13.9 Behaviors of compass-gait model. **a** Schematic of typical compass-gait model. The red and blue lines are the stance and swing leg of simplest walking model, respectively. **b** The upper graph is the periodic gait time series of $\dot{\theta}_2$ [rad s^{-1}], where the slope is $\gamma = 0.01$. **c** The lower graph is the chaotic gait time series of $\dot{\theta}_2$ [rad s^{-1}], where the slope is $\gamma = 0.019$. The left graph is trajectory in $(\theta, \dot{\theta})$ phase space for periodic gait $\gamma = 0.01$. The center graph is trajectory in $(\theta, \dot{\theta})$ phase space for period 3 gait $\gamma = 0.0125$. The right graph is trajectory in $(\theta, \dot{\theta})$ phase space for chaotic gait $\gamma = 0.019$. The red line is the trajectory of $(\theta_1, \dot{\theta}_1)$ that corresponds to the stance leg. The blue line is the trajectory of $(\theta_2, \dot{\theta}_2)$ that corresponds to the swing leg

$\gamma = 0.01$ is periodic because the intervals between the red and blue dots are almost equal, and the gait with $\gamma = 0.019$ is non-periodic because the intervals between the blue dots are not equal. Figure 13.9c shows graphs in which the trajectories with $\gamma = 0.01, 0.0125$, and 0.019 are drawn in the phase space of $(\theta, \dot{\theta})$. It can be observed in the left and center graphs that θ_1 and θ_2 both follow the same curve and are periodic trajectories, and these gaits have different periods, which are periods 1 and 3, respectively; meanwhile, it can be observed in the right graph that countless curves are superimposed, and the trajectory is irregular. Here, a dynamical system that exhibits irregular and complicated behavior is referred to as chaotic. One of the important characteristics of chaos is the so-called initial state sensitivity, which is the sensitivity to trajectory perturbations. The (maximum) Lyapunov exponent can be used to quantify the initial state sensitivity as the rate of expansion of perturbations applied to the system. The Lyapunov exponent λ is intuitively defined as the following equation:

$$\lambda = \lim_{t \to \infty} \frac{1}{t} \log \frac{\|x_0(t) - x_1(t)\|}{\|x_0(0) - x_1(0)\|}, \tag{13.72}$$

where $x_0(t)$ and $x_1(t)$ are the trajectories whose initial states $x_0(0)$ and $x_1(0)$ are infinitesimally close.

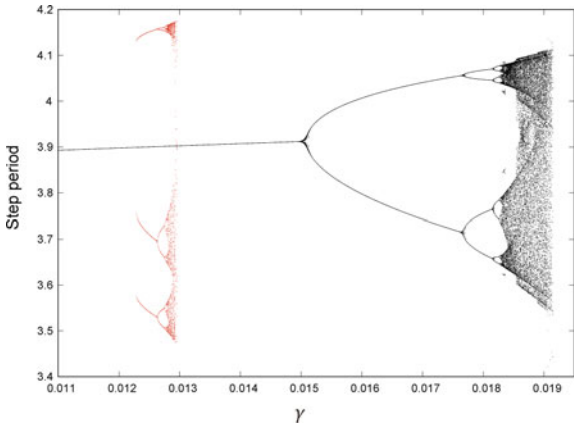

Fig. 13.10 Bifurcation diagram of compass-gait model. The points show the step period of ten different initial states after the transient time. The horizontal axis shows the slope of the inclined ground

A positive Lyapunov exponent indicates that the trajectory has initial state sensitivity. The Lyapunov exponent becomes nonpositive in the case of convergence to a fixed point or periodic oscillation. This Lyapunov exponent is often used as an indicator of chaos for trajectories in closed phase space. In this section, we do not show the analysis of the Lyapunov exponent, but a detailed analysis can be found in Gritli et al. (2014).

Various dynamics, including periodic gait, chaotic gait, and fall, are observed when the slope γ of the incline in contact is changed in a compass-gait model. Such a qualitative change in the system caused by a slight change in the parameters of the dynamical system is called bifurcation. At the bifurcation point, the geometric structure, such as the periodic point of the system or the presence or absence of the attractor, switches discontinuously with respect to the parameter. Figure 13.10 shows the bifurcation diagram of the compass-gait model. The horizontal axis is the inclined slope $\gamma \in [0.011, 0.0195]$, and the vertical axis is the step period, which is the time interval from the occurrence of the impact phase to the next impact phase. For ten different initial values, the step period was plotted for each γ for the gait that did not cause a fall after sufficiently large time steps as the transient time. In the range of $0.014 < \gamma < 0.015$, there is a one-step period, and it is a one-period trajectory. When the slope is subsequently increased, the period doubles to 2, 4, 8, and onward (such a bifurcation is called a period-doubling bifurcation). It can be confirmed that the period-doubling interval roughly converges to the Feigenbaum constants (Garcia et al. 1998), and chaos can be considered to appear in the range of $0.0185 < \gamma < 0.019$ after criticality. A positive Lyapunov exponent was numerically confirmed for the trajectory of the compass-gait model within this range (Gritli et al. 2014). Furthermore, in ranges such as $\gamma > 0.019$, where the incline slope was larger, almost all trajectories resulted in a fall, and walking could not be achieved. A multi-attractor was confirmed in the range of $0.0125 < \gamma < 0.013$ (Gritli et al. 2012). In this range, there were three period attractors that were parallel to the one-period trajectory, and increasing the slope generated a separate period-doubling bifurcation

for the 6-/12-period and three period attractors. The existence of multi-attractors with five periods could be confirmed numerically, even on other slopes.

13.3.3 Basin of Attraction and Riddled Basins

The set of initial values that are attracted to an attractor is called a basin (or basin of attraction). In this study, the basins were confirmed for each gait. Figure 13.11 shows the basins for $\gamma = 0.005, 0.00825$, and 0.014. Simulations were conducted for the initial values in each area, and color coding was used based on the attractor at the site of convergence. Red was the area of the gait where falls did not occur, and blue was the area where falls occurred within the transient time, where brightness indicated the time until the fall, with darker colors indicating a longer time until falling. However, the maximum brightness values were different, with (a)/(b), (c)/(d), and (e)/(f) having values of 50, 100, and 150, respectively. Figure 13.11a, b shows basins at $\gamma = 0.005$. In (a), there is an area where walking is successful and an area where a fall has occurred, with the areas divided by smooth boundaries. Figure 13.11c, d shows the basins at $\gamma = 0.0085$. A fractal basin boundary (or riddled basin) can be confirmed from the basin with successful walking to the basin with falling, which continues to appear in an alternating manner while thinning gradually. Here, (e) and (f) show basins at $\gamma = 0.014$. For this parameter, it can be confirmed that a thinner fall basin is inserted at the boundaries that appear in a fractal manner between the successful walk and fall basins, and a boundary with higher fractal properties than those in (c) and (d) can be confirmed. A fractal is a geometric structure with self-similarity where the same shape as the whole is reproduced when the entire figure is decomposed into several parts. Because the initial value at these boundaries must be determined with infinite accuracy to determine which basin it belongs to (i.e., the final state), these boundaries are referred to as having final state sensitivity (Grebogi et al. 1983). In Akashi et al. (2019), in the compass-gait model, the final state sensitivity was quantified by calculating the uncertainty exponents that were based on the fractal dimension of the boundary. It should be noted that these parameters represent periodic dynamics, as shown in Fig. 13.11, and though they do not have an initial state sensitivity, they do have a final state sensitivity. It has also been confirmed that the changes in the fractal properties observed in (a), (c), and (e) do not correspond to the periodic bifurcation of the gait, as shown in Fig. 13.11 (Akashi et al. 2019).

With this, what does the property revealed here mean to an actual passive dynamic walker? Dice throwing is a deterministic dynamics that can be completely described by the equation of motion; however, it is perceived to generate a probability distribution. This is because of the difficulty in prediction owing to the nonlinear nature of the dynamics involved. In dice throwing, the initial state space, such as the initial posture and velocity of the dice, can be classified into six basins of attraction, where that space ultimately converges into one of the dice faces. These basins are incorporated in a fractal manner, and there is a region in dice throwing where the dice faces are switched because of infinitesimal differences in the initial state (Kapitaniak

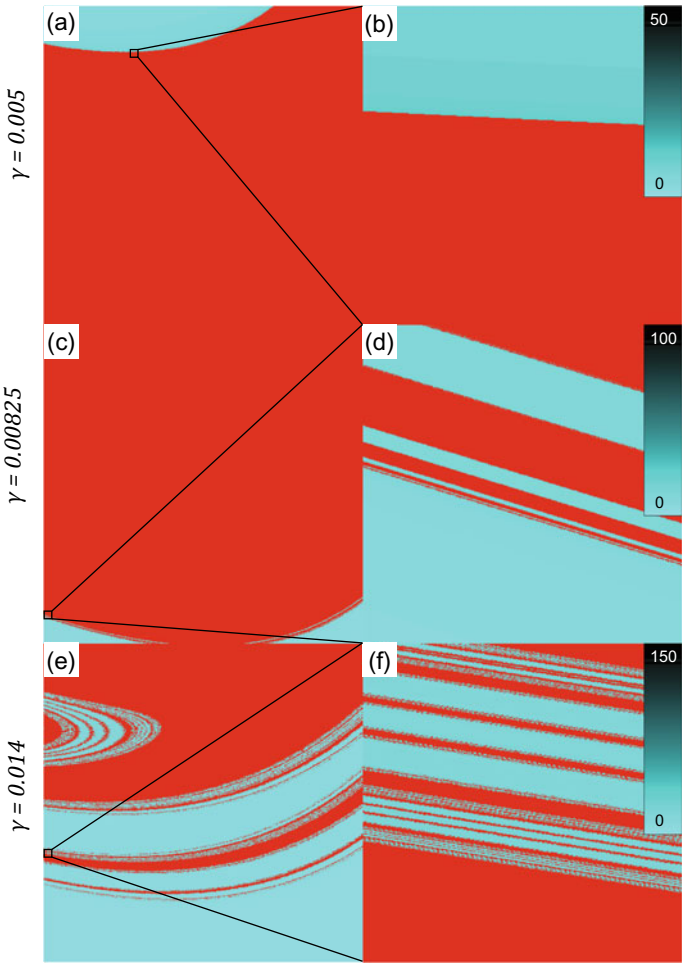

Fig. 13.11 Basins of compass-gait model. Red points show initial states of non-falling. Blue points show initial states of falling, where the gradation represents the time of falling. Slope γ is equal to 0.005 in **a** and **b**, 0.00825 in **c** and **d**, and 0.014 in **e** and **f**. The drawing ranges are $\theta_1 + \dot{\theta}_1 \times \theta_1 - \dot{\theta}_1 = [-0.005, -0.004985] \times [0.29, 0.39]$ in **a**, $\theta_1 + \dot{\theta}_1 \times \theta_1 - \dot{\theta}_1 = [-0.006, -0.001] \times [0.3755, 0.3759]$ in **b**, $\theta_1 + \dot{\theta}_1 \times \theta_1 - \dot{\theta}_1 = [-0.0035, 0.001] \times [0.31, 0.41]$ in **c**, $\theta_1 + \dot{\theta}_1 \times \theta_1 - \dot{\theta}_1 = [-0.0035, -0.005485] \times [0.3176, 0.318]$ in **d**, $\theta_1 + \dot{\theta}_1 \times \theta_1 - \dot{\theta}_1 = [0.0, 0.005] \times [0.35, 0.45]$ in **e**, and $\theta_1 + \dot{\theta}_1 \times \theta_1 - \dot{\theta}_1 = [0.0, 0.00002] \times [0.384, 0.3844]$ in **f**

et al. 2012; Nagler and Richter 2008). In a real system, it is impossible to identify the initial state with virtually infinite accuracy because there are unavoidable errors in the control and observation of the initial values. Therefore, the volume ratio of the basin of the dice face that the dice lands on with respect to the area around a given initial state in the dice throw results in the distribution of that dice face.

The final state sensitivity is not limited to dice throwing, but universally appears in various nonlinear systems. It should be noted that there is no chaos in this parameter, and there is no initial state sensitivity. However, it has a final state sensitivity. Riddled basins also occur in mechanical mechanisms such as magnetic pendulums and billiard systems (Gaspard 2005). In neural networks, which act as controllers, riddled basins appear in the backpropagation process of a feed-forward network (Kolen and Pollack 1990). This signifies that the learning result can change even if the same learning is performed because of slight differences in the initial weight value.

It can be assumed that the fact that a passive dynamic walker has initial state sensitivity or final state sensitivity suggests that the robot body may act 'randomly' similar to a dice. For example, in this fractal basin boundary area, the fate of whether the walker can continue to walk or will fall once the controller lets go of the walker is unknown not only to the controller but also to the walker. This is because, in reality, it is impossible to intentionally specify the initial state of a system with infinite accuracy (this is only possible with Laplace's demon).

In this section, we discuss the dynamics of passive walkers from the perspective of dynamical systems. A passive walker is a model in which the controller is removed, and the focus is only on the interaction between the body and environment. It is a simple model with only four variables as the dimensions of the system state, and only one variable that corresponds to the inclined slope as the underlying parameter. It was confirmed that attempting to understand how such a simple system achieves the dynamics of walking from the perspective of a dynamical system involves not only the periodic gait but also a dynamical system structure that includes numerous factors, such as periodic doubling bifurcations, chaos, multi-attractors, and fractal basin boundaries. Understanding the brain (controller)-body-environment system interaction based on such a dynamical system approach is a similarly powerful method, even in cases involving higher-dimensional systems and controllers (Terajima et al. 2021).

Exercises

1. Explain the following concepts.
   (A) Attractor
   (B) Chaos
   (C) Lyapunov exponent
   (D) Bifurcation
   (E) Basin of attraction
   (F) Fractal

2. Consider a one-dimensional map, called a logistic map, expressed as $x_{t+1} = ax_t(1 - x_t)$. Draw a bifurcation diagram of the logistic map in range of $3.0 < a < 4.0$.

13.4 Controlling Soft Robots

13.4.1 Concept

Sensors and actuators enable robots to function in the real world. The intelligence of robots is achieved through computers, which are based on information, but the real world is governed by the laws of physics. Physical constraints distinguish information-based intelligence from the real world. There are several physical constraints in the real world, however none in the information world. In particular, the information world can accept descriptions that violate physical constraints. Sensing is the process of mapping from the real world to the information world. Even when sensing produces descriptions that violate physical constraints owing to sampling or sensing errors, the descriptions are acceptable in the information world. Alternatively, an action is a mapping from the information world to the real world. When actions computed in the information world violate physical constraints, mapping problems arise. This implies that to deal with mismatches in mapping from the information world to the physical world, a system must have an inherent degrees of freedom. Soft materials can have such inherent degrees of freedom, implying that soft robots can realize map under physical constraints if their bodies and control systems are designed properly. This section demonstrates the contribution of soft materials to map from the information world to the real world using the following basic examples: simultaneous positioning of a soft body and orientation control using soft fingertips.

13.4.2 Simultaneous Positioning of Soft Body

We aim to control multiple points on a soft body. Positioning should be performed by manipulating multiple points except for the positioned points (Fig. 13.12). In other words, we indirectly control the position of the points by controlling the position of the manipulated points using mechanical devices. This positioning is referred to as *indirect simultaneous positioning* (Hirai and Wada 2000), and it is common in the textile industry and medical surgery. This section derives the control law for indirect simultaneous positioning of a two-dimensional elastic body.

We describe a two-dimensional elastic body with a finite number of nodal points, including both the positioned and manipulated points. Let I_p, I_m, and I_o be sets of positioned, manipulated, and nodal points excluding the positioned or manipulated points, respectively. Accordingly, the nodal displacement vector $\boldsymbol{u}_\mathrm{N}$ is divided into the following three collective vectors: $\boldsymbol{u}_\mathrm{p}$, $\boldsymbol{u}_\mathrm{m}$, and $\boldsymbol{u}_\mathrm{o}$, which are represented by I_p, I_m, and I_o, respectively.

We derive the control law for indirect simultaneous positioning based on the static equation, $K\boldsymbol{u}_\mathrm{N} = \boldsymbol{f}_\mathrm{N}$, where K represents the stiffness matrix of the body and $\boldsymbol{f}_\mathrm{N}$ is a set of nodal forces. Because external forces are applied only to the manipulated points, the static equations can be described as follows:

$$\begin{bmatrix} K_{\mathrm{pp}} & K_{\mathrm{pm}} & K_{\mathrm{po}} \\ K_{\mathrm{mp}} & K_{\mathrm{mm}} & K_{\mathrm{mo}} \\ K_{\mathrm{op}} & K_{\mathrm{om}} & K_{\mathrm{oo}} \end{bmatrix} \begin{bmatrix} \boldsymbol{u}_{\mathrm{p}} \\ \boldsymbol{u}_{\mathrm{m}} \\ \boldsymbol{u}_{\mathrm{o}} \end{bmatrix} = \begin{bmatrix} \boldsymbol{0} \\ \boldsymbol{f}_{\mathrm{m}} \\ \boldsymbol{0} \end{bmatrix} \tag{13.73}$$

where $\boldsymbol{f}_{\mathrm{m}}$ denotes the external forces applied to the manipulated points. The first, second, and third rows of the above equation represent the equilibria at the positioned, manipulated, and other nodal points, respectively. We obtain the following from the first and third rows:

$$\begin{bmatrix} K_{\mathrm{pm}} & K_{\mathrm{po}} \\ K_{\mathrm{om}} & K_{\mathrm{oo}} \end{bmatrix} \begin{bmatrix} \boldsymbol{u}_{\mathrm{m}} \\ \boldsymbol{u}_{\mathrm{o}} \end{bmatrix} = - \begin{bmatrix} K_{\mathrm{pp}} \\ K_{\mathrm{op}} \end{bmatrix} \boldsymbol{u}_{\mathrm{p}} \tag{13.74}$$

Let $\delta\boldsymbol{u}_{\mathrm{p}}$, $\delta\boldsymbol{u}_{\mathrm{m}}$, and $\delta\boldsymbol{u}_{\mathrm{o}}$ be small deviations around an equilibrium state. Then, we have the following:

$$\begin{bmatrix} K_{\mathrm{pm}} & K_{\mathrm{po}} \\ K_{\mathrm{om}} & K_{\mathrm{oo}} \end{bmatrix} \begin{bmatrix} \delta\boldsymbol{u}_{\mathrm{m}} \\ \delta\boldsymbol{u}_{\mathrm{o}} \end{bmatrix} = - \begin{bmatrix} K_{\mathrm{pp}} \\ K_{\mathrm{op}} \end{bmatrix} \delta\boldsymbol{u}_{\mathrm{p}} \tag{13.75}$$

We obtain $\delta\boldsymbol{u}_{\mathrm{m}}$ for a given $\delta\boldsymbol{u}_{\mathrm{p}}$ by solving Eq. (13.75). Let $\boldsymbol{u}_{\mathrm{p}}^{\mathrm{d}}$ be the desired displacement vector of positioned points. Then, the small deviation $\delta\boldsymbol{u}_{\mathrm{p}}$ can be replaced by $\alpha(\boldsymbol{u}_{\mathrm{p}}^{\mathrm{d}} - \boldsymbol{u}_{\mathrm{p}})$, where α denotes a scaling parameter. Consequently, we obtain the iterative control law as follows:

1: $\boldsymbol{u}_{\mathrm{m}} \leftarrow \boldsymbol{0}$
2: **repeat**
3: obtain current $\boldsymbol{u}_{\mathrm{p}}$ via sensor
4: $\delta\boldsymbol{u}_{\mathrm{p}} \leftarrow \alpha(\boldsymbol{u}_{\mathrm{p}}^{\mathrm{d}} - \boldsymbol{u}_{\mathrm{p}})$
5: solve Eq. (13.75) to obtain $\delta\boldsymbol{u}_{\mathrm{m}}$
6: $\boldsymbol{u}_{\mathrm{m}} \leftarrow \boldsymbol{u}_{\mathrm{m}} + \delta\boldsymbol{u}_{\mathrm{m}}$
7: guide manipulated points to $\boldsymbol{u}_{\mathrm{m}}$
8: **until** $\left\| \boldsymbol{u}_{\mathrm{p}}^{\mathrm{d}} - \boldsymbol{u}_{\mathrm{p}} \right\| \leq \epsilon$

where ϵ is a small positive constant.

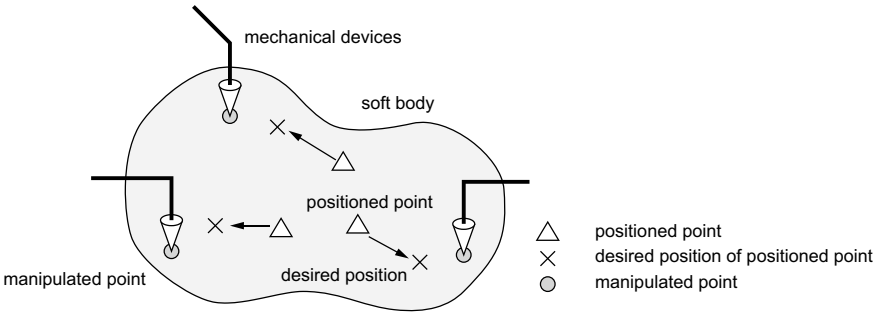

Fig. 13.12 Indirect simultaneous positioning

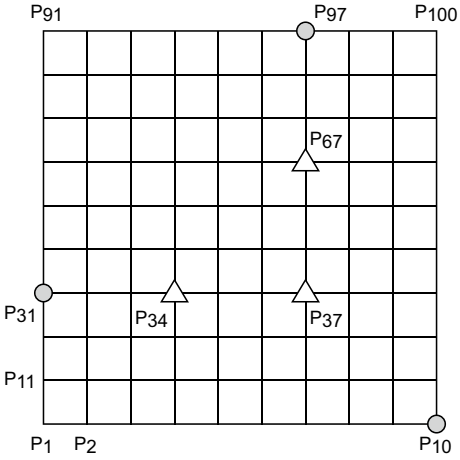

Fig. 13.13 Positioned and manipulated points in simulation

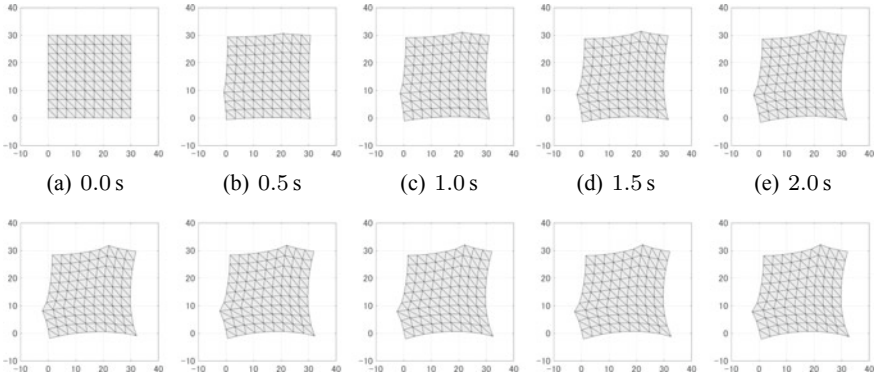

Fig. 13.14 Dynamic simulation of indirect simultaneous positioning

We used a dynamic simulation to validate the aforementioned control law. Figure 13.13 shows a two-dimensional square body. The square region was divided into $9 \times 9 \times 2$ triangles with 10×10 nodal points. Furthermore, let $P_1, P_2, \ldots, P_{10}$ be the nodal points on the bottom edge of the square from left to right, and $P_1, P_{11}, \ldots, P_{91}$ be the nodal points on the left edge of the square from bottom to top. The nodal point in the top–right corner is specified by P_{100}. A set of positioned points is specified by $I_\mathrm{p} = \{P_{34}, P_{37}, P_{67}\}$ and a set of manipulated points is specified by $I_\mathrm{m} = \{P_{31}, P_{10}, P_{97}\}$. The desired displacement vector of the positioned points is $\boldsymbol{u}_\mathrm{p}^\mathrm{d} = [-0.8, 0.1, 0.6, -0.6, 0.1, 0.8]^\mathrm{T}$. Figure 13.14 shows a snapshot of the simulation result of indirect simultaneous positioning of the square body specified by width $w = 30\,\mathrm{cm}$, height $h = 1\,\mathrm{cm}$, Young's modulus $E = 1.0\,\mathrm{MPa}$, viscous

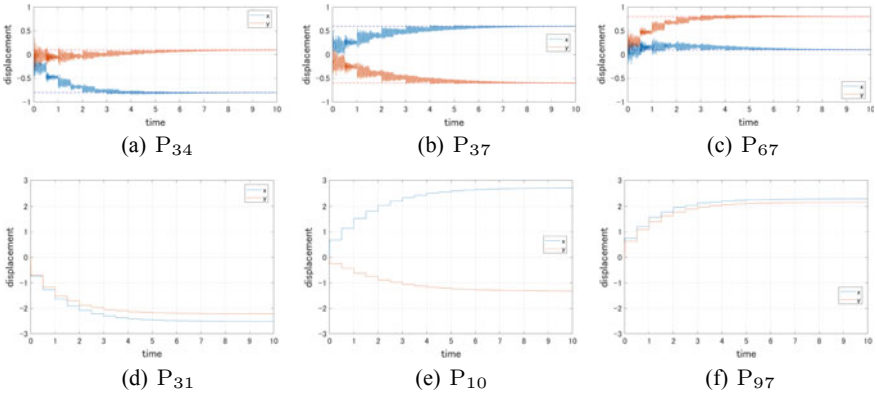

(a) P_{34} (b) P_{37} (c) P_{67}

(d) P_{31} (e) P_{10} (f) P_{97}

Fig. 13.15 Displacement components of positioned and manipulated points

modulus $c = 40\,\text{Pa s}$, Poisson's ratio $\nu = 0.48$, and density $\rho = 1.0\,\text{g/cm}^3$. The estimated parameter values for the control law are Young's modulus $\hat{E} = 0.1\,\text{MPa}$ and Poisson's ratio $\hat{\nu} = 0.45$. Notably, the estimated values are different from the actual values. The scaling parameter is $\alpha = 0.25$. Figure 13.15 shows the displacement components of the positioned and manipulated points. The displacement components of the positioned points are successfully directed to their desired values.

Notably, this control law does not require an accurate elastic body model. This control law functions well even though the estimated physical parameters are different from the actual values. In this control method, the elastic body and control law provides inherent degrees of freedom to cope with the difference between the estimated and actual physical parameters.

13.4.3 Orientation Control Through Soft Fingertips

In this section, we discuss the control of the orientation of the target object held by a soft cover hand with two fingers (Fig. 13.16). Assume that a sensor measures the orientation of the held object and that the rotation of each finger is controlled based on the measured orientation. Let θ_{obj} be the orientation angle of the object and let θ_1 and θ_2 be the rotational angles of the right and left fingers, respectively. The rotational angles increased when the fingers moved inward and decreased when they moved outward. Let $\theta^{\text{d}}_{\text{obj}}$ be the desired angle of the object orientation. The goal of orientation control is to guide θ_{obj} to its desired value, $\theta^{\text{d}}_{\text{obj}}$, by controlling the finger angles θ_1 and θ_2.

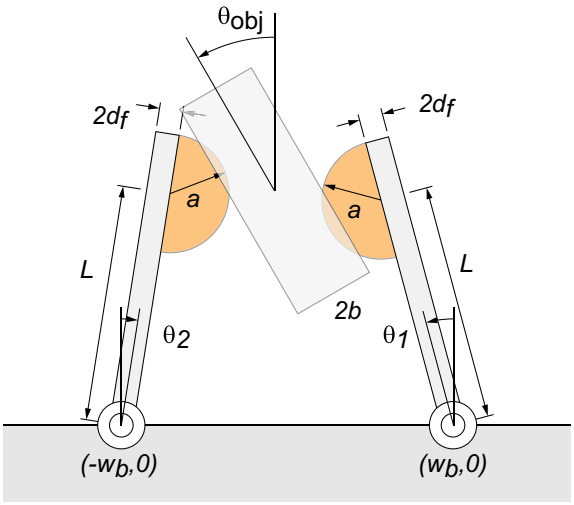

Fig. 13.16 A pair of soft cover fingers manipulating a rectangle object

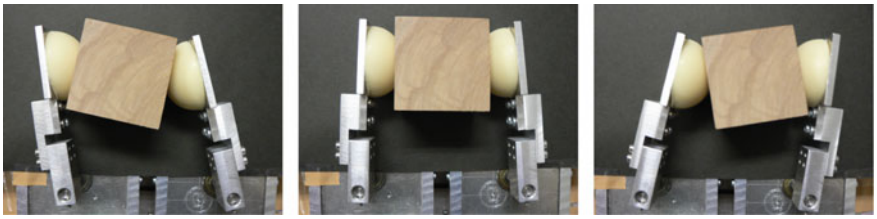

(a) (b) (c)

Fig. 13.17 Orientation of target object grasped by a pair of soft cover fingers

Figure 13.17 shows the dependence of object orientation on the rotation of the two fingers. When both fingers rotate leftward (Fig. 13.17a), the object rotates rightward. Namely, when θ_1 increases and θ_2 decreases, the orientation angle θ_{obj} decreases, implying that when $\theta_{\text{obj}} > \theta_{\text{obj}}^{\text{d}}$, we should increase θ_1 and decrease θ_2 to reduce the orientation angle θ_{obj}. By contrast, when both fingers rotate rightward (Fig. 13.17c), the object rotates leftward. That is, when θ_1 decreases and θ_2 increases, the orientation angle θ_{obj} increases, implying that when $\theta_{\text{obj}} < \theta_{\text{obj}}^{\text{d}}$, we should decrease θ_1 and increase θ_2 to increase the orientation angle θ_{obj}.

We introduced virtual desired angles for the right and left fingers based on the aforementioned observations. We assume that the virtual desired angles are updated at a predetermined time interval T. Let $\theta^{\mathrm{d}}_{1,k}$ and $\theta^{\mathrm{d}}_{2,k}$ be the virtual desired angles in $[kT, (k+1)T]$. The updated laws are as follows:

$$\theta^{\mathrm{d}}_{1,k} = \theta^{\mathrm{d}}_{1,k-1} + K_{\mathrm{I}}(\theta_{\mathrm{obj}}(kT) - \theta^{\mathrm{d}}_{\mathrm{obj}}), \qquad (k = 1, 2, \ldots) \tag{13.76}$$

$$\theta^{\mathrm{d}}_{2,k} = \theta^{\mathrm{d}}_{2,k-1} - K_{\mathrm{I}}(\theta_{\mathrm{obj}}(kT) - \theta^{\mathrm{d}}_{\mathrm{obj}}), \qquad (k = 1, 2, \ldots) \tag{13.77}$$

where K_{I} denotes a positive constant. Their initial values are expressed as follows:

$$\theta^{\mathrm{d}}_{1,0} = K_{\mathrm{I}}(\theta_{\mathrm{obj}}(0) - \theta^{\mathrm{d}}_{\mathrm{obj}}),$$

$$\theta^{\mathrm{d}}_{2,0} = -K_{\mathrm{I}}(\theta_{\mathrm{obj}}(0) - \theta^{\mathrm{d}}_{\mathrm{obj}}).$$

Equations (13.76) and (13.77) show that $\theta^{\mathrm{d}}_{1,k}$ increases and $\theta^{\mathrm{d}}_{2,k}$ decreases when $\theta_{\mathrm{obj}} > \theta^{\mathrm{d}}_{\mathrm{obj}}$, whereas $\theta^{\mathrm{d}}_{1,k}$ decreases and $\theta^{\mathrm{d}}_{2,k}$ increases when $\theta_{\mathrm{obj}} < \theta^{\mathrm{d}}_{\mathrm{obj}}$. We apply the following proportional–derivative (PD) control laws to determine the torques for the rotational motions of the right and left fingers during $[kT, (k+1)T]$:

$$u_1 = -K_{\mathrm{P}}(\theta_1 - \theta^{\mathrm{d}}_{1,k}) - K_{\mathrm{D}}\dot{\theta}_1 + \tau_{\mathrm{b}}, \tag{13.78}$$

$$u_2 = -K_{\mathrm{P}}(\theta_2 - \theta^{\mathrm{d}}_{2,k}) - K_{\mathrm{D}}\dot{\theta}_2 + \tau_{\mathrm{b}}, \tag{13.79}$$

where τ_{b} denotes the positive bias torque that generates the holding force. The aforementioned control law has been demonstrated experimentally, and the object orientation angle θ_{obj} successfully converges to $\theta^{\mathrm{d}}_{\mathrm{obj}}$, whereas θ_1 and θ_2 do not converge to their virtual desired angles, $\theta^{\mathrm{d}}_{1,k}$ and $\theta^{\mathrm{d}}_{2,k}$, respectively (Inoue and Hirai 2009). This implies that Eqs. (13.76) and (13.77) of the control law should accept the deviations of θ_1 and θ_2. When we apply proportional–integral–differential (PID) control laws rather than PD control laws to guide θ_1 and θ_2 to exactly $\theta^{\mathrm{d}}_{1,k}$ and $\theta^{\mathrm{d}}_{2,k}$, θ_1 and θ_2 may diverge or the contact between the fingers and the object may be lost, resulting in object–orientation control failure. Note that the potential energy should reach its local minimum at $\theta^{\mathrm{d}}_{\mathrm{obj}}$ such that the orientation angle θ_{obj} converges to $\theta^{\mathrm{d}}_{\mathrm{obj}}$ in a stable state, and the fingers and object should remain in contact during manipulation. The realization of the virtual desired angles $\theta^{\mathrm{d}}_{1,k}$ and $\theta^{\mathrm{d}}_{2,k}$ may break these conditions, implying that deviations in the control of θ_1 and θ_2 should be allowed.

We used a dynamic simulation to validate the aforementioned control law. First, we described the dynamics of the pair of hemispherical fingertips that manipulated a rectangle. Assume that a hemispherical fingertip of radius a was attached to one end of a rigid plate of thickness $2d_{\mathrm{f}}$. The other end of the plate was connected to a rotational joint fixed to the ground. The distance between the center of the hemispherical fingertip and the rotational joint center was L. Let $[w_{\mathrm{b}}, 0]^{\mathrm{T}}$ and $[-w_{\mathrm{b}}, 0]^{\mathrm{T}}$ denote the positions of the rotational joints of the right and left fingers, respectively. Let

E denotes the Young's modulus of the fingertip material and let d_n and d_t denote the maximum normal and tangential displacements of the fingertip, respectively, and θ be the relative angle between the fingertip and the surface of the manipulated rectangle. The strain potential energy stored in a hemispherical fingertip is expressed as follows:

$$U(\theta, d_\mathrm{n}, d_\mathrm{t}) = \frac{\pi E d_\mathrm{n}^3}{3\cos^2\theta} + \pi E\left(d_\mathrm{n}^2 d_\mathrm{t}\tan\theta + d_\mathrm{n} d_\mathrm{t}^2\right). \tag{13.80}$$

Strain potential energy stored in the two fingertips is given as follows:

$$U = U(\theta_1 - \theta_\mathrm{obj}, d_\mathrm{n1}, d_\mathrm{t1}) + U(\theta_2 + \theta_\mathrm{obj}, d_\mathrm{n2}, d_\mathrm{t1}) \tag{13.81}$$

where d_n1 and d_t1 represent the normal and tangential displacements of the right fingertip, respectively; and d_n2 and d_t2 represent the normal and tangential displacements of the left fingertip, respectively. Assuming that the center of gravity of the rectangle is its center, let $\boldsymbol{x}_\mathrm{obj} = [x_\mathrm{obj}, y_\mathrm{obj}]^\mathrm{T}$ be the positional vector of the center of gravity. Let m_obj and I_obj denote the mass and moment of inertia of the manipulated rectangle, respectively, I_1 and I_2 denote the moment of inertia of the two fingers, and m_n and m_t denote the equivalent masses corresponding to normal and tangential displacements, respectively. The kinetic energy is expressed as follows:

$$T = \frac{1}{2}m_\mathrm{obj}\left(\dot{x}_\mathrm{obj}^2 + \dot{y}_\mathrm{obj}^2\right) + \frac{1}{2}I_\mathrm{obj}\dot{\theta}_\mathrm{obj}^2 + \frac{1}{2}I_1\dot{\theta}_1^2 + \frac{1}{2}I_2\dot{\theta}_2^2 \tag{13.82}$$

$$+ \frac{1}{2}m_\mathrm{n}\dot{d}_\mathrm{n1}^2 + \frac{1}{2}m_\mathrm{n}\dot{d}_\mathrm{n2}^2 + \frac{1}{2}m_\mathrm{t}\dot{d}_\mathrm{t1}^2 + \frac{1}{2}m_\mathrm{t}\dot{d}_\mathrm{t2}^2. \tag{13.83}$$

The work done by the finger torque is described as follows:

$$W = u_1\theta_1 + u_2\theta_2. \tag{13.84}$$

It is assumed that the fingertips roll over the surface of a rectangle without slippage. This yields normal and tangential constraints between the fingertip and surface. Let $\boldsymbol{d}_\mathrm{obj} = [C_\mathrm{obj}, S_\mathrm{obj}]^\mathrm{T}$ and $\boldsymbol{h}_\mathrm{obj} = [-S_\mathrm{obj}, C_\mathrm{obj}]^\mathrm{T}$, where $C_\mathrm{obj} = \cos\theta_\mathrm{obj}$ and $S_\mathrm{obj} = \sin\theta_\mathrm{obj}$. The positional vectors of the centers of the two hemispherical fingertips are represented as follows:

$$\boldsymbol{p}_1 = \begin{bmatrix} w_\mathrm{b} \\ 0 \end{bmatrix} + \begin{bmatrix} C_1 & -S_1 \\ S_1 & C_1 \end{bmatrix}\begin{bmatrix} -d_\mathrm{f} \\ L \end{bmatrix}, \quad \boldsymbol{p}_2 = \begin{bmatrix} -w_\mathrm{b} \\ 0 \end{bmatrix} + \begin{bmatrix} C_2 & S_2 \\ -S_2 & C_2 \end{bmatrix}\begin{bmatrix} d_\mathrm{f} \\ L \end{bmatrix},$$

where $C_1 = \cos\theta_1, S_1 = \sin\theta_1, C_2 = \cos\theta_2$, and $S_2 = \sin\theta_2$. The normal constraints at the two fingertips are as follows:

$$\begin{aligned} C_\mathrm{n1} &= -\boldsymbol{d}_\mathrm{obj}^\mathrm{T}(\boldsymbol{x}_\mathrm{obj} - \boldsymbol{p}_1) - (a - d_\mathrm{n1}) - b = 0, \\ C_\mathrm{n2} &= \quad \boldsymbol{d}_\mathrm{obj}^\mathrm{T}(\boldsymbol{x}_\mathrm{obj} - \boldsymbol{p}_2) - (a - d_\mathrm{n2}) - b = 0. \end{aligned} \tag{13.85}$$

The tangential constraints at the two fingertips are as follows:

$$\begin{aligned} C_{t1} &= \boldsymbol{h}_{obj}^{T}(\boldsymbol{x}_{obj} - \boldsymbol{p}_1) + a(\theta_1 - \theta_{obj}) + d_{t1} = C_{t1}^0, \\ C_{t2} &= \boldsymbol{h}_{obj}^{T}(\boldsymbol{x}_{obj} - \boldsymbol{p}_2) + a(\theta_2 + \theta_{obj}) + d_{t2} = C_{t2}^0, \end{aligned} \tag{13.86}$$

where C_{t1}^0 and C_{t2}^0 are constants determined by the initial contact between the fingertips and the object. These constraints become $\dot{C}_{t1} = 0$ and $\dot{C}_{t2} = 0$. Consequently, four constraints $C_{n1} = 0$, $C_{n2} = 0$, $\dot{C}_{t1} = 0$, and $\dot{C}_{t2} = 0$ are imposed on the system.

This system comprises a pair of soft cover fingers and a rectangular object, a set of generalized coordinates is expressed as $\boldsymbol{q} = [x_{obj}, y_{obj}, \theta_{obj}, \theta_1, \theta_2, d_{n1}, d_{n2}, d_{t1}, d_{t2}]^T$. The Lagrangian of the system is described as follows:

$$\mathcal{L} = T - U + W + \lambda_{n1} C_{n1} + \lambda_{n2} C_{n2},$$

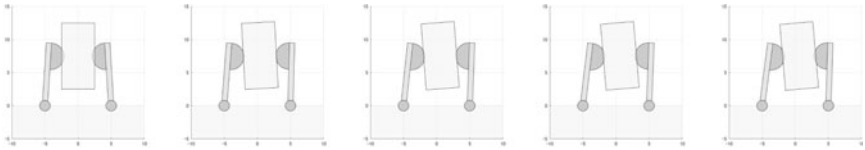

(a) behavior of soft cover hand and object

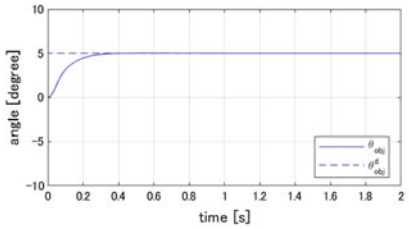

(b) object angle

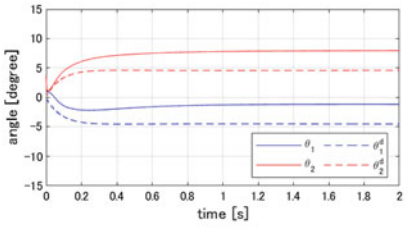

(c) finger angles

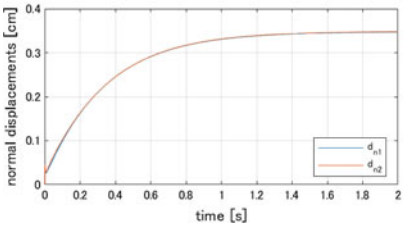

(d) normal displacements

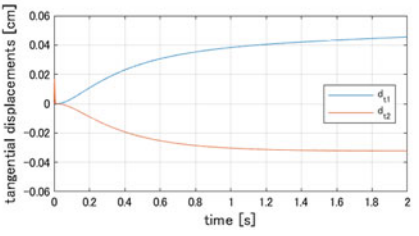

(e) tangential displacements

Fig. 13.18 Dynamic simulation of control law

where λ_{n1} and λ_{n2} are Lagrange multipliers. A set of Lagrange equations of motion and deformation are expressed as follows:

$$\frac{\partial \mathcal{L}}{\partial \boldsymbol{q}} - \frac{\mathrm{d}}{\mathrm{d}t}\frac{\partial \mathcal{L}}{\partial \dot{\boldsymbol{q}}} + \lambda_{t1}\frac{\partial \dot{C}_{t1}}{\partial \dot{\boldsymbol{q}}} + \lambda_{t2}\frac{\partial \dot{C}_{t2}}{\partial \dot{\boldsymbol{q}}} = \boldsymbol{0}, \tag{13.87}$$

where λ_{t1} and λ_{t2} are Lagrange multipliers. The equations for constraint stabilization are as follows:

$$\ddot{C}_{nk} + 2\alpha\dot{C}_{nk} + \alpha^2 C_{nk}^2 = 0, \quad (k = 1, 2), \tag{13.88}$$

$$\ddot{C}_{tk} + \beta\dot{C}_{tk} = 0, \quad (k = 1, 2), \tag{13.89}$$

where α and β are the positive constants.

We can simulate the dynamic behavior of the system by solving the set of Lagrange equations (Eq. 13.87) with constraint–stabilizing equations (Eqs. 13.88 and 13.89). Figure 13.18a shows a snapshot of the simulation result. The object orientation converged to its desired angle (Fig. 13.18b), whereas the joint angles did not converge to their virtual desired values (Fig. 13.18c). Figure 13.18d shows normal displacements d_{n1} and d_{n2} and Fig. 13.18d shows tangential displacements d_{t1} and d_{t2}. The normal displacements d_{n1} and d_{n2} are positive during control, implying that the contact between the fingers and the object is maintained. The intentional use of PD control and soft covering serves as an inherent degrees of freedom to maintain contact between fingers and object.

13.4.4 Challenges and Perspectives

Soft robots have infinite degrees of freedom; however, it is not necessary to control all of them. Instead, we can exploit inherent softness to control a system with soft bodies. Currently, soft sensors are available for soft bodies, implying that control system embodiment in soft robots is possible. In addition, a theoretical analysis based on soft body mechanics is required for a better understanding of soft robot control.

References

Akashi N, Nakajima K, Kuniyoshi Y (2019) Unpredictable as dice: analyzing riddled basin structures in a passive dynamic walker. In: 2019 international symposium on micro-nanomechatronics and human science (MHS), Dec 2019. IEEE, pp 1–6

Antman S (2004) Nonlinear problems of elasticity, 2nd edn. Springer

Broer HW, Takens F (2011) Dynamical systems and chaos. Springer, New York

Fish J, Belytschko T (2007) A first course in finite elements. Wiley. ISBN 978-0-470-03580-1. https://doi.org/10.1002/9780470510858

Garcia M, Chatterjee A, Ruina A, Coleman M (1998) The simplest walking model: stability, complexity, and scaling. J Biomech Eng 120(2):281–288
Gaspard P (2005) Chaos, scattering and statistical mechanics, vol 9. Cambridge University Press
Goswami A, Espiau B, Keramane A (1996) Limit cycles and their stability in a passive bipedal gait. In: Proceedings of IEEE international conference on robotics and automation, Apr 1996, vol 1. IEEE, pp 246–251
Grebogi C, McDonald SW, Ott E, Yorke JA (1983) Final state sensitivity: an obstruction to predictability. Phys Lett A 99(9):415–418
Gritli H, Khraief N, Belghith S (2012) Period-three route to chaos induced by a cyclic-fold bifurcation in passive dynamic walking of a compass-gait biped robot. Commun Nonlinear Sci Numer Simul 17(11):4356–4372
Gritli H, Khraief N, Belghith S (2014) Further analysis of the period-three route to chaos in passive dynamic walking of a compass-gait biped robot. In: Proceedings of the copyright IPCO, pp 123–130
Hirai S, Wada T (2000) Indirect simultaneous positioning of deformable objects with multi pinching fingers based on uncertain model. Robotica 18(1. Millennium issue on grasping and manipulation):3–11. https://doi.org/10.1017/S0263574799002362
Hirsch MW, Smale S, Devaney RL (2012) Differential equations, dynamical systems, and an introduction to chaos. Academic Press
Ijspeert AJ, Crespi A, Ryczko D, Cabelguen JM (2007) From swimming to walking with a salamander robot driven by a spinal cord model. Science 315(5817):1416–1420
Inoue T, Hirai S (2009) Mechanics and control of soft-fingered manipulation. Springer. ISBN 978-1-84800-980-6. https://doi.org/10.1007/978-1-84800-981-3
Kapitaniak M, Strzalko J, Grabski J, Kapitaniak T (2012) The three-dimensional dynamics of the die throw. Chaos Interdiscip J Nonlinear Sci 22(4):047504
Keller HB (1968) Numerical methods for two-point boundary value problems. Blaisdell Publishing
Kolen J, Pollack J (1990) Back propagation is sensitive to initial conditions. In: Advances in neural information processing systems, vol 3
McGeer T (1990) Passive dynamic walking. Int J Robot Res 9(2):62–82
Murray RM, Li Z, Sastry SS (1994) A mathematical introduction to robotic manipulation. CRC Press
Nagler J, Richter P (2008) How random is dice tossing? Phys Rev E 78(3):036207
Nakagawa N, Mochiyama H (2018) Real-time shape estimation of elastic rod using robot manipulator equipped with sense of force. In: Proceedings of the 2018 IEEE/RSJ international conference on intelligent robots and systems (IROS), pp 8067–8073
Obayashi I, Aoi S, Tsuchiya K, Kokubu H (2016) Formation mechanism of a basin of attraction for passive dynamic walking induced by intrinsic hyperbolicity. Proc R Soc A Math Phys Eng Sci 472(2190):20160028
O'Neill B (2006) Elementary differential geometry, Revised 2nd edn. Academic Press
Sugiyama Y, Hirai S (2006) Crawling and jumping by a deformable robot. Int J Robot Res 25(5–6):603–620. https://doi.org/10.1177/0278364906065386
Takano R, Mochiyama H, Takesue N (2017) Real-time shape estimation of Kirchhoff elastic rod based on a force/torque sensor. In: Proceedings of 2017 IEEE international conference on robotics and automation (ICRA), pp 2508–2515
Terajima R, Inoue K, Yonekura S, Nakajima K, Kuniyoshi Y (2021) Behavioral diversity generated from body-environment interactions in a simulated tensegrity robot. IEEE Robot Autom Lett 7(2):1597–1604
Timoshenko SP, Goodier JN (1970) Theory of elasticity, 3rd edn. McGraw-Hill
Zodiac (1996) Theory of robot control. Springer

Chapter 14
Material Intelligence

Yuhei Yamada, Shingo Maeda, Kazuya Furusawa, Masahiro Shimizu, Hiroshi Ito, and Takuma Sugi

Abstract This chapter describes soft robots that use biological and chemical materials. The authors will introduce some attempts to regard them not only as a mere frame of a robot, but also as elements that process information. Section 14.1 describes the use of chemical oscillations in actuators. Section 14.2 described the classification of biomaterials as information processing machines. Section 14.3 discusses the formation of spatial patterns and rhythms by bacteria and animals.

Y. Yamada · S. Maeda (✉)
Department of Mechanical Engineering, Tokyo Institute of Technology, Tokyo, Japan
e-mail: maeda.s.ao@m.titech.ac.jp

Y. Yamada
e-mail: yamada.y.bw@m.titech.ac.jp

K. Furusawa
Department of Applied Chemistry and Food Science, Faculty of Environmental and Information Science, Fukui University of Technology, Fukui, Japan
e-mail: kfurusawa@fukui-ut.ac.jp

M. Shimizu
Department of Systems Innovation, Graduate School of Engineering Science, Osaka University, Toyonaka, Japan
e-mail: m_shimizu@nagahama-i-bio.ac.jp

H. Ito
Faculty of Design, Kyushu University, Fukuoka, Japan
e-mail: hito@design.kyushu-u.ac.jp

T. Sugi
Division of Integrated Sciences for Life, Graduate School of Integrated Sciences for Life, Hiroshima University, Higashihiroshima, Japan
e-mail: sugit@hiroshima-u.ac.jp

Present Address:
S. Maeda
Living Systems Materialogy (LiSM) Research Group, International Research Frontiers Initiative (IRFI), Tokyo Institute of Technology, Yokohama, Japan

K. Suzumori et al. (eds.), *The Science of Soft Robots*, Natural Computing Series,
https://doi.org/10.1007/978-981-19-5174-9_14

14.1 Chemical Information Processing

14.1.1 What Is Chemical Information Processing?

In this section, we explain how soft robots process chemical information. In general, robots have a metal body and a silicon brain. Information processing by semiconductor devices executes precise calculations and enables robots to operate. Thus far, mechatronics has achieved great success in the industrial field. Using such mechatronic technologies, researchers have begun to develop machines and robots that resemble living organisms. However, attempts to replicate the soft mechanisms of living things by extending mechatronic technologies have encountered a roadblock posed by the complexity of biological systems. It is impossible to completely reproduce living organisms using artificial systems. However, it might be feasible to realize machine behaviors and movements that mimic those of living things. For example, if we imagine how many actuators, sensors, programs, and electronic elements are required to imitate the movement of an octopus? If the number of degrees of freedom in the mechanism is extremely large, developing a mechanism that can imitate the movement of an octopus might be possible; however, huge amounts of data from sensor inputs must be processed, and large control programs must be executed. To design autonomous robots capable of performing hardware and software operations in real time, researchers must confront the complexity of mechanical systems. Is reproducing the soft movements of living things the best approach for designing an autonomous machine or robot with a large number of semiconductor devices and programs properly connected to perform sophisticated calculations? We cannot conceive how the assembly of these mechanisms is executed. Soft robotics addresses these issues.

Mechanical systems based on mechatronics are becoming increasingly complex as their performance increases. These facts were empirically expressed by Moore's Law (Moore 1965). The miniaturization of these devices is expected to improve the performance of integrated circuits. Therefore, the limits of miniaturization may be reached one day. Unconventional computing is one approach to overcoming the barrier of increasing machine complexity. Unconventional computing is a field that studies computational methods inspired by chemistry, physics, and biology (Adamatzky et al. 2005; Adleman 1994). For example, DNA computing (Adleman 1994) uses (1) adenine, thymine, guanine, and cytosine pairing in DNA (DNA strand generation) and (2) enzymatic reactions that manipulate DNA strands to perform parallel computations. Understanding DNA computing requires mapping the computational process to a phenomenon. Biochemical reactions can be calculated by mapping them to operations and products to solutions. Thus, biochemical reactions correspond to operations and products correspond to solutions, enabling calculations to be performed. In fact, Adleman (1994) reported that the arithmetic operations (biochemical reactions) of the traveling salesman problem can be completed in a few seconds of parallel computation because many DNA strands that are candidates for the solution are generated simultaneously; however, determining the solution (the product corresponding to the

solution) requires a long time. Therefore, it is necessary to accelerate the process of determining the correct solution.

Reaction diffusion computing has been proposed as a computing method that uses wet systems (Adamatzky et al. 2005). The Belousov–Zhabotinsky (BZ) reaction, which is a typical example of a reaction–diffusion system, has been used for computing operations, such as logic circuits and image processing (Steinbock et al. 1996). The BZ reaction is appealing because spatiotemporal patterns can be constructed in a simple experimental system. Chemical operations can be executed in parallel and spatially if chemical reactions are considered as information processing.

14.1.2 Active Gels

Active gels generate autonomous mechanical motion when nonlinear chemical reactions are coupled with stimuli-responsive gels (Pojman 2004). If the computational solution corresponds to the motion of a system, autonomous robots and machines driven by chemical reactions can be realized. From the perspective of unconventional computing, such autonomous systems can be considered to correspond to a computational process (chemical reaction) and solution (motion). If the control and sensor system processes can be performed by a chain of chemical reactions, the development of new soft machines and robots becomes feasible.

There are two main types of systems that combine nonlinear chemical reactions with stimuli-responsive gels. In the first type, a pH oscillation is produced in the system, and the volume of pH-responsive gels in the system changes (type 1) in response. In the second type, the BZ reaction proceeds inside a stimuli-responsive gel, and the volume of the gel follows that of the BZ reaction (type 2). The pH oscillation in a type 1 system can be realized using the Landolt reaction (Yoshida et al. 1995; Crook et al. 2002) or an enzymatic reaction (Dhanarajan 2002). The interaction of the pH-responsive gel with the non-oscillatory acid autocatalytic chlorite/tetrathionate reaction results in a spatiotemporal pattern of volume changes in the gel (Labrot et al. 2005). The large amplitude of these pH oscillations and large changes in gel volume have a strong visual impact. These pH oscillators typically require continuous-flow stirred-tank reactors, which severely limits the design of the system. Type 2 reactions can be realized by coupling the BZ reaction with a stimuli-responsive gel (Yoshida et al. 1996) (BZ gel). Although the change in volume of the BZ gel was much smaller than the change in pH of the pH oscillator, there was no requirement to prepare continuous-flow stirred-tank reactors.

14.1.3 Belousov–Zhabotinsky Reaction

Chemical oscillation is a chemical reaction in which the concentrations of substances oscillate over time. From a physical perspective, chemical oscillation can be understood as a system in which the concentrations of substances exhibit a limit cycle and is essentially a nonlinear system. The BZ reaction is a typical example of a chemical oscillation. It is a chemical reaction involving the bromination of carboxylic acids through metal-ion catalysis. For example, the BZ reaction can be observed by mixing malonic acid as the reaction substrate, sodium bromate as the oxidant, and a ruthenium complex as the metal catalyst under strongly acidic conditions (Fig. 14.1). Numerous methods for BZ reactions have been reported. Table 14.1 shows a typical procedure for the BZ reaction under unstirred conditions at room temperature.

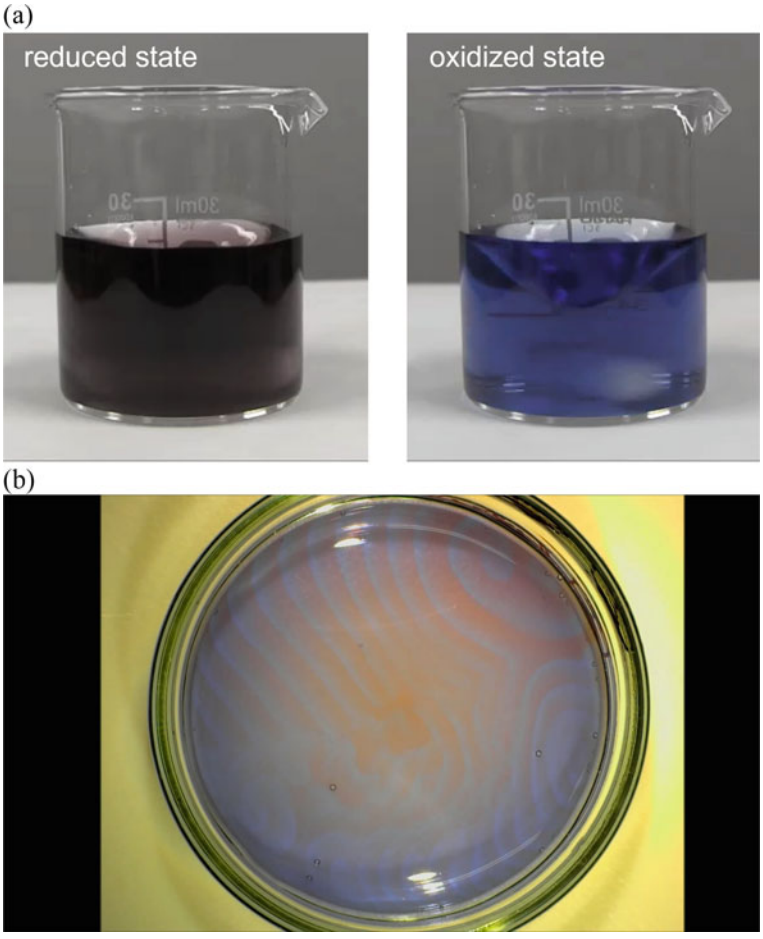

Fig. 14.1 BZ reaction. **a** chemical oscillation and **b** chemical waves

Table 14.1 Recipe for BZ reaction

Chemicals	Concentration [M] (chemical oscillation)	Concentration [M] (chemical waves)
Nitric acid	0.73	0.77
Sodium bromate	0.22	0.12
Ferroin	0.00125	0.0025
Malonic acid	0.05	0.12

The reaction mechanism of the BZ reaction is described by 11 chemical reaction equations known as the Field-Koros-Noyes (FKN) mechanism, proposed by Field, Koros, Noyes, and others (Field and Burger 1985). The FKN mechanism is further reduced to five essential chemical reaction equations known as Oregonator. In the Oregonator, $A = \left[\mathrm{BrO_3^-}\right]$, $B = \left[\mathrm{Org.(organic\ substance)}\right]$, $X = [\mathrm{HBrO_2}]$, $Y = \left[\mathrm{Br^-}\right]$, $Z = \left[M_{\mathrm{ox}}(\mathrm{oxidizedmetal\ catalyst})\right]$, $Y = \left[\mathrm{Br^-}\right]$, $P = [\mathrm{HBrO}]$, and $H = \left[\mathrm{H^+}\right]$, and the reaction process is considered as follows:

$$A + Y \xrightarrow{k_1 H^2} X + P$$

$$X + Y \xrightarrow{k_2 H} 2P$$

$$A + X \xrightarrow{k_3 H} 2X + 2Z$$

$$X + X \xrightarrow{k_4} A + P$$

$$B + Z \xrightarrow{k_5} \frac{1}{2} f Y$$

where f represents the stoichiometric constant. Substances A and B are assumed to be sufficiently abundant in the system compared to substances X, Y, and Z, and are approximated as time-invariant constants. The reaction rate equations for X, Y, and Z then become as follows:

$$\frac{\mathrm{d}X}{\mathrm{d}\tau} = k_1 H^2 A Y - k_2 H X Y + k_3 H A X - 2k_4 X^2$$

$$\frac{\mathrm{d}Y}{\mathrm{d}\tau} = -k_1 H^2 A Y - k_2 H X Y + \frac{1}{2} f k_5 B Z$$

$$\frac{\mathrm{d}Z}{\mathrm{d}\tau} = 2k_3 H A X - k_5 B Z$$

where τ denotes the real time. These equations correspond to elementary processes of the BZ reaction.

Y changes sufficiently fast compared to X and Z that the approximation $\mathrm{d}Y/\mathrm{d}\tau = 0$ is often assumed. With appropriate parameters, these differential equations exhibit a limit cycle. In other words, there is a closed orbit such that the trajectory of the solution converges after sufficient time. The oscillation repeats infinitely in the mathematical model; however, in an actual system, A and B decrease as the reaction proceeds, and the assumption of their abundance eventually becomes incorrect. The model then breaks down, and the oscillation stops.

14.1.4 Belousov–Zhabotinsky Gels

Self-oscillating gels were obtained by copolymerizing a ruthenium catalyst for the BZ reaction into the main chain of a poly(*N*-isopropylacrylamide) (PNIPAAm) gel and inducing the BZ reaction inside the gel (Yoshida et al. 1996). Physical gels, such as alginate gels, and the physical fixation of metal catalysts in water glass or ion-exchange resins can also result in a BZ reaction inside the gels (Yamaguchi et al. 1991); however, the literature contains few experimental studies on the volume oscillation of such gels. In addition, the volumes of gels have been reported to oscillate with the BZ reaction as a result of the physical binding of metal complexes to polymers (Kontop et al. 2011). Unlike the experimental system for pH oscillatory reactions, the BZ reaction is easy to develop because oscillatory reactions and pattern changes can be observed for an extended period in a closed system.

Before explaining the BZ gels, we briefly state the theory of swelling gels. According to Flory's theory (Flory 1953), the affinity between a polymer and solvent is expressed as the χ parameter. In a gel system, a higher χ parameter indicates contraction of the gel, which in turn indicates a decrease in the affinity between the polymer and solvent. Normally, the volume fraction of the polymer in the gel ϕ, is used to describe the thermal equilibrium state and has the following relationship with the volume of the gel:

$$\frac{\phi_0}{\phi} = \frac{V}{V_0} \tag{14.1}$$

where ϕ_0, V, and V_0 denote the volume fractions of the polymer in the gel when the gel is synthesized, the volume of the gel, and the volume of the gel when the gel is synthesized, respectively. Some models of the gel thermal equilibrium state have been proposed. Here, we present a model that uses the Flory model of the gel in the thermal equilibrium state:

$$\phi + \ln(1-\phi) + \chi\phi^2 - \frac{N_\mathrm{c} v_\mathrm{s}}{N_\mathrm{A} V_0}\left[\frac{\phi}{2\phi_0} - \left(\frac{\phi}{\phi_0}\right)^{\frac{1}{3}}\right] = 0 \tag{14.2}$$

where N_c, v_s, and N_A denote the number of polymer chains, the molar volume of the solvent, and Avogadro's constant, respectively. In general, the χ parameter depends on the absolute temperature T as follows:

$$\chi = \frac{1}{k_B}\left(\frac{\Delta h}{T} - \Delta s\right) \tag{14.3}$$

where k_B is the Boltzmann constant and Δh and Δs indicate changes in enthalpy and entropy, respectively. For example, in the case of thermoresponsive gels, a change in the absolute temperature, T, corresponds to a change in the χ parameter. Similarly, changes in the solvent composition, ion strength, and pH corresponds to changes in the χ parameter (Fig. 14.2). The volume of the thermoresponsive PNIPAAm gel exhibited a transition at approximately 33 °C.

Yoshida et al. synthesized a ruthenium monomer and obtained poly(NIPAAm-*co*-[Ru]) gels (Yoshida et al. 1996). They observed periodic swelling and contraction of the gel, which they referred to as a self-oscillating gel. The self-oscillating gel exhibited a displacement of several tens of micrometers, which is a noteworthy result. The change in the ruthenium catalyst, chemically immobilized in the BZ gel, from the reduced state (Ru(II)) to the oxidized state (Ru(III)) corresponded to a change in χ. A larger χ corresponded to contraction of the gel, and χ in the oxidized state was smaller than that in the reduced state. As a result, the volume of the oxidized state of the BZ gel (Ru(III)) was larger than that of the BZ gel in the reduced state (Ru(II)) (Maeda et al. 2016) (Fig. 14.3).

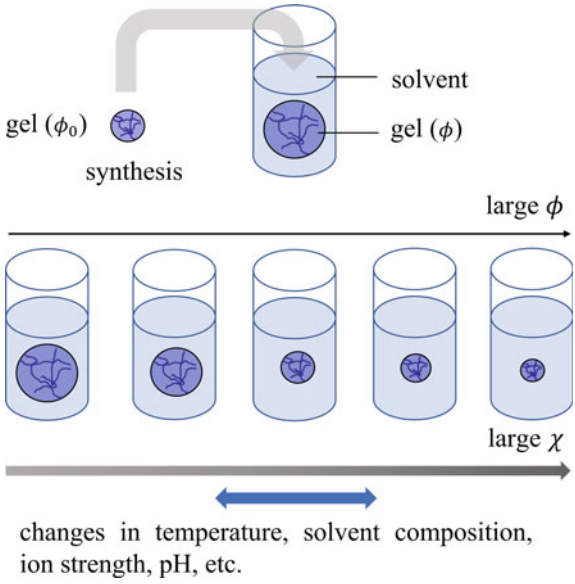

Fig. 14.2 Volume change of gels in response to external changes

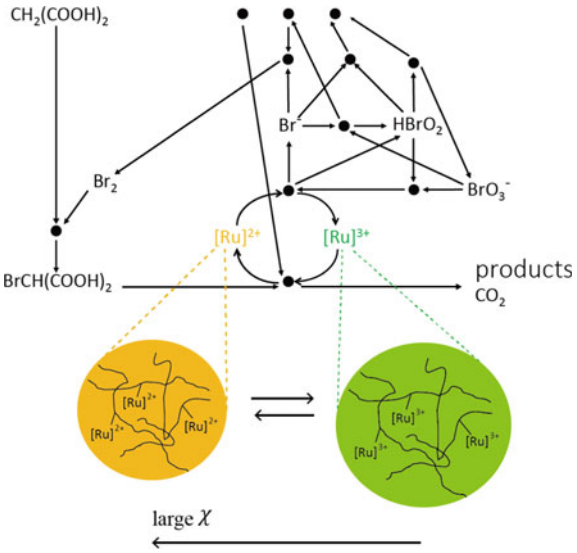

Fig. 14.3 The mechanism of volume expansion of BZ gels

The use of thermoresponsive gels to develop BZ gels has the advantage that the swelling characteristics of the gels can be controlled by changing their temperature. However, because temperature also affects the period of the BZ reaction, independently controlling the amplitude and period of the change in the volume of the thermoresponsive BZ gels is inherently difficult. Figure 14.4 shows the equilibrium states of the reduced and oxidized poly(NIPAAm-*co*-[Ru]) gels as functions of temperature. The difference in volume between the reduced and oxidized poly(NIPAAm-*co*-[Ru]) gels in the higher-temperature range (ii) is larger than that in the lower-temperature range (i). However, in the BZ reaction, the displacement of the poly(NIPAAm-*co*-[Ru]) gel in temperature range (ii) is considerably smaller than that in temperature range (i). This difference is attributed to the ϕ in temperature range (ii) being considerably larger than that in temperature range (i) and to the redox potential of ruthenium in temperature range (ii) becoming extremely low. BZ gels based on non-thermoresponsive gels have been reported (Nakamaru et al. 2009; Yuan et al. 2013). Volume oscillation was realized irrespective of the temperature responsiveness of the BZ gel main chain.

14.1.5 Mathematical Model for Belousov–Zhabotinsky Gels

The concentration change owing to the expansion and contraction of the gel should be considered to describe the elementary process of the BZ gels based on the Oregonator. Here, ϕ denotes the volume fraction of the gel; X, Y, and Z are the ratios of the

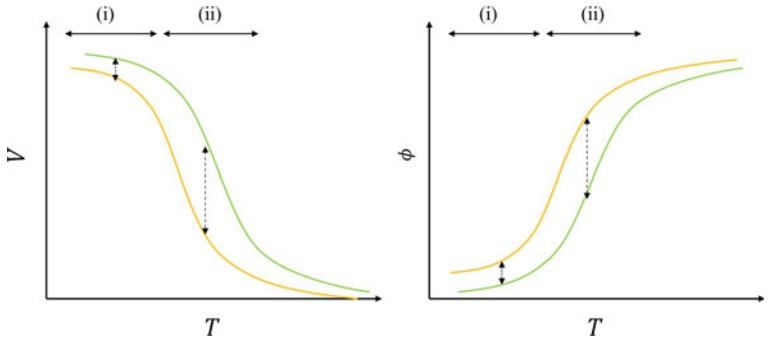

Fig. 14.4 The equilibrium states of reduced and oxidized poly(NIPAAm-*co*-[Ru]) gels

solution volume to the total gel volume; and A, B, and H are the ratios of the solution volume to the gel volume (Yashin and Balazs 2007; Yashin et al. 2012). In this case, A, B, and H change by a factor of $(1-\phi)$ in Oregonator's equation. In addition, when the concentration change owing to the flow of solution into and out of the gel during the volume change is considered, the reaction rate equations for the BZ gel become as follows:

$$\frac{\mathrm{d}X}{\mathrm{d}\tau} = -\frac{X}{1-\phi}\frac{\mathrm{d}\phi}{\mathrm{d}\tau} + (1-\phi)^3 k_1 H^2 AY - (1-\phi)k_2 HXY + (1-\phi)^2 k_3 HAX - 2k_4 X^2 \tag{14.4}$$

$$\frac{\mathrm{d}Y}{\mathrm{d}\tau} = -\frac{Y}{1-\phi}\frac{\mathrm{d}\phi}{\mathrm{d}\tau} - (1-\phi)^3 k_1 H^2 AY - (1-\phi)k_2 HXY + \frac{1}{2} f(1-\phi)k_5 BZ \tag{14.5}$$

$$\frac{\mathrm{d}Z}{\mathrm{d}\tau} = \frac{Z}{\phi}\frac{\mathrm{d}\phi}{\mathrm{d}\tau} + 2(1-\phi)^2 k_3 HAX - (1-\phi)k_5 BZ \tag{14.6}$$

The first term on the right side of each equation represents the inflow and outflow of the solution. To solve this problem, we require an expression for ϕ, which is determined by the balance between the osmotic pressure and viscoelastic properties of the BZ gel. If the osmotic pressure depends on Z and the volume change because if the osmotic pressure change is appropriately faster than the concentration change, then using a proper function Φ, we obtain $\phi = \Phi(Z)$. Equations (14.4)–(14.6) and $\phi = \Phi(Z)$ describe the elementary processes of the chemical reaction in the BZ gel. Following the analysis of Oregonator, we adopt the approximation $\mathrm{d}Y/\mathrm{d}\tau = 0$. In addition, we assume that the effect of volume changes on the concentration is small and adopt the approximation that $\mathrm{d}\phi/\mathrm{d}\tau = 0$. Dimensionless variables are defined as follows:

$$X_0 = \frac{k_3 H A}{2k_4}, \quad Z_0 = \frac{(k_3 H A)^2}{k_4 k_5 B}, \quad \tau_0 = \frac{1}{k_3 H A}$$

$$u = \frac{X}{X_0}, \quad v = \frac{Z}{Z_0}, \quad t = \frac{\tau}{\tau_0}$$

Equations (14.4)–(14.6) then become

$$\frac{\mathrm{d}u}{\mathrm{d}t} = (1-\phi)^2 u - u^2 - fv(1-\phi)\frac{u - q(1-\phi)^2}{u + q(1-\phi)^2} \tag{14.7}$$

$$\frac{\mathrm{d}v}{\mathrm{d}t} = \epsilon\left[(1-\phi)^2 u - (1-\phi)v\right] \tag{14.8}$$

where

$$\epsilon = \frac{k_5 B}{k_3 H A}, \quad q = \frac{2k_1 k_4}{k_2 k_3}$$

Figure 14.5 shows the results of numerical simulations using this model. Parameters u and v oscillate with a constant period after the initial relaxation behavior. As Z corresponds to v, the volume oscillation of the BZ gel follows v. Because the shape of the limit cycle depends on the parameters of the model, the oscillation is controlled by varying the concentration of the chemicals, reaction rate constant, type of catalyst, and amount of gel.

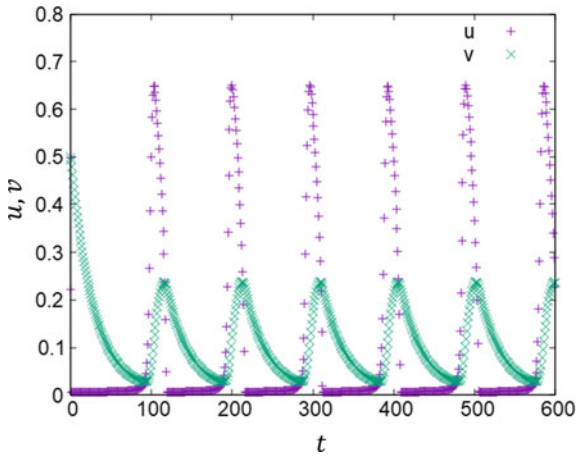

Fig. 14.5 Time series of u and v obtained using a numerical simulation. The parameters are $f = 1, q = 0.008, \epsilon = 0.04$, and $\phi = 0.1$, initial condition is $(u, v) = (0.5, 0.5)$, and time increment is $\Delta t = 1$

14.1.6 Deformation of Belousov–Zhabotinsky Gels

BZ gel is a distinctive material that generates spontaneous motion; however, the displacement of the gel in the longitudinal direction during swelling and contraction is very small (several tens of micrometers), and further research is required to develop it into actuators and mechanical systems. Herein, we introduce a method for inducing bending motion in BZ gels.

Maeda et al. (2007) designed a BZ gel actuator that generates a periodic bending motion by creating a composition gradient inside the BZ gel (Fig. 14.6). Typically, when hydrogels are thermally polymerized, the monomer solution is sealed in a mold and polymerized in a thermostatic bath to maintain a constant temperature in the mold. Maeda et al. sandwiched a monomer solution of a BZ gel between hydrophilic glass and hydrophobic Teflon. BZ gel was prepared as follows: a mixture of *N*-isopropylacrylamide (NIPAAm), a ruthenium complex monomer as the metal catalyst for the BZ reaction, 2-acrylamido-2-methylpropane sulfonic acid (AMPS), *N*,*N*′-methylenebis(acrylamide) (MBAA) as the cross-linker, and a monomer solution consisting of 2,2′-azobis(isobutyronitrile) (AIBN) as the initiator was prepared and purged with nitrogen gas. The prepared monomer solution was injected between a glass and Teflon plate (Fig. 14.6). The solution was then polymerized at 60 °C for 18 h. After gelation, the gel membranes were dialyzed to remove unreacted monomers.

When the BZ gel membranes were subjected to Ru(II) (reduced state) and Ru(III) (oxidized state), the radius of curvature, *R*, of the BZ gel membrane changed. In this experiment, an oxidizing agent was added to the solution to oxidize the BZ gel (Ru(III)). In the thermal equilibrium state, a clear change in *R* was observed. Therefore, we expected that the BZ gel would undergo bending oscillations when the BZ reaction was induced in the gel. One edge of the BZ gel membrane was then physically fixed to the substrate. Chemical waves were generated from one edge of the BZ gel membrane, and the *R* value of the BZ gel increased as the oxidized portion increased. With the disappearance of the oxidized portion, the *R* value of the BZ gel

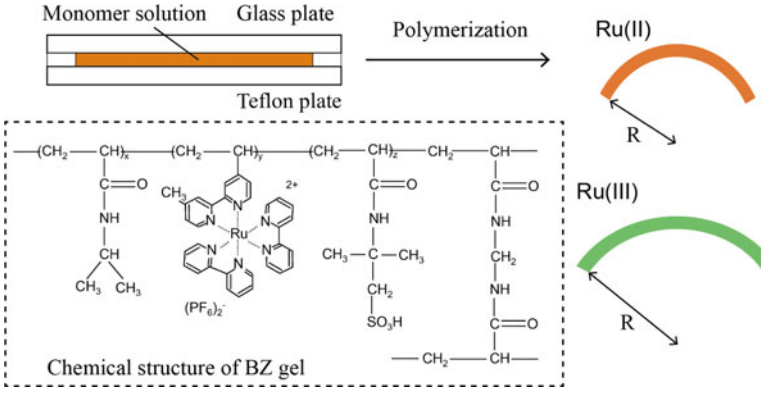

Fig. 14.6 Gradient structure of BZ gels

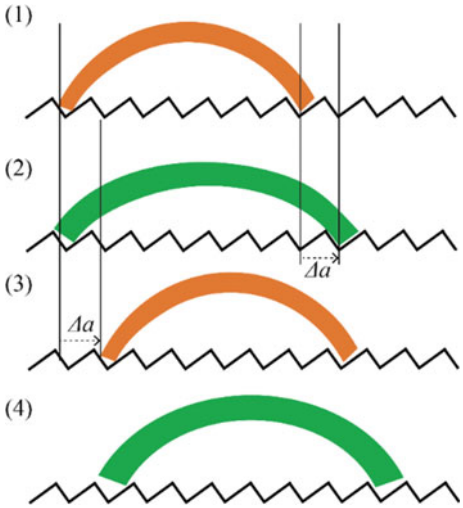

Fig. 14.7 Self-walking gel. Outer solution: 62.5 mM malonic acid, 84 mM sodium bromate, 0.894 M nitric acid

membrane returned to its original state. It was visually confirmed that the bending behavior was synchronized with the chemical wave period of the BZ reaction. A large deformation of the gel, which could not be achieved with conventional self-oscillating gels, was realized. Locomotion of the BZ gel membrane in a single direction has also been realized (Maeda et al. 2007).

Maeda et al. prepared a floor surface with structural asymmetry resembling a microsized sawtooth and placed a bent BZ gel membrane on it (Fig. 14.7). When the BZ gel was oxidized (Ru(III)), it stretched, and the front edge slid forward on the ratchet floor. The back end of the BZ gel did not move backwards. When the BZ gel was transformed to the reduced state (Ru(II)), it bent and its back end slid forward on the ratchet floor. Processes (1) and (2), as shown in Fig. 14.7, were repeated. The BZ gel could move forward by Δa. One cycle of the BZ reaction lasted approximately 112 s, which is very slow forward motion. This gel could potentially function as a new type of artificial muscle, driven only by chemical reactions.

14.1.7 Peristaltic Motion of Belousov–Zhabotinsky Gels

We expect BZ gels to deform if they respond quickly to changes during the chemical oscillation of the BZ reaction. The responsiveness of the BZ gels was improved by synthesizing porous BZ gels. As a result, we directly observed, for the first time, the propagation of local swelling regions (peristaltic motion) in BZ gels (Maeda et al. 2008) (Fig. 14.8). In addition, we placed a cylindrical gel on the BZ gel membrane

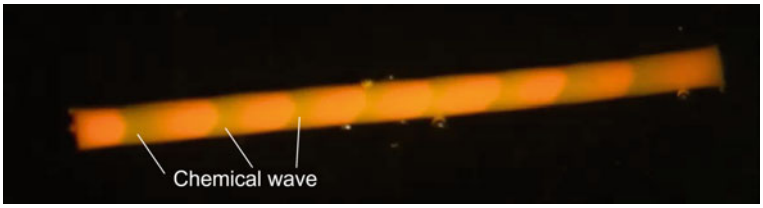

Fig. 14.8 Peristaltic motion of a BZ gel

and successfully transported it in one direction using peristaltic motion (Maeda et al. 2008).

A recipe for a BZ gel that produces peristaltic motion is as follows: BZ gels were synthesized by adding 0.4256 g of NIPAAm, 6 mg of MBAA (cross-linker), 53 mg of ruthenium(4-vinyl-4-methyl-2,2-bipyridine)bis(2,2-bipyridine) bis(hexafluorophosphate), $[Ru(bpy)_3]^{2+}$), and 6.4 mg of AIBN (initiator) to methanol (1.0 g). In advance, the methanol was purged with nitrogen gas. The solution was then thoroughly stirred. AMPS was then added to pure water (1.0 g) and the solution was stirred well. In advance, pure water was purged with nitrogen gas. The two solutions were then combined and mixed thoroughly, and the resultant mixture was injected into a mold. After the injection, the molds were placed in an oven at 60 °C for 20 h. After polymerization, the gels were washed.

14.1.8 Mathematical Model for the Peristaltic Motion of Belousov–Zhabotinsky Gels

In Sect. 14.1.5, we discuss the model for the case where the concentration in the BZ gel varies uniformly. This model provides a good approximation of real phenomena when the size of the BZ gel is small. However, when the size of the BZ gel is larger than the typical spatial period of the BZ gel pattern, the spatial structure of the chemical concentration must be considered. (In our experimental system, the size limit was approximately a few millimeters.)

Based on the model represented by Eqs. (14.7) and (14.8), we consider the simple case where v, which represents the concentration of the metal catalyst fixed on the gel molecule, does not diffuse, whereas u diffuses according to Fick's law, and its diffusion coefficient D is constant. Parameters u and v become functions of position and time, and the governing equations become as follows:

$$\frac{\partial u}{\partial t} = D\nabla^2 u + (1-\phi)^2 u - u^2 - fv(1-\phi)\frac{u - q(1-\phi)^2}{u + q(1-\phi)^2} \tag{14.9}$$

$$\frac{\partial v}{\partial t} = \epsilon\left[(1-\phi)^2 u - (1-\phi)v\right] \tag{14.10}$$

With the initial and boundary conditions, the problem is uniquely determined and the time evolutions of u and v are obtained. Similar to the Oregonator model with a diffusion term, this model exhibits the Turing instability and generates inhomogeneous patterns. The formed pattern strongly depends on the initial and boundary conditions and is typically a striped pattern that emerges from the boundary and moves with constant velocity in this model. Therefore, an information processing mechanism similar to that proposed for reaction–diffusion systems can be developed for BZ gels (Steinbock et al. 1996). Compared with the BZ reaction system, the BZ gel system has the advantage of enabling easy control of boundary conditions. In addition, the concentration in the BZ gel system can change without the inflow or outflow of the material because the concentration and mechanical force are coupled. By exploiting these characteristics, we can realize an information processing mechanism with a higher degree of freedom than that offered by reaction–diffusion systems. Equations (14.9) and (14.10) are simplified models of a real BZ gel and are not necessarily suitable for the quantitative reproduction of the experimental results. A numerical simulation model that reproduces the dynamics of the gel in greater detail was proposed by Balazs et al., who reported the effects of boundary conditions and the response to mechanical stimuli (Yashin and Balazs 2007; Yashin et al. 2012).

14.1.9 Challenges

Numerical simulation methods have been developed for the theoretical modeling of BZ gels. However, the discussion based on theoretical analysis is still unclear. For practical applications, a more comprehensive understanding of the pattern dependence on the boundary and initial conditions is necessary. Understanding dependence in gel systems would enable us to realize complex arithmetic functions in simpler systems than in normal reaction–diffusion systems. Another important issue is understanding how the pattern changes in response to mechanical stimulation of the BZ gels. When we consider a BZ gel as an oscillator, we can build a coupled oscillator network whose interaction corresponds to the mechanical interaction between BZ gels. In this case, a pattern corresponds to the phase of an oscillator, and the frequency of the pattern of the individual BZ gels corresponds to the natural frequency of the oscillator. Once we understand the relationship between the mechanical stimulus and pattern change, with proper system design, we can develop a BZ gel system with various functions, such as associative memory (Nikonov 2015), which is proposed in coupled oscillator systems. In practice, when we develop a device using BZ gel, corrosion is a difficult problem to overcome because the BZ reaction typically requires a strong acid. Thus, the development of a method to keep the BZ reaction solution approximately neutral during the reaction is important.

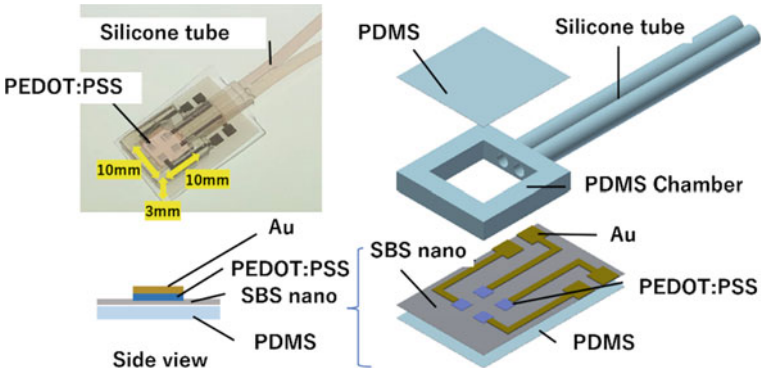

Fig. 14.9 Cell tactile sensor with organic ultraflexible printed electrodes. Reprinted from Shimizu et al. (2020) Copyright 2021 IEEE

14.2 Biological Information Processing

14.2.1 Technology for Autonomous Soft Robots that Process Information Using Biomaterials

Biomaterials are useful for the automation of soft robots. This is because of the ability of biomaterials to process information owing to physiological phenomena. To use biomaterials as robot components, information processing between biomaterials and engineering devices, as well as between biomaterials and engineering devices, must be artificially manipulated. It was shown that a robot can be controlled by neurons for information processing between biomaterials and engineering devices by remotely connecting cultured neurons to a wheeled robot (Warwick et al. 2010a, b). A self-repairable cell tactile sensor was developed using cells as soft tactile sensors, and information was extracted from the cells with organic ultraflexible printed electrodes (Shimizu et al. 2020) (Fig. 14.9). However, information processing between biomaterials remains a relatively new research area. Autonomous soft robots that process information using biomaterials will be feasible if a mechanism that directly uses the brain as a biocomputer and transmits information from the brain to other biomaterials is clarified. In the following section, we introduce the construction of this technology.

14.2.2 Information Processing Between Biomaterials

The fabrication of actuators and sensors using biomaterials has been previously described. In biomaterials, spontaneous biological information processing results in the self-modification of biomaterial structure and function. A robot with a self-modifying function can be realized if assembled using such biomaterials. In contrast,

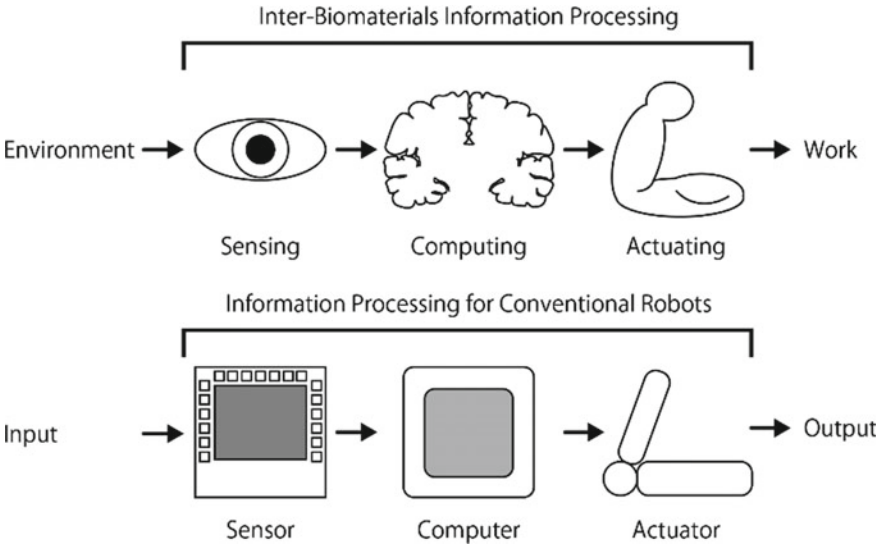

Fig. 14.10 Comparing information processing between biomaterials with that of conventional robots

control devices consisting of biomaterials were not mentioned in the previous sections. Biological control devices are essential for implementing autonomous control and self-modifying functions. This section introduces biomaterials that can be used as living computing units.

To implement the ability to self-modify autonomous work in response to changes in the environment, methods to functionally connect biomaterials are required. The functional connection could result in "the inter-biomaterials information processing" (Fig. 14.10), wherein the environmental information input from the sensor is transmitted to the control device, which then self-modifies the autonomous operation of the actuator through information processing from the sensor input. However, the information processing between biomaterials must be controlled to realize this information processing. Therefore, to build a robot with a self-modifying function, both intra-biomaterial information processing and information processing occurring between different biomaterials must be understood. This section describes the methods used to connect biomaterials and the problems related to the connection.

14.2.3 Living Regulators

Devices that can compute complex calculations similar to humans are ideal regulation devices for developing robots that respond flexibly to changes in environments similar to humans, create better methods of working, and work more safely. There have been studies into connecting the human central nervous system to a robot, such as

brain-machine interfaces; however, these are not robots. Thus, neurons differentiated from human pluripotent stem cells may serve as alternatives to the human central nervous system. These efforts have already been reported, and a few results have been published by (Warwick et al. 2010a, b). However, complex functions have yet to be reproduced using only cultured neurons in circuits. Furthermore, methods to intentionally control the structure of neural circuits using microfluidics have been reported by Gladkov et al. (2017). Neural circuits are limited to a simple architecture and cannot reproduce the complex hierarchical structure of the neural circuit within the brain. This is because the brain is composed of not only neurons but also glial cells and many other types of cells, and all such cell populations are crucial for realizing higher-order brain functions. Therefore, the development of a biomaterial to replace the human brain requires reconstruction of the brains complex hierarchical structure as well as reproduction of the cell population.

Cerebral brain organoids are easy-to-use biomaterials that satisfy these requirements owing to their ability to reproduce the complex hierarchical structure and cell populations by recapitulating the early developmental process of the brain (Lancaster et al. 2013). In addition, a method for differentiating subdomain-specific brain organoids has been developed, which enables the use of living regulators with specific regulatory functions, such as motion regulation (Birey et al. 2017). In contrast, the developmental process of brain organoids cannot completely recapitulate the robust developmental process of the brain. Therefore, the reproducibility of the brain organoids hierarchical structures is extremely low. However, there is a size limitation, wherein the size of brain organoids' that can be produced using a typical protocol is limited to 3–5 mm. Furthermore, although the human neocortex has a multilayered structure comprising of six layers, the formation of the neocortex of brain organoids is limited to a single layer (Lancaster et al. 2013). The computational power of brain organoids and their capability to control robots are currently being investigated. In addition, because brain organoids can reproduce the morphology of the neocortex, which is responsible for the computational function of the cerebrum, and can also include cells expressing genes related to the hippocampus that can play a vital role in memory, they may be used as a powerful biomaterial for constructing robots with autonomous functions.

14.2.4 How to Assemble Robots with Living Regulators

To assemble robots that consist of biomaterials, the materials must be functionally connected. For conventional robots, the roles of various robotic parts were clearly defined and their performance was fully reproducible. In addition, robotic parts were produced to connect with the other parts. Therefore, the method for assembling a conventional robot was determined simultaneously with designing the robotic parts. However, owing to the self-modifying function of biomaterials, their performance, shape, and size change with time; thus, designing an interface for connecting parts is a challenge. Biological information processing between biomaterials results in

autonomous modifications in the function, shape, and size of biomaterials, which may or may not be functionally connected. Therefore, to assemble a living soft robot by combining biomaterials, we must understand how to connect the biomaterials and regulate biological information processing between them.

The simplest method for connecting biomaterials involves co-culturing two or more different engineered tissues in a single culture vessel, which results in a connection through the culture medium (Fig. 14.11a). Co-culturing engineered tissues with two or more culture vessels connected through transportation ducts to perfuse the culture medium between the two is an advanced method (Fig. 14.11b). A typical example is an organ chip wherein cells and engineered tissues are placed in compartments on a small chip consisting of PDMS, and subsequently, different cells and tissues are connected by perfusing the culture medium into a microchannel (Wagner et al. 2013).

Another method involves directly adhering biomaterials with or without biological adhesive materials, such as Matrigel or fibrin (Fig. 14.11c). An assembroid, established by Pasca et al., is a cerebral brain organoid consisting of dorsal and ventral forebrain spheroids that is constructed by direct contact and fusion (Birey et al. 2017). Using the assembroid, a functional connection between the subdomains of the forebrain through a neural circuit was reproduced.

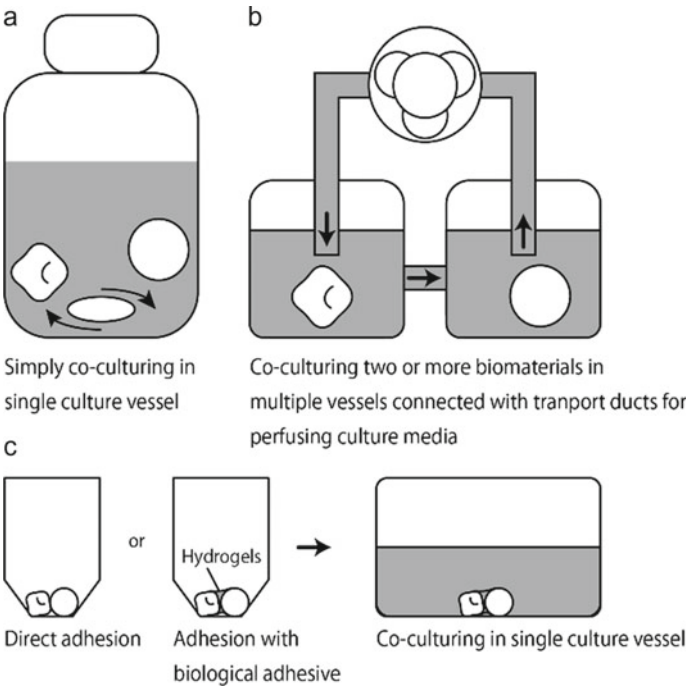

Fig. 14.11 Methods for connecting biomaterials

If biomaterials include cells in nerve tissues and transport ducts, such as blood and lymphatic vessels, the co-culture of biomaterials using the above methods can induce a connection between the biomaterials through neurons and transport ducts (Uzel et al. 2016; Giandomenico et al. 2019; Takebe et al. 2013). These connections can be used as information transmission pathways, as explained in the next section.

14.2.5 Information Transmission Pathways Between Biomaterials

The tissues and organs in our body are comprised of cells and extracellular matrices (ECMs), such as collagen, fibronectin, and laminin, which are adhered to by adhesive proteins. There are two types of adhesion, cell–cell and cell-ECM adhesion, which are crucial for information transmission pathways between intra- and extracellular environments, respectively (Alberts et al. 2014). Because changes in cell adhesion induced by connecting biomaterials affect the biological functions of each biomaterial, it is important to regulate cell adhesion to achieve a functional connection between the biomaterials.

The cells in biomaterials secrete various humoral factors, such as growth factors, into the culture medium. Through the culture medium they affect the biological functions of co-cultured biomaterials; therefore, they can act as messengers between biomaterials. However, to receive information from the biomaterial, another must express a receptor protein corresponding to the humoral factor. The input signal is the humoral factor, intensity of the signal indicates its concentration, and sensitivity is dependent on the expression level of the receptor protein. The outputs obtained from this input include changes in cell proliferation, cell differentiation, morphology, and other biological functions. In an animal body, humoral factors are transported via blood flow through blood vessels; therefore, the latter are also used as information transmission pathways between biomaterials. Similarly, microfluidic devices with microchannels can be used to design information transmission pathways.

However, the biological functions of tissues and organs are regulated by biological information processing through neural circuits. For example, muscle contraction is induced by receiving information transmitted along motor neurons elongated from the motor cortex of the cerebral brain through the spinal cord to the muscle. In contrast, the degree of muscle contraction is monitored by the elongation of sensory neurons in the muscle spindle, and information is transmitted to the brain through the spinal cord. Thus, the position and locomotion of the body are regulated by biological information processing through the neurons. In this context, to regulate the locomotion of robots consisting of living actuators, sensors, and regulators, neurons can be regarded as potent information transmission pathways.

14.2.6 Challenges: Programming Robots with Living Regulators

Animal motion is actively or passively regulated by the brain. The former is a deliberate motion, while the latter is an involuntary exercise. Deliberate motions include locomotion and a change in posture, whereas involuntary motions include breathing, heartbeat, and intestinal peristalsis. The motions are the outputs of biological information processing in the body. Therefore, when implementing autonomous motions for robots using biomaterials, the control type used for designing the work must be considered.

For instance, active control systems must be implemented to develop robots that autonomously collect only red and round balls. In contrast, designing a combination of biomaterials with passive control systems is more suitable for creating robots that autonomously adjust motions in response to changes in ambient temperature. As biomaterials originally possess environmental adaptability, they can be useful for developing robots with passive control systems. Wheeled mobile robots with neural circuits cultured on microelectrode arrays (MEAs), which can autonomously avoid obstacles, can be used to create passive control systems (Warwick et al. 2010a, b). However, developing robots with active control systems using living regulators, such as nerve cells and brain organoids, remains a challenge. Therefore, robots must be educated to implement autonomous and active motions.

The next aspect to consider is the manner in which soft robots are educated using living controllers. Interfaces for education are required to educate living control devices, where sensors for obtaining information regarding objects and environments can be used for education interfaces. In addition, for biological information processing, the devices must have bidirectional communication, which was reported in the case of wheeled mobile robots with nerve cells cultured on an MEA as a control device and an ultrasonic sensor (Warwick et al. 2010a, b). Through bidirectional communication, the robot learned to avoid obstacles at a high rate. Moreover, during the learning process, self-organization of the neural circuit on the MEA can be induced, which, if regulated, can facilitate the use of sensors as an interface for programming the active regulation of robotic motion. However, solutions have not yet been established for cases where obstacles move or appear suddenly, or when autonomous functions other than obstacle avoidance must be implemented simultaneously. Thus, living regulators with hierarchical structures that are more complex than nerve cells simply cultured on MEAs may be used to implement multiple and complex autonomous functions for robots.

14.3 Temporal and Spatial Information Processing

14.3.1 Rhythms and Patterns: The Simplest, but Complex Behaviors in Biology

One of the goals of soft robotics is to build robots that are composed of biomaterials. Why do we discard commonly used metals, but opt for biomaterials made from thousands of different materials? This is simply because current robots cannot perform many phenomena that living organisms can. One of the reasons for this primacy of living organisms is the softness of biomaterials. Proteins are typically soft biomolecules, and a one-dimensional string of polymerized amino acids. Many biological functions of organisms are derived from the dynamics of soft molecules. The softness of cells allows for dynamic changes in size, such as mitosis. Softness of tissues is essential for achieving a supple body.

However, the major disadvantage of biomaterials is that they are designed naturally rather than by humans. Because they are not designed to be used by humans, they are an obstacle to our direct replacement as materials for robots. For example, it is difficult to control the behavior of a cell using the control inputs sent by a computer. Furthermore, ensuring the uniformity of the biomaterial characteristics is difficult. In addition, noise in behavior is inevitable because cellular activities generally arise from stochastic biochemical reactions. Despite these disadvantages, biomaterials are attractive materials for soft robots because they can be used by living organisms. It is not unreasonable to expect that phenomena that exist in living organisms will also exist in artificial ones.

In this section, we focus on spatiotemporal biological patterns as representatives of the complex behaviors exhibited by biomaterials. When biomolecules, cells, and individuals interact, a uniform state of time and space is produced. However, the destabilization of this uniform state over time results in rhythms, and destabilization in space produces spatial patterns. Here, we show that instability can transform a crowd of individual, unintelligent, and difficult to control biomaterials into controllable intelligent devices, which can be a new tool that is applicable in the design of soft robots.

Living organisms exhibit several rhythmic phenomena. For example, cells are repeatedly divided into daughter cells. The c.a. 24-h cycle of physiological phenomena is known as the circadian rhythm. Sleep and nyctinastic movement of leaves are examples of circadian rhythms. Although these rhythms are common in all organisms, their molecular mechanisms that produce them are quite different. Therefore, it is necessary to analyze and develop different methods for their control. Mathematical modeling at the abstract level allows us to analyze them in a common framework.

Furthermore, organisms exhibit spontaneous patterns. For instance, the horizontal pattern on the skin of tropical fish is the most common example. The aggregation of small pigment cells that release transmitting substances results in a skin pattern at the macro level, which can be described using a reaction–diffusion model. Furthermore,

the collection of animals and migrating cells can generate a wider variety of patterns than reaction–diffusion patterns. In addition to biological rhythms, some universal models have been proposed, allowing a unified view of the mechanisms involved.

Understanding how biomaterials produce rhythms and patterns is the first step toward controlling some of the more elusive phenomena of life. In this section, we present two types of biological rhythms and two types of pattern formations, together with their control methods and the mathematical background that underlies them.

14.3.2 Genetic Oscillator

The primary role of DNA in cells is to serve as a memory that stores the inherited genetic information. DNA also functions as an on/off switch that temporally controls gene expression (Alberts et al. 2014). Interestingly, some proteins produced through gene expression control the on/off switch for expression of other genes. For example, approximately 20,000 genes in humans form a network that regulates the expression levels of other genes. The most fascinating results in circadian rhythm research in the twentieth century was that the molecular machinery that generated circadian rhythms, that is, the circadian clock, was a gene network (Nobel 2017). In this subsection, we focus on the genetic oscillators.

Circadian rhythms in animals and plants arise from the negative feedback loop of both the transcriptional and translational processes. Transcription is a copying process that generates mRNA using the information contained in the DNA sequence of a gene as the template. On the other hand, translation is the process that occurs on the ribosomes resulting in the production of proteins based on the based sequence of the mRNA. This set of transcriptional and translational processes is referred to as the central dogma of molecular biology. This is considered to be the most fundamental biochemical reaction in life. Some proteins directly or indirectly inhibit gene expression. This closed structure is called the negative feedback loop of transcription and translation. The TTFL is potentially capable of generating rhythms. Suppose that the central dogma process produces abundant proteins that compose the TTFL. Then, gene expression can easily be turned off or repressed by the proteins, eventually resulting in a reduction in the amount of proteins through spontaneous degradation. The decrease in protein levels causes the gene expression to be restored and the quantity of the protein to the original levels to recover. The sequence of reactions repeats within a period of 24-h, that is, it generates circadian rhythms. In insects and vertebrates, including humans, the *per* gene forms a TTFL, whereas the *CCA1*, *frq, and kaiC* genes form a TTFL in plants, red bread mold, and cyanobacteria, respectively (Fig. 14.12a). Importantly, mutations in these genes can alter the oscillation period or abolish the rhythmicity. These discoveries were made at the end of the twentieth century, and the three discoverers of TTFL in fruit flies won the Nobel Prize in 2017 (Nobel 2017).

The Goodwin model is a mathematical model that represents the closed loop of negative feedback regulation (Goodwin 1965; Kurosawa et al. 2002) (Fig. 14.12b).

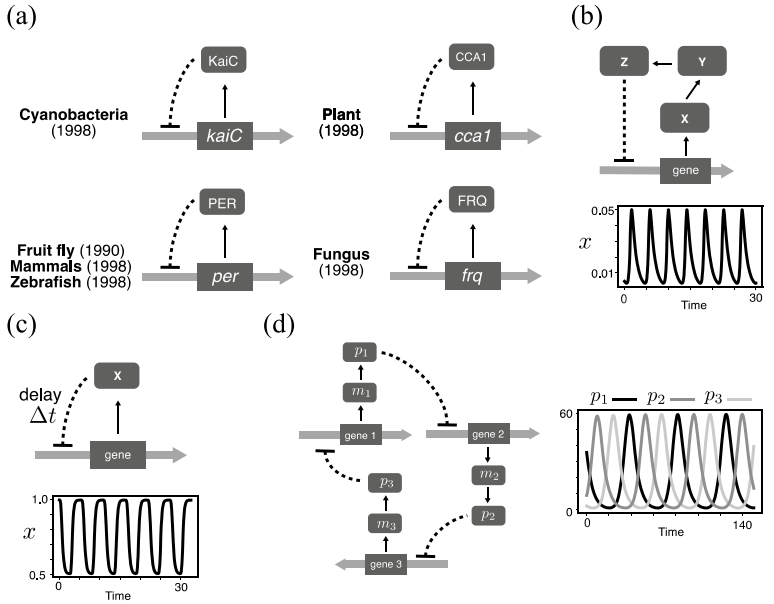

Fig. 14.12 Topology of genetic oscillators **a** The transcriptional and translational negative feedback loops (TTFLs) of clock genes are shared among organisms, however the genes involved are different. **b** Goodwin model describes the dynamics of the amount of mRNA, and nucleic and cytosol proteins in TTFL. The displayed simulation was performed under: $a = d = v = s = 1, u = 10^{-6}, h = 10^{-8}$, and$n = 12$. **c** Goodwin model can be reduced to a one-variable differential equation with delay. The displayed simulation was performed under $k = 1, u = 10^{-6}, \Delta t = 10,$ and $n = 10$. **d** The repressilator is the artificial gene network with a "rock-scissors-paper" relationship. The values of the parameters for the displayed simulation are adopted from Novère 14: $\alpha_0 = 0.2164, \alpha = 216.4, \beta = 0.2,$ and $n = 2$

This model comprises a set of three ordinary differential equations, expressed as follows:

$$\dot{x} = \frac{1}{1 + (z/h)^n} - ax,$$

$$\dot{y} = sx - (d + u)y + vz,$$

$$\dot{z} = uy - vz,$$

where x, y, and$z$ are the variables; $h, a, s, d, u, v,$ and n are the parameters; and the dot hereafter denotes the time derivative, $\frac{\mathrm{d}}{\mathrm{d}t}$. The Goodwin model can generate a self-sustained rhythm and is considered the model for TTFL if the variables x, y, and$z$ represent the amount of mRNA, proteins in the cytoplasm, and proteins in the nucleus, respectively. The production rate of x, $\frac{1}{1+(z/h)^n}$, is a monotonically decreasing function of z, , which corresponds to the autorepression of gene expression by proteins.

Note that the Goodwin model with two variables does not produce a self-sustained rhythm (Kurosawa et al. 2002).

The TTFL in the circadian clock is theoretically identical to the closed-loop control theory. However, the control theory usually intends to stabilize the system with a feedback signal computed based on the differences between the target and current values, leading the system to the desired state. The crucial difference between the control theory and circadian rhythms is whether they desire oscillations or a steady-state, that is, whether the system is unstable or stable. The key point for instability in the biological feedback loop is time delay. In the Goodwin model, transcriptional and translational processes cause time delays to the TTFL. We can provide an example for the TTFL model that explicitly incorporates a time delay as follows:

$$\dot{x}(t) = \frac{1}{1 + (x(t - \Delta t))^n} - kx(t),$$

where $x(t)$ denotes the level of clock proteins at time t and Δt denotes the time delay. The first term on the right-hand side represents auto-negative feedback with a time delay (Fig. 14.12c).

Non-circadian rhythms can be generated by TTFL. In vertebrate embryos, a 2-h oscillation of *Hes7* gene expression is involved in somite formation (Hirata et al. 2002; Bessho et al. 2003). Subsequently, *Hes7* forms a negative feedback loop, similar to the circadian clock. Changing the time delay by slight modulation of the transcriptional system modulates the oscillation period, resulting in an increase in the number of somites (Takashima et al. 2011).

In the field of synthetic biology, the artificial construction of such a genetic oscillator in the cell has been actively pursued. A pioneering work on artificial genetic oscillators is the so-called "repressilator" by Elowitz and Leibler (2000) (Fig. 14.12d). They inserted three genes with rock-paper-scissors relationships into *Escherichia coli*: gene A represses gene B, gene B represses gene C, and gene C represses gene A. The structure of the repressilator can be mathematically modeled as follows:

$$\dot{m}_1 = -m_1 + \frac{\alpha}{1 + p_3^n} + \alpha_0$$

$$\dot{m}_2 = -m_2 + \frac{\alpha}{1 + p_1^n} + \alpha_0$$

$$\dot{m}_3 = -m_3 + \frac{\alpha}{1 + p_2^n} + \alpha_0$$

$$\dot{p}_1 = -\beta(p_1 - m_1)$$

$$\dot{p}_2 = -\beta(p_2 - m_2)$$

$$\dot{p}_3 = -\beta(p_3 - m_3),$$

where m_i, is the amount of mRNA of gene i and p_i is the amount of protein produced from gene i. The actual repressilator implemented in *E. coli* cells showed expression rhythms with a period of several hours; however, it was far from an accurate clock, with a large deviation in periodicity. However, since then, improvements have been made to the genetic oscillator to make it more accurate and controllable (Stricker et al. 2008).

14.3.3 Protein Oscillator

The TTFL has a dogmatic position in the study of circadian rhythms. However, researchers in the field of cyanobacterial circadian rhythm have proposed a mechanism that is very different from that of TTFL. Initially, while studying the transcription-translation loop of KaiC, they observed that KaiC undergoes a molecular modification called phosphorylation and that the amount of phosphorylated KaiC oscillates within approximately 24-h period (Iwasaki et al. 2002). Oscillations in the amount of phosphorylated KaiC have been reported to occur, even under dark conditions (Tomita et al. 2005). This fact came as a shock to cyanobacterial researchers because in cyanobacteria transcription and translation are almost completely abolished in the dark; however, they could still exhibit rhythmicity, suggesting a failure of the TTFL theory. Shortly after this discovery, it was observed that the ratio of phosphorylated KaiC oscillates simply by mixing the three proteins KaiA, KaiB, and KaiC with ATP in a test tube (Nakajima et al. 2005) (Fig. 14.13a). This was the first example of an artificial circadian clock. However, the mechanism by which the protein clock ticks is still under debate. Several mathematical models have been reported, such as the report by Zon et al. (2007). This situation contrasts with the famous model proposed for the chemical oscillator, the BZ reaction, known as the Oregonator (Zhabotinsky 1991).

One of the experimental approaches to understanding the nature of biological rhythms is the perturbation of the system parameters based on bifurcation theory (Strogatz 2019). Bifurcation theory classifies qualitative changes in a system when its parameters change. According to the bifurcation theory, self-sustained oscillations can be classified into two types: the first scenario is the transition from self-sustained oscillations to damped oscillations, called the Hopf bifurcation. The second scenario is the transition from self-sustained oscillations to an excitable system called saddle node on invariant circle (SNIC) bifurcation. In the case of Hopf bifurcation, the rhythm disappears owing to a reduction in amplitude, while in the case of SNIC bifurcation, the rhythm disappears owing to a divergence of the oscillation period to infinity. When the artificial protein oscillator is subjected to a change in the system parameters by lowering the temperature, the rhythm disappears owing to the reduction in amplitude, that is, the Hopf bifurcation causes loss of rhythmicity (Murayama et al. 2017) (Fig. 14.13b, c). As predicted by bifurcation theory, below the bifurcation

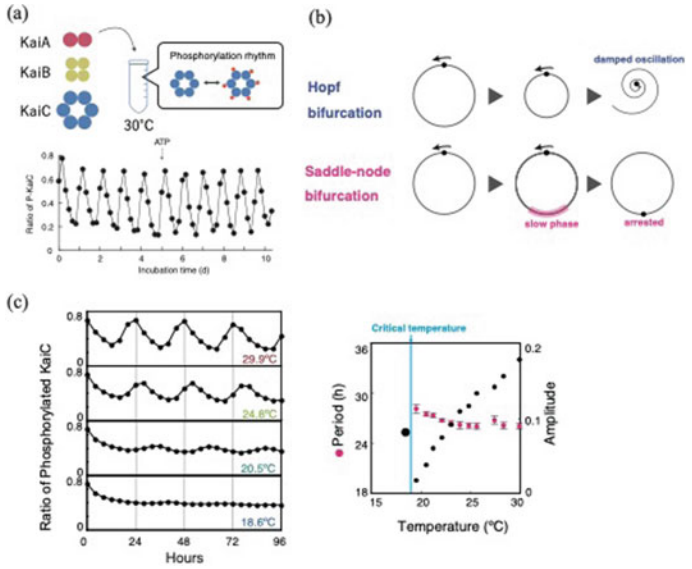

Fig. 14.13 Artificial circadian clock in a test tube. **a** KaiC phosphorylation rhythms can be reconstituted by mixing Kai proteins. **b** The loss of rhythmicity can be classified into typical scenarios based on the bifurcation theory. In the scenario, referred to as the Hopf bifurcation, the amplitude of the oscillations decreases to zero when lowering the temperature and a stable fixed point (closed circle) can be created at the critical temperature. Below the critical temperature, the limit cycle oscillator transforms into a damped oscillator that winds around the fixed point and eventually converges on the fixed point below the critical temperature. However, in the scenario, referred to as SNIC bifurcation, the velocity of angular direction becomes slower at a specific phase, causing a bottleneck. The period of oscillations approaches infinity, and a pair of stable and unstable fixed points (closed and open circles) is created at the critical temperature. Below the critical temperature, the oscillator transforms into an excitable system. **c** Oscillation amplitude and period of the reconstituted KaiC phosphorylation rhythm under different temperature conditions. Reprinted from Murayama et al. (2017), Ito et al. (2007)

temperature, the protein oscillator behaves as a damped oscillator. Temperature cycles with a resonant frequency can recover the oscillation amplitude of a cold-induced damped oscillator, as occurs in mechanical systems.

What is noteworthy about this artificial clock is the fact that the reconstituted KaiC phosphorylation possesses the remarkable property of temperature compensation (Nakajima et al. 2005; Murayama et al. 2017) (Fig. 14.13c). Most biochemical reactions were temperature dependent. In general, the reaction rate doubled when the temperature increased by 10 °C. If the rate constants of all biochemical reactions were involved in the circadian rhythm owing to a temperature rise of 10 °C, then the oscillation period should be halved. However, this was not the case with the circadian rhythm. The period of circadian rhythm in cyanobacteria and other organisms, regardless of the environmental temperature (i.e., winter or summer), was always approximately 24-h (Dunlap et al. 2003). This super-simplified biological clock, which consists of only three proteins, shows temperature compensation.

The KaiC phosphorylation rhythm may be a milestone in the development of a temperature-compensated artificial clock.

14.3.4 Synchronization of the Biological Rhythms

Synchronization involves sharing the same frequency among interacting self-sustained oscillators (Pikovsky et al. 2003). Many biological processes use synchronization. One of the most famous is the synchronization of circadian rhythms with the movement of the sun. The period of our circadian rhythm deviates slightly from 24-h. However, the periodic input of sunlight adjusts the period of the circadian rhythm to a 24-h period (Dunlap et al. 2003). Without this synchronization process, it would be difficult to go to bed on a regular basis. The heart is composed of a population of cardiomyocytes. If the cardiomyocytes do not show synchronized contraction rhythms, the heart would not be able to pump, resulting in arrhythmias (Sakamoto et al. 2021). In addition, in Southeast Asia, thousands of male fireflies are known to swarm around trees and flicker synchronously (Buck and Buck 1966). Note that there are two types of synchronizations: forced synchronization, which affects only one direction, as in the case of the sun and circadian rhythms, and mutual synchronization, which affects each other without a leader, as in the case of fireflies.

We consider the synchronization mechanism using a simple mathematical model. As an example, we consider a circadian rhythm periodically illuminated by the sun. The most important concept, here, is "phase." The trajectory of a self-sustained oscillator in multidimensional state space can be represented by a closed orbit, or called the "limit cycle" in mathematics. The limit cycle is attractive, that is, if the initial state is outside the closed orbit, the system asymptotically approaches the closed orbit. We then assign a quantity, the phase, which increases linearly along the limit cycle. Similarly, we assign values of the phase to the entire state space such that the rule of linear increase on-time holds even when the oscillator is outside the limit cycle. In other words, we consider a "field" of phase (Fig. 14.14a). Considering the dynamics in terms of phase, the self-sustained oscillator can be reduced to the following one-dimensional system:

$$\dot{\theta} = \omega.$$

The two phases of the human circadian rhythm and sun are denoted by θ and Θ, respectively. Assuming that the frequencies of the circadian rhythm and the sun are represented by ω and Ω, respectively, and that the sun affects the progress of the circadian rhythm, θ and Θ will follow the differential equation:

$$\dot{\theta} = \omega + f(\Theta, \theta),$$

where the function f represents the external force exerted by the sun. It is known that when the external force is minimal, by the approximation called averaging, the

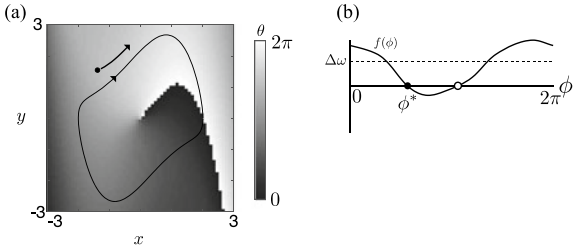

Fig. 14.14 Dynamics of phase. **a** The field of phase, $\theta(x, y)$ for van der pol equation, $\dot{x} = y$, $\dot{y} = \left(1 - x^2\right)y - x$. The black curve represents the limit cycle. Even if the initial state is outside of the limit cycle, the evolution of phase obeys $\dot{\theta} = \omega$. **b** Phase portrait of ϕ. The phase difference spontaneously settles down to the fixed point, which corresponds to synchronization of the sun and circadian rhythm

function f can be described by the phase difference between the sun and the circadian rhythm, $\Theta - \theta$. By applying this, we obtain the following:

$$\dot{\theta} = \omega + f(\Theta - \theta).$$

Note that $\dot{\Theta} = \Omega$. Introducing the phase difference $\phi = \Theta - \theta$, reduces it to a differential equation of ϕ, thus,

$$\dot{\phi} = \dot{\Theta} - \dot{\theta} = \Delta\omega - f(\phi),$$

where $\Delta\omega = \Omega - \omega$. The differential equation in one-variable can be analyzed using the phase portrait, that is, the graph of $\phi - \dot{\phi}$ (Fig. 14.14b). If $\Delta\omega - f(\phi)$ intersects with the abscissa $\dot{\phi} = 0$, then the state of the system moves toward a fixed point $\dot{\phi} = 0$ regardless of the initial phase difference. This is a synchronous state. Moreover, if the difference between the maximum and minimum values of $f(\phi)$ is sufficiently large, synchronization can be achieved for a wide range of $\Delta\omega$.

From the above discussion, we can observe that synchronization is universal for systems with a limit cycle. In other words, synchronization is a feature embodied in a self-sustained oscillator. Therefore, a special device is not required to achieve synchronization. Synchronization requires only self-sustained oscillators interacting with sufficiently strong coupling (Pikovsky et al. 2003).

Synchronization among many oscillators has attracted the interest of both theoreticians and experimentalists. The coupled phase oscillators can be easily extended to interacting N oscillators as follows:

$$\dot{\theta}_i = \omega_i + \frac{1}{N}\sum_{j=1}^{N} A_{ij} f\left(\theta_j, \theta_i\right),$$

where A_{ij} is the coupling strength between ith and jth oscillators. When the coupling method is uniformly all-to-all and function f can be described as a sinusoid, we can obtain the Kuramoto model as follows:

$$\dot{\theta}_i = \omega_i + \frac{K}{N}\sum_{j=1}^{N}\sin\left(\theta_j - \theta_i\right).$$

The model has been intensively investigated as a toy model of a large set of coupled oscillators because the synchronization-desynchronization transition of the model is analytically tractable (Kuramoto 2012).

Recently, there have been few reports on the control of synchronous phenomena in living organisms. For instance, the oscillator of Kai proteins causes mutual synchronization (Ito et al. 2007). *E. coli* cells that incorporate genetic oscillators can synchronize by releasing substances that diffuse out of cells (Danino et al. 2010). On the contrary, the circadian rhythms of the plant leaves are synchronized. Successive dark stimulations have been reported to desynchronize plant rhythms (Fukuda et al. 2013).

14.3.5 Biological Pattern Formation by Reaction–Diffusion Systems

The formation of an organism from a single fertilized egg has long been studied in developmental biology. Researchers in this field have tackled the question of how unspecialized stem cells know their locations and spontaneously differentiate into specific organ cells depending on their location. The historical concept is that some hypothetical molecules, so-called "morphogens," diffused from a specific location and formed a gradient. The cells were then differentiated based on the concentrations of the morphogens. Several morphogens have been identified in *Drosophila* embryos. However, this morphogen model would be limited to explaining a simple form of organisms, and it would be difficult to apply it to more complex patterns.

One epoch-making discovery is that the periodic skin pattern of fish can be regarded as a Turing pattern (Kondo and Asai 1995; Kondo and Miura 2010). In his original paper, Turing stated that a system consisting of a hypothetical pair of interacting molecules, referred to as a reaction–diffusion system, could generate periodic patterns (Turing 1990). A reaction–diffusion system could produce spot, stripe, or maze patterns, which fully explained most fish skin patterns. Since this discovery, reaction–diffusion systems have been identified in other biological systems, such as equally spaced patterns of hair follicle cells, teeth and lung branching, and skeletal patterns of limbs. Moreover, interacting pairs of biomolecules involved in these patterns have been identified (Kondo and Miura 2010).

Several attempts to construct artificial reaction–diffusion systems using cells have been reported. For example, an *E. coli* population that releases two artificial diffusible molecules interacts with each other and generates a spot pattern (Karig et al. 2018).

Another group reported a reaction–diffusion system with genetically modulated mammalian cells releasing two proteins, Nodal and Lefty, which are commonly utilized in development (Sekine et al. 2018). However, they have not yet succeeded in creating a stable pattern similar to that of a fish.

14.3.6 Biological Pattern Formations by Active Matters

Other than reaction–diffusion systems, some patterns can be generated by self-propelled elements, as observed in nonliving things, such as colloids and cytoskeletons, and in living things, such as biofilms of motile bacteria, flocks of birds, schools of fish, and crowds of humans (Vicsek and Zafeiris 2012). Why do randomly moving particles collectively generate patterns without knowing their positions in the entire structure? The research field of active matter physics focuses on the mechanisms of such pattern formations. Active matter refers to systems composed of elements that are self-propelled by energy dissipation. The goal of active matter physics is to obtain the universal laws underlying collective pattern formation.

The theory of active matter physics suggests that no matter how complex a collective motion is, a small number of simple rules it. The Vicsek model is a candidate-unified description of the collective motion of self-propelled particles (Vicsek et al. 1995) and can be described as a set of two difference equations as follows:

$$\boldsymbol{x}_i(t+1) = \boldsymbol{x}_i(t) + v_0\left(\boldsymbol{e}_x \cos\theta_i + \boldsymbol{e}_y \sin\theta_i\right)\Delta t,$$

$$\theta_i(t+1) = \langle\theta(t)\rangle_r + \eta_i \xi,$$

where $\boldsymbol{x}_i$ and θ_i denote the position and direction of the velocity of the particle i;$\langle\theta(t)\rangle_r$ is the average of the velocities of particles within a given distance r; η denotes the noise intensity; ξ denotes a random variable uniformly distributed in $[-\pi, \pi]$. The Vicsek model predicts that only short-range alignment interactions are required to form a long-range ordered phase with long-range correlation, as occurs in many collective motions. The model has two control parameters: the density of the particles and the amplitude of the noise η_i. The ordered pattern appears under conditions of higher density and lower noise (Fig. 14.15a). Vicsek et al. (1995) initiated theoretical studies on active matter and introduced many other theoretical works. Thus, experimental realizations based on these theories are gaining more attention.

Experimental studies on the collective behavior of animals have been performed using non-animal models or animal models. A typical approach for non-model animals is to record the trajectories of individual animals by attaching small GPS devices to their bodies. Nagy et al. obtained tracked logs of homing pigeons flying in flocks of up to 10 individuals using lightweight GPS devices, and analyzed their correlations in velocity (Nagy et al. 2010). This report showed that most flights produced a

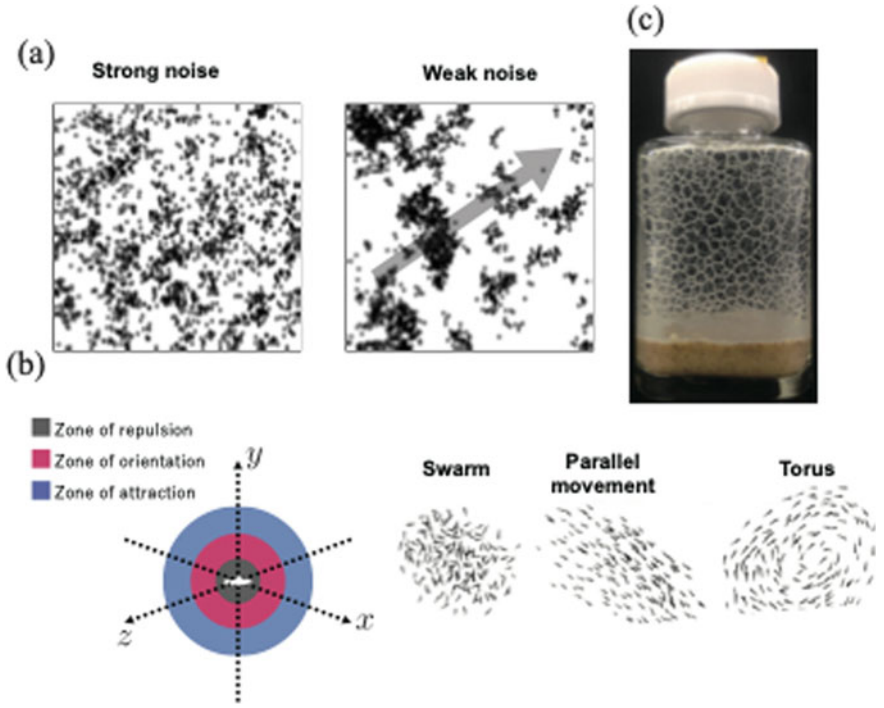

Fig. 14.15 Pattern formations by active matters. **a** Pattern formation by Vicsek model. When noise intensity is strong, the individual particles move in all directions. For weak noise, the particles spontaneously form some clusters and move to the unique direction. **b** Couzin's model for schooling fish. The model assumes three interaction zones centered around each individual fish. The innermost sphere is the zone of repulsion; if other individuals enter this zone, the individual moves away from them in the opposite direction. The middle area is the zone of orientation; the individual aligns with the mates in this zone. Finally, the outermost area is the zone of attraction; the individual continually attempts to go toward the averaged positions of individuals within this attractive zone. This model shows swarm, parallel movement, and torus patterns. **c** Dynamical network of collective nematode on the lateral surface of the glass bottle. Reprinted from Sugi et al. (2019) and Couzin et al. (2002)

robust hierarchical network in flocks containing leader–follower relationships; individuals occupying positions near the front of the flock tend to play leadership roles, which are determined by individual navigational performance. Couzin et al. proposed a model for the school of fish (Couzin et al. 2002). This model, with different parameter values, reproduced some behavioral patterns such as swarm, torus, and parallel movements (Fig. 14.15b).

Regarding the collective behavior of humans, the social force model introduced by Helbing and Molnar described the emergent pattern in human crowds (Helbing and Molnár 1995). In this model, each pedestrian moved according to two forces: the driving force toward a destination and repulsive "social" force from other pedestrians and walls. This social force model allowed to simulate crowd movements such as two pedestrian streams in opposite directions in a corridor and crowds exiting a metro

station. Control methods for human movement have been proposed based on this model in the fields of traffic engineering and social psychology.

The difficulty in reproducing the collective behavior of animals in the laboratory has hampered experimental verification. The authors constructed dynamic pattern formations using the nematode *Caenorhabditis elegans* (Sugi et al. 2019) (Fig. 14.15c). The pattern of insects can occur on a Petri dish, which allows us to change environmental parameters, such as temperature or humidity. Moreover, the movement of these model organisms can be controlled by light using optogenetics. The details are described in the cutting-edge column "*C. elegans.*"

14.3.7 Introductory Books and Articles on Biological Rhythms and Patterns

First, we introduce books on the theory described in this section. A self-sustained oscillator is the topic of a field in applied mathematics called nonlinear dynamics. Strogatz (2019) provided a readable introduction to nonlinear dynamics together with many practical examples. Winfree (2001), who pioneered the phase model, is classic not only for synchronization but also for the theory of biological rhythms. Pikovsky et al. (2003) presented a wide range of experiments and theories on synchronization. Phillips et al. (2012) devoted an entire chapter to reaction–diffusion systems in biological systems. Pismen (2021) described theories on active matter, together with many biological (and non-biological) examples.

On the experimental side, Johnson and Rust (2021) is the most recent book on cyanobacterial circadian rhythms. Dunlap et al. (2003) is a slightly old textbook, but it is good to grab the concepts appearing in research on circadian rhythms. An article by the Nobel Foundation describing the works by Nobel laureates in 2016 and around (Nobel 2017), is also a good and short introduction to overview the history of circadian research. The plain textbook on synthetic biology is from Kuldell et al. (2015). This textbook was written for non-biologists and contained many practical protocols. Some review articles are good at providing a glimpse of the latest developments in synthetic genetic oscillators, for example, Li and Yang (2018).

14.3.8 Conclusions and Challenges for Artificial Biological Rhythms and Patterns

In this section, we introduce some biological rhythms, patterns, and their theoretical background. However, there are still many problems that must be solved to incorporate them into a soft robot. The first is the existence of intrinsic noise, which is peculiar to living organisms. Biochemical reactions, such as gene expression, show

noisy behaviors owing to fluctuations in the small number of molecules (Elowitz et al. 2002). In addition, cells and organs are highly time-varying systems compared to mechanical systems, that is, the responses to inputs are not always identical but depend on unknown and uncontrollable internal variables. Although biological rhythms and patterns are relatively reproducible phenomena, it is difficult to control them in the same manner as conventional robots.

There are three approaches to address these inevitable problems. First, to standardize biological components, as taught by the engineering tradition. Second, to develop "soft" control methods. Rhythm generation and pattern formation are qualitative changes, as noted above. Qualitative control is possible even if quantitative control is difficult. Organisms often seem to provide quantitative control and settle for qualitative control. Convincingly, we refer to this qualitative approach as "soft" control. In control engineering, robust control has been proposed, which considers the uncertain variability of the system (Dullerud and Paganini 2000). This policy is close to soft control and should be strongly promoted to control biomaterials and living organisms. The last approach is to operate the organism as a soft robot. The reservoir computation described in Chap. 15, which uses the object itself as a computational resource, is similar to this spirit. It is necessary to consider how to integrate living things, artificial objects, and the interface between them.

We believe that these approaches can provide insights on the topics pursued by biologists. Soft robotics should provide tools to solve complex biological tissues, such as biological clocks and morphogenesis, and could revolutionize biology.

Exercises

- (1-1) Perform a numerical simulation of the model represented by Eqs. (14.7) and (14.8). Draw nullclines in the (u, v) plane, and plot the trajectory obtained by numerical integration at regular time intervals. Change each parameter and observe how the behavior changes.
- (1-2) Plot the $\chi - \phi$ graph from Eq. (14.2) with $\frac{N_c v_s}{N_A V_0} = 0.001$ and $\phi_0 = 0.1$. Confirm that the behavior changes when χ is approximately 0.5.
- (2-1) Consider the problems regarding co-culturing different biomaterials in single culture vessels.
- (2-2) Describe the three types of methods used for connecting the biomaterials.
- (2-3) Discuss differences in two dimensionally cultured neurons and cerebral brain organoids.
- (2-4) Classify motion regulations mentioned below into active or passive regulations.

  A: Heartbeat
  B: Locomotion
  C: Bowel Peristalsis
  D: Typing Keyboard

- (3-1) Simulate the Goodwin model with the same parameters as those in Fig. 14.12c. Find the integer value of n_c at which the self-sustained oscillation is nullified. What types of bifurcation occur?
- (3-2) Suppose that two persons, A and B, listen to each other's clapping and attempt to clap synchronously. A and B clap with a period of 1 s normally, that is, when they do not care about the other person's sounds. However, they tuned the time of the next clap based on the previous time difference of their clapping. Let the times of the nth clap of A and B be a_n and b_n, respectively. We assume that the following difference equations hold:

$$a_{n+1} - a_n = 1 + k \sin 2\pi (b_n - a_n),$$

$$b_{n+1} - b_n = 1 + k \sin 2\pi (a_n - b_n).$$

- Let $x_n = a_n - b_n$ be the time difference of the guy's nth clapping. By subtracting the above difference equations, show the following difference equation:

$$x_{n+1} = x_n - k \sin 2\pi x_n.$$

- For a small x_n, one can linearize the sinusoidal function in the above equation, that is, $\sin 2\pi x_n \sim 2\pi x_n$. Find the general term of x_n based on the linearized difference equation. For the range of k, the clapping of A and B synchronizes, that is $\lim_{n\to\infty} x_n \to 0$.
- Numerically, calculate the evolution of x_n based on $x_{n+1} = x_n - k \sin 2\pi x_n$ and then check the range of k for synchronization. Confirm that the range is identical to that of Exercise (3–2)b.
- Observe the chaotic behavior of x_n in simulation when k is large enough.
- (3-3) Implement the Vicsek model by visualizing simulations (e.g., processing). It was verified that the pattern changed with the density of the particles, as shown in Fig. 14.15a.
- (3-4) The chemical oscillator introduced in Sect. 14.2 and biological clocks in this section are self-sustained oscillators. Therefore, how are they different? What advantages and disadvantages do they bring to the construction of soft robots?

References

Adamatzky A, De Lacy CB, Asai T (2005) Reaction-diffusion computers. Elsevier, New York

Adleman L (1994) Molecular computation of solutions to combinatorial problems. Science 266:1021–1024

Alberts B, Jhonson A, Lewis J, Morgan D, Raff M, Roberts K, Walter P (2014) Molecular biology of the cell, 6th edn. Garland Science, New York

Anish PD, Misra GP, Siegel RA (2002) J Phys Chem A 106(38):8835–8838

Bessho Y, Hirata H, Masamizu Y, Kageyama R (2003) Periodic repression by the bHLH factor Hes7 is an essential mechanism for the somite segmentation clock. Genes Dev 17:1451–1456
Birey F, Andersen J, Makinson CD, Islam S, Wei W, Huber N, Christina Fan H, Cordes Metzler KR, Panagiotakos G, Thom N, O'Rourke NA, Steinmetz LM, Bernstein JA, Hallmayer J, Huguenard JR, Paşca SP (2017) Assembly of functionally integrated human forebrain spheroids. Nature 22:54–59
Buck J, Buck E (1966) Biology of synchronous flashing of fireflies. Nature 211:562–564
Couzin ID, Krause J, James R, Ruxton GD, Franks NR (2002) Collective memory and spatial sorting in animal groups. J Theor Biol 218:1–11
Crook CJ, Smith A, Jones AL, Ryan A (2002) J Phys Chem Phys 4:1367–1369
Dhanarajan AP, Misra GP, Siegel RA (2002) Autonomous chemomechanical oscillations in a hydrogel/enzyme system driven by glucose. J Phys Chem A 106:8835–8838
Danino T, Mondragón-Palomino O, Tsimring L, Hasty JA (2010) Synchronized quorum of genetic clocks. Nature 463:326–330
Dullerud GE, Paganini FA (2000) A course in robust control theory. Texts Appl Math 36:281–307
Dunlap JC, Loros JJ, Decoursey PJ (2003) Chronobiology: biological timekeeping. Sinauer Associates, Massachusetts
Elowitz MB, Leibler SA (2000) Synthetic oscillatory network of transcriptional regulators. Nature 403:335–338
Elowitz MB, Levine AJ, Siggia ED, Swain PS (2002) Stochastic gene expression in a single cell. Science 297:1183–1186
Field RJ, Burger M (1985) Oscillations and traveling waves in chemical systems. John Wiley & Sons, New York
Flory PJ (1953) Principles of polymer chemistry. Cornell University Press, London
Fukuda H, Murase H, Tokuda IT (2013) Controlling circadian rhythms by dark-pulse perturbations in Arabidopsis thaliana. Sci Rep 3:1–7
Giandomenico SL, Mierau SB, Gibbons GM, Wenger LMD, Masullo L, Sit T, Sutcliffe M, Boulanger J, Tripodi M, Derivery E, Paulsen O, Lakatos A, Lancaster MA (2019) Cerebral organoids at the air-liquid interface generate diverse nerve tracts with functional output: Nat Neurosci 22:669–679
Gladkov A, Pigareva Y, Kutyina D, Kolpakov V, Bukatin A, Mukhina I, Kazantsev V, Pimashkin A (2017) Design of cultured neuron networks in vitro with predefined connectivity using asymmetric microfluidic channels. Sci Rep 7:15625
Goodwin BC (1965) Oscillatory behavior in enzymatic control processes. Adv Enzyme Regul 3:425–438
Helbing D, Molnár P (1995) Social force model for pedestrian dynamics. Phys Rev E 51:4282–4286
Hirata H, Yoshiura S, Ohtsuka T, Bessho Y, Harada T, Yoshikawa K, Kageyama R (2002) Oscillatory expression of the bHLH factor Hes1 regulated by a negative feedback loop. Science 298:840–843
Ito H, Kageyama H, Mutsuda M et al (2007) Autonomous synchronization of the circadian KaiC phosphorylation rhythm. Nat Struct Mol Biol 14:1084–1088
Iwasaki H, Nishiwaki T, Kitayama Y et al (2002) KaiA-stimulated KaiC phosphorylation in circadian timing loops in cyanobacteria. Proc Natl Acad Sci USA 99:15788–15793
Johnson CH, Rust MJ (2021) Circadian rhythms in bacteria and microbiomes. Springer, Cham, Switzerland
Karig D et al (2018) Stochastic turing patterns in a synthetic bacterial population. Proc Natl Acad Sci 115:6572–6577
Kondo S, Miura T (2010) Reaction-diffusion model as a framework for understanding biological pattern formation. Science 329:1616–1620
Kondo S, Asai R (1995) A reaction-diffusion wave on the skin of the marine angelfish pomacanthus. Nature 376:765–768
Kontop Y, Nashimova I R, Rambidi N G, and Khokhlov A R (2011) Chemomechanical oscillations in polymer gels: effect of the size of samples. Polym Sci Ser B 53:121–125

Kuldell N, Bernstein R, Ingram K, Hart KM (2015) Biobuilder: synthetic biology in the lab. O'Reilly Media, California
Kuramoto Y (2012) Chemical oscillations, waves, and turbulence. Springer Science and Business Media, Berlin
Kurosawa G, Mochizuki A, Iwasa Y (2002) Comparative study of circadian clock models, in search of processes promoting oscillation. J Theor Biol 216:193–208
Labrot V, Kepper P D, Boissonade J, Szalai I, and Gauffre F (2005) Wave patterns driven by chemomechanical instabilities in responsive gels 109:21476–21480
Lancaster MA, Renner M, Martin C-A, Wenzel D, Bicknell LS, Hurles ME, Homfray T, Penninger JM, Jackson AP, Knoblich JA (2013) Cerebral organoids model human brain development and microcephaly. Nature 501:373–379
Li Z, Yang Q (2018) Systems and synthetic biology approaches in understanding biological oscillators. Quant Biol 6:1–14
Maeda S, Hara Y, Sakai T, Yoshida R, and Hashimoto S (2007) Self-walking gel. Adv Mater 21:3480
Maeda S, Hara Y, Yoshida R, and Hashimoto S (2008) Peristaltic motion of polymer gels. Angew Chem Int Ed 47:6690
Maeda S, Kato T, Otsuka Y, Hosoya N, Matteo C, and Laschi C (2016) Large deformation of self-oscillating polymer gel, Phys Rev E 93:010501(R)
Moore GE (1965) Cramming more components onto integrated circuits. Electronics 114–117
Murayama Y, Kori H, Oshima C et al (2017) Low temperature nullifies the circadian clock in cyanobacteria through Hopf bifurcation. Proc Natl Acad Sci USA 114:5641–5646
Nagy M, Akos Z, Biro D, Vicsek TH (2010) Hierarchical group dynamics in pigeon flocks. Nature 464:890–893
Nikonov DE, Csaba G, Porod W et al. (2015) Coupled-oscillator associative memory array operation for pattern recognition. IEEE J Explor Solid-State Comput Devices Circuits 1:85–93
Nakajima M, Imai K, Ito H et al (2005) Reconstitution of circadian oscillation of cyanobacterial KaiC phosphorylation in vitro. Science 308:414–415
Nakamaru S, Maeda S, Hara Y, and Hashimoto S (2005) Control of autonomous swelling-deswelling behavior for a polymer gel. J Phys Chem B 113:4609–4613
Nobel Prize Outreach AB (2017) Discoveries of molecular mechanisms controlling the circadian rhythm. https://www.nobelprize.org/prizes/medicine/2017/advanced-information/, Accessed 25 Dec 2021
Novère NL (2013) Elowitz2000–Repressilator. BioModels. https://www.ebi.ac.uk/biomodels/BIOMD0000000012/, Accessed 25 Dec 2021
Pojman JA, and Tran-Cong-Miyata Q, Eds. Nonlinear dynamics in polymeric systems. ACS Symp Ser 869
Phillips R, Kondev J, Theriot J, Garcia HG, Orme N (2012) Physical biology of the cell. Garland Science, New York
Pikovsky A, Rosenblum M, Kurths J (2003) Synchronization: a universal concept in nonlinear sciences. Cambridge Univ Press, Cambridge
Pismen L (2021) Active matter within and around us: from self-propelled particles to flocks and living forms. Springer, Cham, Switzerland
Sakamoto K et al (2021) Emergent synchronous beating behavior in spontaneous beating cardiomyocyte clusters. Sci Rep 11:1–2
Sekine R, Shibata T, Ebisuya M (2018) Synthetic mammalian pattern formation driven by differential diffusivity of Nodal and Lefty. Nat Commun 9:5456
Shimizu M, Fujie T, Umedachi T, Shigaki S, Kawashima H, Saito M, Ohashi H, Hosoda K (2020) Self-healing cell tactile sensor fabricated using ultraflexible printed electrodes. In: Proceedings of the 2020 IEEE/RSJ international conference on intelligent robots and systems, pp 8932–8938
Steinbock O, Kettunen P, Showalter K (1996) Chemical wave logic gates. J Phys Chem 100(49):18970–18975
Stricker J et al (2008) A fast, robust, and tunable synthetic gene oscillator. Nature 456:516–519

Strogatz SH (2019) Nonlinear dynamics and chaos: With applications to physics, biology, chemistry, and engineering. CRC Press, Florida
Sugi T, Ito H, Nishimura M, Nagai K H (2019) C. elegans collectively forms dynamical networks. Nat Commun 10:1
Sumino Y, Nagai KH, Shitaka Y et al (2012) Large-scale vortex lattice emerging from collectively moving microtubules. Nature 483:448–452
Takashima Y, Ohtsuka T, González A, Miyachi H, Kageyama R (2011) Intronic delay is essential for oscillatory expression in the segmentation clock. Proc Natl Acad Sci 108:3300–3305
Takebe T, Sekine K, Enomura M, Koike H, Kimura M, Ogaeri T, Zhang R-R, Ueno Y, Zheng Y-W, Koike N, Aoyama S, Adachi Y, Taniguchi H (2013) Vascularized and functional human liver from an iPSC-derived organ bud transplant. Nature 499:481–484
Tomita J, Nakajima M, Kondo T, Iwasaki H (2005) No transcription-translation feedback in circadian rhythm of KaiC phosphorylation. Science 307:251–254
Turing AM (1990) The chemical basis of morphogenesis. Bull Math Biol 52:153–197
Uzel SGM, Platt RJ, Subramanian V, Pearl TM, Rowlands CJ, Chan V, Boyer LA, So PTC, Kamm RD (2016) Microfluidic device for the formation of optically excitable, three-dimensional, compartmentalized motor units. Sci Adv 2:e1501429
Vicsek T, Zafeiris A (2012) Collective motion. Phys Rep 517:71–140
Vicsek T, Czirók A, Ben-Jacob E, Cohen I, Shochet O (1995) Novel type of phase transition in a system of self-driven particles. Phys Rev Lett 75:1226–1229
Wagner I, Materne E-M, Brincker S, Süβbier U, Frädrich C, Busek M, Sonntag F, Sakharov DA, Trushkin EV, Tonevitsky AG, Lauster R, Marx U (2013) A dynamic multi-organ-chip for long-term cultivation and substance testing proven by 3D human liver and skin tissue co-culture: lab on a chip 13:3538–3547
Warwick K, Xydas D, Nasuto SJ, Becerra VM, Hammond MW, Downes JH, Marshall S, Whalley BJ (2010a) Controlling a mobile robot with a biological brain. Def Sci J 60(1):5–14
Warwick K, Xydas D, Nasuto SJ, Becerra VM, Hammond MW, Downes JH, Marshall S, Whallay BJ (2010b) Controlling a mobile robot with a biological brain. Defence Sci J 60(1):5–14
Winfree AT (2001) The geometry of biological time. Springer, New York
Yamaguchi T, Kuhnert L, Nagy-Ungvarai Z, Mueller SC, Hess B (1991) Gel systems for the Belousov-Zhabotinskii reaction 95:5831–5837
Yashin VV, Balazs AC (2007) Theoretical and computational modeling of self-oscillating polymer gels. J Chem Phys 126(124707):1–17
Yashin VV, Kuksenok O, Dayal P, Balazs AC (2012) Mechano-chemical oscillations and waves in reactive gels. Rep Prog Phys 75(066601):1–40
Yoshida R, Ichijo H, Hakuta T, Yamaguchi T (1995) Self-oscillating swelling and deswelling of polymer gels. Macromol Rapid Commun 16:305–310
Yoshida R, Takahashi T, Yamaguchi T, Ichijo H (1996) Self-oscillating gel. J Am Chem Soc 118:5134–5135
Yuan P, Kuksenok O, Gross DE, Balazs AC, Jeffrey SM JS, Nuzzo RG (2013) Soft Matter 9:1231–1243
Zhabotinsky AM (1991) A history of chemical oscillations and waves. Chaos 1:379–386
Zon JS, van Lubensky DK, Altena PRH, ten Wolde PR (2007) An allosteric model of circadian KaiC phosphorylation. Proc Natl Acad Sci 104:7420–7425

Chapter 15
Information Processing Using Soft Body Dynamics

Kohei Nakajima, Hideyuki Sawada, and Nozomi Akashi

Abstract In this chapter, we address how the introduction of softness into robots will enable unprecedented information-processing functionalities. In Sect. 15.1, we show how softening a robot's body activates the control outsourcing to the body. Based on several examples, we provide an overview of the key concept of "embodiment," under which an intelligent system is viewed as a brain–body–environment system. In Sect. 15.2, we present simple examples to introduce how machine learning techniques for soft robots can be used effectively. In Sect. 15.3, building on the contents of the previous sections, we introduce the concept of physical reservoir computing. We delve into the mathematics of the information-processing capabilities brought about by softness, based on the example of a computer with an octopus arm and a soft interface called a soft keyboard.

15.1 Outsourcing Control to a Soft Body: Embodiment Perspectives

15.1.1 The Universal Gripper

Assume you have a drinking glass right in front of you. Normally, you would have no difficulty lifting the glass with your hands. However, even such a seemingly simple control action would be extremely difficult to execute without the characteristic of "softness." Imagine lifting the glass with metal thimbles attached to the tips of your five fingers (Fig. 15.1). You will notice (try it!) that the task becomes increasingly

K. Nakajima (✉)
Graduate School of Information Science and Technology, The University of Tokyo, Tokyo, Japan
e-mail: k-nakajima@isi.imi.i.u-tokyo.ac.jp

H. Sawada
Department of Applied Physics, Faculty of Science and Engineering, Waseda University, Tokyo, Japan

N. Akashi
Graduate School of Informatics, Kyoto University, Kyoto, Japan

K. Suzumori et al. (eds.), *The Science of Soft Robots*, Natural Computing Series,
https://doi.org/10.1007/978-981-19-5174-9_15

Fig. 15.1 It is difficult to lift a drinking glass with metal thimbles attached to the tips of your fingers

difficult. It is now difficult to grasp and lift glass because of the slippery contact surfaces between the metal thimbles and glass. This should make it clear that the human hand makes effective use of softness. In other words, owing to the elastic force or "springiness" of the hand, the surface of the hand deforms to match the shape of the drinking glass as you grip it, and the friction of the skin can be successfully harnessed to lift it.

It is precisely this kind of "softness" that can be used for an effective robot hand. This is the concept behind a "universal gripper" (Fig. 15.2a) (Brown, 2010). The universal gripper has a very simple structure, principally a granular material in a balloon (Fig. 15.2b). The soft balloon-shaped gripper was pressed against an object to be lifted so that it deformed around it. The air was then evacuated from the gripper, which allowed it to successfully lift the object (Fig. 15.2c). This is an application of a property called the "jamming transition of granular material" (Majmudar 2007). A variety of objects, ranging from fragile eggs to heavy metal tools, can be lifted using this technique. Interestingly, although the object may change, the sequence of controls for pressing the gripper against it remains exactly the same. The control system deforms the balloon filled with granular material, which adapts to match the shape of the object to grip it. It is also interesting to note that research shows that the force produced when lifting an object varies depending on its shape (Fig. 15.2d). The phenomenon observed here is sometimes called "morphological computation" because, in a sense, these changes in morphology execute the computations required for control (Pfeifer 2006).

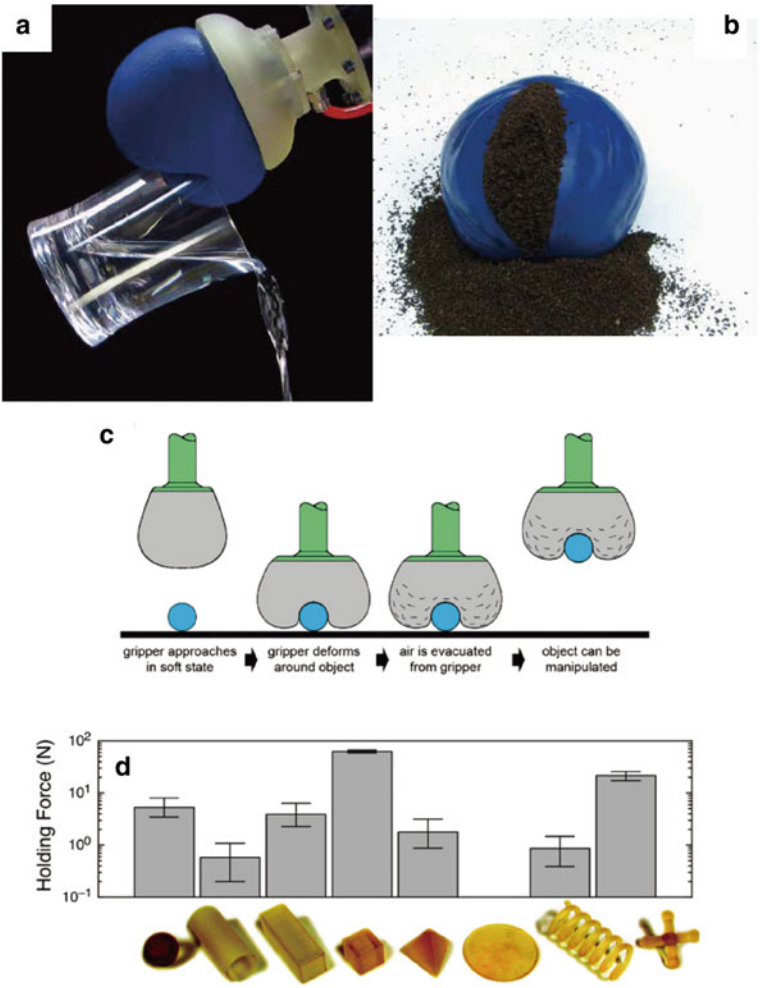

Fig. 15.2 **a** The universal gripper, which is capable to lift a drinking glass with ease. **b** The balloon is filled with granular material, and a jamming transition is used to adjust the softness. **c** How the universal gripper grasps an object. **d** The holding force of the universal gripper varies with the shape of the object. The horizontal axis shows objects with different shapes, and the vertical axis shows the holding force. **a** and **b** are reprinted from https://www.creativemachineslab.com/jamming-gripper.html. **c** and **d** are reprinted from Brown (2010)

15.1.2 Intelligent Systems as Brain–Body–Environment Systems

The above example is one of the behavioral controls made possible by softness. This concept of outsourcing functions is normally assumed to be performed by the controller on the shape and material properties of the body, and its interaction with

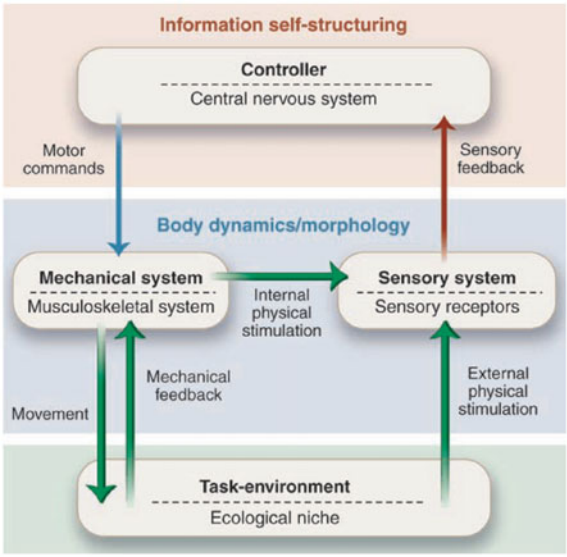

Fig. 15.3 Dynamical interactions in the embodiment model. Reprinted from Pfeifer (2007)

the environment is a well-known concept in robotics (Pfeifer 2006, 2007, 2001). The concept is occasionally proposed under a rubric prefixed with the term "embodied," such as embodied intelligence, embodied robotics, or embodied cognitive science. This section uses the term "embodiment" as a general term for the concept that is common to all of them. A simple summary of the concept of embodiment is shown in Fig. 15.3 (Pfeifer 2007). The diagram illustrates how the capabilities of intelligent systems, including both living things and robots, are achieved through dynamic interactions between the brain or controller, body, and environment.

Now, consider the control of a robot hand used in automobile assembly. The task environment is fixed. In other words, the belt conveyor delivers the car being assembled to a specified position in the execution environment of the robot hand, and the robot hand precisely inserts predetermined parts into predetermined positions. This process was repeated until the automobile was fully assembled. Here, the task environment was restricted, the shapes of the robot's body and parts being handled were limited, and control was implemented precisely. Subsequently, we considered a situation in which the types and shapes of the parts to be inserted by the robot's hand change periodically. In this case, because the parts that interact with the robot hand change to achieve the same control as before, it is necessary to adapt to these changes each time. According to the concept of embodiment, there are two possible courses of action: (1) assuming that the robot's shape is fixed and refining the controller to handle objects that change over time; or (2) changing the shape of the robot's body and refining the controller accordingly. In the example of a universal gripper, it is precisely the introduction of "softness" into the robot's body that makes it possible to adapt to objects that change from one minute to the next without changing the controller. In this manner, when considering robot control, we need to only consider

how to refine the controller. However, rather than focusing only on the controller, it is better to consider achieving control of the system as a whole, considering the dynamic interaction between the robot's body and the task environment.

The perspective of the brain–body–environment system is extremely useful for broadly understanding the structure of the system. Consider the following examples. The first is a bipedal walking robot, called a passive dynamic walker (McGeer 1990; Coleman 1998; Collins 2001) (Fig. 15.4a). The passive dynamic walker, whose body resembles a compass (a traditional drawing instrument consisting of two arms linked by a movable joint), is known for its ability to implement extremely natural bipedal walking. It walked with impressive naturalness, as expected from the bipedal walking control of a typical humanoid robot (see "Andy Ruina Cornell Walker" on YouTube: https://www.youtube.com/watch?v=_2pAMe_5VeY). However, surprisingly, the robot did not have a controller. In other words, by providing a well-designed body and task environment, the laws of physics alone are sufficient to implement bipedal locomotion. According to the previously provided schematic of the brain–body–environment system, this is an extreme example of bipedal walking control achieved solely through the interaction of the body–environment system. In other words, control that you would expect to be implemented by the brain (controller) appears to be outsourced to the interaction of the body and environment.

Similar examples are everywhere once you begin looking for them, particularly in the natural world. Another extreme example that was confirmed in the natural world is the passive swimming by dead fish Beal (2006) (Fig. 15.4b). In this example, a dead fish is first submerged in a tank of water, and a current is then created in the tank. Remarkably, the dead fish began to swim quite spontaneously (the video analyzed in the cited reference (Beal 2006) can be found at https://vimeo.com/44887922). In addition to the naturalness of swimming, dead fish are not swept away by the current, but swim upstream in the opposite direction. Significantly, because the fish is dead, the brain does not function at all. When inserting a cylinder into the tank

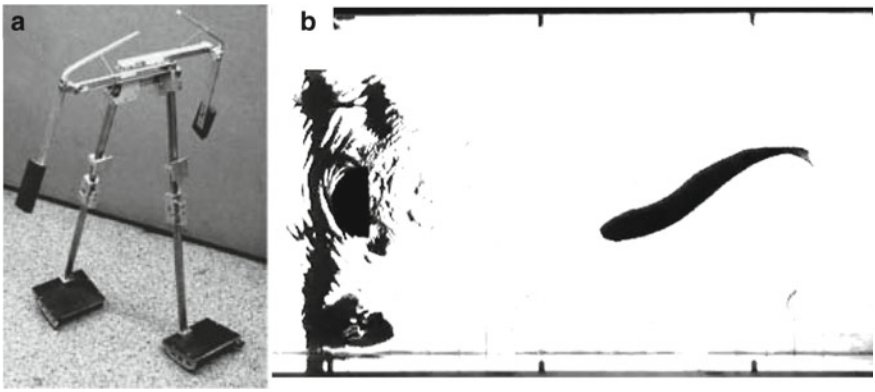

Fig. 15.4 Example of a passive dynamic walker. Reprinted from Collins (2001) (**a**). Placing a dead fish in a tank and introducing a current causes passive swimming (**b**). Reprinted from Beal (2006)

and generating a current, a special vortex called a Kármán vortex is formed behind the cylinder. The dynamic interaction between this Kármán vortex, the fish's natural body form, and its springy material properties is thought to be what allows the fish's dead body to execute this natural swimming behavior. Here, the control we expect to be implemented by the brain (controller) is outsourced to the dynamic interaction between the body and environment. Analyses show that fish utilize passive swimming when alive (Liao 2003; Liao 2004).

Once we introduce the perspective of the brain–body–environment system, we can observe that "softness" plays a role in all aspects of our daily lives. For example, we are familiar with soft rubber automobile tires. Trains, on the other hand, run along rails with hard wheels. What is the difference? Introducing softness (tires) to the contact surface between the environment and the car's body allows one to drive anywhere without staying on fixed rails (of course, you must stay on well-paved roads). This is because the softness of tires allows them to tolerate and adapt to changes in the environment. It was reported that in Formula One racing and similar sports, a slight change in the rubber material of the tires can affect race times (https://en.wikipedia.org/wiki/Formula_One_tyres#Tyre_summary). In other words, the soft tire material influences, and you might even say "controls," the speed and performance of the vehicle. In this sense, the car is a soft robot. This is another example of a link between the body and control.

15.1.3 Evolutionary Robotics: Design Principle of Brain–Body–Environment Systems

Many attempts have been made to design an intelligent system from a brain–body–environment system perspective. Numerous examples of such approaches have been cited in (Pfeifer 2001), including behavioral control design techniques based on subsumption architecture (Brooks 1986), the constructivist approach of Braitenberg's vehicles (Braitenberg 1986), and sensory–motor coordination (Pfeifer 1997). This section will not examine each of these in detail but will look at the concepts that underlie them.

Normally, when constructing an intelligent system, we extract and segment the characteristics of the intelligence we wish to realize and then try to build the corresponding functional units. This can be considered a top-down approach based on the creators' intentions. However, as we have seen, from the perspective of the embodiment concept, the functional units identified in our segmentation are not always the ones adopted in living organisms. Rather, these functions are often implemented non-locally throughout the brain–body–environment system. Because the brain, body, and environment are inextricably linked, it is difficult to understand how these functions are implemented as a whole by looking at them separately. The multiple approaches described above are all designed to incorporate the functions exerted by the overall brain–body–environment system as much as possible to prevent any pre-specified

segmentation from getting in the way. This implies that these approaches are based on the bottom-up approach. As an example, this section introduces an evolutionary robotics approach for the design of soft intelligent systems.

In the evolutionary robotics approach, computer simulation is generally used to implement the physical environment, body, and controller of an intelligent agent in a computer, and then genetic algorithms are used to optimize various parameters of the agent (the controller, body, and sometimes even the environment) based on the provided task (or evaluation function) (Nolfi 2000; Cliff 1993; Harvey 1997; Sims 1994; Floreano 1996; Lipson 2000). In this approach, because the evaluation function is typically defined to evaluate functionalities and behaviors that span the entire brain–body–environment system, it is possible to introduce a bottom-up approach for designing intelligent systems. The parameters to be optimized vary depending on the research topic; for example, one can optimize the controller for a given robotic body, or even think about co-evolving the controller and body (Cheney 2018). Of course, there are many implementations that utilize real robots (Cliff 1993; Floreano 1996; Lipson 2000). The drawbacks are that the genetic algorithm generally requires a long time and significant computational resources to evolve the optimal agent, and, as some researchers have noted, the wide gap between the simulated world and real world indicates that the optimal solution in the computer does not necessarily work in the real world, leaving us with numerous future research challenges (Bongard 2013). In this regard, several approaches have recently been proposed to optimize physical systems using a gradient descent method (Hermans 2014; Wright 2022). These schemes are intended to save computational time for optimization. However, to calculate the gradient, some differentiable models of the target systems should be prepared, which cannot always be obtained in general, and this approach still shares the sim-to-real problems with the approach based on genetic algorithms. Further developments are expected in the future.

Consider the example of an evolutionary robotics approach applied to a soft robot (Corucci 2016). It uses a physics engine called VoxCAD, which consists of a three-dimensional mesh of voxels (Hiller 2014) that can simulate the contraction and deformation of voxels (Fig. 15.5a). A meshed fluid resistance model is introduced to represent the underwater environment (Fig. 15.5a). Now, we consider the evolution of a soft robot that swims underwater in this environment. The properties of interest are the shapes of the robots and their control. These properties are represented by compositional pattern-producing networks (CPPNs), which are tuned using genetic algorithms. First, a cube called a workspace is created, in which the physical shape of the robot is determined by positioning the voxels (Fig. 15.5b). Two specific types of voxels are available: those capable of contraction (active) and that are not (passive). The first CPPN (CPPN1) accepts as input the coordinates (x, y, z) in the workspace, distance, d, from the center of the workspace, and bias term, b, and outputs whether to place a voxel at the coordinates, and if so, whether it is active or passive. When an active voxel is positioned in the workspace, the second CPPN (CPPN2) represents the frequency and phase offset of its contraction motion. Thus, provided the input information specified above, it outputs the frequency and phase offset of the active voxels' contraction motion (Fig. 15.5b).

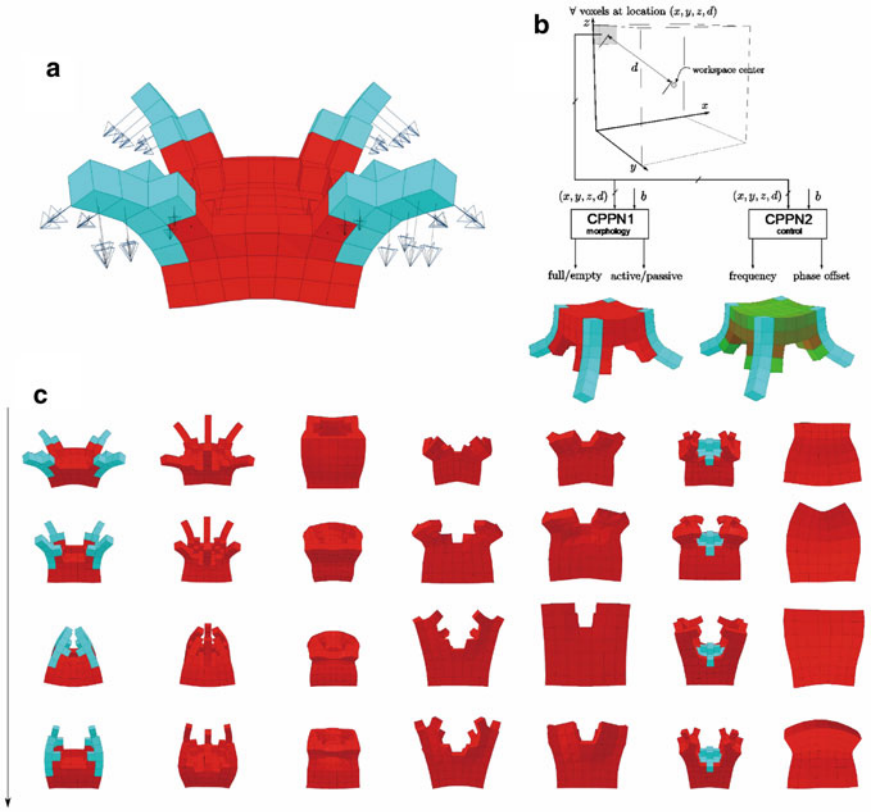

Fig. 15.5 Soft robot made of a deformable 3D mesh. The red ("active") voxels can be actuated to vibrate, while the blue ("passive") voxels remain passive. The arrows illustrate the resistance forces applied during swimming (**a**). Representation of the body and control of the soft robot by compositional pattern-producing networks (CPPNs). Two CPPNs are used, both accepting as input the coordinates (x, y, z) in 3D space and distance d from the workspace center. CPPN1 specifies whether to place the voxel at those coordinates and, if so, whether the voxel is active or passive. CPPN2 outputs the frequency and phase offset of the active voxel. These two CPPNs are evolved using a genetic algorithm (**b**). Examples of evolved soft robots (**c**). You can observe the behavior at https://youtu.be/4ZqdvYrZ3ro. **a** and **c** are reprinted from (Corucci 2016). **b** is reprinted from Corucci (2018)

Subsequently, to drive evolution, an evaluation function is formulated based on the following three goals. The first is to maximize the distance traveled over a given amount of time. The second is to minimize the energy used in swimming (i.e., to minimize the number of active voxels to be utilized). The third is to minimize the total number of voxels (i.e., to minimize the materials required to create the robot). The first goal is related to swimming, and the other two are indicators of swimming efficiency and robot costs. Given the aforementioned goals, several initial robots were prepared using randomly configured CPPNs (CPPN1 and CPPN2). The evaluation

function then generates a value for the behavior of each robot in each generation, and the highest CPNN parameters are passed on to the next generation. This yields a slightly modified version of the robot in the next generation, whose behavior is then evaluated in turn. By repeating this process, it is possible to evolve robots from generation to generation and then observe the behaviors that emerge. Figure 15.5c shows the behaviors of robots with the highest evaluation function values from the final generation. If their behavior is observed at https://youtu.be/4ZqdvYrZ3ro, their similarities to living organisms can be noticed. In Corucci (2018), the researchers investigated whether exaptation occurred when the environment switched from land to water during the evolutionary process.

In recent years, this method has been used to design soft robots (or biological machines) using biological tissues (Kriegman 2020). This type of robot is called a xenobot because it is composed of cells from the African clawed frog (*Xenopus laevis*) (Kriegman 2020; Blackiston 2021). The shape of the xenobot's body is designed in a simulation using a genetic algorithm to perform a specific task (Fig. 15.6a–g). Here, the voxel-based simulator (Hiller 2014) and CPPN-based method introduced earlier are used (Kriegman 2020). The actual size of a xenobot is less than 1 mm wide, and it is composed of skin and heart muscle cells derived from stem cells harvested from early (blastula stage) frog embryos (Fig. 15.6h). The skin cells provide rigid support for the body, and the heart cells act as small motors, contracting and expanding in volume, to propel the xenobot forward. In other words, these cell types correspond to passive and active cells, respectively. Research on xenobots is still in its early stages. The boundary between living organisms and robots is now extremely vague; however, xenobots may be the ultimate soft robots.

15.2 Machine Learning for Soft Robots

15.2.1 Basic Concepts

The geometric transformation based on the mathematically determined description is used to control conventional mechanical systems; however, soft robots and systems with continuously deformable bodies accept flexible deformation by applied force or articulatory actions. The machine learning approach works effectively for establishing the relationship between the applied force and the resulting deformation. In this section, simple examples of the use of machine learning techniques are introduced.

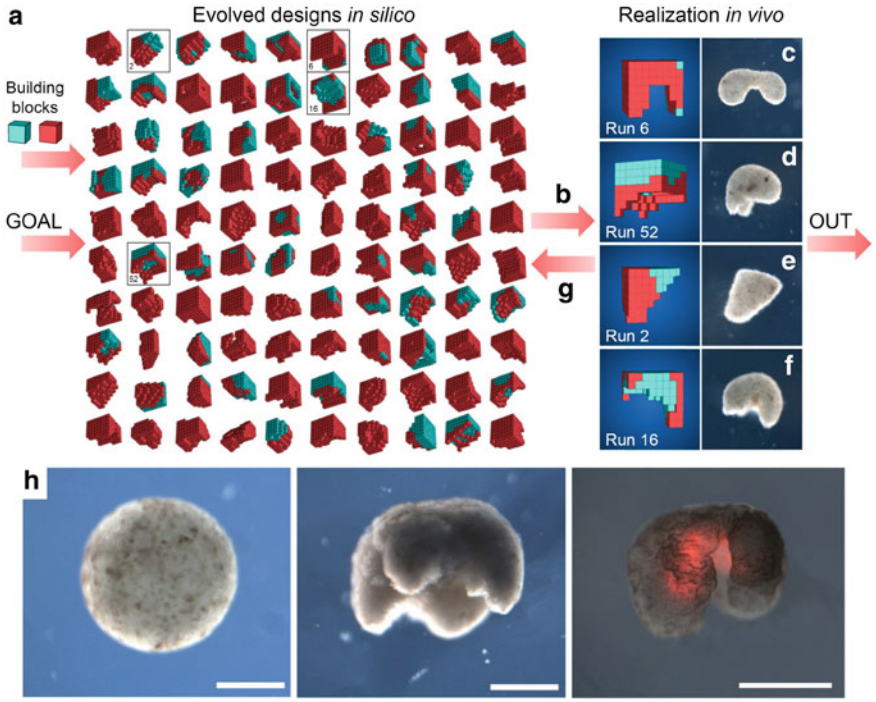

Fig. 15.6 Designing a xenobot using a genetic algorithm. The task and body design are set using a voxel-based simulator, and agents are evolved in the computer (in silico) using a genetic algorithm (**a**). The red voxels can be actuated and vibrate (active), while the blue voxels are passive. Subsequently, the best agents are selected by investigating how robust they are against actuation phase shift (**b**). Based on the design of the selected agents, xenobots are constructed in vivo using skin and heart muscle cells derived from stem cells of the African clawed frog. They are placed in a Petri dish, and their behavior is evaluated to identify whether it is consistent with the desired behavior (**c**–**f**). Discrepancies between in silico and in vivo behavior are reflected in the constraint conditions of the genetic algorithm to encourage a more sophisticated evolution (**g**). Aggregation of pluripotent blastula cells prepared from African clawed frog embryos (left). The shape of this aggregation changes based on the design created by the genetic algorithm (center). Fluorescent pigment can be used to confirm that the active cells are arranged in accordance with the design (right) (**h**). In each photograph, the length of the scale bar corresponds to 500 μm. . This figure is reprinted from Kriegman (2020)

15.2.2 Self-organizing Map

Self-organizing feature maps (SOM), introduced by Teuvo Kohonen in 1982, refer to the brain's mechanisms of self-organization. SOM can construct a mapping structure that preserves neighborhood relations by updating weight vectors in the learning algorithm (Kohonen 1982, 1989, 1998). Figure 15.7 shows a typical mapping structure that presents a map from the input pattern vector space R_m onto a two-dimensional

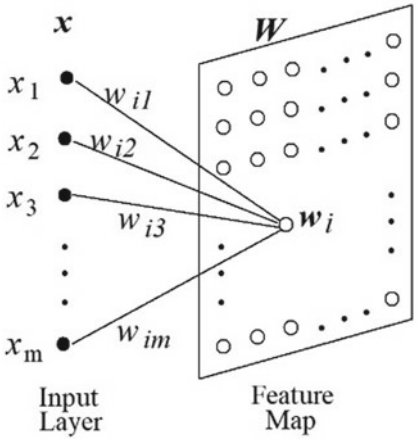

Fig. 15.7 Structure of self-organizing feature map

feature map $\boldsymbol{w}_i = [w_{i1}, w_{i2}, \ldots, w_{im}]^{\mathrm{T}} \in R_m$. The weight vector $\boldsymbol{w}_i$ at node i on the feature map is fully connected to input nodes x_j $[j = 1, \ldots, m]$.

The learning algorithm updates the weight vectors $\boldsymbol{w}_i$-s. Competitive learning is used, in which the winner c is the output unit with the weight vector that is closest to the current input vector $\boldsymbol{x}(t)$ selected at time t in the learning.

$$c = \arg\min_i \{\|\boldsymbol{x} - \boldsymbol{w}_i\|\} \tag{15.1}$$

Using the winner c, the weight vectors $\boldsymbol{w}_i$-s are updated based on the rule shown below:

$$\boldsymbol{w_i}(t+1) = \boldsymbol{w_i}(t) + h_{ci}(t)[\boldsymbol{x}(t) - \boldsymbol{w_i}(t)] \tag{15.2}$$

$$h_{ci}(t) = \begin{cases} \alpha(t) \cdot \exp\left(-\frac{\|r_c - r_i\|^2}{2\sigma^2(t)}\right) & (i \in N_c) \\ 0 & (i \notin N_c) \end{cases}$$

where $\| r_c - r_i \|$ represents the distance between a unit c and i-s in the output array and N_c represents the neighborhood of node c. $\alpha(t)$ represents a learning coefficient, which gradually reduces as the learning proceeds. $\sigma(t)$ represents a coefficient representing the width of the neighborhood area.

15.2.3 Data Classification Using Soft Tactile Sensors

Neural networks have been effectively applied to data classification and recognition. In this section, the classification of data obtained using tactile sensors is introduced. The authors have focused on the physical properties of a shape-memory alloy (SMA)

related to the material temperature and applied external force, which are the shape-memory effect and the pseudoelasticity, and are developing a tactile sensor using SMA wires (Miyatoda 2019). The structure of the tactile sensor is shown in Fig. 15.8. By moving the sensor on an object, the vibratory stimuli generated at the contact point between the object surface and tip of the pin are applied to the SMA wire, causing a change in the electrical resistance of the SMA wire. The change in the resistance was measured by a specially designed electric circuit, and the measurement data obtained by different materials and moving speeds are shown in Fig. 15.9. The measurement data change not only with different objects but also in accordance with the moving speed. To robustly classify objects from tactile data against the uncertainty of measurement conditions, we applied a deep neural network.

We conducted an experiment for classification using five objects with different textures and pattern periodicity: stone, plastic tabletop, fabric rug, mesh rubber, and scotch tape. For learning, we moved the sensor on the objects at different speeds, 150 times for each object, and the data were recorded at a sampling rate of 500 Hz and fed to the network. In the test performance, 77% of the classifications were successful.

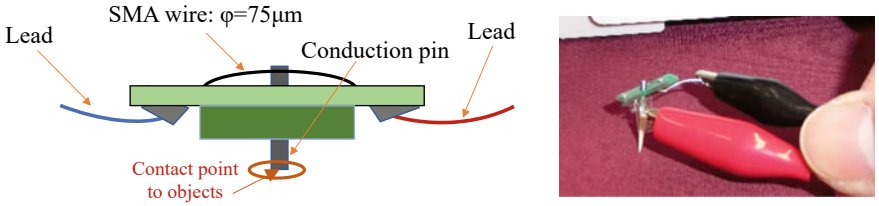

Fig. 15.8 Tactile sensor using a SMA wire

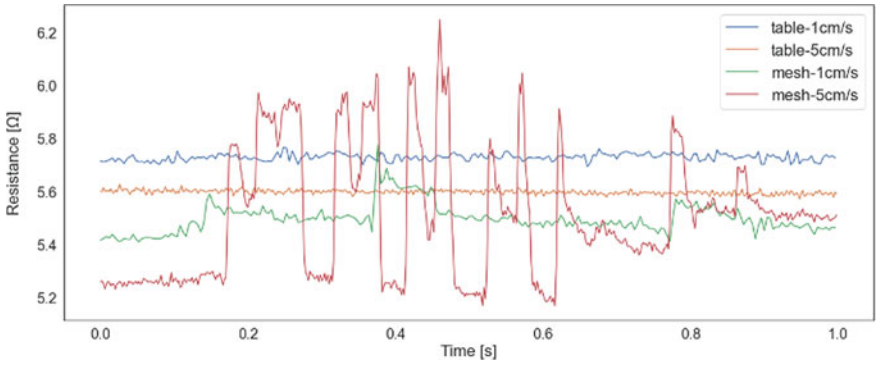

Fig. 15.9 Measurement data of two objects with different moving speed

15.2.4 *Autonomous Learning the Speaking Skill of a Talking Robot*

Machine learning was also used to control the actuators and robotic actuation. Based on the reproduction of human vocal systems, a talking robot was developed (Sawada 2015; Thanh 2016). Humans are born with vocal organs for vocalization; however, newborn babies cannot speak like adults. During the speech acquisition period following birth, they practiced vocalization with caregivers through trials and errors. Once speaking skills are acquired, we do not need to notice how we articulate the vocal organs during speech. When learning a new language, we must make unknown sounds by properly articulating the vocal organs. The articulation of vocal organs in the mouth is not observable, so we must estimate it by listening to the generated vocal sounds to match the unknown sounds. To realize the autonomous learning of human-like vocalization using a mechanically constructed talking robot, a self-organizing neural network was used to associate the articulation of mechanical vocal systems and vocal sounds produced.

The talking robot mainly consists of an air pump, artificial vocal cords, resonance tube, nasal cavity, and microphone connected to a sound analyzer, which corresponds to the lung, vocal cords, vocal tract, nasal cavity, and human audition. The construction of the talking robot system is shown in Fig. 15.10.

A neural network (NN) was used to autonomously associate vocal tract shapes with the produced vocal sounds. The associated relations enable the robot to estimate the articulation of the vocal tract to generate particular vocal sounds even if they are unknown, owing to the inference ability of the NN. During the learning process, the network learns the motor control commands by inputting the resonance characteristics as teaching signals. The network acquires the relationship between sounds and the cross-sectional areas of the vocal tract. After learning, the NN was connected in series to the vocal tract model. The corresponding shape of the vocal tract was

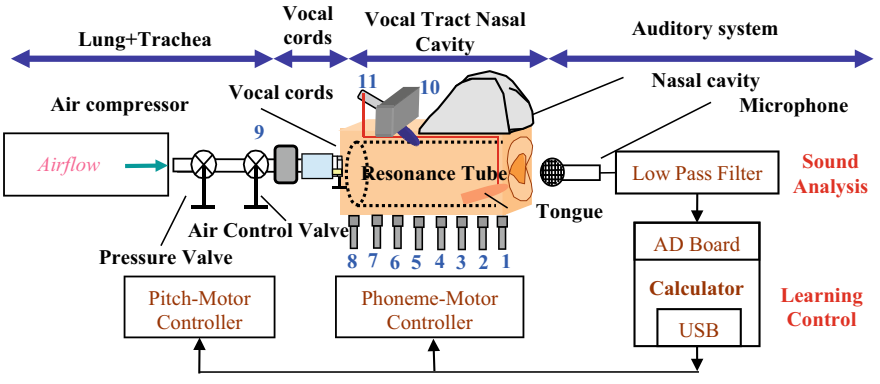

Fig. 15.10 Construction of a talking robot

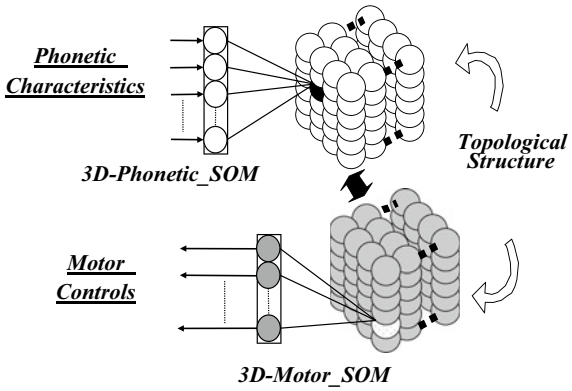

Fig. 15.11 Structure of dual-SOM

associatively obtained by inputting the sound parameters of the desired sounds into the NN.

In this study, the authors introduced a self-organizing neural network (SONN) by combining a three-dimensional SOM (3D-SOM) with an NN. The SONN had a three-dimensional mapping space in which the phonetic characteristics of voices generated by the robot were located. Voice articulations were autonomously recreated by selecting cells on the map.

The 3D-SOM has a three-dimensional mapping space, and its characteristics can be located three dimensionally similar to those of a biological brain. In this study, we used two 3D-SOMs, one for constructing the topological relations among the control commands and the other for establishing the relations of the phonetic characteristics. After the learning of two 3D-SOMs, the association between the two 3D maps was established using an NN based on the topological relations of motor control commands with phonetic characteristics. This algorithm is known as dual-SOM (Kitani et al. 2011), as shown in Fig. 15.11.

In the learning phase, the talking robot generates various voices by randomly changing its vocal tract shape. Generated voices and the original vocal tract shapes have a physical correspondence because different voices are produced by the resonance phenomenon of the articulated vocal tract. This indicates that similar phonetic characteristics were generated by similar vocal tract shapes. By adaptively associating the 3D-Phonetic_SOM with the corresponding 3D-Motor_SOM using an NN, the talking robot autonomously learns vocalizations similar to a human baby by articulating its vocal tract. After learning the relationship between the 3D-Phonetic_SOM and 3D-Motor_SOM, the robot autonomously spoke using its vocal systems.

15.2.5 Challenges

In this section, the self-organizing map and neural network are introduced as machine learning techniques. Two examples of machine learning being used to control soft

robots and soft sensors are also presented. Machine learning techniques are able not only to flexibly establish the relation between the applied force and resulting deformation of soft bodies, but also to effectively extract the physical features of the soft bodies and their deformation to understand their physical properties. Deep neural networks are expected to contribute effectively to the understanding of the physical properties of softness.

15.3 Information-Processing Capabilities of Soft Bodies

15.3.1 Reservoir Computing: Utilizing Dynamics for Information Processing

Brain (controller), body, and environmental systems are all examples of intelligent systems. Behavior control is not always conducted by the controller alone, but rather by the interaction between the body and the environment. These principles can be understood as properties of nonlinear dynamics. In particular, when a soft body is adopted, it can deform and generate an extremely diverse set of dynamics. What type of information processing and control are implemented in a soft body that generates such diverse dynamics? Answering this question requires a thorough understanding of the dynamics and information processing implemented. In this chapter, we introduce a framework called "reservoir computing," which utilizes dynamics as an information-processing device (Nakajima 2021).

Reservoir computing was introduced as a learning method for recurrent neural networks (Jaeger 2001b, a; Maass 2002) in the early 2000s (for details of the origin and establishment of reservoir computing, please check (Jaeger 2021a, b)). However, owing to the special nature of its system configuration, it has spread not only to the neural network and machine learning fields, but also to various other fields, such as nonlinear dynamics, (applied) physics, materials science, and device science. One such approach, physical reservoir computing (Nakajima 2020; Tanaka 2019), is a framework that utilizes the dynamics of physical systems as computational resources. Within this framework, it has been demonstrated that various physical systems can be used as reservoirs for information-processing resources, including quantum dynamics (Fujii 2017; Nakajima 2019; Tran 2021; Ghosh 2021; Fujii 2021), optics (Larger 2012; Brunner 2013; Vandoorne 2014; Larger 2017; Kanno 2021; Dambre 2021), spintronics (Torrejon 2017; Furuta 2018; Tsunegi 2018; Tsunegi 2019; Taniguchi 2021; Riou 2021; Akashi 2022), fluids (Fernando 2003; Goto 2021), electrochemical currents in solution (Kan 2022), biological systems (including cultured neural networks (Kubota 2019; Yada 2021), plants (Pieters 2022), and ecosystems (Ushio 2021)). As discussed later, the application of this technique to soft robots is the subject of this chapter. As a preliminary step, we first formalize the prerequisite concept of reservoir computing and present an echo state network as a concrete example. Subsequently, pertaining to the relationship between

dynamics and information-processing capability, we discuss topics, such as the echo state property and its relationship with bifurcation structures. Finally, we introduce memory capacity and information-processing capacity, which are common metrics for evaluating information-processing capability.

15.3.1.1 Formalization of Reservoir Computing

In this section, we present the formalization of reservoir computing. Reservoir computing operates under a system comprising three layers: input, intermediate, and output layers (Fig. 15.12). The input at time $t \in \mathbb{Z}$ is denoted by $\mathbf{u}_t \in U$, the intermediate layer by $\mathbf{x}_t \in X$, and the output layer by $\hat{\boldsymbol{y}}_t \in Y$. Sets U, X, and Y are the sets of possible states of the input, intermediate, and output layers, respectively. The intermediate layer is also known as a reservoir, and $\mathbf{x}_t$ is the reservoir state or reservoir variable. Here, we consider a version of reservoir computing where the time t is discrete; however, even in the case of a continuous time $t \in \mathbb{R}$, discretization with suitable sampling can yield discrete-time reservoir computing. In physical reservoir computing, a physical system that changes in continuous time is handled in the intermediate layer; however, it can be discretized using this method. The time evolution of the reservoir state is described by the following dynamical system with inputs:

$$\mathbf{x}_t = \mathbf{F}(\mathbf{x}_{t-1}, \mathbf{u}_t),$$

where $\mathrm{F} : X \times U \to X$. The reservoir variable $\mathbf{x}_t$ is determined from the previous reservoir state and current input (Fig. 15.12a). The output layer is derived from the current intermediate layer state, as follows:

$$\hat{\boldsymbol{y}}_t = \mathbf{G}(\mathbf{x}_t).$$

where $\mathrm{G} : X \to Y$.

The specific form in which the inputs are provided as feedback, such as $\mathbf{u}_t = \boldsymbol{y}_{t-1}$, is called a closed-loop configuration (Fig. 15.12b). The case of externally

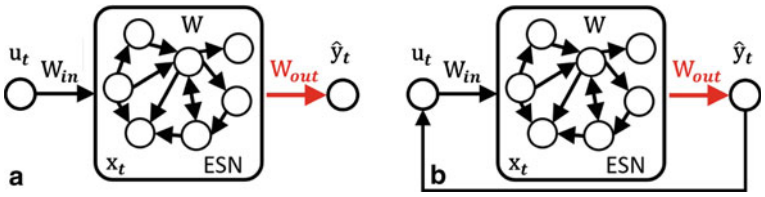

Fig. 15.12 Two typical system configurations used in reservoir computing. **a** Open-loop configuration and **b** closed-loop configuration. The figure is an example of an ESN, where the red part is adjusted by training

provided inputs instead of feedback is called an open-loop configuration. In an open-loop configuration, learning multiple functions on the same input (multitasking), or learning additional functions on the fly, is easy and safe. This is because, in reservoir computing, the intermediate layer is not tuned for a particular task; thus, the readout function **G** does not interfere with the learning process. A closed loop can be used for predicting dynamics (Pathak 2018), controlling a central pattern generator (Wyffels 2009), etc.

15.3.1.2 Echo State Network

Here, we introduce the echo state network (ESN), which is a representative example of reservoir computing, to observe the concrete configuration of reservoir computing. An ESN is a type of recurrent neural network (Fig. 15.12). The states of the input, intermediate, and output layers, each of which is composed of multiple nodes, can be described as follows: $\mathbf{u}_t = (u_t^1, \ldots, u_t^{N_{\text{in}}})^\top \in \mathbb{R}^{N_{\text{in}}}$, $\mathbf{x}_t = (x_t^1, \ldots, x_t^N)^\top \in \mathbb{R}^N$, $\hat{\mathbf{y}}_t = (y_t^1, \ldots, y_t^{N_{\text{out}}})^\top \in \mathbb{R}^{N_{\text{out}}}$. At time t, the i th reservoir node x_t^i, the j th input node u_t^j, and the l th output $\hat{y}_t^l$ follow the following equations:

$$x_t^i = f\left(A_{\text{cp}} \sum_{j=1}^{N} w^{ij} x_{t-1}^j + A_{\text{in}} \sum_{j=1}^{N_{\text{in}}} w_{\text{in}}^{ij} u_t^j\right),$$

$$\hat{y}_t^l = \sum_{i=0}^{N} w_{\text{out}}^{il} x_t^i,$$

where f denotes the activation function and $f(\cdot) = \tanh(\cdot)$. $\mathrm{W}_{\text{in}} = \{w_{\text{in}}^{ij}\}$ represents the input weight matrix, and each element is randomly determined from a uniform distribution in the range $[-1, 1]$. $\mathrm{W} = \{w^{ij}\}$ represents a coupled weight matrix, each element is randomly determined from the uniform distribution in the range $[-1, 1]$, and the spectral radius (the maximum value of the absolute value of the eigenvalues) is normalized to one. A_{cp} denotes the coupling strength, which is the spectral radius of matrix $A_{\text{cp}}\mathrm{W}$. To obtain the output, we add x_t^0, where x_t^0 is a bias term that is one at all times t. $\mathbf{W}_{\text{out}} = \left\{w_{\text{out}}^{ij}\right\}$ is the output weight matrix whose values are determined by training. Training is typically performed using linear or ridge regression. The ridge regression minimizes the cost function as follows:

$$\frac{1}{T} \sum_{t=1}^{T} \left(\hat{y}_t^l - y_t^l\right)^2 + \alpha \sum_{i=0}^{N} \left(w_{\text{out}}^{il}\right)^2$$

where T denotes the size of the training data, y_t^l is the target for output $\hat{y}_t^l$, and α is a ridge parameter, which is a constant. Limiting the training to the linear matrix

of the output in this manner has the advantage of reducing the calculation cost and ensuring that the global optimum solution can be obtained.

Recurrent neural networks have been commonly used in robotics as brain-type controllers with internal dynamics (Tani 2016). In soft robotics, they are not only used in this manner (Kuwabara 2012; Li 2012a, b, c, 2013) but also as a tool to augment sensing (e.g., for indirect sensing tasks) (Thuruthel 2019; Loo 2022; Soter 2020; Wakabayashi 2022; Tanaka 2022a). One of the key issues in sensing soft robots is maintaining the softness of the platform. However, sensory devices are typically rigid, and it is preferable to detach these sensors and replace their functionality using machine learning techniques. ESNs are actively used for this purpose, because they are easy to implement on a physical platform (i.e., the training procedure is easy and quick). For example, they are used to emulate the functionality of a laser displacement meter that measures the length of a pneumatic artificial muscle by considering the applied pressure (and also the resistance of the rubber tube in some cases) as an input. It has been demonstrated that ESNs are good at dealing with hysteresis and can predict the length of a target pneumatic artificial muscle with high precision (Sakurai 2020; Sun 2021, 2022a, b).

Note that in physical reservoir computing, reservoir variables are acquired by sensing the physical system, which are often constrained in number. To secure the computational nodes under such constraints, time (Appeltant 2011) and spatial multiplexing (Nakajima 2019) were used. The time multiplexing method, which acquires the reservoir variable multiple times at different times for a single input application, was typically used in physical reservoir computing because it could increase the computational nodes virtually and simply by fixing the physical setups and changing the number of samplings. In the spatial multiplexing method, the same input was provided to multiple devices, and the reservoir variable was obtained from them in parallel, thereby multiplexing the reservoir variable. Both methods improved the performance of the reservoir compared with the case where multiplexing was not performed.

15.3.1.3 Echo State Property

Here, we introduce the theory and specifications of the properties of a reservoir (a dynamical system with inputs) that should be suitable for reservoir computing. A reservoir is a dynamical system with inputs to obtain the desired outputs $\boldsymbol{y}_t \in Y$ from an input sequence $\mathcal{U}_t = (\ldots, \mathbf{u}_{t-1}, \mathbf{u}_t) \in U^{\mathbb{N}}$. We typically consider information processing, which requires a reproducible response. In other words, when the same input sequence is used, the reservoir should respond in the same manner. This property of a reservoir is called the echo state property (ESP) (Jaeger 2001b, a).

Reservoir $\mathrm{F} : X \times U \to X$ (assuming the compact condition is satisfied) is said to have ESP if the following holds: For the left-infinite sequence of arbitrary inputs $\mathcal{U}_t \in U^{\mathbb{N}}$ and the left-infinite sequences $\ldots, \mathbf{x}_{t-1}, \mathbf{x}_t \in X^{\mathbb{N}}$ and $\ldots, \mathbf{x}'_{t-1}, \mathbf{x}'_t \in X^{\mathbb{N}}$ of two arbitrary reservoir states such that $\mathbf{x}_i = \mathbf{F}(\mathbf{x}_{i-1}, \mathbf{u}_i), \mathbf{x}'_i = \mathbf{F}\left(\mathbf{x}'_{i-1}, \mathbf{u}_i\right)$, it is the case that $\mathbf{x}_t = \mathbf{x}'_t$. ESP was defined in the context of reservoir computing, and it is

closely related to the concept of common input-induced synchronization in nonlinear dynamical systems. When ESP is satisfied, reservoir $\mathbf{F} : X \times U \to X$ can be rewritten in the form $\mathbf{E} : U^{\mathbb{N}} \to X$. Such a function is called an input echo function, which corresponds to the phenomenon of generalized synchronization of inputs in nonlinear dynamics (Abarbanel 1996; Lu 2018; Inubushi 2021). (Although our discussion on ESP is based on the original definition of Jaeger's in (Jaeger 2001b, a), it is important to note that the concept of ESP is still being researched and developed (Yildiz 2012; Manjunath 2013).

The ESP of the reservoir can be checked by calculating the following quantity (referred to here as a synchronization index) based on the definition of EPS or common input synchronization (Snyder 2013).

$$\mathcal{F}(S, T) = \frac{1}{T} \sum_{t=S}^{S+T} ||\mathbf{x}_t^1 - \mathbf{x}_t^2||,$$

where $S, T >> 0$ represent the transient and evaluation times, respectively. $\mathbf{x}^1$ and $\mathbf{x}^2$ represent the reservoir states with different initial values and common inputs, and $||\cdot|| : X \to \mathbb{R}$ is the norm of the reservoir state. If $\mathbf{x}^1$ and $\mathbf{x}^2$ are subject to common input synchronization, $\mathcal{F}(S, T) \simeq 0$. Therefore, when $\mathcal{F}(S, T)$ is sufficiently close to zero, the system can be considered to have an EPS. However, we are only identifying the common input synchronization for a particular input and the initial state; this is different from the judgment of common input synchronization for an arbitrary input sequence and the initial state, as in the ESP definition.

15.3.2 *Reservoir Dynamics and Its Information-Processing Capacity*

A direct link exists between the dynamics of the reservoir and ESP. A special form of the Lyapunov exponent, called the conditional Lyapunov exponent (sub-Lyapunov exponent), was introduced by Pecora (1990). The conditional Lyapunov exponent is defined as follows: a dynamical system $F : X \to X$ is decomposed into two partial systems $G : V \times W \to V$ and $H : V \times W \to W$. Here, $X = V \times W$, and we set $x_t = [v_t; w_t]$ for $v_t = G(v_{t-1}, w_{t-1})$ and $w_t = H(v_{t-1}, w_{t-1})$. At this time,

$$\lambda_V = \lim_{t \to \infty} \frac{1}{t} \log \frac{\|v_t^0 - v_t^1\|}{\|v_0^0 - v_0^1\|}$$

is called a conditional Lyapunov exponent that is conditioned on V, where v_t^0 and v_t^1 are trajectories on V whose initial states $[v_0^0; w_0]$ and $[v_0^1; w_0]$ are infinitesimally close.

The conditional Lyapunov exponent limits the space for calculating the initial state sensitivity to the subspace V. In other words, in a dynamical system with an

input, such as a reservoir, the conditional Lyapunov exponent can be calculated conditionally in the reservoir space without calculating the Lyapunov exponent in the dynamical system $X \times U$ with the reservoir and the entire input. Instead, it can be calculated by the conditional Lyapunov exponent, where reservoir space X is set as V and input space U as W in the definition. At this time, if the conditional Lyapunov exponent is negative, then it is shown that G causes common input-induced synchronization for partial system H (Pecora 1990). Specifically, in a reservoir, calculating the Lyapunov exponent conditioned on the reservoir space enables determination of the presence of an ESP.

Numerical and analytical studies have been conducted to determine whether bifurcations appear in an ESN (Verstraeten 2007; Massar 2013). When changing the spectral radius A_{cp} as a parameter, at $0 < A_{\mathrm{cp}} < 1$, the Lyapunov exponent exhibits negative ordered dynamics, and the network has ESP; however, when $A_{\mathrm{cp}} > 1$, the Lyapunov exponent exhibits positive chaotic dynamics, and ESP is lost (note that by increasing the strength of inputs in ESN, the chaotic dynamics can be suppressed, and as a result, the critical line is shifted to the originally chaotic side). This implies that, on the chaotic side, the reservoir dynamics cannot be used for reproducible information processing in general (it is important to note that the breakdown of ESP is more important than "edge of chaos" for understanding information-processing capability (Jaeger 2021a, b)).

In a dynamical system with an input, an input-induced bifurcation is generated by changing only the input of the system. For example, when considering random noise as an input, noise-induced chaos (Crutchfield 1982) results, in which an originally ordered dynamical system changes to a chaotic system owing to the noise input. Conversely, noise-induced order changes an originally chaotic dynamical system to an ordered system owing to the noise input (Matsumoto 1983). These are collectively known as noise-induced phenomena. It is also known that ordered and chaotic states may alternate owing to periodic inputs other than noise or input delays. As aforementioned, noise-induced order is also generated in an ESN by gradually increasing the input intensity A_{in} (Molgedey 1992; Haruna 2019). Although details are not presented in this book, methods that effectively implement learning while suppressing chaos by applying feedback (Sussillo 2009) and designing the reservoir so that the ESP is partially established while maintaining the original chaos (Laje 2013) have been shown to allow for the construction of dynamics that cause chaotic itinerancy (Inoue 2020).

A physical reservoir is a physical device; therefore, adjusting the parameters inside a reservoir requires changing the physical configuration, and it is not always possible to make unlimited adjustments. Therefore, input-induced bifurcation is important in a physical reservoir because it can be induced by adjusting only an input designed to be externally changeable. For example, in physical reservoir computing that uses a spin-torque oscillator, changing the input intensity has been shown to induce both noise-induced order and chaos, resulting in extremely rich dynamics (Akashi 2020).

15.3.2.1 Memory Capacity and Information-Processing Capacity

Here, we introduce the measures of information-processing capability of a reservoir—memory capacity (MC) and information-processing capacity (IPC)—which are indices of general information capability that do not depend on specific tasks (Jaeger 2001b, a). We also introduced the effective dimension D_{rank} of a reservoir, which is closely related to the above two measures. In the following, the input space is set as $U = \mathbb{R}^1$, and the reservoir state space is $X = \mathbb{R}^N$. It is also assumed that the input is generated from an independent and identically distributed (i.i.d.) uniform random numbers in the interval $[-1, 1]$. The input series up to the time step T is expressed as $\mathcal{U}_T = (\ldots, u_{T-1}, u_T) \in \mathbb{R}^{\mathbb{N}}$. We also consider the reservoir states, outputs, and target series from time step 1 to time step T as $\mathcal{X}_T = (\mathbf{x}_1 \ldots \mathbf{x}_T) \in \mathbb{R}^{N \times T}$, $\widehat{\mathcal{Y}}_T = (\hat{y}_1, \ldots, \hat{y}_T) \in \mathbb{R}^T$, and $\mathcal{Y}_T = (y_1, \ldots, y_T) \in \mathbb{R}^T$.

First, we introduce the MC. The memory function $m(d)$ is the normalized squared correlation between the current state $\mathbf{x}_t$ of a reservoir and the input u_{t-d} from d time steps ago and is expressed as follows:

$$m(d) = \frac{\langle u_{t-d}\mathbf{x}_t\rangle^\top \langle \mathbf{x}_t \mathbf{x}_t^\top \rangle^{-1} \langle u_{t-d}\mathbf{x}_t\rangle}{\langle u_{t-d}^2 \rangle},$$

where $\langle u_{t-d}^2 \rangle$ is the average of u_{t-d}^2 through t. Here, $0 \leq m(d) \leq 1$ always holds true. The case $m(d) = 0$ occurs when the reservoir cannot recall the input from d units ago, and $m(d) = 1$ when the reservoir can completely recall the input from d units ago. The memory capacity $\mathrm{MC}[\mathcal{X}_T, D]$ is the sum of $m(d)$ up to $d = 0, \ldots, D$. In other words,

$$\mathrm{MC}[\mathcal{X}_T, D] = \sum_{d=0}^{D} m(d).$$

Furthermore, D_{rank} is the number of linearly independent reservoir variables, that is, the rank of the covariance matrix $\mathcal{X}_T = (\mathrm{x}_1 \ldots \mathrm{x}_T)$ of the reservoir variables from time 1 to a sufficiently large time T. In other words,

$$D_{\text{rank}}(\mathcal{X}_T) = \mathrm{rank}\big(\mathcal{X}_T^\top \mathcal{X}_T\big).$$

D_{rank} is the (effective) dimension of the reservoir. At this time, the following relationship holds between MC and dimension:

$$\lim_{D \to \infty} MC[\mathcal{X}_T, D] \leq D_{\text{rank}}(\mathcal{X}_T) \leq N.$$

If the reservoir has an ESP, then the equal sign of the left equation holds when the reservoir is a linear dynamical system, and the shortage of MC against D_{rank} can be estimated to be used for nonlinear memory (Dambre 2012).

Subsequently, we introduce IPC, which is an extension of MC (Dambre 2012). Capacity $C[\mathcal{X}_T, \mathcal{Y}_T]$ is defined as follows:

$$C[\mathcal{X}_T, \mathcal{Y}_T] = 1 - \frac{\min_{W_{\text{out}}} \text{MSE}\left[\mathcal{Y}_T, \widehat{\mathcal{Y}}_T\right]}{\left\langle y_t^2 \right\rangle} = \frac{\langle y_t \mathbf{x}_t \rangle^\top \left\langle \mathbf{x}_t \mathbf{x}_t^\top \right\rangle^{-1} \langle y_t \mathbf{x}_t \rangle}{\left\langle y_t^2 \right\rangle}.$$

Here, the predicted value $\widehat{y}_t$ is the value obtained by a linear transformation of the reservoir states $\mathbf{x}_t$, and W_{out} is the linear operator. Furthermore, $\text{MSE}[\mathcal{Y}_T, \widehat{\mathcal{Y}}_T]$ is the mean squared error expressed as $\text{MSE}\left[\mathcal{Y}_T, \widehat{\mathcal{Y}}_T\right] = \frac{1}{T}\sum_{t=1}^{T}\left(y_t - \widehat{y}_t\right)^2$. Capacity is a generalization of memory function, and similar to memory function, $0 \leq C[\mathcal{X}_T, \mathcal{Y}_T] \leq 1$. When $C[\mathcal{X}_T, \mathcal{Y}_T] = 0$, the reservoir cannot reconstruct the target sequence. When $C[\mathcal{X}_T, \mathcal{Y}_T] = 1$, the target sequence can be perfectly reconstructed.

Furthermore, because the target sequence should be generated through a nonlinear function that considers a previous input sequence in temporal learning tasks, this function can be expressed as $g(\mathcal{U}_t) \mapsto y_t$ and it can be decomposed into the linear summation of the following orthogonal polynomial $\{g_l(\mathcal{U}_t)\}_{l=0,1,\ldots}$

$$g_l(\mathcal{U}_t) = \prod_{d=0}^{\infty} \mathcal{P}_{k_{l,d}}(u_{t-d}).$$

Here, $k_{l,d} \geq 0$ is a sequence of degrees for g_l, and $P_n(u)$ is an n-degree Legendre polynomial in the form

$$\mathcal{P}_n(u) = \sqrt{\frac{2n+1}{2}} \frac{(-1)^n}{2^n!} \frac{d^n}{du^n}(1-u^2)^n (n = 0, 1, \ldots).$$

$S(D, K)$ is the set of orthogonal basis g_l that is limited up to a delay D and the total degree $K = \sum_{d=0}^{D} k_{l,d}$. Here, considering $\mathcal{G}_T^l = \{g_l(\mathcal{U}_1), \ldots, g_l(\mathcal{U}_T)\}$, the information-processing capacity $\text{IPC}[\mathcal{X}_T, D, K]$ which is limited up to the delay D and total degree K and the memory capacity $\text{MC}[\mathcal{X}_T, D]$ can be rewritten as follows:

$$\text{IPC}[\mathcal{X}_T, D, K] = \sum_{g_l \in S(D,K)} C\left[\mathcal{X}_T, \mathcal{G}_T^l\right],$$

$$MC[\mathcal{X}_T, D] = IPC[\mathcal{X}_T, D, 1] = \sum_{g_l \in S(D,1)} C\left[\mathcal{X}_T, \mathcal{G}_T^l\right].$$

Specifically, IPC is the sum of all capacities for all orthogonal basis polynomials, and the MC is limited to linear polynomials. Here, the following two important properties hold for the number D_{rank} of linearly independent reservoir variables in system $\mathcal{X}_T$.

$$\lim_{D\to\infty} \mathrm{MC}[\mathcal{X}_T, D] \leq \lim_{K,D\to\infty} \mathrm{IPC}[\mathcal{X}_T, D, K] \leq D_{rank}$$

If the ESP of $\mathcal{X}_T$ holds, then

$$\lim_{K,D,T\to\infty} \mathrm{IPC}[\mathcal{X}_T, D, K] = D_{rank}.$$

In practical situations, when capacity is calculated from a finite amount of data, the finite-size effect creates a problem. Therefore, a method is introduced in which a threshold value is set and the capacity $C[\mathcal{X}_T, \mathcal{Y}_T]$ whose value is below the threshold value is set to zero (Dambre 2012). That is, the capacity $C_\varepsilon[\mathcal{X}_T, \mathcal{Y}_T]$, which is limited to the threshold value ε, is used and defined as follows:

$$C_\varepsilon[\mathcal{X}_T, \mathcal{Y}_T] = \begin{cases} C[\mathcal{X}_T, \mathcal{Y}_T] & (C[\mathcal{X}_T, \mathcal{Y}_T] \geq \varepsilon) \\ 0 & (C[\mathcal{X}_T, \mathcal{Y}_T] < \varepsilon) \end{cases}.$$

The appropriate ε value to reduce the finite-size effect depends on the amount of data and its statistical properties. An appropriate method for determining ε includes preparing a large amount of pseudo-data that are shuffled in the time direction using the surrogate method, estimating the magnitude of the finite-size effect from these data with significant difference tests, and adopting this as ε (Kubota 2021).

Currently, IPC cannot be used for all types of input sequences, and it has various limitations. In a study that proposed IPC (Dambre 2012), the input sequence was assumed to be uniformly distributed i.i.d., however many of the tasks in reality do not show i.i.d. but have a temporal structure (i.e., time correlation), and IPCs cannot be directly used in those situations. Similarly, a multi-input system cannot be evaluated using current IPCs. The IPC is still being expanded, and there are generalizations for various i.i.d. distributions for input sequences, such as non-uniformly distributed binary distributions and normal distributions, as well as calculations of time-dependent IPCs (Kubota 2021). It is expected that such expansions will lead to the evaluation of IPCs in a wider range of situations as well as an understanding of the relationships between tasks and information-processing devices. The code is available on GitHub (https://github.com/kubota0130/ipc).

15.3.3 Physical Reservoir Computing in Soft Robots

Soft robots are generally underactuated systems, in which the number of actuators is small relative to the number of degrees of freedom, and a wide variety of dynamics are produced during actuation. These dynamics are often high dimensional and nonlinear and exhibit context-dependent behaviors. These properties render the application of conventional control techniques extremely difficult. Facing these difficulties, we consider the following. Can these diverse dynamics be used as computational resources for information processing? In other words, the dynamics of the soft

body can be used as a reservoir. Below are several case studies implemented based on this concept. Here, it can be observed that although controlling the complex dynamics of a soft robot is difficult, the dynamics can serve as an effective computational resource if used as a reservoir. We see how the difficulties in controlling a soft robot can be reconsidered as an advantage of control through physical reservoir computing techniques.

15.3.3.1 Muscular-Hydrostat Computers

The octopus arm is made of muscle tissue referred to as a "muscular-hydrostat" (Trivedi,; 2008) (this muscular-hydrostat is also present in elephant noses and human tongues). This muscle tissue has the property of maintaining a constant volume, for example, compressing one side causes an extension on the other side. An octopus takes advantage of these characteristic connections to achieve supply control of the body under dynamic stiffness and relaxation of its muscle tissue. What types of information-processing characteristics do this special muscle tissue have? Here, a muscular-hydrostat model was constructed using a mass-spring system and was used as a reservoir to clarify the computational characteristics of the muscular-hydrostat (Nakajima 2013a). In this study, the actual muscle arrangement and the muscular-hydrostatic properties were considered, making it a model with biological plausibility (Kang 2012). As a related topic, physical reservoir computing that utilizes a randomly coupled mass-spring system and tensegrity has also been proposed (Hauser 2011; Caluwaerts 2013; Caluwaerts 2014). As shown in the left of Fig. 15.13a, the spring arrangement corresponding to the transverse and longitudinal muscles was adopted such that the volume of the truncated cone was kept constant. A weighted force was applied to each spring as an input, and the response was read out with the length of the spring as the state of the system. Information processing was conducted by learning this weight. Here, it is shown that the basic configuration of this muscular-hydrostat can already emulate some types of dynamical systems; in particular, it was concluded that the memory capacity changed in a very characteristic manner by introducing the time multiplexing method and changing the input/output and system timescales (Nakajima 2013a).

The entire octopus arm can then be used as a reservoir. To that end, a model was constructed that vertically combined the muscular-hydrostat system built earlier. It was adjusted so that it would be approximately the same length as an actual octopus arm, considering the friction of water when moving the arm from a hydrodynamic perspective (Nakajima 2013b). Values obtained from the muscle tissue of actual organisms were used (e.g., for the spring constant); however, it has been shown that this parameter can also be changed as a simulator for soft robotic arms (Kang 2012). Here, the input was set as an adjustment of the angle of the base of the arm, and the dynamics of the length of all springs were used as the reservoir (Fig. 15.13a, center). As a result, it was possible to easily perform the benchmark task of a normal recurrent neural network, and by feeding back the output to the next input (i.e., closed-loop setting), it was possible to control the trajectory of the base of its own arm using the

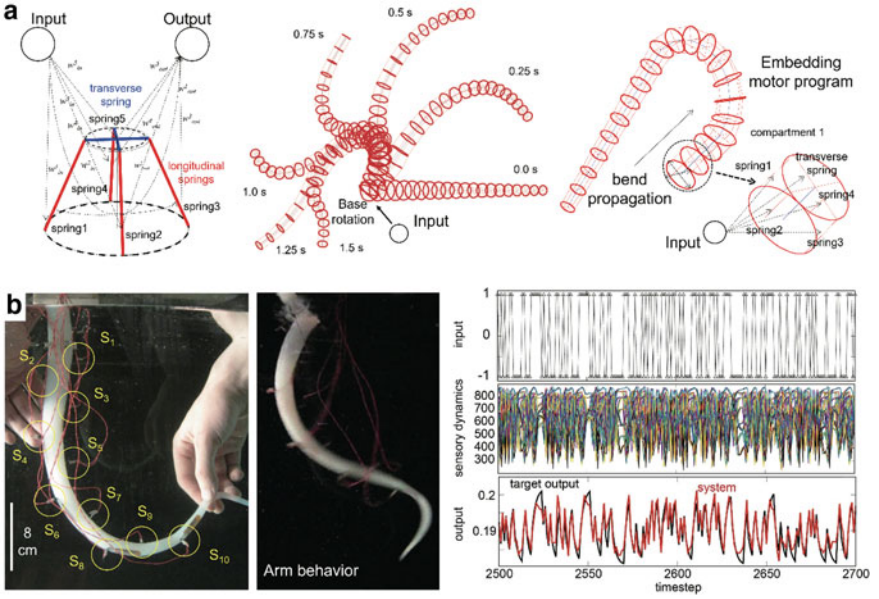

Fig. 15.13 **a** Example of muscular-hydrostat computers. (Left) A system where a muscular-hydrostat system was constructed by implementing the property that tries to keep the volume constant in the mass point spring system and adjusting it to the actual muscle arrangement of the octopus arm and parameters of the muscle tissue of the actual organism. This system is used in the same manner as a neural network. (Center) An octopus arm-type system that is constructed by combining the system on the left on a rod. The base is driven, and the resistance estimated by hydrodynamics is applied assuming underwater conditions. (Right) A concept is proposed in which the octopus arm-type system is used to implement a traveling wave of arm flexion from the base to the tip, called "bend propagation," using only the dynamics of the arm itself. **b** Soft robotic arm made of silicone (Left). Ten bend sensors are embedded inside. The base part is moved from side to side to generate the passive dynamics of the arm (Center). The plot on the right is an example of implementing information processing by injecting a random binary input into the system (top row), generating passive dynamics, and using the time series of the sensor as a reservoir (center row). Here, an example that emulates a nonlinear autoregressive-moving-average model is shown (bottom row)

dynamics of its own passive soft body. The embedded control command is a limit cycle that is often used as a central pattern generator (CPG) to guide the locomotion of a robot. Interestingly, it was observed that the part of the body used differed depending on the type of task, and it was suggested that the suitability of the calculation depends on the shape of the body. Until now, benchmark tasks for performance evaluation of recurrent neural networks have been implemented, and it is important to confirm whether the behavior control that an octopus actually performs can be embedded using this method. In this regard, it would be biologically beneficial to understand whether bend propagation, which is the octopus's characteristic reaching style, could be embedded exclusively with arm dynamics. The implementation scheme for this line was devised in a previous study (Nakajima 2017) (Fig. 15.13a, right).

Subsequently, a silicone-based octopus arm-type soft robotic arm was created and tested (Nakajima 2014) (Fig. 15.13b, left). Ten bend sensors were embedded inside, which could detect the local bending of the arm in real time. Furthermore, the density of the silicone was made similar to that of a living octopus. The arm was suspended in an aquarium and driven by an actuator attached to the base to generate soft body dynamics (Fig. 15.13b, center). Here, the sequence of inputs was mapped to the actuator command, and the sequence of bend sensor values that were obtained based on the generated dynamics was used as the reservoir. (Attempts have been made to introduce a difference in timescale between the input/output relationship and the reservoir, increase the number of computing elements by the time multiplexing method, and improve the computational capacity (Nakajima 2018a).) First, to determine the information-processing capability, it was verified whether it has the extent to which it can retain the memory of past inputs (Nakajima 2014; Nakajima 2018a) and whether it is possible to emulate a parity checker (Nakajima 2014) or a nonlinear autoregressive-moving-average model (Nakajima 2018a, 2015a) (Fig. 15.13b, right). The results show that, although dependent on the input method and strength, a computational capability equal to or greater than that of an echo state network with the same number of computing elements could be obtained, depending on the task. Common input synchronization of the soft robotic arm has also been investigated using centerline tracker (Inoue 2022), and it has been shown to have ESP (Kagaya 2022). Although a normal echo state network can achieve all tasks with a reasonably high accuracy, the octopus arm is not an all-purpose system and has many strengths and weaknesses for the task. This property is thought to be formed by special conditions, such as the shape of the octopus arm, the underwater implementation environment, and how the actuation influence is transmitted to the body (Nakajima 2015b). It also has implications when studying the role of body shape in living organisms. It has also been shown that this silicone octopus arm can be used to feed back the output to the input of the actuator in the next time step to embed a square-wave-like repetitive motion (Nakajima 2014). This result shows that the nonlinear dynamical system can be implemented using the body as a computational resource without externally providing any nonlinearity and memory that are necessary for control.

15.3.3.2 Quadruped Robot with Soft Spine

This control framework is not limited to platforms such as octopus arms. An application to a quadrupedal robot is presented herein. The fastest-running animal on the ground is the cheetah. Horses run fast as well, but not as fast as cheetahs. What is the difference? Several researchers in the field of biomechanics believe that the difference lies in the movement of the spine and are conducting research along these lines (this is called the "spinal engine hypothesis" in the field of biomechanics (Gracovetsky 1988)). The horse's spine is straight and unchanged during running, and the

horse appears to be strongly kicking the ground with its shoulder muscles. Meanwhile, the cheetah's spine moves actively, accompanied by whole-body movement, with the spine movement as the driving force.

How can spine motion affect the overall locomotion behavior? To investigate this issue, a quadruped robot called "Kitty" has been developed (Zhao 2013) (Fig. 15.14a). In contrast to most quadrupedal robots, this robot did not have actuators on the shoulders. Instead, the spine was made of silicone. The cable that passed through was controlled by an actuator, and changes in the spine shape were induced by deforming the silicone. The concept was to implement locomotive control using only spinal movement. The results showed that multiple gates could be implemented simply by activating the spine using an external control command. In this case, can this control be implemented not as an external control but as a computational resource for the dynamics of the spine? Here, a large number of pressure sensors were embedded in the spine, and the series obtained by detecting the dynamics of the sensors was used as a reservoir (Fig. 15.14b). The output, calculated by the linear sum of the sensor values, became the input to the motor at the next time step through the feedback loop. The results show that various gates can embed the dynamics of a single soft spine as a computational resource (Fig. 15.14c). These results have important implications for robot control, as well as biological locomotive control.

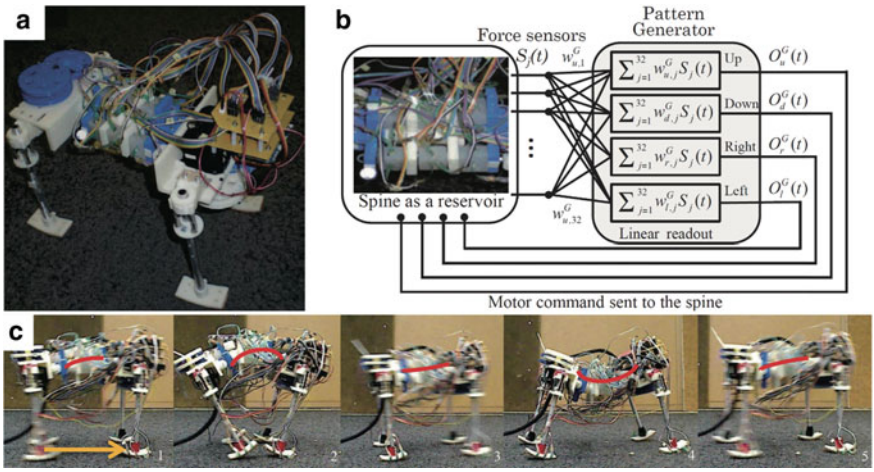

Fig. 15.14 **a** Quadruped robot "Kitty." The part corresponding to the spine is made of silicone, and it contains a large number of pressure sensors. A cable is passed through the silicone part, and pushing and pulling of the cable changes the state of the spine and achieves locomotion. Here, in contrast to a normal quadruped robot, each arm does not have a motor. **b** The silicone spine dynamics are utilized as a reservoir. **c** Photograph of Kitty, driven by the CPG that is embedded in the dynamics of the spine. The CPG was successfully embedded

15.3.3.3 Soft Interface

Subsequently, an implementation not for a soft robot but for a simple interface called a "soft keyboard" was introduced (Nakajima 2018b). Soft silicone was prepared, and a large number of sensors were placed inside it. Pressing on silicone with a finger and deforming it results in the sensor moving based on its dynamics. The time-series data are considered to be the response of the reservoir, and characters are written by learning the linear weight of the readout that is installed for each response (Fig. 15.15a). Here, an example is provided in which a simple mock-up system is constructed and experiments are conducted, assuming a keyboard that draws cursive letters on a two-dimensional display, which is often used as a task for recurrent neural networks.

In Fig. 15.15b, a minimal system (called a "soft module" here) was constructed in which a rectangular cuboid made of silicone with a length and width of 10 cm and depth of 3 cm was prepared and 16 force sensors (Tomo 2016) were embedded inside it (Fig. 15.15b). Each sensor can detect the force in the x-, y-, and z-directions each time and monitor the effect of silicone deformation in real time. Here, not only

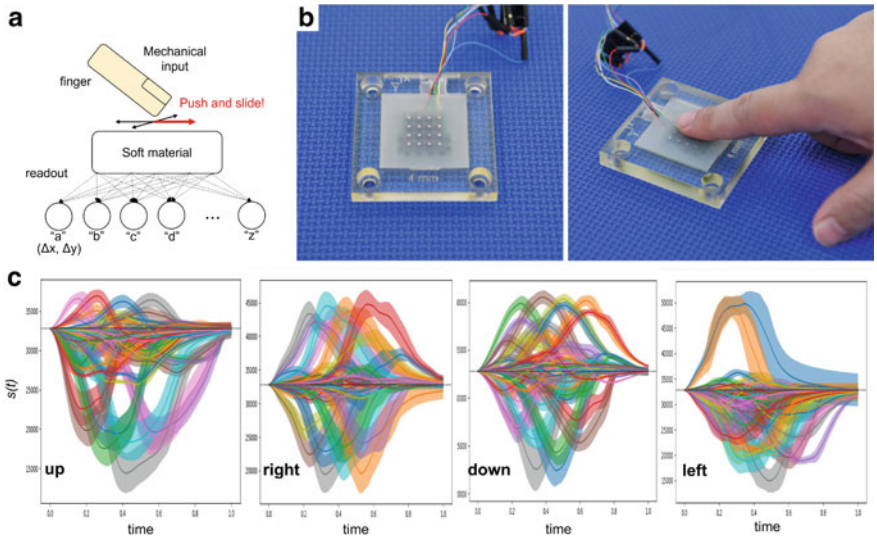

Fig. 15.15 **a** Information-processing scheme that utilizes the dynamics of deformation of soft materials. A multitasking technique can be used to embed multiple characters simultaneously for a finger movement. **b** Soft module appearance (left). Sixteen force sensors are embedded inside the silicone. Each sensor can detect the force in the x-, y-, and z-directions. The user lightly presses the soft module with a finger and slides it (right). The sensor detects the corresponding deformation of the silicone in real time. **c** Average response characteristic $\langle s(t) \rangle$ when the soft module is pushed in various directions (up, right, down, left). The colored area in the width direction of each line indicates the standard deviation interval. Each has its own unique dynamics depending on how the finger is moved. In reality, the dynamics of displacement $v(t)$ are also used as reservoirs, but they are not shown here

were the $16 \times 3 = 48$ responses ($s(t)$) adopted but also the amount of each change ($v(t) = s(t) - s(t-1)$) as computational resources. In other words, the number of sequences read from the soft module as a reservoir time series was 96. The user gently pressed the top of this soft module with their finger and slid their finger either up, down, left, or right to induce deformation in the silicone (Fig. 15.15b, right). Figure 15.15c shows the average response curve (average of 20 times) of $s(t)$ and $v(t)$ corresponding to each finger movement of a user. It can be observed that a large variety of dynamics were obtained.

The external mechanical stimulus by a finger was used as the input, and the responses of 96 computational elements ($s(t)$ and $v(t)$ were collectively referred to $x_i(t)$) and used as a reservoir time series. As aforementioned, the task was to draw cursive letters on a two-dimensional display, and there are multiple methods to implement this. Here, the focus is on the simple movement of a single finger (e.g., up), and the task of associating a certain character with the reservoir series obtained by the movement of the finger is considered with a linear transformation (i.e., adjusting linear readout weights). Here, the start and end of the stimulus were clear when the response of $v(t)$ was considered. Furthermore, because the output is the movement of a point in a two-dimensional plane, it is considered to be composed of two output nodes, which are set as Δx and Δy, respectively (Fig. 15.15a). The reason why the displacement was used as an output here was to enable cursive writing to be started regardless of the position of the starting point on the display at the time the writing commenced.

Subsequently, the learning process for readout weight w is described. Here, the user used a cursive written on the display with a digital pen as the target. Next, the soft module was stimulated 15 times for each finger movement of interest (e.g., up). The response of the reservoir time series at that time was recorded, and it was linearly associated with the output of the target. In this study, learning was conducted using ridge regression. Furthermore, the task performance was evaluated using the weights learned here, with the user implementing a new stimulus of the soft module, and comparing the output drawn on the display with the target.

Figure 15.16 shows the cursive drawn by the user using the readout weight obtained as a result of the aforementioned learning process. Here, the finger movement was fixed, and the cursive types were uppercase letters, lowercase letters, and numbers. As shown in the figure, the cursive is written correctly for almost all characters. An interesting aspect that was noticed at the time of implementation was that even if the soft material was limited to certain movements and stimulated, the speed and the way in which the force was applied changed each time. The cursive drawn changed accordingly. In other words, the user could control the expression of the characters by touching the material. This is a characteristic that is unique to this setting because it utilizes the dynamics of user interaction itself as a computational resource instead of pressing a button and associating it with a cursive, for example.

The dynamics of deformation of soft materials can be used for information processing, such as drawing cursive characters. As with the physical reservoir computing framework, the essential technical aspects are to ensure the nature of

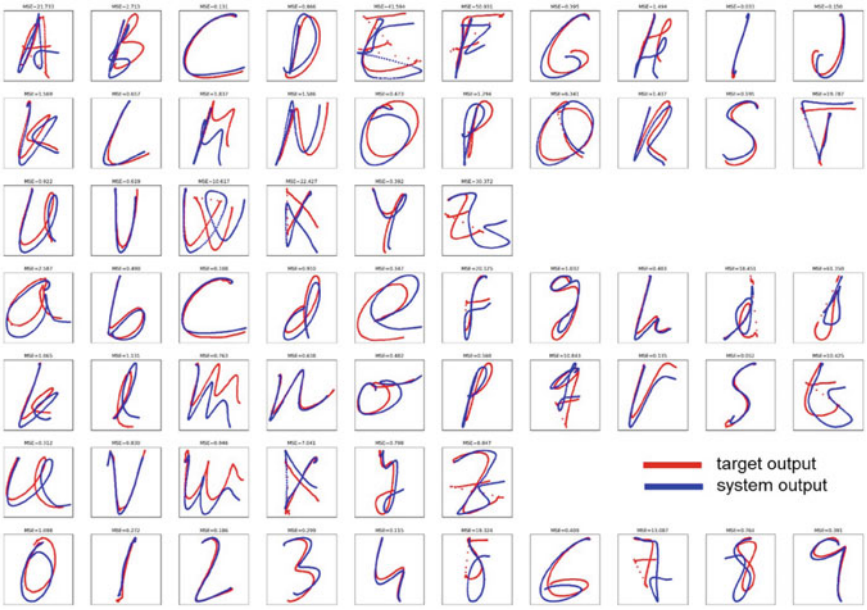

Fig. 15.16 Example of drawing cursive (uppercase, lowercase, numbers) using the dynamics of silicone deformation. The blue line is the actual system output, and the red line is the target. Results when the finger movement was fixed to up are shown as an example.

the diverse dynamics (here, soft material deformation) of the reservoir and to determine how to monitor this without damaging it. In this regard, for example, if the flexible sensor technology that has been developed in recent years is combined with the physical reservoir computing framework, it could be immediately implemented while maintaining its information-processing capacity potential to the maximum extent without destroying the soft material dynamics. This line of research has been conducted in (Tanaka 2021, 2022b; Sakurai 2022). The physical reservoir computing framework using soft materials is expected to provide a wide range of new implementation opportunities by combining materials with emerging soft technologies.

Exercises

- (1-1) Explain the following terms.

  (A) Jamming transition
  (B) Embodiment
  (C) Passive dynamic walkers
  (D) Subsumption architectures
  (E) Braitenberg's vehicles
  (F) Evolutionary robotics

- (2-1) Try to find a technical paper that introduces a machine learning technique for controlling soft robots/actuators/sensors.
- (2-2) Considering the mathematical properties of machine learning techniques, propose a possible application for controlling a soft robot or soft body.
- (3-1) Consider your own physical reservoir, based on a soft robot. Discuss its setup, functionality, and advantages in detail.

References

Abarbanel HD, Rulkov NF, Sushchik MM (1996) Generalized synchronization of chaos: the auxiliary system approach. Phys Rev E 53(5):4528

Akashi N, Yamaguchi T, Tsunegi S, Taniguchi T, Nishida M, Sa-kurai R, Wakao Y, Nakajima K (2020) Input-driven bifurcations and information processing capacity in spintronics reservoirs. Phys Rev Res 2(4):043303

Akashi N, Kuniyoshi Y, Tsunegi S, Taniguchi T, Nishida M, Sakurai R, Wakao Y, Kawashima K, Nakajima K (2022) A coupled spintronics neuromorphic approach for high-performance reservoir computing. Adv Intell Syst 4:2200123

Appeltant L, Soriano MC, Van der Sande G, Danckaert J, Mas-sar S, Dambre J, Schrauwen B, Mirasso CR, Fischer I (2011) Information processing using a single dynamical node as complex system. Nat Commun 2(1):1–6

Beal DN, Hover FS, Triantafyllou MS, Liao JC, Lauder GV (2006) Passive propulsion in vortex wakes. J Fluid Mech 549:385–402

Blackiston D, Lederer E, Kriegman S, Garnier S, Bongard J, Levin M (2021) A cellular platform for the development of synthetic living machines. Sci Robot 6(52):eabf1571

Bongard J (2013) Evolutionary robotics. Commun ACM 56(8):74–83

Braitenberg V (1986) Vehicles: Experiments in synthetic psychology. MIT Press

Brooks R (1986) A robust layered control system for a mobile robot. IEEE J Robot Autom 2(1):14–23

Brown E, Rodenberg N, Amend J, Mozeika A, Steltz E, Zakin MR, Lipson H, Jaeger HM (2010) Universal robotic gripper based on the jamming of granular material. Proc Natl Acad Sci 107(44):18809–18814

Brunner D, Soriano MC, Mirasso CR, Fischer I (2013) Parallel photonic information processing at gigabyte per second data rates using transient states. Nat Commun 4(1):1–7

Caluwaerts K, D'Haene M, Verstraeten D, Schrauwen B (2013) Locomotion without a brain: physical reservoir computing in tensegrity structures. Artif Life 19(1):35–66

Caluwaerts K, Despraz J, Işçen A, Sabelhaus AP, Bruce J, Schrauwen B, SunSpiral V (2014) Design and control of compliant tensegrity robots through simulation and hardware validation. J R Soc Interface 11(98):20140520

Cheney N, Bongard J, SunSpiral V, Lipson H (2018) Scalable co-optimization of morphology and control in embodied machines. J R Soc Interface 15(143):20170937

Cliff D, Husbands P, Harvey I (1993) Explorations in evolutionary robotics. Adapt Behav 2(1):73–110

Coleman MJ, Ruina A (1998) An uncontrolled walking toy that cannot stand still. Phys Rev Lett 80(16):3658

Collins SH, Wisse M, Ruina A (2001) A three-dimensional passive-dynamic walking robot with two legs and knees. Int J Robot Res 20(7):607–615

Corucci F, Cheney N, Giorgio-Serchi F, Bongard J, Laschi C (2018) Evolving soft locomotion in aquatic and terrestrial environments: effects of material properties and environmental transitions. Soft Rob 5(4):475–495

Corucci F, Cheney N, Lipson H, Laschi C, Bongard J (2016) Evolving swimming soft-bodied creatures. In: ALIFE XV, the fifteenth international conference on the synthesis and simulation of living systems, late breaking proceedings, vol 6

Crutchfield JP, Farmer JD, Huberman BA (1982) Fluctuations and simple chaotic dynamics. Phys Rep 92(2):45–82

Dambre J, Verstraeten D, Schrauwen B, Massar S (2012) Information processing capacity of dynamical systems. Sci Rep 2(1):1–7

Dambre J, Katumba A, Ma C, Sackesyn S, Laporte F, Freiberger M, Bienstman P (2021) Computing with integrated photonic reservoirs. In: Reservoir Computing. Springer, Singapore, pp 397–419

Fernando C, Sojakka S (2003) Pattern recognition in a bucket. In European conference on artificial life. Springer, Berlin, Heidelberg, pp 588–597

Floreano D, Mondada F (1996) Evolution of homing navigation in a real mobile robot. IEEE Trans Syst, Man, Cybern, Part B (Cybern) 26(3):396–407

Fujii K, Nakajima K (2021) Quantum reservoir computing: a reservoir approach toward quantum machine learning on near-term quantum devices. In: Reservoir computing. Springer, Singapore, pp 423–450

Fujii K, Nakajima K (2017) Harnessing disordered-ensemble quantum dynamics for machine learning. Phys Rev Appl 8(2):024030

Furuta T, Fujii K, Nakajima K, Tsunegi S, Kubota H, Suzuki Y, Miwa S (2018) Macromagnetic simulation for reservoir computing utilizing spin dynamics in magnetic tunnel junctions. Phys Rev Appl 10(3):034063

Ghosh S, Nakajima K, Krisnanda T, Fujii K, Liew TC (2021) Quantum neuromorphic computing with reservoir computing networks. Adv Quant Technol 4(9):2100053

Goto K, Nakajima K, Notsu H (2021) Twin vortex computer in fluid flow. New J Phys 23(6):063051

Gracovetsky S (1988) The spinal engine. Springer Verlag GmbH

Haruna T, Nakajima K (2019) Optimal short-term memory before the edge of chaos in driven random recurrent networks. Phys Rev E 100(6):062312

Harvey I, Husbands P, Cliff D, Thompson A, Jakobi N (1997) Evolutionary robotics: the Sussex approach. Robot Auton Syst 20(2–4):205–224

Hauser H, Ijspeert AJ, Füchslin RM, Pfeifer R, Maass W (2011) Towards a theoretical foundation for morphological computation with compliant bodies. Biol Cybern 105(5):355–370

Hermans M, Schrauwen B, Bienstman P, Dambre J (2014) Automated design of complex dynamic systems. PLoS ONE 9(1):e86696

Hiller J, Lipson H (2014) Dynamic simulation of soft multimaterial 3d-printed objects. Soft Rob 1(1):88–101

Inoue K, Kuniyoshi Y, Kagaya K, Nakajima K (2022) Skeletonizing the dynamics of soft-continuum body from video. Soft Rob 9(2):201–211

Inoue K, Nakajima K, Kuniyoshi Y (2020) Designing spontaneous behavioral switching via chaotic itinerancy. Sci Adv 6(46):eabb3989

Inubushi M, Yoshimura K, Ikeda Y, Nagasawa Y (2021) On the characteristics and structures of dynamical systems suitable for reservoir computing. In: Reservoir computing. Springer, Singapore, pp 97–116

Jaeger H (2001a) The "echo state" approach to analysing and training recurrent neural networks-with an erratum note. Bonn, Germany: German National Research Center for Information Technology GMD Technical Report 148(34):13

Jaeger H (2001b) Short term memory in echo state networks, vol 5. GMD-Forschungszentrum Informationstechnik, Bremen, Germany

Jaeger H (2021a) Foreword to the book reservoir computing: theory, physical implementations, and applications. In: Reservoir computing: theory, physical implementations, and applications (pp V–X). Springer Nature

Jaeger H (2021b) Foreword to the book reservoir computing: theory, physical implementations, and applications. Natural Computing Series. Springer Nature, pp V–X

Kagaya K, Yu B, Minami Y, Nakajima K (2022, April) Echo state property and memory in octopus-inspired soft robotic arm. In: 2022 IEEE 5th International conference on soft robotics (RoboSoft). IEEE, pp 224–230

Kan S, Nakajima K, Asai T, Akai-Kasaya M (2022) Physical implementation of reservoir computing through electrochemical reaction. Adv Sci 9(6):2104076

Kang R, Branson DT, Guglielmino E, Caldwell DG (2012) Dynamic modeling and control of an octopus inspired multiple continuum arm robot. Comput Math Appl 64(5):1004–1016

Kanno K, Uchida A (2021) Performance improvement of delay-based photonic reservoir computing. In: Reservoir computing. Springer, Singapore, pp 377–396

Kitani M, Hara T, Sawada H (2011) Autonomous voice acquisition of a talking robot based on topological structure learning by applying dual-SOM. Trans Jpn Soc Mech Eng Ser C 77(775)

Kohonen T (1982) Self-organized formation of topologically correct feature maps. Biol Cybern 43:59–69

Kohonen T (1989) Self-organization and associative memory. Springer-Verlag, Berlin, third edition

Kohonen T (1998) The self-organizing map. Neurocomputing 21:1–6

Kriegman S, Blackiston D, Levin M, Bongard J (2020) A scalable pipeline for designing reconfigurable organisms. Proc Natl Acad Sci 117(4):1853–1859

Kubota T, Takahashi H, Nakajima K (2021) Unifying framework for information processing in stochastically driven dynamical systems. Phys Rev Res 3:043135

Kubota T, Nakajima K, Takahashi H (2019) Echo state property of neuronal cell cultures. In: International conference on artificial neural networks. Springer, Cham, pp 137–148

Kuwabara J, Nakajima K, Kang R, Branson DT, Guglielmino E, Caldwell DG, Pfeifer R (2012) Timing-based control via echo state network for soft robotic arm. In The 2012 international joint conference on neural networks (IJCNN). IEEE, pp 1–8

Laje R, Buonomano DV (2013) Robust timing and motor patterns by taming chaos in recurrent neural networks. Nat Neurosci 16(7):925–933

Larger L, Soriano MC, Brunner D, Appeltant L, Gutiérrez JM, Pes-quera L, Mirasso CR, Fischer I (2012) Photonic information processing beyond Turing: an optoelectronic implementation of reservoir computing. Opt Express 20(3):3241–3249

Larger L, Baylón-Fuentes A, Martinenghi R, Udaltsov VS, Chembo YK, Jacquot M (2017) High-speed photonic reservoir computing using a time-delay-based architecture: million words per second classification. Phys Rev X 7(1):011015

Li T, Nakajima K, Kuba M, Gutnick T, Hochner B, Pfeifer R (2011) From the octopus to soft robots control: An octopus inspired behavior control ar-chitecture for soft robots. Vie et milieu 61(4):211–217

Li T, Nakajima K, Calisti M, Laschi C, Pfeifer R (2012a) Octopus-inspired sensorimotor control of a multi-arm soft robot. In: 2012a IEEE International conference on mechatronics and automation. IEEE, pp 948–955

Li T, Nakajima K, Cianchetti M, Laschi C, Pfeifer R (2012b) Behavior switching using reservoir computing for a soft robotic arm. In: 2012b IEEE International conference on robotics and automation. IEEE, pp 4918–4924

Li T, Nakajima K, Pfeifer R (2013) Online learning for behavior switching in a soft robotic arm. In: 2013 IEEE International conference on robotics and automation. IEEE, pp 1296–1302

Liao JC (2004) Neuromuscular control of trout swimming in a vortex street: implications for energy economy during the Karman gait. J Exp Biol 207(20):3495–3506

Liao JC, Beal DN, Lauder GV, Triantafyllou MS (2003) Fish exploiting vortices decrease muscle activity. Science 302(5650):1566–1569

Lipson H, Pollack JB (2000) Automatic design and manufacture of robotic lifeforms. Nature 406(6799):974–978

Loo JY, Ding ZY, Baskaran VM, Nurzaman SG, Tan CP (2022) Robust multimodal indirect sensing for soft robots via neural network-aided filter-based estimation. Soft Rob 9(3):591–612

Lu Z, Hunt BR, Ott E (2018) Attractor reconstruction by machine learning. Chaos: An Interdisc J Nonlinear Sci 28(6):061104

Maass W, Natschläger T, Markram H (2002) Real-time computing without stable states: a new framework for neural computation based on perturbations. Neural Comput 14(11):2531–2560
Majmudar TS, Sperl M, Luding S, Behringer RP (2007) Jamming transition in granular systems. Phys Rev Lett 98(5):058001
Manjunath G, Jaeger H (2013) Echo state property linked to an input: exploring a fundamental characteristic of recurrent neural networks. Neural Comput 25(3):671–696
Massar M, Massar S (2013) Mean-field theory of echo state net-works. Phys Rev E 87(4):042809
Matsumoto K, Tsuda I (1983) Noise-induced order. J Stat Phys 31(1):87–106
McGeer T (1990) Passive dynamic walking. Int J Robot Res 9(2):62–82
Miyatoda A, Shigemune H, Miwa T, Sawada H (2019) A tactile sensor using a shape-memory alloy wire during vibration. IEICE Trans J102-C(9):241–248
Molgedey L, Schuchhardt J, Schuster HG (1992) Suppressing chaos in neural networks by noise. Phys Rev Lett 69(26):3717
Nakajima K (2020) Physical reservoir computing: an introductory perspective. Jpn J Appl Phys 59(6):060501
Nakajima K, Li T, Hauser H, Pfeifer R (2014) Exploiting short-term memory in soft body dynamics as a computational resource. J R Soc Interface 11(100):20140437
Nakajima K, Fujii K, Negoro M, Mitarai K, Kitagawa M (2019) Boosting computational power through spatial multiplexing in quantum reservoir computing. Phys Rev Appl 11(3):034021
Nakajima K, Fischer I (2021) Reservoir computing: theory, physical implementations, and applications. Springer, Singapore
Nakajima K, Hauser H, Kang R, Guglielmino E, Caldwell DG, Pfeifer R (2013a) Computing with a muscular-hydrostat system. In: 2013a IEEE international conference on robotics and automation. IEEE, pp 1504–1511
Nakajima K, Hauser H, Kang R, Guglielmino E, Caldwell DG, Pfeifer R (2013) A soft body as a reservoir: case studies in a dynamic model of octopus-inspired soft robotic arm. Front Comput Neurosci 7:91
Nakajima K, Hauser H, Li T, Pfeifer R (2015a) Information processing via physical soft body. Sci Rep 5:10487
Nakajima K, Schmidt N, Pfeifer R (2015b) Measuring information transfer in a soft robotic arm. Bioinspiration Biomimetics 10(3):035007
Nakajima K, Hauser H, Li T, Pfeifer R (2018) Exploiting the dynamics of soft materials for machine learning. Soft Robot 5(3): 339–347
Nakajima K, Inoue K, Kuniyoshi Y, Somlor S, Tomo TP, Schmitz A (2018b) Soft keyboard: a novel user interface for soft devices. In Proceedings of the international symposium on nonlinear theory and its applications (NOLTA2018b), pp 147–150
Nakajima K (2017) Muscular-hydrostat computers: physical reservoir computing for octopus-inspired soft robots. In: Brain evolution by design. Springer, Tokyo, pp 403–414
Nolfi S, Floreano D (2000) Evolutionary robotics: The biology, intelligence, and technology of self-organizing machines. MIT Press
Pathak J, Hunt B, Girvan M, Lu Z, Ott E (2018) Modelfree prediction of large spatiotemporally chaotic systems from data: a reservoir computing approach. Phys Rev Lett 120:024102
Pecora LM, Carroll TL (1990) Synchronization in chaotic systems. Phys Rev Lett 64(8):821
Pfeifer R, Scheier C (1997) Sensory- motor coordination: the metaphor and beyond. Robot Auton Syst 20(2–4):157–178
Pfeifer R, Lungarella M, Iida F (2007) Self-organization, embodiment, and biologically inspired robotics. Science 318(5853):1088–1093
Pfeifer R, Bongard J (2006) How the body shapes the way we think: a new view of intelligence. MIT Press
Pfeifer R, Scheier C (2010) Understanding intelligence. MIT Press
Pieters O, De Swaef T, Stock M (2022) Leveraging plant physio-logical dynamics using physical reservoir computing. Sci Rep 12(1):1–14

Riou M, Torrejon J, Abreu Araujo F, Tsunegi S, Khalsa G, Querlioz D, Bortolotti P, Leroux N, Marković D, Cros V, Yakushiji K, Fukushima A, Ku-bota H, Yuasa S, Stiles MD, Grollier J (2021) Reservoir computing leveraging the transient non-linear dynamics of spin-torque nano-oscillators. In: Reservoir computing. Springer, Singapore, pp 307–329

Sakurai R, Nishida M, Jo T, Wakao Y, Nakajima K (2022) Durable pneumatic artificial muscles with electric conductivity for reliable physical reservoir computing. J Robot Mechatron 34(2):240–248

Sakurai R, Nishida M, Sakurai H, Wakao Y, Akashi N, Kuniyoshi Y, Minami Y, Nakajima K (2020) Emulating a sensor using soft material dynamics: a reservoir computing approach to pneumatic artificial muscle. In: 2020 3rd IEEE International conference on soft robotics (RoboSoft). IEEE, pp 710–717

Sawada H (2015) A talking robot and its autonomous learning of speech articulation for producing expressive speech. Emergent Trends Robot Intell Syst, Adv Intell Syst Comput 316:93–102

Sims K (1994) Evolving 3D morphology and behavior by competition. Artif Life 1(4):353–372

Snyder D, Goudarzi A, Teuscher C (2013) Computational capabilities of random automata networks for reservoir computing. Phys Rev E 87(4):042808

Soter G, Hauser H, Conn A, Rossiter J, Nakajima K (2020, October) Shape reconstruction of CCD camera-based soft tactile sensors. In: 2020 IEEE/RSJ International conference on intelligent robots and systems (IROS). IEEE, pp 8957–8962

Sun W, Akashi N, Kuniyoshi Y, Nakajima K (2022b) Self-organization of physics-informed mechanisms in recurrent neural networks: a case study in pneumatic artificial muscles. In: 2022b IEEE 5th International conference on soft robotics (RoboSoft). IEEE, pp 409–415

Sun W, Akashi N, Kuniyoshi Y, Nakajima K (2021) Physics-informed reservoir computing with autonomously switching readouts: a case study in pneumatic artificial muscles. In: 2021 International symposium on micro-nanomehatronics and human science (MHS). IEEE, pp 1–6

Sun W, Akashi N, Kuniyoshi Y, Nakajima K (2022) Physics-informed recurrent neural networks for soft pneumatic actuators. IEEE Robot Autom Lett 7(3):6862–6869

Sussillo D, Abbott LF (2009) Generating coherent patterns of activity from chaotic neural networks. Neuron 63(4):544–557

Tanaka G, Yamane T, Héroux JB, Nakane R, Kanazawa N, Takeda S, Numata H, Nakano D, Hirose A (2019) Recent advances in physical reservoir computing: a review. Neural Netw 115:100–123

Tanaka K, Yang S-H, Tokudome Y, Minami Y, Lu Y, Arie T, Akita S, Takei K, Nakajima K (2021) Flapping-wing dynamics as a natural detector of wind direction. Adv Intell Syst 3:2000174

Tanaka K., Minami Y, Tokudome Y, Inoue K, Kuniyoshi Y, Nakajima K (2022a) Continuum-body-pose estimation from partial sensor information using recurrent neural networks. IEEE Robot Autom Lett 7(4):11244–11251

Tanaka K, Tokudome Y, Minami Y, Honda S, Nakajima T, Takei K, Nakajima K (2022) Self-organization of remote reservoirs: transferring computation to spatially distant locations. Adv Intell Syst 4:2100166

Tani J (2016) Exploring robotic minds: actions, symbols, and con-sciousness as self-organizing dynamic phenomena. Oxford University Press

Taniguchi T, Tsunegi S, Miwa S, Fujii K, Kubota H, Nakajima K (2021) Reservoir computing based on Spintronics technology. In: Reservoir computing. Springer, Singapore, pp 331–360

Thanh NV, Sawada H (2016) A talking robot and its real-time interactive modification for speech clarification. SICE J Control, Meas, Syst Integr 9(6):251–256

Thuruthel TG, Shih B, Laschi C, Tolley MT (2019) Soft robot perception using embedded soft sensors and recurrent neural networks. Sci Robot 4(26):eaav1488

Tomo TP, Wong WK, Schmitz A, Kristanto H, Sarazin A, Jamone L, Somlor S, Sugano S (2016) A modular, distributed, soft, 3-axis sensor system for robot hands. In: 2016 IEEE-RAS 16th international conference on humanoid robots (humanoids). IEEE, pp 454–460

Torrejon J, Riou M, Araujo FA, Tsunegi S, Khalsa G, Querlioz D, Bortolotti P, Cros V, Yakushiji K, Fukushima A, Kubota H, Yuasa S, Stiles MD, Grollier J (2017) Neuromorphic computing with nanoscale spintronic oscillators. Nature 547(7664):428–431

Tran QH, Nakajima K (2021) Learning temporal quantum tomography. Phys Rev Lett 127(26):260401

Trivedi D, Rahn CD, Kier WM, Walker ID (2008) Soft robotics: biological inspiration, state of the art, and future research. Appl Bionics Biomech 5(3):99–117

Tsunegi S, Taniguchi T, Miwa S, Nakajima K, Yakushiji K, Fu-kushima A, Yuasa S, Kubota H (2018) Evaluation of memory capacity of spin torque oscillator for recurrent neural networks. Jpn J Appl Phys 57(12):120307

Tsunegi S, Taniguchi T, Nakajima K, Miwa S, Yakushiji K, Fu-kushima A, Yuasa S, Kubota H (2019) Physical reservoir computing based on spin torque oscillator with forced synchronization. Appl Phys Lett 114:164101

Ushio M, Watanabe K, Fukuda Y, Tokudome Y, Nakajima K (2021) Computational capability of ecological dynamics. bioRxiv

Vandoorne K, Mechet P, Van Vaerenbergh T, Fiers M, Mor-thier G, Verstraeten D, Schrauwen B, Dambre J, Bienstman P (2014) Experimental demonstration of reservoir computing on a silicon photonics chip. Nat Commun 5(1):1–6

Verstraeten D, Schrauwen B, d'Haene M, Stroobandt D (2007) An experimental unification of reservoir computing methods. Neural Netw 20(3):391–403

Wakabayashi S, Arie T, Akita S, Nakajima K, Takei K (2022) A multitasking flexible sensor via reservoir computing. Adv Mater 34:2201663

Wright LG, Onodera T, Stein MM, Wang T, Schachter DT, Hu Z, McMahon PL (2022) Deep physical neural networks trained with backpropagation. Nature 601(7894):549–555

Wyffels F, Schrauwen B (2009) Design of a central pattern generator using reservoir computing for learning human motion. In: 2009 Advanced technologies for enhanced quality of life. IEEE, pp 118–122

Yada Y, Yasuda S, Takahashi H (2021) Physical reservoir computing with FORCE learning in a living neuronal culture. Appl Phys Lett 119(17):173701

Yildiz IB, Jaeger H, Kiebel SJ (2012) Re-visiting the echo state property. Neural Netw 35:1–9

Zhao Q, Nakajima K, Sumioka H, Hauser H, Pfeifer R (2013) Spine dynamics as a computational resource in spine-driven quadruped locomotion. In: 2013 IEEE/RSJ International conference on intelligent robots and systems. IEEE, pp 1445–1451

Chapter 16
Toward Understanding and Manipulation of Collective Behaviors Using Nematode *Caenorhabditis elegans*

Takuma Sugi and Hiroshi Ito

Although experimental studies on the physics of active matter are rapidly developing, experiments using animals remain challenging. Some nematodes species, particularly parasitic nematodes, have long been known to swarm in their habitats to survive desiccation for extended periods (Gray and Lissmann 1964; Gaugler and Bilgrami 2004). The free-living nematode *Caenorhabditis elegans*, a commonly used laboratory animal model (Brenner 1974), is genetically tractable and may offer an opportunity to experimentally examine the collective behavior of animals under the control of a wide variety of parameters. Large numbers of propagated worms collectively formed a dynamic network pattern (Sugi et al. 2019). This pattern comprised a large number of compartments surrounded by bundle-shaped worm aggregates, and was dynamically remodeled over time by repeated coalescence and division of compartments within approximately 100 s. This network pattern formation required self-propelled activity, because no clear self-organized pattern was observed for dead worms.

Why do randomly moving animals form this network pattern without knowing their locations in the entire structure? To elucidate the mechanism underlying this pattern formation, behavioral data from *C. elegans* were collected at the single-worm level. The sparsely isolated worms moved clockwise or anticlockwise circular trajectories with gradual changes in the rotation rate. From the detailed trajectory analysis of 38 worms, the standard deviation and correlation time of the rotation rate were estimated to be $\sigma_\omega = 0.155$ rad/s and $\tau = 27$ s, respectively. It can be observed from $\tau\sigma_\omega = 0.67 \times 2\pi$ rad that worms tend to move halfway around with an almost constant rotation rate.

T. Sugi (✉)
Program of Biomedical Science, Graduate School of Integrated Sciences for Life, Hiroshima University, Hiroshima, Japan
e-mail: sugit@hiroshima-u.ac.jp

H. Ito
Faculty of Design, Kyushu University, Fukuoka, Japan

K. Suzumori et al. (eds.), *The Science of Soft Robots*, Natural Computing Series,
https://doi.org/10.1007/978-981-19-5174-9_16

We further analyzed the pair interactions of worms by observing a high number of random collisions between worms in close proximity. In 43 pairs of collision events, the outgoing angles were near zero or pi, regardless of the value of the incoming angles. This result indicates that collisions cause the worms to align or anti-align, implying a nematic rather than a polar order. These short-range nematic alignments and smooth turning of *C. elegans* are reminiscent of microtubules driven by axonemal dynein *c* (Sumino et al. 2012; Nagai et al. 2015). The hexagonal lattice of vortices formed by microtubules was reproduced by a simple agent-based model in which the agents had a memory of the rotation rate. To confirm whether the collective pattern formation of *C. elegans* could be reproduced by the minimal model, we modified the model by adding two characteristics shown by the single-worm-level analysis: attraction caused by surface tension ($\boldsymbol{F}^{\mathrm{a}}_{ij}$) and repulsion owing to the excluded volume of worms ($\boldsymbol{F}^{r}$). The model is expressed as follows:

$$\dot{\boldsymbol{r}}_i = \boldsymbol{e}_{\theta_i} + \sum_{r_{ij}<r^r} \boldsymbol{F}^{\mathrm{r}}_{ij} + \sum_{r^{\mathrm{r}}<r_{ij}<1} \boldsymbol{F}^{\mathrm{a}}_{ij}$$

$$\dot{\theta}_i = \omega_i + \frac{1}{N_i} \sum_{r^{\mathrm{r}}<r_{ij}<1} \sin 2\left(\theta_j - \theta_i\right)$$

$$\dot{\omega}_i = -\frac{\omega_i - \omega_0}{\tau} + \sqrt{\frac{2}{\tau}}\sigma_\omega \xi_i$$

$$\boldsymbol{F}^{\mathrm{r}}_{ij} = k^{\mathrm{r}}\left(r_{ij} - r^{\mathrm{r}}\right)\boldsymbol{e}_{ij}$$

$$\boldsymbol{F}^{\mathrm{a}}_{ij} = \frac{k^{\mathrm{a}}}{r_{ij}}\boldsymbol{e}_{ij}$$

where $\boldsymbol{r}_i$, θ_i, and ω_i represent the position, direction of motion, and rotation rate of the particle i, respectively. $\boldsymbol{e}_{\theta_i}$ denotes the unit vector in the direction of θ_i, which indicates that the isolated particles move at a speed of one. The repulsive force $\boldsymbol{F}^{\mathrm{r}}_{ij}$ was exerted on particle i by particle j in a circle with radius of r^{r} and center at $\boldsymbol{r}_i$. The direction of $\boldsymbol{F}^{\mathrm{r}}_{ij}$ was the same as the unit vector from particle i to particle j, $\boldsymbol{e}_{ij}$. When $r^{\mathrm{r}} < r_{ij} = \left|\boldsymbol{r}_i - \boldsymbol{r}_j\right| < 1$, the attractive force $\boldsymbol{F}^{\mathrm{a}}_{ij}$ was exerted by particle j. The inverse of the distance of the particles was chosen to represent the dependence of $\boldsymbol{F}^{\mathrm{a}}_{ij}$ on the distance from the neighbors, with reference to Ref (Kralchevsky and Nagayama 2000). In the area where $\boldsymbol{F}^{\mathrm{a}}_{ij}$ was applied, particle i aligned head-to-head or head-to-tail with particle j. The alignment interaction term was normalized by the number of interacting particles to avoid excessively strong interactions. When the average ($\omega_0 = 0.0035$) and standard deviation ($\sigma_\omega = 0.35$) of the rotation rate and rotational correlation time ($\tau = 10$) corresponding to the aforementioned estimated values were used, a collective network pattern was obtained in the simulation.

The *C. elegans* collective behavior system provided an opportunity for experimental verification of the above mathematical model by controlling the parameters of the model by changing environmental conditions and genetic perturbations (Corsi et al. 2015). First, an analysis of the density dependence showed that a high density was required in the experiment and simulation. Furthermore, the attraction force

was controlled in both experiment and simulation. In the experiment, we controlled the attraction force between the worms in a network formed on the lid of a plastic petri plate by increasing the humidity inside the plate. As humidity increased, the compartment size of the network also increased. Eventually, the network collapsed and many clusters of simple worm aggregates remained. In the simulation, as the attraction force parameter k^{a} in the model increased, the compartment sizes of the network also increased, resulting in network collapse. These similar experimental and simulation results verified the dependency of the model on the attraction force parameter.

The accumulated genetic resources and tools developed for *C. elegans* allowed us to control the model parameters. Therefore, we controlled the parameters ω_0 and σ_ω of the model in both experiments and simulations. In the experiments, we observed pattern formation in the *mec-4* mutant because this mutant moved along a circular trajectory with a higher curvature than that of the wild-type worm (Cohen et al. 2012). We observed that the compartment sizes of the networks formed by the *mec-4* mutants were smaller than those of wild-type worms. In the simulations, particles traveling with higher ω_0 and σ_ω values formed smaller compartments, suggesting that the model also reproduced the experimental results.

We constructed an experimental system for optical manipulation of the network. This optogenetic system enables transient perturbation of worm aggregations by the optical activation of mechanosensory neurons. Blue light illumination has been known to competitively drive reversal, accelerate forward movements, and induce movement in halted worms (Stirman et al. 2012). Upon illumination, the bundles started to collapse. Subsequently, the bundles recovered their original shape as long as the duration of illumination was not long (< 2 s). However, illumination with mild light intensity for a prolonged duration (> 30 s) broke the bundle, and the worms formed different bundles after the light was turned off. In the simulations, to inactivate the particles, the terms $\boldsymbol{e}_{\theta_i}$ in the first equation and ω_i in the second equation were multiplied by zero for 30% of the particles. The sudden change from the behavior of inactive particles to that of normal particles collapses the network structure. Once the ratio of inactive particles returned to its initial value, the network was reformed. Therefore, the simulation results were consistent with those of the optogenetic experiments. This optogenetic manipulation system offers great opportunities for manipulating the collective patterns of *C. elegans*, which might provide clues for the development of algorithms for controlling self-propelled particles.

Considered together, the findings on collective pattern formation in *C. elegans* allowed experimental verification of the previously proposed model through parameter controls. This verification indicates that the local nematic alignment and smooth turning of worms underlie the collective network formation. Experimental studies support the notion that local alignment interaction is generally one of the key factors in collective pattern formation by active matter.

References

Brenner S (1974) The genetics of *Caenorhabditis elegans*. Genetics 77(1):71–94. https://doi.org/10.1093/genetics/77.1.71

Cohen E, Yemini E, Schafer W, Feitelson DG, Treinin M (2012) Locomotion analysis identifies roles of mechanosensory neurons in governing locomotion dynamics of *C. elegans*. J Exp Biol 215(20):3639–3648. https://doi.org/10.1242/jeb.075416

Corsi AK, Wightman B, Chalfie M (2015) A transparent window into biology: a primer on *Caenorhabditis elegans*. Genetics 200(2):387–407. https://doi.org/10.1534/genetics.115.176099

Gaugler R, Bilgrami AL (2004) Nematode behaviour. CABI

Gray J, Lissmann HW (1964) The locomotion of nematodes. J Exp Biol 41(1):135–154

Kralchevsky PA, Nagayama K (2000) Capillary interactions between particles bound to interfaces, liquid films and biomembranes. Adv Colloid Interface Sci 85(2–3):145–192. https://doi.org/10.1016/s0001-8686(99)00016-0

Nagai KH, Sumino Y, Montagne R, Aranson IS, Chaté H (2015) Collective motion of self-propelled particles with memory. Phys Rev Lett 114(16):168001. https://doi.org/10.1103/physrevlett.114.168001

Stirman JN, Crane MM, Husson SJ, Gottschalk A, Lu H (2012) A multispectral optical illumination system with precise spatiotemporal control for the manipulation of optogenetic reagents. Nat Protoc 7(2):207–220. https://doi.org/10.1038/nprot.2011.433

Sugi T, Ito H, Nishimura M, Nagai KH (2019) *C. elegans* collectively forms dynamical networks. Nat Commun 10(1):1–9. https://doi.org/10.1038/s41467-019-08537-y

Sumino Y, Nagai KH, Shitaka Y, Tanaka D, Yoshikawa K, Chaté H, Oiwa K (2012) Large-scale vortex lattice emerging from collectively moving microtubules. Nature 483(7390):448–452. https://doi.org/10.1038/nature10874

Chapter 17
Peristaltic Mixing Pump Based on Intestinal Peristalsis Motion Using Soft Actuators

Taro Nakamura

Keywords Peristaltic motion · Intestine · Mixer · Pump · Mixing pump · Enteric nervous system · Smooth muscle · Longitudinal muscle · Circular muscle

17.1 Basic Concepts

Peristalsis is a series of contractions and relaxations of muscles arranged in a circular shape in a certain direction. This movement, which is primarily driven by smooth muscles (non-skeletal muscles), is known as the digestive system transport of the human body and the method of earthworm movement.

In particular, the peristaltic motion observed in the human intestinal structure allows the muscles of the intestinal tract to repeatedly contract and relax, thereby conveying intestinal contents while mixing them as if being rubbed and squeezed. The intestine is composed of numerous motor and sensory nerves that are distributed and form a network throughout the enteric nervous system. The intestine is controlled by an autonomous decentralized control using this neuronal network. These intestinal peristalsis functions are expected to be applicable in soft robotics.

A peristaltic mixing pump was developed based on the peristaltic motion of the intestines. Because the peristaltic mixing pump has the following features, it is

T. Nakamura (✉)
Department of Precision Mechanics, Faculty of Science and Engineering, Chuo University, Bunkyo-ku, Tokyo, Japan
e-mail: nakamura@mech.chuo-u.ac.jp

K. Suzumori et al. (eds.), *The Science of Soft Robots*, Natural Computing Series,
https://doi.org/10.1007/978-981-19-5174-9_17

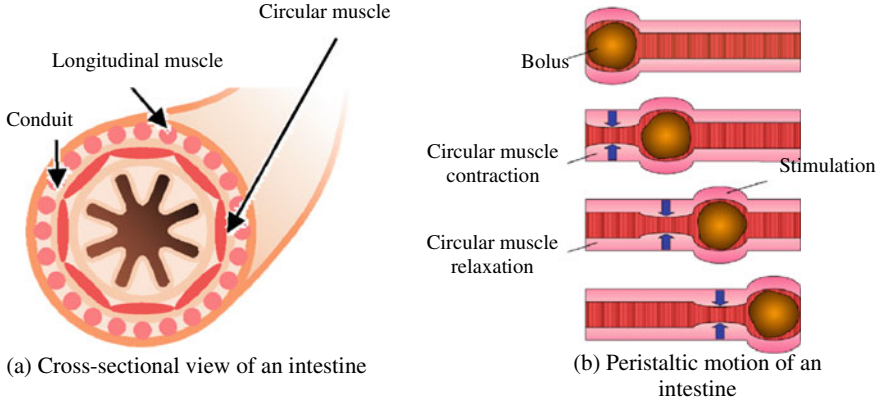

Fig. 17.1 Schematic of the intestinal tract and motion

expected to have practical use in various fields, such as chemical and food processes and the transportation of cement and slurry in the construction field.

- The squeeze flow generated by the peristaltic motion enables efficient conveying and mixing of high-viscosity solid–liquid mixture flows and slurries with low pressure and shear stress.
- The mixing and conveying processes can be carried out continuously rather than in batches.
- There is little loss owing to viscous friction between the fluid and pipe wall because the actuators and sensors are distributed. Therefore, it is suitable for the long-distance conveyance of high-viscosity fluids and slurries.

17.2 Topic and Principle: Intestinal Anatomy and Peristaltic Motion Patterns

17.2.1 Structure of the Intestinal Tract

A cross-sectional view of the intestinal tract is shown in Fig. 1a. The intestine is comprised of two types of muscle layers: longitudinal and circular. Contraction and relaxation of these two types of muscles generate peristalsis.

17.2.2 Generation of the Peristaltic Motion

The actual pattern of intestinal motility is complex (Sarna 2010). If these motions are to be realized as mechanical devices, it is necessary to focus on and select simple

and useful motions. An example of useful motion in intestinal peristalsis is shown in Fig. 1b. When the intestine comes into contact with the bolus, the annulus muscle contracts to extrude it. After the contraction, it relaxes and returns to its original state. By propagating this movement repeatedly, the bolus, which easily changes in shape, is transported and mixed as if kneaded.

17.3 Topic and Principle: Focusing on Mechanisms for Peristaltic Motion

To realize the peristaltic mechanism as a soft robot based on the intestine, it is necessary to have a flexible pipe shape that can contract in the axial direction of the pipe, similar to the longitudinal muscle motion, and contract in the radial direction, similar to the motion of circular muscles. The two contraction/relaxation actions in the axial and radial directions create an elliptical motion inside the flexible pipe, which squeezes out the material to be mixed and transported.

Various devices that imitate the peristaltic motion of living bodies have been proposed. These devices require a relatively small force to transport objects. For example, Spillman (1978) developed a peristaltic-type conveyor consisting of a roller and rubber tube. The transfer device by Mangan et al. (2005) used an annularly arranged McKibben-type artificial muscle.

In addition, Dirven et al. (2013) realized the peristaltic motion of the esophagus and stomach by connecting a circular soft actuator consisting of four chambers in the axial direction and applying pressure inside the chambers (Esser et al. 2018). Furthermore, a peristaltic mixing pump developed by Suzuki et al. (2010) successfully mixed and transported solid–liquid mixtures and high-viscosity fluids by reproducing longitudinal and circular muscles using pneumatic artificial muscles and an inner tube, respectively (Figs. 2a, b). These mixers and pumps are expected to be used for mixing and transporting solid rocket fuel (Yoshihama et al. 2018), lifting and transporting earth and sand at construction sites, transporting coolant and oil (Falk et al. 2021) and in medicine.

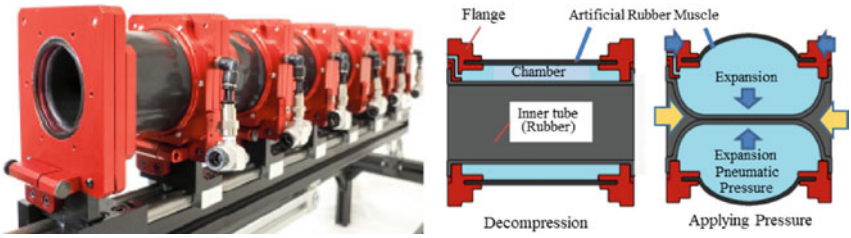

(a) Peristaltic mixing pump using artificial muscle (b)Inner structure of the mixing pump

Fig. 17.2 Overview of a peristaltic mixing pump using pneumatic artificial muscles (Suzuki et al. 2010; Oshino et al. 2021)

However, in the field of microsize, peristaltic motion has been realized using various actuators. For example, Smits (1990) conducted advanced research on the driving principle of a piezoelectric microperistaltic pump. In addition, an electrostatically actuated microphone pump was developed by Xie et al. (2004). Guo et al. (2008) realized peristalsis by applying a shape memory alloy (SMA) to the contraction of a circular muscle. Microperistaltic pumps using electroactive polymers (EAPs) (Lotz et al. 2009) and optically controllable bio-actuators (Yamatsuta et al. 2019) have been reported.

17.4 Topic and Principle: Focusing on the Sensor and Control System for Peristaltic Motion

The intestine has a nervous system (enteric nervous system) that constitutes a reflex arch without a reflex center (Jabbur et al. 1988). Therefore, the intestine is independent of brain commands. To simplify the intestinal nervous system, the intestinal tract can be regarded as a unit separated by a certain length (Wood 2006). When a unit receives a stimulus from the bolus, the nerve signals in that unit and propagated nerve signals from neighboring units cause the muscles in that unit to contract and relax.

The motor neural system of the intestine was applied using a peristaltic mixing pump. (Kano et al. 2013) developed an autonomous decentralized control scheme using coupled oscillators with local sensory feedback and simulated various mechanical motions of the intestine. (Oshino et al. 2021) equipped a peristaltic mixing pump with various sensors to estimate the mixing state of various transported materials using machine learning. In addition, (Matsui et al. 2021) equipped a peristaltic mixing pump with a control method based on the motion generation mechanism of intestinal peristalsis and achieved an adaptive control method based on the state of the conveyed material.

References

Dirven S et al (2013) Design and characterization of a peristaltic actuator inspired by esophageal swallowing. IEEE/ASME Trans Mechatron 19(4):1234–1242

Esser F et al. (2018) Development and characterization of a novel biomimetic peristaltic pumping system with flexible silicone-based soft robotic ring actuators. In: Living machines 2018, vol 10928. LNCS (LNAI), pp 157–167

Falk J et al. (2021) Biomimetic soft robotic peristaltic pumping system for coolant liquid transport. In: Technologies for economic and functional lightweight design, pp 173–181

Guo S et al. (2008) SMA actuator-based novel type of peristaltic micropump. In: International conference on information and automation, pp 1620–1625

Jabbur SJ et al (1988) The enteric nervous system: an overview. Med Res Rev 8(3):459–469

Kano T et al (2013) Generating situation-dependent behavior: decentralized control of multi-functional intestine-like robot that can transport and mix contents. J. Rob Mechatron 25(5):871–876

Lotz P et al. (2009) Peristaltic pump made of dielectric elastomer actuators. In: Electroactive polymer actuators and devices. International Society for Optics and Photonics, vol 7287

Mangan EV et al (2005) A biologically inspired gripping device. Ind Robot 32:49–54

Matsui D et al. (2021) Proposal of a decentralized peristaltic movement generation based on actual intestines and verification by content transfer experiment. In: IEEE/SICE international symposium on system integration (SII), vol 161

Oshino S et al (2021) Generalization capability of mixture estimation model for peristaltic continuous mixing conveyor. IEEE Access 9:138866–138875

Sarna SK (2010) Colonic motility: from bench side to bedside. In: Colloquium series in integrated systems physiology: from molecule to function to disease. Morgan & Claypool Life Sciences, San Rafael

Smits JG (1990) Piezoelectric micropump with three valves working peristaltically. Sens Actuators a: Phys 21(1–3):203–206

Spillman J (1978) Peristaltic conveyors, the chartered mechanical engineer. J Inst Mech Eng 25(5):55–57

Suzuki K et al. (2010) Development of a peristaltic pump based on bowel peristalsis using artificial rubber muscle. In: Proceedings of the IEEE/RSJ international conference on intelligent robots and systems (IROS2010), pp 3085–3089

Wood J (2006) Integrative functions of the enteric nervous system. Physiol Gastrointest Tract 1:671–688

Xie J et al (2004) Surface micromachined electrostatically actuated micro peristaltic pump. Lab Chip 4(5):495–501

Yamatsuta E et al (2019) A micro peristaltic pump using an optically controllable bioactuator. Engineering 5(3):580–585

Yoshihama S et al. (2018) Mixing of solid propellant by peristaltic pump based on bowel peristalsis. In: Proceedings of the IEEE international conference on intelligent robots and systems (IROS), pp 3862–3868

Index

A
Achilles tendon, 50
Active control, 338
Active gel, 321
Active matter, 348, 350, 393, 395
Actuator, 138
Adaptive landscape, 43
Amorphous, 120, 134
Anchoring mechanism, 73
Anchor models, 44
Artificial muscles, 47
Attractor, 303, 305, 306, 308

B
Backbone curve, 289
Basin of attraction, 308
Belousov-Zhabotinsky reaction, 321–324, 326, 329, 330, 332
Bending motion, 261
Bifurcation, 303, 305, 306, 308
Bifurcation theory, 343
Biochemical reaction, 320
Biodegradability, 184
Biodegradable polymers, 186
Bio-hybrid robots, 172, 256
Bio-inspired robotics, 40
Biomimetic robotics, 40
Biorobotics, 39
Bird, 98
Bistable mechanism, 32
Brain–body–environment systems, 359, 362
Brain Organoid, 335, 336, 338, 351
Braitenberg's vehicles, 362, 386

C
Caterpillar, 74–79
Cation, 238
C. eleagns, 393–395
Cell culture, 176
Chaos, 304, 305, 308
Charge-carrier mobility, 215
Chemical structure, 130
Circadian rhythms, 339, 340, 342–347, 350
Classification of actuators, 225
Classification of polymer structures, 130
Collective behavior, 393, 394
Comparative anatomy, 54
Compass-gait model, 301–306
Compliant mechanism, 31
Compositional pattern producing networks, 363–365
Configuration, 132
Conformation, 133
Connective tissue, 50
Constitutive equation, 292
Continuum mechanism, 31
Continuum robot arm, 65–72
Crosslinking density, 154
Crystalline, 120
Curvature, 291
Cyanobacteria, 340, 343, 344

K. Suzumori et al. (eds.), *The Science of Soft Robots*, Natural Computing Series,
https://doi.org/10.1007/978-981-19-5174-9

D
Deformable linear model, 281
Deformable planar model, 281
Dielectric elastomer actuators, 238
Drawing, 124
Drone, 93

E
Earthworm, 73–76, 79–83
Echo state network, 371, 373, 374, 376, 382
Echo state property, 372, 374
Efficiency, 221
E-kagen, 8
Elasticity, 31
Elastomer, 239
Electro-active polymer, 138
Electrohydrodynamic (EHD) pump, 236
Electrostatic (HASEL) actuators, 235
Elliptical motion, 73
Embodiment, 357, 360, 362, 386
End-effectors, 60
Equilibrium, 32
Equilibrium type actuator, 222
Euler equation, 293
Evolutionary robotics, 362, 363, 386
Evolutionary Trekkers, 44
Evolvabots, 44

F
Final state sensitivity, 306, 308
Fixed point, 303, 305
Flapping, 94, 98–100
Flexibility, 197
Flexible-link manipulator, 66
Flexural rigidity, 198
Flight, 92–94
Fluidic pressure sources, 232
Fluid-structure interaction, 99
Fractal, 306, 308
Frame, 289
Frenet-Serret formulas, 291
Functional morphology, 54

G
Gear pump, 234
Gelatin, 186
Gels, 152
Geometrically deformable robot, 281
Golgi tendon organ, 51
Grasping, 60
Gravity compensation mechanism, 52
Grippers, 60
Growth, 172

H
Humido-sensitive, 141
Hydraulically amplified self-healing, 235
Hydrostatic skeleton, 67
Hyper-redundant manipulator, 66–70

I
Iikagen, 8
Indirect simultaneous positioning, 309
Inherent degrees-of-freedom, 309
Initial state sensitivity, 304, 306, 308
Insect, 98
Intervertebral disk, 53
Ionic polymer–metal composites, 238

J
Jamming transition, 358, 386
Joint rotation, 259

K
Kinematics, 289
Kinetic energy, 286
Kirchhoff elastic rod, 292

L
Lamella, 135
Levenberg-Marquardt method, 299
Ligaments, 49
Light-emitting diode, 210
Living regulator, 334, 335, 338
Lyapunov exponent, 375, 376

M
Manipulation, 60
Maxwell stress, 240
McKibben artificial muscle, 233
MEXT Grant-in-Aid, 3, 8
Micro-vibration, 250
Modulus of rigidity, 292

Moment of inertia of the cross section, 292
Muscle contraction, 177
Muscular-hydrostat, 380
Musculoskeletal robots, 48
Musculoskeletal system, 47

N
Nafion, 244
Neural network, 367–371
Newton method, 299
Nodal displacement vector, 283
Nodal point, 283
Non-dimensionalization, 297
Nonequilibrium type actuator, 222

O
Octopus, 380–382
Olfactory sensor, 180
Optogenetics, 395
Orientation, 121
Orientation matrix, 290

P
Partition number, 294
Passive dynamic walker, 300, 301, 306, 308
Passive control, 338
Passive dynamic walker, 361, 386
Pattern formation, 324, 332
Photocurable resin, 158
Photodetector, 214
Photovoltaics, 210
PH-responsive, 136
Phylogenetic comparative methods, 43
Physical reservoir computing, 371, 372, 374, 376, 379, 380, 385, 386
Physiological cross-sectional area (PCSA), 51
Poisson's ratio, 292
Polar moment of inertia of the cross section, 292
Polymer, 120
Polymer crystal, 134
Potential energy, 32, 284
Power conversion efficiency, 212
Protein, 187
Pseudoelasticity, 250

R
Reaction diffusion computing, 321
Reaction-diffusion system, 347, 348, 350
Reservoir computing, 371–374
Riddled basin, 306, 308
Robotic hands, 60
Robotics-inspired biology, 39
Rod integration, 297
Rubber, 145

S
Self-organizing map, 366, 370
Self organizing neural network, 369, 370
Self-sustained oscillation, 343, 352
Setae, 73, 79, 81
Shape-memory alloy, 368
Shape-memory alloy wires, 255
Shape memory effect, 250
Shooting method, 296
Skeletal muscles, 50
Slug, 72, 74, 75
Snap buckling, 35
Snap motor, 34
Snap-through buckling, 35
Soft cover hand, 312
Soft-material robot, 280
Soft fluidic actuators, 228
Soft keyboard, 384
Soft material affected by biological process, 171
Special orthogonal group, 290
Speech articulation, 369
Spinal engine, 382
Starch, 187
Stiffness matrix, 292
Strain, 197
Strain potential energy, 292
Strain sensor, 205
Stretchability, 197
Subsumption architectures, 362, 386
Synchronization, 345–347, 350, 352

T
Tactile actuator, 254
Tactile sensing, 252
Temperature sensor, 208
Template models, 44
Tendon, 50
Thermomechanical actuators, 249
Thermomechanical pump, 233
Thermo-responsive, 136
3D printing, 157

Torsion, 291
Transistor, 214

U
Universal gripper, 357, 358, 360

V
Vertebrate animals, 50

W
Wing, 93, 94, 98–100
Work, 221

X
Xenobot, 365

Y
Young's modulus, 50, 197, 292